BEST PRACTICE PROTOCOL FOR THE VALIDATION OF AEROSOL, CLOUD, AND PRECIPITATION PROFILES (ACPPV)

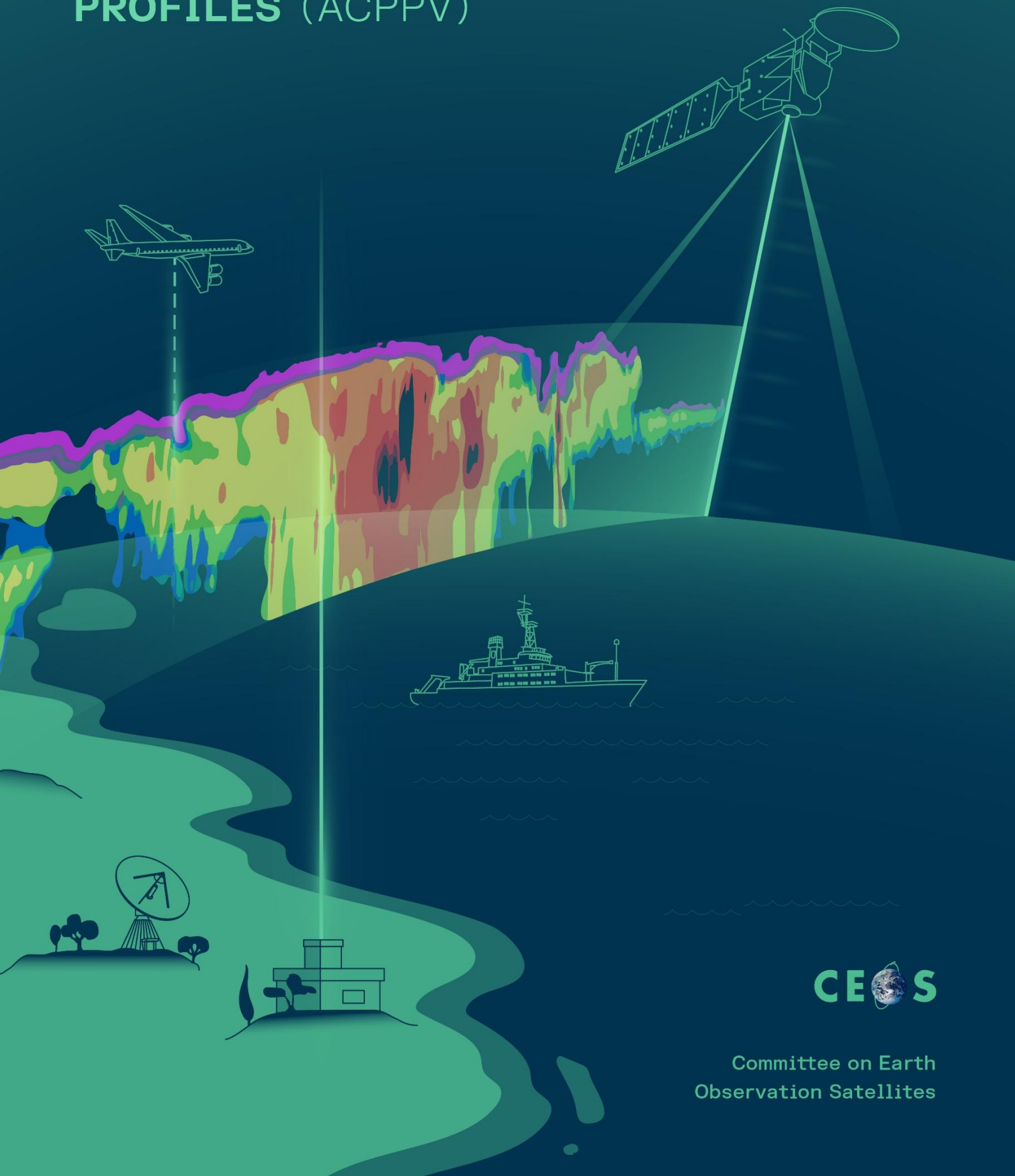

CEOS

Committee on Earth Observation Satellites

BEST PRACTICE PROTOCOL FOR THE VALIDATION OF AEROSOL, CLOUD, AND PRECIPITATION PROFILES (ACPPV) CONSORTIUM

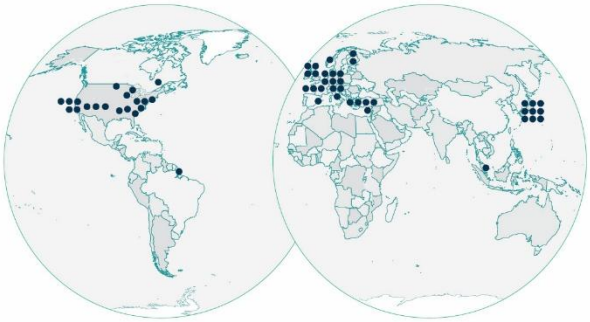

Best practices for the validation of Aerosol, Cloud, and Precipitation Profiles (ACPPV)

Lead Authors: Amiridis, V.[1], Marinou, E.[1], Hostetler, C.[2], Koopman, R.[3], Cecil, D. J.[4], Moisseev, D.[5], Tackett, J.[2], Gross, S.[6], Baars, H.[7], Redemann, J.[8], Marenco, F.[9], Baldini, L.[10], Tanelli, S.[11], Fielding, M.[12], Janisková, M.[12], Tanaka, T.[13], O'Connor, E.[14], Fjæraa, A. M.[15].

Contributing Authors: Paschou, P.[1,16], Voudouri, K. A.[1,16], Ferrare, R.[2], Burton, S.[2], Schuster, G.[2], Kato, S.[2], Winker, D.[2], Shook, M.[2], Bley, S.[7], Haarig, M.[7], Floutsi, A. A.[7], Wandinger, U.[7], Trapon, D.[7], Pfitzenmaier, L.[17], Papagianopoulos, N.[18], Mona, L.[18], Posselt, D.[11], Mason, S.[12], Rennie, M.[12], Benedetti, A.[12], Hogan, R.[12,19], Sogacheva, L.[14], Balis, D.[16], Michailidis, K.[16], van Zadelhoff, G. J.[20], Nowottnick, E.[21], Yorks, J.[21], Mroz, K.[22], Donovan, D.[20], L'Ecuyer, T.[23], Okamoto, H.[24], Sato, K.[24], Henderson, D. S.[25], Nishizawa, T.[26], Barker, H.[27], Cole, J.[27], Qu, Z.[27], Clerbaux, N.[28], Nakajima, T. Y.[29], Chase, R.[30], Wolff, D.[31], Landulfo, E.[32], Kirstetter, P. E.[33,34], Mather, J.[35], Ohigashi, T.[36], Ryder, C.[19], Tzallas, V.[37], Tsikoudi, I.[1,38], Tsekeri, A.[1], Tsichla, M.[1,39], Koutsoupi, I.[1,38], Kubota, T.[13], Siomos, N.[40], Takahashi, N.[41], Horie, H.[42], Suzuki, K.[43], Mace, J.[44], Prakash, G.[45], McLean, W.[46], Borderies, M.[47], Mangla, R.[48], Escribano, J.[49], Moradi, I.[50,51], Zhang, J.[52], Rubin, J.[53], Ikuta, Y.[54], Marbach, T.[55], Bojkov, B.[55], Accadia, C.[55], Fougnie, B.[55], Spezzi, L.[55], Bozzo, A.[55], Chimot, J.[55]., Jafariserajehlou, J.[55], Flament, T.[55], Mattioli, V.[55], Strandgren, J.[55], Barlakas, V.[56], and Kollias, P.[57,58].

Affiliations:

[1]Institute of Astronomy, Astrophysics, Space Applications & Remote Sensing (IAASARS), National Observatory of Athens (NOA), 15236 Athens, Greece

[2]NASA Langley Research Center, Hampton, Virginia, United States

[3]European Space Research and Technology Center, European Space Agency (ESA/ESTEC), Keplerlaan 1, 2201 AZ Noordwijk, The Netherlands

[4]NASA Marshall Space Flight Center, Earth Science Branch, 320 Sparkman Dr NW, AL 35805, Huntsville, United States

[5]Institute for Atmospheric and Earth System Research, Faculty of Science, University of Helsinki, Helsinki, Finland

[6]Institut für Physik der Atmosphäre, Deutsches Zentrum für Luft- und Raumfahrt (DLR), Weßling 82234, Germany

[7]Leibniz Institute for Tropospheric Research (TROPOS), Permoserstraße 15, 04318 Leipzig, Germany

[8]School of Meteorology, University of Oklahoma, Norman, Oklahoma, United States

[9]The Cyprus Institute, 20 Konstantinou Kavafi Street, 2121 Nicosia, Cyprus

[10]National Research Council, Insitute of Atmospheric Science and Climate (CNR-ISAC), Via Fosso del Cavaliere, 100, 00133, Roma, Italy

[11]Jet Propulsion Laboratory, California Institute of Technology, Pasadena, California, United States

[12]European Centre for Medium-Range Weather Forecasts (ECMWF), Reading, United Kingdom

[13]Earth Observation Research Center, Japan Aerospace Exploration Agency (JAXA), Tsukuba, Ibaraki 305-8505, Japan

[14]Finnish Meteorological Institute, Climate Research Programme, Erik Palménin aukio 1, FI-00560, Helsinki, Finland

[15]Climate and Research Institute NILU, P.O. Box 100, 2027 Kjeller, Norway

[16]Laboratory of Atmospheric Physics, Physics Department, Aristotle University of Thessaloniki, University campus, 54124 Thessaloniki, Greece

[17]University of Cologne, Institute of Geophysiks and Meteorology, Pohligstraße 3, 50969 Cologne, Germany

[18]Istituto di Metodologie per l'Analisi Ambientale (IMAA), Consiglio Nazionale delle Ricerche (CNR), C.da S. Loja, 85050 Tito (PZ), Italy

[19]Department of Meteorology, University of Reading, Reading, United Kingdom

[20]Royal Netherlands Meteorological Institute (KNMI), De Bilt, the Netherlands

[21]NASA Goddard Space Flight Center, Mail Code 612, MD 20771 Greenbelt, United States

[22]National Centre for Earth Observation, University of Leicester, Leicester, United Kingdom

[23]Department of Atmospheric and Oceanic Sciences, Cooperative Institute for Meteorological Satellite Studies, University of Wisconsin-Madison, Madison, WI, United States

[24]Research Institute for Applied Mechanics, Kyushu University, Fukuoka, 816-8580, Japan

[25]Space Science and Engineering Center, University of Wisconsin-Madison, Madison, WI, United States

[26]Earth System Division, National Institute for Environmental Studies, Tsukuba, 305-8506, Japan

[27]Environment and Climate Change Canada, Toronto, ON, Canada

[28]Royal Meteorological Institute of Belgium, Brussels

[29]Tokai University, Research and Information Center (TRIC), 4-1-1 Kitakaname Hiratsuka, Kanagawa 259-1292, Japan

[30]Cooperative Institute for Research in Atmosphere (CIRA), Colorado State University, Fort Collins, Colorado, United States

[31]Mesoscale Atmospheric Processes Lab, NASA Wallops Flight Facility, 34200 Fulton Street, N159/E220, VA 23337 Wallops Island, United States

[32]Instituto de Pesquisas Energéticas e Nucleares, Cidade Universitária, São Paulo, Brazil

[33]School of Meteorology & School of Civil Engineering and Environmental Science, University of Oklahoma, Oklahoma, United States

[34]National Severe Storms Laboratory, NOAA, Oklahoma, United States

[35]Pacific Northwest National Laboratory, Richland, Washington

[36]National Research Institute for Earth Science and Disaster Resilience (NIED), Tsukuba, Ibaraki, Japan

[37]European Space Agency, ESA-ESRIN, Via Galileo Galilei, 1, 00044, Frascati RM, Italy

[38]Department of Physics, National and Kapodistrian University of Athens, 157 84 Zografou, Athens, Greece

[39]Environmental Chemical Processes Laboratory, Department of Chemistry, University of Crete, Greece

[40]Meteorologisches Institut, Ludwig-Maximilians-Universität München, Germany

[41]Institute for Space-Earth Environmental Research, Nagoya University; Nagoya 464-8601, Japan

[42]Radio Research Institute, National Institute of Information and Communications Technology, Koganei, Tokyo 184-8795, Japan

[43]Atmosphere and Ocean Research Institute, The University of Tokyo, Chiba, 277-8564, Japan

[44]University of Utah, Department of Atmospheric Sciences, Salt Lake City, United States

[45]Oak Ridge National Laboratory: Oak Ridge, TN, United States

[46]University of Westminster, London, United Kingdom

[47]Université de Toulouse, Météo-France, CNRS, Toulouse, France

[48]Centre for Remote Imaging Sensing and Processing, National University of Singapore, Singapore

[49]Barcelona Supercomputing Center (BSC), Barcelona, Spain

[50]Earth System Science Interdisciplinary Center, University of Maryland, College Park, College Park, Maryland, United States

[51]NASA Global Modelling and Assimilation Office, Greenbelt, Maryland, United States

[52]University of North Dakota, Department of Atmospheric Sciences, United States

[53]U.S. Naval Research Laboratory, Washington, D.C., 20375, United States

[54]Metrological Research Institute, Japan Meteorological Agency, Tsukuba, Japan

[55]The European Organisation for the Exploitation of Meteorological Satellites (EUMETSAT), Eumetsat Allee 1, D-64295, Darmstadt, Germany

[56]CS Group - Germany GmbH, Berliner Allee 65, 64295 Darmstadt, Germany

[57]Stony Brook University, Division of Atmospheric Sciences, Stony Brook, New York, United States

[58]Brookhaven National Laboratory, Department of Environmental and Climate Science, Upton, New York, United States

Contents

Chapter 1: Introduction

1.1. Objectives of the document

Aerosols, clouds, precipitation, and the processes governing their interactions are the grand challenges for current climate science, of the highest priority for the climate science-policy interface, and of great relevance for both Working Groups I and III of the upcoming 7th IPCC cycle. Satellite missions such as CALIPSO and CloudSat have demonstrated the value of aerosol and cloud profiling techniques on understanding the processes governing aerosol-cloud-radiation interactions. The EarthCARE mission will ensure the continuity of these efforts and further advance synergies of space-borne lidar and cloud radar profiling. Following EarthCARE, the Atmosphere Observing System (AOS) of NASA will further shed light over the unknown links between aerosols, clouds, atmospheric convection, and precipitation.

The geophysical validation of spaceborne high-resolution profilers for aerosols, clouds and precipitation presents unique challenges. As indicated in the following section, several CEOS agencies are preparing profiler missions, and the need for a common practice capturing lessons learned from earlier missions was identified by the CEOS Working Group Calibration and Validation, and its implementation is tracked under its action item CV-22-01. The present document is a response to this action item.

The best practice convergence process, culminating in this document, is aimed at the optimization of Calibration and Validation techniques (Cal/Val) in terms of instrumentation, sampling strategies and scenarios, and intercomparison methodologies. For this, the scientific communities involved in past missions have reviewed lessons learned and identified areas where convergence on similar approaches is beneficial.

The approaches and recommendations provided in this document cover correlative site selection, correlative instrument selection, data processing and quality control, campaign criteria, configurations, scenarios, and collocation methods, along with intercomparison methodologies, including handling of wavelength differences. In addition, for increased statistical relevance of the intercomparison with ground sites, guidance and recommendations for intercalibration between networks are included, to achieve a “network of networks” to compensate for the sparse overpasses per site, and avoid biases.

In view of the complexity and diversity of geophysical scenarios and retrievals of aerosol, cloud, and precipitation regimes, the best-practice convergence process and also this entire document is aimed at knowledge exchange and conveying lessons learned, rather than definition on single and strict protocols that have been agreed in some other domains with fewer degrees of freedom.

In the context of the convergence, several dedicated studies have been performed on historic datasets, in order to arrive at recommendations on open issues. Community open source tools have been developed in addition, to facilitate the efforts of the Cal/Val communities.

In this Chapter, we overview key missions addressed in the ACPPV document along with the targeted satellite products for Cal/Val. Furthermore, we review the content included in the following chapters, in terms of available platforms and measurements for validation purposes,

methods for Cal/Val, suggestions on issues concerning scene representativeness, and existing gaps in our Cal/Val knowledge.

1.2. Overview of past, present, and future space missions for aerosol, cloud, and precipitation profile observations, and the role of the validation programme

Key spaceborne missions for aerosol, cloud, and/or precipitation profiling include the Tropical Rainfall Measuring Mission (TRMM) launched by NASA and JAXA in 1997 (Kummerow et al., 2000), CloudSat launched by NASA and CSA in 2006 (Stephens et al., 2008), the Cloud-Aerosol Lidar and Infrared Pathfinder Satellite Observations (CALIPSO) mission launched by NASA and CNES in 2006 (Winker et al., 2010), the Global Precipitation Mission (GPM) launched by NASA and JAXA in 2014 (Hou et al., 2014; Skofronick-Jackson et al., 2017), Aeolus Earth Explorer launched by ESA in 2018 (Stoffelen et al., 2005), the Earth Cloud Aerosol and Radiation Explorer (EarthCARE) launched by ESA and JAXA in 2024 (Illingworth et al., 2015), the future Atmosphere Observing System (AOS) Precipitation Measurement Mission (PMM), and the Cloud Aerosol LIdar for Global scale Observation of the ocean-Land-Atmosphere system (CALIGOLA) mission slated to launch in the early 2030s. Cal/Val activities for these missions generally include combinations of statistical comparisons with data from existing ground-based sites and networks, near-real-time (NRT) validation through monitoring in an assimilation system, airborne field campaigns motivated by the particular missions, and leveraging relevant measurements or flight opportunities from field campaigns that have broader science goals.

The TRMM satellite featured a 13.8-GHz (Ku-band) Precipitation Radar (PR) built by JAXA, which was the first precipitation radar in space (Kummerow et al., 2000). The TRMM PR collected reflectivity data, allowing the derivation of rain rates at 250-m intervals in the vertical swath over 200 km wide. The TRMM Microwave Imager (TMI) allowed retrievals of surface rain rates over a wider (~700 km) swath while constraining combined retrievals of the precipitation profiles where the swath overlapped that of the radar. The TRMM satellite was launched in a tropical (35° inclination) orbit on November 27, 1997. In order to extend the life of the planned 3-year mission, the satellite was boosted from its original 350 km orbit to 402 km beginning August 22, 2001. It remained in orbit until it was decommissioned on April 15, 2015. Its validation program included airborne field campaigns based in Florida (USA, 1999), Kwajalein Atoll (Yuter et al., 2005), and Brazil (Silva Dias et al., 2002). The aircraft carried “satellite simulator” payloads in these campaigns, providing higher-resolution analogs to the satellite measurements. Other airborne instrumentation provided complementary measurements to expand the remote sensing capabilities and provide direct in situ observations. The field campaigns featured ground-based supersites with enhanced remote sensing and in situ measurements, although the aircraft was not constrained to only focus on the supersite locations. Besides those dedicated field campaigns, long-term statistics were accumulated from fixed sites with ground-based radars, rain gauges, and disdrometers (Wolff et al., 2005). Measurements from an operational weather radar network were leveraged as a “Validation Network” via special data processing after TRMM satellite overpasses of rain events near those radars.

CloudSat (Stephens et al., 2008) and CALIPSO (Winker et al., 2010) launched together in 2006, with the W-band cloud profiling CloudSat radar and the Cloud-Aerosol Lidar with

Orthogonal Polarization (CALIOP) dual-wavelength (532 nm and 1064 nm) lidar to distinguish aerosols from clouds. CloudSat and CALIPSO flew in formation along the same track, separated from each other by about 15 seconds, and also aligned with other satellites in the Afternoon-Train constellation (A-Train). The CALIPSO and Cloudsat Validation Experiment (M. J. McGill et al., 2007) was conducted in June 2006, immediately following commissioning of both satellites. That experiment included deployment of a W-band radar and elastic backscatter lidar on the ER-2 aircraft, an HSRL on a King Air, and in situ cloud samplers on a Lear Jet. A dedicated validation field campaign was conducted for CloudSat in southeastern Canada (Barker et al., 2008). Another field campaign focused on validating cool-season, high-latitude, light precipitation retrieval approaches by CloudSat and GPM was conducted in Finland (Petersen et al., 2011). Besides these validation field campaigns, the CloudSat program leveraged long-term systematic measurements from ground-based sites, and validation opportunities associated with airborne science campaigns (Stephens et al., 2008).

Over its 17 years of operation, the CALIOP lidar on CALIPSO benefited from extensive ground and airborne validation efforts. The most impactful in terms of algorithm assessment and improvement were 147 airborne HSRL underflights, 70 of which were flown on a total of 8 campaigns dedicated solely to CALIPSO validation with the remaining flights conducted as opportunities arose during science-focused field missions. The HSRL data were used to assess CALIOP Level-1 calibration (Getzewich et al., 2018; Kar et al., 2018; Rogers et al., 2011) and Level-2 aerosol backscatter, extinction, optical depth, aerosol type, and aerosol detection sensitivity (Burton et al., 2013; Rogers et al., 2014; Thorsen et al., 2017). Validation efforts also heavily leveraged ground-based remote sensors in many locations, most significantly the EARLINET lidar network (Pappalardo et al., 2010).

The GPM satellite was launched in 2014, expanding from the TRMM heritage with a Dual-frequency (Ku- and Ka-band) Precipitation Radar (DPR) built by JAXA and a GPM Microwave Imager (GMI) (Hou et al., 2014; Skofronick-Jackson et al., 2017). The dual-frequency radar measurements allow improved determination of precipitation rate profiles, and a 65° inclination expands the mission focus to include snowfall detection (Iguchi, 2020; Kojima et al., 2012). The GPM ground validation program (Petersen et al., 2020) included a broader range of airborne field campaigns, consistent with the broader range of environments measured by GPM. These included partnering in campaigns with abundant snow and mixed-phase precipitation in Canada (Skofronick-Jackson et al., 2015), Sweden, and Korea, and campaigns featuring thunderstorms (Jensen et al., 2016), flood events (Petersen & Krajewski, 2013), and orographic precipitation (Barros et al., 2014; Houze et al., 2017) in the U.S and Brazil. The airborne field campaigns focused on well-instrumented ground-based sites, featuring combinations of radars, profilers, disdrometers, and other sensors. As with the TRMM field campaigns, the satellite simulator aircraft were not limited to measuring only over ground-based instrumentation. The fixed sites with ground-based precipitation measurements and remote sensors collected both rain and snow data. The TRMM Validation Network was expanded and enhanced, with the GPM Validation Network (Gatlin et al., 2020; Schwaller & Morris, 2011) taking advantage of polarimetric radar measurements from nearly 100 ground radars over CONUS as well as partner sites in Brazil, Korea, and Europe. A well-instrumented, long term super-site was established as the NASA Wallops Precipitation Research Facility (PRF) at NASA Goddard Space Flight Center Wallops Flight Facility on Wallops Island, Virginia. The PRF hosts multi-frequency radars (S-, C-, X-, Ka-, Ku-, K- and W-band), as well as numerous disdrometers, rain gauges and vertical profilers.

The Aeolus wind mission of ESA hosted the first space-based Doppler wind lidar worldwide (ALADIN), operating at 355 nm (Stoffelen et al., 2005). The mission successfully fulfilled its objective to demonstrate the Doppler wind lidar technique for measuring wind profiles from space. The unique Aeolus datasets found a range of applications, demonstrating the benefits of space-based wind profiling for NWP and the study of atmospheric circulation, precipitation systems, aerosol transport and interactions with clouds and radiation. For the validation of Aeolus, an Announcement of Opportunity (AO) call for Cal/Val support studies took place in 2007. The AO focussed on the validation of the Aeolus wind and optical properties products. 17 proposals including ground-based and airborne validation experiments along with NWP data assimilation studies were received from teams all around the globe (a detailed description of the Cal/Val proposals can be found in (Straume et al., 2019)). Activities of special interest included near real-time validation through monitoring in NWP data assimilation systems, tropical stratospheric balloon experiments, and the inclusion of collocated measurements in polar areas. Furthermore, a dedicated large-scale experimental campaign with the participation of groups from both the EU and NASA has been organized by ESA to support the validation of Aeolus and the preparation of the ESA missions EarthCARE and WIVERN. The so-called Joint Aeolus Tropical Atlantic Campaign (JATAC) included both surface and airborne deployments on Cabo Verde (2021/2022) and the US Virgin Islands (2021). The JATAC campaign started in July 2021 with the deployment of ground-based profiling instrumentation at Cabo Verde. By mid-August 2021, the CPEX-AW campaign started its operations from the US Virgin Islands with NASA's DC-8 flying laboratory. In September 2021, a European aircraft fleet was deployed to Cabo Verde with the DLR Falcon-20 and the Safire Falcon-20 carrying remote sensors and in-situ instrumentation, and the Aerovizija Advantic WT-10 light aircraft for in-situ aerosol characterization. The JATAC activities restarted in June 2022 with the one-month deployment of UAVs by the Cyprus Institute to Mindelo for in-situ aerosol measurements. Moreover, NASA deployed the DC-8 aircraft to Sal with the same payload set-up of 2021 for a full month intensive campaign period in the framework of the CPEX-CV activity in September 2022. As for 2021, the Aerovizija Advantic WT-10 light aircraft took part in the campaign with its in-situ aerosol measurements from Mindelo. In total, around 60 scientific flights of the four aircraft were performed, with an additional 25 UAV flights operated by the Cyprus Institute in the framework of the JATAC activities. 23 Aeolus orbits were underflown, four of which in 2021 featured simultaneous observations by three aircraft (DLR/Safire/Aerovizija), with a perfect collocation of Aeolus and ground-based observations for two cases. Also in 2022, NASA and Aerovizija succeeded to perform a collocated flight of Aeolus and the ground-based observation. Overall, the joint activities have resulted in a high-quality and comprehensive dataset to support a wide range of tropical atmospheric research, the validation of Aeolus and other satellites, and have provided key reference data for the development of future EO missions.

EarthCARE is a satellite mission implemented by ESA in cooperation with JAXA, aiming to measure global profiles of aerosol, cloud and precipitation properties together with radiative fluxes and derived heating rates (Illingworth et al., 2015). The data will be used in particular to evaluate the representation of clouds, aerosols, precipitation and associated radiative fluxes in weather forecasting and climate models. The satellite scientific payload consists of the Atmospheric Lidar (ATLID) operating at 355 nm to provide vertical profiles of aerosols and thin clouds, the highly sensitive Cloud Profiling Radar (CPR) operating at 94 GHz (W-band), equipped with Doppler measurement capability, to provide measurements of clouds and precipitation, the Multi-Spectral Imager (MSI) with channels in the visible, near infrared,

shortwave and thermal infrared, and a Broad-Band Radiometer (BBR) to provide measurements of top-of-the-atmosphere radiances and fluxes. The EarthCARE mission has been specifically defined with the basic objective of improving the understanding of cloud-aerosol-radiation interactions so as to include them correctly and reliably in climate and numerical weather prediction models. The validation program of EarthCARE consists of correlative observations of cloud, aerosol, precipitation, and radiation properties. These observations will be delivered by ground-based sites, aircraft and UAVs, and other satellites that are being identified by an open process including announcements of opportunities from ESA/JAXA and the response of the validation teams (similarly to Aeolus). The validation teams and respective proposals are reviewed by the Agencies and during the Joint ESA/JAXA Validation Workshops, before being incorporated into the EarthCARE Validation Team (ECVT). Activities supported already include: (a) pre-launch campaigns and Fiducial Reference Measurement (FRM) developments for radars and lidars (FRM4RADAR, eVe, EMORAL); (b) development of suborbital-to-orbital simulators; (c) collaboration with networks and Research Infrastructures (e.g EARLINET, CloudNet, AERONET, ACTRIS), supported also by the European Commission through the ATMO-ACCESS project; (d) ESA-JAXA coordination through the joint Scientific Validation Implementation Plan (Koopman, 2021) (e) near-real time validation through monitoring in NWP data assimilation systems; (f) lessons learned / best practice convergence on validation of aerosol, cloud and precipitation profiles in collaboration with CALIPSO, Cloudsat, Aeolus, and AOS scientists. Along with the aforementioned activities, field campaigns with mobile ground-based instruments and airborne systems will constitute a very important part of the validation strategy for EarthCARE.

The AOS Precipitation Measuring Mission (PMM) is planned to include a Ku-band Doppler radar built by JAXA and a pair of passive microwave radiometers provided by CNES, to be launched by NASA on two satellites flying in formation in a 55° inclination orbit. The Doppler radar will add vertical velocity information to more traditional precipitation information, both for assessing dynamics (in cloud vertical motion) and refining precipitation retrievals (through the use of particle fall speed information). The short temporal offset between radiometer measurements on the two satellites is intended to add information about vertical velocities and convective ice flux. By processing through the diurnal cycle, PMM will capture a variety of storms in different parts of their lifecycles.

An AOS-Cloud mission launched by NASA is expected to include a Doppler radar capable of measuring clouds and precipitation. It may be limited by attenuation in deep, strong convection and heavy precipitation, but should bring higher sensitivity than PMM in cloud and snow scenes that are especially important from polar orbit. Another AOS mission, with a partnership between NASA and CSA, is expected to bring passive remote sensing measurements that could aid vertical profile retrievals that use active remote sensors in the same orbit. A multi-frequency lidar capable of aerosol and cloud profiling is planned for the CALIGOLA mission, led by ASI with a partnership from NASA (Di Girolamo et al., 2023). If flown in formation, the combination of lidar with a cloud-capable Doppler radar allows the examination of aerosol-cloud-precipitation interaction processes.

Validation for the AOS missions will largely be conducted through a suborbital science program whose focus is not exclusively on validation. This suborbital program is intended to fill gaps by measuring processes and conditions that are difficult to observe from satellites. Many of these measurements, including in situ particle measurements and higher resolution, higher sensitivity analogs of the satellite-based remote sensors, will also align with satellite

validation needs. Airborne field campaigns after key satellite launches will be planned based on the science needs and opportunities, with ground-based networks and super-sites leveraged and potentially augmented with additional instrumentation.

1.3. Validation objectives for space profilers

1.3.1. What to validate

Validation can include assessment of the quality of direct measurements and straightforward derivatives of those measurements (Level 1), of derived geophysical variables (Levels 2 and 3), and the accuracy and representativeness of physical assumptions or parameterizations used in retrieval algorithms. This document largely focuses on validation of retrieved geophysical variables, whether by statistical validation (comparison with independent measurements of those geophysical variables that act as reference), physical validation (measurements relevant to retrieval algorithm assumptions), and NRT validation through monitoring in a data assimilation system. To this extend, a verification on whether the applied design meets the defined requirements, and whether the physical assumptions and/or parametrizations used in the retrieval algorithm result in the expected outcome for product levels 1–3, is also performed within the validation exercise.

A plethora of geophysical variables can be used to describe aerosol, cloud, and precipitation vertical profiles - it is not practical to attempt to list them all, nonetheless to validate them. A particular mission will have its own requirements, identifying those geophysical variables that must be validated. This document addresses some of the more fundamental geophysical variables that may be retrieved by spaceborne lidar or radar for aerosol, cloud, and precipitation vertical profiling.

The geophysical variables to be validated can be grouped by the type of instrument enabling their retrieval, or by classes of the variables themselves (see *Chapter 2* for details). Macrophysical variables include cloud or aerosol layer height, depth, and type (e.g., mineral dust, smoke, ice cloud, liquid cloud). Cloud properties include optical thickness and vertical profiles of extinction, water content, and aspects of the particle size distribution. It is useful to separate these cloud properties into liquid and ice categories. Similarly, aerosol properties include optical thickness and extinction profiles, and it is useful to treat these properties separately by aerosol species. Precipitation rate and mass are also typically separated by phase, with rain rate and snow rate presenting different retrieval and validation challenges. For some of these geophysical variables (e.g., rain rate and snow rate), it is practical to limit validation to the surface, although a retrieval product may apply to the full vertical profile.

1.3.2. How to validate

Depending on the geophysical variable to be validated from the space profilers for aerosols, clouds and precipitation, a validation study can be performed using different types of instruments such as lidars, radars, other remote and in-situ sensors, or synergistic observations of them. The instruments can be deployed on a variety of platforms (ground-based fixed or mobile, airborne, spaceborne) and can be part of a permanent installation or of an ad hoc deployment within the framework of a field campaign. An extended discussion about the capabilities of each sensor is given in *Chapter 3*.

For lidars, different techniques can be implemented that make use of specific interaction processes between the emitted radiation and the atmospheric constituents at a single or at multiple wavelengths, e.g. elastic-backscatter lidar, Raman lidar, high-spectral-resolution lidar, and polarization lidar. The lidar techniques are capable of profiling aerosol and thin-cloud properties. The combination of different lidar techniques or even lidar products from single or multi-wavelength measurements allow the data users to obtain information not only about the optical properties of the particles but also to characterize the particles in terms of their size, shape, and type (e.g. Amiridis et al., 2005; Burton et al., 2012; Floutsi et al., 2023; Gross et al., 2013; Haarig et al., 2018).

For radars, different frequencies are used for depicting the properties of the particular target and the interactions of these targets with the atmosphere, resulting in a wide range of radar types such as weather and micro rain radars, cloud radars, wind radars, as well as scanning radars operating in various radar bands. In principle, radars are capable of providing profiles of cloud and precipitation properties, characterization of cloud particles and hydrometeors, and monitoring of cloud and precipitation systems (e.g. Hogan, 1998; Kollias et al., 2007). Shorter wavelengths provide higher resolution but are more susceptible to attenuation by precipitation, while longer wavelengths offer better penetration through precipitation layers and are suitable for weather forecasting. The choice of wavelength/frequency depends on the desired trade-offs between resolution, penetration, and the atmospheric effects for a given application. Moreover, dual-polarization radar techniques can be used to improve the quality of radar observations of precipitation microphysics, precipitation evolution, and hydrometeor classification (e.g. Bringi & Chandrasekar, 2001). Doppler radars additionally measure the velocity of targets toward or away from the radar. These are commonly used from the ground to diagnose horizontal wind patterns. From a vertically-oriented viewpoint (profilers, and downward-looking spaceborne or airborne Doppler radars), the Doppler velocity combines vertical air velocity with particle fall speed.

In addition, passive sensors can provide reference measurements for the validation of columnar integrals of profiling products. Such sensors can be spectroradiometers, photometers, solar occultation, and limb scattering measurements, which obtain column-integrated aerosol and cloud properties such as the particle size, the aerosol and cloud optical thickness, the extinction coefficient, the cloud top height (e.g. Chiu et al., 2010; Kahn et al., 2010; Sinyuk et al., 2020; Thomason et al., 2010). Furthermore, observations suitable for validation purposes can be provided from in-situ techniques which deliver information of the targeted parameter for the exact location of the in-situ instrumentation. For example, observations of the particle concentration, composition, number size distribution of aerosols or cloud droplets, shape, hygroscopicity, and optical properties can be obtained from in-situ sensors like nephelometers, filters and impactors, particle counters, particle/cloud/precipitation probes and precipitation sensors (e.g. Anderson & Ogren, 1998; Baumgardner et al., 2017; Delahaye et al., 2015; Formenti et al., 2003; Lieke et al., 2011). In addition, for precipitation estimation, both rain gauges and disdrometers are critical tools needed to provide rain rates and particle size distributions at the surface. Video-based disdrometers, such as the Two-Dimensional Video Disdrometer (2DVD; Schönhuber et al., 2007) and the Precipitation Imaging Package (PIP; Pettersen et al., 2020), allow for direct measurement of particle size and shape of liquid and solid precipitation. In general, in-situ measurements should be used with caution when compared to remote sensing observations and special corrections should be applied regarding the environmental conditions (e.g.

humidity corrections need to be applied to remote sensing observations to match dry in-situ measurements; the size range of the samples probed by different in-situ instrumentation should be synthesized to much remote sensing etc, see for example Tsekeri et al., (2017).

All mentioned instrument types have differences in the applied measuring techniques and methods used for the retrieval of the products, and the volume of the atmospheric sample. As such, they can be used individually and independently for providing observations of aerosols, clouds and precipitation. However, the synergistic use of observations from collocated instruments, which could also lead to retrieval of extra parameters incorporating measurements from multiple instruments, allows the increase of the information content of the observation targets and, in a broader point of view, to provide complementary information on the atmosphere and its constituents. Synergistic approaches can be applied not only between remote and in-situ sensors but also between different types of remote sensors (e.g. lidar-radar, lidar-photometer, lidar-radar-radiometer; Gasteiger, et al., 2011a; Illingworth et al., 2007; Lopatin et al., 2021; Marenco et al., 2011; Sato & Okamoto, 2011).

The individual observations of aerosols, clouds and precipitation for calibration and validation studies can be provided from ground- or space-based instrumentation or from instrumentation deployed onboard aircraft, drones, and balloons. The space-based observations from remote sensing instrumentation onboard satellite missions can be used for validation purposes on an instrument onboard another mission given that there is an operational lifetime overlap between the two of them (cross-validation). For ground-based observations, several networks have been established aiming to provide quantitative and comprehensive databases with observations over broader areas. A database of comprehensive measurements can also be provided through intensive field campaigns, but they lack the climatological and statistical significance that a network could provide in terms of monitoring the variability over the operation site. Moreover, the networks may include supersites where multiple instruments are deployed (remote sensing and/or in-situ) targeted on a specific atmospheric component (e.g. aerosols, clouds, radiation) or a combination of components (e.g. aerosols and clouds) where synergistic observations can also be available. For example, the US Department of Energy Atmospheric Radiation Measurement (ARM) facility, the Network for the Detection of Atmospheric Composition Change (NDACC), and the pan-European Aerosol, Clouds and Trace Gases Research Infrastructure (ACTRIS) provide reference measurements, which can be used from the broader climate and Earth Observation communities. Besides the multi-instrument networks and Research Infrastructures (RIs), single-instrument networks also exist for providing targeted observations of the atmospheric components on a global or a regional scale. For example, for weather radars there are networks in Europe (OPERA), Japan (JMA's Weather Radar Observation Network), and the U.S. (NEXRAD); for lidars there are networks in Asia (AD-NET), Europe (EARLINET), Latin America (LALINET), and the global NASA (MPLNET) network, and for photometers and radiometers there are the AERONET, SKYNET, and WMO-PFR networks.

Moreover, there are mobile systems that can be transportable either themselves (e.g. the ground-based lidars of ESA or the ACTRIS mobile facilities), or installed onboard ship- or air-borne platforms (NASA ER-2, UK FAAM, DLR HALO and Falcon 20; Research Vessels Polastern, Meteor, Sonne). These observational platforms often deploy a variety of remote sensing and/or in-situ instrumentation for aerosol, clouds and precipitation measurements and participate in experimental campaigns for providing reference measurements for intensive observation periods to support Cal/Val activities.

The overarching objective of a validation exercise is to evaluate the degree of consistency between the satellite-based instrument (to-be-validated) and the reference instruments that have been described above. Sources of inconsistency may include the instrumental or processing algorithm issues, the differences in the retrieval techniques and the assumptions and limitations made, or the sources of the auxiliary data (e.g. meteorological profiles) required for the retrieval. All these issues and differences can be quantified through the measurement uncertainties of each instrument. Some types of systematic and random uncertainties can be characterized following specific calibration activities and quality assurance and control procedures. A detailed discussion on the data quality assurance and quality control (QA/QC) is provided in *Chapter 3*.

An important factor that must be taken into account is the spatiotemporal representativeness of the datasets used for Cal/Val, which includes the spatial and temporal coverage of the instruments and criteria for collecting collocated observations. Other key aspects should be considered, including scene homogeneity, ocean/land differences, topography etc. The concept of creating collocated observations in time and space is driven by the differences in the spatial and temporal sampling among different instruments and measurement techniques along with the need of a statistically significant dataset suitable for the validation exercise. To this end, thresholds are often used to generate a dataset of collocated observations between the reference and the “to-be-validated” instruments. In principle, the applied thresholds take into account the distance between the geographical position of the observation volumes and the time difference between acquisition times of the instruments. Moreover, complementary or auxiliary data such as air-mass back-trajectories and information about the cloud coverage above a site can be used to better collocate datasets, e.g. from a ground-based station and a satellite overpass.

1.4. Definitions and validation metrics

This section provides an overview on the terminology that is widely used across the Earth Observation community including key terms and metrics for the validation of the data originated from space-based sensors, as well as definitions of the environmental and/or physical parameters that are measured from Earth Observation remote sensing and in-situ instrumentation.

1.4.1. Key terms

A table listing the definitions and source of key terms that are used in this document is provided below.

Table 1.1. *Definitions of key terms used in the ACPPV document and their sources*

Term	Definition	Source(s)
Verification	The provision of objective evidence that specified requirements have been fulfilled. Verification should not be confused with calibration and not every verification is a validation.	ISO/TS 19159-1:2014
Calibration	(1) The process of quantitatively defining the system responses to known, controlled signal inputs.	ISO/TS 19101-2:2008,

	(2) An operation that, under specified conditions, in a first step, establishes a relation between the quantity values with measurement uncertainties provided by measurement standards and corresponding indications with associated measurement uncertainties and, in a second step, uses this information to establish a relation for obtaining a measurement result from an indication. A calibration may be expressed by a statement, calibration function, calibration diagram, calibration curve, or calibration table. In some cases, it may consist of an additive or multiplicative correction of the indication with associated measurement uncertainty.	ISO/TS 19159-1:2014
Validation	The process of assessing, by independent means, the quality of the data products derived from the system output.	ISO/TS 19159-1:2014
Correction	The compensation for an estimated systematic effect. The compensation can take different forms, such as an addend or a factor, or can be deduced from a table.	ISO/TS 19159-1:2014
Measurement	A set of operations having the object of determining the value of a quantity.	ISO/TS 19101-2:2008
Resolution	The smallest difference between indications of a sensor that can be meaningfully distinguished.	ISO 19101-2:2018
Raw data	The physical telemetry payload data as received from a detector of the instrument, i.e. a serial data stream without de-multiplexing.	CEOS/WGISS/DSIG/GLOS
Level 0 data	The reconstructed unprocessed data at full space-time resolution with all available supplemental information to be used in subsequent processing appended.	CEOS/WGISS/DSIG/GLOS
Level 1A data	The reconstructed unprocessed data at full resolution, time-referenced, and annotated with ancillary information, including radiometric and geometric calibration coefficients and geo-referencing parameters computed and appended but not applied to the Level 0 data.	CEOS/WGISS/DSIG/GLOS
Level 1B data	The radiometrically corrected and calibrated data in physical units at full instrument resolution.	CEOS/WGISS/DSIG/GLOS
Level 1C data	The Level 1B data but orthorectified, re-sampled to a specified grid	CEOS/WGISS/DSIG/GLOS
Level 2 data	The retrieved geophysical parameters (e.g. aerosol backscatter coefficient, depolarization ratio, Radar reflectivity, Doppler Velocity, cloud liquid and ice water content) at the same resolution and location as Level 1B source data.	CEOS/WGISS/DSIG/GLOS
Level 3 data	The retrieved geophysical parameters which have been spatially and/or temporally re-sampled (i.e. derived from Level	CEOS/WGISS/DSIG/GLOS

	1 or 2 products), usually with some completeness and consistency. Such re-sampling may include averaging and compositing.	
Correlative measurements	Geophysical parameter data, measured or collected by other means than by the instrument itself, used as correlative or calibration/validation data for that instrument data. It includes data taken on the ground, on the ocean or in the atmosphere.	CEOS/WGISS/ DSIG/GLOS
Fiducial reference measurements	A suite of independent ground measurements that provide the maximum scientific utility/return on investment for a satellite mission by delivering, to users, the required confidence in data products, in the form of independent validation results and satellite measurement uncertainty estimation, over the duration of the mission. The FRMs follow the guidelines outlined by the GEO/CEOS Quality Assurance framework for Earth Observation (QA4EO).	(Donlon et al., 2014)
Remote sensing measurements	A measurement of a quantity from a distance. Remote sensing is the collection and interpretation of information about an object without being in physical contact with the object.	ISO/TS 19101-2:2008, (Sayer, 2020)
In-situ measurements	A direct measurement of a quantity in its original place.	ISO/TS 19159-1:2014
Temporal collocation	The degree to which measurements are aligned in time.	(Loew et al., 2017)
Spatial collocation	The degree to which measurements are aligned in space.	(Loew et al., 2017)
Representativeness	The extent to which a set of measurements taken in a given space-time domain reflect the actual conditions in the same or different spacetime domain taken on a scale appropriate for a specific application.	(Nappo et al., 1982)
Accuracy	The combination of bias and precision, defined as the overall distance between measured and reference value	(Walther & Moore, 2005)
Precision	The absence of variability or variance (i.e. the random error) of the measured value generated by the measurement error, the sample variation, and the estimation variance of the measuring procedure	(Walther & Moore, 2005)
Uncertainty	The non-negative parameter characterizing the dispersion of the quantity values being attributed to a measurand, based on the information used. Note: The measurement uncertainty includes components arising from systematic effects, such as components associated with corrections and the assigned quantity values of measurement standards, as well as the definitional uncertainty. Sometimes the estimated systematic effects are	ISO/IEC Guide 99:2007

	not corrected for but, instead, associated measurement uncertainty components are incorporated.	
Error (of measurement) or Bias	The measured quantity value minus a reference quantity value. Note: The concept of measurement error can be used both a) when there is a single reference quantity value to refer to, which occurs if a calibration is made by means of a measurement standard with a measured quantity value having a negligible measurement uncertainty or if a conventional quantity value is given, in which case the measurement error is known, and b) if a measurand is supposed to be represented by a unique true quantity value or a set of true quantity values of negligible range, in which case the measurement error is not known.	ISO/IEC Guide 99:2007; (Walther & Moore, 2005)
Systematic error (of measurement)	The component of measurement error that in replicate measurements remains constant or varies in a predictable manner. Notes: 1. A reference quantity value for a systematic measurement error is a true quantity value, or a measured quantity value of a measurement standard of negligible measurement uncertainty, or a conventional quantity value. 2. The systematic measurement error, and its causes, can be known or unknown. A correction can be applied to compensate for a known systematic measurement error. 3: The systematic measurement error equals the meas-urement error minus the random measurement error.	ISO/IEC Guide 99:2007
Random error (of measurement)	The component of measurement error that in replicate measurements varies in an unpredictable manner. Notes: 1. A reference quantity value for a random measurement error is the average that would ensue from an infinite number of replicate measurements of the same measurand. 2. The random measurement errors of a set of replicate measurements form a distribution that can be summarized by its expectation, which is generally assumed to be zero, and its variance.	ISO/IEC Guide 99:2007

1.4.2. Validation metrics

A key element in a validation study is the statistical analysis of the differences between the measurements of a new instrument to be validated and a reference instrument (von Clarmann, 2006). As such, the use of statistical metrics is required when testing the quality of the data products derived from the space profilers for aerosol, clouds and precipitation properties while using reference measurements. The used metrics such as mean bias, standard deviation, and root mean square error fall under the terms of bias, accuracy, and precision. The qualitative concepts of these three key terms will be presented below, based on the literature review of (Walther & Moore, 2005).

The term bias is used to define the difference between a measured quantity value and a “true” or reference quantity value, thus it is indicative of an overestimation or underestimation of the reference values. Another word for “bias” is also the “error” of the measurement (ISO/IEC Guide 99:2007). Moreover, it can be classified as a measurement, a sampling or an estimation bias (Kotz et al., 1988). The measurement bias can be caused by errors in the measuring procedures (e.g. wrong calibration procedure) meaning that the measured values are systematically biased away from the reference values, thus, it does not depend on the sampling effort. The sampling bias can be caused by unrepresentative sampling of the measured quantity, and it is independent of the sampling effort (e.g. when an airborne in-situ sensor for particle concentration measurements performs more measurements below the mineral dust layer than inside the dust layer, then the particle concentration measurements below this dust layer will not give an unbiased measurement of the particle concentration inside the layer). On the other hand, the estimation bias can be decreased with increased sampling effort and it refers to a biased estimation method or measuring procedure for which the average of repeated value estimates deviates from the reference value in a consistent way. The estimation bias is also called systematic error of the measurement (ISO/IEC Guide 99:2007). The most common bias metric is the mean error or mean bias, i.e. the mean of the differences between the measured value and the reference/true value (Table 1.1), and it indicates whether the true value is under- or overestimated by the measuring procedure.

The term precision is used to define the degree of variability or variance (i.e. the random error) of the measured value generated by the measurement uncertainty, the sample variation, and the estimation variance of the measuring procedure. In contrast to bias, precision is independent of the reference value and its magnitude depends on the resolution of the measuring instrument. However, higher resolution may allow greater variance of the measured quantity, but does not always result in higher precision. Common metrics for precision are the variance (mean of the squared differences between the measured value and the mean measured value), and the standard deviation (square root of variance) which is in the same scale as the mean error (Table 1.1). However, the precision metrics do not require the knowledge of the true value, thus they cannot evaluate the performance of an instrument without the use of complementary bias or accuracy metrics.

The term accuracy is the combination of bias and precision and defines the overall distance between measured and true value. For example, when the measuring instrument and/or the measuring procedure are more biased and less precise, the overall ability of the measured value to be an accurate estimation of the reference/true value is decreased. Common accuracy metrics are the mean or median absolute error, the mean square error (mean of the squared differences between measured and reference values), and the root mean square error (Table 1.1). The advantage of mean/median absolute error is that it eliminates the effect of outliers while the mean square error and the root mean square error tend to be dominated by the outliers. On the other hand, the mean square error incorporates the concepts of bias and precision as it is the sum of the mean error and the variance (Casella & Berger, 1990), thus a measurement with small variance and small bias is of high accuracy. The advantage of root mean square error is that it scales back the mean square error to the measurement scale.

Table 1.2. *Performance measures for bias, precision, and accuracy where n is the sample size, x_i is the measured value and $\underline{x}$ is the mean measured value, $x_{ref,i}$ is the reference/true value, Σ is the summation formula.*

Bias	
Mean Bias	$MB = \frac{1}{n}\sum_{i=1}^{n}(x_i - x_{ref,i}),$
Precision	
Variance	$Var = \frac{1}{n-1}\sum_{i=1}^{n}(x_i - \bar{x})^2$
Standard Deviation	$STD = \sqrt{Var} = \sqrt{\frac{1}{n-1}\sum_{i=1}^{n}(x_i - \bar{x})^2}$
Accuracy	
Mean Absolute Error Median Absolute Error	$Mean\ AE = \frac{1}{n}\sum_{i=1}^{n}\lvert x_i - x_{ref,i}\rvert,$ $Median\ AE = median(\lvert x_i - x_{ref,i}\rvert)$
Mean Square Error	$MSE = \frac{1}{n}\sum_{i=1}^{n}(x_i - x_{ref,i})^2$
Root Mean Square Error	$RMSE = \sqrt{\frac{1}{n}\sum_{i=1}^{n}(x_i - x_{ref,i})^2}$

1.5. ACPPV document structure

Chapter 2 of this document describes products that may require validation, from past, current, and future aerosol, cloud, and precipitation profiling missions. This includes some description of retrieval algorithms, as validation includes testing algorithm assumptions. The chapter is organized by measurement type, and by mission. *Chapter 3* describes a variety of instruments and networks that are (or recently have been) available for validation data collection. Some challenges in using validation data from such a variety of sources pertain to data access and data formats. *Chapter 4* discusses considerations for correlative metadata, data formats, and data access along with Findable Accessible Interoperable Reusable (FAIR) data principles. *Chapters 5, 6, and 7 provide guidance for conducting validation activities for the lidar and aerosol products (Chapter 5), for the radar and cloud products (Chapter 6), and for statistical validation techniques (Chapter 7)*. While much of this document focuses on using independent measurements to validate spaceborne profilers, *Chapter 8* turns toward validation using numerical models via data assimilation. Finally, *Chapter 9* addresses some of the current (early 2020's) gaps in the state of our knowledge and capabilities, and resulting challenges for validation of aerosol, cloud, and precipitation profiles.

2. Chapter 2: Validation needs for space profilers

2.1. Overview of the Chapter

The focus of this chapter is on the validation of vertical profiles of parameters associated with aerosol, clouds, and precipitation as measured by space-borne active sensors (i.e. lidars and radars). These profiles may range in nature from mainly direct observables (e.g. lidar attenuated backscatter, radar reflectivity and Doppler mean velocity), to quantitative inversion products (e.g. lidar derived extinction profiles, radar derived ice-water-content profiles and microphysics parameters), to qualitative products (e.g. classification of cloud particles and aerosol type).

Validation (see *Chapter 1* for the definition) implies the use of independent measurements, that can be collected by instruments having different characteristics with respect to satellite instruments to achieve an independent assessment of satellite products but also to provide feedback for improving retrieval methods, which implies also a feedback on the assumptions adopted to develop the retrieval algorithms. The GPM Ground Validation (Petersen et al., 2020) refers to these two aspects as direct statistical validation and physical validation. While the statistical validation relies on long term measurements obtained from operational or scientific networks, and fiducial networks or supersites, physical validation is usually related to targeted measurement campaigns including those typically conducted in the pre-launch phase to set-up algorithms.

Since each recent (some of them are described in *Chapter 1*) and future satellite missions has its own characteristic sets of observing systems with their associated products and specific retrieval methods, aspects like the characteristics of sensors, the spectral range exploited, and the set of assumptions adopted in retrieval must be taken into account in terms of validation requirements. Usually, satellite missions draft a specific validation plan that takes into account science objectives and innovative elements of the mission, such as technology advancements and related new methods and products that were not available in the previous missions (e.g. Doppler capability of lidar in Aeolus or in EarthCARE radar, the use of dual-frequency in radar the GPM radar, co-location of multiple instruments on the same platform). For this reason, new missions set new challenges for validations.

Therefore, drafting a document about general validation needs with an outlook to future missions is not an easy task, although there is a noticeable experience developed along past and current missions. Some of the high-level (interacting) considerations to be taken into account when planning or conducting validation activities are:

- The horizontal and vertical resolution of the space-based profiles measurements and products and their associated uncertainty.
- The data availability and the degree of co-location between the space and terrestrial instruments involved.
- The temporal and spatial scales of the geophysical target(s) in question.

All of these factors come into play in determining the effective validation strategies but can affect in different ways the validation, depending on the sensor and the target geophysical products. For example, the validation of L1 CALIOP attenuated backscatter profiles was successfully carried out via satellite underflights with a nadir-viewing airborne HSRL (Rogers

et al., 2011). Success was ensured by conducting flights along the satellite track timed for temporal coincidence at a point on the track and focusing on validation comparisons in the free troposphere between the boundary layer and aircraft altitude where there was low spatial and temporal variability in aerosol backscatter. On the other hand, validation of cloud observations using ground-based observations usually must involve longer-term statistical comparisons (Protat et al., 2009), mainly because, in general, clouds and precipitation as well are much more variable in time and space than aerosols.

For aerosols, in areas far from sources, tropospheric aerosol optical properties can typically be considered coherent on horizontal scales on the order of several tens of km and on temporal scales of a few hours. For clouds the temporal and spatial scales depend on the cloud type, however, as a general rule the variability associated with clouds is much higher than with aerosols ranging from less than a few minutes and 100's of meters for boundary-layer cumulus clouds to a few minutes and less than a few km for cirrus clouds. Similar considerations can be also applied to precipitation that follows different time and space scales, for example in convective events and in stratiform events. Horizontal and temporal scales can sometimes be evaluated after each event using imagery products from e.g. geostationary imagers and ground-based radar networks or modeling tools, but in general this remains a challenge to be addressed case-by-case.

For lidars, especially, the target's optical depth and its associated variability is also an important consideration. For optically thin targets, signal profiles may be averaged together to increase the signal-to-noise ratio as well as the representativity of the observation, which may be considered a valid average. If significant and highly variable extinction is present, then any retrieval based on the average signals will become suspect because of the non-linear equations that model the instrument response. This is also an important distinction between lidar aerosol and cloud observations. In the case of radar observations, especially at frequencies like the Ka (36 GHz) of GPM and the W-band (94 GHz) of Cloudsat and EarthCARE, the effect of attenuation depends on the radar frequency and could not be a concern for cloud observation but can be in case of liquid precipitation. Moreover, attenuation effects are different if the same precipitating structure is observed from a satellite or from a ground-based profiler: in observing precipitating clouds in stratiform regime with say, at 94 GHz radar, attenuation due to propagation through liquid precipitation and the melting layer affects measurements collected by profilers at ground, but not measurements collected by the satellite-borne radar. Geophysical retrievals will present a completely different error structure.

Expected uncertainties related to satellite products and uncertainties of corresponding correlative estimates, collected from ground or, in general, from a suborbital platform must be taken into consideration as part of the validation study. Although key system parameters are carefully monitored, also with external calibrator and precise specifications are defined in the pre-launch phase and to verify their behavior in time, this is not always the case of the expected accuracies of geophysical products (this happens for GPM, which set a requirements on accuracy of mass weighted mean drop diameter - (Skofronick-Jackson et al., 2018), which are defined through pre-launch experiments or through simulations and have a complex dependency on the scene observed.

Instrument instantaneous footprints are also a factor, for lidars this is usually not a significant concern. However, for space-based radars cloud and precipitation variability on the foot-print scale can be important and can have a significant effect both on reflectivity measurements

and especially with observed Doppler velocities leading to the fact that cloud edges should be treated with caution (Kollias et al., 2023). This fact will have an obvious impact on strategies needed to validate Doppler velocity estimates from space-based radars.

Several strategies and methods are available for validation. While discussing validation techniques that will be the aim of other chapters, this one focuses on validation needs, by illustrating satellite retrieval techniques for main profile products to discuss the expectations for validation and the experience carried out in past experiences.

The discussion is separated based on the instruments and instrumental synergies and considers the validation approaches adopted in the different satellite missions. The chapter begins with lidar products from CALIPSO, CATS, Aeolus, and EarthCARE, followed by cloud-focused radar products as in CloudSat, EarthCARE, or precipitation-focused as in TRMM/GPM, and offers also an initial survey of the products of the planned INCUS mission. The discussion is separated by mission since each mission has peculiar characteristics, both in terms of instruments and the physical basis of the recovery approaches adopted for the development of L2 products, probably being EarthCARE due to the payload and the number of products delivered by ESA and JAXA (see table A2.1 for a summary of the products made available by the two agencies) as the most complex one. Instrument synergies will be the subject of Section 2.4, which discusses the long-term CloudSat/CALIPSO experience and new EarthCARE synergy products. Radiative products, both from CloudSat/CALIPSO and EarthCARE, are included in Chapter 2 (section 2.5).

All the sections of Chapter 2 have been developed following possible a similar scheme, i.e. starting with the description of the algorithms and products (important to highlight the hypotheses used in the algorithms used and which are the subject of physical validation) followed by a discussion of the validation approaches, which may be "lessons learned" from validation programs of completed missions, or ongoing missions like GPM with a long-term validation experience, or "validation needs" for ongoing or future missions which can provide new products compared to previous missions that will likely require new methods for validation. Issues relating to instrument calibration are also taken into consideration (see Chapter 1 for the definition of calibration). A final section attempts to summarize the content of the chapter considering macrocategories of products and a critical discussion of the corresponding validation means used or planned by the different missions.

2.2. Lidar products

2.2.1. CALIPSO products

The CALIPSO (Cloud–Aerosol Lidar and Infrared Pathfinder Satellite Observations) satellite mission was a joint endeavor between NASA and the French Space Agency Centre National d'Études Spatiales (CNES). Its primary payload was CALIOP, standing for Cloud–Aerosol Lidar with Orthogonal Polarization, a three-channel elastic backscatter lidar operating at 532 and 1064 nm, with depolarization sensitivity in the 532 nm channel. Launched on April 28, 2006, CALIPSO embarked on a mission initially planned for three years flying in formation along the same track with CloudSat which hosted a W-band radar (see section 2.4.1 for the CALIPSO/CloudSat synergy) to probe the vertical structure and properties of clouds and aerosols. The mission, which concluded on August 1, 2023, marked a significant milestone as the first enduring lidar satellite mission and CALIOP lidar collected science measurements

from 2006-2023 that have provided significant insight into the role of clouds and atmospheric aerosols in determining weather, climate, and air quality.

2.2.1.1. CALIOP level 1B data products

The primary measurables were vertical profiles of parallel and perpendicular attenuated backscatter at 532 nm and total (parallel + perpendicular) attenuated backscatter at 1064 nm. Given the high vertical and horizontal sampling of the lidar, CALIOP measurements were capable of discerning cloud and aerosol layers at a wide range of spatial resolutions, from the surface up to 36 km in altitude. The fundamental calibration technique for CALIOP was molecular normalization of the 532 nm nighttime channel based on the MERRA-2 reanalysis model molecular number density from 36-39 km (Kar et al., 2018). The 532 nm daytime channel is calibrated by matching attenuated scattering ratios between the day and night at lower-stratospheric altitudes that are spatially homogeneous (Getzewich et al., 2018). Lastly, the 1064 nm calibration technique transfers the 532 nm calibrations to 1064 nm based on the predictable ratios of 1064 nm to 532 nm attenuated backscatter for cirrus (Vaughan et al., 2019). To achieve acceptable SNR when deriving calibration coefficients, the calibration process averages data in multiple neighboring orbits as a function of granule elapsed time. The calibration coefficients are a strong function of latitude, and they vary also over time. Perpendicular attenuated backscatter is calculated using polarization gain ratios (PGR) derived from bi-monthly on-orbit PGR calibration operations at night and derived from backscatter returns of optically thick cirrus during the day that are smoothed and stored in a lookup table (Getzewich et al., 2024). These processes capture the systematic change in PGR values over the course of the mission. Table 2.1 reports a summary of CALIOP level 1B data products.

2.2.1.2. CALIOP level 2 data products

To identify atmospheric features, CALIOP level 2 processing uses a threshold-based feature detection algorithm to iteratively search for features from finer to coarser horizontal averaging resolutions (Vaughan et al., 2009). This allows detecting layers at varying backscatter intensity while improving SNR with each subsequent average. Cloud and aerosol layers are discriminated based on comparing five lidar observables to a five-dimensional probability distribution function of values expected for these two feature types (Liu et al., 2019). Aerosol layers in the troposphere are each subtyped into one of seven classifications, consisting of pure types (clean marine, dust, smoke), mixtures (dusty marine, polluted dust, polluted continental/smoke), and background aerosol (clean continental). The subtyping algorithm for tropospheric aerosol uses thresholds of CALIOP observables based in part on AERONET cluster analysis with refinements added for mixtures (Kim et al., 2018; Omar et al., 2009). Stratospheric aerosol layers are subtyped into one of four classifications (volcanic ash, sulfate, smoke, polar stratospheric aerosol) using thresholds of estimated particulate depolarization ratio empirically derived from major stratospheric injections during the CALIPSO mission (Tackett et al., 2023). The thermodynamic phase for cloud layers (ice, water, oriented ice) is determined based on depolarization ratio and integrated attenuated backscatter measurements (Avery et al., 2020).

Following atmospheric layer identification and typing, CALIOP level 2 processing retrieves profiles of extinction coefficients. These retrievals are either unconstrained, whereby a lidar ratio is assumed based on the feature type/subtype, or they are “constrained” by an estimate

of the layer two-way transmittance which allows a lidar ratio to be estimated (Young et al., 2018). Except for layers classified as ice clouds where the lidar ratio is assigned based on the layer centroid temperature, default lidar ratios for unconstrained retrievals are fixed values for each subtype that are occasionally adjusted in the retrieval process to achieve a solution. Extinction profiles are reported separately for aerosol and cloud features. Additionally, two independent retrievals in CALIPSO processing determine column particulate optical depths (1) above opaque water clouds based on the technique of Hu et al., (2007), and (2) over ocean based on atmospheric attenuation of the ocean surface lidar return, named ODCOD (Ryan et al., 2024).

Table 2.1 *CALIOP Level 1B and level 2 Data Products.*

CALIOP level 1B data products
Calibrated, geolocated, vertical profiles (AMSL) of:
- Total attenuated backscatter 532 nm
- Perpendicular attenuated backscatter 532 nm
- Total attenuated backscatter 1064 nm
CALIOP level 2 layer product
For each layer detected:
- Top/base altitudes
- Feature type (cloud or aerosol)
- Feature subtype
- Layer-integrated volume depolarization ratio 532 nm, attenuated backscatter 1064 nm, attenuated backscatter color ratio (all measured quantities)
- Layer optical depth 532 nm, 1064 nm
- Ice-water path (cloud only)
Column retrievals:
- Column aerosol optical depth 532 nm, 1064 nm
- Column cloud optical depth 532 nm
- Column stratospheric aerosol optical depth 532 nm, 1064 nm
- Above-opaque water cloud column optical depth 532 nm
- Ocean surface derived column optical depth 532 nm
CALIOP level 2 profile products
Vertical profiles including:
- Aerosol extinction coefficient, backscatter coefficient, perpendicular backscatter coefficient 532 nm, 1064 nm
- Aerosol particulate depolarization ratio 532 nm
- Cloud extinction coefficient, backscatter coefficient, perpendicular backscatter coefficient, particulate depolarization ratio 532 nm
- Ice-water content (cloud only)
- Atmospheric volume description / vertical feature mask

2.2.1.3. CALIOP level 3 products

CALIOP level 3 products are also constructed from quality-assured level 2 retrievals for tropospheric aerosol, stratospheric aerosol, ice clouds, and cloud occurrence (Kar et al., 2019; Tackett et al., 2018; Winker et al., 2024). These products contain monthly averages or

histograms, on an equal angle latitude-longitude-altitude grid. The detail of CALIOP Level 3 products is provided in Table 2.2.

Table 2.2 *CALIOP Level 3 Data Products*

Description	**Variables**
CALIOP level 3 tropospheric aerosol product	
Reported for cloud-free, all-sky, cloudy-sky transparent, cloud-sky opaque. Day/night separate. Equal angle latitude-longitude-altitude grid.	Aerosol extinction coefficient mean 532 nm
	Aerosol occurrence by subtype
	Column AOD mean 532 nm
CALIOP level 3 stratospheric aerosol product	
Reported for all aerosol and background-only. Nighttime only, above tropopause. Zonal averages. Equal angle latitude-altitude grid.	Total attenuated backscatter coefficient 532 nm
	Particulate extinction and particulate backscatter coefficients 532 nm (Fernald retrieval)
	Stratospheric optical depth 532 nm
CALIOP level 3 ice cloud product	
Equal angle latitude-longitude-altitude-histogram grid. Day/night separate.	Ice cloud extinction coefficient 532 nm histogram
	Ice water content histogram
	Ice cloud occurrence
CALIOP level 3 cloud occurrence product	
Equal angle latitude-longitude-altitude-histogram grid. Day/night separate	Water cloud occurrence
	Ice cloud occurrence
	Unknown phase cloud occurrence

2.2.1.4. CALIOP calibration and validation

The primary validation needs for CALIOP level 1B data are quantitative assessments of the attenuated backscatter calibration coefficients and the PGR values. Validation data is required for both day and night, and separately for both wavelengths because assumptions underpinning the backscatter calibration methods are different for 532 nm night, 532 nm day, and 1064 nm. In addition, co-located observations are needed at varying latitudes to ensure that the calibration coefficients remain accurate over the course of each orbit. This analysis typically involves comparisons of attenuated backscatter profiles in particulate-free regions from either airborne or ground-based lidar data. Given the SNR of CALIOP observations, numerous collocated measurements are required to create statistically significant comparisons. The CALIPSO project relied heavily on collocated underflights of the NASA Langley Research Center airborne HSRL for assessing calibration accuracy during the mission lifetime (Getzewich et al., 2018; Kar et al., 2018; Rogers et al., 2011; Vaughan et al., 2019) and other underflight experiments (Marenco et al., 2014). Collocated ground-based lidar observations of attenuated backscatter measurements were also a valuable source of validation (Mamouri et al., 2009; Wu et al., 2010).

An important validation step was incorporated into the CALIOP level 1B data verification strategy as data was generated, prior to public release. The CALIPSO team formalized a science impact test plan that specified quantitative metrics which must be met based on statistical analysis of each month of data produced. These tests confirmed that (1) the assumptions underlying the calibration strategies for all three channels are correct and (2) the accuracy of the calibrated signal in the science region (<36 km) is within an acceptable margin. Furthermore, time series of attenuated scattering ratios were evaluated for each month to identify and correct any errors caused during the production process.

CALIOP PGR values are also important to validate because volume depolarization ratios are among the most influential measurables that level 2 feature typing and subtyping algorithms use for classification. Strongly depolarizing features such as cirrus have provided useful validation targets (Sassen et al., 2012). Since the CALIPSO PGR values vary diurnally, a proper validation must assess both day and night depolarization ratio measurements.

Validation of CALIOP level 2 retrievals was a continual process throughout the mission because it required statistical comparisons of a wide variety of atmospheric feature types with limited sources of independent measurements. The primary needs of level 2 validation are for feature detection capability and the accuracies of cloud-aerosol discrimination, aerosol subtyping, cloud thermodynamic phase determination, default lidar ratios, retrieved extinction profiles, and retrieved column optical depth.

Feature detection capability is important to characterize because CALIOP level 2 typing, subtyping, and extinction retrievals only operate on detected layers. Weakly scattering or vertically diffuse layers can go undetected, particularly in the daytime due to solar noise, which can cause underestimates in total column optical depth (Thorsen et al., 2017; Toth et al., 2018). Previous validation strategies identified minimum thresholds for layer detection in terms of either backscatter, extinction, or optical depth using collocated lidar, in-situ, and MODIS observations (Sheridan et al., 2012). Accurate detection of cloud geometric thickness is also important. Co-located airborne CPR measurements, CloudSat observations, and ground-based lidar have been used to evaluate CALIOP top and base altitudes (Kim et al., 2011; McGill et al., 2007). Cloud-aerosol discrimination validation is critical because erroneously including clouds in aerosol-only observations can lead to large biases. Particular attention is warranted in regions where discrimination is difficult, for example where high-altitude dust and cirrus co-exist and where strongly backscattering dust plumes could be misclassified as clouds (Liu et al., 2019).

Aerosol subtyping and cloud thermodynamic phase determination are important to validate because the classifications from these algorithms determine the initial lidar ratios used in CALIOP extinction retrievals. Unconstrained retrievals are most common for aerosol layers, where the default lidar ratio is based on the ascertained subtype. Because default lidar ratios for aerosol layers vary by nearly a factor of three, incorrect aerosol subtyping can cause large biases or failures in extinction retrievals due to incorrect lidar ratio selection. CALIOP aerosol subtyping has been evaluated using different methods, including comparisons against collocated airborne HSRL classifications resulting from an independent subtyping scheme that uses aerosol intensive property measurements (Burton et al., 2013). Ground based Raman lidar and AERONET typing retrievals provided valuable comparative observations (Ansmann et al., 2021; Mielonen et al., 2009). Likewise, incorrect cloud thermodynamic phase determination can also lead to lidar ratio selection errors for unconstrained retrievals. It is

especially important to validate that the correct phase is assigned to cirrus since these layers typically exist above all others and any bias due to incorrect lidar ratio selection will propagate to layers at lower altitudes in the extinction retrieval (Young et al., 2013). The IIR instrument on board the CALIPSO satellite has proved to be a critical asset for verifying the accuracy of CALIOP cloud phase classifications (Avery et al., 2020; Garnier et al., 2023).

Cloud lidar ratios, either retrieved or assumed by CALIOP level 2 processing, have been validated by a variety of methods. Dedicated co-located flights of the Cloud Physics Lidar were used to evaluate cirrus lidar ratios retrieved by CALIOP during the CALIPSO-CloudSat Validation Experiment in 2006 (Hlavka et al., 2012). SODA retrievals, derived from CloudSAT and CALIOP measurements of the ocean surface return, also provided meaningful insight for cirrus lidar ratio validation (Josset et al., 2012) and water cloud lidar ratio validation (Deaconu et al., 2017). The IIR instrument on board CALIPSO provided a means to establish a temperature-dependent multiple scattering factor required for CALIOP lidar ratios based on constrained retrievals of ice clouds (Garnier et al., 2015; Young et al., 2018).

Aerosol lidar ratios vary between different types and natural variability exists within each type (Floutsi et al., 2023). Hence, validating default lidar ratios for each subtype is an important priority for CALIOP. Default lidar ratios for tropospheric aerosol types were initially assigned based on aerosol models derived from AERONET cluster analysis (Omar et al., 2009). These values were re-evaluated and refined based on statistical analysis of airborne HSRL data (Rogers et al., 2014) and ground-based AERONET and EARLINET observations (Papagiannopoulos et al., 2016; Sayer et al., 2012). As of 2024, efforts are underway to replace the CALIOP default lidar ratio for marine aerosol layers with regionally and seasonally varying climatological averages of lidar ratio retrievals constrained by SODA, ODCOD, and MODIS (Trepte et al., 2023). Independent oceanic observations of lidar ratios will be needed to validate this new strategy.

Validation of retrieved extinction profiles and column optical depth is important and difficult because multiple error sources can impact the retrieval, including undetected features, incorrect lidar ratio assignment, and calibration uncertainty (Young et al., 2013). Each of these factors must be assessed to gain an accurate assessment of the validity of CALIOP extinction and optical depth retrievals. Case studies of collocated airborne HSRL measurements are ideal for evaluating CALIOP extinction retrievals and teasing apart these factors (e.g. Kacenelenbogen et al., 2011; Rogers et al., 2014). Collocated MODIS and AERONET observations are valuable for statistical comparisons (e.g. Kim et al., 2013; Kittaka et al., 2011; Omar et al., 2013).

Validating CALIOP tropospheric level 3 products is especially challenging because it requires global independent observations which do not exist from the ground at all locations. Further exacerbating this challenge, level 3 products are monthly averages of CALIOP overpasses within a given latitude-longitude grid (typically 4-5 per month at midlatitudes, many more near high latitudes), making temporal collocation tricky. Therefore, most validation work would need to be regional, focusing on comparing level 3 latitude-longitude grids containing fixed ground-based observations that can be sampled on the same days of the CALIOP overpasses. Comparing CALIOP level 3 products to monthly averages from other satellite observations is helpful for sanity checks, but care must be taken in interpreting these non-temporally collocated comparisons (Kotarba, 2022b). Validating CALIOP level 3 stratospheric aerosol retrievals is more tractable since stratospheric aerosol tends to be uniformly distributed in

between major events, thereby requiring less stringent spatiotemporal collocation. Comparisons against monthly averaged spaceborne solar occultation and limb scattering measurements are fruitful for validation (Kar et al., 2019). Despite the challenges of validating level 3 products, the CALIOP team found that closely examining level 3 data was tremendously beneficial for sanity checking level 2 data products. This is because the averaging process required to make level 3 data tends to elucidate systematic errors in level 2 retrievals. Comparing against independent observations is a means to identify these level 2 errors and identify refinements.

2.2.2. CATS products and their validation

The Cloud-Aerosol Transport System (CATS) was a lidar technology demonstration that profiled the atmosphere from the International Space Station (ISS) from 15 February 2015 to 30 October 2017 (Yorks et al., 2016, 2021). During its lifetime, CATS operated in two distinct science modes: science mode 1 from 15 February 2015 until 21 March 2015 and science mode 2 from 25 March 2015 until end of operations. In Mode 1, CATS provided total attenuated backscatter and volume depolarization ratio measurements at 532 and 1064 from two fields of view, separated by 7 km on the ground. In Mode 2, CATS provided total attenuated backscatter and volume depolarization ratio measurements from 1064 nm only. CATS data products were produced at three levels. CATS Level 0 data products include photon counts acquired at raw data resolution (350 m horizontal and 60 m vertical) downlinked from the ISS and are assigned as a “day” or “night” granule based on ISS broadcast ancillary data (BAD) and a threshold for solar background contributions to the total signal. In both modes, level 1 (L1) data products, which are further described in Section 2.2.2.1, were provided at 350 m horizontal and 60 m vertical resolution. CATS level 2 (L2) data products, described in Section 2.2.2.2, include both layer integrated and profile data products at 5 km horizontal and 60 m vertical resolution. A key feature of CATS was the capability to provide expedited near-real time (NRT) data products within 6 hours to the global modeling and hazard detection communities.

2.2.2.1. CATS Level 1 Data Products and Validation

CATS Level 1A data products include normalized relative backscatter (NRB) for all parallel and perpendicular channels. L1A data products are range corrected, normalized to laser energy, geolocated, and then are correcting raw L0 data for detector nonlinearity (dead-time correction) using precomputed look-up tables. The data is then corrected for molecular folding to remove atmospheric contributions that have been folded from above the data frame into the measured signal and then are background subtracted to remove solar contributions to the total signal. CATS L1A products were produced at raw data resolution.

CATS L1B data products, described in Yorks et al. (2016), consist of (1) total attenuated backscatter at 1064 nm (both operating modes), (2) perpendicular attenuated backscatter at 1064 nm (both operating modes), (3) total attenuated backscatter at 532 nm (Mode 1 only), and (4) perpendicular attenuated backscatter at 532 nm (Mode 1 only). These parameters are scaled through calibration by normalizing the 532 and 1064 L1A NRB signal to the atmospheric signal between 22 and 26 km, which includes the Rayleigh backscatter profile and backscatter from background aerosols in the lower stratosphere (Pauly et al., 2019). Rayleigh backscatter profiles were computed using collocated NASA Modern-Era Retrospective analysis for Research and Applications version 2 (MERRA-2) (Gelaro et al.,

2017) profiles of temperature, pressure, and ozone. For stratospheric aerosol loading in the CATS calibration window, CALIPSO V4 L1B data was used to construct monthly climatologies of scattering ratios to correct for stratospheric aerosol contributions to the total signal in the calibration region. Production of CATS L1B data also includes correction for the relative gain between perpendicular and parallel channels, known as the polarization gain ratio (PGR).

Validation of the CATS L1 data products has been performed by comparing the L1B calibrated attenuated backscatter profiles to collocated airborne and ground-based attenuated backscatter profiles. Pauly et al. (2019) compared the mean attenuated backscatter profiles from eight clear-sky, nighttime overpasses (40 profiles, ~10km) to the mean attenuated backscatter from the ground-based Leipzig PollyXT lidar. CATS passed an average distance of 40 km from the Leipzig site and 30 min of PollyXT data were averaged for each validation case (36,000 profiles/case). Pauly et al. (2019) also compared the CATS 1064 nm attenuated backscatter profiles to Cloud Physics Lidar (CPL) airborne attenuated backscatter profiles collected during two underflights of the ISS ground track. The mean attenuated backscatter profiles were computed for clear sky regions over a 55-70 km span for both CATS (165-210 profiles) and CPL (280-360 profiles). The PGR is computed using the ratio of CATS daytime parallel to perpendicular solar background signals scattered from optically thick ice clouds, which are summed over an entire granule. Yorks et al. (2015) validated the CATS PGR using a CPL underflight that occurred during local nighttime hours and included observations of dense ice clouds along the ISS track. The 1064 nm depolarization ratios in the dense ice clouds from CATS were validated against the CPL 1064 nm depolarization ratios from CPL, which flew about a 30-minute segment below the ISS. Biases were then used to further correct the CATS 1064 nm perpendicular attenuated backscatter in operating Mode 1.

2.2.2.2. CATS Level 2 Data Products and Validation

CATS L2 data products include 1) atmospheric feature detection for determination of the vertical feature mask (VFM) that includes cloud-aerosol discrimination (CAD), cloud phase determination, aerosol typing, and 2) retrievals of cloud and aerosol optical properties. The first step in CATS level 2 data processing is feature detection, which uses the attenuated scattering ratio to discriminate particulate contributions to the profiles, as done by CALIPSO and CPL (Mace & Zhang, 2014). Owing to CATS primarily operating in single-wavelength Mode 2, the feature detection developed by Vaughan et al. (2009), was modified for 1064 nm. Additional differences between CALIPSO and CATS feature detection are provided in detail in Yorks et al. (2021). One distinct new addition to the CATS feature detection algorithm was the CATS Cloud-Embedded-in-Aerosols-Layers (CEAL) routine that was developed to isolate low-level clouds within aerosol layers. CATS feature detection was performed at two horizontal resolutions: 5 km and 60 km. All nighttime feature detection was performed at 5 km which daytime feature detection was performed at both 5 km and 60 km, owing to the lower SNR during daytime viewing conditions.

The objective of the CATS CAD is to determine whether a detected feature is cloud or aerosol. The CATS CAD uses a multidimensional probability density function (PDF) as done with CALIPSO using CPL airborne measurements as inputs, as CPL provides volume depolarization ratio measurements at 1064 nm. Inputs to the CATS CAD are layer integrated attenuated backscatter, 1064 nm layer-integrated volume depolarization ratio, layer thickness, mid-layer altitude, temperature profiles from MERRA-2, and layer-integrated color ratio for Mode 1 only. An overview of the CATS CAD is provided in Figure 2.1.

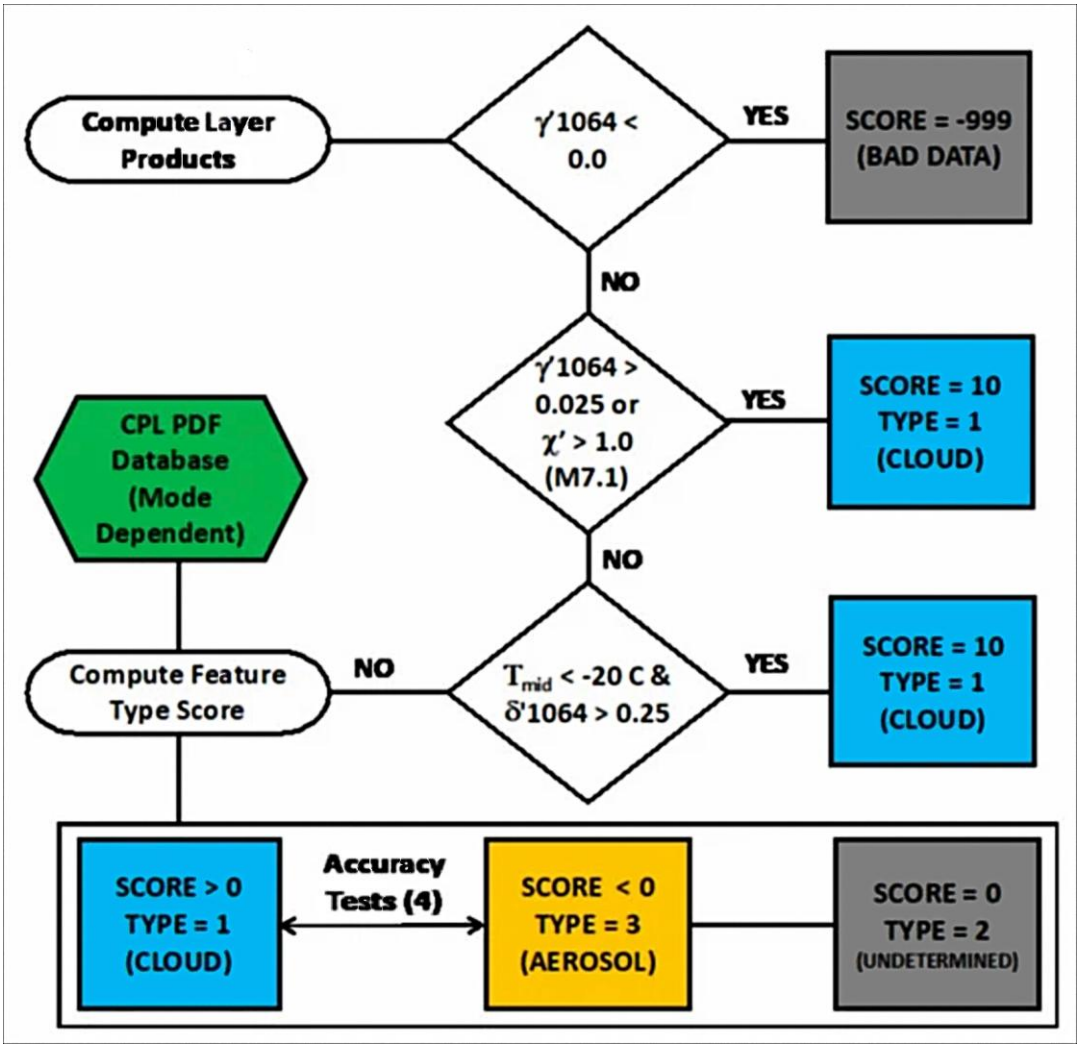

Figure 2.1 *CATS Cloud-Aerosol-Discrimination Schematic (from Yorks et al. (2021))*

Following the CAD, cloud phase and aerosol typing algorithms are evoked to assist with lidar ratio determination for optical property retrievals. Inputs to the CATS cloud phase algorithm include layer-integrated attenuated backscatter, layer-integrated volume depolarization ratio, cloud thickness, and temperature from MERRA-2 to assign either ice, liquid, or undetermined cloud types. Inputs to the CATS aerosol typing algorithm include layer-integrated attenuated backscatter and volume depolarization ratio, aerosol altitude and thickness, surface type, and layer-integrated color ratio in the case of Mode 1. Additionally, as described in Nowottnick et al. (2022), MERRA-2 aerosol typing is evoked conservatively to help discriminate between smoke and polluted continental layers. CATS cloud phase and aerosol type is used primarily to select a lidar ratio to retrieve particulate backscatter and extinction when the constrained method cannot be used (see CATS ATBD). Detailed descriptions of the various techniques to retrieve CATS optical quantities are provided in the CATS ATBD.

CATS L2 data products include both profile (vertically resolved) and layer (feature integrated) files. All products are reported at 5 km horizontal resolution. Primary products in each level 2 file type are provided in Table 2.3.

Table 2.3 *CATS Level 2 Layer and Profile Data Products.*

Parameter	Wavelength	Notes
Layer Products		
Top/base altitudes	N/A	cloud or aerosol
Feature type	N/A	cloud or aerosol
Feature subtype	N/A	cloud phase, aerosol type
Layer-integrated attenuated backscatter	532* and 1064 nm	*Mode 1 only
Layer-integrated volume depolarization ratio	532* and 1064 nm	*Mode 1 only
Layer optical depth	532* and 1064 nm	*Mode 1 only
Ice-water path	532* and 1064 nm	Ice clouds, *Mode 1 only
Profile Products		
Particulate extinction coefficient	532* and 1064 nm	*Mode 1 only
Particulate backscatter coefficient	532* and 1064 nm	*Mode 1 only
Ice-water content	532* and 1064 nm	Ice clouds, *Mode 1 only

Validation of CATS L2 products has primarily been focused on aerosol extinction/optical depth. Proestakis et al. (2019) used EARLINET observations to validate near-coincident CATS 1064 nm backscatter coefficients and to evaluate day-night feature detection sensitivity. Lee et al. (2019) evaluated CATS aerosol optical depths by comparing them to near-coincident AERONET and MODIS aerosol optical depths (AODs), as well as an intercomparison between CATS and CALIPSO AODs at 1064 nm. Nowottnick et al. (2022) used near-coincident measurements of aerosol extinction from the Micro-Pulse Lidar Network (MPLNET) to validate diurnal variability in smoke distributions observed by CATS in Kuching, Malaysia. Yu et al. (2021) compared CATS dust optical depths to AERONET ground sites and MISR (the Multi-angle Imaging Spectroradiometer aboard NASA's Terra satellite) observations. For clouds, Noël et al. (2018) compared CATS cloud detection frequencies to the Lidar Nuages et Aérosols (LNA) lidar at the Site Instrumenté de Recherche par Télédétection Atmosphérique (SIRTA) ground site in Paris, as well as the Atmospheric Radiation Measurement (ARM) lidars at the Southern Great Plains (SGP) and Eastern North Atlantic (ENA) sites.

2.2.2.3. CATS Near-Real-Time (NRT) Data Products

Owing to operating on the ISS, CATS was able to downlink raw data and process NRT data products to data users within 6 hours of acquisition. The CATS NRT data product was provided at 5 km horizontal and 60 m vertical resolution and contained total attenuated backscatter, volume depolarization ratio, VFM, and associated uncertainties and quality flags. For NRT products, Rayleigh backscatter profiles were computed using collocated profiles of temperature, pressure, and ozone from the NASA Goddard Earth Observing System - Forward Processing (GEOS-FP) for CATS NRT products, owing to the longer latency of MERRA-2 production. CATS NRT products were not validated during mission operations.

2.2.2.4. CATS Data Availability

CATS quick look and individual file data can be found at: https://cats.gsfc.nasa.gov/data/browse/. Data may also be found at the NASA Atmospheric Science Data Center (ASDC): https://www.earthdata.nasa.gov/eosdis/daacs/asdc.

2.2.3. Aeolus products and validation

Launched on 22 August 2018, the Aeolus mission provided global profiles of the horizontal wind speed as well as extinction and backscatter information on clouds and aerosols. The satellite carried a single instrument, the Atmospheric Laser Doppler Instrument (ALADIN) operating at 355 nm wavelength, the first Doppler Wind Lidar (DWL) in space, measuring direct wind profiles from Earth's surface up to an altitude of about 30 km in clear air, inside thin clouds and aerosols, and on top of thick clouds. The instrument includes a Rayleigh and a Mie receiver to measure the molecular and the particulate laser return signals. As a High Spectral Resolution Lidar (HSRL), ALADIN is able to independently measure the particle extinction and co-polarized particle backscatter coefficients.

The operational mission ended on 30 April 2023 followed by a series of experimental end-of-life activities before its assisted re-entry on 28 July 2023. In these 4.5 years of operations, ALADIN emitted 7.1 billion UV laser shots at 355 nm. Aeolus was flying in a polar dawn-dusk orbit at an altitude of 320 km with a 7-days repeat cycle. The number of orbits per day was 15 summarizing to 111 orbits per week.

2.2.3.1. Level 1B products

The Level 1B products contain the preliminary Horizontal Line-Of-Sight (HLOS) winds, useful signals for the Rayleigh and Mie receivers, product confidence data (e.g. random and systematic errors and product quality flags) and processed calibration files (instrument characterization, instrument settings and calibration processor output). Standard atmospheric corrections, receiver response and bias correction are applied to the L1B product.

2.2.3.2. Level 2B wind product

The Level 2B wind product is a geo-located HLOS wind observation with actual atmospheric correction applied to Rayleigh channel (Rennie & Isaksen, 2020) . The correction of atmospheric temperature and pressure broadening effects is done in the processing using collocated auxiliary meteorological information (AUX_MET) from the ECMWF model. The product is classified into Rayleigh–clear winds, indicating observations in clear air (from molecular return signal) and Mie–cloudy winds, indicating winds retrieved from aerosol or cloud particle backscatter (Rennie et al., 2020; Tan et al., 2008). For most parts of the mission, one measurement consisted of 18 accumulated backscattered laser pulses, corresponding to 2.9 km. The setting has been adjusted during the mission to mitigate the instrument degradation and to optimize the SNR ratio. Rayleigh-clear winds typically have a horizontal resolution of 87 km, which corresponds to 30 measurements, while only 3 measurements were accumulated for Mie-cloudy winds resulting in a horizontal resolution of 8.7 km (Lux et al., 2020; Rennie et al., 2021). Each profile consists of 24 range bins dividing the atmosphere into boxes with varying vertical resolution between 250 m and 2 km. The thickness of these range bins was defined through range bin settings, which have been changed and updated multiple times during the mission. The main reason to change or add range bin settings was to address

particular scientific and Aeolus mission objectives. Some of the settings were changed seasonally, while others were long term and meant to support data assimilation by NWP centers. In the case of dedicated science objectives, validation campaigns or specific events such as volcanic eruptions or smoke, a limited spatial box could be defined.

2.2.3.3. Level 2A aerosol/cloud product

The Aeolus Aerosol and Cloud Optical Properties Product Level-2A (L2A) includes retrievals derived from multiple algorithms SCA, MCA, and MLE monitored and improved at Météo France CNRM and TROPOS (Flamant et al., 2022). The historical Standard Correct Algorithm (SCA) is a direct inversion of the lidar equation without a-priori conditions (Flament et al., 2021). The SCAmid corresponds to an average over consecutive vertical bin to compensate for noise. The Mie Channel Algorithm (MCA) relies on the Mie channel and climatological data using fixed extinction-to-backscatter ratio. The Maximum Likelihood Estimation (MLE) is based on a physically constrained optimal estimation (Ehlers et al., 2022). Particulate extinction and backscatter with corresponding variances and Quality Check (QC) flags are provided at coarser horizontal resolution Basic Repeat Cycle (BRC), also referred as observation, aligned with signal accumulation over ~87km. The SCA attenuated backscatters are given at finer horizontal sampling measurements (~2.9km to ~17.4km depending on settings) as the MLEsub particulate extinction and backscatter which accumulates measurement per sub-BRC profiles. A group product with feature detection and a model-based scene classification are included.

The L2A product also comprises retrievals from algorithms AEL_FM and AEL_PRO developed at KNMI anticipating further missions such as EarthCare and Aeolus 2. AEL-FM provides a feature-mask at the highest resolution measurement. AEL-PRO is a Multi-scale Optimal-Estimation procedure for retrieving cloud and aerosol extinction and lidar-ratio.

2.2.3.4. Validation of Aeolus products

Since Aeolus' main objectives were to demonstrate the Doppler Wind Lidar technology in space and to improve weather forecasting an appropriate calibration and validation approach was essential for the success of the mission. A comprehensive description of the Cal/Val needs is provided in the Aeolus Scientific Calibration and Validation Requirements document (ESA, 2019b). An overview of all planned Aeolus validation activities from external teams (at the beginning of the mission) including guidance and recommendations for the acquisition of collocated data is provided in the Aeolus Scientific Calibration and Validation Implementation Plan (ESA, 2019a).

The assessment of the Aeolus L2B wind product quality relies mainly on the quantification of wind biases and random errors (scaled MAD, RMSE, STD). For this purpose, collocated independent reference measurements are needed, such as from super pressure balloons, radiosondes, ground-based Radar Wind Profilers (RWP) and Doppler Wind Lidars (DWL). Further, geostationary satellites provide Atmospheric Motion Vectors (AMVs) on a global scale with a very high temporal sampling. However, AMVs are only single-layer winds representative for the top of clouds or water vapor features and the assignment of the corresponding altitude is very uncertain. Super-pressure balloons float horizontally in a particular layer of the atmosphere and thus don't provide vertical information. In contrast, radiosondes measure the entire wind profile but only on a single case basis. Remote sensing instruments onboard

research aircrafts have proven to be very valuable, as they can measure multiple profiles along the satellite track (Bedka et al., 2021; Lux et al., 2020; Witschas et al., 2020). Furthermore, pre-launch validation campaigns with the ALADIN airborne demonstrator from DLR were considered to be very valuable for improving the calibration strategy and for quantifying the uncertainties of the retrieved winds (Lux et al., 2018).

The quality assessment of the wind product using independent reference measurements is complemented by NWP monitoring using the ECMWF mode (Rennie et al., 2021). Because each L2B wind dataset also provided the predicted winds from the ECMWF model collocated and converted to the Aeolus HLOS wind, the NWP monitoring was a very powerful tool throughout the whole mission. It also helped to correct systematic biases (e.g. due to temperature fluctuations across the primary mirror of the telescope, (Weiler et al., 2021)) and to improve calibrations (e.g. NWP-based calibration of the Mie winds, (Marseille et al., 2022)) during mission operations. The L2B wind processor further provides an estimated error which mainly accounts for the instrument noise. Independent validation activities showed that this error estimate is underestimated (Bley et al., 2022; Borne et al., 2024).

Profiles of backscatter coefficient, extinction coefficient and depolarization ratio measured by ground-based or airborne-based lidars operating at 355 nm are needed for independent validation of the Aeolus L2A aerosol and cloud product. Because Aeolus only measured the co-polar component of the backscattered signal, the backscatter coefficient is significantly underestimated in case of non-spherical particles (e.g. dust). Thus, ground-based lidars need to be operated at 355 nm and derive backscatter coefficient, extinction coefficient and depolarization ratio in order to derive the parallel-component of backscatter signal of Aeolus. Cloud contamination can significantly influence the intercomparison of extinction and backscatter profiles from multiple observing platforms with varying spatial resolution. Adequate spatiotemporal averaging can reduce the impact of representativeness errors, but not the impact of cloud contaminated profiles. Therefore, a cloud flag based on the AUX_MET data was introduced to the L2A product to support validation teams in the selection of aerosol-only profiles. This update was requested by external validation teams.

In four years of L2A validation with the EARLINET lidar network, 2313 overpasses have been collected. After cloud screening, the number of collocated measurements reduced to 556 and after further manual data screening, 282 collocated profiles remained for statistical validation which is only 12% of the initially collected data. This means that only 6 collocations can be used for a single station per year assuming one overpass per week. This example demonstrates the challenges when performing statistical validation of aerosol backscatter/extinction profiles.

Statistical comparison between Aeolus backscatter profiles and collocated measurements from ground-based lidars at Cape Verde (e.g. multiwavelength Raman polarization and water-vapor lidar PollyXT, ESA eVe reference polarization lidar (Paschou et al., 2022)) have revealed an underestimation of the Aeolus backscatter in the Saharan Air Layer, which can be explained by the missing cross-polarization component of the backscattered signal. After conversion of the ground-based lidar measurement to the Aeolus-like co-polar signal, the deviation is reduced, but not fully, which indicates that the differences are due to multiple reasons (e.g. range bin overlap especially at coarse vertical resolution, non-perfect cross-talk correction between the Rayleigh and Mie signal, signal loss and cloud contamination in lowermost bins). Preliminary analysis of Aeolus backscatter and extinction profiles collocated

with NASA DC-8 aircraft measurements from the High Altitude Lidar Observatory (HALO) showed solid agreement for pure dust layer below clear sky conditions, the statistics appearing degraded for dusty mix with marine aerosols in lower altitudes.

Both the horizontal and the vertical resolution has changed multiple times over the course of the mission. This has direct impacts on the quality and the representativeness of the data. On one hand, finer aerosol layers can be detected or sharper wind gradients observed with smaller range bins, on the other hand smaller range bins also lead to higher random errors. The heterogeneous Aeolus sampling both vertical and horizontal should be considered for validation activities. The flexible Range Bin Settings (RBS) results in multiple vertical grids per orbit. This leads to higher Signal to Noise Ratio (SNR) for thicker bins but with less chance to get bins homogeneously populated in particles.

2.2.4. EarthCARE ATLID products and validation

2.2.4.1. ESA ATLID and ATLID-synergy products

EarthCARE payload includes the Atmospheric Lidar (ATLID) system, to provide vertical profiles of aerosols and thin clouds. ATLID onboard EarthCARE is a high-spectral-resolution lidar (HSRL) operating at 355 nm with a high-spectral resolution receiver and depolarisation channel (do Carmo et al., 2021). An overview of the EarthCARE processing chain is provided by Eisinger et al. (2024).

Several processors produce products based on processing on lidar measurements. Table 2.4 lists main processors, and corresponding products and provides references to specific processors and processors.

Table 2.4 *ESA ATLID level 2 processor (in grey) and products*

ATLID Feature Mask (A-FM, (van Zadelhoff et al., 2023))
● Probability of particle return detection on a scale from 0 (clear sky) to 10 (clouds or aerosols present).
ATLID Profile Processor (A-PRO, (Donovan et al., 2024))
● Aerosol-oriented extinction and backscatter retrieval (A-AER) ● Cloud and aerosol Extinction, Backscatter, and Depolarization procedure (A-EBD) that provides profiles of ○ particle backscatter coefficient ○ particle extinction coefficient ○ lidar ratio ○ particle linear depolarization ratio ● Target classification (A-TC, (Irbah et al., 2023)) ● Ice Microphysical property Estimation (A-ICE)
ATLID Layer Products processor (A-LAY, (Wandinger, et al., 2023a))
● Cloud top height ● Aerosol layer heights ● Layer mean optical properties ○ Backscatter ○ Extinction ○ lidar ratio ○ particle linear depolarization ratio ○ aerosol optical depth (AOD) ● AOD, stratospheric AOD, sum of layer AOD

2.2.4.2. Validation of ESA ATLID products

The spaceborne lidar ATLID and its products need to be validated in many ways.

Firstly, the cross-talk between the detection channels has to be known. Even if it was characterized on ground before launch, it is suggested that in-flight operations need calibration and validation. There is the spectral cross talk between the Mie and the Rayleigh channel which will affect the results, especially the extinction coefficient and there is the polarization cross talk between the Mie channel and the cross-polar channel which especially affects the measured depolarization ratio. Besides internal calibration and verification procedures, suborbital validation is essential to prove the correctness of the derived L2 products. The A-FM processor provides an operational output for evaluating the crosstalk correction & calibration in the EarthCARE L1 A-NOM data. From the pixels assigned as clear-sky (with no features present above), the 'clear-sky-averaged' profiles for the three ATLID channels, the co-polar Mie channel, the cross-polar Mie channel and the co-polar Rayleigh channel, are created and can subsequently be compared to the theoretical clear sky profiles. Offsets and trends in these 'feature-free' or 'clear-sky' profiles, and therefore appropriate cross-talk corrections, can be identified and looked into for further evaluation on the exact causes.

Profiles of the extinction coefficient and the depolarization ratio measured by ground-based or airborne lidar systems are an important input for the validation of the cross-talk influenced quantities. Issues like the spatio-temporal collocation or the wavelength transformation (if the suborbital measurement is not at the same wavelength as the spaceborne lidar) are discussed in *Chapter 5* where guidance for validation is given. The quality assurance is essential for the suborbital validation data and needs to be documented well.

The L2 products from the above-mentioned processors need to be validated. High quality profiles of the particle backscatter coefficient, extinction coefficient and particle linear depolarization ratio at the same ATLID wavelength, i.e. 355 nm, are best suited to validate EarthCARE's lidar products. All other quantities like the aerosol layer heights, the AOD, the profile of the lidar ratio and target classification can be derived from these profiles. Using a different wavelength is possible, however the transformation to 355 nm needs to be well documented and based on previous multiwavelength observations. Multiwavelength lidar (depolarization) observations with their higher information content are especially helpful for the validation of the target classification and the evaluation of the Hybrid End-to-End Aerosol Classification (HETEAC) model on which the aerosol typing is based (Wandinger, et al., 2023b). Additional collocated in-situ measurements of aerosol and ice-crystal habits are beneficial for this evaluation as well. The algorithm developers have indicated that the feature detection and target classification (e.g., aerosol cloud discrimination) is a major uncertainty in their algorithms and needs to be validated with close collocation.

2.2.4.3. JAXA ATLID L2 products

As JAXA L2 products (Sato et al., 2024), the JAXA ATLID products (including the ATLID-MSI) synergy are listed in Table 2.5 and are obtained by using different retrieval method than the method by which the above-mentioned ESA L2 products are estimated (Nishizawa et al., 2024).

Table 2.5 *JAXA ATLID and ATLID-MSI synergy products*

ATLID one-sensor Cloud Aerosol Products (ST)
● Feature mask ● Aerosol and cloud extinction coefficient, backscatter coefficient, lidar ratio, and depolarization ratio ● Target mask (aerosol and cloud type) ● Planetary boundary layer height
ATLID one-sensor Aerosol Component Product (ER/LR)
● Extinction coefficient for the major aerosols in the atmosphere ○ water soluble particles (WS) ○ light absorbing carbonaceous particles (LAC) ○ mineral dust (DS) ○ sea-salt (SS)
ATLID-MSI synergy sensor Aerosol Component Product (ER/LR)
● Extinction coefficient for WS, LAC, DS, and SS ● air-column mean mode-radii of fine-mode and coarse-mode aerosols

The JAXA EarthCARE products are divided into two categories, Standard Product (ST) and Research Product (ER/LR). The JAXA L2 ATLID one-sensor and ATLID-MSI synergy algorithms have been extended from those developed for CALIOP and MODIS to produce JAXA A-train products and ground-based HSRL and Raman lidar measurements. The algorithm to estimate the feature mask product adopts vertically varying criteria function determined from ATLID observables considering the signal-to-noise ratio of all the ATLID channels and spatial continuity (coherent filter) (Hagihara et al., 2010, 2014; Okamoto et al., 2024). The aerosol and cloud optical properties such as extinction coefficient are retrieved by the maximum likelihood estimation using the Gauss-Newton method and line-search method with spatial smoothing to achieve robust retrieval (Kudo et al., 2016). Aerosol-type classification is performed using a two-dimensional diagram of lidar ratio and depolarization ratio, which is constructed by combining cluster analysis using the AERONET L2 product with non-spherical dust data obtained from lidar observation. Cloud type classification algorithm uses the two-dimensional diagrammatic method of signal attenuation and depolarization ratio developed for CALIOP cloud-type classification (Yoshida et al., 2010). PBL height is estimated by a method using wavelet covariance transform (e.g. Kim et al., 2021). The algorithms for estimating aerosol component products (ER/LR products), which are based on algorithms developed for ground-based lidar and CALIOP and validated (Kudo et al., 2023; Nishizawa et al., 2007, 2011), retrieve the vertical profiles of aerosol components by the MAP method using difference in sensitivity to depolarization and lidar ratio for each aerosol component, under which the optical properties and shape of each component are modeled.

2.2.4.4. Validation of JAXA ATLId L2 products

The JAXA ATLID L2 product validation uses ground-based observation networks such as AD-Net and SKYNET and ship-borne measurement (Katsumata et al., 2020) to attempt validation against various aerosol species. Comparison with HSRL and Raman lidar measurements at the same wavelength as ATLID (i.e., 355nm) is essential for the validation of optical properties such as extinction coefficients, and HSRL and Raman lidars implemented at AD-Net sites are used together with HSRL installed at the EarthCARE super-site in Koganei, Tokyo, Japan (Jin et al., 2020, 2022; Nishizawa et al., 2017). In addition, comparisons with AOD at UV

wavelengths obtained from the SKYNET skyradiometer are also performed. The feature mask, target mask and PBL height products are also validated by the products derived from ground-based 355nm HSRL and Raman lidar measurements. For these products, ground-based lidar data at other wavelengths (e.g. 532nm, 1064 nm) are used in terms of increased validation opportunities, although some differences in the criterion and retrieval method used in the estimation should be noted. The aerosol component products are validated by the products derived from ground-based 355nm HSRL and Raman lidar measurements with skyradiometer measurements.

2.3. Radar products

2.3.1. CloudSat radar products

CloudSat launched in June 2006, carrying the first millimeter-wavelength cloud radar in space. Operating at 94 GHz (W-band), the nadir-pointing Cloud Profiling Radar (CPR) provided the first near-global (82°S to 82°N) measurements of the vertical structure of clouds and light precipitation (Stephens et al., 2008). The CPR ceased operations on December 20, 2023. For most of its lifetime, CloudSat flew in formation with several other Earth observing satellites in the A-Train constellation making 14 orbits per day in a sun-synchronous orbit with equatorial crossing times of 1:30am and 1:30pm (L'Ecuyer & Jiang, 2010).

The CPR data record spans more than 17 years that can be divided into two epochs: a period where measurements were collected during both day and night prior to a battery anomaly in April 2011, followed by a period of daytime-only observations after the data collection resumed in early 2012 (Stephens et al., 2018). CloudSat's standard products consist of vertical profiles of reflectivity (corrected for attenuation from atmospheric gasses), cloud occurrence, cloud phase, cloud liquid and ice water contents, and radiative fluxes and heating rates. CloudSat also supplies scalar estimates of near-surface precipitation occurrence and phase as well as profiles of light rain and snowfall intensity. It should be noted that, while this section describes CloudSat's radar-only, or RO, products, many of the mission's most widely used cloud products are those that include information from the Cloud Aerosol LIDAR and Infrared Pathfinder Satellite Observations (CALIPSO) lidar. Combined CloudSat and CALIPSO products will be discussed in Section 2.4.1.

CloudSat's RO data products are listed in Table 2.6. All have undergone several refinements from their initial post-launch releases in 2007, but most follow the same theoretical concepts and retrieve similar geophysical parameters as originally designed, with some additions. At the time of writing, Release 05 (R05) is the most recent version of all CloudSat products available through the CloudSat Data Processing Center (DPC). One final post-mission revision is underway that will culminate in the final Release 06 (R06) version of all products, but the anticipated updates should not change the summary presented here. The reader is directed to the Process Description and Interface Control Documents (PCICDs) for each algorithm found on the DPC website (www.cloudsat.cira.colostate.edu) for additional details.

Table 2.6 *CloudSat Radar-Only Data Products*

Product	Description
Level -1	
1B-CPR	Backscattered power profile
Level-2	
2B-GEOPROF	● Radar reflectivity profile ● Vertical cloud mask ● Gaseous attenuation profile
2B-CLDCLASS	Cloud classification
2B-CWC	Cloud liquid and ice water content profile
2C-PRECIP-COLUMN	Surface precipitation occurrence and type
2C-RAIN-PROFILE	Rainfall rate profile
2C-SNOW-PROFILE	Snowfall rate profile; snow particle size distribution profile

Backscattered Power (1B-CPR)

The most fundamental CPR data product used in scientific analyses is the Level-1 range-resolved backscattered power product, 1B-CPR (Tanelli et al., 2008). 1B-CPR reports calibrated, geolocated profiles of backscattered power sampled at 240 m vertical resolution along with estimates of the noise floor and surface backscatter cross-section and several other instrument characteristics such as transmit power and radar coefficient. A full description of the CloudSat Level-1B algorithm can be found in the corresponding PCICD.

More relevant to this discussion is the output, calibrated radar backscattered power that effectively defines the vertical and spatial resolution of all subsequent Level-2 products. Aside from a short period prior to 15 August 2006, the CPR has pointed forward by 0.16° off-nadir to avoid specular reflection from flat surfaces. The CPR's 3.3 ms pulse and beam pattern translate into an approximately 480 m along-track resolution which is sampled every 240 m to generate the profiles reported in 1B-CPR. The CPR has a 1.4 km instantaneous field of view on the surface which is stretched to 1.7 km in the along-track direction by spacecraft motion over the 0.16 second integration time (Tanelli et al., 2008). The absolute calibration of the CPR was established via coordinated underflights with airborne W-band radar (e.g. the CALIPSO-CloudSat Validation Experiment, CCVEx; (McGill et al., 2007)). Subsequent monitoring via surface backscatter and other indirect methods has demonstrated that, aside from an expected slow degradation of the radar sensitivity, the CPR maintained a remarkably stable calibration over its lifetime.

Geometric Profile (2B-GEOPROF)

1B-CPR provides the primary observational input to the series of CloudSat Level 2 algorithms reported in Table 2.6. These algorithms are run sequentially, starting with CloudSat's geometric profile algorithm, or cloud mask, 2B-GEOPROF, which identifies atmospheric layers that contain significant radar echo from hydrometeors (as opposed to noise or ground clutter) based on CPR radar returns. To maximize the detection of thin clouds and minimize false detection, the 2B-GEOPROF algorithm employs a spatial box filter in both the vertical and along-track directions centered on each range bin to identify coherent signals in the 1B-CPR backscatter profile (Marchand et al., 2008). To further improve detection capability, an independent cloud mask generated by applying an along-track moving average to the observed backscatter power is also generated and used to create a combined cloud mask. A confidence is assigned to each cloudy range bin at the native CloudSat resolution based on the results of these two methods of cloud identification. The primary validation needs for 2B-GEOPROF are precise measurements of cloudy layers from radar with higher vertical and spatial resolution and more sensitivity. Elements of the methodology such as the averaging scales used, and the cloud probability thresholds adopted can also be tuned to strike an optimal balance between false detections and missing clouds using ground-based and suborbital observations.

2B-GEOPROF also reports the surface bin and identifies ground clutter-contaminated range bins with a cloud mask value of 5. Furthermore, unlike precipitation radars, water vapor can significantly attenuate W-band radar, especially in the tropics where two-way attenuation from the surface to the satellite can exceed 5 dB. 2B-GEOPROF supplies an estimate of profile of attenuation due to gases (water vapor and the less pronounced effects of oxygen) based on ECMWF analyses that is generally applied to correct the reported unattenuated reflectivity profiles before subsequent cloud and precipitation retrievals. Both the ability of the algorithm to discriminate between clouds and ground clutter as well as the estimated attenuation profile require verification against independent observations.

Cloud Scenario Classification (2B-CLDCLASS)

All cloudy scenes observed by CloudSat are classified into one of eight canonical cloud types recognized universally by surface observers. The cloud classification algorithm, 2B-CLDCLASS, classifies clouds as either St, Sc, Cu, Ns, Ac, As, deep convective, or high cloud, based on their cloud top temperature, cloud base height, horizontal and vertical dimension, and maximum reflectivity which indicates the presence of precipitation (Sassen et al., 2008; Sassen & Wang, 2008). Both rule-based and fuzzy logic approaches have been employed. Cirrus, cirrocumulus, and cirrostratus are all considered high clouds for the purpose of the classification while Cu includes both cumulus congestus and fair-weather cumulus. Radiance observations from the Moderate Resolution Imaging Spectroradiometer (MODIS) aboard Aqua are used to supply texture information to the algorithm. Like 2B-GEOPROF, the validating 2B-CLDCLASS requires precise delineation of cloud boundaries (both horizontal and vertical). In situ measurements of cloud phase and precipitation presence at the horizontal and spatial resolution of the CloudSat field of view are also required. Validation observations are also used to tune thresholds in the rule-based approach or refine training datasets in the fuzzy logic-based method.

Cloud Water Content (2B-CWC-RO)

2B-CLDCLASS determines the phase of the hydrometeors that may exist in each cloud observed by CloudSat. The cloud water content product, 2B-CWC-RO, utilizes this information to provide quantitative estimates of cloud liquid and ice water content and effective radii for each cloud layer observed by CloudSat's CPR. 2B-CWC is a combination of two distinct algorithms, one that applies to liquid clouds (Austin & Stephens, 2001) and the other that applies to ice clouds (Austin et al., 2009). Each algorithm applies optimal estimation to retrieve size distribution parameters and associated uncertainties for the liquid- and ice-phase portions of cloudy profiles that are used to compute corresponding liquid and ice water contents. In addition to qualitative information from 2B-CLDCLASS, 2B-CWC-RO applies temperature thresholds to ECMWF analysis temperature profiles to separate the liquid, ice, and mixed portions of clouds that extend across these thresholds. The liquid- and ice-only retrievals are combined to produce continuous profiles of liquid and ice water content at the standard 240 m CloudSat range bin resolution.

The 2B-CWC-RO output requires three forms of validation: a priori algorithm assumptions and thresholds, profiles of retrieved size distribution parameters and liquid and ice water content, and uncertainties. Verifying and improving algorithm assumptions requires observations of temperature-dependent ice and liquid particle number concentrations and effective radii in a wide range of cloud types and environments to form the a priori distributions and covariances employed in the retrieval. Validating the 2B-CWC-RO products themselves, requires coincident measurements of liquid and ice water contents and effective radii from airborne sensors in clouds sampled by CloudSat. Since 2B-CWC-RO produces explicit uncertainty estimates linked to the a priori, measurement, and forward model error covariance matrices, it is important to verify that the differences between in situ and remotely-sensed cloud properties obey approximately Gaussian distributions and fall within the stated standard deviations.

Precipitation (2C-PRECIP-COLUMN, 2C-RAIN-PROFILE, 2C-SNOW-PROFILE)

All cloudy scenes observed by CloudSat are also probed for the presence of precipitation. CloudSat's 2B-PRECIP-COLUMN product uses attenuation- and multiple-scattering-corrected reflectivity to identify precipitating (raining and snowing) radar profiles (Haynes et al., 2009). All CloudSat profiles are classified as either not precipitating or assigned a probability that they contain rain, snow, or mixed-phase precipitation based on applying thresholds to corrected reflectivity in the lowest usable range bin above the ground clutter. Rain and snow are discriminated by applying a melting model to temperature and humidity profiles from ECMWF analyses. Any precipitating profile with more than 90% of the hydrometeor mass melted is classified as rain while any profile with less than 10% melted is classified as snow. Profiles with melted fractions between 10 and 90% are classified as mixed phase to reflect uncertainty in the phase classification.

Even more so than GPM, attenuation from hydrometeors significantly impacts the CloudSat reflectivity profile to the point where rainfall can completely attenuate the radar signal well above the surface. To mitigate this challenge, CloudSat's precipitation products also make use of the surface backscatter return to estimate PIA (L'Ecuyer & Stephens, 2002). Unlike GPM, the PIA information is not used to tune the assumed DSD, but rather used to provide a first-order attenuation correction to the reflectivity profile and a rough estimate of rainfall

intensity assuming that rain is vertically uniform below an estimated rain top height (e.g. Meneghini et al., 1983). The top of the rain column is estimated by searching for an inflection point in the reflectivity profile noting that strong attenuation when rainfall is present causes reflectivity to decrease significantly toward the surface. Comparing the estimated rain top height to the local freezing level also provides a means for identifying convective cores whenever the rain top exceeds the freezing level by more than 1 km.

While not a profile product, output from 2C-PRECIP-COLUMN is used to drive retrievals of rainfall and snowfall intensity and its output must be validated to characterize the quality of the subsequent precipitation intensity retrievals. Assessing this product requires measurements of near-surface precipitation phase and measurements of two-way attenuation at W-band due to hydrometeors for coincident CloudSat under flights. More generally, independent observations of surface winds and surface radar backscatter can also be used in the algorithm to refine relationships used to derive PIA constraints.

All raining scenes identified by 2C-PRECIP-COLUMN are further processed by the 2C-RAIN-PROFILE algorithm. L'Ecuyer & Stephens (2002) demonstrated that the (Hitschfeld & Bordan, 1954) attenuation correction method rapidly becomes unstable even in light rain (>1 mm h^{-1}) so the algorithm uses PIA estimates based on observed surface backscatter as a strong constraint via optimal estimation. The algorithm models attenuation from both rain and cloud water (Lebsock et al., 2011) and inverts the radar equation to retrieve surface rainfall rate and profiles of precipitating liquid and ice water content consistent with CPR reflectivities (Lebsock & L'Ecuyer, 2011). The algorithm also outputs estimated hydrometeor attenuation profiles and a multiple-scattering correction that accounts for multiple-scattering within the CloudSat field of view. Surface rainfall rate and coincident profiles of rain drop size distribution and the ratio of ratio of total water content that resides in the form of cloud droplets to raindrops are needed to validate the 2C-RAIN-PROFILE product. Satellite under flights with higher spatial resolution airborne W-band radar can be used to validate the associated multiple-scattering corrections.

W-band radar also provides the most direct measure of falling snow from space across the full range of snowfall regimes (Kollias et al., 2007). Snow particle size distributions (PSDs) and snowfall intensities for all snowing scenes identified by 2C-PRECIP-COLUMN are estimated in CloudSat's 2C-SNOW-PROFILE algorithm. The algorithm applies an optimal estimation approach to retrieve the slopes (L) and intercepts (N_0) of exponential snow particle PSDs ($N(D) = N_0 e^{-LD}$) in each CloudSat range bin from observed CPR reflectivities (Wood & L'Ecuyer, 2021). The algorithm utilizes temperature-dependent first guesses and novel particle scattering models derived from ground-based observations (Wood et al., 2015). In principle, validating 2C-SNOW-PROFILE outputs requires snow particle size distribution and snowfall rate measurements from CloudSat under flights but any measurements relating snow microphysical and scattering properties to surface snowfall rate in distinct environments have proven useful for verifying algorithm assumptions.

At present, scenes determined to contain possible mixed-phase precipitation (modeled melted fractions at the surface between 10% and 90%) are not processed. This precipitation category can best be interpreted as an 'uncertain phase' flag for which algorithm assumptions appropriate for determining surface precipitation phase are not known. Validation datasets providing explicit discrimination of precipitation phase at the surface as a function of temperature, dew point temperature, and other cloud characteristics may provide an avenue

for expanding the application of CloudSat's precipitation intensity algorithms to more of these uncertain scenes.

Following the discussion of key CloudSat products and applied calibration/validation methods, the Table 2.7 aims to highlight, in a validation perspective, which geophysical products can be expected from correlative to the benefit of CloutSat products validation.

Table 2.7 *CloudSat Level-2 Geophysical Property Profile Parameters to Validate*

Qualitative Parameters	Description	Resolution (spatial; vertical)
Cloud presence	Probability of hydrometeor echo in radar volume	CloudSat FoV; 240 m
Cloud type	Qualitative cloud type	CloudSat FoV; Column
Cloud phase	Layer cloud phase: liquid, ice, mixed	CloudSat FoV; 240 m
Precipitation presence	Precipitation confidence: possible, probable, certain	CloudSat FoV; Surface range bin
Precipitation phase	Rain, snow, mixed/uncertain	CloudSat FoV; Surface range bin
Cloud liquid and ice water content	Layer liquid and ice water content (g m^{-3})	CloudSat FoV; 240 m
Rainfall rate	Rainfall rate profile (mm h^{-1})	CloudSat FoV; 240 m
Snowfall rate	Snowfall rate profile (mm h^{-1} water equivalent)	CloudSat FoV; 240 m
Snow particle size distribution	Profiles of slope (L) and intercept (N_0) parameter	CloudSat FoV; 240 m

2.3.2. GPM precipitation radar products

2.3.2.1. GPM Dual-frequency Precipitation Radar (DPR) products

The Global Precipitation Measurement (GPM) is a NASA/JAXA satellite mission conceived to provide measurements of precipitation worldwide every three hours (Hou et al., 2014; Skofronick-Jackson et al., 2017). On February 27th, 2014, the GPM Core Observatory (CO) satellite was launched and started its operation in March 2014. The satellite orbits the Earth 16 times per day using a non-sun-synchronous orbit between 65°S and 65°N latitude. The GPM CO carries an instrumentation that includes the Dual-Frequency Precipitation Radar (DPR) consisting of a Ku-band radar (KuPR; 13.6 GHz) and a Ka-band radar (KaPR; 35.5 GHz). The GPM-CO follows the Tropical Rainfall Measuring Mission (TRMM), also a joint mission of JAXA and NASA. In orbit since 1997 to 2015, it was the first mission using a satellite equipped with a radar conceived to measure precipitation, namely the Precipitation Radar (PR), that operated at the single frequency of 13.8 GHz in the Ku-band (Kozu et al., 2001;

Kummerow et al., 1998; Okamoto, 2003; Takahashi et al., 2016). With respect to TRMM, the GPM CO satellite uses a non-sun-synchronous orbit with an inclination of over 65° to provide measurements at mid-latitudes through 16 orbits per day, that were excluded by the TRMM's orbit, with an inclination of 35°. The major innovation of GPM-CO is the addition of Ka-band radar designed for increased sensitivity and to take advantage of dual frequency measurements for more accurate classification of precipitation and retrieval of precipitation properties that include Drop Size Distribution (DSD) estimation.

During ten years of operation, both scanning modes and products have evolved. Focusing on the DPR Level 2 products, the version 03 adopted at launch, was replaced by updates and the current one effective from July 1st 23 is the V07B. The reference for the L2 products is the Algorithm Theoretical Basis Document (ATBD) document, the latest concerning V07B being (Iguchi et al., 2023). Although algorithms have been modified and improved since the at-launch version and the set of output products enriched, some original ideas and the overall processing architecture have been preserved.

A major change affected the scanning mode of the two radars. DPR radars are not nadir looking profilers but have scanning capabilities that allow investigating horizontal structure of clouds and precipitation. The KuPR performs a cross-track scan (Normal Scan, NS) consisting of 49 beams with incidence varying from −17° to +17° with respect to nadir, resulting in a scan width at ground of 245 km. The native range (i.e. height) resolution was 0.250 km, but, after oversampling, profiles are presented at a resolution of 0.125 km. KaPR operated two different scans. The matched scans (MS) make 25 angle bins in the inner swath with central beam at nadir, to match the beams of KuPR with a range resolution resampled to 0.125 km with a cross-track coverage between -8.5° and 8.5° corresponding to a 125 km swath at ground. A high sensitivity scan (HS) was performed in an interleaved mode, again in the inner swath, but allowing an increased sensitivity at the expense of rage resolution that was 0.5 km (3.33 μs pulse duration) resampled to 0.250 km L2 products. Dual frequency methods were possible only in the inner swath. The ground resolution (footprint size) of DPR in the different modes was about 5 km at surface but the minimum detectable reflectivity was estimated in 15.46 dBZ for the Ku_PR, and 19.18 and 13.71 dBZ, for the Ka_PR in MS and HS mode, respectively (Masaki et al., 2020) implying that, at best range resolution KuPR is more sensitive than KaPR. Such sensitivities are suitable for a wide range of liquid and solid precipitation, according to the mission goals.

In November 2023, GPM-CO performed two orbit boost maneuvers that raised its altitude from 400 km to 435 km in order to allow its life to extend in the early 2030, to make the GPM mission overlap with the satellites of Atmosphere Observing System (AOS) mission planned by NASA, JAXA, and other agencies, allowing intercalibration between the GPMs' and AOS satellites' instruments.

Proper radar calibration is essential for retrieving high quality precipitation products and profiles. The GPM DPR uses an active calibration procedure described in Masaki et al. (2020), where four years of calibration results are reported. A ground-based active calibrator to assure that the spaceborne radar at both Ka- and Ku-bands are calibrated within ± 1 dB. Calibration consistency between GPM KuPR and TRMM PR measurements of natural scatterers was exploited by Kanemaru et al. (2020) to estimate actual parameters of the radars.

Later, the high sensitivity beams of the interleaved mode were redirected to the outer swath; since then the Ku-band and Ka-band beams have been approximately matched over the full 245 km swath (JAXA/NASA, 2018, (Awaka et al., 2021)). From 21 May 2018, the KaPR HS scan was modified to make beams to match those of the Ku-band in the two bands from -17° to -8.5° and from +8.5° to +17°, i.e., the outer swath. As a result, matched dual-frequency products are possible for the full swath (FS). After testing (Awaka et al., 2021; Seto et al., 2020, 2021), such products were available from December 2021 as Version 07A.

Geophysical products pertain to Level 2 (L2) processing, obtained from Level 1 products that contain pre-processed radar measurements, surface type classification, but also ancillary variables useful for L2 processing. The L2 algorithms yield single frequency (SF) products, that involve measurements from one of the two radar and dual frequency (DF) products, that advantage on dual-frequency radar measurements and are available for different scans depending on the acquisition data (i.e. before or after 21 May 2018).

The processing for DPR L2 products follows the architecture in Figure 2.2, which is basically the same since Version 03 although the 6 modules underwent different and significant changes. The architecture is generic enough to describe both DF and SF products although details of single modules can contain significant differences. The following subsection summarizes the 6 interconnected modules and a new module added in Version 07 (Trigger module). Output L2 files contain many variables, many of which are used internally by the processing modules. Specific tables of this document report a selection of major geophysical outputs available. A field with the same name can follow a different coding if obtained with DF or SF algorithms. See Iguchi et al. (2023) for a complete list of products. It should be noted that the latest version of TRMM products were obtained with a processing similar to that of DPR (Stocker et al., 2018).

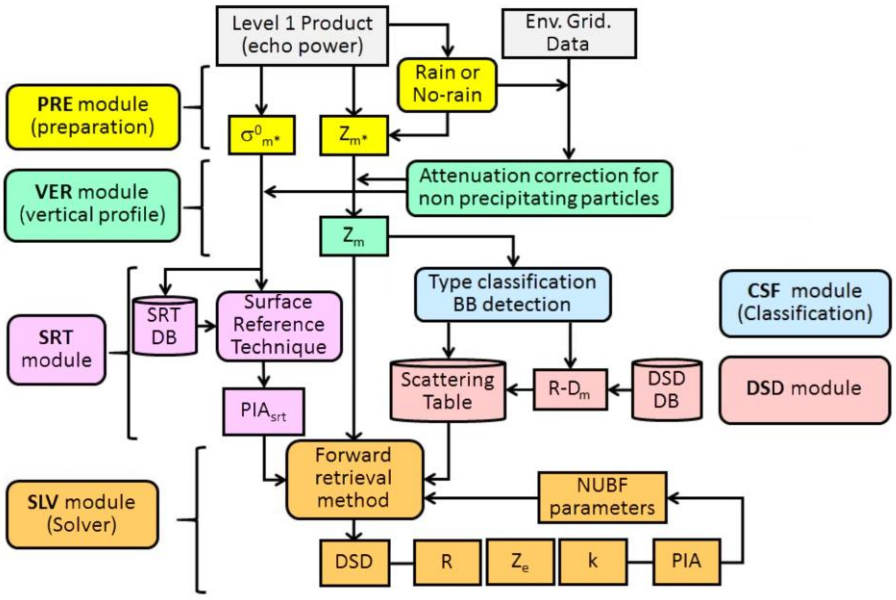

Figure 2.2 *Schematic diagram of the standard DPR algorithm (From Iguchi et al. (2023)).*

Preparation (PRE) module

The *Preparation* (PRE) is an interface module that prepares raw Level 1 input products and external information to be used by the other modules of the L2 processing. Using the measurement of the power received by the two radars, system parameters, orbit, and scan geometry, it computes the reflectivity factors, reduces the influence of clutter (Kanemaru et al., 2021; Kubota et al., 2016, 2018), identifies the surface range bin (using power measurements) and lower clutter-free bin (CFB, i.e. the one with reliable precipitation measurements closest to the terrain). The height CFB depends on the orography and the range resolution of the considered product and on the local zenith angle that increases as a function of the distance from the nadir and at the edges of the outer swath. Differences of the CFB height with respect to that at nadir can exceed 1 km, while are lower in the inner swath. L2 products are also provided below the CFB through extrapolation. Finally, *Preparation* identifies the pixels with precipitation that will undergo further processing and provides the measurements of the normalized surface cross section (NRCS) used for the attenuation correction (Kanemaru & Hanado, 2023).

Vertical profile (VER) module

The main function of the *VER* module is to provide vertical profiles of environmental parameters such as pressure, temperature, water vapor, and cloud liquid water by ingesting the ancillary environmental data provided by the Japan Meteorological Agency (JMA) Global Analysis (GANAL) product. From these data, the attenuations resulting from the non-precipitating particles, such as water vapor, molecular oxygen, and cloud liquid water, are computed and used to correct the measured reflectivities (Kubota et al., 2020).

Classification (CSF) module

The CSF module classifies precipitation according to categories such as stratiform and convective, as well as precipitation that is neither stratiform nor convective. In addition, it provides information on the bright-band characteristics (bright-band top, peak, and bottom ranges) using two different products (Awaka et al., 2016, 2021; Awaka & Brodzik, 2019), one being DF specific (Le et al., 2016), flags associated with heavy ice precipitation (HIP), anvil precipitation, the surface snow, and graupel and hail. Table 2.8 summarizes the information available from the CSF module. All the outputs are provided as 2D matrices defined by the number of beams depending on the scanning mode, and the number of scans.

Table 2.8 *Summary of major CSF Output Variables*

Geophysical information	**Description**
Bright band characteristics	Bright band detection flag, peak, bottom, width
Melting Layer	Melting layer top, bottom (DF)
Precipitation classification	Classification is provided in terms of stratiform, convective, other, transition, convective winter (DF only)
Shallow rain	Shallow rain (isolated or non-isolated) detected.
Heavy ice precipitation (HIP)	HIP detection flags, height of bottom and top of detected HIP
Hail	Hail detection flag
Anvil precipitation	Anvil precipitation detection flag

DSD module

This module plays a critical module for retrievals, providing the size distribution models employed for different hydrometeors, along with, mass densities, dielectric constants, and fall velocities of the particles are also specified in the module. For the DPR algorithms, the drop/particle size distribution is assumed to follow a normalized gamma model that, with the shape parameter μ=3, takes the form of a 2-parameter PSD that can be expressed in terms of the mass weighted mean drop diameter D_m (mm^{-1}) and the "normalized intercept parameter" N_w (mm^{-1} m^{-3}), related to liquid water content LWC and D_m is factorized as

$$N(D;N_w,D_m) = N_w f(D,D_m)$$

Limiting to a 2-parameter form is somehow necessary for algorithms relying on no more than two measurements, which are the equivalent reflectivities measured by the two radars. An R-D_m is assumed that allows, in the SLV module, to apply the proper retrieval algorithm.

Based on different CSF outputs, a profile is subdivided through nodes that imply the use of different particle models and related scattering tables. In general, particles are modeled as a mixture of air, water, and ice expressed with different volume ratios. Being DSD set in the rain phases, conversion of diameter is obtained by assigning to D the role liquid equivalent diameter for melting or ice drops and maintaining the same mass flux between the different phases of precipitation (see Table 2.9 for a summary of outputs).

Table 2.9 *Summary of DSD outputs*

Geophysical information	***Description***
Phase	3D matrix (bin x ray x scan) with a code indicating temperature and bright band limits
Nodes	5 bins partitioning the profiles in segments used in solver retrievals.
Parameters of *R-D_m* relation	Available on the five nodes

Surface Reference Technique (SRT) module

The primary purpose of *SRT* is to estimate path integrated attenuation (PIA) using the surface returns (Meneghini et al., 1983), a technique already applied at Ku-band for TRMM (Iguchi et al., 2000). The SRT charges differences of the NRCS in rain and no-rain areas to the attenuation due to rain, although NRCS changes also because of wind and rain over the ocean (Tanelli et al., 2005), especially far from nadir, and by rapidly changing scattering properties over land. Meneghini et al. (2021) presents an overview of the recent implementations of the SRT along with an assessment of their performance. The module implements different versions of SRT, based on the NRCS provided through the PRE module. One uses rain-free areas close to a rainy area whose NRCS are averaged to obtain the reference NRCS for rain areas. Different estimates are obtained using different averaging and the SRT module arrives at four PIA spatial reference estimates. The different estimates are combined into an effective PIA estimate by weighting the individual estimates by a factor that is inversely proportional to the variance of the reference estimate. A further method obtains the reference NRCS in a target area when rain is absent from time averaging and obtained values are applied to estimate the PIA in the presence of rain.

Similarly, differential PIA estimates are obtained from the difference between the NRCS at the two frequencies. Since rain-free NRCS are correlated at the two frequencies, the variance of the rain-free reference estimate is typically smaller than the SF counterparts resulting in more accurate estimates of differential PIA and, eventually, of the precipitation estimates.

A further PIA estimation method combines the SRT with the Hitschfeld & Bordan (1954) method since the first works well in heavier rain and the opposite is true for the second. The methods are combined with weights inversely proportional to the variance of their estimates.

The Solver (SLV) module

The SLV module uses a set of inputs from other modules, namely the measured reflectivities (from PRE), the PIAs from *SRT* corrected by the output for non-precipitating particles from *VER* and the *R-D_m* relations, along with phase information from the *DSD* module. The output is a set of "columns" of parameters including precipitation rate *R* in mm^{-1} h^{-1}, parameters of DSD (D_m, N_w) effective (corrected) reflectivity and specific attenuation *k* (dB/km). DPR algorithms (both DF and SF) relies on a relationship between rain rate R and D_m adjusted by a parameter ε determined through a series of equations aiming at reconciling inconsistencies between PIA obtained by the different attenuation estimation techniques with the PIA obtained at ground from DSD profiles. A detailed description of latest versions of the algorithms along with a rigorous mathematical formulation and preliminary validation can be found in Liao & Meneghini (2019, 2022) and Seto et al. (2021), which also describes the derivation of the scattering table and the $R-D_m$ relation as well as the procedure correction for non-uniform beam filling (NUBF).

The SF algorithms took origin from the one used for the TRMM Ku radar algorithm developed using relations between intrinsic reflectivity at Ku band and the specific attenuation *k*. In GPM it has been replaced by an equivalent of the $R-D_m$ relation that has the advantage of linking geophysical parameters and not frequency-dependent parameters. The advantages of the dual-frequency algorithm rely on the increased reliability of the dual-frequency SRT and the availability of a method called ZfKa, a method with similarities to SRT, but can use measurements from KuPR or KaPR. This is different from the pre-launch and at-launch versions of the algorithms, where dual frequency retrievals were based on DFR (the ratio between reflectivities at Ka and Ku band), which is, theoretically, an estimate of D_m (Mardiana et al., 2004). However, this approach was proven to be unstable also after validation.

The rationale of the algorithm can be explained in a narrative form as follows. Having assumed a gamma DSD with a fixed shape parameter, it is possible to establish an R- D_m for various effective reflectivities. In this way, given an effective reflectivity factor and an initial value of ε, an (R, D_m) pair can be obtained, and, using the tables established in the DSD module, the corresponding N_w and specific attenuation coefficient *k* can be obtained as well. The process starts from the top, where the measured reflectivity is supposed to be unattenuated and can be corrected iteratively using the estimated *k*. Once the procedure is applied to the entire column, a PIA profile is also obtained. The process is repeated with different ε profiles to minimize the retrieved PIA at the surface level with the SRT-estimated PIA is chosen (Liao & Meneghini, 2019). Table 2.10 summarizes information available from the SLV module. Outputs can be presented as 3D (bin x ray x scan) or 2D (bin x scan) matrices. The latter are used sometimes to express the value of profiles at certain surfaces or their integration along the vertical (not shown in the table).

Table 2.10 *Summary of major SLV Output Variables*

Geophysical information	Description
Solver Flag (2D)	For each profile indicates the presence of precipitation, the location below surface or a bad quality of the measurements
Bin echo bottom (2D)	The range bin 176 (or 88 in HS) is at the ellipsoid. The bottom of echo is specified.
Particle size distribution(3D)	Profiles of N_w, D_m
PIA (2D)	Path integrated attenuation by precipitation consistent with DSD profiles (different from SRT estimate by an offset tha is provided as output)
Reflectivity factor (3D)	Effective reflectivity factor profile consistent with DSD
Precipitation rate (3D)	Profiles of precipitation rate in mm/h
Precipitable water (3D)	Profiles of precipitable water in g/m^3
Correction factor “epsilon” (3D)	Adjustment from the original distribution (ε =1 mean no adjustment)
Correction for NUBF (2D)	Parameters used to correct for NUBF (not applied if the ratio between the rain area and FOV is equal to 1)

The TRG module

This module is implemented as a new standard product in L2 algorithm V07 and is executed before the call to the SLV module to identify the presence of multiple scattering and NUBF. Detection of multiple scattering is based on identification in the measured Ku and Ka-band reflectivity profiles of the “Multiple-Scattering tail” or “Ghost Echo” that decay from a maximum value reached above, or around the 0°C isothermal to a minimum value that appears below the surface following a smooth curve with a concave shape. This behavior was first observed on the CloudSat DPR (Battaglia et al., 2008; Tanelli et al., 2012) and TRMM PR data. The occurrence is quite rare but is more frequent in Ka band (Battaglia et al., 2015; Battaglia et al., 2014a). A further multiple scattering feature is the “DFR Knee” (Battaglia et al., 2014a). Being multiple scattering triggered by large frozen hydrometeors in the upper troposphere and affects more Ka-band than Ku, the slope of the measured reflectivity of KaPR diminishes towards the surface and can become smaller than that at the Ku-band, which is unlikely under single scattering.

A second algorithm aims to diagnose NUBF at Ka-band based on consistency between PIA at the two frequencies and the PIA related to DSD retrievals in the hypothesis of absence of NUBF. Deviations from this behavior are indications of NUBF (Seto et al., 2021).

2.3.2.2. GPM DPR validation

An integral part of a successful satellite mission to measure global rainfall is a robust and active ground validation program. The GPM Ground Validation (GV) was designed from the start as a key part of the overall GPM program. During the TRMM era, GV was limited to simple comparisons of rain rates observed by the TRMM PR and/or TMI instruments to surface measurements from radars and/or rain gauges, which is referred to as “Statistical Validation.” During TRMM, it became obvious that a more robust GV program needed to be developed to

better aid satellite algorithm developers to improve the physics of their algorithms rather than just tweaking their outputs. So, for GPM, a three-tiered approach was developed (Hou et al., 2014): 1) *Statistical Validation*, as done during TRMM; 2) *Physical Validation,* where the emphasis was on better understanding the physics and microphysics of different precipitating systems; and 3) *Hydrological Validation*, which emphasized improving precipitation retrievals on large scale areas (e.g. watersheds).

To address this new paradigm, the GPM Ground Validation (GV) was launched to assess and improve the performance of the different releases of the DPR algorithms. The program was included various field campaigns targeting specific precipitation, such as heavy snow and mixed-phase precipitation (Skofronick-Jackson et al., 2015), thunderstorms (Heymsfield et al., 2015; Jensen et al., 2016), intense rain and floods (Petersen & Krajewski, 2013), and orographic precipitation (Houze et al., 2017), in addition to supporting to international campaigns. To obtain continuous correlative precipitation measurement, fixed sites with dual-polarization scanning radars such as the GPM Validation Network consisting of S-band radars from the U.S. NEXRAD, network raingauge and disdrometers of different kind (Schwaller & Morris, 2011). In addition, the GPM established an international cooperation for GV to obtain information from different regions of the globe. Many validation studies have been conducted that provided useful feedback to the algorithm developers, despite known issues related to validation. Comparison results have shown some variability that can be charged to different climatologies but also to issues like space and time mismatches between the spaceborne and ground instruments an instrument specific issues, differences in frequencies (that implies different attenuation effects), the presence of blind ranges in both in satellite and ground-based radars (GR) that does not allow a direct comparison between surface in situ measurements with DPR measurements collected aloft. In case of point measurements (disdrometers or rain gauges), the attempt is to compare continuous measurements in time at a single location, with satellite nearly instantaneous but spatially averaged measurements. GPM Level I requirements specified that DPR rain estimate biases relative to ground radars should be within ± 50% at rates of 1 mm hr-1 and within ± 35% at rates of 10 mm h^{-1} (Petersen et al., 2016). Figure 2.3 shows the Normalized Mean Absolute Error (NMAE), Root Mean Squared Error (RMSE) and Bias when comparing the DPR Ku rain estimates to the Kwajalein S-band polarimetric radar estimates. The green polygons outline requirement boundary for 1 and 10 mm/h illustrating that indeed the Level I requirements are met.

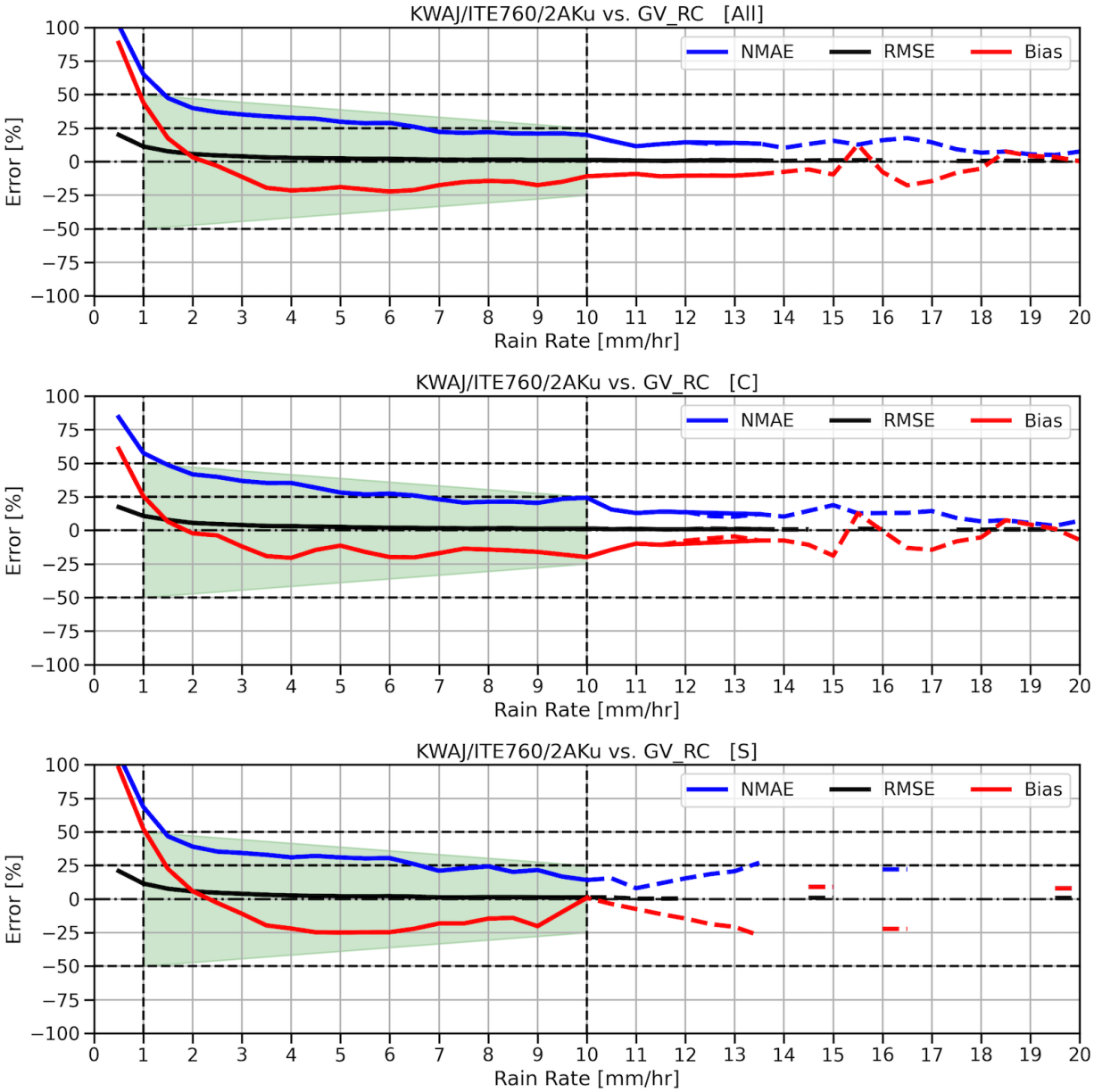

Figure 2.3 *Statistical comparison between ground-based radar rain estimates at Kwajalein Atoll to DPR Ku (V07). GPM Level I requirements stated that biases between DPR Ku and ground radars should be within ± 50% at 1 mm hr-1 and ± 25% at 10 mm hr-1. The panels show the biases met requirements (green shaded polygon) for "All" rain types (top), "Convective" (middle), and "Stratiform" (bottom). The blue lines represent the Normalized Mean Absolute Error (NMAE), the black lines represent the Root Mean Squared Error (RMSE), and the red lines represent the Bias = (GV - DPR)/GV in percent.*

Biswas & Chandrasekar (2018) using the VN network found correlations between reflectivity from DPR and GR of ~0.9 at Ku-band and ~0.85 at Ka-band with higher values in stratiform rain. Other studies targeting precipitation rates were conducted with radar in Switzerland, were a DPR underestimation of winter precipitation was found (Speirs et al., 2017), in Italy (Petracca et al. (2018), who pointed out the issue of characterizing the quality of GR estimates), UK (Watters et al., 2018), and finally, in Germany, where a three year of comparison of DPR precipitation rates with those from precipitation product of the German Weather Service correlation provided a correlation coefficient of 0.61 and the root mean square error of 1.83

mm h^{-1} (version 5). Dense gauge networks were used for precipitation rate comparison (Lasser et al., 2019; Tan et al., 2018) since they can account for the variation of rain within the DPR footprint. However, they cannot account for the vertical variation of rain within the sampling volume and between the surface and the DPR useful measurement closer to the terrain (actually several hundred meters above the surface, depending on the orography).

Concerning snow, GRs have also been used for the validation of snow products. Le & Chandrasekar (2019) evaluated the surface snowfall flag using GR dual-pol classification capabilities, while Mroz et al. (2021) compared the DPR snowfall rate with the US MRMS radar snow product (https://www.nssl.noaa.gov/projects/mrms/) over from November 2014 to September 2020, highlighting a DPR underestimate snowfall rates by a factor of two attributed to the complexity of the ice scattering properties and the limitations of the remote sensing systems such as the limited DPR sensitivity.

For ground-based radars, there are several statistical and data-driven methods available, but most facilities do not have active calibrators to employ. For dual-polarized radars, the properties of the precipitation system can be used to estimate the absolute calibration of the radar. Chandrasekar et al. (2015) discuss multiple techniques for the calibration of radar reflectivity.

Gorgucci et al. (1992) developed a technique that uses a combination of differential reflectivity and differential phase measurements in rain to estimate the absolute calibration of reflectivity. Scarchilli et al. (1996) quantified the consistency between reflectivity Z_H, differential reflectivity Z_{DR}, and specific differential phase (K_{DP}). Gorgucci et al. (1999) showed via theoretical calculations and radar observations that the three polarization diversity measurements, Z_H, Z_{DR}, and K_{DP}, lie in a constrained space that can be approximated by a three-dimensional surface. Most of these previously mentioned techniques required the presence of large rain rates (greater than 50 mm h^{-1}) at the S-band for a sufficiently reliable K_{DP} measurement to be observed.

Ryzhkov, Giangrande, et al. (2005) used Area-Time Integrals (ATI) to develop a self-consistency methodology that did not require large rain rates. In this method, measured K_{DP} is compared to an estimated K_{DP} derived as a function of Z_H and Z_{DR}. The bias between observed Z_H and the absolute reflectivity was then quantified as the Z_H needed for the respective ATIs to agree.

Once an absolute calibration has been determined, GPM GV uses a technique referred to as the Relative Calibration Adjustment (RCA) (Marks et al., 2011; Silberstein et al., 2008; Wolff et al., 2015) to monitor the system calibration on an hourly or daily basis. In this method, the 95th percentile of clutter-area reflectivity was found to be quite stable in the absence of any external calibration differences. Louf et al. (2019) utilized both self-consistency and RCA techniques to post-calibrate over 20 years of data observed by the Australian Bureau of Meteorology C-band Polarized (CPOL) radar. GPM GV utilizes both methodologies for routine quality control and calibration of NASA's POLarimetric (NPOL) radar (Wolff et al., 2015) and other GV radars.

GR and disdrometer were used also for microphysics. Using C-band dual-pol radars and GPM products in Italy, a good agreement between the Dm estimates was found, pointed out by an absolute bias generally lower than 0.5 mm (D'Adderio et al., 2019). Based on the S-band

radars of the VN network, the DPR Dm estimate was found to be generally affected by a 0.2 mm bias, with an overestimation of ~0.5–0.6 mm in convective precipitation (Gatlin et al., 2020).

An increasing number of studies have been conducted to compare the DPR rain and DSD estimates to ground-based disdrometer measurements. Starting from version 4 of DPR products, studies show a Dm was in good agreement with disdrometer measurements but uncertainties in normalized intercept parameter (N_w) occurred (this is consistent with findings obtained with dual-pol radars). Studies based on long-term datasets of disdrometer were performed in China (Wu et al., 2019) with five years of Parsivel measurements, in Italy with a network of disdrometers (Adirosi et al., 2021) some of which operated in the period 2014 to 2020 and in North Taiwan (Seela et al., 2024). All of them generally agree on the different behavior of Dm and Nw, although report different values of uncertainties for the different DPR modes.

In general, DPR precipitation retrieval algorithms are complex and use many assumptions. Detecting specific issues in DPR algorithms based on specific GV is not a straightforward process. Despite this, the performance of different versions of the algorithms has improved significantly with respect to the performance of the DPR algorithms at launch.

2.3.3. EarthCARE Cloud Profiling Radar product

EarthCARE is equipped with a 94-GHz Cloud Profiling Radar (CPR), developed by JAXA and the National Institute of Information and Communications Technology (NICT). It is a coherent pulse radar using the same frequency as the CloudSat CPR although its minimum sensitivity is better than -35 dBZ at 20-km height ASL with 10 km horizontal integration, (i.e. 5 dB better than CloudSat due to lower orbit and the larger antenna of 2.5-m diameter) to measure profiles of reflectivity, and for the first time from space, Doppler velocity. The range of the Doppler velocity depends on the pulse repetition frequency (PFR). The unfolded Doppler Velocity (i.e. the Nyquist velocity, takes the value from 5.7 to 6.0 ms^{-1} for high PRF and from 4.9 to 5.2 ms^{-1} for low PRF, respectively (Hagihara et al., 2023; Okamoto, Sato, Nishizawa, Jin, Nakajima, et al., 2024), with an accuracy of at least 1.3 ms^{-1} from specification for homogeneous cloud echoes of more than -19 dBZ integrated over a 10 km horizontal distance.

The transmit pulse width is 3.3 microseconds corresponding to the vertical resolution of 500m (the same as CloudSat CPR). However, the received echo is over-sampled to achieve a 100 m resolution (it was 250 m in CloudSat after oversampling). The vertical observation ranges from -1 km below the surface to a height of 16, 18, or 20 km, which is selectable according to latitude. The PRF varies with satellite altitude and observation height considering the contrasting needs for Doppler accuracy and width of vertical range. The antenna allows an instantaneous footprint size of 750 m at the ground while averaged data are produced every 500 m along the track. To compare, the instantaneous footprint of the CloudSat CPR measures 1.4 km in diameter and is integrated over 0.16 seconds, resulting in an effective footprint of 1.4 km by 1.8 km produced every 1.1 km.

The CPR Level 1 product contains radar reflectivity and Doppler velocity detected from cloud and precipitation particles that can be used to derive L2 products also in synergy with other EarthCARE instruments. The CPR uses several methods to calibrate and verify performance along time including also internal sources to monitor transmit power and receiver. External

calibration means for Transmitter, Receiver and end-to-end include ARCs (Active Radar Calibrator) at ground which can also provide the antenna pattern and pulse shape during overpasses.

For the sea surface calibration, the EarthCARE satellite performs a roll maneuver at regular intervals (e.g. once a month) in order to take into account NRCS sea variability on wind and incidence angle. CPR level 1 processing also includes detection surface echo bin, estimation of NRCS and calculation of Doppler velocity of the surface, while CPR Level 1b product contains the measured radar reflectivity and vertical Doppler velocity profiles.

2.3.3.1. ESA EarthCARE cloud products and their validation needs

The National Aeronautics and Space Administration (NASA) A-Train satellite constellation, as demonstrated by Stephens et al. (2002), showcased the potential of W-band radar observations from space. The EarthCARE mission, recently launched on 28 May 2024, introduces the first space-borne cloud profiling radar (CPR) with Doppler capability (Kollias et al., 2023), which in comparison to its predecessor CloudSat, boasts higher sensitivity (5-6 dB more sensitive), better vertical sampling (100 versus 240 m), improved along-track resolution (500 versus 1100 m), a smaller Instantaneous Field of View (IFOV, 800 versus 1400 m), and includes Doppler velocity measurements (Illingworth et al., 2015). Leveraging these advancements, the EarthCARE CPR is poised to generate an improved set of radar observables, encompassing radar reflectivity, Path Integrated Attenuation (PIA), and Doppler velocity. Following post-processing and quality control, these observables are fed into the CPR-only Cloud and Precipitation Microphysics Retrieval (C-CLD) product.

The Cloud and Precipitation Microphysics (C-CLD) represents an L2 data product that leverages data from the EarthCARE 94-GHz Doppler Cloud Profiling Radar (CPR) to furnish microphysical details regarding cloud and precipitation systems. Adopting a profile-by-profile approach, the C-CLD algorithm utilizes radar-only measurements, including CPR feature mask and radar reflectivity (C-FMR), CPR Cloud Doppler parameters (C-CD), and CPR target classification (C-TC), as detailed by Kollias et al. (2022). Employing an optimal estimation (OE) approach, the algorithm balances information derived from the CPR measurements with a-priori knowledge about the climatology of cloud and precipitation systems. Its primary goal is to retrieve profiles of two moments of the particle size distribution (PSD), specifically, the mean mass-weighted diameter and the condensed water mass content in the CPR measurement volumes. Initially, the C-TC hydrometeor classification output is used to determine the occurrence of specific hydrometeor types (such as ice cloud, snow, rimed snow, melting snow, cold rain, warm rain, non-drizzling liquid cloud, drizzling liquid cloud), playing a crucial role in selecting the appropriate branch of the C-CLD retrieval process. In scenarios involving drizzle-free and lightly drizzling warm clouds, the OE framework is substituted with climatological relationships linking measured reflectivities to the microphysical parameters of interest. The algorithm's outputs feed into the composite cloud and aerosol profiles product (Cole et al., 2023), contributing essential data for further analysis, as explained in Eisinger et al. (2024). The discussion below highlights the key components of the algorithm. For more detailed information on the C-CLD algorithm, please refer to Mroz et al. (2023).

As depicted in the flowchart presented in Figure 2.4, the C-CLD processor exhibits a modular structure. Specific algorithms have been designed to retrieve various cloud system types, encompassing liquid clouds, drizzle, ice/snow, cold rain resulting from snow melting aloft, and

warm rain. The choice of algorithm relies on the radar-based Target Classification product (C-TC). The retrieval process for liquid clouds and light drizzle relies on power law relationships, as more sophisticated methods yield comparable uncertainties in microphysical parameters

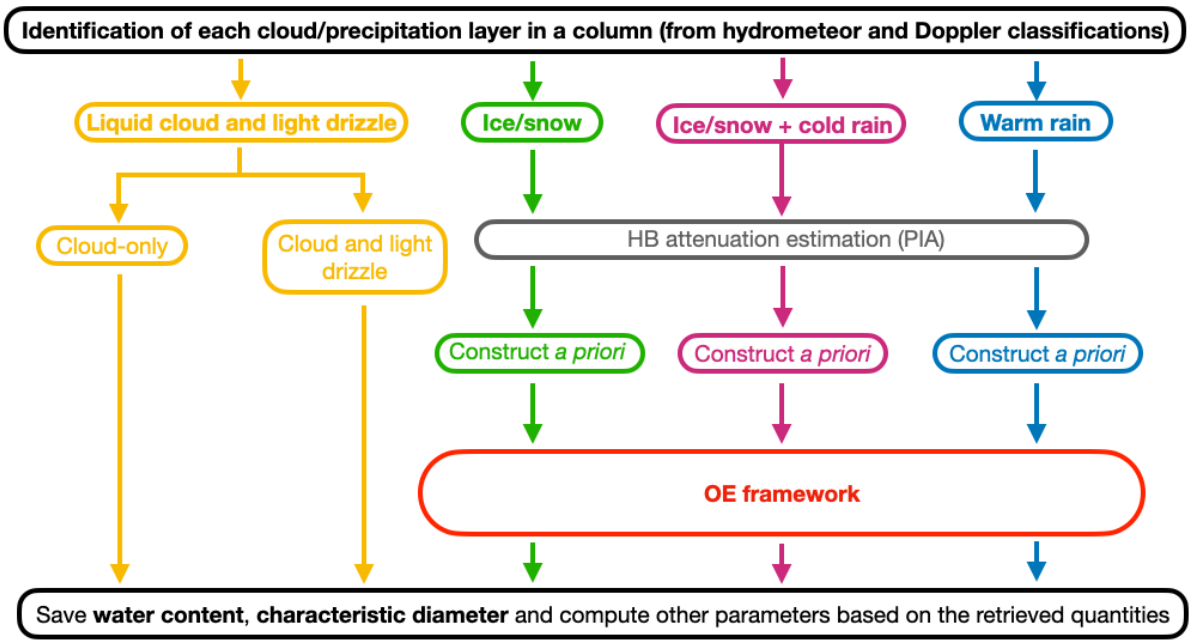

Figure 2.4 *Schematic diagram of the standard C-CLD algorithm (Mroz et al., 2023)*

For profiles containing only liquid clouds, the vertical structure of cloud Liquid Water Content (LWC) is deduced from reflectivity values using the LWC − Z_e relationship

$$LWC = <A> Z_e^{1/2},$$

with the value of <A> determined from path-integrated attenuation estimates. The retrieval of LWC for light drizzling clouds combines an estimate of cloud mass content based on the adiabatic profile assumption and the LWC derived from reflectivity (Baedi et al., 2000; Sauvageot & Omar, 1987). It's important to note that the retrieval of heavy drizzle is incorporated within the rain retrieval process, categorized as a subset of warm rain.

For solid precipitation, ice clouds and rain, the C-CLD algorithm employs an Optimal Estimation framework. This framework seamlessly integrates all available information from the EarthCARE CPR with statistical knowledge about the precipitation process. The statistical insights into the precipitation process stem from a dataset of NASA disdrometer data (Dolan et al., 2018). This dataset is utilized to create joint probability distribution functions of microphysical parameters relevant to the algorithm, so-called “a-priori” estimates.

Similar to the DPR retrieval, the drop/particle size distribution assumes a normalized gamma model in which the shape parameter (μ) is dependent on the mass-weighted (melted-equivalent) diameter (D_m) through

$$\mu = 10\, D_m^{-0.8} - 4,$$

as this relation is deduced from the NASA disdrometer data. The PSD is parameterized using the concept of double moment normalization, with mass-weighted mean diameter (D_m) and condensed Mass Content (MC) being used as the characteristic parameters:

$$N(D; D_m, MC) = MC\, f(D; D_m) ,$$

where f denotes the shape function of the DSD model. Estimating vertical profiles of D_m and MC for clouds and precipitation across the entire tropospheric column is the primary task of the C-CLD algorithm.

The disdrometer dataset also plays a role in establishing forward model relations between bulk precipitation properties and radar observables, and the associated simulation uncertainty is quantified, with quantified associated simulation uncertainty. Different modules of the C-CLD algorithm share forward model components; for instance, the radar simulator in cold rain is the same as in warm rain, and the simulation of snow overlying cold rain mirrors that of snow falling on the ground.

The scattering properties of snow particles are obtained using the discrete dipole approximation corresponding to realistic snowflake shapes (Leinonen et al., 2016). These snowflakes consist of dendrites of different sizes and are subject to varying degrees of riming. The terminal velocity of ice crystals and snowflakes was estimated using the hydrodynamic model of Böhm (1992). In contrast, the scattering properties of rain are less variable and are simulated using the T-matrix approximation assuming the aspect ratio of raindrops follows the formula of Brandes et al. (2005). Terminal velocities were estimated from a dataset of Gunn & Kinzer (1949).

The effectiveness of the C-CLD retrieval framework was evaluated using simulated observations from the EarthCARE CPR in high-resolution weather system simulations across three distinct climatological settings (Donovan et al., 2023): tropical climate, humid continental climate (Halifax), and mid-latitude conditions over North America (Baja). This evaluation demonstrated that the CPR reflectivity and Doppler radar measurements provide sufficient information to confidently retrieve two moments of the PSD, especially in rain, where Doppler measurements offer additional value. On average, D_m of rain can be estimated within a precision of 23% while the uncertainty of the MC estimate is estimated to be 67%.

However, the retrieval of D_m for ice poses the most significant challenge, as the terminal velocity of snowflakes is not strongly dependent on particle size. Additionally, simulations used for validation lack precipitation events with melted equivalent D_m exceeding 1 mm. These conditions pose a particular challenge for W-band retrievals due to significant signal attenuation and saturation of radar reflectivity and Doppler measurements (Mróz et al., 2020). There is a need for increased effort in validating the product in this regime, as it is crucial for accurate precipitation quantification. Notably, 88% of the total precipitation volume reported by NASA disdrometers is generated by DSDs with D_m greater than 1 mm.

The C-CLD algorithm was crafted to align with ground-based disdrometer measurements, a strategy that proves advantageous for precipitation quantification. However, this approach may introduce biases in radiative closure studies, as the assumptions about the DSD shape derived from disdrometer data might not accurately represent light rain and drizzle (Bringi et al., 2020). Furthermore, the same disdrometer data were used to derive assumptions for snow, based on the assumption that rain originates from snow melting and neglects interactions

between hydrometeors en route to the disdrometer. Particle concentration has also been adjusted to accommodate differences in sedimentation velocities of snow and rain particles, ensuring mass flux preservation.

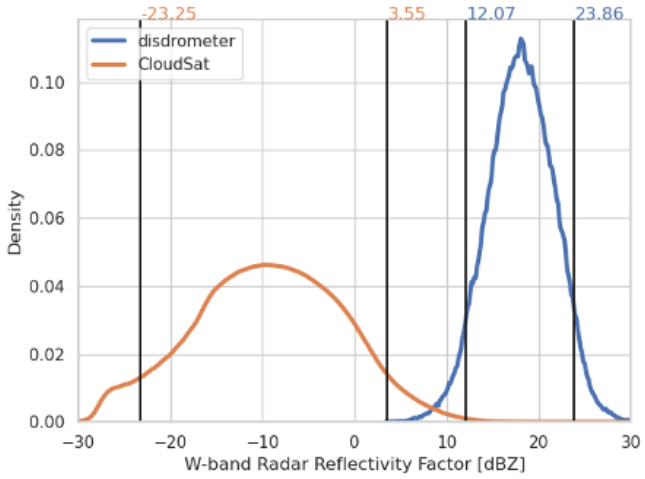

Figure 2.5 *Probability distribution functions of W-band radar reflectivity in rain. The orange line shows CloudSat effective reflectivity from the 2C-RAIN-PROFILE product, while the blue line represents simulated reflectivity based on NASA disdrometer measurements. The vertical lines indicate 5th and 95th percentiles.*

For instance, the validity of the μ-D_m relationship used across the size range becomes questionable for D_m values below 0.8 mm, as traditional disdrometers face challenges in capturing small drops. Notably, only 5% of CloudSat retrievals in rain align with radar reflectivity exceeding 3.5 dBZ, while disdrometer-simulated reflectivities never dip below this threshold. Conversely, 95% of disdrometer data corresponds to W-band reflectivity greater than 12 dBZ, a threshold exceeded in only 0.2% of CloudSat rain measurements (Figure 2.5). This stark contrast underscores the complementary nature of these two datasets, offering valuable insights into rain processes across different regimes. However, it also implies that the C-CLD product may not be well-suited for light rain conditions as it is biased toward higher precipitation rates. This proposition warrants testing with real data rather than relying solely on model simulations, which inherently carry some assumptions about the DSD.

Furthermore, this underscores the radar community's need for broader access to DSD datasets that encompass the entire spectrum of particle sizes, from drizzle to precipitation mode. To our knowledge, such datasets are scarce in airborne measurements, where the primary focus tends to be on ice microphysics. Ground-based efforts in this direction have only started in recent years (Bringi et al., 2020) and, unfortunately, are not totally available to the public. To address this knowledge gap, utilizing data from vertically pointing radars, particularly those operating in W or G bands, becomes a viable alternative. These radars not only provide accurate wind retrievals, crucial for high-quality DSD products (Battaglia et al., 2014b; Schoger et al., 2021), but also offer sensitivity surpassing that of the EarthCARE radar. Moreover, their sample volumes are significantly larger than those of disdrometers, enhancing compatibility with space-borne observations.

Finally, characterizing the distribution of the liquid cloud mass in the radar profiles, including supercooled clouds, is essential for reducing uncertainties in path-integrated attenuation simulations and retrieved rain/snow mass content below the liquid cloud. As suggested by Battaglia & Panegrossi (2020), this issue can be mitigated by assimilating the W-band brightness temperatures in the retrieval. This opportunistic measurement, estimated from the receiver noise, has been proven to provide important insight on the cloud and precipitation microphysics (Lebsock & Suzuki, 2016).

In addition, in order to produce realistic transitions in the retrieved state vector between consecutive profiles, future algorithms could make use of the two-dimensional information provided by the radar. This should help not only in preserving the continuity of the state vector but also in the quantification of NUBF (and its correction) and in the detection of non-precipitating liquid clouds whose boundaries tend to have long correlation lengths and therefore can be detected outside from precipitating systems where they may be visible and extrapolated inside precipitating systems where their signal is masked by the larger hydrometeors.

2.3.3.2. JAXA EarthCARE cloud products

2.3.3.2.1. JAXA EarthCARE CPR and CPR-synergy products

JAXA EarthCARE products are divided in two categories, Standard Product (ST) and Research Product (ER/LR). Majority of the algorithms in the Standard Products are already well researched and have heritage from past studies. They are strongly promoted to be developed, which are processed and released from JAXA Mission Operation System. The algorithms of the Research Product contain new research developments that are challenging, yet scientifically valuable. They are promoted to be developed and are processed and released as standard products when the release criteria are satisfied from either JAXA Earth Observation Research Center and/or Japanese Institute/Universities. The CPR L2 products are processed using 1-km and 10km horizontally integrated CPR reflectivity and Doppler velocity. Both versions of the products are reported at each 1km and 100m horizontal and vertical grid spacing. The overview of the major JAXA L2 products and algorithms are provided in Okamoto, Sato, Nishizawa, Jin, Nakajima, et al. (2024) and Figure 2.6 shows the flow of the JAXA L2 cloud products.

Table 2.11 provides a taxonomy of both Level 1 and Level 2 CPR products. Details of processing are provided in the ATBD (JAXA, 2024). Stand-alone CPR products are obtained by L1 products, although some basic corrections are applied at Level 2, such as the clutter echo correction, and gas attenuation correction for reflectivity and Doppler unfolding, the latter likely occurring in strong rainfall. Products are obtained at 1 km and 10 km horizontal integration resolution and associated quality flags are provided. Processing includes surface detection and the estimation of NRCS (normalized radar cross section), Gas attenuation correction (obtained by NWP and ITU specific recommendations) and PIA (Path Integrated Attenuation) estimation. Finally, the processing maps the products onto the joint standard grid (JSG grid) for EarthCARE.

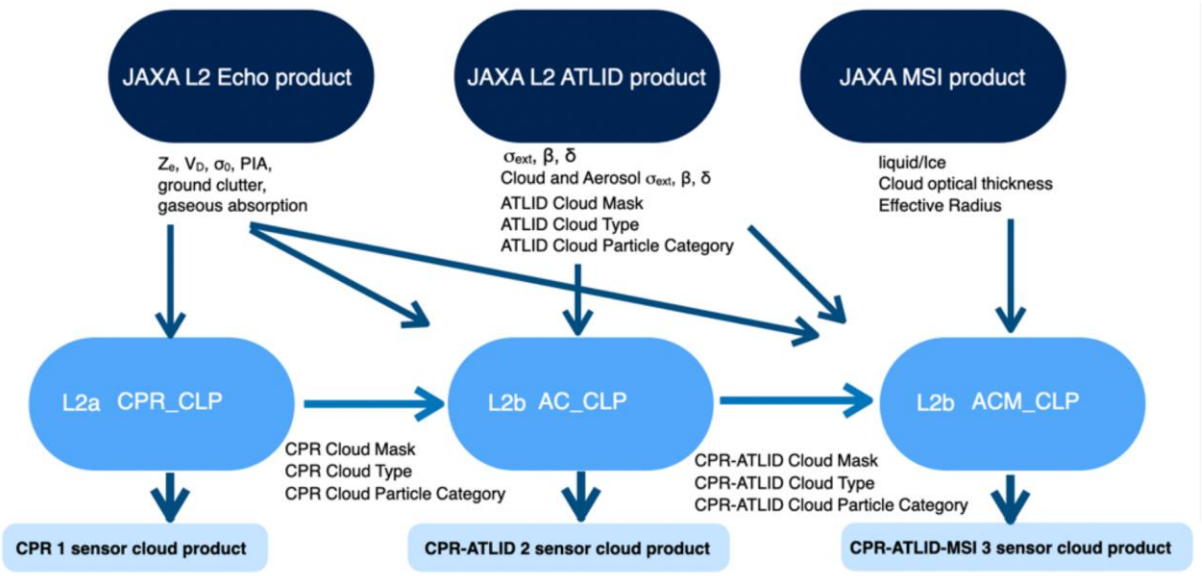

Figure 2.6 *Flow of the JAXA L2 cloud products (from Figure 1 of Sato et al. (2024))*

Table 2.11 *Name and primary parameters of CPR-only and CPR synergy products (please refer to text and JAXA EarthCARE CPR ATBD Level 2, 2024, for a more precise description of parameters)*

Product	Primary parameter	Product Type
• CPR one-sensor Received Echo Power and Doppler Product (L1b)	(1) Received Echo Power (2) Radar Reflectivity Factor (3) Surface Radar Cross Section (4) Doppler Velocity (5) Pulse Pair Covariance (6) Spectrum Width	ST
• CPR One-sensor Echo Product (L2a)	(1) Integrated radar Reflectivity (2) Integrated Doppler Velocity (3) Gas Correction factor	ST
• CPR One-sensor Cloud Product (L2a) • CPR-ATLID Synergy Cloud Product (L2b) • CPR-ATLID-MSI Synergy Cloud Product (L2b)	(1) cloud mask (cloud and precipitation) (2) cloud type: warm water, supercooled water, randomly oriented ice crystal (3D-ice), horizontally oriented plate (2D-plate), 3D-ice + 2D-plate, liquid drizzle, mixed-phase drizzle, rain, snow, mixed-phase cloud, water + liquid drizzle, water + rain, melting layer (3) cloud particle category: warm water, super-cooled water, 2D-plate, 2D-column, bullet rosette/3-D aggregate type, droxtal/compact type,	ST

	Voronoi/irregular type, fractal snow aggregates (4) cloud-and precipitation-microphysics: Effective radius(Reff)/LWC/IWC/Number concentration (No), Reff1, Reff2, WC1, WC2, Cloud phase1, Cloud phase2, No1, No2, LWP/IWP (5) Optical Thickness	
• CPR One sensor Doppler Product (L2a)	(1) Doppler velocity correction value (considering inhomogeneity) (2) Doppler Velocity Unfolding value	ER/LR
• CPR One sensor Rain and Snow Product (L2a) • CPR One sensor Vertical Velocity Product (L2a) • (CPR-ATLID Synergy Rain and Snow Product (L2a) • CPR-ATLID Synergy Vertical Velocity Product (L2a) • CPR-ATLID-MSI Synergy Cloud Doppler Product (L2a) • CPR-ATLID-MSI Synergy Rain and Snow Product (L2a) • CPR-ATLID-MSI Synergy Vertical Velocity Product (L2a)	(1) Attenuation Corrected Radar Reflectivity Factor (2) LWC*/IWC*/No*/LWP*/IWP* /Rain Rate/SnowRate /OpticalThickness* (3) In-cloud Doppler velocity/Vertical Air Motion / Sedimentation velocity (* ST with Doppler)	ER/LR

JAXA EarthCARE L2 CPR Echo Product

The primary parameters contained in the JAXA CPR L1b Received Echo Power and Doppler Product are received echo power, radar reflectivity factor, surface radar cross section, Doppler velocity, covariance of pulse pair, and spectrum width. The JAXA L2a CPR Echo Product contains, integrated radar reflectivity factor integrated Doppler velocity and gas correction factor as primary standard product. For research products, the JAXA L2a CPR Doppler product contains corrected Doppler velocity considering inhomogeneity and Doppler velocity unfolding. These products are developed by National Institute of Information and Communications Technology (NICT) (Okamoto, Sato, Nishizawa, Jin, Nakajima, et al., 2024).

JAXA EarthCARE L2 cloud- and precipitation- Products

The JAXA L2 cloud algorithms consists from cloud mask, cloud type, cloud microphysics and vertical velocity products and have been extended from those developed for CloudSat, CALIPSO and MODIS to produce KU-JAXA EarthCARE A-train products (provided via JAXA A-Train Product Monitor). The KU CloudSat-CALIPSO merged data sets and cloud products (developed by Kyushu University), CALIPSO aerosol products (developed by National Institute for Environmental Studies (NIES)), MODIS cloud products (developed by Tokai University) are provided and updated to the latest version by JAXA EarthCARE Research A-Train Product Monitor

(https://www.eorc.jaxa.jp/EARTHCARE/research_product/ecare_monitor_e.html). These L2 products were assessed using simulated EarthCARE L1 orbit data created from the Japanese global cloud-resolving model, the Nonhydrostatic Icosahedral Atmospheric Model (NICAM) with Joint simulator (Okamoto, Sato, Nishizawa, Jin, Nakajima, et al., 2024).The standard cloud products are derived without the usage of Doppler velocity (V_D). Similar products are produced for the research products but derived by additional use of V_D. Brief description is provided in the following.

(1) cloud mask (cloud and precipitation) products

The JAXA standard L2 CPR cloud mask algorithm considers the signal to noise ratio and spatial continuity (coherent filter) to identify significant signals from noise, reduce the misclassification of clouds, and to assign a confidence level (Hagihara et al., 2010, 2014; Okamoto, Sato, Nishizawa, Jin, Ogawa, et al., 2024). Here, in order to remove the effect due to noise, a threshold for the radar echo power proposed by Okamoto et al. (2007, 2008) are used, which was evaluated against lidar and sky camera. The Doppler function is used to improve discrimination between clouds, precipitation and phase of precipitation for ER/LR products (Okamoto, Sato, Nishizawa, Jin, Ogawa, et al., 2024). For the CPR-ATLID synergy products, the hydrometeor mask and aerosol mask for ATLID use vertically varying criteria function determined from ALTID observables and atmospheric profiles, and a spatial coherent filter for the hydrometeor mask (Hagihara et al., 2010; Nishizawa et al., 2024; Okamoto, Sato, Nishizawa, Jin, Ogawa, et al., 2024). The cloud masks for ATLID and CPR are combined to produce CPR cloud mask (C1), ATLID cloud mask (C2), CPR and ATLID cloud mask (C3), CPR or ATLID cloud mask (C4) products (Okamoto, Sato, Nishizawa, Jin, Ogawa, et al., 2024).

(2) cloud particle (cloud and precipitation) type products

The JAXA Standard L2 CPR-cloud particle type algorithm, extended from Kikuchi et al. (2017) primary uses information of radar Z_e and temperature from the European Center for Medium-range Weather Forecasting (ECMWF) to infer cloud phase, shape and orientation, cloud or water or ice precipitation (Okamoto, Sato, Nishizawa, Jin, Ogawa, et al., 2024). Two-dimensional diagrams of Z_e and temperature, normalized radar cross section, vertical Z_e profile and a spatial continuity test scheme are used to discriminate nine hydrometer types (warm water supercooled water, 3D-ice, 2D-plate, liquid drizzle, mixed-phase drizzle, rain,snow, melting layer). The CPR particle discrimination scheme is trained with CALIOP cloud particle type classification (Yoshida et al., 2010) and Tropical Rainfall Measuring Mission (TRMM) radar measurements collocated with CloudSat radar (Kikuchi et al., 2017). JAXA Research L2 CPR- cloud particle type algorithms further combine V_D in addition to Z_e for improved discrimination of clouds and liquid precipitation (Okamoto, Sato, Nishizawa, Jin, Ogawa, et al., 2024). To improve the CPR estimates, the JAXA L2 CPR-ATLID and CPR-ATLID-MSI synergy cloud particle type algorithms further combines the ATLID-only hydrometeor particle type (Nishizawa et al., 2024; Okamoto, Sato, Nishizawa, Jin, Ogawa, et al., 2024), which produces 7 particle types (e.g., warm water, super-cooled water, 2-D plate, 3-D ice, 2D-plate and 3D-ice mixture, mixed phase (water+3D-ice), unknown), and produces total 14 type classification (warm water, supercooled water, randomly oriented ice crystal (3D-ice), horizontally oriented plate (2D-plate), 3D-ice + 2D-plate, liquid drizzle, mixed-phase drizzle, rain, snow, mixed-phase cloud, water + liquid drizzle, water + rain, unknown and melting layer) (Okamoto, Sato, Nishizawa, Jin, Ogawa, et al., 2024). The liquid- and ice- phase discrimination in the ATLID-

only hydrometeor particle type algorithm was developed based on 355nm Multiple-Field-of-view Multiple Scattering Polarization Lidar developed in Nishizawa et al., 2021; Okamoto, Sato, Nishizawa, Jin, Ogawa, et al. (2024).

(3) cloud particle category products

JAXA L2 cloud particle category product enables a more detailed comprehensive exploration of the dominant particle habit category contained within each JSG grid (warm water, super-cooled water, 2D-plate, 2D-column, bullet rosette/3-D aggregate type, droxtal/compact type, Voronoi/irregular type and fractal snow aggregates) (Sato et al., 2024). For ice phase particles, the 2-D ice, 3-D ice, snow and mixed-phase particle types in the CPR-only and synergy cloud particle type products are further classified into 6 ice categories based on Sato & Okamoto (2023), where estimation of cloud particle category was demonstrated using complementary observations from CALIPSO lidar. The cloud particle category product is based on information from ATLID depolarization ratio and lidar ratio (Okamoto et al., 2019, 2020). This ATLID-based classification method is extended to cloud scenes detected by CPR, and the CPR-ATLID and CPR-ATLID-MSI cloud particle category products are created (Sato et al., 2024).

(4) In-cloud velocity products

The JAXA Research L2 CPR vertical velocity product reports the Doppler velocity at cloud and precipitation masked radar bins. Doppler velocity folding is corrected based on vertical and horizontal patterns of Z_e and V_D (Okamoto, Sato, Nishizawa, Jin, Nakajima, et al., 2024). The in-cloud vertical velocity can be derived from the difference between V_D and the estimated reflectivity-weighted particle sedimentation velocity (V_{tz}). Further, simultaneous microphysics, sedimentation velocity, and vertical air-motion(V_{air}) retrieval algorithm combining CPR Z_e, V_D and their normalized vertical structures, ATLID backscattering coefficient and depolarization ratio are also developed for the JAXA Research L2 CPR-ATLID/CPR-ATLID-MSI synergy vertical velocity products (Sato et al., 2009).

(5) cloud- and precipitation- microphysics products

The JAXA L2 CPR, CPR-ATLID and CPR-ATLID-MSI synergy algorithms for cloud and precipitation extend previous algorithms developed for CloudSat and CALIPSO synergy. Lidar depolarization ratio was combined with Z_e and β to retrieve the microphysical properties of mixture of 2D and 3D nonspherical ice particle types based on physical optics (Iwasaki & Okamoto, 2001) and the discrete dipole approximation (DDA) (Okamoto, 2002; Sato & Okamoto, 2006) from CloudSat and CALIPSO, where the variation of mean lidar ratio was treated (Okamoto et al., 2010). Further, a framework to extend the applicability of the microphysics retrieval algorithm to the entire cloud and precipitating region observed by CloudSat or CALIPSO was developed (Sato & Okamoto, 2011, 2020).

The JAXA L2 CPR, CPR-ATLID and CPR-ATLID-MSI synergy algorithms retrieve the microphysics corresponding to each particle category (Sato et al., 2024). ATLID σ_{ext}, δ, β and CPR Z_e, V_D, and s_0/PIA are used to determine the microphysics. The single scattering properties of the nonspherical ice particle categories are calculated using physical optics (Borovoi et al., 2012) and modified geometrical optics integral equation methods (Masuda et al., 2012) for the ATLID specification (Okamoto et al., 2019, 2020) and using the discrete dipole approximation (DDA) and finite difference time domain method (FDTD) for the CPR wavelength, and multiple scattering effects are estimated based on Sato et al. (2018, 2019)

and Sato & Okamoto (2020). The cloud microphysics scheme considers the maximum of two different size distributions at each JSG grid (i.e., Reff1, Reff2, WC1, WC2, No1, No2, Cloud phase 1, Cloud phase 2).

Additional information about cloud properties are obtained also from MSI sensors. The JAXA L2 MSI one-sensor Cloud Products for liquid clouds and the JAXA L2 MSI one-sensor Ice Cloud Product report cloud mask from the cloud/clear discrimination algorithm (CLAUDIA) and cloud properties such as cloud optical thickness from the cloud microphysical properties algorithm (CAPCOM) (Ishida & Nakajima, 2009; Nakajima et al., 2019), respectively. The CPR-ATLID-MSI synergy algorithms use the output from JAXA L2 MSI and improve the CPR- and CPR-ATLID microphysics retrieval.

2.3.3.2.2. Validation needs and observations planned for EarthCARE

Evaluation of EarthCARE cloud mask, cloud particle type, cloud/precipitation microphysics and corrected Doppler velocity products can be categorized into those using (1) ground-based radar and synergistic sensors, (2) Space borne sensors and (3) JAXA EarthCARE L1 synthetic data from the Nonhydrostatic ICosahedral Atmospheric Model (NICAM) and Joint-Simulator.

(1) Evaluation of EarthCARE products by ground-based radar and synergistic sensors

Several unique collocated radar and lidar instruments installed at EarthCARE super-site in Koganei, Tokyo (Japan), are planned for the evaluation of EarthCARE measurements and products.

- There are two 94GHz cloud radars installed targeting EarthCARE; High-sensitivity Ground-based Super Polarimetric Ice-crystal Detection and Explication Radar (HG-SPIDER) and Electronic Scanning SPIDER (ES-SPIDER) (Horie et al., 2000).
- HG-SPIDER has a minimum sensitivity of -40dBZ at 15km and exceeds -60dBZ at 1km. Although, it is expected that higher sensitivity of EarthCARE CPR will detect more thin ice clouds and low-level clouds that consist of small particles compared with CloudSat, some clouds with Z_e smaller than the CPR minimum sensitivity may not be detected. HG-SPIDER with its high sensitivity can provide an assessment of the limitation of CPR cloud detections. The Doppler function of HG-SPIDER can be utilized to first evaluate EarthCARE CPR velocity products. Aliasing correction in CPR velocity products will be tested by using the HG-SPIDER data where much higher accuracy of V_D is expected. V_D from HG-SPIDER is also crucial for the evaluation of cloud particle types because precipitation can be easily discriminated. ES-SPIDER has an electrically scanning function so that horizontal inhomogeneity of clouds can be detected. By using ES-SPIDER, non-uniform beam filling (NUBF) effect in V_D measured by EarthCARE can be evaluated.
- There are several lidars with new capabilities developed to aid the CPR- and CPR-synergy cloud and velocity products for EarthCARE. Multiple-Field-of-view Multiple Scattering Polarization Lidar (Nishizawa et al., 2021; Okamoto et al., 2016) can be used to investigate the effect of multiple scattering on microphysics retrieval and test multiple scattering schemes (Sato et al., 2018, 2019; Sato & Okamoto, 2020). High spectral resolution lidar (HSRL) (Jin et al., 2020, 2022) is effective for cloud particle/aerosol typing (Kong et al., 2022; Okamoto et al., 2019, 2020). Doppler lidar information is another key source of information to evaluate velocity products. For the

evaluation of air-motion and terminal velocity products, wind profiler and Doppler lidars (Coherent Doppler lidar at 2μm (Iwai et al., 2013) and incoherent (direct detection) Doppler lidar (Ishii et al., 2022) can be effective. Doppler radars with different frequencies produce different Doppler velocity for the same target, and the same is true for the difference between radar and lidar Doppler velocity. Therefore, terminal velocity and air motion comparisons among radars or lidar are preferable. Wind profiler has been proven to be effective to validate V_{air} retrieved from 94GHz cloud radar. Full one-to-one validation of the retrieved V_{air} has been performed by collocated 94GHz Doppler cloud radar and VHF Doppler radar measurement (Equatorial Atmospheric Radar) every 3 min. The spatial structure of the retrieved in-cloud up-/downward V_{air} agreed closely with direct measurements (Sato et al., 2009). A large improvement in the microphysical retrieval was achieved due to accurate estimation of V_{tz} from V_D.

- Ground-based validation of solid/liquid precipitation products from satellites is not trivial due to differences in sampling areas, blind zones close to the ground where satellite measurements are unreliable, and the imitation of overpasses with precipitation. The use of a longer radar wavelength has the advantage of being less affected by attenuation from hydrometeors. The disdrometer and Micro Rain Radar, a 24 GHz (K-band) Doppler radar profiler are relatively common precipitation instruments suitable for unattended operation and available in many ground observation sites worldwide and in most of the research stations in Antarctica observation sites. Recent studies in Antarctica (Bracci et al., 2021) have demonstrated the usefulness of the synergy in providing reliable information on precipitation for the validation of satellite products. During the EarthCARE validation activities, a validation methodology for space-borne Doppler radar (here after K2W methodology) was developed which obtains the 94 GHz (W-band) radar reflectivity and Doppler profiles from radar Doppler spectrum at 24 GHz (K-band) and disdrometer observations through frequency conversion (Bracci et al., 2023). This K2W approach allows comparison and validation of radar reflectivity and Doppler profiles between ground-based and satellite-borne radar using affordable and low-maintenance instrumentation at the surface. By defining the appropriate sampling strategies and frequency conversion procedure for the simulation of space-borne measurements using ground-based observations, assessment of the K2W conversion methodology with coincident CloudSat measurements concluded that the K2W methodology could evaluate space-borne W-band radar reflectivity and Doppler velocity within 0.2 dB and 0.2 m s^{-1} for snow precipitation, respectively. Latest assessment of EarthCARE CPR Doppler velocity measurement accuracy from global simulations for precipitation suggests values <0.5 m s−1 for Z_e > 0 dBZ at 10 km integration for low pulse repetition frequency (PRF) case and a smaller value for high PRF case (Hagihara et al., 2023). The unattenuated W-band profile obtained by the K2W methodology is also useful to evaluate spaceborne W-band radar retrievals. The K2W method can provide particle velocity - diameter relation (i.e., habit information) and particle size distribution (therefore ice/liquid water content and effective radius) information at high temporal resolution along with the simulated W-band Doppler spectrum within and above the blind zone of EarthCARE CPR. The K2W method has a wide application and is highly valuable for long-term validation of satellite measurements and products. For the vertical profile, ground-based radars at different frequencies have been used for the validation of radar precipitation products. In the case of hydrometeor type discrimination, the dual

wavelength ratio (DWR) and the Doppler velocity difference from synergy analysis of X-, Ka- and W-band radar have been used.

(2) Assessments of EarthCARE products using Space borne sensors

There are several candidates such as CloudSat, CALIPSO, MODIS, AMSR-E, CERES to evaluate EarthCARE CPR and synergy products. As an example, the recent advancement in ice-particle backscattering theories (Okamoto et al., 2019, 2020) enables a more comprehensive exploration of the geographical distribution and seasonal dependence of ice-particle shape categories before Sato & Okamoto (2023). These datasets are used to statistically assess the EarthCARE hydrometeor category product. The new particle type discrimination data obtained in such study are also expected to be useful for deriving the ice particle fall velocity information globally, a key parameter in ice cloud parameterizations, which affects cloud amount, and the appropriate ice optical models to calculate ice cloud radiative fluxes. The EarthCARE single sensor and synergy sensor products can also be evaluated using the same products produced with higher-order synergy algorithms. The JAXA L2 four-sensors synergy radiative products (developed by University of Tokyo), generated by radiative transfer simulations with retrieved cloud and aerosol microphysical profiles used as input, are assessed for the consistencies among the retrieved microphysical profiles and the radiative fluxes through comparing the simulated and measured radiative fluxes as a “radiative closure assessment” (Yamauchi et al., 2024). This assessment is conducted through one-dimensional radiative simulations using MSTRN-X (Nakajima et al., 2000; Sekiguchi & Nakajima, 2008) that generate the radiative flux of the standard product (Yamauchi et al., 2024), and through three-dimensional radiative transfer simulations using MC-star (Okata et al., 2017) that generates the research product of radiative flux and heating rate.

(3) Assessments of the JAXA L2 products using JAXA EarthCARE L1 synthetic data from the Nonhydrostatic ICosahedral Atmospheric Model and Joint-Simulator

Simulated L1 satellite data are highly required for the development and assessment of L2 retrieval algorithms and products before launch. For this purpose, JAXA’s EarthCARE L1 synthetic data are constructed (Roh et al., 2023) using a 3.5km horizontal-mesh global storm-resolving model simulation performed with NICAM (Satoh et al., 2008, 2014; Tomita & Satoh, 2004) and a satellite simulator (Hashino et al., 2013, 2016). CPR Radar reflectivity, Doppler velocity and ATLID data were simulated by the EarthCARE Active Sensor Simulator (EASE) (Nishizawa et al., 2008; Okamoto et al., 2007, 2008), MSI signals were calculated by System for Transfer of Atmospheric Radiation (RSTAR) (Nakajima & Tanaka, 1986, 1988), and the radiative fluxes were simulated by the Model Simulation Radiation Transfer code (MSTRN) - X (Sekiguchi & Nakajima, 2008). This JAXA L1 synthetic data have helped to assess the expected errors of the EarthCARE CPR Doppler velocity obtained from pulse-pair covariances for different pulse-repetition-frequencies (PRF), along-track integration, and with and without unfolding corrections (Hagihara et al., 2021, 2023), as well as the MSI spectral misalignment (SMILE) effect on the cloud retrieval (Wang et al., 2023). JAXA L1 synthetic data are also being used to evaluate and improve the cloud, precipitation and aerosol retrieval algorithms (Nishizawa et al., 2024; Okamoto, Sato, Nishizawa, Jin, Ogawa, et al., 2024; Sato et al., 2024).

2.3.4. INCUS Mission Overview

The INvestigation of Convective UpdraftS (INCUS) mission was competitively selected as the 3rd NASA Earth Ventures Mission (EVM-3) and is planned to be operating in orbit with possible overlap to EarthCARE (with launch planned for no earlier than 2026). INCUS will provide the first tropics-wide investigation of the evolution of the vertical transport of air and water by convective storms (convective mass flux), one of the most influential, yet unmeasured atmospheric processes.

The goal of INCUS is to understand why, when and where tropical convective storms form, and why only some storms produce extreme weather. To this end, state of the art atmospheric modeling, a novel observing strategy and a machine-learning retrieval approach are essential integrated components. The INCUS observing concept hinges on the observation of the change of the vertical profile of the measured effective radar reflectivity factor Z_m by three copies of the Ka-band Dynamic Atmospheric Radar (DAR) over the timescale of 30 to 120 seconds (i.e., commensurate to convective processes), and on the near-simultaneous and collocated observations of brightness temperature by the multi-channel, scanning, millimeter-wave radiometer (Dynamic Microwave Radiometer, DMR) over a wider swath inclusive of the narrow swath where the radar measurements are acquired. The former provides the means to observe the vertical evolution of the water condensate at a particular location, while the latter provides the information needed to put that particular small-scale observation in the larger context of the storm or the atmospheric environment surrounding it. The DAR and DMR have significant heritage from their predecessors: the technology demonstrations in orbit of RainCube and TEMPEST-D, respectively. The primary difference between DAR and RainCube is that each radar will use a 1.6 m antenna (instead of RainCube's 0.5m) with 7 beams partly overlapped in the cross-track direction (instead of RainCube's single beam).

The primary scientific objective of INCUS is different, and yet related to EarthCARE's. Both missions include a significant component aiming at improving our understanding of convection and cloud dynamics: but the W-band instantaneous Doppler measurements by the EarthCARE CPR and the vertical change Ka-band reflectivity over 30 to 120 second baselines are expected to have quite different strengths and weaknesses. Given their unprecedented nature it is conceivable that joint analysis of their data, if made possible by their respective periods of operation in space, will reveal opportunities for cross-comparison and vicarious validation in some atmospheric scenarios, while providing completely complementary information or extension of applicability in other scenarios. The products released by INCUS are summarized in Table 2.12.

Table 2.12 *INCUS products*

Product Name	Description
Level 1 Products	
1A-PWR and 1B-ZM	Received power [dB] from each DAR, calibrated and geolocated, converted to measured reflectivity factor Zm [dBZ]. 1B-Zm includes also an echo mask and surface normalized radar cross section [dB].
1C-ZRG and 1C-ZPAC	Equivalent radar reflectivity factor Zm from all spacecrafts, resampled on a regular grid. ZRG includes relative pointing error correction, ZPAC includes both pointing and advection corrections.
1B-Tb	Calibrated DMR brightness temperature (Tb) [K]
Level 2 Products	
2B-MASS	Vertical profile of condensate for each radar profile [kg m-3]
2B-MASS-RATE	Profile of temporal change in condensate for each radar pair [kg m-3 s-1]
2B-FLUXES	Profile of vertical mass flux of air and condensed-water estimated for every detected updraft [kg m-2 s-1]
2B-DT	2 min evolution of local advection, condensate and vertical fluxes in each cloud column
2A-HD	IWP [kg m-2] derived from the radiometer brightness temperature 1B-Tb
Level 3 and 4 Products	
3A-LIFE	Storm-centric LEVEL 2 and AUX data reported at half-hourly temporal resolution, labeled by storm
3B-CONV	Storm-wide statistics of vertical flux and environmental data, labeled by storm
4-CONV	Convection nowcasting system machine learning from 3B-CONV
Auxiliary Products	
AUX-GEOIR	Lifecycle from geo-IR, convection type from cold Tbs, anvil size from IR Tb threshold
AUX-REANAL	Large-scale environmental variables include CAPE, RH, T and shear
AUX-RSURF	Surface precipitation from Integrated Multi-satellite Retrievals and GPM (IMERG)
AUX-LIGHT	Lightning locations and flash rates from ground-based networks and spaceborne sensors
AUX-GPM-KA	Coincident (GPM combined retrievals of IWC) and (DPR Z_e)

2.4. Synergistic products

The exploitation of the complementary characteristics of lidar and cloud radar for the synergistic detection and retrieval of the profile of clouds, aerosols and precipitation was established in ground-based ((Donovan, 2003; Hogan & Connor, 2004; Illingworth et al., 2007; van Zadelhoff et al., 2004), and many others) and airborne ((Tinel et al., 2005), and others) applications ahead of the age of spaceborne radar-lidar synergy, beginning with the launches of CloudSat and CALIPSO in 2006.

While radar-lidar synergy from space has enabled unprecedented detail in the detection and measurement through the profile of the atmosphere, its insights are not omniscient. Lidar is sensitive to aerosols and small ice particles, but strong interactions with liquid cloud droplets quickly extinguish the lidar beam. Cloud radars are capable of detecting ice and liquid clouds, but the radar reflectivity is dominated by larger snowflakes, drizzle and raindrops. The radar beam is most strongly attenuated by liquid hydrometeors, and subject to multiple scattering in

heavily precipitating profiles. While the combination of lidar and radar measurements allows detection of targets from cirrus to the surface, synergistic radar and lidar measurements are mostly available near the tops of ice clouds where the lidar is not yet extinguished (e.g. the first three to five optical depths). In complex and layered cloud scenes, many uncertainties remain.

In this section we provide an overview of available synergistic CloudSat-CALIPSO products from the A-Train of satellites (Section 2.4.1), and of upcoming synergistic products from ESA for the EarthCARE mission (Section 2.4.2), whereas JAXA EarthCARE products involving radar were described in section 2.3.2.1.

We distinguish between two broad categories of synergistic products:

- Synergistic target classifications exploiting the complementary detection and classification from radar and lidar, in combination with a numerical weather forecast model profile of atmospheric temperature, to produce a near-complete profile of clouds, aerosols and precipitation in the atmosphere. This may be either a combined radar-lidar algorithm (e.g. DARDAR-MASK; (Ceccaldi et al., 2013)) or a two-stage production model (e.g. EarthCARE's ESA AC-TC product, which is a relatively simple merging of the ESA A-TC and C-TC) or the JAXA CPR-ATLID synergy products described in Section 2.3. Most of these products owe to the experience of A-train satellite synergy products.

- Geophysical retrievals exploiting radar and lidar measurements, as well as synergies with imaging radiometers. We may distinguish between different approaches to synergistic retrievals. For CloudSat-CALIPSO, distinct synergistic retrieval products for ice and snow have been created: DARDAR-CLOUD (Delanoë & Hogan, 2008, 2010) and 2C-ICE (Deng et al., 2010, 2013, 2015). For retrievals of other classes of hydrometeors, other synergies are applied, such as radar-radiometer for liquid cloud water content (Leinonen et al., 2016), or lidar-radiometer retrieval of liquid cloud (Schulte et al., 2023). For ESA EarthCARE products, a single unified synergistic retrieval estimates the properties of ice clouds, snow, liquid clouds, rain and aerosols simultaneously (Mason et al., 2023).

2.4.1. CloudSat-CALIPSO Synergy Products

The most heavily utilized products developed under the CloudSat mission are those that incorporate measurements from the CALIOP lidar to detect thin and boundary-layer clouds missed by CloudSat because their backscatter signals fall below the minimum detectable signal of the radar or are obscured by ground clutter. Capturing these clouds is critical for mapping the three-dimensional distribution of clouds and quantifying their impact on Earth's radiation budget (e.g. Henderson et al., 2013). Indeed, the synergy of radar and lidar measurements for providing a more complete description of global cloudiness was the primary motivation for flying CloudSat and CALIPSO in a tight formation (L'Ecuyer & Jiang, 2010). As a result, each of the CloudSat cloud products described in Section 2.3.1 have corresponding radar-lidar synergy products that include CALIOP information to augment CloudSat measurements.

Many CloudSat-CALIPSO synergy products are discriminated by appending -lidar to the name of an original radar-only product (Table 2.13). An exception is two widely used ice cloud microphysics products, 2C-ICE and raDAR/liDAR (DARDAR), that combine radar and lidar measurements seamlessly via optimal estimation to derive profiles of ice water content and particle size. Complete algorithm descriptions for each of these products can be found in Cazenave et al. (2019) and Deng et al. (2015), respectively. In all cases listed in Table 2.14, however, CloudSat and CALIOP synergy products report similar parameters to the radar-only parameters listed in Table 2.10. However, the combination of radar and lidar information occasionally allows additional parameters to be retrieved that can also be verified via sub-orbital measurements. Some examples of associated validation needs are described below.

Table 2.13 *CloudSat-CALIPSO Synergy Products (not comprehensive).*

Product Name	Description
2B-GEOPROF-LIDAR	Cloud layer boundaries
2B-CLDCLASS-LIDAR	Cloud classification
2C-ICE	Cloud ice water content and effective diameter profiles
Combined CloudSat-CALIPSO Snow (C3S)	Virga; shallow snowfall intensity
DARDAR	Ice cloud visible extinction; Lidar ratio; Ice particle number concentration

Cloud Boundaries and Phase

Soon after the launch of CloudSat and CALIPSO the radar-only CloudSat 2B-GEOPROF and 2B-CLDCLASS products underwent revisions to include additional information supplied by the CALIOP lidar. The 2B-GEOPROF-LIDAR product summarizes all hydrometeor layers identified by either the CloudSat or CALIOP or both and identifies which sensor detected the cloud. This provides a much more comprehensive picture of the vertical character of global cloudiness than either sensor alone and adds some new requirements for ground validation efforts. Like the original 2B-GEOPROF cloud mask, the primary validation for this product consists of measurements of cloud vertical boundaries and horizontal scales from airborne or ground-based radar and lidar. Merging spaceborne radar and lidar measurements, however, is complicated by their distinct footprints as well as the fact that the instruments fly on distinct platforms. Specific uncertainties in cloud geometric profiles owing to footprint mismatches between the CloudSat and CALIOP need to be assessed statistically using multiple A-Train under flights.

The CloudSat 2B-CLDCLASS-LIDAR product builds on its radar-only predecessor by including lidar-detected clouds and adding a much more robust discrimination of cloud phase that incorporates lidar linear depolarization ratio and new classification rules based on combined radar and lidar backscatter measurements. Additional measurements of the vertical profiles of cloud liquid and ice water contents are required to validate the vertical profile of cloud phase (liquid, ice, or mixed) output by 2B-CLDCLASS-LIDAR.

Ice Clouds (2C-ICE and DARDAR)

The CloudSat 2C-ICE and DARDAR ice cloud microphysical property retrievals (Deng et al. (2015) and Cazenave et al. (2019), respectively) use simultaneous measurements of radar and lidar backscatter to improve radar-only ice cloud water content and particle size retrievals.

The underlying principle of both algorithms is the same: radiation in the vastly different regions of the electromagnetic spectrum spanned by the lidar (visible) and radar (microwave), exhibit distinct sensitivities to ice cloud particles providing independent information for retrieving cloud properties. There are, however, several challenges in combining profiles of radar and lidar backscatter owing to the different instrument spatial and vertical resolutions and their susceptibility to attenuation and multiple scattering. Both algorithms employ variational schemes to seamlessly integrate these distinct profile measurements and retrieve cloud microphysical properties on a common vertical resolution. The output from these products is not too different from 2B-CWC and can generally be validated using similar airborne in situ measurements. However, both algorithms output profiles of visible extinction at the resolution of the CloudSat field of view and vertical range bin that also need to be validated. DARDAR further retrieves lidar extinction-to-backscatter ratio that can be evaluated using airborne multi-wavelength lidar or high spectral resolution lidar (HSRL).

Snow (Combined CloudSat-CALIPSO Snow, C3S)

Recognizing the value of exploiting synergies between radar and lidar for characterizing deep and shallow snowfall, respectively, a new synergy product has recently been developed that refines surface snowfall estimates from 2C-SNOW-PROFILE using CALIOP observations. The Combined CloudSat-CALIPSO Snowfall (C3S) applies a series of CALIOP-based tests to every CloudSat profile to correct false and missed snowfall detections in the radar blind zone. Ground clutter between the surface and about 1 km (somewhat higher over land) in radar reflectivity profiles leads to two common errors in CloudSat snowfall: reporting no snow from shallow snow that resides entirely in the blind zone and reporting surface snowfall based on snow signals aloft that don't reach the surface. C3S utilizes CALIOP measurements in the radar blind zone to identify shallow snowfall in scenes with no discernable radar backscatter and snow virga in scenes where a gap exists in lidar backscatter between radar-detected snowfall aloft and the surface (L'Ecuyer et al., 2024). A lidar-based snowfall estimate trained using observations from Summit Station, Greenland is further used to supply an estimate of snowfall intensity when CALIOP observes shallow snow.

Combining CloudSat and CALIPSO snowfall measurements adds two new variables relative to the radar-only product described above that need to be validated. Ground-based or airborne observations are needed to verify the frequency of snow virga reported in C3S while CALIPSO surface snowfall estimates need to be validated against in situ surface snowfall measurements, especially in shallow snow events.

Table 2.14 *CloudSat-CALIPSO Synergy Profile Products not captured in Table 2.10*

Qualitative Parameters	**Description**	**Resolution (spatial; vertical)**
Cloud phase	Layer cloud phase: liquid, ice, mixed	CloudSat FoV; 240 m
Virga presence	Precipitation confidence: possible, probable, certain	CloudSat FoV; Column
Shallow snowfall rate	Surface snowfall rate (mm h^{-1} water equivalent)	CloudSat FoV; Surface

2.4.2. ESA EarthCARE synergy products

EarthCARE synergy is based on the atmospheric lidar (ATLID) and cloud profiling radar (CPR), with additional contributions from the multispectral imager (MSI). The ESA EarthCARE radar-lidar synergy products comprise the ATLID-CPR target classification (AC-TC) and the ATLID-CPR-MSI cloud-aerosol-precipitation product (ACM-CAP).

AC-TC determines the location, extent and context of what can be retrieved in ACM-CAP, so development on the two products has been closely coordinated. In general, the target classification product is formulated to be explicit about the detection limits of the radar and any uncertain or incomplete classifications, such as highlighting volumes that "may contain liquid" once the lidar beam is extinguished. In some cases, judgment on these unknowns must be made within the retrieval: for example, ACM-CAP may optionally place supercooled liquid clouds wherever the radar detects rimed snow.

2.4.2.1. AC-TC

EarthCARE's synergistic target classification AC-TC consists of a pixel-wise combination of the CPR radar and ATLID lidar target classifications (C-TC and A-TC, respectively) using a decision matrix. The full description of all three products is provided in Irbah et al. (2023). In many parts of the atmosphere only one product provides information: AC-TC inherits pure lidar classifications of aerosols and ice clouds not detected by the radar, and the radar classification of precipitation dominates when the lidar is extinguished. In some cases, synergistic radar-lidar information yields a new classification that is not included in either of the input products: e.g. mixed-phase cloud, where radar identifies ice cloud and lidar liquid cloud; in other situations, the synergy may provide clarification: e.g. an uncertain discrimination between optically thin ice and aerosols by the lidar may be resolved if the radar detects ice clouds.

AC-TC necessarily inherits any limitations of the radar and lidar instruments that are not resolved by radar-lidar synergy. Once the lidar beam is extinguished in optically thick clouds, the target classification is solely determined by the radar, with the additional information that the presence of liquid cloud (or, indeed, aerosols) is unknown. When undetected by the active instruments, the effects of undiagnosed liquid cloud may be non-negligible in terms of radar attenuation, microwave emission, and shortwave radiation—with the latter affecting both assimilation of MSI solar channels in the ACM-CAP retrieval, and in terms of radiative closure assessments against EarthCARE's broadband radiometer (BBR; in the ACMB-DF product). Undiagnosed liquid clouds may be isolated cloud layers at any level where the radar does not detect targets (e.g. supercooled layers below an optically thick anvil cloud, or boundary-layer clouds below optically thick cloud layers aloft), as well as areas where the radar does detect another class of hydrometeor (e.g. embedded mixed-phase layers within optically thick ice clouds and snow, or warm liquid clouds that are coincident with rain).

Where radar is obscured by surface clutter, attenuated, or affected by multiple scattering in heavy precipitation, C-TC uses contextual information to provide some guidance to the user on the likely contents of pixels in which no useful radar measurements are available:

- Regions of surface clutter that are contiguous with precipitation have classes denoting, e.g. "possible rain", "possible snow", based on the classification immediately above the clutter zone.

- Where the CPR becomes strongly affected by attenuation or multiple scattering various “heavy precipitation” classes are assigned all the way to the surface.

These contextual classes are inherited in AC-TC, and need to be further interpreted within geophysical retrievals to decide if—and, if so, how—to represent hydrometeors that are undetected by radar-lidar synergy.

Validation needs related to the limitations of the lidar:

- Quantify the undiagnosed presence of mixed-phase cloud layers embedded within deep and complex cloud scenes.

- Quantify the undiagnosed presence of liquid clouds coincident with rain or below optically thick clouds aloft.

- Validate the discrimination between aerosols and optically thin ice clouds

Validation needs related to the limitations of the radar:

- Quantify the undiagnosed presence of shallow cloud within surface clutter (especially in complex and layered scenes, where lidar is not available)

- Quantify the continuity of precipitation throughout the surface clutter zone.

- Quantify the continuity of heavy precipitation when the radar is fully attenuated or dominated by multiple scattering.

- Validate the classification of rimed snow

While direct validation of the target classification product is possible and necessary, the critical importance of an accurate target classification for the formulation of a geophysical retrieval means that there is also scope for an indirect evaluation based on the performance of retrieval products and ultimately the radiative closure assessment. Of special importance would be:

- Evaluation of how clouds undiagnosed by radar-lidar synergy are interpreted within retrievals and radiative closure assessments

- Quantifying the sensitivity of the radiative closure assessment to the accurate detection and thermodynamic phase classification of cloud-tops, especially of mixed-phase clouds from radar-lidar synergy.

2.4.2.2. ACM-CAP

ACM-CAP is novel among spaceborne synergistic retrievals in that it performs a unified retrieval of all clouds, precipitation and aerosols in the atmospheric column. The ACM-CAP product and the underlying optimal estimation retrieval algorithm CAPTIVATE are described in Mason et al. (2023). The unified approach maximizes the use of the synergy of profiling radar and lidar measurements, with passive or integrated measurements such as thermal infrared and solar channels from the MSI radiometer, or the path-integrated attenuation from CPR—especially in complex and layered scenes.

Some novel aspects of the CAPTIVATE retrieval have been developed in preparation for EarthCARE’s Doppler radar and high-spectral resolution lidar, but cannot be directly tested in application to CloudSat-CALIPSO retrievals, and have been evaluated so far only in ground-

based or airborne applications. Some novel aspects of ACM-CAP that will require validation include (see Table 2.15):

- In ice clouds and snow, the retrieval of an ice density factor, chiefly constrained by the terminal fallspeeds of snowflakes implied by the radar mean Doppler velocity. This allows the representation of a transition between aggregate snowflakes and denser graupel particles ((Mason et al., 2018, 2019); using ground-based Doppler radars from the BAECC campaign); however, the retrieval of snow microphysics is not fully constrained at a single radar wavelength (or even two), and will need to be applied cautiously.
- In rain, the use of mean Doppler velocity observations to constrain an additional parameter of the drop size distribution (DSD), based on the relation between raindrop size and terminal velocity ((Mason et al., 2017); using airborne Doppler radars from the TC4 campaign). This should improve the capacity to resolve microphysical processes through the rain profile, as well as regional and regime-specific variability in the DSD.
- In aerosols, the retrieval of pre-determined aerosol species is specified by A-TC using the HETEAC scheme (Wandinger, et al., 2023a), based on the lidar extinction-to-backscatter and depolarization ratios measured by ATLID. ACM-CAP takes the scattering properties of these species as given, and retrieves the number concentration of the dominant HETEAC species in each volume, using a Kalman smoother to resolve large-scale features from the measurement noise.
- Informed by the uncertainties in AC-TC related to the detection of liquid cloud layers below or embedded within cloud and precipitation, certain assumptions can be configured to enable the retrieval of a simple profile of liquid cloud that is not detected by the active instruments, e.g. within rain, or where rimed snow is diagnosed. In testing with A-Train and synthetic data, it has been found that including these undiagnosed liquid cloud layers can facilitate better representation of solar radiances and radar path-integrated attenuation, with improvements in radiative closure and rain retrievals; however, the widespread applicability of these assumptions and their optimal configuration are yet to be evaluated

Table 2.15 *ACM-CAP validation needs according to observational constraints and target class*

	Observational constraints			
Target class	**Radar**	**Lidar**	**Synergetic**	**Indirect**
Ice cloud & snow	Microwave scattering properties Ice particle density (i.e. riming)	Optical scattering properties Lidar ratio	Ice effective radius Mixed-phase cloud	Assumptions of continuous mixed-phase precipitation when radar is fully attenuated or dominated by multiple scattering in ice/snow
Liquid clouds	Cloud/drizzle partitioning	Droplet number concentration	Properties and structure of mixed-phase cloud tops Contribution of solar radiances	Vertical profiles of undiagnosed liquid cloud: Embedded mixed-phase layers Supercooled liquid Collocated with rain Boundary layer clouds in layered scenes
Rain	DSD parameters (D0 & Nw) in warm and cold rain Collision/coalesence and evaporation processes			Assumptions of continuous precipitating through surface clutter zone Assumptions of continuous heavy precipitation when radar fully attenuated or dominated by multiple scattering
Aerosols		Microphysical properties of HETEAC & HETEAC-2 species Spatial smoothness		

2.5. Radiative flux and heating rates products

2.5.1. CloudSat-CALIPSO Radiative Flux and Heating Rate Profiles

A primary objective of cloud radar and lidar measurements is to characterize atmospheric aerosol and clouds with sufficient accuracy to estimate their influence on Earth's radiative balance. To these ends, two widely used datasets have been produced that couple CloudSat and CALIPSO retrieved products, along with ancillary temperature, humidity, and surface property information, to broadband radiative transfer models to estimate vertical profiles of radiative fluxes and heating rates. Due to the integrating nature of these derived products, they provide an opportunity to assess the integrated by assessing the degree to which radiative closure can be achieved from the underlying atmospheric reconstructions.

The CloudSat 2B-FLXHR-LIDAR product (Henderson et al., 2013) provides vertical profiles of shortwave (SW) and longwave (LW) radiative fluxes and heating rates. These calculations employ a two-stream plane-parallel doubling-adding radiative transfer model (Henderson et al., 2013; L'Ecuyer et al., 2008). The vertical profiles are derived from radar and lidar backscatter data from the CloudSat CPR and CALIOP aboard CALIPSO. European Centre

for Medium-Range Weather Forecasts (ECMWF) analyses provide ancillary temperature and humidity profiles. Spectral surface albedo and emissivity are assigned using the International Geosphere–Biosphere Programme (IGBP) global land surface classification (Henderson et al., 2013), supplemented by snow and sea ice measurements from the Near-real-time Ice and Snow Extent (NISE) dataset.

Though it employs somewhat different ancillary inputs and methods, the CERES-CALIPSO-CloudSat-MODIS (CCCM) algorithm also derives LW and SW radiative flux and heating rate profiles largely based on radar and lidar measurements from CloudSat and CALIPSO. CCCM uses the enhanced CERES-MODIS cloud property retrieval algorithm that uses cloud altitude information from CALIOP and CPR to produce more reliable estimates of effective radius, effective diameter, and cloud optical depth and distribute them vertically using the lidar-derived vertical feature mask. Temperature, humidity, and ozone profiles are specified based on the Goddard Earth Observing System (GEOS) Data Assimilation System reanalysis while spectral surface albedos for each IGBP surface type are specified using MODIS-derived albedo product. LW and SW radiative flux and heating rate profiles at 137 atmospheric layers are computed from these inputs using the CERES two-stream flux model. Ham et al. (2017) provide a complete description of the CCCM approach, including the methods used to merge cloud and aerosol information obtained over the different MODIS, CALIPSO, and CloudSat fields of view.

The radar and lidar data allow for a detailed representation of vertical cloud properties, enhancing the depiction of multilayered cloud structures and improving the assessment of cloud impacts on top-of-atmosphere (TOA) and surface radiation (Hang et al., 2019; L'Ecuyer et al., 2019). The FLXHR-LIDAR algorithm utilizes ice and liquid effective radius, ice water content (IWC), and liquid water content (LWC) from the CloudSat radar-only 2B-CWC-RO product. However, there are cases where the cloud layer is detected by CALIPSO alone or when cloud parameters are not available from the CWC-RO product. To address this, cloud properties for ice clouds detected by CALIPSO are derived from the CloudSat 2C-ICE product (Deng et al., 2013), and mixed-phase clouds are more explicitly represented (Tricht et al., 2016), resulting in improved surface flux comparisons against ground sites in Greenland (McIlhattan et al., 2017). Additionally, auxiliary cloud information from MODIS is incorporated to constrain single-layer liquid cloud cases. The CloudSat 2B-FLXHR-LIDAR also provides aerosol information extracted from the CALIPSO 5-km aerosol layer product (Omar et al., 2009; Young & Vaughan, 2009). Aerosol optical properties are assigned to each aerosol layer on the basis of the aerosol optical depth and mean radius from CALIPSO following the method of D'Almeida et al. (1991) and Deepak & Gerber (1983), similar to the models used by the Spectral Radiation-Transport Model for Aerosol Species (SPRINTARS) global transport model (Takemura et al., 2002).

Radiative heating rate profiles derived from A-train data with 2B-FLXHR-LIDAR and CCCM have been compared by Ham et al. (2017). Although the observations used to derive the heating rates are the same, namely observations taken by CoudSat, CALIPSO, and MODIS, heating rates of two data products [FLXHR-LIDAR (Henderson et al., 2013) and CCCM (Ham et al., 2022)] are significantly different over some regions. The difference is partly caused by the difference in cloud vertical profiles. CALIPSO and CloudSat are unable to provide a full vertical profile of deep convective clouds. In addition, some of the small boundary layer clouds (e.g. fair weather cumulus) are likely to be missed by CALIPSO due to cloud overlap and by CloudSat due to surface clutter (Marchand et al., 2008). These clouds introduce the

uncertainty in heating rate computations. While satellite-based active sensors tend to miss boundary layer clouds, ground-based active sensors tend to miss high cirrus (Thorsen et al., 2011).

Irradiance profiles measured by aircraft under clear-sky conditions have also been used to evaluate modeled irradiance and aerosol radiative effect profiles (e.g. Fiebig et al., 2002; Redemann et al., 2000; Russell et al., 1997). The focus of these evaluations is on aerosol optical properties used in the computations. While aerosol properties are relatively spatially uniform and do not change significantly with time during the aircraft measurements, cloud properties are highly inhomogeneous and change with time. Therefore, evaluating irradiance profiles under cloudy conditions by aircraft is more challenging compared to the evaluation of clear-sky irradiance profiles.

While evaluating cloudy-sky irradiance profiles with aircraft observations is difficult, computed TOA and surface irradiances have been evaluated with observations. For TOA irradiance, computed irradiances are compared with irradiances derived from broadband radiance observations and angular distribution models (Ham et al., 2022; Kato et al., 2011). When NASA's A-train observations are used for the evaluation, cloud properties over the CALIPSO and CloudSat ground track whose width is ~1.4 km do not cover the entire CERES footprint, which is approximately 20 km in diameter. When the ground-track within a CERES footprint is cloud free according to CALIPSO and CloudSat, the cloud fraction of the entire CERES footprint of approximately 3 out of 10 CERES footprints (i.e. 30%) can be up to 15% (Ham et al., 2015). The cloud contamination is mitigated by using 3D cloud fields constructed by the EarthCARE cloud-construction algorithm (Barker et al., 2011). The bias error of modeled radiances with a 3D Monte Carlo code decreases from 2.9 Wm^{-2} sr^{-1} to 2.1 Wm^{-2} sr^{-1} compared to observed CERES radiances when the 3D construction algorithm is used to obtain full footprint coverage of clouds (Ham et al., 2015).

Surface observations have also been used to evaluate modeled surface irradiances. Because of nadir-view only observations by satellite-based active sensors, a 150 km radius centered at a ground site is used to collocate satellite and surface observations (e.g. Kato et al., 2011). Because the distance between the ground site and satellite observation is larger than evaluations of surface irradiances computed with imager derived cloud properties, the noise in the comparison tends to be larger. To reduce the noise, Kato et al. (2011) use all CERES footprints within a 150 km radius from a surface site and average them. They also average irradiances observed at the site within 15 min from the overpass time. This averaging reduces the relative RMS difference to ~10% for downward longwave irradiances (Kato et al., 2011), which is comparable to the relative RMS difference of instantaneous downward longwave irradiance computed with retrieved cloud properties form passive sensors reported by Scott et al. (2022).

While TOA and surface observations can provide validation data for an extended time as long as satellite and surface observations continue, aircraft observations can only provide data for relatively short time periods. When Level 3 data products (gridded irradiances) need to be evaluated, multiple flights with well-coordinated flight patterns are needed to increase the statistical significance of the difference between modeled and observed irradiances (Smith et al., 2017). However, when irradiances are computed with a high resolution using active sensor derived cloud properties, achieving statistical significance with a few flights might be possible. An aircraft flies below or above clouds and measures downward or upward irradiances nearly

collocated with satellite observations by pyranometers and pyrgeometers. Because irradiances are modeled at ~1 km resolution over the ground track of the active sensors with a 3D radiative transfer model, many ~1 km irradiance comparisons are possible. This allows us to compare not just the mean irradiance over a flight-leg under the ground track of active sensors, but also compare the distribution of ~1 km irradiances.

2.5.2. EarthCARE radiative products

2.5.2.1. Introduction

Following prior related satellite missions such as CERES, CloudSat, and CALIPSO, EarthCARE will routinely produce numerous shortwave (SW) and longwave (LW) radiative products. These products result from application of atmospheric radiative transfer (RT) models to geophysical properties inferred from EarthCARE observations, NWP model estimates, and auxiliary sources. Additionally, EarthCARE will employ observations of broadband (BB) radiances, made by its BB radiometer (BBR), and its RT model-generated counterparts to conduct a continuous radiative closure assessment of its inferred cloud and aerosol properties. As these inferences do not utilize BBR data, with some BBR measurements stemming from the fixed nadir view of its other sensors, its radiative assessments have the potential to form a stringent test of the chain of processes that culminate at the mission's objective of providing cloud and aerosol properties well enough that when used in RT models, estimated top-of-atmosphere (TOA) SW and LW fluxes are, more often than not, within 10 W m^{-2} of estimates obtained from BBR data.

There are several variables related to EarthCARE's RT modeling effort that will be in need of verification. These include data and assumptions that will go into the RT models as well as their outputs. The following sections give brief overviews of these variables.

2.5.2.2. Overview

Geophysical variables retrieved from observations made by EarthCARE's lidar (ATLID), cloud-profiling radar (CPR), or multi-spectral imager (MSI) sensors are referred to as L2 products. Products that arise from a single sensor's data are designated as L2a, while all others are L2b products. Most L2 products are reported on the Joint Standard Grid (JSG), which has horizontal resolution of ~1 km and extends across-track 35 km to the right and 115 km to the left, relative to the satellite's motion vector, thereby covering the MSI's swath. Vertically-resolved L2 variables, defined from nadir observations, are at 0.1 km-thick layers extending from surface to 30 km. Together they form the L2-plane.

Figure 2.7 summarizes the flow of products leading to, and including, EarthCARE's ex situ radiative closure experiment. It begins with L2b variables and auxiliary information, from NWP model reanalysis and climatological statistics (Qu, Donovan, et al., 2023), being used by the 3D Scene Construction Algorithm (SCA) (Barker et al., 2011; Qu, Barker, et al., 2023).

Information from the SCA gets ingested into various forward radiative transfer models (Cole et al., 2023) that predict profiles of BB radiative fluxes as well as upwelling BB radiances at TOA, commensurate with observations made by the BBR. The essence of the closure assessment, which marks the end of version 1 of EarthCARE's production chain, is comparison of TOA *pseudo-fluxes* derived from modeled and measured radiances and averaged over domains D that measure n_{access} JSG pixels along-track by $2m_{access}+1$ JSG

pixels across-track half-width. The current plan (Qu, Barker, et al., 2023) is n_{access} = 21 and m_{access} = 2, implying that closure assessments are done for *D* measuring ~ 5x 21 km, or ~100 km^2, which follows from BBR development guidelines.

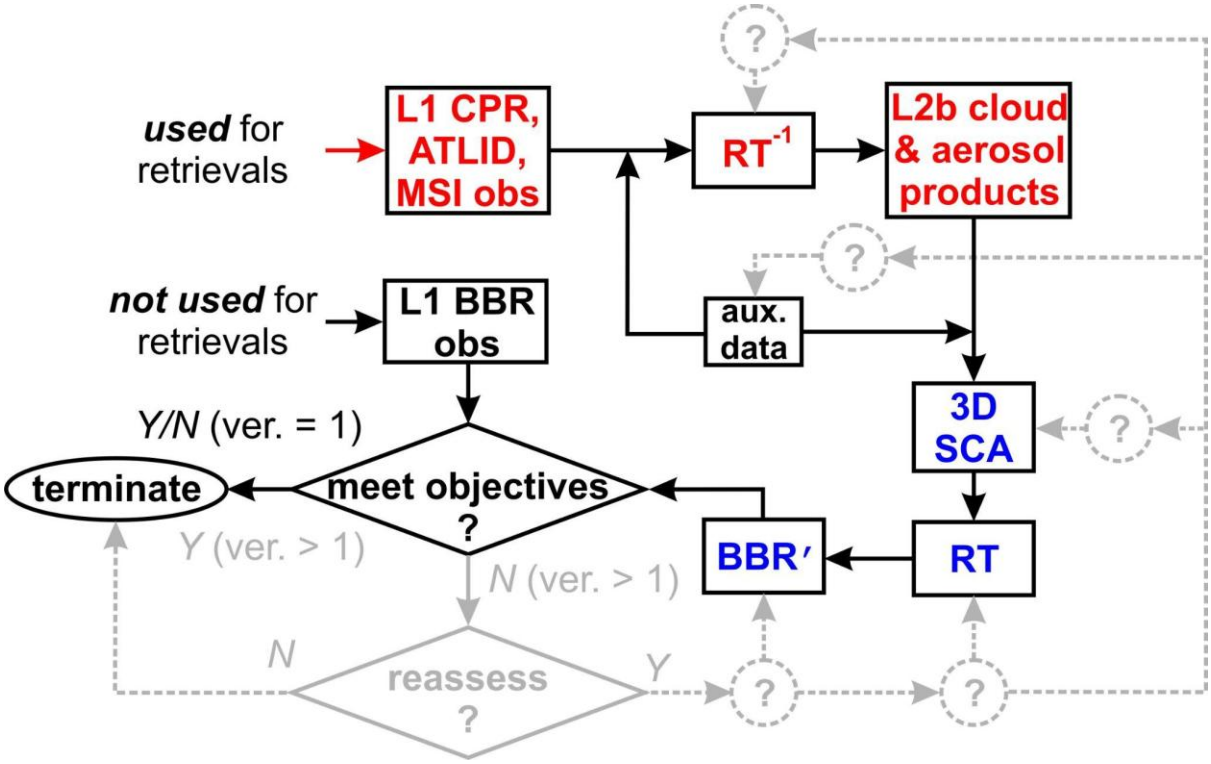

Figure 2.7 *Flowchart shows EarthCARE's RT effort. Version 1 (ver. = 1) represents EarthCARE's initial processing plan. It terminates unconditionally after comparing modeled to measured BBR quantities and reporting the likelihood of their differences being within W m^{-2}. For subsequent processings (ver. > 1), if modeled and measured BBR quantities compare unsatisfactorily, potentially all steps in the processing chain will be interrogated and possibly adjusted until some level of satisfaction is reached.*

2.5.2.3. 3D Scene Construction Algorithm (SCA)

In light of EarthCARE's ambitious goal of limiting differences between measured and modeled TOA fluxes to ± 10 W m^{-2} when averaged over "assessment domains", the success of its radiative closure programme depends on reducing errors and uncertainties in: BBR measurements; variables needed by RT models that are not provided by EarthCARE observations; and RT models. This includes issues of observational geometry facing use of BBR data for closure assessment. First, L2-retrieved profiles are ~1 km in diameter, while the BBR was designed to perform best for footprints of ~10 x 10 km. For this configuration, fluxes and radiances computed for sequences of retrieved profiles contribute only ~10% to BBR pixels. Second, at only ~1 km wide, net horizontal fluxes for each retrieved column, and sequences of them (Barker & Li, 1997; Marshak et al., 1998). This requires that 3D RT models, as opposed to their ubiquitous 1D counterparts, are needed for EarthCARE's radiative closure assessment (Illingworth et al., 2015). Hence the need for 3D arrays of data that describe the Earth-atmosphere system adjacent to the ~1 km-wide retrieved L2-cross-section.

Fortunately, point-spread function widths of BBR native radiances are ~0.7 km, and this offers much flexibility to the design of the closure assessment (e.g. Tornow et al., 2015). The extreme

case is to use a single along-track line of BBR radiances that overlap the ~1 km wide curtain of L2-retrieved profiles, referred to hereinafter as the L2-plane. Presumably, however, this would degrade BBR performance and thus weaken closure assessments. Alternatively, one could attempt an across-track "broadening" of the L2-plane so as to cover as many BBR native radiances as necessary. Regardless of the route taken and the size of domains over which closure assessments are performed, there is constant lateral flow of photons both within assessment domains *and* between assessment domains and their adjacent areas. Taking these issues together, it was decided that EarthCARE utilize 3D RT models as much as possible (Illingworth et al., 2015).

The core of the SCA is passive narrowband radiance-matching, has been presented, assessed, and applied elsewhere (Barker et al., 2011; Qu, Barker, et al., 2023; Sun et al., 2015). Using MSI radiances, the SCA associates an off-nadir JSG pixel with its closest matching nadir pixel. L2b profiles, and surface properties, associated with the donor nadir pixel get replicated at the off-nadir recipient to form a 3D surface-atmosphere system around, and consisting entirely of data in, the L2-plane.

Thus far, the SCA's reconstructed radiances have been assessed with MODIS observations and model-generated radiances. The bigger challenge, however, is verification of its 3D geophysical fields. Barker et al. (2021) performed a partial verification using an entirely virtual system, but as yet this portion of the SCA has not been assessed with real observations. Suggestions for verification tests include collocation of passive satellite imagery with surface-based scanning active sensors and/or arrays of surface-based radiometers.

2.5.2.4. RT model input requirements

Following previous satellite missions (e.g. Kato et al., 2013; L'Ecuyer et al., 2008), EarthCARE computes SW and LW BB flux and HR profiles by applying 1D RT models to each JSG profile in the L2-plane. It makes a step forward, however, with its operational use of BB 3D RT models for both SW and LW.

The 3D RT solvers are Monte Carlo solutions of the plane-parallel 3D RT equation. The SW model produces profiles of fluxes and HRs, and TOA BB radiances commensurate with the BBR's three telescopes. The LW model computes the same radiances along with an upwelling flux at a "reference height" as defined by Angular Distribution Models (ADMs) (see (Velázquez-Blázquez, Baudrez, Clerbaux, & Domenech, 2024)). All 3D RT computations are done for "radiation computation domains" that consist of a closure assessment domain and surrounding buffer-zones that marginalize and minimize impacts due to use of cyclic boundary conditions.

RT model inputs

The requirements of EarthCARE's RT models are like those of all other multi-layer RT models. They need, at as high spatial and temporal resolution as possible, profiles of atmospheric pressure, temperature, humidity, and various trace gases. These profiles will come from NWP model reanalyses via X-MET process files and climatological assumptions of gaseous concentrations. These quantities are assumed, in practice, to be errorless, which is, as everyone knows, untrue. Ideally, they should be quantified with some confidence and used to help estimate uncertainties in RT modeled radiances and fluxes, for these uncertainties will have an impact on the quality of radiative closure assessments.

Additionally, all RT models surface optical properties are required. Ideally, this includes spectral values of albedo and emissivity, as well as associated bidirectional reflection distribution functions (BRDFs). For open water surfaces with surface winds, Hansen et al. (1983) definition of albedo is assumed to be spectrally-invariant, while Huang et al. (2016) formulation of emissivity is used. SW BRDFs are handled by Cox & Munk (1956) ergodic wave parametrization.

For snow-free land, SW surface albedos are calculated from climatological BRDF parameters for 16-day periods based on 12 years of MODIS MCD43GF data (Schaaf et al., 2002). Terrestrial snow albedos for the same spectral bands are based on Moody et al. (2007) whose calculations were, in turn, based on climatological statistics of Northern Hemisphere white-sky albedos for 16 International Geosphere–Biosphere Program (IGBP) ecosystem classes with accompanying snow. For ice-covered land or water surfaces, BB averaged albedos are provided by X-MET. While the SW 3D RT model has the provision to use (Rahman et al., 1993) land surface BRDF model, global spectral parameters were deemed to be too lacking for operational use. Hence, for all land surfaces, the Lambertian assumption is used.

Where possible, 1D and 3D RT models use the same atmospheric and surface optical properties. Optical properties for pristine atmospheres, free of aerosol and cloud, come from the RRTMG models (Iacono et al., 2008; Morcrette et al., 2008). The default is for 1D and 3D RT models to use ACM-CAP profiles of retrieved cloud and aerosol properties. Otherwise, L2a-composite profiles are used (see (Cole et al., 2023)). The 3D RT solvers use detailed representations of all scattering phase functions while the 1D solvers use just the corresponding asymmetry parameters. The other cloud and aerosol optical properties are used by both models.

2.5.2.5. RT model outputs

An obvious set of predicted variables that could be verified are surface irradiances. These quantities arise from entirely different photon pathlength and scattering distributions than upwelling quantities at TOA, which are all that a satellite works with. The following surface variables should be considered:

- direct-beam BB SW irradiance (all-sky conditions for both 1D and 3D RT models)
- diffuse-beam BB SW irradiance (all-sky conditions for both 1D and 3D RT models)
- down-welling BB SW irradiance (all-sky conditions for both 1D and 3D RT models)
- down-welling BB LW irradiance (all-sky conditions for 1D RT models)

The more challenging verification measurements to make are from an elevated platform, which is likely to be aircraft, but could be balloon or tower as well. The obvious measurements are BB up- and down-welling SW and LW irradiances at some altitude. The obvious location to make these observations is along paths that under fly EarthCARE; i.e., along the L2-plane. A potential useful test of the SCA might be to fly parallel to, but at some distance removed from, the L2-plane and make up- and down-welling irradiance measurement. While EarthCARE does not archive these quantities, they could be produced easily using 1D RT results along the L2-plane and indices that come from the SCA. Doing this for the SW 3D RT and 3D LW model, however, would be more complicated, and requiring specialized versions of the ACM-

RT processor. Naturally, when making observations such as these an (array of) aircraft would also be equipped with other instruments ranging from remote sensors, to in situ particle samples, to extinctiometers.

At this point, it is difficult to see how meaningful and reliable “observations” of flux convergence (i.e., radiative heating rates) can be made. As such, reference here is limited to level fluxes.

2.5.2.6. Radiative closure assessment

The integrity of a radiative closure assessment rests much on reliable quantification of uncertainties associated with both modeled and measured variables that are to be compared. Regarding uncertainties for modeled radiances and fluxes, the main concern is provision of uncertainties for input variables be they geophysical retrievals or state variables provided by NWP reanalyses or climatological records. The obvious way to estimate uncertainties for retrieved variables is via multiple realizations of retrieval algorithms subject to ranges of assumptions, parameter settings, and L1 measurement uncertainties. These coupled with plausible ranges of estimated state variable would be ingested into the RT models resulting in distributions of radiances and fluxes.

When closure assessments are confined to L1-level radiances, measurement uncertainties will likely be small. This is why EarthCARE’s assessments are based on summations of up to three BBR radiances, using the same summation weights for both measured and modeled radiances (i.e., rudimentary yet straightforward ADMs) (Barker et al., 2021). If, however, one intends to perform assessments using estimates of TOA fluxes, additional uncertainties enter the fray via ADMs (Velázquez-Blázquez, Baudrez, Clerbaux, & Domenech, 2024; Velázquez-Blázquez, Baudrez, Clerbaux, Domenech, et al., 2024), as well as definition of upwelling flux at TOA. Clearly, such a flux is not meant to be that that would be measured by a down-facing pyranometer for its view would vastly exceed that of the small assessment domain. On the other hand, definition of flux at the top of a small narrow column is rooted in notions of 1D RT, but EarthCARE has decidedly moved away from that paradigm.

While there are no intentions to perform radiative closure assessments using measurements other than those made on EarthCARE, EarthCARE’s RT models could be altered easily to produce estimates of radiances other than that align with the BBR. For instance, more often than not, EarthCARE L2-columns are in the field-of-view of other satellites, most notably geostationary satellites. Generally, their view(s) of an L2-column can be expected to differ radically from the BBR’s. As such, comparing their measured radiances to corresponding estimates from EarthCARE’s altered RT models represents an additional constraint on closure assessment in which new (radiative) information gets utilized. The same goes for airborne or surface-based radiometers. As they stand, EarthCARE’s RT models do not produce radiances at these levels, but they could with minor modifications. A point to remember is that photon path length and number of scattering event distributions differ greatly between transmitted and reflected SW radiation and downwelling LW radiation at the surface and upwelling LW radiation at TOA. Thus, closure assessments of satellite-based retrievals performed with quantities measured at the surface can be very powerful; notwithstanding problems associated with potentially poor sample sizes.

2.6. Conclusions

Based on the discussions in previous sections, this section summarizes the main suggestions and recommendations from developers' experiences, along with the anticipated validation needs for new mission products, particularly focusing on profile validation.products validation.

The importance of sensor calibration reflected in Level 1 products has been highlighted for all the missions. Different missions and instruments have used different approaches. Methods described in previous sections include monitoring satellite-borne sensors (active and passive) and internal parameters using internal references. Calibration verification includes end-to-end methods, and typically applied are generally:

a) Measurements collected in the presence of favorable conditions of stable natural targets, like cirrus clouds, or reference surfaces. Observations can be planned to monitor calibration over time and, in some cases, latitude dependency.

b) Comparison with measurements from ground-based profiling instruments (as in Pauly et al. (2019) for CATS), possibly (but not necessarily) at similar wavelengths to the satellite-borne instruments. This assumes that the ground instrument is properly calibrated, in Chandrasekar et al. (2015) for ground-based, scanning radars used for GPM DPR product validation.

c) Underflights to collect coincident measurements obtained with wavelengths comparable (or not) with that of satellite-borne instrument (e.g., the CALIPS-CloudSat Validation experiment with coordinated underflights but many others are mentioned in the chapters) are considered important and effective for validation.

d) Active calibrators (e.g., for GPM DPR and EarthCARE CPR).

e) Self-consistency checks among measured parameters.

Particular attention is given to critical behaviors of instruments that critically impact the retrievals, such as the ATLID spectral cross talk between the Mie and the Rayleigh channel that is monitored from the impact it has on specific measurements. A specific Level 1 product has been designed to facilitate its monitoring.

Concerning L2 products, they are typically obtained through complex processing, like those described by the flow charts in figures 2.1, 2.5, 2.6, 2.7. A common first step of L2 processing is the discrimination of signal from noise in measurements available from the L1 products. Parameters of thes module, specific for each mission/sensor, are determined in various ways, including statistical analysis or simulated scenes (Donovan, 2003). This very important step affects all subsequent processing, implying the correct detection and delineation of layers of clouds and aerosols.

Measurements from the ground are important in validating the determination of layers in profiles, whether they are clouds or aerosols. They can be conducted not necessarily using the same wavelength as the satellite-borne instrument, have been used, since using multiple wavelengths can help identify more features of the scene observed from the satellite than a single instrument (see considerations in sections 2.3.3.1 and 2.3.2.2) and, depending on the achievable resolution, a more precise delineation of boundaries of detected layers.

A common product of atmospheric profiling missions is the classification that can be either a cloud classification (e.g., liquid or ice, convective/stratiform) or an aerosol typing. In this case, in situ measurements from underflights have been used along with statistics provided by measurement networks as in Sato & Okamoto (2006). In the experience of CALIPSO, ground-based Raman lidar and AERONET classification products have been beneficial for statistical validation of aerosol typing.

For validation of profiles of cloud and precipitation, the availability of reliable profiles of particle size distribution seems essential to validate most of the products, whether they are profiling or columnar. In addition to airborne campaigns, such profiles can be achieved by ground-based Doppler profilers and/or multi-frequency radar profilers. However, since one of the key factors affecting the uncertainties of radar products is the attenuation, especially at W-band (that of CloudSat and EarthCARE CPR), the use, in ground-based radars, of frequencies less prone to attenuation than W, has also been proposed (see section 2.3.3.2.2 where the use of K-band profilers is mentioned for EarthCARE in Antarctica). However, chances of overpasses in the presence of clouds and precipitation over fixed installations are not so many and lack of colocated measurements can be mitigated using networked profilers and operational, scanning dual polarization weather radar, massively used in the validation of GPM both for validating precipitation microphysics products and their compliance with mission requirements and classification (see section 2.3.2.2 on GPM validation). It should be noted that the problem of obtaining coincident measurements even from a network of lidar was also highlighted for Aeolus validation of aerosol/backscatter extinction profiles. (see 2.2.3)

A recent novelty from space missions is the Doppler capability, present in recent missions Aeolus (the Atmospheric Laser Doppler Instrument ALADIN) and EarthCARE with the Doppler Cloud Profiling Radar. Co-located and independent measurements were used for validation of Aeolus wind products (section 2.3.3), like super pressure balloons, atmospheric motion vectors from geostationary satellites, although their limitation is validating vertical profiles. Useful indications for Aeolus were obtained using remote sensing instruments research aircrafts, but useful feedback was obtained also by comparing winds from ECMWF converted into ALADIN observations.

The new Doppler capabilities and products of EarthCARE CPR deserve novel approaches. A combination of two Doppler radars operating at 94 GHz operating in the supersite of Koganei (Japan) has been proposed (see section 2.3.3.2.2). One radar has a sensitivity higher than EarthCARE CPR and the other has scanning capability to detect the possible presence of NUBF. Moreover, VHF profilers allow separating the contribution of air motion from the sedimentation velocity. As previously mentioned, chances for coincident measurements in the presence of clouds or precipitation are not too many and therefore, more accessible and available radars at frequencies different from 94 GHz, including those operational of weather services can be proposed also for Doppler products.

This section underscores the significance of the experiences discussed, particularly in relation to the development of robust and efficient validation activities. These activities are crucial for gathering valuable information that can enhance the retrieval algorithms integral to Level 2 products. Despite the challenges and complexities associated with these activities, their importance cannot be overstated. The results derived from validation activities play a pivotal role in refining satellite products, further emphasizing the necessity of these validation endeavors.

3. Chapter 3: Survey of validation measurements

Plain language summary:

This chapter provides an overview of instruments and systems of instruments (hereafter “measurement systems”) that are available for the validation of spaceborne atmospheric profiling instruments. We start with a description of instrument types, broken down by application, i.e., aerosol, cloud, and precipitation measurements (3.2). We then provide surveys of specific instruments and instrument suites that are available for validation of measurements in each of the three applications, with discussions separated between ground-based, airborne, and space-borne systems (3.3). This subchapter includes a list of airborne platforms that have been used extensively for validation purposes. The ground-based and airborne categories are further broken down into remote sensing and in-situ instruments, while the spaceborne remote sensing category discusses primarily intercalibration approaches. After the instrument survey, we discuss the validation measurements in their ability to represent the spatiotemporal variability of validation scenes (3.4), followed by a discussion of measurement quality (3.5), which we define primarily as measurement uncertainty, sensitivity, and quality assurance protocols. We proceed to discuss methodologies for remote sensing system synergy, i.e., the opportunity to combine different data sources to improve the ability to address a validation need (3.6). Conceptual recommendations for how to use the various validation measurements described in this chapter will be provided in *Chapters 5, 6, and 7*.

3.1. Introduction

In this chapter, we survey the tools available to validate the vertical profiles of aerosol, cloud, and precipitation properties retrieved from spaceborne sensors. Validation of observations from active spaceborne remote sensing measurements is severely challenged by their typically small spatial footprints near the satellite ground-track. For aerosols, clouds, and precipitation whole properties vary greatly in space and time, this means that validation measurements have to be carefully coordinated to be meaningfully interpreted for the purpose of satellite measurement validation. We discuss the instruments available for such validation efforts and provide examples of previous successful validation exercises. In addition to the instruments themselves, we provide surveys of the platforms that these instruments have been deployed on. We discuss in some detail the requirement to characterize the spatiotemporal variability of the geophysical variables, and how that variability needs to be incorporated into the validation studies themselves. Inherently, the diversity of tools discussed here varies greatly in their spatial resolution and in their ability to characterize the spatiotemporal variability of observables. Figure 3.1 shows a schematic of the trade space between measurement resolution and spatiotemporal representativeness for the instrument and platform combinations discussed in this chapter.

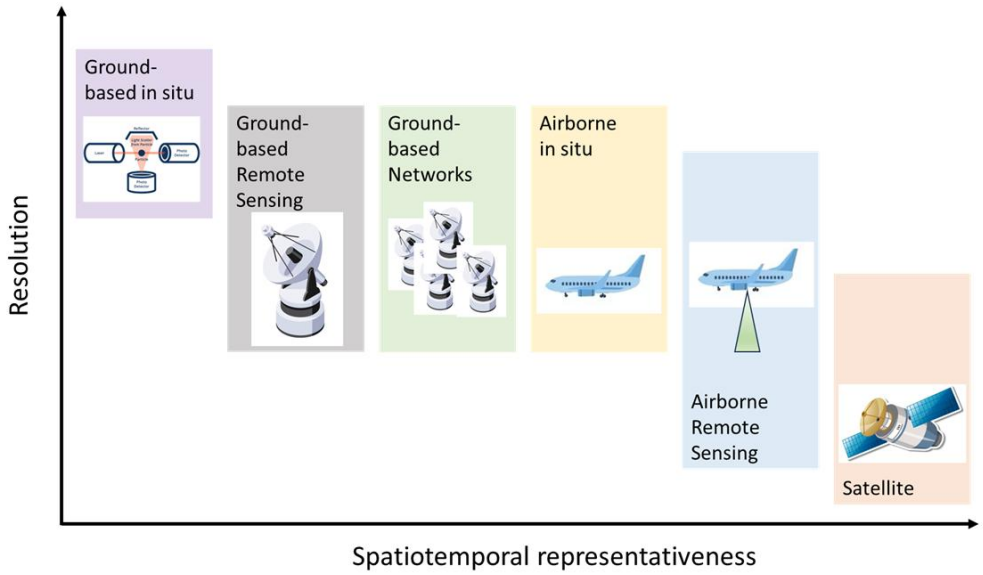

Figure 3.1. *Trade-space between measurement resolution and spatiotemporal representativeness for a variety of instrument type and platform combinations discussed in this chapter.*

3.2. Types of validation instruments

3.2.1. Lidar

Elastic backscatter lidar / Ceilometer

The simplest systems are the so-called elastic backscatter lidars, measuring the attenuated backscattered signal at one or more wavelengths. The relative contribution of molecular scattering processes to the backscatter signal depends on the wavelength, with a higher contribution at short wavelengths and vice versa. Thus, measurements at longer wavelengths are well suited for detecting aerosols and cloud particles and determining their layer boundaries, while shorter wavelengths may be useful for particle type characterization. The signal scattered from molecules in aerosol and cloud-free regions is used as a reference for the Fernald/Klett (Fernald, 1984; Klett, 1985) lidar inversion to derive extinction and backscatter profiles. For longer wavelengths, a calibration method using returns from stratocumulus clouds has been proposed (O'Connor et al., 2004). For all methods, the extinction-to-backscatter ratio (lidar ratio) has to be assumed or derived from additional auxiliary data, and this introduces uncertainties in the derived parameters. We note that the lidar ratio assumption can be better constrained if the aerosol optical depth of the aerosol layers is known a priori, for example from sun photometric observations (Marenco et al., 1997; Takamura et al., 1994) or from satellite instruments (Burton et al., 2010; Painemal et al., 2019); the lidar ratio can be constrained using lidar observations alone where molecular signals can be clearly measured below and above an aerosol layer (Di Girolamo et al., 1994). Among the elastic backscatter lidars, the ceilometers represent a subspecies: they are low-power, simple and robust, fully automated systems, usually measuring at longer wavelengths. Ceilometers are often employed in networks to determine aerosol and cloud layer boundaries on national and continental scales.

Raman lidar

The aerosol Raman lidar technique makes use of the inelastic scattering by air molecules, adding an additional detection channel to the elastic one. In this way, it enables the measurement of the extinction coefficient independently (Ansmann et al., 1992). Combining the elastically backscattered and the inelastically backscattered signals, one can also derive the lidar ratio and the backscatter coefficient. In most systems, the vibrational-rotational Raman technique is used. This technique is limited by the solar background, and often this results in a limitation to nighttime observations, whereas the pure rotational Raman technique (e.g. Veselovskii et al., 2015) is able to deliver the extinction coefficient at daytime as well, at least over a somewhat larger height range. The DOE ARM program operates vibrational-rotational Raman lidars that provide daytime and nighttime measurements of water vapor and aerosol (e.g. Thorsen et al., 2015; Turner et al., 2002). As the Raman lidar technique exploits the scattering by molecules, most systems are deployed at shorter wavelengths, with the exception of Haarig et al. (2016), who reported rotational Raman measurements at 1064 nm as well. Multiple wavelengths (e.g. 355 nm and 532 nm) can be used to provide information on the backscatter and extinction wavelength dependence (i.e. Angström exponent and color ratio).

High-Spectral-Resolution Lidar (HSRL)

The high-spectral-resolution lidar technique (Shipley et al., 1983) exploits the difference in Doppler broadening of backscattered light by particles and molecules (quasi-elastic scattering). Through optical filtering, the molecular- and particle-dominated backscattered signal can be separately determined and thus the extinction coefficient and backscatter coefficient (and thus the lidar ratio) can be directly derived. Conceptually, this is similar to the aerosol Raman technique. The advantage of HSRL over Raman lidar is the better signal-to-noise ratio, making it more suitable when the limitations due to large background signals are critical (daytime observations or fast-moving platforms). Continuous ground-based observations with HSRL systems are rare, due to the large effort in maintaining stable instrument conditions (e.g., temperature of the laser). The HSRL technique is widely used for airborne (e.g. Esselborn et al., 2008; Hair et al., 2008) and spaceborne applications (Ansmann et al., 2007; do Carmo et al., 2021; Liu et al., 2024; Wehr et al., 2023) because a short signal averaging period is sufficient to retrieve high-quality measurements. Adding a second (or more) wavelength in a multiwavelength HSR lidar enables the determination of the extinction and backscatter Angström exponents and the color ratio (Ferrare et al., 2023; Gross et al., 2013).

Polarization lidar

A polarization lidar is an elastic backscatter, Raman, or HSR lidar with the additional capability of measuring the cross-polarized (depolarised) elastic return signal. The depolarisation signal helps distinguish non-spherical atmospheric particles such as mineral dust, volcanic ash, and ice crystals from spherical particles like sulfate aerosols, pollution, and water droplets. From the volume depolarization ratio and the backscatter coefficient, the particle depolarization ratio can be determined. Calibration of the polarization channels is crucial for retrieving high-quality observations (Freudenthaler, 2016; Freudenthaler et al., 2009). Polarization-sensitive lidar measurements can be performed at different wavelengths (e.g. Burton et al., 2015; Gross,

Tesche, et al., 2011), but also using different polarization states, i.e.circular or linear polarization (Sassen, 2003).

Lidar capability combinations and information content

The combination of different lidar techniques (e.g. multi-wavelength lidar and polarization sensitive high spectral resolution or Raman lidar) allows the determination of higher level products, e.g., the Angström exponent and color ratio and thus information on the size range (coarse vs. fine) of the measured particles or hydrometers. Combining information about the lidar ratio and the depolarization ratio allows a first discrimination between aerosol types (Burton et al., 2012; Floutsi et al., 2024; Gross, Tesche, et al., 2011; Wandinger, et al., 2023b). The combination with multi-wavelength information further refines this aerosol typing (Gross et al., 2013). The combining information about the depolarization, color ratio, and lidar ratio also allows the estimation of aerosol components (Nishizawa et al., 2007, 2011; Sugimoto et al., 2003). In specific cases, multi-wavelength depolarization measurements can even allow inferences about the aerosol lifecycle (Gross et al., 2013; Gross, Freudenthaler, Schepanski, et al., 2015; Haarig et al., 2018) as well as different aerosol mixtures (Gross et al., 2016; Gross, Tesche, et al., 2011; Tesche et al., 2009).

Table 3.1. *Derived quantities and geophysical variables observed by different types of lidars*

Derived Quantities / Geophysical Variables	Elastic backscatter lidar	Raman lidar	HSR lidar	Polarization-sensitive lidar
Layer heights	X	X	X	
Backscatter coefficient	(X)4	X2	X	
Extinction coefficient	(X)4	X2	X	
Lidar ratio		X2	X	
Depolarization ratio				X
Ångström exponent	(X1)	x1	x1	
Colour ratio	(X1)	x1	x1	
Aerosol optical depth	(X)4	X	X	
Cirrus optical depth	(X)4	X	X	
Aerosol typing		X3	X3	X

[1]for multiwavelength option only, [2]mostly restricted for nighttime, [3]in combination with polarization-sensitive measurements, [4]quantity retrievable with additional assumptions on the atmospheric layers.

3.2.2. Radar

Radars that are used in the atmospheric sciences and meteorology can be divided into two types: weather (precipitation) and cloud radars. Weather radars operate at cm-wavelengths, and are intended to provide large-scale observations, with a maximum range of a few hundred kilometers, of cloud and precipitation systems. The majority of weather radars are part of national weather radar networks. Cloud radars operate at mm-wavelengths and are intended

for relatively short-range observations: the typical range is about 10-20 km. Given the wavelength, cloud radar systems are smaller than precipitation radars and are ideally suited for airborne and spaceborne deployments.

Table 3.2. *Overview of different types of radars*

Type of radar	Frequency / GHz	Wavelength / cm	Liquid clouds	Ice clouds & snow	Rain
Weather radars					
S	2 — 4	7.5 — 15	—	+	++
C	5 — 8	3.75 — 7.5	—	+	++
X	8 — 12	2.5 — 3.75	—	+	++
Cloud radars					
Ka	27 — 40	0.75 — 1.11	+	++	+
W	75 – 110	0.273 — 0.4	+	++	+
G	110 — 300	0.273 — 0.091	-/+	++	—
Other types					
Ku	12 — 18	2.5 — 1.67	—	+	+
K-band profilers (aka MRR*)	24.23	1.23	—	+	+
cm-wavelength profilers			—	+	++
Multi-frequency systems (e.g. Ku/Ka, Ka/W, cm-/mm- wavelengths)			++	++	++

*Micro Rain Radar

Precipitation (weather) radars

The majority of weather radars operate at either S or C-bands, which correspond to wavelengths of 10 and 5 cm, respectively. In the last two decades, X-band weather radars have been more frequently used for weather observations. Typical weather radar measurements include radar reflectivity factor and Doppler velocity. The dual-polarization radar variables, such as differential reflectivity, co-polar correlation coefficient, and specific differential phase, significantly improve observations of precipitation microphysics, precipitation evolution, hydrometeor classification, and quantitative precipitation estimation. They are used to improve the quality of radar observations (Bringi & Chandrasekar, 2001). It was shown that such observations provide valuable data for the validation of satellite-based precipitation products (e.g. Chandrasekar et al., 2008).

Typical weather radar observations are collected using a set of plan position indicator (PPI) scans carried out at different elevation angles, normally ranging between 0.5 and 20 deg.

Research radars also perform range-height indicator (RHI) scans, which have better vertical resolution. The sensitivity of weather radars usually ranges between -35 and -50 dBZ at 1 km distance. These sensitivity values are comparable to what is achieved by cloud radars, but other limiting factors affect the applicability of weather radars for cloud studies (Kollias et al., 2007; Maesaka, 2018). At short ranges, weather radars tend to have larger clutter contamination than cloud radars (Kollias et al., 2007). Bragg scatter, visible in cm-wavelength radar observations (10 dBZe with an S-band radar, 0 dBZe with a C-band radar, and −10 dBZe with an X-band radar), can mask shallow liquid clouds (Knight & Miller, 1993).

Cloud radars

Cloud radars are mm-wave radars that typically operate in Ka or W-bands (Kollias et al., 2007). Recently, cloud radars operating in G-band were introduced (Battaglia et al., 2014a). These new radar systems show promise in improving the characterization of ice clouds (Cooper et al., 2021). Given the higher frequencies of the cloud radars as compared to a typical precipitation radar, cloud radars tend to be more sensitive. Their sensitivity is ideally in the order of -50 dBZ at 1 km. They also provide a higher spatial resolution thanks to a narrower beam width for a given aperture. Note that thanks to their sensitivity these radars are also well suited for studying weak precipitation events, such as drizzle and snow. The downside of the higher radar frequency is that the cloud radar observations are more affected by attenuation by water vapor, clouds, and precipitation (e.g. Tetoni et al., 2021), which tend to limit the maximum range.

The radar reflectivity factor is the main radar variable used for the retrieval of cloud and precipitation properties (e.g. Tetoni et al., 2022). The reflectivity factor depends on the size distribution, shape, and dielectric properties of observed hydrometeors. Sizes of observed hydrometeors range from around 5-10 μm for cloud water droplets, 100 μm - 3 mm for ice crystals, 0.1-8 mm for raindrops, and 0.5 mm - 5 cm for snowflake aggregates. The range of sizes implies that for some hydrometeors non-Rayleigh scattering effects (and sometimes multiple scattering) should be taken into account.

The difference in scattering regimes provides an opportunity for retrieving effective particle size by utilizing multifrequency observations (e.g. Matrosov, 2011). In such observations, one frequency is selected such that the observed particles fall within the Rayleigh scattering size range and the other frequency is higher where non-Rayleigh scattering occurs. In addition to using differences in scattering, differences in path attenuation between several frequencies can be used to improve retrievals of cloud microphysical properties (Hogan, 1998).

Dual-polarization radar

Dual-polarization radar observations are valuable for precipitation microphysics studies and for quantitative precipitation estimation (Chen et al., 2017). They provide information about hydrometeor shapes, sizes, composition, and phase (liquid, ice) by interpreting radar waves probing clouds and precipitation with two orthogonal polarizations (Tetoni et al., 2021). For example, in the case of hydrometeors in the liquid phase, the value of dual-polarization technology builds on the relationship between the size and the shape of raindrops. Raindrop size changes are more prevalent in the horizontal dimension, i.e. raindrops become more oblate as they become larger. Common dual-polarization variables include the radar reflectivity factor at horizontal polarization (Z), the differential reflectivity (ZDR), the specific

differential phase shift (KDP), and the co-polar correlation coefficient (ρHV). Z is a size-sensitive radar product proportional to the returned signal power, which is also proportional to the sixth power of the horizontal dimension of particle D^6 when Rayleigh scattering applies as illuminated particles are small compared to the radar wavelength. In the radar sampling volume, Z is proportional to the particle number density and measured as the sum of all scattering particles. ZDR is the difference (in logarithmic scale) between the returned powers of the vertically and horizontally polarized radar waves, and it provides an indication of the particles' shapes and sizes. KDP is the difference between the phases of the vertically and horizontally polarized radar waves, and it is proportional to the concentration of nonspherical (large) particles. ρHV is the correlation between the horizontally and vertically polarized received pulses and a measure of the homogeneity in size and shape of hydrometeors within a radar resolution volume. Z, ZDR, and KDP are used for applications such as hydrometeor classification, particle size distribution estimation, and quantitative precipitation estimation. In addition to being used for hydrometeor classification, ρHV is commonly used for quality control of dual-polarization radar data.

Other radar types

There are a number of radars that do not fall within the above-specified categories but are used for cloud and precipitation studies. These radars are wind profilers (Williams et al., 1995), and vertically pointing and scanning radars operating in various radar bands that are used for cloud and precipitation studies. These radars include vertically pointing cm-wavelength radars typically operating in X- or C- bands. Since the launch of TRMM and GPM (https://gpm.nasa.gov/missions/GPM), the Ku-band radars have also been used. Relatively inexpensive micro rain radars (MRR), which operate at 24 GHz, have shown to be very valuable for precipitation studies by providing high-resolution vertical profiles of reflectivity and Doppler velocity.

3.2.3. Other remote sensing instruments and techniques

Spectroradiometers

Spaceborne imaging spectroradiometer retrievals can provide constraints useful in the context of validating profiling instruments, e.g., column AOD measurements that can be used to validate vertically-integrated aerosol extinction profiles from lidar. They provide important constraints for retrieving column average lidar ratios that can further be used to improve backscatter lidar retrievals of aerosol extinction profiles (Burton et al., 2010). AOD derived from the passive instruments may be more accurate than the AOD derived from the lidar, but in other cases, the lidar retrievals of AOD using the HSRL molecular channel are likely to be more accurate than spectroradiometer retrievals of AOT over land. Cloud top height and cloud optical thickness (COT) retrieved from these instruments can also be used to validate retrievals of these parameters from spaceborne lidar and radar. However, the cloud top height derived from spectroradiometers is a 'radiative height' and in many cases not comparable with the geometric cloud top height measurements, especially for semi-transparent clouds. Thus its use has to be handled with care for validation purposes (Haarig et al., 2023). Short-wave spectroradiometers measure TOA reflectances at multiple wavelengths. Clouds are detected by evaluating contrast relative to background surface reflectance at different wavelengths, while cloud top heights are retrieved using the CO_2 slicing technique to determine cloud top pressure and NCEP GFS data to convert to height (Frey et al., 2008; Menzel et al., 2008).

COT is retrieved by comparing measured reflectances at targeted wavelengths to values in lookup tables for ice and water clouds computed from radiative transfer model calculations of plane-parallel clouds over a dark surface (Platnick et al., 2003). AOD is retrieved by eliminating cloudy pixels, correcting for atmospheric gaseous absorption and attenuation, subtracting surface reflectances, and then similarly comparing these measured spectral reflectances to a lookup table of modeled aerosol optical properties (Levy et al., 2013). Though the underlying principle is the same for aerosol retrievals, different algorithms exist to account for surface brightness regimes (ocean, vegetation, desert).

Multi-angle spectroradiometers also provide retrievals of cloud top height, COT, and column AOD, though with expanded information content provided by observing the atmosphere at multiple viewing angles. Aerosol and cloud top heights are retrieved by the observed parallax between measurements at different angles, corrected for atmospheric winds (Moroney et al., 2002). Therefore, these retrievals are less reliant on the accuracy of measured radiances. Retrievals of COT are determined from measured radiances at visible wavelengths (Marchand et al., 2010) and estimates of microphysical aerosol properties are also possible, including SSA and particle size (Kahn et al., 2010). Multi-angle polarization-sensitive spectroradiometers observe the polarization state of the reflected radiances, principally enabling the retrieval of additional aerosol properties.

Solar occultation scattering

Spaceborne solar occultation and limb scattering measurements provide a means to validate aerosol and polar stratospheric cloud observations in the stratosphere along with cirrus altitudes. Typical vertical resolutions are on the order of 1 km (Taha et al., 2021). Instruments employing the solar occultation technique vertically scan the sun as it rises and sets along the limb of the Earth, and pass the light through a grating spectrometer to achieve vertical profiles of extinction at multiple wavelengths (Thomason et al., 2010). This allows observations of stratospheric aerosol, trace gases, and polar stratospheric clouds. The occultation technique is beneficial because it is self-calibrating, making measurements highly accurate, and the multiple wavelengths observed facilitate the retrieval of intensive aerosol properties. It is also applied to lunar and stellar targets. Because the occultation technique relies on a bright target passing across Earth’s limb, measurement opportunities are less common than for other techniques. Detection of subvisible and visible cirrus is also possible with these instruments using measurements of extinction and their ratios at different wavelengths (Schoeberl et al., 2021).

The spaceborne limb scattering technique observes the limb of the Earth's atmosphere that is illuminated by the sun, thereby allowing more measurement opportunities than solar occultation. Extinction is retrieved from the multi-wavelength radiance measurements using a radiative transfer model and assumptions on the optical properties of aerosol present in the stratosphere (Taha et al., 2021). Instruments using the limb scattering technique provide vertical profiles of aerosol extinction that are directly comparable to extinction retrievals from lidar, with the highest accuracy in the stratosphere.

Ground-based photometer

A photometer is a passive ground-based instrument that uses the direct radiation from the sun (sun photometer) or moon (lunar photometer) to derive aerosol and cloud optical thickness

(Chiu et al., 2010; Sinyuk et al., 2020). The Ångström exponent of aerosol optical thickness (columnar extinction Angstrom exponent) is derived from the observation at several wavelengths. The sun photometer is limited to daytime observations, while the lunar photometer is limited to nighttime observations of the moon. Photometers are globally widespread and organized in networks such as the Aerosol Robotic Network (AERONET, (Holben et al., 1998)) or SKYNET (Nakajima et al., 2007, 2020). Sun photometers are often also sky radiometers, providing measurements of diffuse light at different scattering angles (during Almucantar or Principle Plane measurements). This allows the retrieval of column-integrated aerosol microphysical properties, e.g. particle size distribution, refractive index, absorption optical depth, asymmetry parameter, and phase function. Photometer measurements can be used to validate column-integrated aerosol or cloud extinction (AOD, COD) from active and passive spaceborne sensors.

3.2.4. In-situ instruments

Aerosol, cloud, and precipitation particles are complex and can be described under several perspectives, approaches, and techniques, yielding information on concentration, particle size distribution (PSD), particle shape, hygroscopicity, optical properties, phase, and composition, all of which vary in space and time. Satellite calibration and validation efforts may need to cover most of the above-mentioned perspectives, although some properties may be more directly linked to remote sensing observables (e.g., scattering and extinction, single-scattering albedo, refractive index) while the connection must be made for others through complex retrievals (e.g., particle speciated composition, particle shape, and size distribution).

Each in-situ observation only provides information where the instrument is located. Extensive spatial networks are possible, enabling mapping for statistical validation at the surface to identify first-order discrepancies between spaceborne and ground-based estimates that require in-depth examination, to characterize uncertainties in satellite retrievals, and to estimate the convergence of these two types of estimates. Yet, such networks are usually limited to the surface and can be hard to relate to spaceborne measurements (which are more representative of the atmospheric column). Mobile platforms (using aircraft, balloons, and UAVs: covered in section 3.3.2.2) can provide better spatial and/or vertical coverage for in-situ observations. They are usually preferred to improve the understanding of the physical relationships between aerosols, clouds, and precipitating particles, although due to the cost involved their use is usually temporally limited compared to long-term ground-based networks. Moreover, they are useful to understand the relationship between the microphysical properties and the radiances observed by satellite sensors at different frequencies. For aerosols, size distribution and size-resolved shape, phase, composition, and mixing state are required for the evaluation of remote sensing retrieval schemes as well as bulk properties (concentration, extinction). For clouds and precipitation, size distribution, phase, and composition are the targeted properties.

Nephelometers measure the aerosol scattering coefficient, usually at multiple wavelengths, with high temporal resolution (Anderson & Ogren, 1998). **Aethalometers** measure the aerosol absorption coefficient. When combined, the extinction coefficient can be derived for a direct comparison to lidar profiles and multispectral imagers (the latter usually report the aerosol optical thickness, i.e. the column-integrated extinction), and the single-scattering albedo (useful to estimate the contribution to absorption, that can be related to species such as black carbon).

The collection of samples using **filters** (Formenti et al., 2003) or **impactors** (Lieke et al., 2011) allows offline analysis to yield information on aerosol particle shapes, composition, and mixing state. Information that can be derived from samples typically reflects the bulk properties, but can also be more detailed with for example a particle-by-particle image and the observation of the size-resolved elemental or mineralogical composition.

Optical Particle Counters (OPCs) or scattering probes are amongst the most useful in-situ instruments, although their use in cal/val activities is mainly indirect. They provide particle size distribution (PSD), from which a mass size distribution and a mass concentration can also be estimated. Aerosol size, concentration, and number density span several orders of magnitude, and suborbital constraints on them are very important to constrain a priori assumptions in satellite retrievals, despite their observational uncertainties. OPCs are broadly deployed on aircraft (Baumgardner et al., 1992; Osborne & Haywood, 2005; Ryder et al., 2015; Turnbull et al., 2012); and many others) and UAVs (Kezoudi et al., 2021; Renard et al., 2016; Smith et al., 2019). PSD measurements allow for the reduction in uncertainties on parameters useful to remote sensing, such as the lidar ratio (Jager & Hofmann, 1991; Marenco et al., 2016) and the specific extinction (Marenco et al., 2011). Furthermore, OPCs offer a complementary picture to the remote sensing observations, and the validation occurs from the coherence of the enhanced knowledge brought by the closure of the two approaches (Tsekeri et al., 2017).

Recent advances in scattering probes for cloud research involve the acquisition of scattered light at multiple and larger scattering angles (e.g., the Small Ice Particle Detector, PHIPS HALO and the Backscatter Cloud Probe) which allows one to distinguish between solid ice and liquid water drops. Baumgardner et al. (2017) summarize the different types of in-situ cloud probes that exist, and McFarquhar et al. (2017) describe the different algorithms that are used to process data from these probes. Although we generally distinguish cloud probes from aerosol probes, they can be exploited synergistically (i.e. to make observations of large aerosol particles such as mineral dust; see Ryder et al. (2015)).

Optical array probes (OAPs) illuminate an array of photodiode detectors and count the number of diodes shadowed by each particle (Knollenberg, 1970). This allows the acquisition of two-dimensional images of the particles and infer information on their size and shape. The cloud probes cover the size range from 15 μm to 1 mm, and precipitation probes cover the size from about 1 mm to 1 cm. Examples of these probes include Two-Dimensional Cloud and Precipitation spectrometers (2DC and 2DP), Cloud Imaging and Precipitation Imaging Probes (CIP and PIP), and the Two-Dimensional Stereo Probe (2DS) that uses two separate orthogonal arrays oriented horizontally and vertically to obtain particle images.

High-resolution particle imagers are distinguished from OAPs in that an actual two-dimensional image of a hydrometeor is obtained. Examples of such probes include the Cloud Particle Imager (CPI), the High-Speed Imaging Probe (HSI), and the imaging component of the PHIPS HALO probe. The images have higher resolution than available with OAPs but typically have smaller sample volumes that are not always well-defined, complicating the numerical calculation of size-resolved and bulk properties.

Bulk liquid water probes are heated wires that are typically used to measure the total amount of liquid water in clouds but do not provide information on how this mass is distributed with particle size. Examples of these probes include the King Probe, the Johnson-Williams probe, and the LWC sensor on the WCM-2000 and Nevzorov probes.

Bulk total water content (TWC) probes measure the total water content regardless of phase. Examples of these probes include the Counterflow Virtual Impactor (CVI), and the Nevzorov probe.

Holographic probes, such as the Holographic Detector for Clouds (HOLODEC, (Fugal & Shaw, 2009)) provide information on the three-dimensional position, shape, and size of each particle in a sample volume, as derived from an interference pattern of the incident wave and light scattered by an illuminated particle. The time and computer power needed to reconstruct the holograms limit the extensive use of this probe.

Other probes provide measurements of cloud bulk extinction and the observation of supercooled water.

Among precipitation sensors, **rain gauges** directly measure precipitation rates or time accumulations and provide reliable records frequently spanning more than 100 years, useful for long-term studies, extremes, and trends. Their global distribution is heterogeneous, with higher densities in more populated regions and lower densities in rural and remote areas. Critically, the number of gauges available also depends on their temporal sampling resolution, with stations sampling at finer scales being rarer. The spatial representativeness of each gauge measurement depends on the autocorrelation distance of precipitation (e.g. Delahaye et al., 2015). While the autocorrelation increases with time integration, it varies greatly with the precipitation regime and is typically short for extreme events (e.g., convective events; (Lebel et al., 1987)). Rain gauges provide local quantitative accuracy that can be combined with the spatial distribution of precipitation provided by weather radar observations to derive more accurate surface precipitation estimates.

Disdrometer observations are useful for providing a temporally continuous record of the size distribution and falling velocity of precipitation at the surface. The measured drop size distribution is then used to derive other moments of the size distribution, such as reflectivity. These observations are also spatially limited at the point of measurement. Precipitation estimates from active and passive sensors rely on relations between precipitation rate and remote sensing observations (e.g., radar reflectivity to rain rate, i.e., the Z–R relations) that are moments of the PSD.

3.2.5. Synergistic observations for enhanced validation capabilities

In this section, we describe two types of synergistic observations for enhanced validation capabilities. The first is synergistic retrievals of geophysical variables using observations from multiple instruments, a process that normally increases the information content, thereby often reducing the reliance on a priori assumptions in retrievals. The second type of synergistic observation refers to collocated observations from multiple instruments to provide complementary views of the observation target without using the measurements from multiple instruments in a joint retrieval network. An example of the latter is the use of lidar and radar to detect cloud boundaries. Rather than providing a comprehensive survey of each synergistic observation type, we provide only a few illustrative examples of synergistic retrievals that are relevant for the validation of the spaceborne observations considered here.

Synergistic Retrievals: Lidar + sun photometer

By collocating an elastic backscatter system with a ground-based sun photometer, the aerosol optical depth measured by the sun photometer can be used as a constraint on the lidar inversion problem, because the AOD is the column integral of aerosol extinction (e.g. Ganguly et al., 2009; Lopatin et al., 2013, 2021; Marenco et al., 1997; Takamura et al., 1994).

In addition, it has been shown that lidar and sun-photometer measurements can be used in synergy to retrieve microphysical particle properties and concentration (Gasteiger, et al., 2011a). Lidar measurements provide vertical information at a limited number of wavelengths (usually 3 wavelengths) and sun photometers (Haarig et al., 2023) can only provide columnar information but usually at several spectral channels (standard AERONET sun photometers with 8 wavelengths). The inversion of microphysical aerosol properties such as size and number concentration from the measured optical properties is an ill-posed inverse problem (e.g. Müller et al., 1999). State-of-the-art lidar systems provide the profiles of 3 backscatter coefficients, 2 extinction coefficients, and at least 1 depolarization ratio (Engelmann et al., 2016; Müller et al., 2014; Veselovskii et al., 2015). The additional use of the spectral information from a sun photometer constrains the inversion (Gasteiger, et al., 2011a) and improves the results (e.g., in the framework of the Generalized Retrieval of Atmosphere and Surface Properties (GRASP), (Kudo et al., 2016; Lopatin et al., 2013, 2021). However, this requires optical modeling assuming realistic particle properties (Gasteiger, et al., 2011b).

Synergistic Retrievals: Lidar + polarimeter

Similar to the combination of lidar and other measurements that constrain column-integrated aerosol properties, recent work has focused on combining lidar measurements with polarimetric observations of total and polarized radiances. This approach was the fundamental methodology considered for the retrieval of higher-level aerosol properties for the NASA AOS mission. In an early application to airborne lidar and polarimeter observations, HSRL-derived AOD and aerosol vertical distributions were used to improve the aerosol retrievals from an airborne polarimeter. More recently, the approach was used to derive full profiles of aerosol microphysical and radiative properties from joint airborne lidar and polarimeter observations in a full Bayesian optimal estimation framework (Xu et al., 2021).

Synergistic Retrievals: Remote sensing + in-situ measurements

Remote sensing and in-situ techniques are quite different in the methods used and in the atmospheric volumes that they can sample. However, they offer complementary information on the atmosphere and its constituents, and it can be at times really useful to combine them in order to increase our knowledge of the atmosphere and the techniques themselves. In most of the examples that we give below, these techniques have been combined ad hoc to answer specific questions that have arisen for a given experiment; therefore, we do not have the ambition of being exhaustive.

An application of remote sensing and in-situ synergy allows one to compute mass concentrations of a chosen aerosol type from lidar observations of the full aerosol mixture, complemented with airborne PSD measurements. This was done on the occasion of the eruption of Eyjafjallajökull when it was important to quantify atmospheric volcanic ash in terms of absolute concentration, to address aviation safety concerns (Marenco et al., 2011). The in-situ measurements permitted the evaluation of a coarse extinction fraction (making it possible

to disregard the scattering contribution of fine particles, which is believed not to be volcanic ash) and a coarse mode-specific extinction (mass-to-extinction conversion factor). These quantities, evaluated on a flight-by-flight basis, were used to convert lidar-derived aerosol extinction to ash concentration, expressed in micrograms per cubic meter. The relatively large uncertainty of those conversions (estimated to be a factor of 2) was deemed smaller than many other uncertainties on volcanic ash quantitative estimates so that the derived dataset was found very useful for both model and satellite validation (see e.g. World Meteorological Organisation, 2015).

As a general consideration, OPCs offer a complementary picture to remote sensing, so that combining their observations reduces the knowledge gap on the aerosol mixture under examination. If the goal is validating the remote sensing observations, the validation occurs from the coherence of the enhanced knowledge brought with the closure of the two approaches. If the goal is retrieving information on the atmosphere that neither method can provide alone, then we can speak of a true synergistic retrieval. The latter concept is exemplified for example with the In-situ/Remote sensing aerosol Retrieval Algorithm (IRRA) (Tsekeri et al., 2017). In that study, airborne in-situ measurements and lidar remote sensing were combined to retrieve vertical profiles of ambient optical and microphysical properties of an aged smoke plume. Observations included lidar extinction profiles, the in-situ dry PSD, dry scattering and dry absorption, and the chemical composition. The combination of these pieces of information allowed the characterisation of the aerosol growth due to humidity content and the ambient PSD.

Synergistic Use of Observations: lidar and radar

Active remote sensing with lidar and radar provides height-resolved information on aerosol and cloud distribution and properties. Due to the different wavelengths of lidar and radar, they are sensitive to different properties. Measuring at shorter wavelengths, the lidar is sensitive to the particle concentration and can detect small particles and hydrometeors. However, the signal can be extinguished at high particle concentrations or from large particles or droplets. The radar, in contrast, is sensitive to the particle size and thus misses aerosols and small hydrometeors. Due to this different sensitivity, both instruments complement each other (Ewald et al., 2021; Stephens et al., 2018). This provides information on the full extent of the vertical aerosol and cloud distribution.

Synergistic Retrievals: lidar and radar

Since the radar reflectivity is proportional to the sixth moment of the particle size distribution (PSD), and the lidar backscatter coefficient is proportional to the second moment of the PSD, two moments of the PSD can be determined in the overlap region of both instruments from synergistic use of the two measurements.

The first steps towards a synergistic lidar-radar retrieval to derive ice microphysical properties from lidar and radar backscatter were done by Intrieri et al. (1993), and Okamoto (2003). The methods use the differences in backscatter returns widely separated in wavelength to derive information on the characteristics on sizes of the scatterers. However, their approaches are based on an assumed extinction-to-backscatter ratio (lidar ratio). Donovan & van Lammeren (2001), and Tinel et al. (2005) solved that problem by replacing the unknown lidar ratio with the ratio between radar reflectivity Ze and extinction α within the lidar equation. This approach

retrieves the extinction α independently of assumptions on the particle size spectra and particle density. These methods are still limited to regions where both cloud radar and lidar measurements are available. Recent approaches try to combine lidar and radar measurements within a framework that naturally bridges the gap between these altitude regions: For the ground-based measurement network Cloudnet (Illingworth et al., 2007), various techniques for ice clouds (Delanoë & Hogan, 2008; Donovan & van Lammeren, 2001; Tinel et al., 2005) have been incorporated into a combined cloud product. For satellites, the CAPCOM approach (Sato & Okamoto, 2011) will combine radar and lidar measurements from EarthCARE; it is based on an optimal estimate of cloud properties including specular reflection of ice crystals and residual Doppler particle fall speeds (Sato et al., 2009) to retrieve cloud particle phase, size, and their number concentration. The CAPTIVATE approach (Mason et al., 2023) is based on a variational optimal estimation algorithm (VarCloud/DARDAR, (Delanoë & Hogan, 2008, 2010)) which combines radar, lidar, and infrared radiance measurements in a unified framework. The current version of the VarCloud algorithm was transformed from C++ to Python (VarPy) to make it more flexible and to allow the use of different wavelength combinations from different platforms (Cazenave et al., 2019). Furthermore, the capability of Varpy was extended to also account for mixed-phase clouds (Aubry et al., 2024).

Synergistic Retrievals of Precipitation: Weather Radar + Gauges

Remote sensing is the only way to explicitly observe the spatial distribution of precipitation. However, complex interactions between the spatiotemporal variability of precipitation processes, underconstrained relationships between precipitation-related quantities and remote sensing measurements, sensor resolution, sensitivity, calibration, and the indirect nature of precipitation retrievals introduce complications. In the last decades, weather radar systems have become a valuable tool to fill multiple observational gaps in time, surface 2D and 3D. As active sensors, ground-based radars provide range-resolved information on precipitation that is not available from gauges and from most satellite sensors. Radar systems reveal precipitation characteristics, including intermittency, types (e.g., stratiform, convective, snow, and hail), and rates, with better resolution than gauges and better accuracy than satellites. Through real-time and high-resolution volume scanning, weather radars offer more comprehensive information on the horizontal and vertical structure of precipitation. Radar networks upgraded with dual-polarization technology give additional insights into precipitation microphysics specifically on the size, shape, orientation, and phase of hydrometeors. Ground-based weather radar data are now widely used by national weather services for quantitative precipitation estimation (QPE) at fine scales (e.g., 1 km/5 min). Radar QPE is subject to specific uncertainties (i.e., sensor calibration, attenuation depending on the radar frequency, ground clutter, and beam blocking, variation of reflectivity with height, conversion from radar moments to precipitation rate, etc. (e.g. Berne & Krajewski, 2013; Delrieu et al., 2009). The characterization of these uncertainties has motivated studies for several decades. Radar–rain gauge merging approaches combining the fine spatio-temporal resolution of radar and the local accuracy of gauges have been proposed for QPE (e.g. Delrieu et al., 2014) and are applied operationally, while novel approaches are being developed to integrate uncertainty as part of the quantitative estimation process (e.g. Kirstetter et al., 2015; Neuper & Ehret, 2019). To overcome these individual sensor limitations, it is crucial to recognize that no single sensor combines accuracy, resolution, and representativeness over relevant spatial and temporal scales. Achieving these characteristics requires an expert combination of observations that

maximize each sensor's advantages while minimizing its weaknesses. Ultimately, such a combination does not produce perfect estimates with no uncertainty, but estimates with uncertainties that are deemed sufficiently low.

3.3. Specific instruments

3.3.1. Ground-based observations

3.3.1.1. Fixed-location systems and networks

A typical goal of measurement networks is to provide measurements over a broad and diverse geographical area. There is, of course, a tradeoff between spatial coverage and site complexity. Many measurement networks that are particularly focused on broad spatial coverage tend to have focused and limited measurement capabilities. Some applications, in particular those that study the interactions among system components, require more comprehensive measurements at a single location and time. Historically, requirements for such comprehensive measurements were met through intensive field campaigns. Such field studies have been invaluable; however, they are very limited in time so do not sample seasonal or interannual environmental variability, which may be important for understanding physical processes. Supersites address the dual need for comprehensive and long-term measurements. Supersites may be operated as a single system or a limited network but are constrained in spatial coverage.

Some networks described below include supersites, which we define as sites with expansive suites of instrumentation and/or sites that serve multiple user communities (e.g., aerosols, clouds, radiation). The measurement scope of supersites is not truly comprehensive but depends on the science goals of the target science community. For sites supporting studies of climate processes, and particularly the earth's energy balance, measurements of the components of the atmosphere and earth surface that impact that balance are needed. This includes measurements of cloud and aerosol optical properties, profiles of the atmospheric thermodynamic state, precipitation properties, and surface properties including temperature and (over land) soil moisture. For some applications, additional detailed measurements may be required, such as measurements of aerosol chemical properties and trace gases, which may serve as aerosol precursors. As with any network, there is a trade-off with increasing complexity.

Examples of programs that operate supersites include the US Department of Energy Atmospheric Radiation Measurement (ARM) facility and the pan-European Aerosol, Clouds and Trace Gases Research Infrastructure (ACTRIS). ARM and ACTRIS provide measurements to support the global climate research community and other earth science applications. Both programs are described in brief below.

Table 3.7. *Available networks, deployed instruments, location, number of stations, and corresponding products*

Networks	Type	Geographical Coverage	Number of Stations	Products
Multi-Instrument				
ACTRIS	Multi-Instrument	Europe***	112	1-9, 11
ARM	Multi-Instrument	Global	6*	All products listed in Chap. 2
NDACC	Lidar, FTIR, Various Spectrophotometers and Radiometers	Global	70	1,2,3,4
Lidar Networks				
GALION	Framework for lidar networks below	Global		
AD-NET	Lidar	East Asia	22	1,2,3,4,5,7,8,9
EARLINET	Lidar	Europe	22	1,2,3,4,5,6,7,8,9
LALINET	Lidar	South America	7	1,2,3,4,6,7
MPLNET	Micropulse Lidar	Global	72	1,2,5
E-profile	Ceilometers	Mainly Europe	280**	1, 2a
Radar Networks				
NEXRAD	S-Band radar	USA	159	10, 11, 12
OPERA	C-Band, X-Band, S-Band radars	Europe	200	10, 11, 12
Radiometers				
AERONET	Sun photometer	Global	1146	6,9
SKYNET	Sun photometer	Asia + Europe	159	6,9

(1) Layer heights, (2) backscatter coefficient, (2a) attenuated backscatter, (3) extinction coefficient, (4) lidar ratio, (5) depolarization ratio, (6) angström exponent, (7) colour ratio, (8) cirrus optical depth, (9) aerosol optical depth, (10) rain rate, (11) atmospheric movement, (12) radar reflectivity

* In 2024-2025, ARM locations will include: US Southern Great Plains (Oklahoma), US North Slope of Alaska, Southeastern US (Bankhead National Forest in Alabama), Graciosa Island (Azores), and Cape Grimm, Australia (location of 6th observatory to be announced in August).

** Considering only E-PROFILE network

***and selected non-European sites

Multi-instrument networks

ACTRIS - The Aerosol, Clouds and Trace Gases Research Infrastructure (ACTRIS; https://www.actris.eu/) is the pan-European research infrastructure that is currently operating in 22 countries and combines observations from 112 facilities. The ACTRIS infrastructure

includes aerosol in-situ, aerosol remote sensing, cloud in-situ, and cloud remote sensing measurement facilities as well as reactive trace gas in-situ measurements and remote observations.

The cloud remote sensing facilities carry out observation using Doppler Cloud Radars (Ka- and/or W-band), microwave radiometers for profiling of temperature and humidity, and observations of liquid water path, and Doppler lidars for wind profiling. Additionally, automatic low-power lidars or ceilometers are used for cloud profiling purposes.

ARM - The ARM user facility includes a network of six atmospheric observatories. Multi-year ARM sites (www.arm.gov) overlapping with EarthCARE will be the U.S. Southern Great Plains, North Slope of Alaska, and Southeast U.S. and the Eastern North Atlantic in the Azores. Each observatory includes cloud radar, backscatter or extinction lidar, thermodynamic profiling, various radiometers, and aerosol in-situ instruments. Two of the observatories are deployed for approximately a year at a time on a proposal-driven basis. See additional information in section 3.3.1.1.

NDACC (https://ndacc.larc.nasa.gov/) - NDAAC (Network for the Detection of Atmospheric Composition Change) is a Network of various types of instrumentation such as Brewer Spectrophotometer, Dobson Spectrophotometer, FTIR Spectrophotometer, Lidar, Microwave Radiometer, Sondes, UV and Visible Spectro & Radiometers and is composed of more than 70 globally distributed, ground-based, remote-sensing stations with more than 160 currently active instruments. Most of the products are related to greenhouse gases, trace gases and aerosols in the stratosphere, and UV radiation.

Lidar networks

GALION - GAW Aerosol Lidar Observation Network and other networks - The World Meteorological Organization (WMO) Global Atmospheric Watch (GAW) Aerosol Lidar Observation Network (GALION) was formed in 2008. GALION is a lidar network of networks organized through the GAW program to coordinate network activities and provide comprehensive profiling of atmospheric aerosols, clouds, gases, and thermodynamic structures. GALION chair and steering committee leadership is run by the heads of the individual lidar networks. Each GALION network is an official GAW contributing network.

AD-NET (https://www-lidar.nies.go.jp/AD-Net/) - AD-Net is a lidar network for continuous observation of vertical distributions of Asian dust and other aerosols in East Asia (Shimizu et al., 2004). The standard lidar system in AD-Net is a two-wavelength (1064 nm, 532 nm) polarization-sensitive (532 nm) Mie-scattering lidar (Sugimoto et al., 2008). Extinction coefficient estimates for non-spherical and spherical aerosols are also derived with the method using the backscattering and depolarization ratio (Shimizu et al., 2004; Sugimoto et al., 2002). For quantitative analysis of aerosol optical characteristics, HSRLs (Jin et al., 2020, 2022) and Raman lidars (Nishizawa et al., 2017) have been constructed at primary sites. At present, there are 22 stations, the majority in Japan, some in South Korea, Mongolia, and Thailand. Also, some stations are collocated with SKYNET skyradiometers.

EARLINET (https://www.earlinet.org) - The European Aerosol Research Lidar Network, EARLINET (Pappalardo et al., 2014), was established in 2000 as a research project with the goal of creating a quantitative, comprehensive, and statistically significant database for the horizontal, vertical, and temporal distribution of aerosols on a continental scale. Since then

EARLINET has continued to provide the most extensive collection of ground-based data for the aerosol vertical distribution over Europe.

A major part of the measurements is performed according to a fixed schedule to provide an unbiased statistically significant data set. Additional measurements are performed to specifically address important processes that are localized either in space or time. Back-trajectories derived from operational weather prediction models are used to characterize the history of the observed air parcels, accounting explicitly for the vertical distribution. EARLINET is a key component of the ACTRIS infrastructure, which represents a big step towards better coordination of the atmospheric observations in Europe towards the establishment of the European component of an Integrated Atmospheric Global System as part of GEOSS, the Global Earth Observation System of Systems (GEOSS, 2005). Several active stations distributed over Europe are part of the network. Most but not all of the participating stations are members of ACTRIS. The organization of the observing capabilities including Quality Assurance and Data Center services is now handled by ACTRIS. EARLINET remains a network for lidar expertise and scientific applications. EARLINET is also a contributing network to the GAW Programme.

LALINET (http://lalinet.org/) - The Latin America Lidar Network (historically LALINET is also known as ALINE) is a Latin American coordinated lidar network measuring aerosol backscatter and extinction profiles for climatological studies of the aerosol distribution over Latin America, as well as other atmospheric species such as ozone and water vapor. This federative lidar network aims to establish a consistent and statistically sound database for the enhancement of the understanding of aerosol distribution over the continent and its direct and indirect influence on climate. At present, there are 14 stations in LALINET, however after the pandemic of COVID there is a restructuring of the network. Most of the stations operate multiwavelength backscatter lidars, some have Raman channels and a few depolarization.

MPLNET (https://mplnet.gsfc.nasa.gov/) - The NASA Micro-Pulse Lidar Network (MPLNET; (Welton & Campbell, 2002)) is a federated network of Micro-Pulse Lidar (MPL; (Spinhirne et al., 1995)) systems designed to measure aerosol and cloud vertical structure, and boundary layer heights. The data are collected continuously, day and night, over long time periods from sites around the world. Most MPLNET sites are co-located with sites in the NASA Aerosol Robotic Network (AERONET). MPLNET is also a contributing network to the World Meteorological Organization (WMO) Global Atmospheric Watch (GAW) Aerosol Lidar Observation Network, GALION. MPLNET data have contributed to many studies and applications. Key focus areas for MPLNET include (i) domestic and international aerosol and cloud research, (ii) climate change and air quality studies, (iii) support for NASA satellite and sub-orbital missions, and (iv) aerosol modeling and forecasting.

MPLNET is composed of NASA sites and others run by, or with help from, partners from around the world. Principal investigators for individual network sites may be from NASA, other US government agencies, universities, or foreign institutions. MPLNET core activities and the NASA staff are funded by the NASA Radiation Sciences Program and the NASA Earth Observing System (EOS). The evolution of the MPL from the initial (Spinhirne et al., 1995) optical design to the standard design now used in MPLNET is described in detail by Campbell et al. (2002) and Welton & Campbell (2002), including on-site maintenance, and calibration techniques. Post 2002 enhancements include a new data system, telescope, fiber-coupled detectors, and a new laser. Post 2013 changes: The original MPL design from the early 1990s

was unpolarized, providing only total signal power. The MPL was first polarized with an approach described by Flynn et al. (2007). In total, there are 81 sites in MPLNET, 23 active.

E-PROFILE (https://e-profile.eu/) - E-PROFILE is part of the EUMETNET (https://www.eumetnet.eu/) Composite Observing System, EUCOS, managing the European networks of radar wind profilers (RWP) and automatic lidars and ceilometers (ALC) for the monitoring of vertical profiles of wind and aerosols including volcanic ash. E-PROFILE coordinates the measurements of vertical profiles of wind from radar wind profilers (vertically pointing Doppler radars) and weather radars from a network of locations across Europe and provides the data to the end users. The main goal is to improve the overall usability of wind profiler data for operational meteorology and to provide support and expertise to both profiler operators and end users.

Due to technical advances of the last years, ceilometers (automatic low-cost lidars) provide nowadays not only cloud base height but also information on the vertical distribution of aerosols derived from the backscatter profile. To make this new observation capacity available, E-PROFILE is developing a framework to produce and exchange profiles of attenuated backscatter profiles. Automatic lidars and ceilometers of stations across Europe are added to the operational network.

Weather radar networks

Because weather radars typically operate as part of national weather radar networks (e.g. United States Weather Surveillance Radar Doppler (WSR-88D) radar network) or are a part of networks, such as OPERA (European Operational Programme for the Exchange of weather RAdar information), they can provide synoptic scale observations.

OPERA - In Europe, national weather services are responsible for observing the weather in their respective countries. However, they also collaborate under the umbrella of the European Meteorological Services Network, EUMETNET. The work of weather radar within EUMETNET is coordinated by the Operational Program for Exchange of Weather Radar Information (OPERA), which was established in 1999. The development and activities of OPERA are described in Saltikoff et al. (2019) and Huuskonen et al. (2014). The OPERA network consists of 30 members operating over 200 radars, mostly in C-band but with some in X- and S-bands. Currently, about 70% of the radars have dual-polarization capability, but dual-pol variables are not yet collected within OPERA. The production lines consist of three components: CUMULUS/STRATUS for gathering and distributing incoming single-site radar data, CIRRUS for producing 5-minute maximum reflectivity composites with 1 km spatial resolution, and NIMBUS for generating rain rate and 1-hour rainfall accumulation composites, wind profile products, and quality-controlled volume data.

Four filters are centrally applied for quality control: an anomaly-removal module (Peura, 2002), a hit-accumulation filter (Scovell et al., 2013), beam blockage correction (Henja & Michelson, 2012), and a satellite-based filter of residual non-precipitation echoes based on the EUMETSAT Nowcasting SAF Precipitating Clouds product (Marcos & Rodríguez, 2019). A quality indicator, defined as the minimum of the first three quality indicators presented above, is added to the radar metadata. Finally, this quality indicator is weighted according to the distance from the radar and the height of the beam above the ground and used for generating the OPERA composite products. In 2022, an open climatological OPERA-based radar

precipitation dataset, EURADCLIM (EUropean RADar CLIMatology), was published (Overeem et al., 2023). This dataset covers a variety of climates from Mediterranean to temperate, mountain, continental, and arctic regions. In processing the dataset, additional algorithms are applied to remove non-meteorological echoes, and gauge adjustment is applied hourly. The rerun of EURADCLIM is performed once a year over the entire period, using all available rain gauge data, and the dataset is extended with one year of data.

NEXRAD or **Nexrad (Next-Generation Radar)** and the **Multi-Radar/Multi-Sensor System (MRMS)** - NEXRAD is a network including high-resolution S-band Doppler weather radars at 159 locations. They are operated by the National Weather Service (NWS) which is an agency of the National Oceanic and Atmospheric Administration (NOAA) within the United States Department of Commerce, the Federal Aviation Administration (FAA) within the Department of Transportation, and the U.S. Air Force within the Department of Defense.

The standard operation is in the S-band range, at a frequency of around 2800 MHz, with a typical gain of around 53 dB using a center-fed parabolic antenna. The pulse repetition frequency (PRF) varies from 318 to 1300 Hz with a maximum power output of 700 kW at Klystron output, although dependent on the volume coverage pattern (VCP) selected by the operator. All systems within NEXRAD have a dish with a diameter of 9.1 m (30 ft) and an aperture diameter of 8.5 m (28 ft). Using the predetermined VCPs, the NEXRAD systems have a traditional elevation minimum and maximum ranging from 0.1 to 19.5 degrees, although the non-operational minimum and maximum can span from −1 to +45 degrees. The antenna can, however, not be manually steered by the operator. Spatial resolution varies with data type and scan angle – level III data has a resolution of 1 km x 1 degree in azimuth, while super-res level II, (implemented in 2008 nationwide), has a resolution of 250m by 0.5 degrees in azimuth below 2.4 degrees in elevation. The National Centers for Environmental Information (NCEI) provides access to archived NEXRAD Level-II data and Level-III products.

In Norman, Oklahoma, a project built upon data collected by the NEXRAD network is the NOAA's Multi-Radar/Multi-Sensor system (MRMS: https://www.nssl.noaa.gov/projects/mrms/), developed by researchers at the National Severe Storms Laboratory (NSSL) and the University of Oklahoma (OU). The MRMS system automatically combines information from all ground-based radars comprising the National Weather Service's NEXRAD network, performs quality control procedures (Lakshmanan, 2007), mosaics radar data onto a common 3D grid, and generates a suite of severe weather and hydrometeorological products including precipitation. Other data sources are used, that include hourly analyses and forecasts from the High-Resolution Rapid Refresh (HRRR) and the Rapid Refresh (RAP) numerical weather prediction models (Benjamin et al., 2004) as well as rain gauge networks, upper air soundings, geostationary satellite observations, and surface observations. Surface precipitation accumulations are blended with collocated rain gauge networks to arrive at ground-based estimates of rainfall. The uniqueness of the MRMS system lies in its high resolution (1 km horizontal) and high-frequency product generation (2 min). A significant amount of research has been conducted over the past 10 years to improve the data quality and accuracy of the MRMS rainfall products (e.g. Kirstetter et al., 2015; Lakshmanan, 2007). The NEXRAD network was upgraded with dual-polarization technology in 2013, which benefitted radar quality control, hydrometeor classification, and quantitative precipitation estimation (QPE). The MRMS system was transitioned to operations at the National Centers for Environmental Prediction (NCEP) in Fall 2015, and more recently, MRMS dual-polarimetric QPE was transitioned to operations in October 2020. OU/NSSL's MRMS system has emerged

as the state-of-the-art in ground-based precipitation measurement in terms of spatial and temporal consistency, accuracy, and product resolution (Zhang et al., 2016).

Radiometer networks

AERONET - The AErosol RObotic NETwork (AERONET) program (Holben et al., 1998) has provided accurate remote sensing of aerosol optical and physical properties and a limited set of cloud properties for an extensive geographic distribution that includes all continents and many island sites, with some locations operating for almost 30 years now. AERONET-derived aerosol properties have been used for the validation of satellite retrievals of AOD (Remer et al., 2002; Sayer et al., 2012), the characterization of aerosol absorption and size distributions (Dubovik et al., 2002), for the validation of model estimates (Kinne et al., 2003) and to improved forecasts (Rubin et al., 2017) of aerosol properties. These investigations primarily depend on the highly accurate observations of extensive properties such as AOD from direct solar beam transmittance and as more data become available, they include the intensive aerosol products retrieved from inversion of the radiative transfer equation such as complex index of refraction and particle size distribution. In the context of this report, AERONET measurements can be used for the validation of column-integrated extinction and column-average aerosol properties, such as the lidar ratio.

SKYNET - https://www.skynet-isdc.org/ is a worldwide ground-based radiation observation network with many observation sites in Europe and Asia, focused on research regarding the interaction of aerosols, clouds, and solar radiation (e.g. Nakajima et al., 2007, 2020; Takamura & Nakajima, 2004). In addition to the research goals regarding aerosol-cloud-radiation interactions, the validation of satellite observations climate model simulations, and data assimilations are also within the scientific scope of the SKYNET activity. SKYNET uses a skyradiometer as a standard instrument to provide AOD, SSA, refractive index at several wavelengths from 315nm to 1020nm, and volume size distribution and Ångström exponent of aerosols by inversion estimation using skyrad.pack (e.g. Kudo et al., 2021; Nakajima et al., 1996) and a method using direct solar radiation (Estellés et al., 2012). Calibration using the improved Langley method (Campanelli et al., 2004, 2007; Nakajima et al., 2020), has been routinely performed, along with Inter-calibration of the sun-sky radiometers with a master instrument calibrated using the Langley method at a high mountain performed occasionally.

3.3.1.2. Mobile systems

A mobile system can be transported from one location to another by means of a vehicle (terrestrial, aerial, or ship). Some of these platforms are designed to be operated in motion in a dedicated mode, others are standalone systems that are put in a transport system (Ship, UAV, etc.). These systems can be relocated and thus fill gaps for validation.

Table 3.8. *Example of mobile systems along with instrumentation, operator, reference, and platform*

System	Instrumentation	Operator	Reference	Platform
Multi-instruments (including radar & lidar)				
LACROS	Cloud radar, MWL*, BSRN station, MWR**	TROPOS	(Radenz et al., 2021)	Mobile station
BALI system	Scanning Basta (W-Band) radar, lidar 532/808nm	LATMOS	(Delanoë et al., 2016)	Mobile instruments
Multi-Wavelength Radars				
Poldirad/Basta	Polarization C-Band radar, Basta (W-Band) radar	DLR	(Delanoë et al., 2016; Hagen et al., 2021)	Mobile instrument
SAPHERALER	W- and X-Band radars (ballon)	CNES		Balloon
Radars				
BASTAs	W-Band radar	LATMOS	(Delanoë et al., 2016)	Mobile instruments
X-Band Trailer	X-Band radar	NOA		Trailer
Horus	S-Band phased-array			Truck
PX-1000, RaXPol	X-band radar			Truck
PAIR	C-Band phased-array			Truck
Sea-Going Polarimetric (SEA-POL)	C-Band radar			Ship
Lidars				
OCEANET	MWL, sky camera, MWR, sun photometers	TROPOS	(Engelmann et al., 2016)	Ship
PollyNET	PollyXT MWL	TROPOS	polly.tropos.de	Mobile Instrument
MAMS	MWL, photometers	ACTRIS-FR		Mobile instrument
Aerosol platform	MWL, sun photometer	NOA		Mobile Instrument
EVE lidar	Polarization lidar system	NOA	(Paschou et al., 2022)	Mobile instrument
EMORAL	MWL	Univ. Warsaw		Van
POLIS	MWL	Univ. Munich	(Freudenthaler et al., 2018; Gross, Freudenthaler, Wirth, et al., 2015)	Mobile Instrument

*Multi-wavelength lidar, **Microwave radiometer

In addition to these mobile systems operated by specific institutions, the ARM user facility includes two deployable systems referred to as ARM Mobile Facilities (AMFs). The mobile observatories include a similar set of instruments as the multi-year sites introduced in section 3.3.1.1. The AMFs are deployed on a proposal-driven basis. Calls for proposals are typically published around the end of the calendar year in most years on the ARM field campaign webpage. The next planned deployments are in Tasmania, Australia, and Baltimore, U.S..

3.3.2. Airborne observations

3.3.2.1. Available airborne platforms and previously deployed instruments

A number of different high and low-flying aircraft are available to be equipped with adjustable in-situ and remote sensing payload for aerosol, cloud, and precipitation studies.

Table 3.9. *General information on airborne platforms and measurements*

Aircraft / Operator	Altitude range [m]	Range or Endurance [h]	Remote Sensing (Payload Accommodations)	In-situ Instruments flown
FAAM	10,000	5	Aerosol LIDAR, MARSS radiometer, ARIES infrared hyperspectral, SWS/SHIMS visible hyperspectral	various in-situ probes for chemistry, aerosol and cloud measurements; hygrometer; dropsondes
HALO	15000	10	WALES HSRL and WV DIAL, Cloud radar, multi-spectral imager, solar and thermal radiation, MWR	various in-situ probes for aerosol and cloud measurements, dropsondes
DLR Falcon	9000	4-5	various wind lidars	various in-situ probes for aerosol and cloud measurements, hygrometer, dropsondes
LOAC Voltaire				Light Optical Particle Counter
Strateole			BeCOOL lidar	backscatter tethered sonde, etc.
ATR42	1500		RASTA and BASTA radars, LNG lidar, ALIAS lidar, Radiometers	various in-situ probes for cloud measurements
STRATOBUS			BASTA	
Polar 5	4200	2300 km	MIRAC radar / radiometer, AMALI lidar	various in-situ probes for cloud measurements
Norwegian Aircraft				Nevzorov probe (LWC, TWC)
NASA LaRC B-200	8,534	6.2	HSR Lidar, water vapor+HSR lidar, Polarimeters, Spectro-radiometers	various in-situ probes for aerosol and cloud measurements, dropsondes
NASA Gulfstream III	13,716	7.5	Backscatter Lidar, HSR Lidar, water vapor DIAL+HSRLPolarimeters, Spectroradiometers	dropsondes, trace-gas probe (PICARRO)
NASA Gulfstream V	15,500	13	Backscatter Lidar, HSR Lidar, water vapor DIAL+HSR lidar, Polarimeter, Spectroradiometer	
NASA ER-2	21,336	12	Cloud and precipitation radars (9.6, 13.5, 35, 94 GHz), Backscatter Lidar, HSR Lidar, WV DIAL+HSRL, polarimeter, radiometers	
NASA WB-57	18,288	6.5	Cloud and precipitation radars (13.5, 35, 94 GHz)	
NASA DC-8 (expected to be decommissioned in mid-2024)	12,800	12	Cloud and precipitation radars (13.5, 35, 94 GHz)	
NASA P-3	9,100	10	Cloud and precipitation radars (13.5, 35, 94 GHz); HSRL	
NASA 777-200ER (expected to come online in late 2025)			tbd	tbd
Canadian Convair			94 GHz cloud radar, (355nm) backscatter Lidar	
ATMOSLAB	12,000	3.5	MULTIPLY HSRL (355,532,1064)	N/A
USRL (UAVs)	6,000	0.83	N/A	OPCs, aethalometer, backscatter sondes, gas concentration measurements, temperature, humidity, aerosol sample collection
various UAVs			WALI Lidar	Various instruments

In addition to the several aircraft mentioned earlier, airborne measurements can be obtained with smaller systems, such as balloons and UAVs. These systems do not have the flexibility and the endurance of larger aircraft, nor the ability to carry multiple instruments as part of their payload. However, they are cheaper to deploy and can provide valuable insights on atmospheric properties (see e.g. Kezoudi et al., 2021; Renard et al., 2016; Smith et al., 2019).

3.3.2.2. Airborne in-situ systems

Different aerosol and cloud in-situ instrument packages are deployed on the different airborne platforms to answer research questions for the specific scientific missions. The instrument package, a short description and the corresponding references are listed in the following.

Table 3.10. *Airborne in-situ packages and corresponding references.*

Instrumentation package	Description	Reference
FAAM core aerosol and cloud instruments	PCASP, CDP, CIP15, CIP100, 2DS, SID2, nephelometer, PSAP, meteorological variables, LWC, TWC, dropsondes	(Abel et al., 2014, 2017; Darbyshire et al., 2019; Rosenberg et al., 2012; Ryder et al., 2015, 2018; Tsekeri et al., 2018; Young et al., 2016)
HALO in-situ packages	PCASP, CDP, CIP, CIP, 2DS, SID, PIP, CAS-DEPOL, nephelometer, PSAP, CPC, Grimm OPC, TD, meteorological variables, LWC, TWC, dropsondes	(Krämer et al., 2020; Voigt et al., 2017)
Falcon cloud and aerosol packages	PCASP, CDP, CIP, CIP, 2DS, SID, PIP, CAS, nephelometer, PSAP, UHSAS, meteorological variables, LWC, TWC, dropsondes	e.g. (Petzold et al., 2011; Voigt et al., 2010; Weinzierl et al., 2017)
USRL dust/cloud instrument set	POPS, UCASS, COBALD, impactors	(Kezoudi et al., 2021)
Langley Aerosol Research Group Experiment (LARGE)	CN counter, Nephelometer, Optical particle counter	Microsoft Word - LARGE SEAC4RS Experiment Description.docx (nasa.gov)

PCASP = Passive Cavity Aerosol spectrometer Probe, CDP = Cloud Droplet Probe, CIP = Cloud Imaging Probe [CIP15 = 15 µm size resolution, CIP100 = 100 µm size resolution], SID = Small Ice Detector mark 2, PSAP = Particle soot absorption photometer, POPS = Portable Optical Particle Spectrometer, UCASS = Universal Cloud and Aerosol Sounding System, COBALD = Compact Optical Backscatter Aerosol Detector

3.3.2.3. Airborne remote sensing systems

Depending on the mission the airborne platforms are equipped with different instrumentation; among those active and passive instruments for aerosol, cloud, and radiation measurements. The instruments most frequently deployed on airborne platforms together with short descriptions and references for further specification are listed in the following.

Table 3.11. *Airborne remote sensing instruments, short description, and the corresponding references.*

Instrument / payload	Description	Reference
FAAM aerosol lidar	Airborne backscatter lidar at 355 nm	(Kealy et al., 2017; Marenco et al., 2011, 2014, 2016; O'Sullivan et al., 2020)
WALES lidar	Combined airborne depolarization sensitive (532 and 1064 nm) HSRL (532 nm) and WV differential absorption lidar	(Esselborn et al., 2008; Wirth et al., 2009)
FALCON wind lidars	Direct detection wind lidar system at 355 nm and Coherent wind lidar system at 2 µm	(Reitebuch et al., 2009; Witschas et al., 2017)
BeCOOL lidar	Balloon-borne micro lidar	(Ravetta et al., 2020)
LNG lidar	Airborne depolarization sensitive HSRL (355 nm)	(Bruneau et al., 2015)
ALIAS lidar	Airborne backscatter lidar at 355 nm	(Chazette et al., 2020)
Amali lidar	Polarization-sensitive (532 nm) backscatter lidar (355/532 nm or 532/1064 nm)	(Stachlewska et al., 2010)
NASA HSRL-2	High Spectral Resolution Lidar, HSRL-capable (ext+back) at 355/532nm, backscatter at 1064nm, depol at 355/532/1064nm	(Burton et al., 2018; Ferrare et al., 2023; Hair et al., 2008; Rogers et al., 2009)
NASA Cloud Physics Lidar	Backscatter at 355/532/1064nm	(McGill et al., 2002)
NASA HALO lidar	Combined airborne depolarization sensitive (532 and 1064 nm) HSRL (532 nm) and WV differential absorption lidar	(Carroll et al., 2022)
WALI lidar	Water vapor and aerosol Raman lidar at 355 nm	(Chazette et al., 2014)
NASA ER-2 High-Altitude Cloud and Precipitation Radars	HIWRAP (Ku/Ka), CRS (W), and EXRAD (X) Doppler Radars	(Heymsfield et al., 2023)
HALO cloud radar	Ka-band radar with Doppler capability	(Ewald et al., 2019)
RASTA	Airborne multi-antenna Doppler cloud radar at 94GHz	(Protat et al., 2004)
BASTA		(Delanoë et al., 2016)
MIRAC radar / radiometer	Airborne continuous wave radar at 94 GHz in combination with 89 GHz passive channel	(Mech et al., 2019)
Cloud and precipitation radars (P-3)		
Convair cloud radar		
specMACS	Hyperspectral imager	(Ewald et al., 2016)
SMART	Airborne hyperspectral observations	(Ehrlich et al., 2012; Wendisch et al., 2001)
HAMP	Microwave package (microwave radiometers at different frequencies)	(Mech et al., 2014)
ATR42 Radiometers		

3.3.3. Spaceborne remote sensing

Multiple spaceborne remote sensing systems have been deployed in the past 30 years that are capable of profiling Earth's atmosphere for validation purposes. Table 3.12 lists current, past, and future instruments. Though some of these instruments are no longer active, inter-validation activities are expected to continue as researchers seek to characterize the accuracy of the observation records they left behind. There is overlap in the operational lifetime of numerous instruments, leading to numerous intercomparison assessments (e.g. Behrangi et al., 2012; Feofilov et al., 2022; Lee et al., 2019; Taha et al., 2021).

Most of these spacecraft occupy sun-synchronous polar orbits, with varying inclinations and fixed equatorial crossing times. CloudSat and CALIPSO originally joined the A-Train satellite constellation in 2006 along with MODIS Aqua and others, allowing ground sampling within ~7 minutes of each other. In 2018, CloudSat and CALIPSO descended from the A-Train, causing their equatorial crossing times to gradually occur later in the day. Collocations with the remaining A-Train satellites became rare, as the orbits precess with respect to one another. CATS and SAGEIII on the International Space Station follow a precessing orbit at a lower inclination, with varying equatorial crossing times which allows sampling of the full diurnal cycle and coincident observations with other spacecraft in polar orbits.

Among the spaceborne lidars operational in the 2000s, most have been elastic backscatter lidars focusing on atmospheric observations (LITE, CALIOP, CATS) and surface observations (ATLAS, GLAS). Though the lidars for the ICESat missions are optimized for surface measurements, these instruments also provide atmospheric measurements suitable for validation. Special handling is required for ATLAS atmospheric observations due to a "folding" effect caused by the instrument's high repetition rate (Palm et al., 2021). The age of spaceborne HSRLs began in the mid-2010's. The HSRL capability was first demonstrated on ALADIN as the primary measurement technique (Schillinger et al., 2003). In 2022, the ACDL HSRL was launched on China's Atmospheric Environment Monitoring Satellite (Ke et al., 2022). The ATLID lidar on the EarthCARE mission will also use HSRL technology (do Carmo et al., 2021).

All the lidars in Table 3.12 provide measurements of the total backscatter return (attenuated backscatter in the case of EB lidars), except ALADIN which only receives the co-polar return of the circularly-polarized light that is emitted. Because the cross-polar component is not measured, the backscatter return will be less than the total backscatter for strongly depolarizing targets such as mineral dust and volcanic ash (Gkikas et al., 2023).

Cloud-aerosol discrimination and aerosol typing retrievals are provided in data products for ATLID, CALIOP, and CATS using slightly different information. For aerosol typing, CALIOP and CATS both rely on altitude, land-surface type, and measurements of attenuated backscatter and depolarization, though at different wavelengths (Kim et al., 2018; Nowottnick et al., 2022; Tackett et al., 2023). CATS also incorporates MERRA-2 reanalysis estimates of sulfate and carbon loading in its typing scheme. Being an HSRL, the ATLID lidar will have the benefit of using measured lidar ratios in addition to depolarization for aerosol typing (Gross, Freudenthaler, Wirth, et al., 2015), though at a shorter wavelength than CALIOP or CATS (Wandinger, et al., 2023b).

Spaceborne atmospheric precipitation measurements began in 1997 with the Precipitation Radar (PR) on board the Tropical Rainfall Measuring Mission (TRMM) platform. The 35-degree inclination of TRMM spacecraft and the Ku band employed are ideal for observing tropical precipitation. Later, in 2006, the W-band CPR on board CloudSat launched in tandem with CALIPSO at the same sun-synchronous orbit. CloudSat and CALIPSO orbited together, measuring the same locations within ~15 seconds of one another. The CloudSat CPR entered daylight-only mode for science collection in 2011 due to issues with the spacecraft battery (Witkowski et al., 2018). In 2015, the Dual-frequency Precipitation Radar (DPR) was launched onboard the Global Precipitation Measurement (GPM) platform with a 65-degree inclination as a successor of the TRMM-PR. It features two radars operating at Ku- and Ka-bands. Relative to the TRMM precipitation radar, the DPR is more sensitive to light rain rates and snowfall. Simultaneous measurements by the overlapping of Ka/Ku-bands of the DPR can provide information on particle drop size distributions over moderate precipitation intensities. The GPM Core Observatory also features the multi-channel GPM Microwave Imager (GMI) which is a conically-scanning multi-channel microwave radiometer with thirteen channels ranging in frequency from 10 GHz to 183 GHz. The GMI uses a set of frequencies that have been optimized over the past two decades to retrieve heavy, moderate and light precipitation using the polarization difference at each channel as an indicator of the optical thickness and water content and precipitation systems. GMI is used as a calibrator of a constellation of spaceborne imagers and sounders to unify precipitation estimates.

Solar occultation measurements from the SAGE series and ACE-MAESTRO also provide profiles of aerosol extinction that can be used for intercomparisons with lidar observations in the stratosphere (e.g. Kar et al., 2019). Cloud/aerosol discrimination becomes challenging near the tropopause for solar occultation measurements (Kovilakam et al., 2023), therefore the most accurate aerosol extinction comparisons are expected within the stratosphere where aerosol is more homogeneously distributed compared to the troposphere.

Spaceborne spectroradiometer measurements from MISR and MODIS provide column AOD and cloud occurrence retrievals based on observed radiances. Being imagers with large swaths, collocations between the scenes observed by these instruments and those of profiling missions can be plentiful. This was particularly true when CALIPSO/CloudSat joined the A-Train with MODIS Aqua, allowing near-nadir collocations separated by ~1 minute until the profiling missions left the A-Train in 2018. Because MISR and MODIS rely on scattered sunlight at visible wavelengths, they provide daytime-only observations. MISR has the additional capability to retrieve layer heights by taking advantage of parallax in the multi-angle fields of view of its cameras.

Table 3.12. *Current and past spaceborne profiling instruments. DW - Doppler wind, EB - elastic backscatter, HSR - high spectral resolution*

Instrument	Description	Variables	Altitude coverage	Latitude coverage	Platform	Years active
ACDL	Lidar, HSR 532 nm	Backscatter, extinction	-2 – 40 km	82° S/N	AEMS	2022-
ATLAS	Lidar, EB 532 nm	Attenuated backscatter, layer height	0 – 14 km	88° S/N	ICESat-2	2018-
ALADIN	Lidar, DW 355 nm	Co-polarized backscatter, extinction, lidar ratio, cloud-aerosol discrimination	0 – 30 km	85° S/N	AEOLUS	2018-2023
ATLID	Lidar, HSR 355 nm	Extinction, backscatter, particle depolarization, lidar	0 – 40 km	83° S/N	EarthCARE	2024-

Instrument	Description	Variables	Altitude coverage	Latitude coverage	Platform	Years active
		ratio, layer height, cloud-aerosol discrimination, aerosol type				
CALIOP	Lidar, EB 532, 1064 nm	Attenuated backscatter, volume depolarization ratio, color ratio, extinction, cloud-aerosol discrimination, aerosol type, cloud ice/water phase, layer height	–2 – 40 km	82° S/N	CALIPSO	2006-2023
CATS	Lidar EB 355, 532, 1064 nm, HSR 532 nm	Attenuated backscatter, volume depolarization ratio, color ratio, layer height, extinction, cloud-aerosol discrimination, aerosol type	–2 – 28 km	51° S/N	ISS	2015-2017
GLAS	Lidar, EB 532, 1064 nm	Attenuated backscatter, layer height, aerosol extinction	–1.0 – 41 km	86° S/N	ICESat	2003-2009
CPR	Radar, Doppler W-band	Radar backscatter, cloud heights, ice/water phase, optical depth	–0.5 – 20 km	83° S/N	EarthCARE	2024-
CPR	Radar, W-band	Radar backscatter, cloud heights, ice/water phase, optical depth	0 – 25 km	82° S/N	CloudSAT	2006-2023
DPR	Radar, Ku & Ka-band	Radar backscatter, reflectivity profiles, cloud heights, cloud type, precipitation heights, precipitation type, precipitation profiles, PSD, surface precipitation	0 – 19 km	65° S/N	GPM	2014-
PR	Radar, Ku-band	Radar backscatter, reflectivity profiles, cloud heights, cloud type, precipitation heights, precipitation type, precipitation profiles, PSD, surface precipitation	0 – 20 km	35° S/N	TRMM	1997-2015
ACE-MAESTRO	Solar occultation spectrophotometer	Stratospheric aerosol & PSC extinction, layer height	0 – 100 km	85° S/N	SCISAT	2003-
SAGE-II	Solar occultation	Stratospheric aerosol & PSC extinction, layer height	10 – 80 km	80° S/N	ERBS	1984-2005
SAGE-III/M3M	Solar occultation	Stratospheric aerosol & PSC extinction, layer height	6 – 30 km	80° S/N	Meteor-3M	2002-2006
SAGE-III/ISS	Solar, lunar occultation, 9 wavelengths	Stratospheric aerosol extinction, layer height	10 –85 km	70° S/N	ISS	2017-
GOMOS	Stellar occultation, 500 nm	Stratospheric aerosol extinction	20 –100 km	82° S/N	Envisat	2002-2012
OMPS-LP	Limb scattering, 6 wavelengths	Stratospheric extinction, layer height	0 – 80 km	81° S/N	JPSS/ S-NPP	2011-
OSIRIS	Limb scattering, 750 nm	Stratospheric aerosol extinction, cloud top altitude	5 –100 km	82° S/N	Odin	2001-
SCIAMACHY	Limb scattering	Stratospheric aerosol extinction	0 – 92 km	82° S/N	Envisat	2002-2012
SGLI	Imaging spectroradiometer, 17 bands	Cloud and aerosol occurrence, cloud height	N/A	90° S/N	GCOM-C	2017-

Instrument	Description	Variables	Altitude coverage	Latitude coverage	Platform	Years active
MISR	Multi-angle imaging spectroradiometer	Column AOD, cloud occurrence, layer height	N/A	90° S/N	Terra	1999-
MODIS	Imaging spectroradiometer, 36 bands	Column AOD, cloud occurrence	N/A	90° S/N	Terra	1999-
MODIS	Imaging spectroradiometer, 36 bands	Column AOD, cloud occurrence	N/A	90° S/N	Aqua	2002-
GMI	Radiometer - 13 bands	Brightness temperatures from 10 GHz to 183 GHz	N/A	65° S/N	GPM	2014 -
POLDER	Radiometer, 9 bands;, polarimeter, 3 bands	Column AOD, cloud occurrence, aerosol layer height	N/A	90° S/N	PARASOL	2004-2013
HARP2	Polarimeter, 4 bands	AOD, aerosol layer height	N/A	90° S/N	PACE	2023
SPEXone	Multi-angle polarimeter, 385-770 nm	AOD, aerosol layer height	N/A	90° S/N	PACE	2023
3MI	Multi-angle polarimeter, 410-2130 nm	AOD, cloud occurrence, aerosol layer height	N/A	90° S/N	Metop-SG A	planned

3.4. Spatiotemporal representativeness/scene homogeneity and colocation criteria for correlative measurements

For the validation of satellite data, measurements are used and combined in different ways, and the validity of the comparisons depends on various factors. Particular attention should be paid to the spatiotemporal representativeness of both the satellite observation to be validated and the suborbital measurement to be used for validation. Depending on the method, a meaningful comparison or validation must take into account the following points, which, among others, also determine the criteria for co-location for the correlative measurements:

- Length and time scale of the analyzed variable
- Scene homogeneity
- Statistical representativeness of the sampling

Especially for the geophysical variables the co-location criteria depend on parameter, scene and even sensor (algorithm). In this subsection, the problem of collocating measurements is outlined, without claiming to be complete. A recommendation concerning e.g. minimum measurement duration around satellite overpass, maximum distance from satellite ground track, geographical location (e.g. ocean, mountainous), and scene homogeneity for specific collocated measurements goes beyond this Chapter and will be addressed in Chapter 5 of this document.

Length and time scale of the analyzed variable

The length and time scale are strongly dependent on the observed variable. While in general aerosol properties have longer temporal and spatial scales, clouds and precipitation properties have relatively large spatial and temporal variability. Those aspects have to be carefully evaluated to define the needs and criteria for co-location and statistical analysis. Aspects to be additionally considered on different assumptions of homogenization include e.g. biases due to differences in sources for meteorological datasets, differences in retrieval techniques which include different approaches of the measurements (e.g., the assumption in the PSD and/or precipitation types to interpret radar reflectivity profiles, lidar integrated extinction with AOD from sun-photometer, the application of night-time derived lidar ratios on daytime retrievals), and the impact of the location (e.g. over land or over ocean).

Validation of aerosol properties is intrinsically linked to the difference in time and location for both observations, often leading to uncertainty due to collocation or representation. To minimize the uncertainty related to collocation, the scales and time at which each property naturally varies must be assessed (e.g. Sayer et al., 2020). The spatiotemporal scales of the extensive and intensive properties are directly linked to the processes governing the emission, transport, removal, and transformation of the aerosol particles.

- Globally, a time difference of 30 minutes typically induces from 0.011–0.035 variation in AOD and 0.03-0.07 variation in aerosol fine-mode-fraction, but there is a large disparity in different regions (Anderson et al., 2003; Sayer et al., 2020; Shinozuka & Redemann, 2011). Biomass burning regions tend to show the largest and fastest sub-daily AOD variability.

- For locations influenced by mixed aerosol types, the distance at which the standard deviation in the aerosol optical depth varies by 0.14 is roughly 50 km, while the similar variation in Angstrom exponent occurs at roughly 20 km (LeBlanc et al., 2022).

- Generelly, for column AOD a spatial and temporal scale recommended for validation is within 30 km and 30 min, respectively (Park et al., 2020).

- Near clouds, the aerosol experiences much greater spatio-temporal variations, with up to 100% change in optical depth, roughly 55% in size occurring at scales of less than 13 km (Eck et al., 2014; Yang et al., 2022).

- However, AOD differences over low-level clouds is similar to that in the neighboring clear skies (< 0.01 in AOD) for the same height levels (Shinozuka et al., 2020).

In a similar way, validation of **cloud** and **precipitation** properties are dependent on time and location of the observations. But, the temporal and spatial scales of cloud and precipitation properties are much more variable than for aerosol properties. This variability requires as much collocated, concomitant, and scaled observations as possible to mitigate unwanted biases and uncertainties in the comparison (e.g. Kirstetter et al., 2012, 2015). Imperfect matches of collocation, differences in time and space and scales of the observations lead to large uncertainties in the comparison and its representativeness. The spatial variability of rainfall at small scales and any resolution difference may cause differences in the statistical sampling properties of the extremely variable rainfall process (e.g. Habib et al., 2004). Such statistical noise when comparing two observations is especially significant for short

accumulation periods (1 hour or less; (Ciach & Krajewski, 1999)). The spatio-temporal scales are linked to the type of cloud and precipitation, the precipitation pattern as well as to the environmental / meteorological situation, e.g. turbulence and convection.

In addition, approaches for one-to-one comparisons account for the resolution of the satellite products and the time averages, the vertical sampling/smoothing of the data and the handling of uncertainties.

Scene homogeneity

To combine satellite- and ground-based measurements, a key piece of information is the spatial representativeness of the surface sites and their area coverage. The same assumption should be taken into account for temporal representativeness as well. One approach is to list and evaluate the methods available to infer the representativeness of a measurement related to the satellite observation (both spatially and temporally). Another approach is to use an ensemble-based method in which a statistical algorithm employs a series of measurements over time, with errors and noise, and generates estimates of unknown variables that show more accurate and precise results than those single measurements alone. This approach relies on estimating a joint probability distribution over the observed variables at each time period the measurements and observations were carried on. In general, conducting these approaches one can get a generally good agreement on large scales, however, the regional context can present significant differences. Ground-based data may strongly profit from information achieved by the use of airborne and satellite data: correlations may be used to define radii and areas of influence for each local station to spread this sparse and valuable information spatially around each site, based on a sound statistical approach. In practical approaches, one would have to consider the time frame in which to conduct the observations carrying one: hourly, daily, monthly, and yearly means in a way the product errors are smeared out as the temporal window increases, one also should consider seasonal approaches and bearing in mind the seasonal hemisphere differences.

These approaches aim to improve the spatial coverage of satellite data and better accuracy/precision from the ground-based measurements and to define collocation requirements.

Statistical representativeness

Highly variable properties often have the need for statistical comparisons. The same is true if the measurement location and the satellite do not have sufficient collocation. Approaches for statistical comparisons, however, have a strong need for performing representativeness analysis. These analyses have to include the collocation and time scale of the measurements, the sampling volume, uncertainties, sensitivities, and resolution. A critical point is also a time shift of the measurements to be compared, as atmospheric properties may be affected by diurnal cycles. Representativeness analysis can be performed using e.g. information from models to investigate the representativeness of the measurement location. Suggested metrics for the comparisons include an evaluation of the distribution as well as its mean, median, and standard deviation.

3.5. Quality of measurements

The comparison of suborbital to satellite observations is only sensible in the context of observational uncertainties because the definition of successful validation is the agreement of two observations within their measurement uncertainties and spatiotemporal sampling context. The primary sources of uncertainties are random and systematic errors in fundamental measurements and in the retrieval algorithms, but the spatiotemporal variation of observables within the measurement volume discussed in section 3.4 provides an additional source of error that is often difficult to quantify. Some types of systematic and random errors can be characterized with careful calibration activities (known unknowns) and quality assurance/control, but some uncertainties in suborbital observations are impossible to constrain, e.g., uncertainties due to covariance of errors in retrievals or uncertainties due to uncharacterized spatiotemporal variability. In subsection 3.5.1, we describe the main sources of uncertainties in suborbital lidar, radar, and in-situ observations as they pertain to validation efforts. In subsection 3.5.2 we describe the quality assurance and control protocols that are ideally applied to these measurements.

3.5.1. Measurement uncertainties

3.5.1.1. Lidar

In order to deliver a ***particle backscatter coefficient***, the molecular contribution of the received backscattered signal has to be subtracted. The pure molecular backscatter coefficient can be determined from temperature and pressure profiles, e.g. from radiosonds or model analysis. With the so-called Rayleigh fit the lidar signal is fitted to the molecular signal in a particle-free height range. This enables us to check the molecular contribution to the signal. At 355 and 532 nm the molecular signal is strong enough to derive a particle backscatter coefficient with low uncertainties. However, at 1064 nm the molecular contribution to the signal is weak. Therefore, it is more challenging to derive a particle backscatter coefficient in the near-infrared (e.g. Vaughan et al., 2019).

There are several techniques to derive the ***particle extinction coefficient***. Elastic backscatter lidars need to assume a lidar ratio (extinction-to-backscatter ratio) which depends on aerosol type and often varies with altitude. Therefore, the uncertainties are higher compared to a direct measurement of the particle extinction coefficient (using the Raman method or HSRL). Observations from sun photometers or satellite spectroradiometers, polarimeters, etc. can be used to constrain the column-integrated extinction coefficient (AOD), where available. Advanced aerosol typing algorithms can help constrain aerosol types and related uncertainties in assumed lidar ratios for elastic backscatter retrievals (Kim et al., 2018; Omar et al., 2009; Tackett et al., 2023).

Raman and HSR lidars provide a direct measurement of the extinction coefficient without additional assumptions. Due to the weaker signals in the Raman channel, and because the extinction profiles are determined from the derivative of the log of the signal (more noisy), longer vertical smoothing intervals are necessary compared to the measurements of the backscatter coefficient. Furthermore, the particle extinction coefficient is not calculated via a signal ratio (as backscatter and depolarization), but uses only one channel. Therefore, the overlap function has to be known to derive the particle extinction coefficient below the full overlap height (Comerón et al., 2023; Wandinger & Ansmann, 2002). Some lidar systems use

dedicated near range telescopes to measure the extinction coefficient closer to the receiving telescope (e.g. Engelmann et al., 2016). This is not an issue from space, because the full overlap is reached well above the heights of interest.

Raman lidar measurements are often limited to night-time observations and longer temporal averaging periods of the extinction coefficient because of the weak signal of the Raman scattering. However, first measurements with the pure rotational Raman technique provided daytime observations of the extinction coefficient (Arshinov et al., 2005; Thorsen et al., 2015; Turner et al., 2002)).

The uncertainties in derived ***lidar ratios*** combine the uncertainties of the particle backscatter and particle extinction coefficient (Gross, Wiegner, et al., 2011). Several recent studies discussed the best settings in terms of vertical resolution of the backscatter (i.e., vertical smoothing) and extinction coefficient (i.e., the number of height bins for the linear regression) in order to calculate the lidar ratio. Iarlori et al. (2015) proposes an effective resolution, where the number of height bins for vertical smoothing of the backscatter is approximately 78% of the number of height levels used to derive the extinction coefficient. Especially in thin aerosol layers the effective resolution of the lidar ratio gains importance.

The main uncertainties of the ***particle depolarization ratio*** emerge from the polarization-sensitive optical components in a lidar system. Proper knowledge of their behavior is essential to reduce systematic uncertainties. Main factors are a misalignment of the plane of polarization in the emitter with respect to the receiver, the diattenuation of the receiver optics, and the gain ratio between the two detection channels needed for the measurement of the depolarization ratio. Belegante et al. (2018) proposed methods to assess the first two uncertainties. The gain ratio should be monitored by frequent Δ90° calibrations (Freudenthaler, 2016; Freudenthaler et al., 2009). A polarimetric lidar simulator enables a complete assessment of the polarization-sensitive parts of a lidar system (Bravo-Aranda et al., 2016).

3.5.1.2. Radar

Radars are widely used for cloud and precipitation studies, but they are subject to specific uncertainties (i.e., attenuation depending on the radar frequency, ground clutter, beam blocking, variation of the reflectivity with height, conversion from reflectivity to precipitation rate, etc. See Delrieu et al. (2009), Villarini & Krajewski, (2010) for a summary). These uncertainties are associated with parameter estimation, as well as with the observational system and measurement principles. Another source of uncertainties is physical processes that are not fully understood.

Radar miscalibration is caused by changes in the radar constant over time. These changes can be related to the deterioration of different radar components and thermal effects. Different methods exist to calibrate radar or monitor its calibration over time (e.g. balloon-borne target, radar profiler, frequency shift reflector, transponder).

Signal attenuation is a common problem with radar systems operating at wavelengths shorter than S-band or C-band (although this attenuation at these frequencies can occur in extreme cases). Attenuation affects radars operating at smaller wavelengths more significantly, however, it has to be taken into account for all evaluations.

A common component in radar applications is to distinguish between meteorological and non-meteorological radar echoes. Ground clutter and partial beam blocking can occur when the radar beam intersects the ground (especially in mountain regions) as well as fixed objects obstructing the radar beam.

Anomalous propagation of the radar beam in the atmosphere causes the beam to propagate at different altitudes than expected. It occurs in the presence of strong gradients of refractivity with height, e.g., in the presence of shallow moist layers or nocturnal inversions.

Partial beam filling can lead to range degradation which is a problem due to the radar beam geometry. At greater ranges, the sampled volume increases, and, therefore, small but intense features of the rain system are averaged out, leading to a bias in the measured reflectivity.

Radar variables sampled aloft with ground radars (e.g., reflectivity, differential phase) are not always representative of the surface precipitation. These variables vary with height because of various precipitation processes (e.g., melting, aggregation, collision-coalescence, evaporation). In addition to the increase in beam elevation with distance, beam widening degrades the vertical sampling of the vertical structure of precipitation. This representativeness issue is increased in complex terrain where ground radars must sample precipitating systems at higher elevation angles. Vertical variations of radar variables are one of the major sources of error in the estimation of precipitation by weather radar. Correcting these errors allows radar variables measured aloft to be projected onto the ground before they are converted into a precipitation rate (Delrieu et al., 2009).

3.5.1.3. In-situ uncertainties

Data from in-situ probes often come along with a value-added product that provides the best estimate of relevant geophysical parameters of interest that are not probe-specific. This enables the use of data by others who are not as familiar with the probes themselves. Quantities included in a value-added product can include the best estimate of particle size distributions over the complete range of particle sizes integrated from contributions of probes that were deemed to before best during the field campaign, as well as best estimates of total particle concentration, mass content, phase, extinction, bulk reflectivity factor and dominant ice crystal shape (or distributions of shape).

It is important to quantify the uncertainties associated with the measurements of aerosol and cloud particle properties. Each probe has to follow its own calibration protocol and the observations are subject to estimation of the uncertainties for the specific instrument.

Broadly speaking, uncertainties include statistical counting errors, errors due to variability in microphysical properties in similar environmental conditions, errors induced by the measurements themselves, and errors associated with the processing of the data. From Poisson statistics, counting errors are proportional to the square root of the number of particle counts in the size bins that the measured particles are sorted into. Provided that the averaging time and bin sizes are chosen appropriately and that probes with sufficiently large sample volumes are used, the statistical counting errors are typically smaller than the degree of variability in cloud and aerosol microphysical properties. Probes and averaging periods must be chosen appropriately due to a trade-off in a sufficiently large sample size and a small enough averaging period to measure the inhomogeneity in the cloud and aerosol fields.

Techniques that extract atmospheric samples through an inlet also need to carefully account for changes in the sample environmental conditions through the inlet (i.e., temperature, pressure, and especially relative humidity). Moreover, air is typically warmed and dried behind an inlet, leading to a loss of the water component of the particles. Knowledge of the humidification curves is required to pass from the properties of the dried particles to the ambient conditions, and this may increase the uncertainty of the observations (depending on the ambient humidity and aerosol type). Inlets may display a size-dependent efficiency, affecting the observed PSDs or mass concentrations before they reach the instruments. It is therefore important that the impacts and characteristics of inlets are reported alongside aerosol measurements.

Some aerosol observations are inextricably linked to the measurement technique rather than a unique geophysical property (e.g., black vs. elemental carbon; condensation nuclei concentration greater than an instrument-defined Kelvin condensation diameter). It is therefore hard sometimes to draw comparisons across in-situ observations from different instrument manufacturers and models or sample treatments, even if the underlying measurement techniques are similar. For example, OPCs do not directly measure size-resolved particle number, but cross-section-resolved particle number (Rosenberg et al., 2012). To relate the cross-section to particle size, an assumption on the refractive index is needed (which depends upon the composition). Moreover, a particle shape is required (usually assumed spherical): large uncertainties for sizing non-spherical particles may arise. Moreover, there is uncertainty in how the size of a non-spherical particle should be defined (e.g. McFarquhar & Black, 2004; McFarquhar & Heymsfield, 1998; Wu & McFarquhar, 2018) and the determination of the sample volume and its size dependence can vary between probes of the same type.

Bulk samples may be altered between the time of collection and the time of analysis because volatile components may evaporate and chemically active components may react, thus affecting the outcome. The state of hydration of the aerosols will also be affected as the sample is exposed to varying temperature and humidity conditions between sampling and analysis.

For optical array probes specifically, care must be taken in how the compressed data are converted into geophysically relevant quantities. Several steps in these algorithms are used, and include algorithms for correcting the sizing of out-of-focus particles and fogged or stuck bits, corrections for shattered particles and interarrival time analysis, and identification of corrupt images and noise removal.

Determining the overload time (i.e. the time when many cloud particles arrive at the same time, preventing some of them from being recorded) can complicate the analysis, especially in updrafts when overloads tend to occur more frequently. There are ongoing efforts to try to provide some standardization and benchmarking of the processing algorithms.

Precipitation gauge measurements can be affected by uncertainties (for example, wind undercatch, evaporation, snow) and lack areal representation, which becomes particularly problematic for intense rainfall with high spatial variability (e.g. Zawadzki, 1975). The spatial representativeness of each gauge measurement depends on the autocorrelation distance of precipitation (for example, Delahaye et al., 2015).

3.5.2. Quality assurance (QA) / quality control (QC)

3.5.2.1. Lidar

Aerosol lidar QA/QC. The quality of aerosol lidar observations depends on multiple factors. Firstly, a proper alignment of the optical components of the emitter and receiver part as well as the alignment with respect to each other is essential. Knowledge of the polarization-sensitive parts in a lidar system determines the quality of polarization measurements. Regular quality control of the lidar is necessary and needs to be documented. There are several protocols usually developed by large lidar networks. Emerging from EARLINET, the ACTRIS Centre for Aerosol Remote Sensing (CARS) does provide standard quality assurance procedures (Freudenthaler et al., 2018). These procedures include the telecover test, the Rayleigh fit, the zero bin test, and the dark signal measurement.

Telecover test. Shortcomings of the optical and optomechanical design or misalignments have their largest effect in the near range. A test for this range is based on the fact that the backscattered photons collected by different parts of the telescope of a lidar system must give the same range dependency of the signal, and if not, the range dependency of the whole signal is uncertain.

Zero bin test. The slope of the signal in the near range changes significantly if the zero bin for the range-corrected signal varies. In case pre-trigger samples are recorded, the zero-bin can easily be detected due to the signal peak from diffuse straylight. In case no pre-trigger samples are recorded, the zero-bin can be detected by means of a near-range target with a known distance to the lidar.

Rayleigh fit. The Rayleigh fit (i.e. the comparison of lidar signals in clean air ranges with the calculated signals from air density) is the only absolute calibration of lidar signals. To be able to calibrate lidar signals with Rayleigh (molecular) backscatter, the optoelectronic detection systems must have a high dynamic range.

Dynamic range. For the photon counting signal dead time correction in the near range is necessary. Due to the large signal in the very near range, the counted photons might not reflect the real signal. In contrast, the analog signal suffers from distortion in the far range. Some lidar systems use combined analog/photon counting data acquisition, for those, signals have to be combined, with carefully determining the appropriate range and signal strength.

Dark signal measurement. Analog signal detection can suffer from signal distortions. These signal distortions can be determined with so-called dark measurements if they are independent of the lidar signal. The measured dark signals without atmospheric backscatter can be subtracted as range-dependent offset from the normal lidar signals.

Furthermore, the quality control of the polarization measurements is discussed by Freudenthaler (2016). Regular **Δ90° calibrations** (Freudenthaler, 2016; Freudenthaler et al., 2009) are recommended to control the gain ratio between the cross and parallel detection channel to ensure a high quality of the measured depolarization ratio.

3.5.2.2. Radar

The quality of cloud and precipitation radar observations can be affected by a number of issues, for example, radar calibration, attenuation, and clutter contamination, to name a few.

The list of potential QA/QC measures is radar-dependent, but radar calibration and calibration monitoring are universally important. There are many papers describing different types of calibration methods. For example, Ewald et al. (2019) gave a comprehensive overview of the calibration of an airborne cloud radar, and Chandrasekar et al. (2015) gave a comprehensive overview of calibration approaches for ground-based radars that are recommended for radars used for the validation of NASA GPM observations. Here we summarize the main calibration approaches and methods for calibration monitoring.

External target calibration. Calibration using external targets with known radar cross sections, such as a sphere or corner reflector, is considered to be the most comprehensive calibration that characterizes all parts of a radar, including transmitter, receiver and antenna. Additionally, by scanning across the target the radar antenna pattern can be characterized. The challenge of this calibration method comes from the need to minimize the background clutter signal and finding a suitable location for the calibration target. This can be achieved either by selecting a calibration target with an RCS that is significantly higher than clutter, or placing the target such that the clutter single is minimized. Various techniques for the deployment of calibration targets are discussed in the literature (e.g. Toledo et al., 2020).

Engineering calibration entails the characterization of radar system subcomponents individually, i.e. by measuring transmit power and characterizing the radar receiver (Chandrasekar et al., 2015; Ewald et al., 2019). This can be performed using either external equipment, such as a signal generator for receiver calibration and power meter for transmitter calibration, or built-in components, e.g. building noise diodes. This calibration method is logistically easier to carry out and does not require the use of an external calibration target. However, it does not allow a characterization of the system as a whole.

Calibration transfer between radars. If external calibration cannot be performed, alternative methods can be used to check the radar calibration. One method is the calibration transfer from one radar to another. This can be done either using other ground-based radar observations, which overlap with the measurements from the uncalibrated radar or using spaceborne radar observations. Both, calibration transfer from a calibrated ground-based radar and comparison of satellite-based radar and ground-based radars are possible. (Li et al., 2005; Protat et al., 2011; Tanelli et al., 2008; Toledo et al., 2020; Warren et al., 2018).

Calibration monitoring using rain observations.

Polarimetric self-consistency. For scanning dual-polarization radars, polarimetric self-consistency (Gorgucci et al., 1992) can be utilized for calibration monitoring purposes (Myagkov et al., 2020). To carry out this method observations of reflectivity factor, differential reflectivity, and specific differential phase in rain are needed. This approach provides a relatively easy method for calibration monitoring, which can be used by scanning radars.

Using disdrometer-based calibration monitoring of raindrop size distributions, expected polarimetric radar variable values can be computed. For the best results, disdrometers and radars should be located with the least possible distance between the radar and disdrometer sampling volumes, ideally within a few tens to a few hundred meters between the observation volumes. Because of the inherent uncertainty in this method, often the comparison is carried out in a statistical sense.

94 GHz reflectivity "saturation" in rain is another calibration monitoring method. It can be applied to W-band cloud radars only, exploiting the fact that at this frequency, the radar reflectivity factor of rain measured at a range of 250 m is approximately constant for a range of rain rates (Hogan et al., 2003), as a result of the combined effects of attenuation and non-Rayleigh scattering.

Radar-rain gauge combination uses the fine spatio-temporal resolution of radar and the local accuracy of gauges for improved QPE (for example, Delrieu et al., 2014) and can be applied operationally. Quality controls can be performed by assessing the local discrepancies between radar and gauge precipitation estimates.

Additional QA/QC can be applied to radar observations. Numerous techniques have been developed over decades of practice, sometimes involving machine learning (e.g. Lakshmanan, 2007) and more recently relying on polarimetric technology to filter out non-weather echoes via hydrometeor classification (e.g. Park et al., 2009). Radar Quality Indices can be computed operationally to qualitatively represent the radar QPE uncertainty associated with reflectivity changes with height and near the melting layer (e.g. Zhang et al., 2011, 2016).

3.5.2.3. In-situ quality assurance

In-situ QA/QC. In section 3.2.4 we have indicated a range of in-situ observations useful for satellite calibration and validation, and each comes with its own QA/QC-specific methods. We will avoid here getting into the details of each instrument and we will approach the issue in general terms, as there are some common points to be considered:

Sampling in clean air flow. Specific issues must be addressed for airborne measurements. The location of probes should be chosen to sample a clean air flow away from the boundary layer of the aircraft where regions of amplified or reduced particle concentrations exist.

Probe design. Moreover, there is the possibility of large ice crystals shattering on probe tips, generating a field of small ice crystals that are measured when swept through the probe sample volume. Probe tips have been redesigned to sweep these artifacts away from probe sample volumes. Further, algorithms based on the distribution of particle interarrival times in a sample volume have been developed that allow for the removal of the majority of these artifacts. In mixed-phase clouds, care must be taken to identify times when icing occurs that can generate spurious data, e.g. bulk water probes can falsely detect cloud conditions if supercooled water has frozen on probe inlets.

Account for changes in the sample conditions. These considerations lead many investigators to carefully condition the sample to a well-controlled, known set of environmental conditions by, for example, active drying, pressure-controlling, and thermally conditioning the inlet sample stream. These limitations can be overcome with open-path probes that sample the ambient air without making use of an inlet.

Sufficiently large sample. To be able to retrieve statistically representative properties of the aerosol and cloud particles a sufficiently large sample needs to be observed. The amount of collection time required for a sample to be significant is dependent upon the sampling method and the atmospheric conditions. On the other hand, a long sampling time affects the data resolution (spatial and/or temporal). A good knowledge of the observation methods allows one to find the optimal compromise between the resolution and statistical significance of the

collected samples, allowing at the same time to reduce statistical uncertainties and to measure inhomogeneity in cloud fields. The relative statistical uncertainty of a sample is typically proportional to $1/\sqrt{N}$, where N is the sample size (Poisson statistics). $N \sim d \cdot t$, where d is the concentr time (McFarquhar et al., 2007).

Redundancy. Often using a broad range of sampling probes is useful to build redundancy, e.g. for field experiments that would be hard to repeat in case of instrumental issues and artifacts. This also reduces uncertainties and instrument-specific interpretations of the observations: when multiple instruments report the same quantity, a reassurance on the results is brought, and when they do not we have a feel of the uncertainties that are directly related to the sampling techniques.

3.6. Recommendation to determine criteria for validation exercises

There are several ways to perform a validation exercise (e.g. Loew et al., 2017) and references herein). Among these, there is the comparison between 'coincident/collocated' observations.

The first step of this process is to generate a statistically significant number of data couples assumed to measure the same variable. Once obtained, this dataset can be used to calculate a metric estimating the differences between the reference and the to-be-validated observations. The final objective of a validation exercise is to identify sources of inconsistency, due to either instrumental or processing algorithm issues, and hopefully to identify sources of uncertainties and give indications for possible improvements; a common by-product is an observation-based estimation of accuracy to complement the ones derived by uncertainty budget.

The produced metrics include several contributions that should be somehow accounted for to correctly interpret the results in terms of the diagnostic of the validated observations. In addition to the uncertainties associated with the reference measurement, there is a contribution due to their representativeness. Besides the fact that the concept of perfectly coincident/collocated observations is practically never satisfied because of the difference in spatial and temporal sampling among different measurement techniques. Because of the trade-off between representativeness and the need to build a statistically significant dataset in the shortest possible time, match-up criteria are generally adopted to generate the couples of 'coincident/collocated' observations. The simplest way to implement the match-up criteria is by adopting, for a given geophysical parameter, two threshold values: one for spatial matching (maximum distance between geographical position associated to the measurements) the other for temporal matching (absolute maximum time lag between acquisition times). Observations are considered matching if the distance and the acquisition time lag are both below the set of adopted thresholds. Thresholds are surely easy to implement to generate couples of matching observations but introduce a discretization that is unphysical. Moreover, there is the issue of objectively defining the threshold values; when adopting this criterion it is difficult to evaluate the uncertainty due to representativeness of the reference measurements. It is not always clear the rationale behind the definition of adopted threshold values. An objective approach to set the threshold values in principle, could be to derive them from the requirements in temporal spatial sampling (e.g. https://space.oscar.wmo.int/observingrequirements).

Even adopting the threshold criteria some improvements can be implemented, e.g.in terms of spatial horizontal variability. Atmospheric variables may have different variability scales meridionally or zonally due to the circulation patterns. This may generate a sort of ellipses, rather than a circle, of spatial match-up area. Similarly, a dependence on the horizontal variability scales is expected also to depend on the atmospheric level.

A different approach, from the adoption of thresholds, can be to evaluate quantitatively the representativeness of each comparison pair taking advantage of the rich literature available for the estimation of representation error, first defined by Nappo et al. (1982), in the process of data assimilation in numerical model (e.g. Janjić et al., 2018). With this approach, a weight, based on the estimation of the representativeness error, can be applied when producing comparison metrics with the advantages of:

- removing the discontinuity due to the application of discriminating thresholds,
- increasing the dimension of the comparison dataset
- accounting explicitly for the representativeness of the reference observation.

From the point of view of practical implementation of both, use of simple/complex sets of thresholds or account for representativeness error, a database of available observations should be used. For the representativeness error estimation it is possible to take advantage of the methods adopted for the assimilation of observations in numerical models.

4. Chapter 4: Correlative metadata and data format

Plain language summary:

The aim of this chapter is to describe the information elements that enable large complex scientific datasets to be easily read, understood, distributed and attributable by both human and machine. This includes both the description of the data format and additional pieces of information that are associated with the dataset.

4.1. Introduction

This correlative metadata and data format chapter describes the requirement and best practices for structure and content of data sets that are used by Cal/Val communities and are related to each other by some common attribute or variable. In order to derive accurate and meaningful results from the correlative measurements, it is crucial to ensure that the metadata and data formats are properly defined and that data are reported accordingly to trusted data archives.

A set of standard metadata in a harmonized vocabulary, and files reported in standard data formats ensure that the information in each dataset is comparable to other datasets. It also avoids information loss in the process of submission and extraction of files, and ensures that the data represents the essence of scientific work at a station and of a Principal Investigator. Exchange of standard metadata between operational data centers helps collecting and displaying relevant information directly in and from the database, in a specified and uniform manner. This is especially relevant for networks that have their own individual databases and from which Cal/Val efforts may harvest the correlative files.

Metadata is essential for facilitating the discovery, access, reuse, and preservation of the data sets. Metadata should include information such as: the title, author, date, location, description, methodology, variables, units, codes, formats, standards, provenance, version, license, and citation of the data sets. Correlative metadata and formats are here based on existing metadata standards or schemas that are widely used in a specific domain or disciplines. For ESA-EarthCARE, for example, the supported data formats are: Hierarchical Data Format (HDF, www.hdfgroup.org) and Network Common Data Form (NetCDF, https://www.unidata.ucar.edu/software/netcdf/) as primary standards, following the Climate Forecast metadata conventions (CF, https://cfconventions.org/; (Hassell et al., 2017)) and/or the GEOMS metadata schemas.

The GEOMS metadata standard is explained in detail in https://evdc.esa.int/documentation/geoms/

4.2. FAIR data principles

The FAIR data principles (Wilkinson et al., 2016) are a set of guidelines to improve the findability, accessibility, interoperability, and reusability of digital assets, such as data sets, software, and metadata (https://www.go-fair.org/fair-principles/). FAIR data principles aim to make data more machine-actionable, meaning that they can be easily discovered, accessed, integrated, and reused by computational systems with minimal human intervention. FAIR data

principles also support the open science movement, which advocates for the sharing and transparency of scientific data and processes.

One of the key aspects of FAIR data principles is the use of metadata, which are structured information that describe, explain, locate, or otherwise make it easier to retrieve, use, or manage an information resource, as described above. The correlative metadata and data format should follow the FAIR data principles to ensure that the data sets are findable, accessible, interoperable, and reusable by both humans and machines. Correlative datasets should also adhere to the “as open as possible, as closed as necessary” motto of the Open Research Europe policy for the Horizon 2020 and Horizon Europe programmes, which means that the data sets should be shared as widely as possible while respecting ethical, legal, and security constraints.

4.3. Data format

Recommended file format types in this best practices document include NetCDF and HDF, which both are self-descriptive and commonly used formats.

The supported metadata standard for these file formats are the Generic Earth Observation Metadata Standard GEOMS. This standard is a further development of the metadata standard previously implemented for the Envisat Cal/Val activity, but the standard is now further generalized and harmonized to be implemented for EVDC, NASA, AVDC (Aura Validation Data Centre) and NDACC (Network for Detection of Atmospheric Composition Change). The GEOMS standard is described in the GEOMS document, added as a chapter Appendix (4.5).

One challenge is the diversity of formats and conventions used by different instruments and data providers. While this challenge is not unique to EarthCARE, specific information about networks relevant to EarthCARE are shown as an example in Table 4.1.

Table 4.1. *List of networks relevant for EarthCARE, together with their data formats, links to the native archives and their ESA EVDC Services readiness levels.*

Network	Format	Description
ACTRIS CLOUDNET	NetCDF	Metadata items and vocabulary following the specifications in https://vocabulary.actris.nilu.no/skosmos/actris_vocab/en/ https://cloudnet.fmi.fi/api/download/
ACTRIS EARLINET	NetCDF	Metadata items and vocabulary following the specifications in https://vocabulary.actris.nilu.no/skosmos/actris_vocab/en/ https://data.earlinet.org/api/services/restapi?_wadl
AD-NET	NetCDF	https://www-lidar.nies.go.jp/AD-Net/
AERONET	ASCII	https://aeronet.gsfc.nasa.gov/new_web/data.html
AERONET-MAN	ASCII	https://aeronet.gsfc.nasa.gov/new_web/maritime_aerosol_network.html
ARM	NetCDF (ASCII and HDF allowed for external data products)	Each datastream can have its own metadata format, with the most recent file header provided in the data product description. (https://www.arm.gov/guidance/datause/formatting-and-file-naming-protocols)
e-Profile	NetCDF	https://archive.ceda.ac.uk/
GALION		TBD
ICARRT (aircraft campaigns)	ICARTT (ASCII)	https://www.earthdata.nasa.gov/s3fs-public/imported/ESDS-RFC-029v2.pdf, https://www.earthdata.nasa.gov/s3fs-public/imported/ESDS-RFC-019-v1.1_0.pdf
LALINET	ASCII	http://lalinet.org/index.php/Pilot2012/MeasurementSpecification
MPLNET	NetCDF	V3 products are NETCDF 4, CF compliant files, with specific data and metadata formats for the NRB, CLD, AER, and PBL products (https://mplnet.gsfc.nasa.gov/product-info/)
NDACC	ASCII Ames or GEOMS compliant HDF4	https://ndacc.larc.nasa.gov/data/formats
OPERA	BUFR or HDF5	https://www.eumetnet.eu/activities/observations-programme/current-activities/opera/
Pollynet	NetCDF	https://polly.tropos.de/
PGN	GEOMS H5	https://www.pandonia-global-network.org/ https://evdc.esa.int
SkyNet	NetCDF	https://www.skynet-isdc.org

To facilitate the conversion of data from native formats to CF or GEOMS and internally between CF and GEOMS, a number of reporting templates and data conversion routines have been made available to data submitters involved in the EarthCARE Cal/Val activities. The file format harmonization is ideally done on input level and before the data is made available to the end users, but assistance for file conversion is also available from EVDC to the groups that do not have expertise or resources to do the file conversion on their side.

Data formatting templates available at: https://evdc.esa.int/tools/data-formatting-templates/

Unformatted ASCII or CSV data, or data from research infrastructures such as ACTRIS-EARLINET or ACTRIS-CLOUDNET supporting the CF standard, requires a GEOMS translation file for converting data to GEOMS before storing the data according to the metadata requirements. A GEOMS translation file is a file that specifies how to map the variables and attributes from native metadata format to GEOMS. This translation file can be written in any scripting language, and is normally only a text file. By using a GEOMS translation file, data

providers can easily format their data according to the GEOMS standard, and make their data available and interoperable for the Cal/Val community.

Different measurement principles (e.g radar and lidar) may have different requirements for how their output data are reported. For example, a measurement principle that relies on spectral analysis may need to report the wavelength, intensity, and resolution of the spectra, while a measurement principle that relies on image analysis may need to report the pixel size, contrast, and orientation of the images. Therefore, each measurement principle requires a specific data reporting template that captures the relevant information and metadata for the data. A data reporting template is a standardized document or format that specifies the structure, content, and style of the data report. A data reporting template can help ensure the consistency, completeness, and quality of the data report, as well as facilitate its discovery, access, reuse, and validation by other users or systems. A data reporting template can also be aligned with the FAIR data principles to make the data more findable, accessible, interoperable, and reusable.

In addition, a number of tools have been set up by EVDC to support the data formatting and submissions to EVDC. The GEOMS online tool available at https://geoms-tool.nilu.no/ is a set of functionalities to support data submitters with these tasks. The tool is easy to use and self-explanatory, and documentation and "how-to" documents are made available at https://evdc.esa.int/documentation/geoms/. The online GEOMS tool uses the metadata templates for each individual and specified measurement principle as input and provides final correlative files in NetCDF or HDF as output.

A GEOMS NetCDF and HDF file format checker has been developed as a collaboration between NASA and ESA, and is made available to users that want to check their files before submitting these to a distributor or archive. The tool is available at https://geoms-tool.nilu.no/geoms_file_format_checker.

4.4. DOIs, re-formatting and re-distributions, licencing

A DOI (Digital Object Identifier) is a unique and permanent identifier for a digital object, such as a research paper, dataset, or software. The purpose of a DOI is to provide a stable, long-lasting link to the digital object, allowing users to easily locate and access it. DOIs are managed by trusted registration agencies, such as CrossRef, DataCite, or mEDRA, and they resolve to a landing page that provides metadata and access to the object being identified.

Having a DOI (Digital Object Identifier) for your publication provides several benefits:

- Permanent and stable access: A DOI provides a permanent and stable link to your publication, ensuring that it remains accessible over time and can be easily located by others.
- Improved discoverability: DOIs make it easier for others to discover your publication through online search engines and databases, increasing its visibility and impact.
- Reliable citing: DOIs help to ensure accurate and reliable citing of your publication by providing a unique identifier that can be easily included in a reference list.
- Increased credibility: By using a DOI, you are demonstrating your commitment to high-quality research and publishing practices, which can increase the credibility of your publication.

- Better data management: DOIs can be used to track and manage data associated with your publication, making it easier to access, analyze, and share your research results.

Overall, having a DOI for your publication helps to ensure its long-term accessibility, visibility, and impact, making it easier for others to find, use, and build upon your work.

Best practices for coining DOIs include:

- Assign unique DOIs: Each DOI must be unique and permanent, and should not change over time.
- Use a trusted DOI registration agency: Use a recognized and trusted DOI registration agency such as CrossRef, DataCite, or mEDRA.
- Ensure resolvability: DOIs should resolve to a landing page that provides metadata and access to the full-text or object being identified.
- Provide complete metadata: The landing page should provide complete and accurate metadata, including title, authors, publication date, and persistent URL.
- Use a consistent format: i.e. a consistent format for coining DOIs, such as the "10.xxxx/yyyyyyyy" format recommended by the International DOI Foundation.
- Update and maintain the DOI record: Regularly update and maintain the DOI record to ensure that it continues to resolve to the correct landing page.

Examples of DOIs (Digital Object Identifiers):

- 10.1038/nature14539
- 10.1016/j.cell.2013.11.049
- 10.1371/journal.pone.0127752
- 10.1186/s13643-020-01356-9

Note that the format of DOIs typically consists of a prefix (e.g. "10."), followed by a unique identifier assigned by the registration agency (e.g. "nature14539," "journal.pone.0127752"). The prefix and identifier together form the complete DOI, which resolves to a landing page that provides metadata and access to the digital object being identified.

A data archive or distributor may issue a DOI on datasets or other data products related to Cal/Val activities. Issuing of the DOI may be done through the DataCite metadata service.

EVDC offers user support related to the coining of the DOIs. This support involves giving the various frameworks access to the EVDC API for generating landing pages, issuing new DataCite repositories and giving access to the DataCite API for coining DOIs. In addition, EVDC provides guidelines for the distribution of DOIs, recommendations on granularity and a list of recommended metadata to include when creating landing pages and coining DOIs.

When a DOI is issued, there are two things to consider: First, one should report metadata following the XML format (see Section 4.4.1 below). Secondly, additional information may be for a landing page. The data resource will then be available through the presentation web page, hereunder a private URL to your landing page. For EarthCARE this may be a presentation webpage on the EVDC server, and as as a sub page of https://evdc.esa.int

A set up jupyter notebooks is set up for self assignment of the DOIs in EVDC. It is recommended that the data submitters from the Cal/Val teams consider adding DOIs to their

data, either via EVDC or any at “home” institutes location, if offered. More information is found at https://evdc.esa.int/documentation/doi-docs/

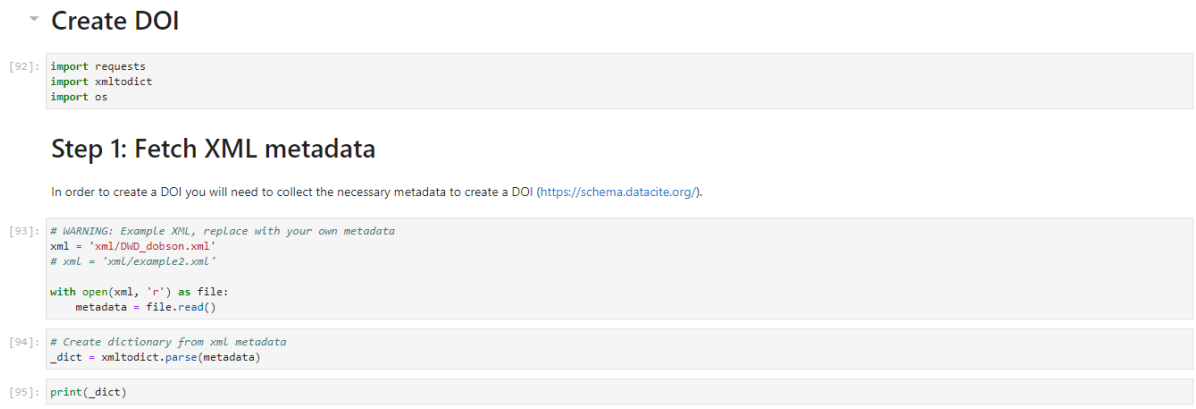

Figure 4.1. *Screendump of the first step of the jupyter notebook for self assignment of DOIs.*

4.4.1. XML metadata and landing pages

Example of how to report metadata in xml:

- Metadata elements
- Name of the creator(s) of the dataset and affiliation
- Title
- Publication year
- Subject (e.g. “Atmospheric Science”)
- Contact person(s)
- Date of collection
- Date of creation
- Size (only if its a dataset, supply size of dataset in megabytes)
- Format (text/plain, netCDF, ASCII etc.)
- Language
- Rights (Any rights information for this resource, licensing, copyright etc.)
- Resource type (should be “Dataset” in most cases)
- Description(s) (you can have one or more description types. Select among the following description types: Abstract, Methods, SeriesInformation, TableOfContents, TechnicalInfo, Other)
- Funder name(s)
- GeoLocation of measuring station(s)

All data objects with a DOI (or a PID) must have a landing page associated with it. The landing page is not so strict in terms of content and shape, but should include the following elements on the page:

- Title
- Image (plot etc.) that describes the dataset, not mandatory but preferable.

- Data policy
- Description of data file (s), including contact person for the specific dataset/subset of the dataset (in case there is data from multiple stations).
- Acknowledgments
- Citation (How to cite the dataset)
- Contact

The landing page can also include a link to the previous (or latest) version.

The metadata schema used for coining the DOIs follows the DataCite metadata schema. For more information visit: https://schema.datacite.org/.

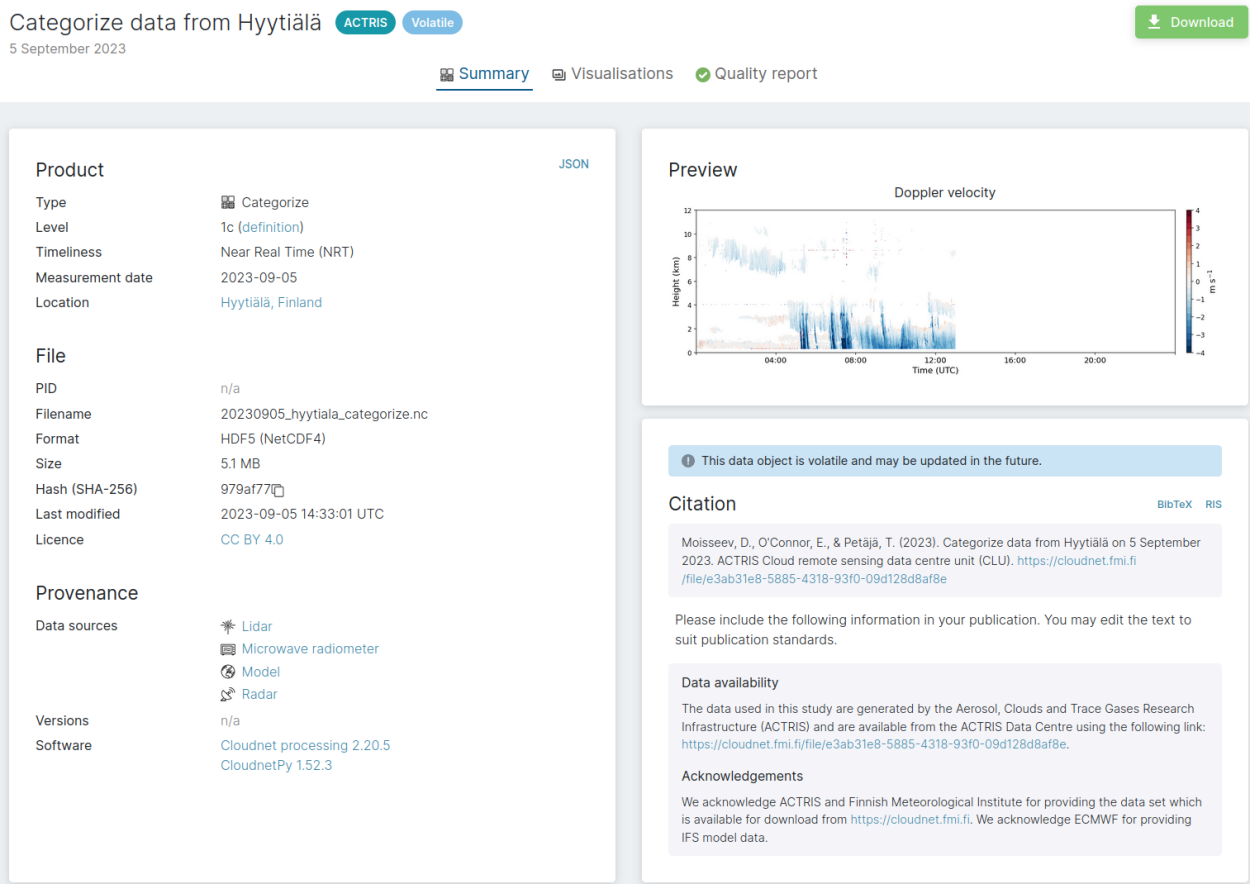

Figure 4.2. *Example ACTRIS DC landing page for a cloud-profiling product*

4.4.2. Granularity

Granularity in DOIs is the level of detail or specificity that a DOI provides for identifying a digital object. For example, a DOI can identify a whole dataset, a subset of a dataset, or a single data file within a dataset. The level of granularity depends on how the data provider assigns and registers DOIs for their data products.

Granularity in DOIs should be carefully considered and balanced by data providers and users, taking into account the nature, purpose, and scope of their data products. It may create

confusion or inconsistency among data users if different levels of granularity are used for citing or accessing the same type of data products. As a general rule in EVDC, the recommendation is to have the granularity of one DOI for each dataset in the GEOMS database, on station or instrument level.

In special cases other granularities can be considered. It is important to consider that when deciding on the granularity, the data user should be kept in mind. If a dataset is produced every day, a collection of datasets over time might be more sensible than a dedicated DOI for each dataset.

4.4.3. Version control

Version control can also be directly referenced through the use of DOIs and PIDs. If datasets are reprocessed, such as when a new processing scheme has been implemented, or a new software version implemented, these are new data objects and should have a new descriptor (PID and DOI). Such new processing can be required due to changes or corrections (bug fixes) in the implementation of an algorithm or software rather than a new implementation. These new or updated data objects can then be linked to the original data object through references to the DOI and PID identifiers; the identifier schemas provide a specific mechanism for linking to new and previous identifiers.

Figure 4.3. *Example provenance on the landing page for a specific product version, with links to the PIDs (and landing pages) for previous and updated versions.*

4.5. Appendix: NetCDF examples

4.5.1. ARM cloud radar (KAZR) file

```
netcdf corkazrcfrgeM1.a1.20190430.000001 {
dimensions:
        range = 600 ;
        time = UNLIMITED ; // (1737 currently)
        sweep = 1 ;
        frequency = 1 ;
        string_length_22 = 22 ;
        r_calib = 1 ;
variables:
        int base_time ;
                base_time:string = "2019-04-30 00:00:01 0:00" ;
                base_time:long_name = "Base time in Epoch" ;
```

```
                base_time:units = "seconds since 1970-1-1 0:00:00 0:00" ;
                base_time:ancillary_variables = "time_offset" ;
        double time_offset(time) ;
                time_offset:long_name = "Time offset from base_time" ;
                time_offset:units = "seconds since 2019-04-30 00:00:01 0:00" ;
                time_offset:ancillary_variables = "base_time" ;
        double time(time) ;
                time:long_name = "Time in seconds since volume start" ;
                time:units = "seconds since 2019-04-30 00:00:01 0:00" ;
                time:standard_name = "time" ;
                time:calendar = "gregorian" ;
        short linear_depolarization_ratio(time, range) ;
                linear_depolarization_ratio:long_name   =   "Linear   depolarization
ratio, channel unspecified" ;
                linear_depolarization_ratio:units = "dB" ;
                linear_depolarization_ratio:coordinates = "elevation azimuth range"
;
                linear_depolarization_ratio:standard_name                          =
"radar_linear_depolarization_ratio" ;
                linear_depolarization_ratio:add_offset = 19.72893f ;
                linear_depolarization_ratio:scale_factor = 0.001267589f ;
                linear_depolarization_ratio:_FillValue = -32767s ;
        short mean_doppler_velocity(time, range) ;
                mean_doppler_velocity:long_name  =  "Radial  mean  Doppler  velocity,
positive for motion away from the instrument" ;
                mean_doppler_velocity:units = "m/s" ;
                mean_doppler_velocity:coordinates = "elevation azimuth range" ;
                mean_doppler_velocity:standard_name                                =
"radial_velocity_of_scatterers_away_from_instrument" ;
                mean_doppler_velocity:add_offset = 0.01556277f ;
                mean_doppler_velocity:scale_factor = 0.0002427116f ;
                mean_doppler_velocity:_FillValue = -32767s ;
        short mean_doppler_velocity_crosspolar_v(time, range) ;
                mean_doppler_velocity_crosspolar_v:long_name  =  "Doppler  velocity,
crosspolar for vertical channel" ;
                mean_doppler_velocity_crosspolar_v:units = "m/s" ;
                mean_doppler_velocity_crosspolar_v:coordinates = "elevation azimuth
range" ;
                mean_doppler_velocity_crosspolar_v:standard_name                   =
"radial_velocity_of_scatterers_away_from_instrument" ;
                mean_doppler_velocity_crosspolar_v:add_offset = 0.f ;
                mean_doppler_velocity_crosspolar_v:scale_factor = 0.f ;
                mean_doppler_velocity_crosspolar_v:_FillValue = -32767s ;
        short reflectivity(time, range) ;
                reflectivity:long_name = "Equivalent reflectivity factor" ;
                reflectivity:units = "dBZ" ;
                reflectivity:coordinates = "elevation azimuth range" ;
                reflectivity:standard_name = "equivalent_reflectivity_factor" ;
                reflectivity:add_offset = -19.72893f ;
                reflectivity:scale_factor = 0.001267589f ;
                reflectivity:_FillValue = -32767s ;
        short reflectivity_crosspolar_v(time, range) ;
                reflectivity_crosspolar_v:long_name   =   "Equivalent   reflectivity
factor, crosspolar for vertical channel" ;
                reflectivity_crosspolar_v:units = "dBZ" ;
                reflectivity_crosspolar_v:coordinates = "elevation azimuth range" ;
                reflectivity_crosspolar_v:standard_name                            =
"equivalent_reflectivity_factor" ;
                reflectivity_crosspolar_v:add_offset = 0.f ;
```

```
                reflectivity_crosspolar_v:scale_factor = 0.f ;
                reflectivity_crosspolar_v:_FillValue = -32767s ;
        short signal_to_noise_ratio_copolar_h(time, range) ;
                signal_to_noise_ratio_copolar_h:long_name = "Signal-to-noise ratio,
horizontal channel" ;
                signal_to_noise_ratio_copolar_h:units = "dB" ;
                signal_to_noise_ratio_copolar_h:coordinates  =  "elevation  azimuth
range" ;
                signal_to_noise_ratio_copolar_h:standard_name                      =
"radar_signal_to_noise_ratio_copolar_h" ;
                signal_to_noise_ratio_copolar_h:add_offset = 7.972565f ;
                signal_to_noise_ratio_copolar_h:scale_factor = 0.001190834f ;
                signal_to_noise_ratio_copolar_h:_FillValue = -32767s ;
        short signal_to_noise_ratio_crosspolar_v(time, range) ;
               signal_to_noise_ratio_crosspolar_v:long_name    =    "Signal-to-noise
ratio, Cross-polar for vertical channel" ;
                signal_to_noise_ratio_crosspolar_v:units = "dB" ;
                signal_to_noise_ratio_crosspolar_v:coordinates = "elevation azimuth
range" ;
                signal_to_noise_ratio_crosspolar_v:standard_name                   =
"radar_signal_to_noise_ratio_crosspolar_v" ;
                signal_to_noise_ratio_crosspolar_v:add_offset = 17.64213f ;
                signal_to_noise_ratio_crosspolar_v:scale_factor = 0.0006878275f ;
                signal_to_noise_ratio_crosspolar_v:_FillValue = -32767s ;
        short spectral_width(time, range) ;
                spectral_width:long_name = "Spectral width" ;
                spectral_width:units = "m/s" ;
                spectral_width:coordinates = "elevation azimuth range" ;
                spectral_width:standard_name = "radar_doppler_spectrum_width" ;
                spectral_width:add_offset = 1.770866f ;
                spectral_width:scale_factor = 5.404583e-05f ;
                spectral_width:_FillValue = -32767s ;
        short spectral_width_crosspolar_v(time, range) ;
                spectral_width_crosspolar_v:long_name = "Spectral Width, Crosspolar
for Vertical Channel" ;
                spectral_width_crosspolar_v:units = "m/s" ;
                spectral_width_crosspolar_v:coordinates = "elevation azimuth range"
;
                spectral_width_crosspolar_v:standard_name                          =
"radar_doppler_spectrum_width" ;
                spectral_width_crosspolar_v:add_offset = 0.f ;
                spectral_width_crosspolar_v:scale_factor = 0.f ;
                spectral_width_crosspolar_v:_FillValue = -32767s ;
        float frequency(frequency) ;
                frequency:long_name = "Transmit center frequency" ;
                frequency:units = "Hz" ;
                frequency:meta_group = "instrument_parameters" ;
        float range(range) ;
                range:long_name = "Range to measurement volume" ;
                range:units = "m" ;
                range:meters_between_gates = 29.97925f ;
                range:meters_to_center_of_first_gate = 100.6792f ;
                range:spacing_is_constant = "True" ;
                range:standard_name = "projection_range_coordinate" ;
                range:axis = "radial_range_coordinate" ;
        float azimuth(time) ;
                azimuth:long_name = "Azimuth angle from true north" ;
                azimuth:units = "degree" ;
                azimuth:standard_name = "sensor_to_target_azimuth_angle" ;
```

```
                azimuth:axis = "radial_azimuth_coordinate" ;
                azimuth:_FillValue = -9999.f ;
        float burst_width(time) ;
                burst_width:long_name = "Transmitter burst width" ;
                burst_width:units = "ns" ;
                burst_width:meta_group = "instrument_parameters" ;
                burst_width:_FillValue = -9999.f ;
        float chirp_width(time) ;
                chirp_width:long_name = "Transmitter chirp width" ;
                chirp_width:units = "ns" ;
                chirp_width:meta_group = "instrument_parameters" ;
                chirp_width:_FillValue = -9999.f ;
        float elevation(time) ;
                elevation:long_name = "Elevation angle from horizontal plane" ;
                elevation:units = "degree" ;
                elevation:standard_name = "sensor_to_target_elevation_angle" ;
                elevation:axis = "radial_elevation_coordinate" ;
                elevation:_FillValue = -9999.f ;
        float fixed_angle(sweep) ;
                fixed_angle:long_name = "Ray target fixed angle" ;
                fixed_angle:units = "degree" ;
                fixed_angle:_FillValue = -9999.f ;
       int n_samples(time) ;
                n_samples:long_name = "Number of Samples used to compute moments" ;
                n_samples:units = "1" ;
                n_samples:meta_group = "instrument_parameters" ;
                n_samples:standard_name                                          =
"number_of_samples_used_to_compute_moments" ;
                n_samples:_FillValue = -9999 ;
        float noise_figure(time) ;
                noise_figure:long_name = "Receiver noise figure estimated from noise
source using y-factor method" ;
                noise_figure:units = "dB" ;
                noise_figure:missing_value = -9999.f ;
                noise_figure:_FillValue = -9999.f ;
        float nyquist_velocity(time) ;
                nyquist_velocity:long_name = "Unambiguous doppler velocity" ;
                nyquist_velocity:units = "m/s" ;
                nyquist_velocity:meta_group = "instrument_parameters" ;
                nyquist_velocity:_FillValue = -9999.f ;
        float prt(time) ;
                prt:long_name = "Pulse repetition time" ;
                prt:units = "s" ;
                prt:_FillValue = -9999.f ;
        float pulse_width(time) ;
                pulse_width:long_name = "Transmitter pulse width" ;
                pulse_width:units = "s" ;
                pulse_width:meta_group = "instrument_parameters" ;
                pulse_width:_FillValue = -9999.f ;
        float r_calib_radar_constant_copol(r_calib) ;
                r_calib_radar_constant_copol:long_name = "Calibrated radar constant
copolar" ;
                r_calib_radar_constant_copol:units = "dB" ;
                r_calib_radar_constant_copol:meta_group = "radar_calibration" ;
                r_calib_radar_constant_copol:standard_name                       =
"calibrated_radar_constant_h_channel" ;
                r_calib_radar_constant_copol:_FillValue = -9999.f ;
        float r_calib_radar_constant_crosspol(r_calib) ;
```

```
                r_calib_radar_constant_crosspol:long_name   =   "Calibrated   radar
constant crosspolar" ;
                r_calib_radar_constant_crosspol:units = "dB" ;
                r_calib_radar_constant_crosspol:meta_group = "radar_calibration" ;
                r_calib_radar_constant_crosspol:standard_name                       =
"calibrated_radar_constant_h_channel" ;
                r_calib_radar_constant_crosspol:_FillValue = -9999.f ;
        float r_calib_two_way_radome_loss_h(r_calib) ;
                r_calib_two_way_radome_loss_h:long_name = "Radar calibration two way
radome loss horizontal channel" ;
                r_calib_two_way_radome_loss_h:units = "dB" ;
                r_calib_two_way_radome_loss_h:standard_name                         =
"radar_calibration_two_way_radome_loss_h_channel" ;
                r_calib_two_way_radome_loss_h:_FillValue = -9999.f ;
        float radar_beam_width_h ;
                radar_beam_width_h:long_name  =  "Half  power  radar  beam  width
horizontal channel" ;
                radar_beam_width_h:units = "degree" ;
                radar_beam_width_h:_FillValue = -9999.f ;
        float radar_beam_width_v ;
                radar_beam_width_v:long_name = "Half power radar beam width vertical
channel" ;
                radar_beam_width_v:units = "degree" ;
                radar_beam_width_v:_FillValue = -9999.f ;
        float radar_measured_sky_noise_h(time) ;
                radar_measured_sky_noise_h:long_name   =   "Measured   sky   noise,
horizontal channel" ;
                radar_measured_sky_noise_h:units = "dBm" ;
                radar_measured_sky_noise_h:_FillValue = -9999.f ;
        float radar_measured_sky_noise_v(time) ;
                radar_measured_sky_noise_v:long_name = "Measured sky noise, vertical
channel" ;
                radar_measured_sky_noise_v:units = "dBm" ;
                radar_measured_sky_noise_v:_FillValue = -9999.f ;
        float radar_measured_transmit_power(time) ;
                radar_measured_transmit_power:long_name  =  "Radar  measured  transmit
peak power" ;
                radar_measured_transmit_power:units = "dBm" ;
                radar_measured_transmit_power:meta_group = "instrument_parameters" ;
                radar_measured_transmit_power:standard_name = "radar_transmit_power"
;
                radar_measured_transmit_power:_FillValue = -9999.f ;
       float receiver_gain_copol(time) ;
                receiver_gain_copol:long_name = "Receiver gain copol" ;
                receiver_gain_copol:units = "1" ;
                receiver_gain_copol:_FillValue = -9999.f ;
        int sweep_end_ray_index(sweep) ;
                sweep_end_ray_index:long_name = "Index of last ray in sweep" ;
                sweep_end_ray_index:units = "1" ;
                sweep_end_ray_index:_FillValue = -9999 ;
        char sweep_mode(sweep, string_length_22) ;
                sweep_mode:long_name = "Scan mode for sweep" ;
                sweep_mode:units = "1" ;
        int sweep_number(sweep) ;
                sweep_number:long_name = "Sweep index number 0 based" ;
                sweep_number:units = "1" ;
                sweep_number:_FillValue = -9999 ;
        int sweep_start_ray_index(sweep) ;
                sweep_start_ray_index:long_name = "Index of first ray in sweep" ;
```

```
                sweep_start_ray_index:units = "1" ;
                sweep_start_ray_index:_FillValue = -9999 ;
        float unambiguous_range(time) ;
                unambiguous_range:long_name = "Unambiguous Range" ;
                unambiguous_range:units = "m" ;
                unambiguous_range:meta_group = "instrument_parameters" ;
                unambiguous_range:standard_name = "unambiguous_range" ;
                unambiguous_range:_FillValue = -9999.f ;
        float latitude ;
                latitude:long_name = "Latitude" ;
                latitude:units = "degree_N" ;
                latitude:standard_name = "latitude" ;
                latitude:valid_min = -90.f ;
                latitude:valid_max = 90.f ;
                latitude:_FillValue = -9999.f ;
        float longitude ;
                longitude:long_name = "Longitude" ;
                longitude:units = "degree_E" ;
                longitude:standard_name = "longitude" ;
                longitude:valid_min = -180.f ;
                longitude:valid_max = 180.f ;
                longitude:_FillValue = -9999.f ;
        float altitude ;
                altitude:long_name = "Altitude" ;
                altitude:units = "m" ;
                altitude:standard_name = "altitude" ;
                altitude:_FillValue = -9999.f ;
        float altitude_agl ;
                altitude_agl:long_name = "Altitude above ground level" ;
                altitude_agl:units = "m" ;
                altitude_agl:standard_name = "height" ;
                altitude_agl:_FillValue = -9999.f ;
        float lat ;
                lat:long_name = "North latitude" ;
                lat:units = "degree_N" ;
                lat:standard_name = "latitude" ;
                lat:valid_min = -90.f ;
                lat:valid_max = 90.f ;
                lat:_FillValue = -9999.f ;
        float lon ;
                lon:long_name = "East longitude" ;
                lon:units = "degree_E" ;
                lon:standard_name = "longitude" ;
                lon:valid_min = -180.f ;
                lon:valid_max = 180.f ;
                lon:_FillValue = -9999.f ;
       float alt ;
                alt:long_name = "Altitude above mean sea level" ;
                alt:units = "m" ;
                alt:standard_name = "altitude" ;
                alt:_FillValue = -9999.f ;

// global attributes:
                :command_line = "kazrcfr_ingest -s cor -f M1" ;
                :Conventions   =   "ARM-1.2   CF/Radial-1.4   instrument_parameters
radar_parameters radar_calibration" ;
                :process_version = "ingest-kazrcfr-1.2-0.el6" ;
                :dod_version = "kazrcfrge-a1-1.0" ;
```

```
                :input_source                                                    =
"/data/collection/cor/corkazrM1.00/KAZR_MOMENTS_20190430-000004.dat" ;
                :site_id = "cor" ;
                :platform_id = "kazrcfrge" ;
                :facility_id = "M1" ;
                :data_level = "a1" ;
                :location_description = "Cloud, Aerosol, and Complex Terrain
Interactions (CACTI), Cordoba, Argentina" ;
                :datastream = "corkazrcfrgeM1.a1" ;
                :antenna_altitude = "3 m" ;
                :antenna_diameter = "2 m" ;
                :comment = "" ;
                :digital_rx_dec = "24" ;
                :fft_len = 512 ;
                :filter_length = "106" ;
                :institution = "Department of Energy Atmospheric Radiation
Measurement Program" ;
                :n_gates = 1024 ;
                :num_spectral_averages = "15" ;
                :pulse_compression_ratio = "13.3" ;
                :range_gate_spacing_m = 29.97925f ;
                :range_offset_ch1 = "  -1.4 m" ;
                :range_offset_ch2 = "  70.7 m" ;
                :software_version = "1.7.6 (Wed Mar 23 17:10:35 UTC 2016 leachman" ;
                :title = "ARM KAZR Moments" ;
                :doi = "10.5439/1478370" ;
                :history = "created by user dsmgr on machine ruby at 2019-04-30
16:30:42, using ingest-kazrcfr-1.2-0.el6" ;
data:

 base_time = 1556582401 ;

 time_offset = 0.951612, 3.025211, 5.098814, 7.172429, 9.246025, 11.319628,
    13.393227, 15.466826, 17.540443, 19.61402, 21.687623, 23.761223,
…
}
***
```

4.5.2. GEOMS HDF/NetCDF file global format attributes

! Global Attributes
PI_NAME=Leblanc;Thierry
PI_AFFILIATION=NASA Jet Propulsion Laboratory;NASA.JPL
PI_ADDRESS=JPL Table Mountain Facility;Wrightwood, CA 92397-0367;UNITED STATES
PI_EMAIL=thierry.leblanc@jpl.nasa.gov
DO_NAME=Leblanc;Thierry
DO_AFFILIATION=NASA Jet Propulsion Laboratory;NASA.JPL
DO_ADDRESS=JPL Table Mountain Facility;Wrightwood, CA 92397-0367;UNITED STATES
DO_EMAIL=thierry.leblanc@jpl.nasa.gov
DS_NAME=Leblanc;Thierry
DS_AFFILIATION=NASA Jet Propulsion Laboratory;NASA.JPL
DS_ADDRESS=JPL Table Mountain Facility;Wrightwood, CA 92397-0367;UNITED STATES
DS_EMAIL=thierry.leblanc@jpl.nasa.gov

DATA_DESCRIPTION=Routine middle atmospheric temperature profile from JPL LIDAR at Mauna Loa Observatory, HI (MLSOL)
DATA_DISCIPLINE=ATMOSPHERIC.CHEMISTRY;REMOTE.SENSING;GROUNDBASED
DATA_GROUP=EXPERIMENTAL;PROFILE.STATIONARY
DATA_LOCATION=MAUNA.LOA.HI
DATA_SOURCE=LIDAR.AEROSOL_NASA.JPL002_GLASS.1.1
DATA_VARIABLES=LATITUDE.INSTRUMENT;LONGITUDE.INSTRUMENT;ALTITUDE.INSTRUMENT;DATETIME;DATETIME.START;DATETIME.STOP;INTEGRATION.TIME;WAVELENGTH_EMISSION;WAVELENGTH_DETECTION;ANGLE.VIEW_ZENITH;ALTITUDE;AEROSOL.RETRIEVAL.METHOD;AEROSOL.BACKSCATTER.RATIO_BACKSCATTER;AEROSOL.BACKSCATTER.RATIO_BACKSCATTER_UNCERTAINTY.ORIGINATOR;AEROSOL.BACKSCATTER.RATIO_BACKSCATTER_UNCERTAINTY.COMBINED.STANDARD;AEROSOL.BACKSCATTER.RATIO_BACKSCATTER_UNCERTAINTY.RANDOM.STANDARD;AEROSOL.BACKSCATTER.RATIO_BACKSCATTER_UNCERTAINTY.SYSTEMATIC.STANDARD;AEROSOL.BACKSCATTER.RATIO_BACKSCATTER_RESOLUTION.ALTITUDE.IMPULSE.RESPONSE.FWHM;RANGE_INDEPENDENT_NORMALIZATION;AEROSOL.BACKSCATTER.COEFFICIENT_DERIVED;AEROSOL.BACKSCATTER.COEFFICIENT_DERIVED_UNCERTAINTY.ORIGINATOR;AEROSOL.BACKSCATTER.COEFFICIENT_DERIVED_UNCERTAINTY.COMBINED.STANDARD;AEROSOL.BACKSCATTER.COEFFICIENT_DERIVED_UNCERTAINTY.RANDOM.STANDARD;AEROSOL.BACKSCATTER.COEFFICIENT_DERIVED_UNCERTAINTY.SYSTEMATIC.STANDARD;AEROSOL.BACKSCATTER.COEFFICIENT_DERIVED_RESOLUTION.ALTITUDE.IMPULSE.RESPONSE.FWHM;NUMBER.DENSITY_INDEPENDENT;PRESSURE_INDEPENDENT;TEMPERATURE_INDEPENDENT;NUMBER.DENSITY_INDEPENDENT_SOURCE;PRESSURE_INDEPENDENT_SOURCE;TEMPERATURE_INDEPENDENT_SOURCE;SOURCE.PRODUCT
DATA_START_DATE=20200124T053201Z
DATA_STOP_DATE=20200124T075457Z
DATA_FILE_VERSION=001
DATA_MODIFICATIONS=Older data versions also available at NDACC in Ames format, filenames: mltp.tll and mltp*.mdl*
DATA_CAVEATS=Profile quality potentially impacted by clouds, aerosol layers, and occasional instrument issues
DATA_RULES_OF_USE=
DATA_ACKNOWLEDGEMENT=Notify PI that data is being used and ask for proper form of acknowledgement
DATA_QUALITY=Full QC/QA completed
DATA_TEMPLATE=GEOMS-TE-LIDAR-AEROSOL-005
DATA_PROCESSOR=GLASS v1.18_20200919
FILE_NAME=groundbased_lidar.aerosol_nasa.jpl002_glass.1.1_mauna.loa.hi_20200124t053201z_20200124t075457z_001.hdf
FILE_GENERATION_DATE=20200928T224850Z
FILE_ACCESS=NDACC;AVDC
FILE_PROJECT_ID=CAMS27
FILE_ASSOCIATION=
FILE_DOI=
FILE_META_VERSION=04R051;CUSTOM

5. Chapter 5: Guidance for the validation of lidar and aerosol products

Plain language summary

The aim of this chapter is to provide guidelines on how to perform a validation study of the Level 1 lidars and Level 2 aerosol profiling products from satellite missions. For this validation, the reference measurements can come from suborbital airborne or ground-based lidars, photometers, and in-situ instrumentation. Moreover, key aspects and considerations that may apply when different types of instruments (remote sensing or in-situ, ground-based or airborne) are used as reference in the validation, are provided. The description of the Level 1 and Level 2 lidar products from past, current and future satellite missions are provided in *Chapter 2*. The description of the different instruments/measurements that can be used for their validation, along with the instrument capabilities, corresponding QA/QC procedures, spatiotemporal criteria, and statistical considerations, is provided in *Chapter 3*.

5.1. General Considerations

When planning Calibration/Validation (Cal/Val) activities, an estimate of the noise in the satellite lidar measurements and an estimate of the desired calibration uncertainty to be achieved should be kept in mind. For the evaluation of satellite lidar measurements using suborbital measurements, we must attempt at finding procedures allowing us to reduce both systematic and random errors in the comparison of these products (Gimmestad et al., 2017).

To reduce random uncertainties, satellite measurements typically require compositing or averaging measurements over larger spatial scales than suborbital measurements. The amount of spatial averaging also depends on the desired level of uncertainty in the satellite measurement. For instance, assessing the uncertainty of CALIOP calibration at 5 km altitude to 2% requires along-track compositing of data over thousands of kilometers. Airborne lidars, flying along the satellite ground track, can measure the same (or similar) aerosol/cloud scene with reduced systematic uncertainties associated with measuring potentially different scenes, and allow greater horizontal averaging scales to reduce the random uncertainties in the satellite measurements. For validation comparisons with ground-based lidars, one should consider that the composited satellite lidar profile can differ from that ground-based measurements due to differences in the geophysical scene and temporal offsets observed by the two instruments. These differences in a geophysical scene should be considered, in order to not introduce systematic errors in the comparison which can affect the resulting assessment of the satellite lidar products.

The number of satellite and suborbital profiles that must be acquired and averaged to be used for cal/val activities depends on the homogeneity of the desired parameter(s) at the altitudes of interest and the extent to which inhomogeneities will introduce systematic errors. In this process, during validation studies, the suborbital measurements used should be carefully examined to consider the atmospheric variability during the satellite data acquisition (e.g. the temporal and spatial scales appropriate for use in evaluating the satellite measurements). As an indicative example, Anderson et al. (2003) used ground-based, airborne, and satellite AOD (Aerosol Optical Depth) aerosol measurements and found large correlations for temporal scales below four hours and distances less than 70 km. However, other studies using airborne

remote sensing measurements have found that the variability in AOD with distance/time varies significantly depending on whether the aerosols are generated locally or transported from long distances (Chang et al., 2021; LeBlanc et al., 2022; Redemann et al., 2005; Rogers et al., 2014; Shinozuka & Redemann, 2011). Moreover, collocated CALIPSO and ground-based lidar measurements within a radius of 100 km have been used (Pappalardo et al., 2010) to investigate the spatio-temporal representativeness of aerosol optical properties under different atmospheric conditions (higher representativity for long scale events) and at different altitudes (smaller representativeness at lower altitudes).

Furthermore, several satellite lidar products that need evaluation are not directly measured through suborbital lidars. For instance, using lidar observations the aerosol classification is approximated through intensive parameters (e.g., extinction-to-backscatter ratio (lidar ratio); LR, particle depolarization ratio, color ratio) or their combination. Therefore, complementary to the Cal/Val activities based on remote sensors, airborne in situ techniques offer a valuable insight for the validation of aerosol products derived by lidar observations (e.g. Sheridan et al., 2012). In situ measurements are valuable for the validation of both aerosol and cloud properties (e.g. using measurements of single-scattering albedo, size distribution and particle shape, liquid water content). Hence, although in situ measurements have their own limitations, it is recognised that they offer complementary information for the atmospheric layers which is invaluable for satellite Cal/Val.

The following subsections present the different approaches that can be followed for the validation of the L1 or L2 satellite lidar products when using different instruments to serve as a reference (from different types of suborbital lidars to photometers and in-situ instrumentation), along with special considerations taking into account the capabilities and limitations of each instrument. Depending on the availability of the reference measurements, the optimum would be to use several of these approaches when performing a validation study (e.g. a lidar and a photometer at the same location/station), as each method has different strengths and weaknesses.

5.2. Validation of Level 1 Lidar products

Spaceborne lidar Level 1 (L1) products include the attenuated backscatter coefficient (here on attenuated backscatter) from elastic and HSRL systems (more details in *Chapter 2*). The direct validation of these lidar L1 products can be achieved using coordinated airborne lidar measurements, and possibly ground-based mobile lidar facilities deployed on the satellite ground-track. In other cases (e.g. using ground-based lidar facilities at a distance from the satellite track), the validation should be performed by assessing statistical properties of the products. Given the narrow footprint of the lidar systems (50 - 350 m) and the revisit time of polar orbits, the use of long term (multi-year) measurements and/or measurements from several locations is preferred to achieve meaningful statistics. Data from lidar networks and observatories with lidar systems are well suited for such tasks.

5.2.1. Attenuated Backscatter

Suborbital lidar measurements have been used to evaluate satellite L1 lidar calibration typically by using molecular (Rayleigh) scattering measured high in the atmosphere. Products and methodologies that have been used, along with aspects to be considered, are presented herein.

- Comparison of **attenuated backscatter profiles calculated from aerosol backscatter profiles** (see Rogers et al., (2011) for HSRL airborne measurements and Mona et al., (2009) for ground-based measurements).

  (a) aspects/steps to be considered for the airborne comparison (e.g. Rogers et al., 2011):

  - choose an altitude range for which the atmospheric backscatter can be accurately estimated, the lidar signal has sufficient Signal-to-Noise-Ratio (SNR), the signal response of the detection system is linear, and use only full overlap regions.
  - convert the unattenuated scattering ratio profile from the HSRL into attenuated backscatter.
  - use the same molecular density profile as used in the processing of the satellite profiles.
  - compute the HSRL attenuated backscatter profile at lower altitudes using the total attenuated backscatter at this altitude with the two-way transmittance from the reference altitude.
  - transfer the computed attenuated backscatter to the satellite calibration reference altitude (e.g. ~30 km for CALIOP) by estimating the attenuation between this altitude and the suborbital calibration altitude (i.e. including molecular scattering and ozone absorption).

  Usually, HSRL measurements have the important advantage of internal calibration to high accuracy (~1-2%) without the need for additional independent information about the aerosol loading at the calibration altitude or an assumption that this region is aerosol-free (e.g. Rogers et al., 2011). But this calibration transfer does not attempt to include attenuation due to clouds or aerosols, hence the satellite feature mask should be used to screen out profiles that include such attenuation. In Rogers et al. (2011) a detailed description of the errors/biases induced in each step of the aforementioned methodology is provided. The biases could be reduced if the suborbital platform flies at a higher altitude, such as in the lower stratosphere, so as to reduce the potential for undetected aerosols and clouds.

  (b) aspects/steps to be considered for the ground-based comparison (e.g. Mamouri et al., 2009; Mona et al., 2009; Pappalardo et al., 2010):

  - use the ground-based derived particle extinction coefficient profiles to calculate the 2-way particle transmittance up to the calibration altitude of the satellite product.
  - compute the attenuated backscatter coefficient using the total backscatter coefficient, and the 2-way transmittances from particles, molecules and ozone.
  - use the same molecular density profile as used in the processing of the satellite profiles (i.e. pressure and temperature fields).

- for daytime measurements, an appropriate lidar ratio (LR) should be selected for the calculation of the particle extinction coefficient from ground-based backscatter lidars. Collocated sun photometer data and multi-wavelength lidar measurements can assist for a representative LR selection.

- in the above methodology, attenuation due to clouds or aerosols is not considered, hence the satellite feature mask should be used to screen out profiles with such attenuation.

- for the investigation of the multiple scattering effects in the spaceborne lidar signals, comparison between satellite and ground-based lidar signals should take into account the multiple scattering effect (Donovan, 2016; Reichardt & Reichardt, 2003; Wandinger et al., 2010).

- The selected spatio-temporal distance between the ground-based and satellite lidar measurement should consider the atmospheric variability. Past EARLINET-based studies have chosen 40 km - 100 km as the maximum horizontal distance for intercomparisons between ground-based lidars and the satellite lidar footprint, and time windows of ±10 min - ±2 hrs (Mamouri et al., 2009; Mona et al., 2009; Pappalardo et al., 2010; Proestakis et al., 2019).

- Comparison of **calibrated attenuated backscatter profiles** measured from airborne backscatter lidars (Hlavka et al., 2005; Pauly et al., 2019). Aspects to be considered:

    - the attenuated backscatter profiles are calibrated by normalizing the signals acquired to a modelled molecular attenuated backscatter profile. The molecular profile ideally is the same as the one used for the retrieval of the satellite products.

    - accurate selection of the scattering ratio that will be applied in the molecular region will lower the uncertainties induced from this step (e.g. Pauly et al., 2019; Vaughan et al., 2010).

- Comparison of **molecular** (**Rayleigh) backscatter signals in aerosol free altitudes** (McGill et al., 2007). Aspects to be considered:

    - accurate calculation of the lidar calibration constant whereby the attenuated backscatter profile is matched to a Rayleigh backscatter profile at aerosol free altitude ranges.

    - complementary comparison with the expected Rayleigh backscatter profile calculated using atmospheric parameters' profiles (e.g., pressure and temperature). Take into account the source of the used atmospheric parameters' profiles (e.g. radiosonde soundings or model outputs).

- Comparison of elastic backscatter measurements at desired wavelength calibrated using aerosol scattering ratio at HSRL-available wavelength (e.g. LaRC HSRL airborne lidar) (e.g. Vaughan et al., 2019). Aspects to be considered:

- identify regions of minimum aerosol scattering using the aerosol scattering ratio at the HSRL-available wavelength.

- choose an altitude range of minimum aerosol loading, where the aerosol scattering ratios at desired wavelength can be estimated using the HSRL-measured scattering ratio and an assumed aerosol backscatter color ratio.

- normalize the elastic backscatter measurements at the desired wavelength in the minimum loading region to a molecular model that incorporates contributions from the estimated aerosol scattering ratio.

- data should be cloud-cleared and averaged over the entire coincident flight path.

- corrections should be applied for additional molecular attenuation between the satellite and the airborne calibration altitude.

Other qualitative approaches:

- Qualitative comparison of **stratospheric aerosol scattering ratio** using airborne backscatter lidar observations (Winker et al., 1996).

- Comparison of the **minimum detectable backscatter associated with aerosol and cloud features** (e.g. McGill et al., 2007 on subvisible cirrus clouds).

Although it seems that for some of the presented approaches more aspects should be considered, one should consider that this is also related to the level of detail treatments that were considered from the authors of the different publications.

5.2.2. HSRL attenuated backscatter

The focus of the community's efforts until now has been on the attenuated backscatter calibration and validation for elastic backscatter lidars. For HSRLs and other more advanced lidars, fundamental calibration and validation will be more difficult, if, by that, we mean calibration of individual measurement channels. These more advanced systems optically separate total attenuated backscatter into channels that optically pass molecular and particle backscatter by different degrees (e.g., for an HSRL system, there can be a channel that is dominated by molecular backscatter with a small amount of particle backscatter "cross-talk" and another that is dominated by particle backscatter with some molecular backscatter cross-talk). Assessing the calibration of the individual channels from such an instrument would ideally be done with an airborne HSRL with identical cross-talk characteristics; however, that is likely to be impractical for a variety of reasons (e.g., lack of airborne instruments employing the same technique with exactly the same cross-talk parameters, cross-talk changing on orbit as a function of laser-to-interferometer tuning, etc.) As a result, spaceborne HSRL calibration assessments will have to involve the reconstruction of space-like channel measurements from the airborne HSRL data set based on assumptions on the cross-talk parameters for both the airborne and spaceborne instruments. Those assumptions will add uncertainty to the calibration assessment. In the case of ATLID, an alternative is an assessment of the L1 data products, i.e., the attenuated Rayleigh backscatter and the attenuated Mie backscatter. Such profiles can be constructed from a suitably designed and calibrated airborne lidar employing

any HSRL technique. Unfortunately, it will be difficult to determine whether differences between the ATLID L1 profiles and the airborne lidar proxy profiles are due to errors in the airborne cross-talk parameters, ATLID cross-talk parameters, or other factors (e.g., gain ratios between the airborne channels or between the ATLID channels). That is, the root cause of differences will be difficult to quantify, making it difficult to correct L1 algorithms based on the validation assessment alone. Overall, the different approaches that can be followed for the validation of Level 1 HSRL attenuated backscatter profiles are summarized herein:

(a) Attenuated backscatter signals from different channels (e.g. EarthCARE Rayleigh, Mie co-polar, Mie cross-polar)

- Use of similar airborne HSRL to separately evaluate Rayleigh and Mie attenuated backscatter signals (using even the same cross-talk).

- Reconstruction of space-like channel measurements from sub-orbital HSRL data set based on assumptions on the cross-talk parameters for both the sub-orbital and space-borne instruments.

(b) Attenuated backscatter data products (e.g. attenuated Rayleigh backscatter, attenuated Mie backscatter)

- Comparison with the same products from airborne HSRL lidars (e.g. comparison of attenuated backscatter profiles calculated from aerosol backscatter profiles, following procedures similar to Rogers et al. (2011), can be used for ATLID products).

- Comparison with the same products derived from ground-based lidars with a lidar simulator tool developed to simulate the spaceborne lidar.

For example, for EarthCARE ATLID L1 products, the CARDINAL Campaign Tool (CCT) lidar simulator has been developed which provides realistic simulations of the ATLID signals and the L1 products of the attenuated particle (Mie) backscatter, the attenuated molecular (Rayleigh) backscatter, and the attenuated cross-polar backscatter. In brief, the simulator make use of airborne or ground-based lidar or radar L2 products and meteorological fields, parameterizes the atmospheric scene using a lidar radiative transfer model and an instrument model based on the ATLID design, in order to simulate the lidar signals that would be recorded from ATLID for the provided atmospheric scene and, finally, derives the corresponding ATLID L1-like products. These products can be directly compared with the collocated measured ATLID L1 products.

Special considerations for L1 validation:

- Thermally driven changes in the alignment between the satellite transmitter and receiver (Hunt et al., 2009) could cause changes between the daytime and nighttime calibration. Due to this reason, frequent daytime and nighttime validation (including periodic under-flights) is needed to monitor the calibration performance over a range of latitudes and seasons (e.g.Getzewich et al., 2018; Rogers et al., 2011).

- For the validation of the L1 lidar products, it is preferred to use suborbital (or other satellite) measurements of the same wavelength. That is because the wavelength

conversion of L1 products is not straightforward. If one needs to use lidar measurements at different wavelengths for the L1 validation, a conversion is needed using Level 2 (L2) products.

5.3. Validation of Level 2 lidar aerosol products

In general, L2 lidar aerosols products are optical and geophysical parameters that can be obtained through a retrieval technique. Spaceborne lidar L2 products may include the following parameters: aerosol optical depth (or thickness), extinction coefficient, backscatter coefficient, lidar ratio, particle linear depolarisation ratio, color ratio, Ångström exponent, aerosol layer height/depth, aerosol layer classification (typing) (see also ch. 2).

There are two main sources of uncertainties affecting the retrieved products. The first involves challenges in accurate identification and characterization of aerosol layers in complex scenes (i.e. aerosol layers with embedded (unfiltered) broken clouds, geometrically thin or low concentration layers (undetected), high concentrations layers with multiple scattering effects or misclassified as clouds). The second comes from the fact that physical assumptions underpinning the retrievals may vary across regions, seasons, and regimes (e.g. lidar ratio assumption, assumptions in aerosol models used). The analysis of these sources should be part of validation activities.

Suborbital lidar and sun photometer measurements have been used extensively to evaluate satellite L2 lidar products, particularly aerosol products. Additionally, in-situ measurements have been partially used for the evaluation of few products. Herein we briefly review the used measurements, along with aspects to be considered, for the different L2 aerosol products.

5.3.1. Aerosol Optical Depth (AOD)

(a) Use of ground-based sun-photometer measurements

Column AOD (or Aerosol Optical Thickness - AOT) can be directly measured through surface photometry. Ground-based photometers directly observe the attenuation of solar/lunar radiation (in the spectral range of 340–1640 nm), and provide accurate measurements of AOD (without interference from land surface reflections) with uncertainty ~ 0.01 – 0.02 (Eck et al., 1999). Furthermore, since AOD varies nearly linearly with wavelength in the log-log space (e.g., Schuster et al., 2006), the reference measurements can be easily interpolated to the satellite's wavelengths throughout the shortwave spectrum. These reference measurements are the 'gold standard' for AOD, and can successfully be used for validation of satellite column AOD products (e.g., Sogacheva et al., 2022). Measurements from the AERONET photometer network (which consists of 1114 sites globally as of Feb 1, 2024; https://aeronet.gsfc.nasa.gov/) have been extensively used for the validation of satellite AOD products from passive and active sensors (e.g. Omar et al., 2013; Schuster et al., 2012 on CALIPSO-Aeronet AOD comparisons). There is also an excellent discussion of the uncertainty associated with satellite-AERONET comparisons by Sayer et al. (2020). For satellite aerosol validation, the AERONET version 3 L2 AOD quality-assured dataset should be used (available within a month after post-field calibration). Furthermore, the Maritime Aerosol Network (MAN) component of AERONET (ship-borne AOD measurements from Microtops II sun photometers; (Smirnov et al., 2009)), provides an opportunity for the validation of satellite AOD products over the oceans. The MAN sun-photometers acquire direct sun measurements (within the

spectral range of 340–1020 nm), and provide columnar optical depth (OD) and water vapour content (Morys et al., 2001), with estimated OD uncertainty less or equal to ±0.02, (i.e. slightly higher than the uncertainty of the AERONET field instruments; (Smirnov et al., 2006)).

Additional aspects to be considered when using ground-based photometer measurements for the validation of satellite lidar-based AOD products: the space-based lidar laser beam rarely passes directly over the vast majority of photometer sites and the overpass repeat cycles are more sparse in time than for passive sensors (e.g., 16-days repeat cycle for CALIPSO). Due to these reasons, during the validation a certain offset distance between the lidar beam and the ground-based sites can be considered, and a longer time period is needed for the collection of the statistically significant/equivalent collocated dataset (in relation to the passive satellite products). Indicatively, users shouldn't expect statistically robust comparisons to AERONET sites in the first years after the launch of a satellite lidar. More specifically, regarding offset distances, good analyses allow "closest approach" distances that are equivalent to the longest averaging distance used in the satellite lidar curtains for the comparisons (Schuster et al., 2012). As an example, CALIPSO provided 5, 20, and 80 km averaging distances for the AOD data products (depending upon the averaging required to detect the aerosol concentration). For aerosol layers retrieved at 80-km averages, the analysis already assumes an 80-km autocorrelation distance and therefore 80-km closest approaches are also valid. Inticatively, Schuster et al. (2012) obtained 677 synchronized clear-sky overpasses at the AERONET sites in a 3-year period, with 80% of those having 80-km averaging in at least one aerosol layer.

Time synchronization is another factor to be considered. Indicatively, AERONET provides AOD measurements every 3 or 15 minutes (Giles et al., 2019, for the Model 5 or older Model 4 Cimels). This means that any satellite overpass can pair with a concurrent AERONET measurement within ∼15 minutes, as long as there are no clouds or an instrument malfunction. If data does become available 1-2 hours later (as some authors allow), it is likely that clouds were present during the overpass and that the clear conditions that AERONET found later (or earlier) were not present during the overpass. Since broken clouds add noise to clear-sky comparisons, comparisons with an hour or two between satellite overpass and AERONET data acquisition should not be included in AOD comparisons. Given the AERONET data acquisition frequency described above, it is reasonable to allow up to ∼30 minutes for comparisons to Cimel Model 4 instruments and ∼5 minutes for Model 5, which allows some flexibility for improperly programmed instruments.

(b) Use of airborne HSRL measurements

Airborne HSRL measurements have several aspects that greatly facilitate their use for the validation of satellite lidar aerosol products. Regarding the validation of AOD:

- The flights can occur over a wide geographical range and sample a wide variety of aerosol types and AOD conditions.

- They can provide a direct, calibrated, and validated measurement of AOD (e.g. Rogers et al., 2009) reported AOD biases from integrated airborne HSRL measurements on the order of 0.005 (and less than 6.5%) when compared with photometer-collocated measurements).

- The airborne HSRL can perform satellite underflights, minimizing spatial and temporal mismatches (e.g. Rogers et al. (2014) show that HSRL AOD measurements going outbound and inbound along CALIPSO tracks were well correlated for temporal differences of less than 90 minutes).

- The measurements have the advantage that the region of incomplete overlap between laser and telescope lies in the upper troposphere or lower stratosphere (depending on the altitude of flight), which have much lower aerosol amounts than in the lower troposphere wherein lies the overlap regions of ground-based lidars (Rogers et al., 2014).

- The evaluation of layer and column AOD can be done during both daytime and nighttime, in contrast to measurements and/or retrievals of AOD from ground-based (e.g. AERONET) and airborne (e.g. polarimeters) passive sensors that require sunlight.

- Measurements of layer AOD are also possible in cases where passive instruments would be limited because of clouds (e.g. above or below clouds).

- In cases of elastic lidars (e.g. CALIOP, CATS), the measurements enable the separation of the impact of the satellite's detection sensitivity and the method inferring the aerosol LR on the layer and column AOD products (e.g. Rogers et al., 2014).

Extensive airborne HSRL measurements have been used to evaluate CALIOP layer and column optical depths (and aerosol LRs) in the North America and Caribbean Sea regions (Rogers et al., 2014). Furthermore, airborne HSRL AOD measurements have been used to evaluate CALIOP above-cloud AOD retrievals derived using the standard CALIOP algorithm as well as a technique that uses liquid water clouds of known reflectivity (Kacenelenbogen et al., 2014). Liu et al. (2015) also used airborne HSRL measurements as part of an extensive investigation to evaluate smoke and mineral dust layers AOD (and LR values) derived using return signals above opaque water clouds. Airborne HSRL measurements of AOD have also been used to evaluate retrievals of AOD derived from CALIOP measurements using the Synergized Optical Depth of Aerosols (SODA) algorithm that uses ocean surface returns measured by CALIOP and CloudSat's Cloud Profiling Radar (Josset et al., 2011; Painemal et al., 2019) as well as from CALIOP alone (Venkata & Reagan, 2016). Additionally, advanced lidars such as ATLID may be expected to provide layer AOD below thin cirrus, in such cases coincident airborne HSRL measurements can be used to evaluate these measurements.

Additional aspect to be considered: for a satellite backscatter lidar (e.g. CALIOP), the AOD could be biased high/low because of an overestimated/underestimated assigned LR for that layer, and biased low in the column AOD due to its failure to detect tenuous aerosols. In order to separate the impact of each of these uncertainties on the layer- and column-AOD products, simultaneous measurements relating to aerosol type, LR, and aerosol backscatter are desired. These measurements would also be required to validate the measurements from more advanced lidars, such as ATLID, that provide direct measurements of the LR and AOD.

(c) Use of satellite products

AOD satellite inter-comparison with passive sensors can be utilized to mitigate the aforementioned satellite-to-ground collocation drawbacks. The passive sensor's large swath can allow a much higher collocation success, and one could anchor the lidar validation via a proxy passive satellite sensor anchor with reasonably well known uncertainties (e.g. Oo and Holz 2011; Kittaka et al., 2011; Redemann et al., 2012; Ma et al., 2013; Kim et al., 2013; Liu et al., 2018). This inter-comparison is particular useful over oceans, where surface reflectance is less uncertain than over land, from either sensor. While the satellite-to-satellite intercomparison is imperfect, it provide an opportunity for a statistically relevant assessment against a data product with peer reviewed accuracy and limitations.

In the AOD satellite-to-satellite inter-comparison, special causion should be given on the impact of the two satellites spatial and temporal sampling (e.g. Redemann et al., 2012; Ma et al. 2013), and on the criteria for screening the collocated dataset (e.g. Redemann et al., 2012). Special focus should be given on adequate cloud screening of the collocated dataset. Indicativelly, Redemann et al. (2012) restricted the CALIPSO-MODIS comparison dataset to scenes with MODIS cloud fraction less than 1%. Additionally, the comparisons over land should be provided with causion, and one should assess whether or not there is consistency with the over-ocean retrievals as far as the geographical distribution of AOD differences between the two sensors is concerned (e.g. Redemann et al., 2012).

5.3.2. Aerosol backscatter and extinction profiles

Validation of the lidar L2 aerosol backscatter and extinction products rely on the intercomparison with suborbital lidar measurements from airborne (e.g. Omar et al., 2009; Winker et al., 2013) and ground-based systems (e.g. Pappalardo et al., 2010; Proestakis et al., 2019). The approaches used, along with the corresponding aspects to be considered are presented herein.

(a) Use of airborne HSRL measurements

Airborne HSRL measurements of aerosol backscatter and extinction profiles provide excellent means for the evaluation of the relevant satellite products, and also the evaluation of the performance of alternative satellite algorithms used to derive these products. Aspects to be considered (in addition to the advantages mentioned already in AOD section):

- The HSRL measurements do not rely on assumptions and/or external information regarding aerosol type or LR, hence they can be used to directly assess the backscatter and extinction products.

- Use of the same molecular density profile as used in the processing of the satellite profiles.

- An extensive dataset of satellite under-flights is valuable for the comparison of the L2 aerosol extinction and backscatter profile products.

- The comparison between the nearly-coincident measurements of the suborbital and satellite platforms can be compared in a probability density distribution space.

- For the interpretation of the differences between the satellite and airborne products, one should consider different effects (e.g. the effect of the selected LR parameter in the case of elastic spaceborne lidars, the SNR effect on undetected aerosol layers, the effect of target misclassifications).

For example, Omar et al. (2009) used airborne HSRL extinction measurements collected during field missions (HSRL-1 data; (Hair et al., 2008)), to evaluate the CALIOP retrievals of aerosol extinction. To this end, they compared probability density distributions (PDFs) of the aerosol extinction products for nearly coincident measurements from the two platforms. They found generally good agreement for the CALIOP products (aerosol extinction biases between 0.0029 to 0.015 km-1 or 24-60%), noting that uncertainties in the CALIOP aerosol extinction profiles can be quite significant (30-200%) in large part due to uncertainties in the LRs used in the retrievals. Kacenelenbogen et al. (2011) used airborne HSRL extinction (and LR) measurements to evaluate CALIOP aerosol extinction profiles (and AODs). They found an overall low bias in CALIOP V2 profiles, due to a combination of low SNR leading to missed detection of aerosols as well as some misclassification of aerosols that led to an underestimation of the LR, and an improvement in V3 CALIOP profiles (after the addition of low-level aerosol levels). Additionally, airborne HSRL measurements acquired over North America and the Caribbean Sea were used to evaluate CALIOP nighttime retrievals of aerosol extinction profiles (Winker et al., 2013). Other studies have used airborne HSRL aerosol extinction profiles to assess new techniques for retrieving aerosol extinction profiles (e.g. Burton et al., 2010; McPherson et al., 2010; Painemal et al., 2019).

(b) Use of ground-based extinction and backscatter profiles derived from Raman or HSRL lidars

Ground-based measurements of aerosol extinction and backscatter profiles from Raman or HSRL lidars are capable of evaluating the corresponding space-based profiles (e.g. Pappalardo et al., 2010). Aspects to be considered for the satellite comparison:

- Use of the same molecular density profile as used in the processing of the satellite profiles.

- In order to minimize the uncertainties related to spatio-temporal collocation, one must assess the scales and time at which each property naturally varies. The spatio-temporal scales at which the aerosol properties vary are directly linked to the processes governing the emission, transport, removal, and transformation of the aerosol particles. Different aerosol layers are observed at different spatiotemporal homogeneities, with biomass burning layers showing the largest and fastest variability.

- The selected distance between the ground-based and satellite lidar measurements should consider the spatial atmospheric variability. Past EARLINET-based studies have chosen 40 km - 100 km as the maximum horizontal distance for intercomparisons between their ground-based lidars and satellite lidar footprint (Mamouri et al., 2009; Mona et al., 2009; Papagiannopoulos et al., 2016; Pappalardo et al., 2010; Proestakis et al., 2019). EARLINET suggests ≤ 100 km as an optimum horizontal distance, also considering that typical averaging of ±30 min for ground-based lidar will smooth out some of the atmospheric variability in the scene.

- The choice of the selected time interval from the ground-based measurements is crucial, and to some extent is related to the selected distance between ground-based and satellite lidar measurement. Past EARLINET-based studies have chosen time windows within ±30 min - ±2 hrs as a correlative period (Mamouri et al., 2009; Mona et al., 2009; Papagiannopoulos et al., 2016; Pappalardo et al., 2010; Proestakis et al., 2019).

- The atmospheric measurements above the ground-based site (e.g. during the time correlative to the satellite), can provide additional information on the scene (un)homogeneity, towards the application of a more strict time interval (i.e. temporal criteria tailored for each case).

- Only cloud-free atmospheric data should be used (e.g. taking into consideration any typing information provided or derived from the satellite and/or ground-based dataset).

- For the investigation of multiple scattering effects in the spaceborne lidar products, a comparison between satellite and ground-based products should take into account the multiple scattering effects on both lidar signals. (e.g. Donovan, 2016; Reichardt & Reichardt, 2003; Wandinger et al., 2010).

(c) Use of ground-based elastic backscatter profiles (e.g. where an LR selection is required) (e.g. Paschou et al., 2023; Proestakis et al., 2019).

In cases of the absence of independent ground-based extinction and backscatter profiles (as for example 1064 nm measurements) and for Aeolus missions (due to the daytime tracks), elastic backscatter profiles are the next best option for the utilization of the ground-based lidar stations towards the validation of the aerosol extinction and backscatter products. For these cases, on top of the aforementioned aspects, the following should be considered for the validation of the satellite products:

- When the elastic backscatter profiles are calculated using assumed LR, an error is introduced in the retrieval. One should be aware of the introduced error and take it into consideration for the interpretation of the results of the comparison. For example, for the EARLINET/ACTRIS elastic backscatter profiles the mean relative uncertainty in the calculation of the aerosol backscatter coefficient is expected to be less than 20 % (Mattis et al., 2016).

- In cases of persistent aerosol layers (e.g. a mineral dust layer detected during nighttime and later-on daytime satellite overpass) one can use the mean/representative layer LR value measured during nighttime (e.g. using Raman channels) to assign a more appropriate LR on the daytime retrieval. This is expected to reduce the errors due to the selected LR value.

- The evaluation should be performed only in the altitudes of the full overlap of the ground-based system. In case a comparison is made in the altitudes below the full overlap, one should clearly mention the ground-based system limitation to capture all the aerosol load in the overlap region.

Special consideration for validation of Aeolus L2 backscatter:

ALADIN lidar onboard the Aeolus mission operated using circularly polarized emission at 355 nm. However, the transceiver concept of ALADIN allowed the detection of only the co-polar component of the backscattered signal. The missing cross-polar component in the detection led to signal loss in cases of depolarizing particles (e.g. mineral dust, volcanic ash, cirrus clouds) and subsequently to the underestimation of the backscatter products and the overestimation of the lidar ratio products. Due to this, in order to account for the undetected signal in validation scenes with depolarizing particles, a harmonization of the reference suborbital backscatter to the Aeolus-like backscatter products is necessary, which is done using suborbital particle linear depolarization ratio measurements (Abril-Gago et al., 2022; Paschou et al., 2022). Abril-Gago et al. (2022), Baars et al. (2021), and Gkikas et al. (2023) validated Aeolus aerosol backscatter products using the aforementioned correction methodology in atmospheric scenes with anthropogenic, mineral dust, mineral dust mixtures, and smoke layers. The conversion formulas cannot be applied when the particles present a preferential orientation (e.g. mineral dust (Daskalopoulou et al., 2023; Ulanowski et al., 2007) and cirrus clouds (Myagkov et al., 2016; Noel & Sassen, 2005; Thomas et al., 1990)) and/or when the multiple scattering effect is not negligible (e.g. inside clouds (Donovan et al., 2015; Jimenez et al., 2020; Schmidt et al., 2013); and inside thick aerosol layers (Wandinger et al., 2010)). For such cases, the particle circular depolarization ratio is required which can be obtained from a circular polarization lidar system. An example of a circular polarization lidar system is eVe, ESA's reference lidar for the Cal/Val of Aeolus aerosol products (Paschou et al., 2022). More specifically, eVe is a combined linear/circular Raman polarization lidar that was specifically developed to address the aforementioned limitations. It incorporates the necessary hardware elements to reproduce the operation of ALADIN and provide ground-based reference measurements for the validation of Aeolus aerosol products (Paschou et al., 2023). With eVe the evaluation of the conversion accuracy and the quantification of the multiple scattering and orientation effects on Aeolus backscatter products was investigated.

5.3.3. Aerosol lidar ratio

(a) Satellite elastic lidar ratio products

Satellite elastic backscatter lidars must assume (or derive) LR values in order to retrieve their aerosol backscatter and extinction profiles. Until now, the validation of these LR assignments (value itself and type) were performed using airborne HSRL and ground-based Raman measurements. More specifically, airborne HSRL LR measurements have been used to assess LRs used in, or derived from, satellite lidar aerosol retrievals. As an example, (Rogers et al., 2014) used extensive daytime and nighttime airborne HSRL measurements and found that the LRs used by CALIOP for marine and mineral dust aerosol types were most comparable with the airborne measurements for these types (71-82% of these aerosol layers were within 30% of the HSRL LR measurements, while only about a third of the CALIPSO cases for other aerosol types were within 30% of the HSRL LRs measurements). Ground based Raman measurements provided by EARLINET stations were used for comparing LR values for each aerosol type with the corresponding CALIPSO assumed values. Papagiannopoulos et al. (2016) used LR observations collected over the EARLINET stations, representing different atmospheric conditions, and found that the mean clean continental LR used in CALIPSO scheme is about 10 sr lower than the value observed in background

European values. For mineral dust particles, the comparison with EARLINET values allowed for an adjustment in the CALIPSO assumed values toward the EARLINET observed mean value of 51 ± 10 sr. Additionally, both ground-based Raman and airborne HSRL LR measurements showed a range of LRs for each of the CALIPSO aerosol types (e.g. Mona et al., 2006), indicating that the use of a single LR to represent each of the aerosol types can lead to significant uncertainties in the retrieved aerosol products, with a possibility to estimate the expected uncertainty induced from the LR assumption of CALIPSO. Furthermore, airborne HSRL measurements have been used to evaluate LRs determined by alternative elastic backscatter lidar retrieval techniques which use column AOD or scattering from the ocean surface/clouds to derive a mean LR. As an example, Painemal et al. (2019) found mean bias differences between CALIOP column LRs derived using a SODA AOD column constraint to be within 5 sr (18%) of airborne HSRL mean LRs, with RMSE differences within 9 sr (32%). It should be considered that the satellite elastic backscatter LR assumed values are constrained by the limitation of its lidar signatures and their sensitivity to the differences between the several types. For the case of CALIPSO, the wide variation of LR values observed from suborbital measurements for particular CALIPSO aerosol types has been attributed in aerosol mixtures beyond the satellite's classification capabilities which are driven mainly by the depolarization.

(b) Satellite HSRL lidar ratio products

Satellite HSRL lidars (e.g. Aeolus, EarthCARE) can directly measure the LR profiles. In particular, Aeolus was the first lidar that directly measured LR from space, but due to the missing of polarization component in the satellite design, only the co-polar LR could be measured (not the total). A description of the methodologies used to evaluate the Aeolus LR products is provided herein, after a short discussion on the spatiotemporal correlation required for the evaluation of the LR products.

For non-depolarized aerosol layers: the undetected polarization issue of Aeolus could be neglected. An example of these type of cases is the validation performed in Baars et al. (2021). In this study, ground-based lidar measurements were used for the validation of Aeolus LR products in long-range transported smoke layers, and found that the Aeolus LR agreed well within the ground-based reference uncertainties in well-pronounced lofted smoke layers. This was possible because the smoke cases considered did not depolarize the light.

In the presence of depolarizing particles (e.g. mineral dust, stratospheric smoke): as already discussed in *section 5.2.1* (for Aeolus backscatter coefficient), due to the missing polarization component of Aeolus (Flament et al., 2021), a conversion should be made to the Aeolus-like LR for using the particle depolarization ratio profiles from the suborbital lidar and assuming randomly oriented particles and negligible multiple scattering (Baars et al., 2021; Flament et al., 2021; Paschou et al., 2022). This conversion is based on the assumption that the same aerosol type can be observed from the satellite and the suborbital platform (i.e. the same aerosol depolarization properties for both measurements).

Consistency check with known aerosol type: If the aerosol type in an atmospheric region is known and correlation (as described above) can be assumed, the LR of the known aerosol types can be used to validate the satellite LR profiles using a consistency check. Flament et al. (2021) and Ehlers et al. (2022) validated the Aeolus LR of a dense mineral dust layer above the Eastern Atlantic Ocean by converting the Aeolus co-polar LR component (e.g. Abril-Gago

et al., 2022; Paschou et al., 2022) and comparing it's consistency with LR literature values (e.g. Floutsi et al., 2023). Note: As LR is an intensive quantity and thus depends only on the aerosol type, it can be used to validate satellite products in case the aerosol type is accurately known (i.e. including also its respective mixing state). As the mixing state can change, it is preferred to do such a validation approach only on pure aerosol types (e.g. Saharan dust). For the cases of pure aerosol types, the LR variability is lower compared to the variability of the aerosol mixtures since it mainly originates from the aerosols' chemical composition (e.g. different mineral dust components).

In fact, validation of the LR is also partly a validation of the aerosol type properties, thus one should refer also to the respective section in this chapter.

For the upcoming EarthCARE mission (where the depolarization component is not missing), similar suborbital LR measurements and approaches can be utilized to evaluate the satellite LR measurements.

(c) Use of in-situ observations for LR assessments

In-situ measurements can be used for the validation of satellite LR products. To compute the LR, we need the measured refractive index, particle size distribution (PSD), and particle shape, all of which can (in principle) be inferred with the right set of in-situ instrumentation. The derivation of particle microphysical properties from in-situ measurements can be quite complex (e.g., a combination of several instruments is needed to have the full set of information) but we report here on a few applications. Jager & Hofmann (1991) used balloon-borne particle counter data to define a seasonally averaged stratospheric volcanic sulfuric acid aerosol size distribution, and from this LR, mass, and area ratios are derived for an appropriate range of refractive indices. Marenco et al. (2016) computed the LR of smoke in the Amazon basin by applying a constraint on the lidar signals, and compared the result to airborne in-situ observations of the PSD, through Mie scattering computations, obtaining an agreement able to validate the LR retrieved. The computation has been repeated for a suitable range of refractive indices, showing that the combination of remote sensing and in-situ techniques could in principle help to put a constraint on the refractive index of smoke.

It should be mentioned here that for the scattering calculations of irregular particle shapes (e.g. mineral dust particles), the calculation of LR is not trivial, especially for large size parameters (e.g. Gasteiger, et al., 2011b). What has been commonly used up to now is the spheroidal shape (e.g. Dubovik et al., 2006), which has limitations in reproducing the backscattering properties of e.g. mineral dust (Gasteiger, et al., 2011b). Thus, further work is needed for developing scattering codes and databases that reproduce the backscattering properties of irregular-shaped particles (e.g. Gasteiger, et al., 2011b; Huang et al., 2023; Saito et al., 2021).

Moreover, for the LR assessment from in-situ observations one should also take into account the particle's hygroscopicity, which changes the LR of the particles in humid ambient conditions (e.g. Tsekeri et al., 2017). In these cases the in-situ derived LR may be different, since it is usually derived for dried particles.

General spatiotemporal consideration of LR products: In contrast to the backscatter and extinction coefficient, the LR and depolarization ratio are intensive properties (i.e. dependent only on aerosol type and not on aerosol load), thus as long as the same particle type is

observed, spatiotemporal correlation (co-location) is not as sensitive as for the extensive quantities (i.e. extinction and backscatter, which depend on aerosol load). This makes the measured LR easier to validate, once correlation between the suborbital and satellite measurements are assured. There are several options to investigate this correlation (Baars et al., 2021):

a) Use of trajectory analysis: calculate backward trajectories to compare the suborbital observation with the satellite observation by taking into account the air motion. In this method, no changes are considered in the air parcels (i.e., no changes in the aerosol properties), which is mainly valid for lofted (or long-range transported) aerosol layers. For aerosol measurements in the planetary boundary layers (PBL), this assumption is not valid.

b) Check the temporal (in)homogeneity in the suborbital observation and horizontal (un)homogeneity in the satellite profiles: A second method to analyze the correlation between the two measurements, is to check for temporal homogeneity (in the ground-based measurements) and horizontal homogeneity (in the airborne and satellite measurements). As an example, if the satellite LR in the targeted aerosol layer is horizontally homogeneous over some tens to hundreds of kilometers and does not change significantly for the ground-based lidar through time, then it can be fairly assumed that the same air mass (i.e., the same containing aerosol property) is observed and hence the LR values can be directly validated. Passive satellite imagery can be used to validate this assumption also.
For the validation of LR measurements in the PBL, where homogeneity cannot be assumed, so far only statistical methods can be considered (e.g., long-term observations at certain places).

5.3.4. Particle depolarization ratio

Particle depolarization ratio is an important satellite L2 product, used widely for the satellite's aerosol typing. As an intensive property, for the validation of this product the spatiotemporal correlation (co-location) is not as sensitive as for the extensive quantities (as long as the same particle type is measured). While the volume depolarization ratio (defined as the calibrated ratio of the measured cross- to the co-polar lidar signals containing the contribution from molecules and particles; (Freudenthaler, 2016) is directly measured, the particle depolarization ratio needs to be retrieved from the measured volume depolarization ratio, the molecular depolarization ratio (calculated for each lidar system; e.g. Siomos et al., 2023) and the retrieved particle and molecular backscatter products (Beyerle, 1994; Biele et al., 2000)). An indirect validation of the particle depolarization ratio includes the validation of the products used for its retrieval (e.g. Burton et al., 2013).

CALIPSO measured the volume (linear) depolarization ratio at 532 nm (polarization calibration procedure described by Powell et al. (2009)) and provided the particle (linear) depolarization ratio as a L2 product. Airborne and ground-based measurements were used for its validation. Ground-based validation using particle depolarization ratio co-located products, led to the suggestion of an improved calculation scheme for the particle depolarization ratio product (Tesche et al., 2013). Airborne validations found that the attenuation of the backscatter by atmospheric features above the measurement height affects the particle depolarization ratio product (Burton et al., 2013). For the validation of CATS 1064 nm volume (linear)

depolarization products, airborne lidar measurements (from the Cloud Physics Lidar) were used to better characterize the gain ratios of the relevant channels (CalWater-2 and CCAVE-15 campaigns).

Suborbital considerations:

(a) For the successful validation of satellite particle depolarization ratio products, calibrated suborbital lidar systems are required (e.g. polarization calibration methodologies developed for ACTRIS lidars: Belegante et al., 2018; Bravo-Aranda et al., 2016; Freudenthaler, 2016).

(b) For certain aerosol types, there is a wavelength dependence of the particle depolarization ratio. Mineral dust exhibits a wavelength-dependent depolarization ratio (Burton et al., 2015; Haarig et al., 2017, 2022; Hofer et al., 2020; Hu et al., 2020). Non-spherical smoke particles in the upper troposphere / lower stratosphere exhibit a distinct and pronounced spectral dependence of the depolarization ratio as well (Burton et al., 2015; Haarig et al., 2018; Hu et al., 2019). On the other hand, the spectral dependence is negligible for almost spherical particles such as pollution, marine aerosol, and smoke under humid conditions. In cases of evaluation of this product with measurements from another wavelength, this wavelength dependence should be considered.

5.3.5. Geometrical properties (Aerosol layer height and depth)

Satellite profiling sensors can detect atmospheric regions where the aerosol load is either significant or relatively homogeneous. In general, the altitude registration of the laser profiles is quite accurate with small height bin assignment errors, hence the most crucial validation concerns the characterization of the layer detection sensitivity. Each mission adopts a different algorithm that fits its goals and operational needs. In general, due to the moving platform, SNR enhancement through data averaging is a common practice for the retrieval of these products. The methods used by different missions are summarized in the chapter Appendix 5.5 (Table 5.1). As an example, the first CALIPSO layer identification algorithm used an adaptive threshold technique on single profiles and multiple profiles to identify tenuous layers (Vaughan et al., 2009), while another algorithm used a two-dimensional and multi-channel feature detection method (Vaillant de Guélis et al., 2021).

Generally, the suborbital lidar aerosol (and cloud) identification techniques detect the layers through one-dimensional (1D) or two-dimensional (2D) approaches. The algorithms to retrieve elevated layers use similar techniques as those for the detection of the PBL. A comprehensive review of the different techniques to retrieve PBL height is given by Kotthaus et al. (2023). A short description of the methodologies used from suborbital measurements for layer identification is presented herein.

- 2D approaches (processes) are widely used in space profilers and have applicability in suborbital profile measurements. They take advantage of the information provided by a continuous series of lidar profiles by searching for cloud and aerosol features in the 2D image. Typically edge detection, sliding window, and image reconstruction techniques are often employed to retrieve a feature mask (Vaillant de Guélis et al., 2021; van Zadelhoff et al., 2023; Vivone et al., 2021).

- Detection algorithms applied to single-shot or averaged profiles (1D approaches). Ground-based systems historically detect layers using single or averaged profiles. Four main approaches are generally employed:

    - the slope-based method, which detects a negative maximum in the derivative with respect to the range of the lidar signal (e.g. Flamant et al., 1997).

    - the threshold-based method, which searches for regions rising significantly above the theoretical clear-air value (e.g. Campbell et al., 2008).

    - a combination of slope-based and threshold-based methods (e.g. Lewis et al., 2013).

    - the wavelet covariance analysis (WCT), which detects a maximum in the correlation function of the lidar signal and a wavelet, usually the Haar wavelet (e.g. Baars et al., 2008; Comerón et al., 2013; Siomos et al., 2018).

In MPLNET, the planetary boundary layer height and the aerosol top height products are derived using a combination of the WCT technique and image processing, following the methodology presented in Lewis et al. (2013). Recently, the ACTRIS/EARLINET database has been enhanced with aerosol layer height and mixing layer height products, defined as the top of the aerosol layer and the top of the convective boundary layer respectively. They are derived using the WCT, following the methodology described by Siomos et al. (2018). In other EARLINET studies (e.g. Michailidis et al. 2023), the center of mass (COM) is used to describe the aerosol layer height of elevated layers and is derived using the methodology of Mona et al. (2006). In AD-NET the boundary layer height is identified using the vertical gradient of the backscatter coefficient with the methodology presented by Sugimoto et al. (2009) and Nishizawa et al. (2017).

<u>Geometrical considerations:</u>

The WCT is a commonly used methodology for layering detection and has been applied to range-corrected signals (Baars et al., 2008), and on lidar products (Michailidis et al., 2023; Siomos et al., 2018). Below some aspects to be considered when applying this methodology are summarized, concerning the wavelength/product/deliation selection (Voudouri et al., 2023): (a) wavelength selection: Infrared wavelengths magnify the differences in the vertical distribution of the aerosols, resulting in layers that are easily identified and can provide more accurate layer detections; (b) product selection: particulate backscatter product is less noisy than the particulate extinction product, hence the application of WCT on this product give more accurate detections; (c) wavelet dilation selection: optimum wavelet dilation values for layering detection are reported between 200 - 600 m, while with > 600 m only thick layers can be detected. In general, the selection of a bigger wavelet dilation value results in a lower number of detected layers (especially for the infrared channel).

For the validation of the aerosol layer height and depth products, the suborbital location and the terrain topography around the satellite overpass should not be neglected. Vertical inconsistencies between suborbital and satellite retrievals over areas with a complex terrain appear (and should be considered) due to the orography that induced disturbances in the aerosol layer heights/depth.

The evaluation of aerosol geometrical properties could give different results in layers with different concentrations and depths, and in daytime/nighttime conditions. Typically, the satellite retrievals will struggle to detect relatively thin layers and layers with low concentrations. Also, the satellite measurements will have less sensitivity during daytime (higher noise), which may result in more undetected layers.

Suborbital lidar measurements are used to evaluate the satellite layer products. This has been done in the past either through a direct comparison of the identified aerosol layers, or through the evaluation of derived products within the detected layers (e.g. AOD). Overall, there is not an absolute reference for layer heights against which a selected layer height technique could be verified. For the CALIPSO mission, one significant concern was the validation of the correct determination of the aerosol layer base (a more difficult product than layer top for a spaceborne lidar). The validation of this parameter was provided using collocated airborne HSRL measurements during campaigns (e.g. the ORACLES campaign; Redemann et al., 2021). Furthermore, several studies that address the satellite's capability for aerosol layer detection, concentrated on characterizing layer detection sensitivity and on the quantification of the undetected-layers effect in the columnar AOD (and subsequent radiative forcing calculations). This was investigated through data intercomparison with MODIS, AERONET, airborne HSRL, ground-based lidar-derived AOD products, and lidar-derived AOD products above opaque clouds. Examples of these studies:

1. Kim et al. (2017) statistically quantified the (AOD) effect of the CALIPSO undetected aerosol layers through AOD intercomparison with MODIS products. This methodology can be applied once the extinction products of a mission are validated, hence one can consider the absence of biases from the detected aerosol layers. A similar approach could also be used with AERONET product intercomparison.

2. Toth et al. (2018) statistically quantified the (AOD) effect of the CALIPSO undetected aerosol layers through intercomparison between CALIPSO profiles with fill-only values and MODIS collocated profiles, in a multiyear approach (4-year collocated dataset).

3. Rogers et al. (2014) compared CALIPSO AOD with airborne HSRL-derived AOD and quantified the undetected aerosol layers during daytime and nighttime.

4. Thorsen et al. (2017) compared CALIPSO AOD with ground-based (ARM) lidar-derived AOD.

5. Liu et al. (2015) compared the CALIPSO L2 AOD with the retrieved AOD from the Opaque Water Cloud technique applied to CALIPSO L1 data where aerosol layers are located above opaque water clouds

One critical aspect of geometrical properties validation is collocation. The bottom, top, and depth of the layers are high variable (the mostly variable properties) hence intercomparison with sub-orbital measurements should be carefully done and should be based on a large number of values of statistical relevance (see also *Chapter 3*).

Additionally, special caution is needed so as to avoid cases of very high AODs (e.g. Chimot et al., 2018; or when AOD is above 2 to 3), in order to exclude cases where the satellite or suborbital lidar beam is totally attenuated. In these cases, the ALH derived from the lidar

retrievals is not representative of the scene, as only part of the aerosol layer is detected. There might be cases when thick absorbing layers shield the backscatter profile at short wavelengths (e.g. 532 nm of CALIPSO), and not at longer ones. In these cases, the observations at the longer wavelengths can be used as a reference point of the underestimation of the geometrical products at the shorter wavelengths.

5.3.6. Aerosol typing/classification

Intensive optical properties are concentration-independent parameters which reveal information about the aerosol type. They can be utilized for aerosol-typing purposes (and thus for the harmonization of satellite records of aerosol properties performed at different wavelengths). The most common intensive optical parameters used for aerosol-typing purposes are the LR, the particle depolarization ratio, and the Ångström exponent. These parameters are common L2 products and their validation has been already discussed in the sections above.

Different satellites utilize different sets of products for aerosol classification, and usually the classes are different for different missions. Indicatively, CALIPSO classification scheme categorize the aerosol layers in eleven types (troposphere: clean marine, dust, polluted continental/smoke, clean continental, polluted dust, elevated smoke and dusty marine; stratosphere: polar stratospheric aerosol, ash, smoke, sulfate, and “unclassified”). The parameters used for this classification are the lidar-derived feature-integrated volume depolarization ratio, attenuated backscatter, feature height, geographical location, underlying surface type, temperature and season (Kim et al., 2018; Omar et al., 2009; Tackett et al., 2023). CATS classification scheme categorize the aerosol layers in similar types (e.g. desert dust, dust mixture, smoke, polluted continental, clean/background, marine, marine mixture, and upper troposphere–lower stratosphere aerosol; (Nowottnick et al., 2022)). Both CALIPSO and CATS (as elastic backscatter lidars) were not able to utilize LR measurements for their classification (as they didn’t perform direct extinction measurements thus the LR was an a priori). Several validation studies have been performed with ground-based lidar systems (e.g. Kanitz et al., 2014), as well as with airborne HSRL LR measurements (Burton et al., 2013). The most common problem was aerosol misclassification, mainly due to the surface-dependent decision tree of the classification scheme. This issue was mainly resolved with the new version updates (Tackett et al., 2023), which led to more accurate feature identification and more reliable extinction retrievals.

Aeolus HSRL aerosol/cloud products are the particle backscatter, particle extinction, and lidar ratio (Ansmann et al., 2007; Flamant et al., 2008; Straume et al., 2020). Aeolus doesn’t have a classification product. The main limitation for this came from the undetected cross-polar component of the emitted circular-polarized light, and the inadequate separation of the aerosol types with only the three available products. This imposes great challenges to aerosol classification based on Aeolus products only (typing may be performed in the case of spherical scatterers or via a synergistic approach with ground-based lidars, supported by back trajectory analysis and other additional information).

Comprehensive collections of suborbital lidar-derived intensive optical properties can be utilized in the development and validation of aerosol typing schemes on both suborbital and satellite lidars. ACTRIS/EARLINET database (Pappalardo et al., 2014, data.earlinet.org)

includes backscatter, extinction, lidar ratio, and particle depolarization ratio profiles over more than 40 stations (at present 33 stations available) over Europe and beyond since 2000 up to now with most of them committed to providing measurements on long term for the next 20 years within ACTRIS (Laj et al., 2024). This database has been used for developing aerosol typing algorithms (Nicolae et al., 2018; Papagiannopoulos et al., 2018), and for comparing and assessing the complementariness of different typing algorithms (Voudouri et al., 2019). Currently, it is under implementation the centralized fully quality-controlled provision of the aerosol typing product for the ACTRIS/EARLINET stations.

Looking also outside Europe, DeLiAn ground-based data collection is available (Floutsi et al., 2023) including globally distributed, long-term, ground-based, multiwavelength Raman and polarization lidar measurements (mainly from the PollyNET network; (Baars et al., 2016; Engelmann et al., 2016)) of the particle (linear) depolarization ratio, the lidar ratio and the Ångström exponent, available at 355 and 532 nm. The dataset includes 13 aerosol type categories (i.e. pure aerosol types and specific aerosol mixtures). DeLiAn collection has been used for the development and validation of aerosol typing schemes of the EarthCARE's Hybrid End-To-End Classification (HETEAC) model (Wandinger, et al., 2023b), which serves as a common baseline for the development, evaluation, and implementation of EarthCARE algorithms. More information about the HETEAC algorithm can be found in the chapter Appendix 5.6.

Aspects to be considered for the validation of spaceborne aerosol typing:

- A first step towards the classification validation is the validation of the L2 products that were used in the classification scheme (described in the sections above). This will provide valuable information on misclassification reasons (e.g. if it is due to the L2 products or the algorithm itself).

- The utilization of suborbital multiwavelength observations can provide additional information on the aerosol types in the scene, and validate the capability of the classification scheme to correctly separate mixtures.

- Intercomparison with a different aerosol typing scheme that uses the same (or different) L2 input parameters can be applied. However, this becomes difficult due to the different nomenclatures and classifications used in the different aerosol typing schemes (Voudouri et al., 2019). For validation purposes, a commonly agreed nomenclature/classification would be highly beneficial.

- Since aerosol typing is usually applied to atmospheric features, a consistency check between the feature identification algorithms (see *Section 5.2.5*) shall be performed.

- Additionally, consistency must be ensured for the atmospheric layer geometrical boundaries (or column, etc.) in consideration.

- L2 products used for aerosol typing can be wavelength-dependent and, therefore, wavelength conversion might be necessary to allow meaningful comparisons. Spectral conversion can be achieved via the aerosol-type-dependent backscatter- and extinction-related Ångström exponents. These conversions can be derived from suborbital lidar measurements, optical models, or data collections (e.g. Amiridis et al.,

2013).

5.3.7. Aerosol microphysical and optical properties

The lidar capabilities are rather limited in terms of the characterization of aerosol microphysical and optical properties (in an extended spectral range than provided by the lidar measurements). However, the validation needs of space profilers include microphysical and optical properties of aerosols too, as e.g. the LR used in the extinction coefficient retrieval of CALIPSO (Kim et al., 2018), or the optical properties in UV/VIS/IR used as input to the radiative closure assessments of EarthCARE (Wandinger et al., 2023a). In this context, validation is also needed for:

Microphysical properties:

- Size distribution, effective radius and spectral refractive index

Optical properties (in the spectral range from UV to IR):

- Extinction and Angstrom exponent (profiles)
- Single-scattering albedo (profiles)
- Asymmetry parameter

These properties can be validated with new products from new passive polarimeters, such as PACE/HARP2, PACE/SPEXone, Metop-SG/3MI and CO2M/MAP, in terms of column-effective values, mainly in the VIS (e.g., Dubovik et al., 2019). The passive polarimeters provide valuable information of particle microphysical properties, depending on their spectral range and accuracy (Mishchenko and Travis, 1997). Their sensitivity is though limited to the vertical distribution of the particles, and the possible change in particle properties at different heights, making the validation of products of profilers a challenging task. New products from the synergy of passive polarimeters and lidar profilers are expected to provide more accurate estimations, including the vertical variability of the microphysical and optical properties of the particles (e.g. Knobelspiesse et al., 2011).

Ground-based retrievals of optical and microphysical properties may also be used for validation. For example, advanced retrievals are provided from the synergy of lidar and sun-photometer measurements from the GARRLiC/GRASP algorithm, which currently is being employed for operational processing within the framework of the European ACTRIS infrastructure (Lopatin et al., 2021). The algorithm provides column-effective values for the microphysical properties of the particles (and profiles of their concentrations), thus the comparison with the corresponding products from space profilers may be challenging in case of large vertical variability.

The validation may also be performed with airborne in-situ measurements, providing profiles of the size distribution, chemical composition (from which the refractive index can be deduced), as well as SSA (from extinction and absorption coefficient measurements) (e.g., Tsekeri et al., 2017). The comparison with in-situ data should always be done with caution, taking into account the different methodologies used (e.g. drying of particles (Tsekeri et al., 2017), undersampling of large sizes (e.g., Ryder et al., 2018), etc.

A less direct way to validate the particle microphysical properties is to use an inversion algorithm (Müller et al., 1999) to retrieve the microphysical parameters from the lidar-derived

optical parameters. This methodology though is limited by the information content in lidar measurements regarding the aerosol properties.

5.4. Summary and Discussion

The validation activities associated with satellite lidar measurements of aerosols have shown that suborbital lidar measurements are critical for properly evaluating the performance of their products. Additionally, the additional wavelengths available from sub-orbital lidar measurements can aid in the development of a dataset that can be used to relate similar suborbital lidar measurements at other wavelengths to the satellite lidar wavelength, thereby helping to facilitate the use of additional suborbital measurements for Cal/Val. The measurements at additional wavelengths, along with measurements of additional aerosol optical properties such as lidar ratio, depolarization ratio, Angstrom exponent etc. provide valuable information for assessing assumptions and constraints associated with aerosol retrieval algorithms (e.g. CALIOP LR assumption). Additionally, extensive sub-orbital lidar measurements have provided the opportunity to acquire data in diverse locations and a wider variety of aerosol types and optical properties. As new aerosol retrieval algorithms are developed, additional lidar Cal/Val activities have provided the datasets needed to assess these retrievals under more diverse conditions and locations.

Airborne lidar measurements provide the means to acquire relevant datasets directly along the satellite track minimizing uncertainties associated with temporal and spatial differences. Airborne measurements permit the acquisition of the required number of satellite profiles to achieve the desired uncertainty while minimizing both systematic and random errors. Additionally, airborne lidar Cal/Val activities have shown the benefits of using airborne lidar systems (with greater measurement capabilities) than the targeted satellite lidar systems. Better SNR and smaller uncertainties in such airborne measurements reduce the number of profiles that must be acquired and averaged together to reduce random uncertainties and achieve the desired level of calibration accuracy. Going one step further, airborne under-flight lidar measurements acquired over a long time period provide the means to monitor the L1 calibration, account for temporal changes in this calibration, and evaluate procedures used to transfer the nighttime calibration to daytime (lessons learned from CALIPSO mission with >16 years under-flights).

Similar airborne lidar measurements will be required for the ATLID and AOS lidar systems. Such measurements will likely be acquired during dedicated Cal/Val field missions and during other science campaigns. While such under-flights could theoretically be conducted during science missions, operational or other constraints may make it difficult, if not impossible, to conduct such flights. For example, the satellite lidar calibration will likely require measurements to check both nighttime and daytime calibration; however, most airborne science missions are conducted during the day due to operational constraints. Conducting additional night flights may require resources that are beyond the science mission’s staffing or funding levels. Additionally, the science mission may require flights to a particular location or need particular observational conditions that preclude sufficient coincidence with the satellite lidar measurements. Science missions necessarily place priority on acquiring suborbital data to meet specific science objectives; satellite Cal/Val, if considered, is typically a lower priority. Consequently, satellite lidar validation typically involves dedicated flight hours and/or dedicated missions that are tailored to acquire the specific data required for Cal/Val.

Such missions that deploy airborne lidar(s) may be more efficiently conducted with small aircraft and so can increase Cal/Val opportunities.

Cal/Val from ground-based mobile lidar systems and ground-based lidar networks provide a less expensive option, with the latter providing usually longer timeseries. The main aspect that needs to be considered when using ground-based network measurements is that the space-based lidar laser beam rarely passes directly over the vast majority of the network sites (e.g., 16-days repeat cycle for CALIPSO). Moreover, a certain spatio-temporal distance between the ground-based and satellite lidar measurements should be considered for the atmospheric variability for the Cal/Val of aerosol products. In order to minimize the uncertainties related to spatio-temporal collocation, one must assess the scales and time at which each property naturally varies. The spatio-temporal scales at which the aerosol properties vary are directly linked to the processes governing the emission, transport, removal, and transformation of the aerosol particles. EARLINET suggests ≤ 100 km as an optimum horizontal distance for intercomparison between ground-based lidars and the satellite lidar footprint and time windows of ±30 min. Moreover, for the investigation of multiple scattering effects in the spaceborne lidar products, comparison between satellite and ground-based products should take into account the multiple scattering effects on both lidar signals. Lastly, the evaluation should be performed only in the altitudes of the full overlap of the ground-based system. In case a comparison is made in the altitudes below the full overlap, one should clearly mention the ground-based system limitation to capture all the aerosol load in the overlap region.

5.5. Appendix: Active satellite layer detection algorithms

Table 5.1. The active satellite layer detection algorithms

Satellite	Lidar	Type	Layer detection method	Reference
CALIPSO	CALIOP	Elastic	Adaptive threshold-based method and multi-profile averaging	(Vaughan et al., 2009)
CALIPSO	CALIOP	Elastic	Multispectral iterative threshold-based method and image reconstruction techniques	(Vaillant de Guélis et al., 2021)
ICESat-2	ATLAS	Elastic	Data aggregation function with an auto-adaptive threshold algorithm	(Herzfeld et al., 2021)
EarthCARE	ATLID	HSRL	Edge detection and smoothing techniques	(van Zadelhoff et al., 2023)
Aeolus	ALADIN	HSRL	Edge detection and smoothing techniques adopted from ATLID	(van Zadelhoff et al., 2023)
ISS	CATS	Elastic	Adaptive threshold-based method and multi-profile averaging	(Vaughan et al., 2009; Yorks et al., 2015)
ISS	CATS	Elastic	Convolutional Neural Networks and denoising techniques	(Yorks et al., 2021)

5.6. Appendix: EarthCARE Aerosol Classification model: HETEAC & HETEAC-Flex

Successful aerosol classification from EarthCARE's (Illingworth et al., 2015; Wehr et al., 2023) UV-Atmospheric lidar (ATLID) is of key importance for achieving one of the EarthCARE

mission's goals, which is radiative closure for each 10×10 km pixel within 10 Wm^-2. To this end, the Hybrid End-To-End Aerosol Classification (HETEAC) model was developed (Wandinger, et al., 2023b). HETEAC's hybrid approach ensures consistency between the theoretical description of aerosol microphysics and the experimentally derived optical properties (Floutsi et al., 2023), while the end-to-end approach allows a complete and uniform representation of the aerosol types in terms of microphysical, optical and radiative properties. In addition, HETEAC serves as the common baseline for the development, evaluation, and implementation of EarthCARE algorithms.

HETEAC considers four aerosol components: two fine modes consist of either weakly or strongly absorbing spherical particles and two coarse modes consist of either spherical or non-spherical particles. The four aerosol components adequately reflect the most frequently observed aerosol types in the troposphere: pollution-related aerosol, fresh smoke, marine particles and mineral dust, respectively.

For each of these components, a mono-modal particle size distribution and a wavelength-dependent complex refractive index is assigned to obtain their microphysical description, based on ESA's Climate Change Initiative (CCI) project Aerosol CCI (Holzer-Popp et al., 2013). The mode radii and refractive indexes are obtained from AERONET and are considered typical for the aerosol components. To describe the scattering of the non-spherical particles, two models were examined. One is the spheroid model introduced by Dubovik et al. (2006) and the other one is proposed by Gasteiger, et al. (2011b). While both models are widely used in several applications (e.g. Dubovik et al., 2006 in Aerosol cci and Gasteiger, et al., 2011b in OPAC), the model and spheroid distribution chosen for HETEAC was the one of Gasteiger, et al. (2011b), mainly due to the degree of reproducibility of the observations.

To account for aerosol mixtures of two or more modes, a multimodal representation is achieved by mixing rules. Each mode has specific scattering properties per unit particle volume, which are then used, in combination with the relative volume contribution of each mode, to derive the optical properties of the aerosol mixture. This procedure results in lookup tables (LUT) of the optical and radiative properties for the different mixing ratios between the aerosol modes at eight wavelengths (Wandinger, et al., 2023c).

Once in orbit, EarthCARE's products will undergo extensive validation from the several cal/val teams. In view of aerosol typing and radiative closure, a novel methodology for the characterization of atmospheric aerosol based on lidar-derived intensive optical properties was developed (Floutsi et al., 2024). The aerosol typing scheme is applicable to both ground- and satellite lidars, which is ideal for cal/val activities.

HETEAC-Flex, applies the optimal estimation method (OEM) to a combination of lidar-derived intensive aerosol properties (i.e., concentration-independent), to determine the statistically most-likely contribution of aerosol component to the observed aerosol mixture, weighted against a priori knowledge of the system. The aerosol components considered to contribute to an aerosol mixture are four, namely fine, spherical, absorbing (FSA); fine, spherical, non-absorbing (FSNA); coarse, spherical (CS); and coarse, non-spherical (CNS). These four components have been selected from lidar-based experimental data set at 355, 532 and 1064 nm. Their optical and microphysical properties serve as a priori for the retrieval scheme and are in accordance with the ones used in the original HETEAC model, to ensure meaningful comparisons. In contrast to HETEAC, which is limited to observations at 355 nm only, the

novel typing scheme is flexible in terms of input parameters and can be extended to other wavelengths to exploit the full potential of ground-based multiwavelength-Raman-polarization lidars and thus reduce the ambiguity in aerosol typing. It is thus an algorithm, able to be applied to EarthCARE but also to other lidar systems providing other or more optical products.

The initial guess of the aerosol components contribution that is needed to kick-off the retrieval scheme is the outcome of a decision tree. Using this initial guess, the lidar ratio (355 and 532 nm), particle linear depolarization ratio (355 and 532 nm), extinction-related Ångström exponent and backscatter-related color ratio (at the 532/1064 nm wavelength pair) are calculated (forward model). The final product is the contribution of the four aforementioned aerosol components to an aerosol mixture in terms of relative volume. Once this product meets certain quality assurance flags, it can be used to provide additional products: (a) aerosol component separated backscatter and extinction profiles, (b) aerosol optical depth per aerosol component, (c) volume concentration per component, (d) number concentration per component, (e) effective radius of the observed mixture and (f) refractive index of the mixture.

6. Chapter 6: Guidance for the validation of radar, cloud and precipitation products

Plain language summary

The aim of this chapter is to provide guidelines on how to perform validation of cloud precipitation products, with a major focus on vertical profiles of cloud and precipitation properties, by using ground and airborne-based remote sensors. The description of the instruments that can be used for such validation and corresponding QA/QC procedures are described in *Chapter 3*, the comprehensive list of geophysical products is given in *Chapter 2*.

This chapter is divided into two parts, the first part focuses on recommendations for validation of level 1 cloud and precipitation radar products. The second part focuses on recommendations for the validation of level 2, i.e. geophysical, cloud and precipitation products. As discussed in previous chapters, some of the level 2 products are derived from synergistic observations by different instrument types and other ancillary data (while level 1 products are instrument specific). Recommendations on the use of synergistic observations and some of the products are derived using observations from multiple spaceborne remote sensors.

6.1. Validation of L1 cloud and precipitation radar products

L1 cloud and precipitation radar products typically include received echo power, transmitted signal power, noise power, range and other variables needed for estimation and geolocation of radar reflectivity values, which are delivered as one of level 2 products. Additionally, depending on each specific mission processing architecture, the following quantities may be included in derived L1 products (often labeled as 1B or 1C) : measured normalized radar cross section of the surface (NRCS, often referred to by the symbol σ^0, measured in dB), measured effective reflectivity factor (often referred to by the symbol Z, or Z_m, measured in dBZ), and some form of echo mask (to classify each pixel according to two or more classes based on its signal to noise or signal to clutter ratio). It is important to note that these quantities are typically not corrected for attenuation (hence the ‘measured’ qualifier): attenuation correction, when implemented, is typically a L2 processing step.

Furthermore, additional products are generated at L1 depending on the nature of the payload itself: for example, a Doppler radar (such as EarthCARE’s CPR) will also include mean Doppler velocity and Doppler spectral width (it will be the first cloud spaceborne radar with Doppler capability). For the purpose of this document, we will use EarthCARE's list of L1 products, including radar reflectivity and Doppler velocity noting that these products will include different levels of corrections between L1B and L1C processed products. Another example is the collocated and spatially resampled multi-radar reflectivity factor fields to be generated by the INCUS mission (where three identical Ka-band radars aim to observe the same storm within a couple of minutes from each other in order to observe their dynamics at those temporal scales).

6.1.1. Level 1 Products derived from backscattered power

One of the key requirements for cloud and precipitation radar missions is the radar reflectivity sensitivity which translates to the minimum detectable precipitation rate or total cloud content.

The TRMM Precipitation Radar (PR), which operated at Ku band (13.8 GHz) between 1997 and 2015, had a sensitivity of approximately 17 dBZ for a 5 km horizontal resolution and 250 m range resolution, and was able to detect rain rates down to approximately 0.7 mm/h. The TRMM PR successor GPM's Dual-frequency Precipitation Radar (DPR), operating at Ku- (13.6 GHz) and Ka- (35.5 GHz) bands (Hou et al., 2014), as well as the ultra-compact RainCube Ka-band radar (Peral et al., 2019) and its successors Dynamic Atmospheric Radars (DAR) on board the INCUS mission (van den Heever et al., 2022) and the ones on board the Tomorrow.io technology demonstrations (Roy et al., 2023) all had, have, or are slated to have comparable sensitivities generally in the +10 to +20 dBZ range (corresponding to rain rates roughly between 0.1 and 1 mm/hr) for resolutions between 3 and 8 km horizontally and 120 to 500 m in range.

For spaceborne cloud radars the sensitivity values are much smaller in order to detect a sufficient fraction of non-precipitating clouds, as well as precipitation lighter than 0.1 mm/hr. The Cloudsat Cloud Profiling Radar (CPR), which operated at W-band (94.05 GHz) between 2006 and 2023, had a sensitivity of about -30 dBZ for a ~1.5 km along-track integration during prime mission (Tanelli et al., 2008), and the expected sensitivity of EarthCARE Cloud Profiling Radar (EC-CPR, also at W-band) is -35 dBZ (for a nominal along-track integration of 10 km). Both these cloud radars were developed with a 500 m range resolution to maximize detection. The Atmosphere Observing System (AOS) mission concept, under formulation as of early 2024, includes both cloud and precipitation radar concepts more capable than all of these predecessors in some respects, but comparable or even with reduced capability for some other aspects.

Calibration of the L1 radar products is an important step in ensuring good quality of radar observations. The Calibration and Validation experience developed for the first two spaceborne precipitation and cloud radars (TRMM/PR and CloudSat/CPR) demonstrated that the most reliable means to achieve the required data calibration are careful analysis of the backscatter from natural targets themselves : sea surface primarily, (see for example Li et al., 2005; Protat et al., 2009; Tanelli et al., 2005), but also land and ice surfaces as well as Rayleigh scatterers in the atmosphere) and use of specific active or passive radar calibrator units on the ground (e.g. Masaki et al., 2020). While in principle ground based or airborne weather and cloud profiling radars provide a wealth of information to compare and validate, it was found that spaceborne radars are typically better calibrated than the ground-based or airborne-radars and can in fact act as 'universal reference' calibrators for the multitudes of ground and airborne radars (e.g. Anagnostou et al., 2001; Kollias et al., 2019; Louf et al., 2019).

One of the first steps of the validation activities is the verification of compliance to the sensitivity requirements. Direct validation of spaceborne radar products can be achieved using coordinated airborne measurements using well instrumented research aircrafts, and possibly mobile facilities deployed on the CPR/PR ground-track. While this type of verification can lead to in-depth understanding of any possible sources of discrepancy (such as, for example, occurrence of multiple scattering as shown in Battaglia et al. (2010)), it is limited in terms of statistical significance by the complexity of obtaining measurements that are precisely collocated in space and time. Similarly, collocation to analogous products from similar spaceborne systems (e.g. Sy et al., 2022; Turk et al., 2021) has been exploited successfully for specific purposes.

On the other hand, the bulk of validation (and tracking of any long-term trends) should be performed by assessing statistical properties of the observables on datasets as large as possible (e.g. Petersen et al., 2020). For this purpose, some relaxation on collocation (spatial and temporal) requirements, and use of long term (multi-year) measurements are preferred in order to achieve meaningful statistics (Protat et al., 2009). For example, data from US Department of Energy Atmospheric Radiation Measurement (ARM) observatories and cloud profiling stations of pan-European Aerosol, Clouds, and Trace Gases Research Infrastructure (ACTRIS) are well suited for such tasks for a mission such as EarthCARE (Eisinger et al., 2024).

It should be noted that spaceborne radars utilize relatively long point target responses (be they implemented with shorter monochromatic pulses, or longer frequency modulated pulses with pulse compression) that result in contamination of near-surface observations by ground echo, typically referred to as “surface clutter”. The surface clutter limits the ability of the spaceborne radars to observe boundary layer clouds and surface precipitation (Christensen et al., 2013; Lamer et al., 2020; Li & Moisseev, 2019; Maahn et al., 2014; Schulte et al., 2023), which have an impact on the interpretation of such geophysical products as precipitation rate, cloud fraction (Lamer et al., 2020; Maahn et al., 2014), etc. This surface clutter contamination, therefore, should be characterized as a part of the calibration/validation activities.

The vertical extent of surface clutter contamination depends on individual system characteristics and the specific nature of the surface being observed. For example, in a scanning radar such as TRMM/PR surface clutter extends only a few hundred m for the center beams (i.e., those closest to nadir) but up to more than 2 km for the most off-nadir profiles. CloudSat’s CPR was affected by clutter generally below 1.3 km because of the nature of the transmitted pulse and receiver filter (which were optimized for high cloud detection), subsequently reduced in Level 1B processing to about 700 m over ocean and flat land by adopting a Surface Clutter Rejection algorithm (Tanelli et al., 2008). EarthCARE CPR will leverage (Eisinger et al., 2024) on the CloudSat experience and is expected to have a reduced surface clutter extent in most profiles thanks to more frequent range sampling and adoption of an improved receiver filter.

In general, validation of the estimated maximum clutter height (that is, the highest sample that is contaminated by ground clutter above the threshold of sensitivity that is otherwise determined by the system noise) has been successfully performed by means of direct, collocated comparisons such as those described above to validate sensitivity (see e.g. Sy et al., 2022).

One other important aspect of spaceborne cloud and precipitation radar calibration and validation of reflectivity products pertains to the use of attenuating frequencies (that is, at Ku band and above) and the downward looking geometry. Useful interpretation of data acquired by radar systems that differ (with respect to the spaceborne radar object of the calibration and validation effort) either by frequency or viewing geometry is definitely possible, and in fact recommended. However, the sometimes subtle and sometimes drastic differences that may be engendered in the observed data by such differences must be carefully accounted for. For example, data from ground-based weather radars at C-band or below are typically associated with radically different spatial resolutions (coarser in vertical and finer horizontally, with respect to spaceborne) and path attenuation effects, while data from ground-based W-band radars are affected by significant path attenuation in the direction opposite to the spaceborne

equivalent. Useful research has been conducted exploiting these differences, but for the specific purpose of Level 1 calibration and validation, strict quality control and screening procedures are necessary to ensure that no unintended biases are folded in the assessment.

6.1.2. Level 1 Products related to Doppler capability

Level 1 products derived from any Doppler radar capability can also be divided in two stages of Level 1 processing as described for example in Eisinger et al. (2024) and Kollias et al. (2023) for the EarthCARE mission. The most fundamental Level 1 product of any Doppler cloud and precipitation radar is the mean, reflectivity weighted, Doppler velocity of the hydrometeors in the sampled volume. In general, the quantity provided by the Level 0 data corresponds to the first normalized moment of the Doppler spectrum as observed and sampled, and it is affected by a number of factors that need to be corrected, or at least mitigated, before it can be interpreted as an unbiased estimate of the desired mean Doppler velocity of the hydrometeors: aliasing, Doppler broadening or biasing introduced by the platform motion combined with the characteristics of pointing and along-track distribution of the hydrometeors within the volume (often referred to as Non-Uniform Beam Filling, NUBF bias), and spectral whitening by thermal noise or distortion by other forms of noise in the radar system are the primary ones (see e.g. Kollias et al., 2023; Sy et al., 2014; Tanelli et al., 2002 and references cited therein). A complete description of all these factors is provided in the cited references, but here it is important to note that for spaceborne radars there can be a significant difference between the values reported in the early stages of Level 1 processing vs those reported in the products at the end of Level 1 processing.

Calibration and Validation activities should be tailored to validate, separately, if possible, the effectiveness of the various corrective algorithms. For example, the CPR Doppler velocity observations depend on antenna pointing accuracy, which can be assessed using Doppler measurements in ice clouds and the Earth's surface (Battaglia & Kollias, 2015; Kobayashi et al., 2003; Tanelli et al., 2005). The climatology of ice cloud properties including the relations between the reflectivity and Doppler velocity at locations spanning from tropical to high-latitudes is needed for the Doppler velocity validation. Is the ensemble of these corrective actions sufficient to cancel out the pointing induced bias? Other examples include: is the Doppler unfolding performing as needed under the cloud or precipitation regimes of interest to a specific mission? Are the associated Quality Control flags raised accordingly? Is the overall performance of the NUBF-correction satisfactory?

Similar considerations apply to the estimation of the Doppler spectral width (i.e., the second moment of the spectrum) which is generally even more challenging from a Low Earth Orbiting platform (see Sy & Tanelli, 2023), unless the radar architecture includes features such as the Displaced Phase Center Antenna (DPCA) approach (Durden et al., 2007, 2023; Nakamura & Furukawa, 2023).

Once these factors are corrected, or at least mitigated, the accuracy and precision of the Doppler products can be addressed. At this stage, and only at this stage, along-track integration as well as along-range averaging can be applied and examined in the context of verifying compliance with the mission requirements, and accounting for the expected performance resulting from the specific mission design parameters. For example, for EarthCARE CPR, the Pulse Repetition Frequency (PRF) depends on latitude, lower PRF observations are carried out over tropics and higher PRF measurements over high-latitude

regions, the validation of whether the Doppler velocity requirement is met should be performed at different geographical regions accounting for such difference.

Validation of these products involves use of similar approaches as those listed for the backscatter power products, with the obvious distinction that the radar assets involved (be they airborne or ground based) must have Doppler capabilities, with performances that are at least comparable to (but preferably better than) the spaceborne radar being validated.

In general, Doppler products are to be validated in the context of two distinct objectives : observation of convective motions (i.e., where the objective is to estimate the vertical air velocity, and typically associated with small-scale variability, large velocities, and significant hydrometeor loading) and observation of cloud and precipitation microphysics (i.e., where the primary goal is to estimate the hydrometeor terminal velocity and the vertical air velocity is assumed to be small, typically associated with the presence of low-density frozen hydrometeors, drizzle or stratiform precipitation). These two objectives may require completely independent validation efforts, but in some cases can be combined (for example by exploiting the natural occurrence of cirrus anvils in proximity of convection).

6.2. Validation of Level 2 cloud and precipitation products

There are several sources of uncertainties affecting the retrieved products. Analysis of these sources should be part of the validation activities. The first involves challenges in accurate identification and characterization of cloud layers in complex scenes, i.e. containing multiple cloud layers. The second uncertainty arises from the fact that physical assumptions underpinning the retrievals may vary across regions, seasons, and regimes.

As described in *Chapter 2* the cloud and precipitation products can be roughly subdivided into the following main categories:

- *Macrophysics*, i.e. cloud top height and vertical profiles of cloud fraction, including phase and particle type
- *Liquid cloud properties*, which include water path and content, effective radius, extinctions and optical thickness, vertical velocity in cloud regions (which is a combination of air and sedimentation velocities)
- *Ice cloud and snowfall*, where in addition to the products listed for liquid clouds, surface snowfall rate, profiles of snow rate, and snow particle median diameter are derived
- *Rain*, this category includes rain water path and rate, median drop diameter, and sedimentation velocity

6.2.1. Macrophysical cloud products

Macrophysical cloud products, i.e. cloud top height, phase, and vertical profiles of cloud fraction and particle type, are typically derived using a multi-sensor approach, where radar and lidar observations are combined. For this reason, a well instrumented ground-based cloud profiling station employs a combination of cloud Doppler radar, lidar (or low-power automatic lidar, known as ceilometer), and microwave radiometer to gather data (Illingworth et al., 2007). Similarly, spaceborne systems, such as CloudSat and Calipso, and EarthCARE's CPR and ATLID (Eisinger et al., 2024), utilize a complementary suite of radar and lidar instruments.

Airborne lidar and radar instruments flying on high-altitude aircraft also serve as key validation tools, especially for cloud top height and vertical profiles of cloud fraction (Stephens et al., 2008; Yorks et al., 2011).

It is, however, expected that the radar/lidar synergy will not fully resolve cloud macrophysical properties in some cases, namely:

1. physical depth of liquid clouds (from space), because lidar signal is attenuated by liquid cloud droplets. For the ground-based observations this is less of a problem, where lidar observations are used for detection of cloud base and radar observations for cloud top
2. liquid water layers embedded in ice (are challenging for both ground-based and space-borne systems)
3. liquid (& liquid-topped mixed-phase) clouds below optically thick ice clouds (for space-borne observations)
4. liquid-topped mixed-phase clouds above optically thick ice clouds or above another liquid layer (for ground-based systems)
5. warm liquid clouds within cold rain (for spaceborne systems), due to attenuation of the lidar signal

As can be seen, because of the differences in observation geometry, ground-based observations are complementary to satellite cloud profiling measurements and can be used to assess validity of cloud macrophysical products in the above-listed complex scenes. It should be noted, however, that multilayer clouds are a challenge for radar/lidar observations, regardless of the platform. In optically thick systems, like deep convective clouds, also cloud radar signals can be significantly attenuated.

For the validation of spaceborn cloud macrophysical products it is recommended therefore to use radar/lidar synergetic observations. Addition of a microwave radiometer would further help to identify the presence of liquid water clouds. Multi-frequency radar observations are useful for characterizing deeper clouds, where W-band radar signals are attenuated (Tridon et al., 2020). Analysis of cloud radar Doppler spectra are useful for multi-layer mixed-phase cloud cases (Schimmel et al., 2022; Shupe et al., 2004, 2008).

The characterization of complex scenes can be enhanced by incorporating coincident active and passive microwave observations. While radar/lidar provides detailed information on the vertical structure of clouds and precipitation, multi-frequency passive microwave observations complement this by capturing information on water vapor, cloud liquid water, and ice. This information helps improve radar/lidar detection, particularly in conditions where radar sensitivity is limited, such as detecting thin or weak precipitation layers (at Ku- and Ka-bands) or deep convection (where W-band is attenuated). Additionally, passive microwave sensors offer global coverage of observations, improving the radar's ability to distinguish between phases, such as liquid versus ice/snow, by providing a broader atmospheric context.

Looking ahead, the potential use of both passive (Eriksson et al., 2020) and active (Battaglia et al., 2014b; Roy et al., 2020) sub-millimeter (sub-mm) wave observations for cloud ice presents an exciting opportunity. Passive sensors covering sub-mm frequencies, such as the Ice Cloud Imager (ICI) on Metop-SGB (Eriksson et al., 2020) and the Arctic Weather Satellite

(ESA), can enhance the identification of ice and mixed-phase clouds, improving synergies with active microwave observations. The combined passive and active retrievals will better constrain the microphysical properties of ice hydrometeors (Pfreundschuh et al., 2020), while synergies with the EARTHCARE's lidar/radar offer further opportunities to enhance supercooled liquid water detection (Camplani et al., 2024). Additionally, a radar operating at G-band (Battaglia et al., 2014b; Roy et al., 2020) will extend radar sensitivity to smaller ice particles and can also be used for profiling water vapor inside clouds by utilizing observations at the water vapor absorption line of 183 GHz (Roy et al., 2020).

6.2.1.1. Collocation considerations

Vertically pointing ground-based cloud radars in combination with microwave radiometers and lidars are a part of a standard setup for cloud and precipitation studies (Clothiaux et al., 2000; Illingworth et al., 2007). The observations from these instruments can be used to derive a time-series of vertical profiles of cloud properties. The satellite-based profilers on the other hand provide vertical observations along the ground track. The active instruments observe in narrow transects that sample only a small percentage of the area over which the cloud is present. This difference in sampling (van de Poll et al., 2006) needs to be considered when the two are compared. Additionally, because the ground track will rarely pass directly above a ground-site no direct comparison is possible. Because of that, use of long term (multi-year) measurements of e.g. cloud top/base height and the reflectivity distributions (Liu et al., 2010; Protat et al., 2009) are preferred in order to achieve meaningful statistical comparison of ground-based and spaceborn cloud observations. The statistical comparison requires use of relatively long datasets, as it is shown that short, few weeks long datasets may not be representative of an observation region (Liu et al., 2010).

Direct validation of the CloudSat and CALIOP cloud products, such as cloud top height and vertical profiles of cloud fraction has been performed by comparing the spaceborne data products to collocated airborne lidar and radar profiles. The CALIPSO-CloudSat Validation Experiment (CCVEX) took place in July and August 2006, intended to validate the newly launched CALIPSO and CloudSat satellites. An elastic backscatter lidar operating at multiple wavelengths and a W-band radar flew on the NASA ER-2 out of Warner-Robbins, Georgia to permit validation over convective clouds and cirrus anvils in the southeast United States. The airplane flew roughly 30-minute segments below the predicted ground tracks of the satellites, centered on the point of coincidence near predicted clouds. The data collected was used to validate CALIOP cloud top heights and detection frequencies (Yorks et al., 2011), as well as CloudSat reflectivity and vertical profiles of cloud fraction (Stephens et al., 2008).

6.2.1.2. Scanning radar observations

Because of relatively narrow swaths of spaceborne cloud and precipitation radars, it is difficult to obtain coinciding ground-based radar observations especially from vertically pointing cloud radars. Using scanning cloud or precipitation radars allows for a more direct comparison between ground-based and spaceborne radar observations, as demonstrated by Hudak et al., 2008.

This approach requires collecting radar volume data, which involves plan position indicator (PPI) scans taken at various elevation angles (see Fig. 6.1 for an example). Number of angles depends on the antenna beamwidth and distance to the ground track. To minimize the time

required for completing a volume scan, sector PPI scans, focusing on a limited azimuth angle in the direction of the ground track, can be utilized. Ideally, such observations should be scheduled using up-to-date orbit prediction information, such that the scans performed at the time of an overpass. See Fig. 6.2 for an example of CloudSat CPR precipitation observations collected on 10 March 2009 and corresponding derived vertical reflectivity factor profiles from University of Helsinki Kumpula radar observations. In the presented case, the Kumpula radar was performing sector PPI scans that started 1 min before the overpass and ended about 1 min after. The nearest distance to the ground track is 30.7 km. From the volume scan the radar cross section was computed using Vaisala IRIS software.

An alternative to a volume scan consisting of PPIs is a set of RHI scans (Fielding et al., 2013; Kollias et al., 2014). This approach is better suited for resolving vertical cloud system characteristics, which tend to change significantly both horizontally and vertically. Important to note, that for distances less than 5 kilometers, the required maximum elevation angle for a PPI volume would surpass 60 degrees, making the volume scan excessively time-consuming. Under these circumstances, conducting an overhead Range Height Indicator (RHI) scan, horizon-to-horizon RHI, aligned parallel to the ground track, could be a better alternative (Kollias et al., 2014).

The scanning radar observations can be used to access such products as cloud top height and phase, vertical profiles of cloud fraction and particle type. We should note, however, that there is a difference in spatial resolution. Weather radars have better horizontal resolutions and lower vertical resolution. The exact resolution values depend on distance. If the weather radar observations are used for validation of target classification products, it should be pointed out that definitions of particle types derived from ground-based radar observations and satellite remote sensors may differ. In the weather radar community hydrometeor classification based on dual-polarization radar observations is more commonly used. This classification provides such classes as rain, snow, melting snow, hail, graupel (Chandrasekar et al., 2013; Ryzhkov, Schuur, et al., 2005; Straka et al., 2000).

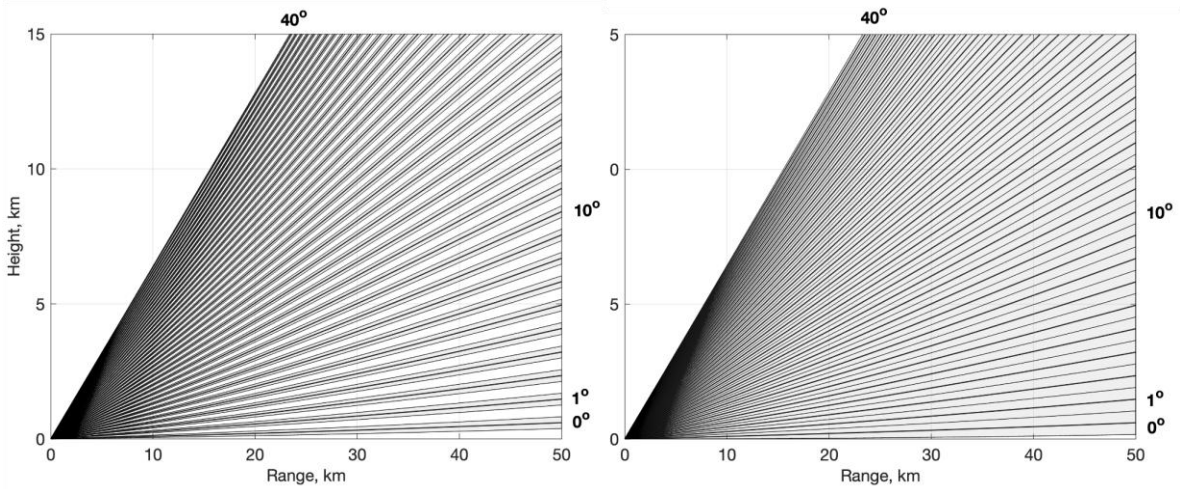

Figure 6.1. *Radar beam height as a function of range. The left panel is for the beam width of 0.5 deg (more typical for cloud radars) and the right panel is for the beam width of 1 deg (typical value for weather radars). The elevation angle changes between 0.5 and 40 deg with a step of 1 deg.*

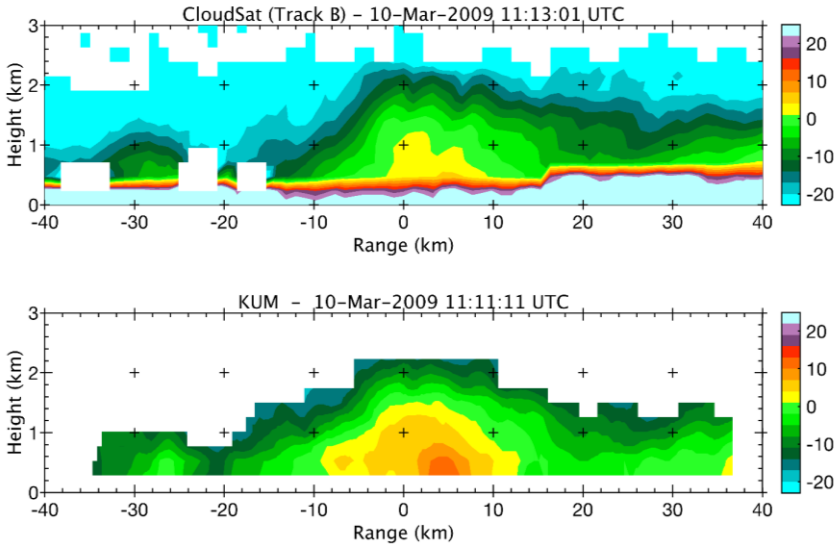

Figure 6.2. *Vertical profiles as observed by the CloudSat CPR at 1110 UTC on 10 March 2009 and corresponding reconstructed vertical profiles from University of Helsinki C-band weather radar observations. The cross section was computed using IRIS software. The distance to the nearest point on CloudSat overpass is 30.7 km.*

The Python ARM Radar Toolkit (Py-ART) (Helmus & Collis, 2016), currently supports estimations of cross sections from radar volumes along one or more azimuth angles using the pyart.util.xsect function. The Py-ART does not seem to be able to compute a cross-section along an arbitrary vector, which is needed for computing vertical profiles along an overpass.

6.2.2. Liquid cloud properties

6.2.2.1. Liquid clouds

Liquid cloud layers can cause significant radar and lidar signal attenuation. The difference in observation geometries between satellite and ground-based remote sensors results in different attenuation profiles. On one hand, this difference poses a challenge for the comparison of statistics of liquid cloud properties derived from satellite and ground-based observations. On the other hand, it allows for the evaluation of how radiatively important liquid clouds not detected by a space-borne lidar are.

Layered clouds, warm liquid clouds embedded within cold rain or liquid cloud layers embedded within ice precipitation also pose challenges. To assess what is missed by satellite observations, synergistic ground-based cloud radar and lidar observations, or profiles of liquid water content observed by aircraft can be used. Additionally, microwave observations of LWP can be used to identify occurrences of liquid water clouds even in cases where water layers are not detected by lidars.

For non-precipitating liquid clouds, LWC can be retrieved using the Frisch et al. (2002) method. If Ka and W-band radar observations are available, LWC can be retrieved using differential attenuation (Hogan et al., 2005). The advantage of the dual-wavelength method is that it does not suffer from the presence of drizzle (Hogan et al., 2005). The presence of drizzle

biases cloud radar reflectivity observations to larger drops that do not contribute significantly to cloud LWC. There are several methods that can be applied for the detection of drizzle. The most promising ones use reflectivity factor and spectra observations (Zhu et al., 2022) or skewness of Doppler radar spectra (Acquistapace et al., 2019).

6.2.2.2. Mixed- phase clouds

Identification of supercooled liquid layers embedded in ice clouds by a lidar is limited to a first layer encountered in the particular viewing geometry. Therefore, new approaches like machine learning based methods for identification of embedded supercooled liquid cloud layers (Schimmel et al., 2022) show a great promise for characterization of such liquid layers. This method is relatively new and requires testing and validation. As a first step, the methodology should be applied, trained, tested and validated at profiling stations located in different geographic locations. For the validation of the method, supporting information such as aircraft observations and collocated soundings are beneficial. Additionally, synergy between active sensors (EARTHCARE Lidar/Radar) and passive sub-mm sensors (AWS, ICI) offers further opportunities to enhance supercooled liquid water detection (Camplani et al., 2024).

6.2.3. Ice cloud and snowfall products

6.2.3.1. Validation of Physical assumptions

The ice particle size distribution is fundamentally important for describing properties of ice clouds and snowfall. It allows linking single particle properties to ice water content and snowfall rate and remote sensing variables. The observations of PSD in ice clouds are typically performed using aircraft probes (Field et al., 2005). The PSD of snowfall can be sampled using surface instrumentation, such as using different kinds of particle imagers and disdrometers (e.g. MASC (Garrett et al., 2012), VISSS (Maahn et al., 2024), PIP (Pettersen et al., 2020), 2DVD (Schönhuber et al., 2007), OSCRE (Kennedy et al., 2022), and OTT Parsivel (Löffler-Mang & Joss, 2000)). Each sensor has its own limitations and advantages, see Table 6.1.

Table 6.1. *Comparison of capabilities of ground-based precipitation instruments, MASC, 2DVD, PIP, VISSS and OSCRE, for measuring falling snow properties. This table attempts to summarize and contrast measurement capabilities*

Instrument / Observations	MASC (commercial)	2DVD (commercial)	PIP (NASA)	VISSS (open source)	OSCRE (open source)
Particle images	(+++) High-resolution images (33.5 µm)	(+) shadow images reconstructed from line-by-line obs.	(+-) Images (blurring limits recognition of details)	(+++) High-resolution images (40-60 µm)	(+++) Adaptable, tested at ~50µm, direct lighting
Particle shapes (especially 3D shape)	(+?) 3 cameras at 70 deg separation A more sophisticated analysis, however a sophisticated approach is needed (Notaroš et al., 2016; Leinonen et al., 2021)	(+) two images at 90 deg Some reconstruction is possible (see Huang and Bringi) – may be complicated by snowflake matching	(-+) Only 2D images are recorded, no 3D reconstruction. Only statistical inferences on the particle shape are possible	(+?) multiple observations from two cameras (typically 2x8 or 2x12 per particle) can be used to derive shape	(-+) Only 2D images are recorded, no 3D reconstruction. Only statistical inferences on the particle shape are possible
PSD For all instruments there is an uncertainty due to size definition	(+) small sampling volume	(+) – snowflake matching is needed, which affects sampling volume	(+?) - Good sampling volume, uncertainty due to size definition (von Lerber et al., 2017)	(++?) very well defined measurement volume, matching required	(+?), similar to PIP, next upgrade uses light to define sampling volume.
Fall velocity High winds and vertical winds if instruments are deployed next to obstacles would cause significant errors	(+-) needs wind shield. High impact of turbulence	(+) – good observations, very wind sensitive	(++) – multiple recording of an ice particles allows for good velocity reconstruction	(++?) multiple recordings (typically 2x8 or 2x12) of an ice particles allows for good velocity reconstruction. High impact of turbulence	(-) While possible at higher frame rates, currently designed to sample blowing snow events where V >> W.

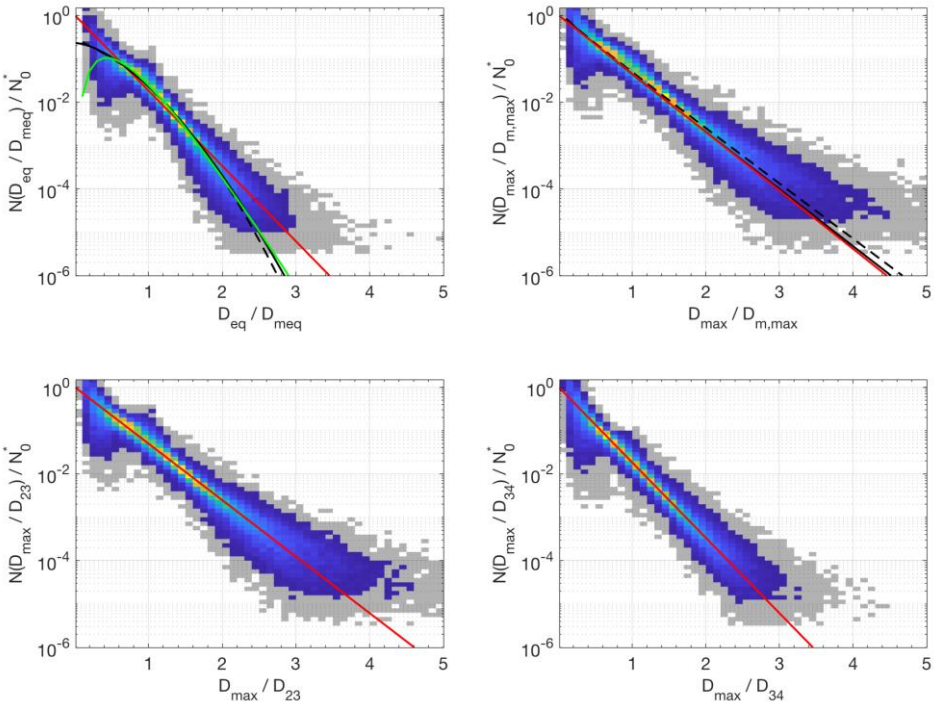

Figure 6.3. *The normalized PSD for snowfall collected during winter 2014-2020 in Hyytiälä, Finland. The top left panel shows PSD as function equivalent melted diameter, the other panels show PSD as a function of particle maximum dimension. The PSD are normalized by using N_0^* and mass weighted mean diameters (top panels), proxy for a mass weighted mean maximum diameter (D23, the ratio of 3 and 2 moments of PSD) and D34 (the ratio of fourth to third moments).*

The shape of observed PSD is often described using a gamma functional form or modified gamma (Delanoë et al., 2014; Testud et al., 2001). This approach allows us to describe PSD using three or four parameters, for gamma and modified gamma shapes respectively. To deduce if PSD converges to an average PSD representative of a cloud type, geographic location, etc., the normalized PSD representation is used (Delanoë et al., 2014; Testud et al., 2001), where observed PSD is presented as $N(D) = N_0^* F(D/D_m)$, where is N_0^* is the scaling parameter and D_m is the mass weighted mean diameter. We should point out that depending on measurement instrumentation and application, where PSD is used, the definition of particle dimension may differ. The following definitions of particle dimension are often used: maximum dimension, area (disc) equivalent diameter, volume equivalent diameter, melted equivalent particle diameter. The use of melted equivalent diameter allows for seamless description of particle properties in precipitation systems, where raindrops and snowflakes follow the same diameter definition.

The normalized PSD representation using mass weighted mean diameter for normalization or expressing PSD as a function of melted equivalent particle diameter requires knowledge of representative mass-dimensional relation or direct observations of particle masses. Because the exponent of mass-size relation is usually close to 2 (Mason et al., 2018; Szyrmer & Zawadzki, 2014), the ratio of third and second moments of PSD can often be used as a proxy for D_m.

To document variability of PSD bulk precipitation (snowfall rate and accumulation) and particle imaging measurements (PSD and particle fall velocity) at the surface in locations where

snowfall occurs should be carried out. To document PSD in ice clouds, aircraft measurements of PSD and IWC are needed.

Lidar ratio (LR). The information of the lidar ratio is an important parameter for the inversion of lidar signals in instruments that do not have Raman channel and space-borne lidars, such as CALIPSO (Cloud-Aerosol Lidar and Infrared Pathfinder Satellite Observations), that depend on a parameterisation that may vary with location. Thus, for satellite retrievals, the selected lidar ratio value can introduce errors into the retrieved extinction and optical depth values of the cirrus layers, as is illustrated by Young et al. (2018). Consequently, information provided by well-calibrated ground-based measurements is quite crucial to verifying and eventually improving the satellite retrievals. The analysis of ground based lidars (Voudouri et al., 2020) of the cirrus cloud properties in the different geographical and climatic counterparts show higher lidar ratio values moving toward the poles, with calculated values of 27±12, 26±6, and 33±7 sr for Gwal Pahari, Elandsfontein and Kuopio, respectively, also confirmed by other studies. New a priori information of the lidar ratio value for the cirrus layers, included in version 4.10 (V4) of the CALIOP data products, led to improvements of the extinction and optical depth estimates of the cirrus cloud layers. Airborne lidar systems provide another source for validating lidar ratio assumptions. Hlavka et al. (2012) used airborne lidar data taken during the CCVEX field campaign (Section 6.2.1), primarily observations of cirrus anvils in the southeast United States, to validate CALIOP lidar ratios and extinction retrievals. When targeting transparent randomly oriented ice (ROI) cloud cases for underflight opportunities, constrained techniques for estimating lidar ratio and extinction from both the airborne and spaceborne lidars provides a robust validation dataset.

Multiple scattering (MS). The influence of multiple scattering on CALIPSO light-extinction profiling in mineral dust is reported by Wandinger et al. (2010). By taking the multiple-scattering effect into account, discrepancies found between ground-based measurements of lidar ratios in pure Saharan dust cases can be explained. An effective lidar ratio of 40 sr applied in the CALIPSO retrievals accounts for the increased atmospheric transmission caused by multiple scattering and gives reasonable backscatter coefficients that compare well with ground-based observations. However, if the same value of 40 sr is applied to convert backscatter into extinction coefficients, a systematic under-estimation of extinction and optical depth by 25%–35% is introduced. This artifact can easily be overcome by applying two different look-up values for the lidar ratio of mineral dust in the CALIPSO retrieval algorithm, i.e., an effective value of 40 sr for the backscatter retrieval and a typical single-scattering value for pure mineral dust (i.e., 50 sr), for the backscatter-to-extinction conversion.

6.2.3.2. Microwave scattering properties of ice particles

To link microphysical properties of ice clouds and remote sensing observations an approach for computing scattering properties of ice particles is needed. For a long time, a so-called “soft-spheroid” particle model was used for modeling scattering from ice particles. In this model, an ice particle was approximated by a spheroid consisting of a mixture of ice and air. This approach allows use of such computationally efficient methods as Mie scattering, and T-matrix. It was found (Botta et al., 2010; Ori et al., 2014; Petty & Huang, 2010; Tyynelä et al., 2011) that for particles roughly larger than wavelength the “soft-spheroid” model results in significant underestimation of the scattering cross sections. To address this problem more realistic looking particle models (e.g. physically based crystals and aggregates, and realistic looking fractal models), see Fig. 6.4, in combination with numerical scattering methods such

as the Discrete Dipole Approximation are used (Kuo et al., 2016; Leinonen & Szyrmer, 2015; Tyynelä et al., 2011).

Figure 6.4. *Three particle models representing an ice particle with the same dimensions and mass. Left panel - aggregate. Middle panel - fractal particle. Right panel – "soft-spheroid". The figure is adopted from Tyynelä et al. (2011).*

There are a number of scattering databases that cover a variety of ice crystal habits, aggregates and rimed particles (see section 6.3). However, the Discrete Dipole Approximation (DDA) method—employed to calculate these properties—is computationally intensive. Consequently, the range of ice particle mass-size relations represented in these databases is constrained. This limitation raises concerns about the adequacy of existing datasets in capturing the full spectrum of ice particle variations required for accurate representations of global ice cloud properties.

Hogan et al. (2017) have proposed to use the Self-Similar Rayleigh–Gans Approximation (SSRGA) for rapid computation of the backscatter cross-section of ice aggregates. SSRGA allows for parametrizing particle structure and scattering properties by using just five parameters. The selection of these parameters, however, needs to be tested.

Validation of scattering properties can be performed by a variety of methods: using closure studies, a combination of in situ observations and collocated radar observations (Falconi et al., 2018; Tridon et al., 2019), using multi-frequency radar observations (Kneifel et al., 2015; Leinonen et al., 2012; Leinonen & Moisseev, 2015), multi-frequency Doppler spectra observations (Kneifel et al., 2016), and passive MW polarimetric observations (Eriksson et al. 2018, McCusker et al. 2024).

It should be noted that the existing scattering databases may not cover all the frequencies or scattering geometries, for example. Kneifel et al. (2018) have summarized the needs for future developments, namely: extending scattering datasets to make them valuable for a wider range of applications; ensuring datasets contain three-dimensional structures of particles and comprehensive metadata; developing in situ forward operators to convert three-dimensional particle models to simulated in situ observations; assessing the physical assumptions used in generating scattering datasets; deriving bulk scattering properties for global applications like numerical weather prediction models; addressing the complexity of orientation and polarimetric variables in scattering databases; including missing particle classes such as melting, oriented, rimed, and accreted ice particles; and ensuring snow particle models are representative of typical temperature and humidity conditions. Additionally, there is also a need for standards and conventions for storing complex scattering datasets, and for databases to cover a wide range of temperatures, particle sizes, and frequencies.

6.2.3.3. Surface snow intensity

The validation of the surface snowfall intensity observations can be carried by matching satellite precipitation estimates to ground-based weather radar observations (e.g. see Mróz et al., 2021; von Lerber et al., 2018). This approach is similar to the validation of rain products discussed in the next section, but there are notable differences. There are still large uncertainties of radar-based estimates of snowfall rate (SR). Typically, a climatologically tuned equivalent reflectivity factor, Ze, - snowfall rate, SR relation is used, see Fig. 6.5. It should be noted that this relation depends on wavelength. To reduce the uncertainty of the radar-based estimate, gauge adjustment can be used.

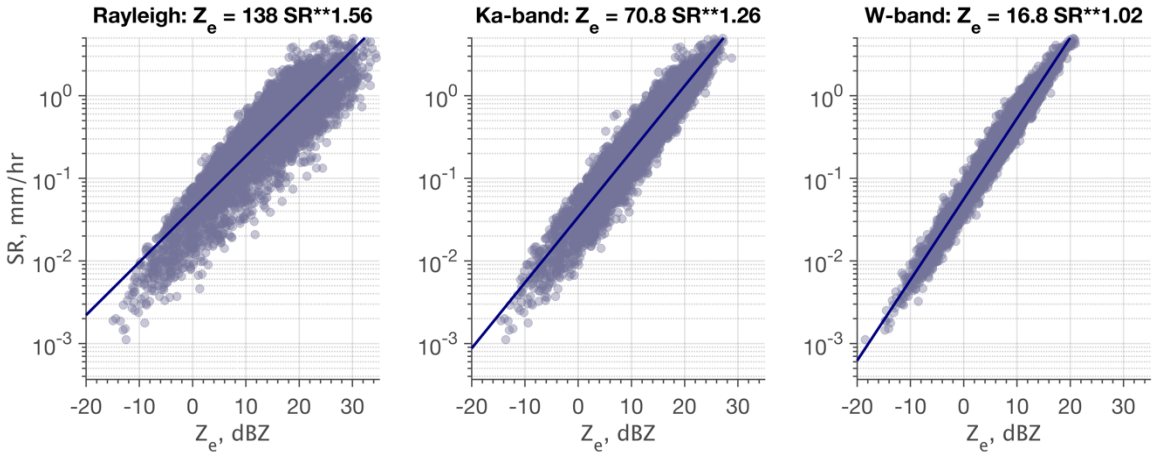

Figure 6.5. *Ze-SR relations computed using von Lerber et al. (2017) observations of m(D) and PSD. The left panel presents a relation for radar wavelengths where Rayleigh scattering assumption can be used, i.e. S and C -bands. The central panel shows the relation for Ka- and the right one for W- bands. For the last two panels datasets of single scattering ice particle properties computed by applying DDA to realistic particle shapes was used.*

What is the main factor affecting the Ze-SR relation? It was shown (Rasmussen et al., 2003; von Lerber et al., 2017, 2018) that the exponent of the relation can be assumed to be constant. The value of it depends on wavelength. The main variation in the Ze-SR comes from the prefactor (Rasmussen et al., 2003; von Lerber et al., 2017, 2018). The prefactor of the Ze-SR is mainly function of the PSD intercept parameter, N_0. The dependence on particle type and mass is secondary, at least at cm-wavelengths (von Lerber et al., 2017). As shown in Fig. 6.6 the prefactor of Ze-SR relation, a_{zs}, changes over three orders of magnitude for Z and C-bands (Rayleigh scattering bands). For higher frequencies this range decreases.

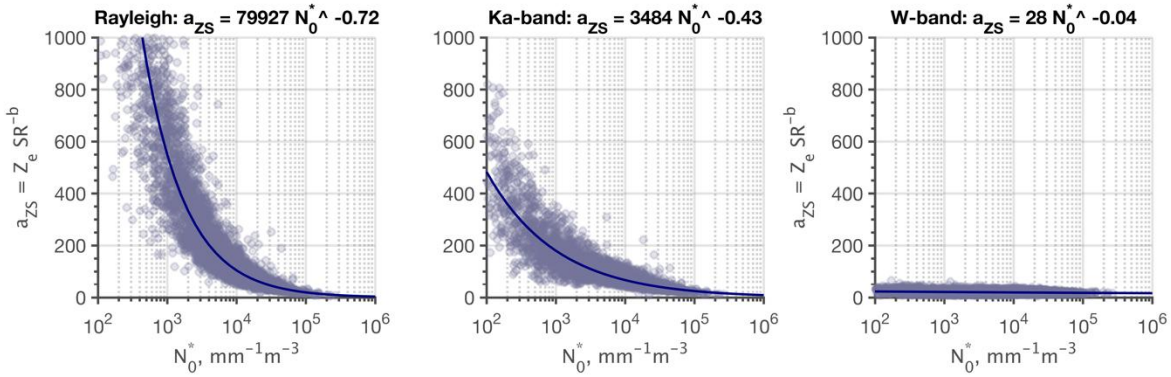

Figure 6.6 *Dependence of the prefactor, a_{zs}, of the Ze-SR relations on N_0 and wavelength. It should be noted that the range of a_{zs} variance decreases as radar frequency increases.*

Given the dependence of the Ze-SR relation on the PSD parameter N_0, the uncertainty of the radar-based snowfall rate estimate can be significantly reduced if N_0 is estimated from other observations, e.g. disdrometer observations (Schoger et al., 2021) or dual-polarization radar measurements (Bukovčić et al., 2020). The reduction in uncertainty is demonstrated in Fig. 6.7. As can be seen the largest impact of N_0 based tuning of Ze-SR is visible for larger wavelengths. At W-band, because the scattering cross sections of snowflakes are roughly proportional to their mass, the uncertainty in Ze-SR estimate mainly depends on m(D) and not on PSD.

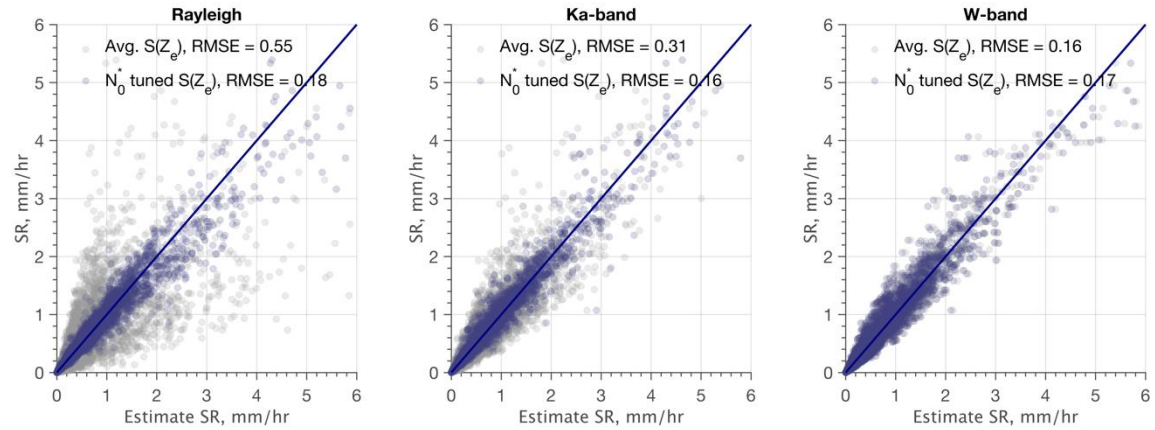

Figure 6.7. *Illustration of the impact of N_0 estimation on RMSE of SR estimate.*

Von Lerber et al. (2018) have proposed two approaches for reporting uncertainty of radar based snowfall estimates. If during the event a storm passed over a well-quiped site where PSD and m(D) observation were recorded, then for this event an event-specific Ze-SR can be computed. Furthermore, instantaneous a_{zs}, estimated every 5 min or so can be computed (von Lerber et al., 2018). The combination of the event-specific Ze-SR relation and the observed range a_{zs} values gives an estimate of the computed snowfall rate. If such observations are not available then our best estimate of the uncertainty is the climatological uncertainty of the Ze-SR relation, as for example shown in Fig. 6.5.

To summarize, for the validation of snowfall rate estimates the following is recommended. The ground-based setup should include:

- Dual-polarization weather radar (or network of such radars)
- Supported by a network of gauges, and
- Ideally one or several sites equipped with disdrometers or snowflake video imagers

The conversion from radar variable to snowfall rate products is carried out using climatologically tuned relations, or event-specific relations. The observations of PSD can be used to assess, in some cases limit, the uncertainty of such estimates.

6.2.3.4. Doppler radar products

In ice clouds vertical air velocities can be assumed to be relatively small, in such cases Doppler velocity observations are related to the hydrometeor terminal velocity. The validation of Doppler products can be approached in a statistical sense, by comparing long-term statistics of observed relations between the reflectivity and Doppler velocity in ice clouds (Kalesse & Kollias, 2013). It should be noted that both radar reflectivity factor and mean Doppler velocity (Kneifel & Moisseev, 2020) depend on the radar wavelength, so care should be taken while comparing observations at different radar frequencies.

6.2.4. Validation of rain products

6.2.4.1. Surface rain intensity and microstructure

The use of the dual-polarization radar observations for precipitation observations allows for more accurate estimates of rain intensity (e.g. Ryzhkov et al., 2022; Ryzhkov, Schuur, et al., 2005) and mass weighted mean diameter, as well as radar data quality control (e.g. Chandrasekar et al., 2013). The data quality control includes radar power calibration (see *Chapter 3*), target classification and data filtering. In addition to radar power calibration, calibration of different reflectivity is needed for precipitation retrievals and target classification. The differential reflectivity calibration can be carried out using “bird-bath” observations, extrapolation of measured Z- Z_{dr} relation in rain, and by tracking receiver calibration using Sun observation.

To derive and validate conversions from radar observations to precipitation intensity, gauge observations can be used. The other important use of gauges is the adjustment of any potential biases in radar precipitation estimates, and deriving merged radar and gauge-based precipitation estimates by using such techniques as kriging, etc. In addition to gauges, disdrometer observations of drop size distributions can be used. The advantage of using disdrometers is that they provide more detailed information on rain microstructure. These observations are used to derive relations for estimating rain intensity that are tuned to a specific geographic region, or rain type (convective or stratiform). However, if compared to gauges, there are typically fewer disdrometers available, so the validation of the retrieved weather radar precipitation products is mainly carried out by gauges (Zhang et al., 2011).

The ground-based setup for the validation of satellite-derived rain products includes:

- Dual-polarization weather radar (or network of such radars)

- Supported by a network of gauges, and
- Ideally one or several sites equipped with disdrometers

The recorded data includes:

- PPI observations of dual-polarization radar variables recorded at the time of the satellite overpass. For research radars the scan schedule can be selected to match the overpass
- Gauge observations of 10 min averaged precipitation intensity and hourly accumulations. These observations are used for verification of ground-based radar precipitation estimates and potential adjustment of these estimates

The conversion from radar variable to rain products is carried out using climatologically tuned relations, derived for example by using disdrometer observations.

6.2.4.2. Melting layer attenuation

For mm-wave profiling radar observations, the melting layer of precipitation poses a significant challenge. Because of non-negligible attenuation, the melting layer affects the retrieval of surface rain intensity from satellite-based radar observations and of ice cloud properties from ground-based observations. There are two main approaches for estimating the radar signal attenuation in the melting layer. The first, is based on modeling the propagation of radio waves through the melting layer. The second, is based on using observations to estimate melting layer attenuation.

There are several melting layer models, that somewhat differ in how changes in microphysical properties due to melting are parametrized and in how EM scattering from melting snowflakes is computed (e.g., D'Amico et al., 1998; Fabry & Szyrmer, 1999; Liao et al., 2009; Matrosov, 2008; Olson et al., 2001; Planche et al., 2014; Russchenberg & Ligthart, 1996; Skaropoulos & Russchenberg, 2003; von Lerber et al., 2015; Zhang et al., 1994). Because melting layer properties depend on the microphysical properties of snow aloft (Li et al., 2020), and as discussed in Section 6.2.3 our knowledge of ice cloud properties is still limited, there is still an uncertainty in how melting layer attenuation depends on ice microphysics. Additionally, the majority if not all models assume continuity of mass flux and size distributions (one snowflake results in one raindrop) across the melting layer. Observations of melting layer properties, however, indicate that these assumptions may not be valid in all cases (Heymsfield et al., 2015; Mróz et al., 2020). Therefore, there is a need to document:

- dependence of melting layer attenuation on snow properties aloft
- and how continuity of mass flux and size distributions across melting layer affects the attenuation

This can be done by using observations. Li & Moisseev (2019) have shown that multi-frequency radar Doppler spectra observations can be used to estimate attenuation in the melting layer. Given the proliferation of measurement sites equipped with multi-frequency radars capable of recording Doppler spectra, more exhaustive analysis covering a range of events with varying precipitation intensities and ice cloud microphysical properties should be possible. This analysis would give us a better understanding on how attenuation at Ka- and W-bands changes, and if current parameterizations are representative of the wide range of

precipitation systems. This analysis could be expanded by using data from aircraft campaigns that combine sampling of melting layer structure and multi-frequency radar observations.

6.3. Useful open-source software packages

There are several open software packages that can be beneficial for validation of cloud and precipitation observations. Majority of them is written is in Python. The list provided below is not exhaustive and we may miss some of the packages, see Heistermann et al. (2015) for the overview of the open-source software development in the weather radar community.

Python packages for analysis of radar data:

- The Python ARM Radar Toolkit (**Py-ART**) (Helmus & Collis, 2016). This Python module was originally developed to facilitate the use of DOE ARM radar data. Since them it includes a large number of useful routines to access, display and analyze radar data
- **Wradlib** is the library for processing weather radar data (Heistermann et al., 2013). This is a community-based library mainly aimed on sharing and documenting efficient algorithms for processing weather radar data

Python packages that can be used for data analysis from variety of instruments, or models:

- **CloudnetPy** is a Python package for processing cloud remote sensing data (Tukiainen et al., 2020). This package is being developed and maintained by the cloud remote sensing data center unit as part of the ACTRIS research infrastructure. It includes routines for reading ACTRIS cloud remote sensing data, from such instruments as cloud radars, lidars and microwave radiometers, and standard cloud retrieval procedures
- Meteorological Python Library for Data Analysis and Visualization (**MetPy**) provides functionality for analyzing and visualizing meteorological datasets (May et al., 2022)

Other useful software:

- **PyTmatrix** is a Python code for computing the scattering properties of homogeneous nonspherical scatterers with the T-Matrix method (Leinonen, 2014). This software is particular useful for deriving radar-based rain retrievals algorithms
- **PAMTRA** is a package that forward models microwave radiometer and full radar Doppler spectra observations of cloudy atmosphere (Mech et al., 2020)
- Collection of ice particle single scattering databases: https://snowport.meteo.uni-koeln.de/snow-scattering/scattering-databases

7. Chapter 7: Statistical validation

Plain language summary

Inter-comparisons between satellite-based remote sensing observations can provide a mechanism for characterizing the behavior of retrievals from spaceborne profiling instruments. Two classes of intercomparisons are possible: near-instantaneous comparisons and climatological comparisons. Near-instantaneous comparisons are less common due to different orbit geometry and overpass times of satellites. Climatological comparisons are more common, whereby data are averaged temporally and spatially prior to comparison. Such analyses can provide useful validation data, though they must be treated carefully to avoid misinterpreting sampling biases caused by differences in observations times and locations. Differences in retrieval algorithms and instrument characteristics must also be considered. This chapter discusses statistical validation techniques from satellite-satellite intercomparisons and highlights the challenges that must be understood to gain meaningful data for validation.

7.1. Overview

Inter-comparisons with other satellite-based remote sensing observations provide a mechanism for characterizing the behavior of retrievals from spaceborne profiling instruments that can help uncover regional systematic biases. Occultation and limb-sounding observations are particularly useful for comparing against spaceborne lidar observations in the stratosphere. In the troposphere, there are not yet satellite instruments in orbit that can be used to directly assess the accuracy of spaceborne profiling retrievals on a global scale. In many cases, passive sensor retrievals are not as accurate as lidar, for example in cloud cover, cloud ice/water phase, and other parameters (Stubenrauch et al., 2024). In the case of cloud top height, lidar and radar can make a direct measurement, whereas some passive retrievals rely on external information for height retrieval. Despite the challenges of finding accurate enough satellite observations to analyze, comparing against independent observations can still help to uncover systematic biases in profiling data, especially with large averaging.

Ideally, the observations being intercompared would observe the same location at the same time throughout their orbits, but historically this has rarely been the case. Apart from CALIPSO and CloudSat which trailed each other by seconds and the remaining A-Train members by minutes, other spaceborne profilers have sampled Earth's atmosphere in different orbits with different equatorial crossing times. Satellite-based radars such as TRMM-PR, CloudSat-CPR, and GPM-DPR had the opportunity for collocated observations, though only near where their orbits intersect. Nevertheless, statistical comparisons are a viable solution for validation, whereby observations from the instruments being intercompared are aggregated monthly, seasonally, or annually. For example, continuous intercomparisons between various cloud products from different long-term satellite data records are essential to improve our understanding of the observed cloud properties. An important question arises when differences are observed in these intercomparisons: are the differences caused by instrument performance issues, natural variability, or sampling artifacts due to lack of spatial and temporal collocation? Differences also arise from the use of distinct instruments aboard each satellite, as well as differences in retrieval algorithms, all of which needs to be accounted for. Since the aim of the guidance in this report is to assist in understanding instrument performance issues,

intercomparisons between aggregates of non-collocated measurements need to be cognizant of the impacts of natural variability and any potential sampling biases that are expected.

There are two classes of intercomparisons to consider. (1) Near-instantaneous comparisons where the two satellite-based instruments measure approximately the same location at a similar time. Spatiotemporal constraints are enforced to ensure the same airmass is sampled, with tighter constraints yielding fewer collocation opportunities. (2) Climatological comparisons where monthly, seasonal, or annual averages for the two instruments are compared over a given region without regard for which specific days are sampled or enforcing strict coincident criteria. The underlying assumption is that the climatological average from each instrument is reflective of what actually occurred in the atmosphere, so they can be compared directly with any remaining differences being reflective of instrument performance. The stringency of collocation requirement depends on whether the validation target is tropospheric aerosol, clouds, or stratospheric aerosol to account for the different autocorrelation length scales of these features.

7.2. Near-instantaneous comparisons

The most accurate approach for cross-validation between two satellite remote sensing observations requires collocation in space and time. Various criteria have been applied based on the type of remote sensors being compared (active-to-passive vs active-to-active) and the spatiotemporal variability of the atmospheric features (clouds, aerosols, precipitation etc.).

Comparing active lidar or radar measurements to passive column observations provide more near-instantaneous collocations given the wider swath of passive sensors. This enables tighter spatiotemporal constraints on the definition of collocation, minimizing the effects of sampling and natural variability of the atmospheric features. Two sensors flying in the same orbit, such as CALIOP/CALIPSO and MODIS/Aqua, further enable collocations at fine temporal and spatial scales. Kotarba (2020) collocated the centers of MODIS and CALIOP instantaneous fields of view (IFOVs) with an average spatial separation of 418 m and temporal separation of 81 s. These fine spatial and temporal scales are critical for comparing cloud and convection properties, which have autocorrelation lengths that depend on the parameter being investigated. For example, Wood and Hartmann (2006) found the spatial variability of cloud liquid water path existed primarily on horizontal scales of 10 - 50 km. Cloud ice-water phase heterogeneity also varies regionally on relatively fine scales (Sokol and Storelvmo, 2024). Kittaka et al. (2011) required each 5 km CALIOP footprint to fall within a 10 km MODIS Aqua L2 pixel, yielding 2 min temporal collocation for their AOD assessment. This criterion is sufficient to capture typical aerosol variability, because the autocorrelation length scale for tropospheric aerosol is expected to be on the order of 40 – 400 km (Anderson et al., 2003).

Near-instantaneous comparisons of two active sensors can be challenging given their narrow IFOVs compared to passive sensors. Opportunities for near-instantaneous collocation are rarer, so collocation criteria must be lessened. For aerosol intercomparisons between CATS and CALIOP which have very different orbit inclinations, Lee et al. (2019) required retrievals from each instrument to be within +/-30 min and 0.4° lat/lon. A similar time of day was sampled by both instruments due to CALIOP's fixed equatorial crossing times. In another study, Sellitto et al. (2020) noted improved consistency between observations of high clouds when CATS-CALIOP collocations were constrained to +/-3 hours. On the other hand, the ALADIN/CALIOP cloud occurrence comparisons of Feofilov et al. (2022) examined a more challenging situation.

Overflights by these satellites are separated by 4.5 hours, with ALADIN crossing the equator at dusk/dawn and CALIOP in the afternoon/night. A spatial criterion of 1° lat/lon was imposed to constrain the expected fractional standard deviation of cloud water content and the study arrived at a < 6 hour criteria to balance temporal representativeness versus number of collocation opportunities. Citing cloud observation studies, Feofilov et al. (2022) rationalize the 6-hour criteria by noting that diurnal changes in oceanic cloud distributions are expected to be small within this timeframe. The length of the temporal constraint is dependent on the diurnal variability of the atmospheric feature being compared. Precipitation over South America and Africa, as well as ice clouds over the tropics and cumulus clouds over land, vary significantly over a 6-hour period (Nesbitt et al., 2000; Noël et al., 2018).

Temporal constraints for spaceborne precipitation radar intercomparisons are typically 15-20 minutes (e.g., Casella et al., 2017; Tang et al., 2017; Chase et al., 2022). Due to the scale dependence of precipitation frequency, the spatial resolution of each instrument must be made compatible to ensure similar precipitation patterns are sampled (Behrangi et al., 2012). For example, the footprint of CloudSat-CPR was much smaller than other spaceborne radars such as TRMM-PR and GPM-DPR which required CPR data to be averaged to match the coarser resolution footprints (Tang et al., 2017). In a comparison of rain fraction between CPR and five other spaceborne instruments, Behrangi et al., 2012 determined a relationship between number of CPR footprints required to achieve identical rain fraction in a coarser resolution footprint as a means to ensure compatible sampling with the other instruments.

Useful metrics for near-instantaneous comparisons of profiling retrievals are the mean relative bias and the de-biased standard deviation which characterizes the relative precision between the instruments (von Clarmann, 2006; Wang et al., 2020):

$$\bar{b}(z) = 100 \times \frac{1}{n(z)} \sum_{i=1}^{n(z)} \frac{x_i(z) - x_{i,ref}(z)}{x_{i,ref}(z)}$$

$$\sigma(z) = \sqrt{\frac{1}{(n(z)-1)} \sum_{i=1}^{n(z)} \left(b_i(z) - \bar{b}(z)\right)^2}$$

7.3. Climatological comparisons

Intercomparisons of climatological averages can be an effective method to elucidate systematic biases while reducing the effects of random variability (Hegglin et al., 2021). If the atmosphere is randomly sampled by both instruments and artifacts are removed, then any bias can be diagnosed by the difference between their averages: $\bar{b}(z) = \bar{x}(z) - \bar{x}_{ref}(z)$, where $\bar{x}_{ref}$ is the reference measurement (von Clarmann, 2006). On the other hand, climatological averages risk masking instrument performance issues or introducing artificial biases if sampling is not handled carefully. Because patterns of cloudiness and aerosol occurrence vary regionally, it is important that intercomparisons sample the same regions as much as practical to ensure random sampling of similar populations. In the case of background stratospheric aerosol observations, similar latitude bands can be a good enough constraint as aerosol in the stratosphere tends to become homogeneously distributed around the planet over time. This is not always the case in the weeks following major volcanic aerosol or wildfire smoke injections where the aerosol mass steadily circumnavigates across longitudes and

disperses across latitudes (e.g. Khaykin et al., 2020). The higher amount of heterogeneity in the troposphere typically necessitates regional analyses versus zonal means.

A typical strategy for spaceborne climatological intercomparisons is to average each set of observations on an equal-angle latitude-longitude grid over a monthly or seasonal time period and then compare the averages. This is a level 3-style comparison. Several aspects of the sampling process that impact these level 3 averages can complicate intercomparisons. The latitude-longitude grid size should be selected such that the spatial correlation scale of the quantity being aggregated fits within the grid. This size can be larger for tropospheric aerosol compared to clouds because the scales of variability are smaller relative to aerosol (McComiskey and Feingold, 2012); e.g., mineral dust plumes in the Saharan air layer span hundreds of kilometers, whereas variability within a field of trade wind cumuli occurs at shorter lengths. It is also important that identical aggregation methods are used for climatological intercomparisons. Derived mean AOD is highly dependent on the choice of aggregation method and weightings in level 3 products, causing differences of 30% depending on the distribution of aerosol sampled, cloud coverage, and other factors (Levy et al., 2009). Using a consistent averaging method minimizes the chance of apparent biases between climatological averages.

A best practice for level 3 comparisons is to avoid aggregating over space-time intervals that are too small because sampling biases (i.e., representivity errors) can dominate the total uncertainty. The potential for sampling biases in level 3 averages is more likely with spaceborne profiling instruments relative to passive imagers because the instantaneous ground field of view is much smaller. Consequently, only a small area within each lat-lon grid cell is sampled by a series of transects. For observations from polar-orbiting platforms, the density of observations is greatest for grid cells at high latitudes where multiple days are sampled over a month, whereas the density is least near the equator and only a few days are sampled. This has implications on comparing the apparent state of the atmosphere between spaceborne profiles with different repeat cycles causing dissimilar days of the month to be sampled. In regions where aerosol events are episodic, non-daily sampling tends to yield AOD averages that are lower estimates (Sayer et al., 2010). According to Kotarba (2022b), because lidars do not sample a given lat-lon grid daily, it can take 10 years of lidar cloud amount measurements to approach what would have been observed with a 1-day revisit time, assuming a 16-day repeat cycle and a 10° lat-lon grid. Nonetheless, the authors conclude that the sampling errors introduced in cloud climatologies due to repeat cycle differences are similar for currently operating spaceborne lidars.

The size of lat-lon grid cells also impacts the ability to represent the true state of the atmosphere. In a study on the impact of transect sampling on cloud climatology, Kotarba (2022a) demonstrated that errors decrease in gridded cloud amount, cloud optical thickness, and cloud top height as the choice of grid size increases from 1° to 5° for annual averages. At the same time, the underestimate in cloud amount increases. It is therefore critical to use consistent grid sizes when intercomparing climatological averages between instruments to avoid artificial biases due to sampling.

The standard metric for climatological intercomparisons is the standard error on the mean (SEM) which assumes random sampling from the same population. It is most useful when random measurement errors are larger than natural variability, as is the case for passive imagers that can thoroughly sample a given lat-lon grid cell. However, when the sampled

observations are sparse, as is the case with monthly lidar transects through a small grid cell, the SEM can under or overestimate the actual uncertainty relative to the mean (Toohey and von Clarmann, 2013). Based on these sample biases inherent to transect sampling with spaceborne lidars, gridded intercomparisons between such instruments should adopt confidence intervals as metrics for assessment rather than (or in addition to) simple means, medians or SEM analyses (Kotarba, 2022b; Kotarba & Solecki, 2021). Comparing probability density functions is an even better assessment method (e.g. Winker et al., 2024).

Global averages alone are not well suited for rigorous intercomparisons seeking to quantify instrument performance. Sampling biases can vary regionally, and the efficacy of capturing natural variability (which also varies regionally) might not be the same between each instrument (Kahn et al., 2011). As a result, compensating biases can hide instrument performance issues in the average making interpreting such intercomparisons difficult or misleading. Different types of retrieval errors are found in different cloud types and may be of either sign, exacerbating the difficulty of interpreting global averages. At a minimum, comparisons of globally averaged gridded quantities should apply an inverse cosine (latitude) weighting to avoid over-emphasizing contributions near the poles due to denser sampling. Globally-averaged intercomparisons should be supported by a regional analysis to diagnose differences in regional sampling biases between the instruments or aggregation strategy. Analyzing at regional scales helps to isolate particular cloud regimes or dominant aerosol types, though with the possibility of yielding insufficient observations to be statistically significant. Zonally-averaged statistics within distinct longitude bands that are segregated by altitude can also be useful for profiling intercomparisons. Intercomparisons of precipitation rates observed by spaceborne radar benefit when stratified by rainfall regime to help bound natural variability and reveal instrument biases (Berg et al., 2009). It is also important to stratify by rain-rate regime when the instruments being compared have dissimilar sensitivities to precipitation intensity.

Differences in the time of day sampled for spaceborne intercomparisons can lead to apparent biases that are an expected consequence of diurnal variability. Convection over land is often greatest in the late afternoon relative to that observed in the morning hours, leading to higher cloud top observations and more precipitation (Nesbitt et al., 2000; Noël et al., 2018). Similarly, smoke plume injection heights are greater in the late afternoon when wildfires are most active (Nowottnick et al., 2022). For tropospheric aerosol and cloud analyses, it is important to either (1) constrain the overpass times for satellite intercomparisons to sample comparable portions of the diurnal cycle in order minimize biases due to natural temporal variability, or (2) acknowledge the influence of this variability as a source of uncertainty in the intercomparison interpretation. As an example, the CATS/CALIOP climatological comparison of Asian mineral dust by Ren et al. (2023) restricted observations to the hours containing the CALIPSO equatorial crossing time to match the time of day sampled. Stratospheric aerosol intercomparisons are expected to be impacted less by differences in sampling time due to a lack of diurnal variability.

Intercomparisons of stratospheric aerosol is a simpler task for climatological averages compared to the troposphere due to its lesser heterogeneity and fewer expected types of particulates. Several intercomparisons of the vertical structure of stratospheric aerosol exist in the literature that evaluate solar occultation and limb profiling observations against spaceborne lidar measurements (e.g. Kar et al., 2019; Rieger et al., 2019; Taha et al., 2021). Typically, the intercomparison approach involves comparing monthly averages from each

instrument, zonally averaged onto 5° – 10° latitude grids and averaged or interpolated upon a common altitude grid. In general, averages being compared should cover the same time-frame for as long as possible; in the realm of stratospheric trace gasses, 4 – 5 years is advisable (Hegglin et al., 2021).

The multi-instrument mean (MIM) relative difference is a useful comparison metric for stratospheric aerosol, computed as the percent difference of one instrument relative to the mean of the instruments being compared:

$$\Delta\bar{x} = 100 \times \frac{\bar{x} - \bar{x}_{MIM}}{\bar{x}_{MIM}}$$

This metric is preferable to a traditional relative difference when assessing the consistency between two retrievals with comparable uncertainty so that neither instrument is favored, though unphysical behavior or sampling biases in one instrument can impact its value (Hegglin et al., 2021). Additional metrics in Table 7.1 provide valuable insights in climatological intercomparisons.

Table 7.1. Common metrics for validating satellite data records. Adapted from the ESA Cloud Climate Initiative Product Validation and Intercomparison Report (ESA, 2020).

Metric	Description
Bias	Mean difference between used and reference dataset. See also Table 1.1.
bc-RMSE	Bias corrected root mean squared error quantifying the precision of the dataset of interest and the reference dataset.
Stability	The variation of the bias over a multi-annual time period, computed against a reference “truth” trend. Can only be computed to within the accuracy of the “truth” trend.
POD	Probability of Detection. The fraction of correct reports of a particular category of the dataset, relative to all reference reports of this category.
PDF	Probability density function (frequency distribution or histogram)
FAR	False Alarm Rate. The fraction of incorrect reports of a particular category of the dataset relative to all reports of this category for the same dataset.
Hit Rate	The total fraction of all correct reports of the dataset, relative to all reference reports.
KSS	Hanssen-Kuipers Skill Score. The correct reports of the dataset, with random correct and unbiased reports subtracted from those.

7.4. Quantities to be compared

Extensive intercomparisons have been conducted between the most commonly used satellite data records. Tables 7.2 and 7.3 list the most common satellite records and observables that have been historically used for satellite-to-satellite intercomparison studies. A more

comprehensive list of satellite-based instruments and their observables is given in Table 3.12. Most tropospheric aerosol studies compare column-integrated AOD to collocated MODIS observations (e.g. Kim et al., 2014; Liu et al., 2018; Ma et al., 2013; Redemann et al., 2012). Stratospheric aerosol intercomparisons rely on aerosol extinction or scattering ratio measurements provided by limb profiling instruments (e.g. Kar et al., 2019; Kovilakam et al., 2023). Cloud intercomparisons involve various observables including top heights/pressures, cloud fraction, thermodynamic phase, ice water path, and ice water content. These studies used collocated CloudSat and MODIS observations (e.g. Chan and Comiso, 2011; Schulte et al., 2023) as well as long-duration satellite climate data records (Karlsson and Devasthale, 2018) to evaluate the CLARA-A2, ESA Cloud CCI V3, ISCCP-H, and PATMOS-x records). Cloud observations were also compared against several well-validated datasets under the Product Validation and Intercomparison Report of the ESA Cloud Climate Change Initiative project. Snowfall and precipitation intercomparisons have been conducted between the GPM-DRP and CloudSat (e.g. Casella et al., 2017).

Table 7.2. *List of satellite datasets for intercomparisons.*

Satellite dataset	Description	Orbit	Comparison type
ADM-Aeolus	Active Doppler lidar measurements	Polar	Aerosol, cloud
CALIPSO-CALIOP	Active lidar measurements	Polar	Aerosol, cloud
ISS-CATS	Active lidar measurements	Inclined	Aerosol, cloud
MODIS Collection 6.1	Visible and infrared radiance measurements, optical depth, microphysical properties.	Polar	Aerosol, cloud
GCOM-C/SGLI	Visible and infrared radiance measurements.	Polar	Aerosol, cloud
SAGE III/ISS	Solar, lunar occultation measurements	Inclined	Stratospheric aerosol
OMPS-LP	Limb scattering measurements	Polar	Stratospheric aerosol
GOMOS	Stellar occultation measurements	Polar	Stratospheric aerosol
OSIRIS	Limb scattering measurements	Polar	Stratospheric aerosol
AMSR-E LWP	Passive microwave observations of liquid water path over ocean	Polar	Cloud
CLARA-A3	Visible and infrared Advanced Very High Resolution Radiometer (AVHRR) observations	Polar	Cloud
Cloud_cci V3	AVHRR, ATSR2, AATSR observations	Polar	Cloud
CLAAS-3	SEVIRI observations from MSG satellites	Geostationary	Cloud
EUMETSAT OCA CDR	SEVIRI observations from MSG satellites, climate data record (CDR)	Geostationary	Cloud
DARDAR	Active lidar/radar observations of ice water path	Polar	Cloud
CloudSat 2C-ICE	Active lidar/radar observations of ice water content	Polar	Cloud
GOES-ABI	Visible and infrared observations	Geostationary	Cloud
Himawari	Visible and infrared observations	Geostationary	Cloud

ISCCP-H	Visible and infrared observations from both geostationary and polar-orbiting satellites	Polar and geostationary	Cloud
PATMOS-x	Visible and infrared AVHRR observations	Polar	Cloud
GPM DPR	Rain and rainfall rate	Inclined	Precipitation

Table 7.3. *Common satellite observables for intercomparison studies.*

Product	**Description**	**Comparison type**
Extinction coefficient	Vertical profile	Aerosol
Backscatter coefficient	Vertical profile	Aerosol
Backscatter scattering ratio	Ratio of particulate + molecular backscatter to molecular backscatter	Aerosol
Aerosol optical depth	Vertically integrated extinction	Aerosol
Aerosol layer top height	Geometric top of aerosol layer	Aerosol
Fractional Cloud Cover	Cloud fractional coverage derived from CMA. Usually also separated to low, mid-level, and high clouds as defined by the ISCCP classification (Rossow and Schiffer, 1999).	Cloud
Cloud Mask	Binary cloud mask per pixel.	Cloud
Cloud Optical Thickness	Vertical integral of the absorption coefficient and the scattering coefficient.	Cloud
Cloud Phase	Thermodynamic phase of the observed cloud.	Cloud
Cloud Top Temperature	Retrieved temperature at the top of the observed cloud.	Cloud
Cloud Top Pressure	Retrieved atmospheric pressure at the top of the observed cloud.	Cloud
Cloud Top Height	Retrieved height of the top of the observed cloud.	Cloud
Joint Cloud property Histogram	Spatially resolved 2D histogram of COT and CTP for each grid cell.	Cloud
Ice Water Path	Vertically integrated ice water content for the observed cloud layers.	Cloud
Liquid Water Path	Vertically integrated liquid water content for the observed cloud layers.	Cloud
Ice water content	Range-resolved ice water content.	Cloud
Cloud water content	Range resolved cloud water content.	Cloud
Rain rate	Range-resolved snowfall rate.	Precipitation
Snowfall rate	Range-resolved snowfall rate.	Precipitation

7.5. Summary

Satellite-to-satellite intercomparisons provide useful diagnostic information to assess the performance of spaceborne profiling instruments and their geophysical retrievals. Differences in sampling due to orbital geometry, field of view, and equatorial crossing time make such intercomparisons challenging. This chapter highlighted the primary contributors to sampling biases and the methods developed by researchers to understand and mitigate these issues. The most direct intercomparisons are near-instantaneous in space and time. Co-location constraints should consider particulate type and its autocorrelation length scale to ensure similar airmasses are sampled. Most often, adequate sampling is the greatest challenge for near-instantaneous intercomparisons. Climatological, level-3 style intercomparisons offer the potential to identify systematic biases in spaceborne profiling retrievals. Regional intercomparisons aggregated over large enough time scales to observe similar atmospheric states are recommended to avoid sampling biases that would complicate the ability to discern retrieval performance. Differences in repeat cycles can necessitate long duration averaging for meaningful lidar climatological intercomparisons. Several useful metrics were introduced. Probability distributions and confidence intervals are recommended as valuable climatological intercomparison analysis tools. Global averages alone are not recommended to assess instrument performance due to the potential for regional variability masking systematic instrument biases. A host of current and past satellite-based instruments have served in validating spaceborne profiler retrievals. Despite the practical challenges of statistical intercomparisons, methods such as these will continue to be important contributors to validating the spaceborne profiling instruments of the future.

8. Chapter 8: Near-real time validation through monitoring in an NWP data assimilation system

8.1. Overview of the Chapter

The traditional approach to validation of satellite measurements is to correlate observations from similar instruments, either from the ground, from aircraft or from other space-borne sensors (cross-validation). However, this technique often requires a lot of time to be effective; for example, individual ground sites may only achieve one or two useful overpasses per month, or the representativity error of in-situ observations can be significant. In this section, we will discuss an alternative approach that uses numerical weather prediction (NWP) model or atmospheric composition model data assimilation systems to validate new sensors. Instead of cross-validating with other sensors, observations are monitored against simulated observations from within an NWP or atmospheric composition model's forecast generated within their assimilation systems.

Data assimilation systems produce atmospheric model analyses — a best-estimate of the current state of the atmosphere — by combining millions of observations from across the globe with a previous model forecast. The more the analysis is constrained by a diverse set of observations, the closer the analysis is to the truth and therefore the more powerful a monitoring system is likely to be for validation. Since NWP analyses now incorporate a wealth of observations related to clouds (e.g. Geer et al., 2017) NWP-based monitoring leverages indirect comparisons against all these observations. For observations related to aerosols, atmospheric composition model analyses can be used. Monitoring against simulated observations from models has a number of additional advantages: for example, comparisons can be made at any point in time or space, and the model analyses are created frequently, so observations can be monitored in near-real time. By comparing observations collected over a long time period and over many geographic regions, the sampling noise in any individual observation is significantly reduced allowing the rapid detection of systematic instrument issues.

The monitoring of observational data against a numerical model's output is also a fundamental step of quality control before performing data assimilation since it helps identify problems with observations and/or the model. It also provides a template to understand and to exploit the new observations in an optimal way, before they become fully active in the analysis system. A data monitoring system also gives feedback to instrument mentors on potential measurement issues in a timely manner. As we will show, coupling observational information with model information allows for the quicker detection of errors than using observational information alone.

8.2. Key considerations for monitoring observational data against model data

8.2.1. Atmospheric model analysis or re-analysis

An NWP model analysis' primary function is to provide an estimate of the atmospheric state to use as the initial conditions for generating a weather forecast. Similar to an NWP model, an atmospheric composition model provides a weather forecast, but simultaneously produces a

composition forecast. Either way, analyses from these models are produced by combining observations of the atmospheric state with a previous forecast using a data assimilation system. Observations are compared with a set of simulated observations derived from the previous forecast (a departure) via an observation simulator, and, if a difference is found, the model analysis is pulled towards the observations. The amount the analysis is pulled towards an individual observation depends on the expected error of both the observation and model background, and the magnitude of the departure.

Before assimilation, all observations enter a monitoring system which performs a series of statistical checks to assess the quality of the data. New observations will typically be monitored for several months before being assimilated operationally. Alternatively, new observations can be compared to reanalysis data. Reanalysis offer a higher quality analysis of the atmospheric state, but are run several days behind real-time to allow a greater number of observations to be included in the assimilation system. For example, the ERA5 reanalysis (Hersbach et al., 2020), uses re-processed observations, and observations that were not available in near-real time, to generate analyses that are better-constrained and generally closer to the truth than the analyses issued from operational weather forecasting. On the other hand, reanalysis data are usually at lower resolution and this could compromise the accuracy of the simulated observations compared to NRT high-res operational analyses.

8.2.2. Observation simulators

The primary requirement for monitoring observations against model data is a simulator to convert model variables to model equivalent observations. Note that the terminology varies according to the application, for example in retrievals, the simulators are known as ‘forward models’, while in data assimilation they are known as ‘observation operators’. Their complexity also varies according to the application, as compromises need to be made between precision and computational cost/speed. However, all simulators of active profiling observations share similar characteristics. Firstly, model hydrometeor or aerosol amounts must be converted to bulk optical (scattering and absorption) properties at the measurement wavelength, often via an off-line look-up table because calculation of scattering properties is computationally very demanding. Typically, single scattering optical properties are integrated over a chosen particle size distribution (PSD). These bulk optical properties are then passed, along with other atmospheric properties such as temperature and water vapor, to a scattering model or a radiative transfer model that simulates the active measurements.

One challenge in the simulation of observations from model data lies in the approximations that must be made in the observation simulator. For example, any given PSD may provide a reasonable approximation to the true PSD in some circumstances, but is unlikely to be realistic in all cases. In addition, desert dust or ice hydrometeor properties are notoriously difficult to constrain, and the need to choose one particular shape to describe a diverse set of hydrometeors or aerosol particles in a variety of different cloud/aerosol systems undoubtably introduces uncertainty into the observation monitoring and assimilation process.

Nonetheless, significant progress in simulating radar and lidar observations has been made, particularly since the launch of CloudSat and CALIPSO. In preparation for the monitoring and assimilation of EarthCARE data, a cloud radar and lidar simulator has been included in the ECMWF Integrated Forecast System (IFS). The simulator uses a triple-column approach to represent sub-grid condensate variability (Fielding & Janisková, 2022) coupled with the Liu

(2008) and Yang et al. (2000) ice optical properties databases, while choosing microphysical assumptions to be as consistent as possible with the IFS NWP model (see Fielding & Janisková, 2020 for full details). Likewise, aerosol backscatter and extinction operators have been included in the IFS composition configuration (IFS-COMPO) and have been used to model observations from CALIPSO initially and more recently from Aeolus. The simulator uses a look-up table of aerosol optical properties and the speciated aerosol concentrations predicted by the IFS-COMPO used operationally by the Copernicus Atmosphere Monitoring Service (CAMS) for the global aerosol forecasts.

The active sensor module developed for the Community Radiative Transfer Model (CRTM) offers the ability to simulate radar reflectivity across various instruments and zenith angles, given the availability of specific CRTM coefficients tailored to each instrument (Moradi et al., 2023). This simulator incorporates a comprehensive scattering database created through the discrete dipole approximation method, encompassing 19 distinct forms for both frozen and liquid hydrometeors (Eriksson et al., 2018; Moradi et al., 2022). Rigorous validation of the CRTM active module has been performed using CloudSat's observations at 94 GHz. Figure 1 shows an example of simulated versus observed CloudSat reflectivities for a tropical cyclone where the CloudSat passed over the eye of a tropical cyclone. This study employed cloud liquid, rain, and cloud ice water content profiles from the CloudSat level 2B-CWC-RVOD dataset, derived using an algorithm based on CloudSat radar reflectivity and Aqua MODIS cloud optical depth. Snow water content was obtained from the 2C-SNOW-PROFILE dataset, while graupel was likely included within the ice water content. ERA-Interim atmospheric profiles were used for radiative transfer simulations, as they are validated and accurate for gas attenuation calculations. Hail scattering was not considered due to the lack of hail water content data (the readers are referred to Moradi et al. (2023) for the details). The CRTM active sensor module is currently being integrated into the Joint Effort for Data assimilation Integration (JEDI) framework for radar observation assimilation into NOAA and NASA models.

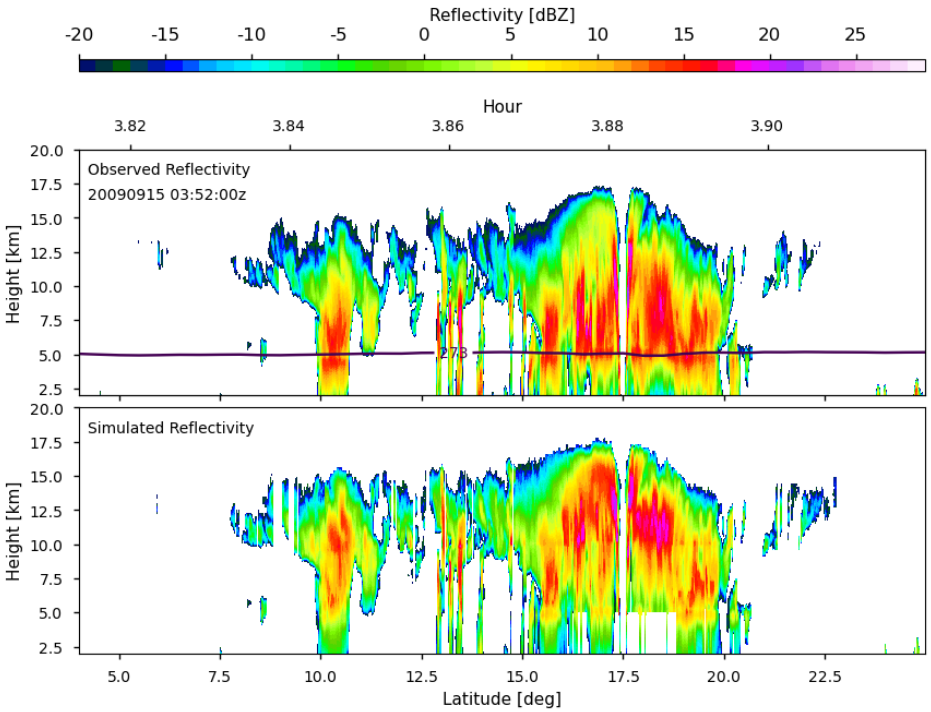

Figure 8.1. *Simulated versus observed CloudSat reflectivities.*

JMA uses different observation simulators for data assimilation and model validation. In the DPR assimilation, the observation operator is simplified and does not compute attenuation because it uses an attenuation-corrected reflectivity observation. In addition, since the DPR assimilation is limited to the liquid phase, a look-up table for Mie scattering is used (Ikuta et al., 2021). In the model validation, the observation operator uses SCATDB (Liu, 2008) assuming that solid precipitation is a non-spherical particle, and attenuation is also computed (Ikuta et al., 2021).

8.2.3. Data assimilation system

Data assimilation systems contain many tools that can be leveraged for observation monitoring. So, although not strictly necessary, monitoring observations 'on-line' through a data assimilation system has many advantages.

Screening:

Firstly, observations undergo quality control and screening to ensure that both observations and model equivalents are of suitable quality to be assimilated. For monitoring, this screening is relaxed so that observation issues can be detected, but it is important that any known issues are removed. For example, when assimilating CloudSat radar reflectivity, Janisková & Fielding (2020) screen profiles where multiple scattering is suspected because their radar simulator assumes only single scattering. The screening therefore removes situations where the model may be systematically biased compared with the observations.

Bias correction:

Data assimilation systems assume that all observations are unbiased with respect to the simulated observations. In practice, any comparison between observations and models contains some amount of systematic bias, either from the observations or the model, so the bias is mitigated with a bias correction scheme. Bias correction schemes can either be adaptive (e.g., VarBC,) or climatological. Bias correction can help with monitoring new observations by removing model biases, and also by enabling bias-free observations to be compared with the new observations.

Observation errors:

Fundamental to data assimilation, observation errors help control the weight of individual observations compared to the model background by specifying the amount of random error expected in the difference between the observations and the model. When observations are only monitored and not assimilated, these observation errors can still be leveraged to apply statistical significance tests to bias estimates or the setting and triggering of data quality alarms. Taking an 'error inventory' approach, Janisková & Fielding (2020) separate the observation error into three components: measurement error, observation operator error, and sampling error. For profiling observations with a narrow swath, sampling error typically dominates (Fielding & Stiller, 2019). Observation operator error also contains a significant contribution to the total random error, mostly from microphysical uncertainties. Alternatively, statistical relationships between the model variables and observations can be (e.g. Desroziers et al., 2005).

8.3. Principles of data quality monitoring using data assimilation

8.3.1. Description of monitoring using data assimilation

The purpose of the monitoring is to provide detailed statistical information on the quality and availability of the different components of the observing system. The monitoring results are primarily produced to help improve the usage of observations within the data assimilation systems.

Using an automatic data checking system, the production of alarm messages is triggered if an anomaly is detected in the quality or the availability of the data assimilated by the model. Two kinds of ranges are usually used by the automatic checking: 'soft' and 'hard' limits. Soft limits are updated automatically based on the statistics of the measurements in the past 20 days. Hard limits are set manually and can be adjusted as needed. A severity level is also assigned to each alert depending on the magnitude of the anomaly.

Statistical 'indicators', whose ranges are monitored, are chosen to represent different aspects of an observation. In a monitoring system these indicators can be typically, but not exclusively, one of the following:

- mean first guess departures (i.e. difference between observations and model equivalent)
- standard deviation of first guess departures
- average analysis increment
- standard deviation of analysis increments
- number of observations

These indicators can also be subset by height or geolocation.

Before observations are included in the automatic monitoring system, we must first define hard limits for each indicator that will be used. One way to do this is by examining a climatology of the data (assumed to be free of any errors) and setting the limits using some threshold in the standard deviation.

8.3.2. Statistical basis of validation through monitoring

The detection of a sudden change in calibration:

If the correlation between the observations and simulated observations is sufficiently strong, then monitoring the mean of first guess departures is a powerful method to detect changes in instrument calibration. To understand the importance of this correlation between observations the following conceptual model provides a theoretical basis.

We first assume that our profiling instrument takes unbiased samples, y_t, from a 'true' global distribution of clouds or aerosols, Y_t, drawn from a gaussian distribution with mean $\bar{y}_t$ and standard deviation σ_t, where σ_t can be interpreted as the natural variability of clouds and precipitation or aerosol particles. Now suppose after some time during its mission, the

instrument develops a fault that induces a systematic bias. If we define this systematic bias as ε_o, we can define each sample, y_o, as:

$$y_o = Y_t + \varepsilon_0,$$

such that the calibration error can be computed as

$$\varepsilon_o = \bar{y}_o - \bar{y}_t.$$

Assuming the global mean, $\bar{y}_t$, has been found through a period of monitoring before the fault developed (i.e. where ε_o =0), then the standard error in the estimate of the calibration error is the same as the standard error of the observation:

$$\Delta y_o = \Delta \varepsilon_o = \frac{\sigma_0}{\sqrt{n}},$$

where n is the number of independent samples drawn from Y_t. Finally, the number of samples required to detect a calibration error, with a probability greater than P_d, can be found by combining eq. 5 with the complementary error function:

$$P_d = 1 - erfc\left(\frac{n\varepsilon_0 - \sqrt{n}\sigma_o}{\sqrt{2}\sigma_o}\right)$$

In the case of monitoring against an NWP or atmospheric composition analysis, we can say that the model also makes observations, but from a 'model world' global distribution of clouds, Y_b, drawn from a gaussian with mean $\bar{y}_b$ and standard deviation, σ_b , where Y_b are correlated with Y_o. Monitoring first-guess departures therefore gives:

$$y_o - y_b = Y_o - Y_b + \varepsilon_o.$$

Again, assuming the global mean is known, the standard error in the mean of first-guess departures is:

$$\Delta \varepsilon_{o-b} = \sqrt{\frac{\sigma_o^2 + \sigma_b^2 - 2\rho\sigma_o\sigma_b}{n}},$$

where ρ is the correlation between the 'random' variables Y_o and Y_b. Assuming a similar magnitude for σ_o and σ_b, then we can see that $\Delta \varepsilon_{o-b}$ is less than $\Delta \varepsilon_0$when the correlation between simulated and real observations is greater than 0.5. This tells us that monitoring first guess departures to detect a change in calibration will require less samples than monitoring observations alone, hence an instrument error would be detected faster. Note if the correlation between model and observations is perfect then the change in calibration is known from one observation. However, if the correlation is less than 0.5, the additional noise from the model makes it harder to detect a calibration change. As an example, the model correlation with cloud radar reflectivity is around 0.7 so the number of samples required to detect a change in calibration is approximately 4 % less.

Detection of drifts in calibration

To understand the skill of the monitoring system to detect a problem in the quality of observations, experiments with artificially degraded CloudSat data are performed.

Experiments are performed for the period of two months where the CloudSat radar calibration is assumed to drift after day 10. The drift is set to a 1% decrease per day, which leads to a total bias of 3 dB after two months. We compare the monitoring of stand-alone observations to the monitoring of observation and model related variables to investigate whether there are any advantages in considering FG departures compared to using CloudSat observations alone.

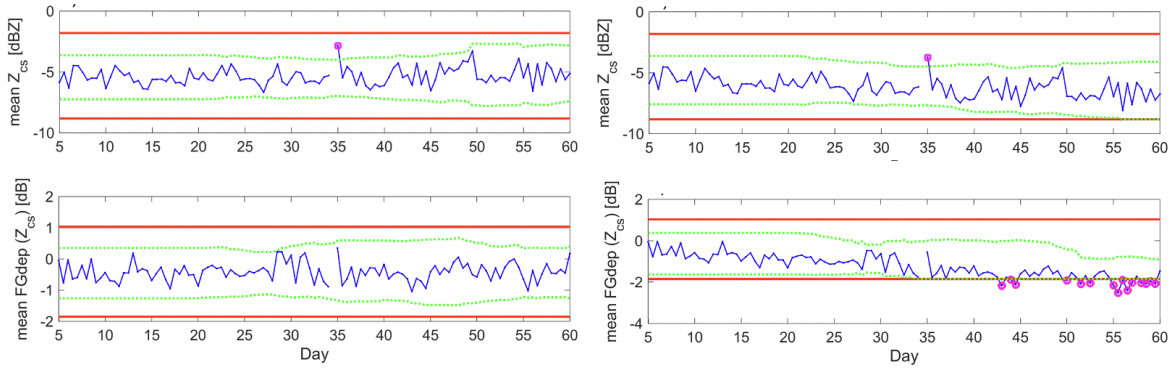

Figure 8.2. *Example of monitoring global 12-hour mean CloudSat radar reflectivity (top) and mean CloudSat radar reflectivity minus simulated radar reflectivity (bottom). Left panels show monitoring with zero bias, while right panels have a drift of 1% per day applied after day 30. Red lines show hard limits, while green dashed lines show soft limits; see text for details.*

Figure 8.2 shows the monitoring of observation-only indicators, where the bias has been introduced. Although a drift can be seen by eye in the global mean radar reflectivity (top right panel in Fig. 8.2), no additional alerts are triggered compared to the control (top left panel in Fig. 8.2). However, when using the global mean FG departures (bottom right panel in Fig. 8.2), the drift is detected with alerts triggered around 30 days after the bias was introduced. Because the drift is gradual, the alerts are triggered by the hard limits rather than the soft limits. The soft limits are more likely to detect any sudden jumps in calibration or instrument issues.

Using monitoring for relative calibration

Another possible application of a monitoring system is to use it for calibration of instruments against other instruments included in the monitoring system. If the bias between a similar, well-calibrated instrument and the model is known, then the new instrument could be calibrated to have the same bias with the model as the similar instrument. For this approach to be reliable, several assumptions must be valid, such as the model's bias against reality should be the same, which could be problematic if the model biases are different for different cloud/aerosol regimes or seasons. Nevertheless, a monitoring system could provide a useful sanity check on the calibration of a new instrument.

8.4. Demonstration of monitoring L1 data in global NWP systems

8.4.1. Example of monitoring CloudSat, CALIPSO cloud information

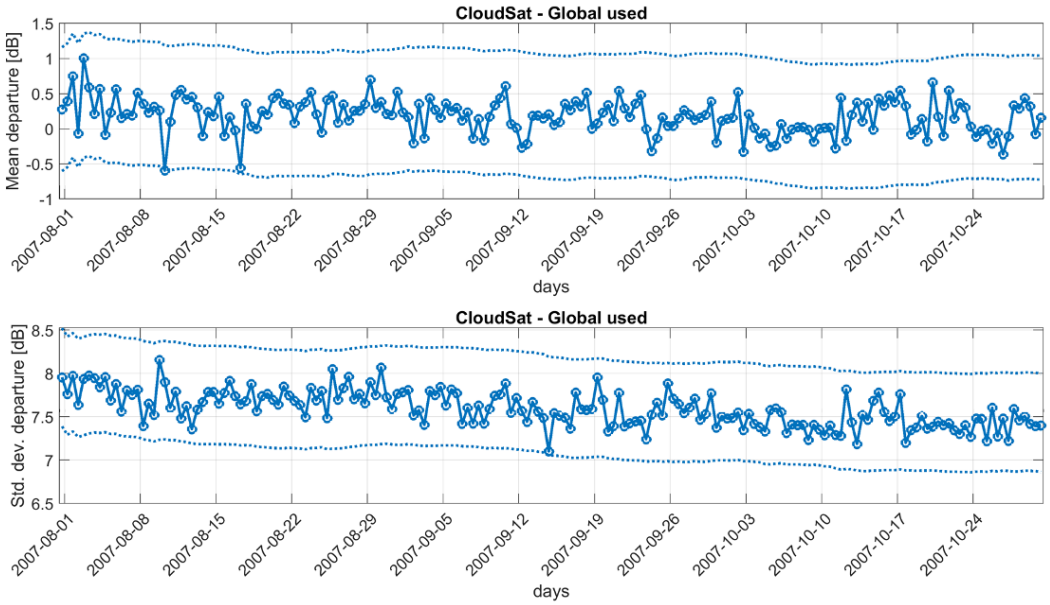

***Figure 8.3**. Three months of monitoring the mean (top) and standard deviation (bottom) of CloudSat radar reflectivity departures using the ECMWF model. Each circle represents a single data assimilation window (12 hours). The dotted line shows the mean plus and minus three times the standard deviation.*

The monitoring of CloudSat radar reflectivity is demonstrated over a 3-month period between August 2007 and October 2007. To begin with the 'used' first-guess departures (those that pass screening, so would have been assimilated) of CloudSat radar reflectivity from the control experiments are monitored. The mean of all FG departures in each 12-hour assimilation window (Fig. 8.3) are remarkably stable over the period, with 95 % of global means after bias correction of between 0-1 dB. For reference, the dynamic range of radar reflectivity measurements from CloudSat is between -30 and 20 dBZ. The standard deviation of first guess departures gives a measure of the fidelity of the model to represent clouds and precipitation, and also the accuracy of the observation operators. Unlike the global mean bias, the global standard deviation of first guess departures (Fig. 8.3) does show some seasonality. The greatest standard deviations are found at the start and end of the period, which coincides with Northern Hemisphere summer. The seasonal effects are more pronounced when looking at the data regionally (not shown), where both the Arctic and North Hemisphere regions share the same signal. It is likely that the seasonality is due to the greater number of convective clouds and precipitation in summer months, which are more difficult for the model to represent. On the other hand, the standard deviation of FG departures in the tropics are very stable throughout the year.

As an example of monitoring lidar observations, the passive monitoring of CALIPSO lidar backscatter first-guess departures (Fig. 8.4) during 2007 revealed a known quality issue with the data that could have been overlooked in an assimilation experiment. The global mean first-

guess departure can be seen to be around 1.3 dB for most of the experimental period, but drops to under 1 dB for the period between 21 August 2007 and 7 September 2007. The reason for the change in bias is due to the CALIOP lidar changing its tilt from 0.3 to 3 degrees during the period. Horizontally aligned ice crystals can cause enhanced backscatter due to specular reflection, so, as expected, changing the pointing angle of the lidar to be off-nadir reduces the bias in the observations. A small reduction in the standard-deviation of FG departures can also be detected when the lidar was pointing off-nadir, suggesting that the specular reflection was also increasing CALIPSO's observation error. For the remaining experiments, the lidar was pointing at 3 degrees off-nadir, as CALIOP changed its tilt definitively from 28 November 2007 onwards.

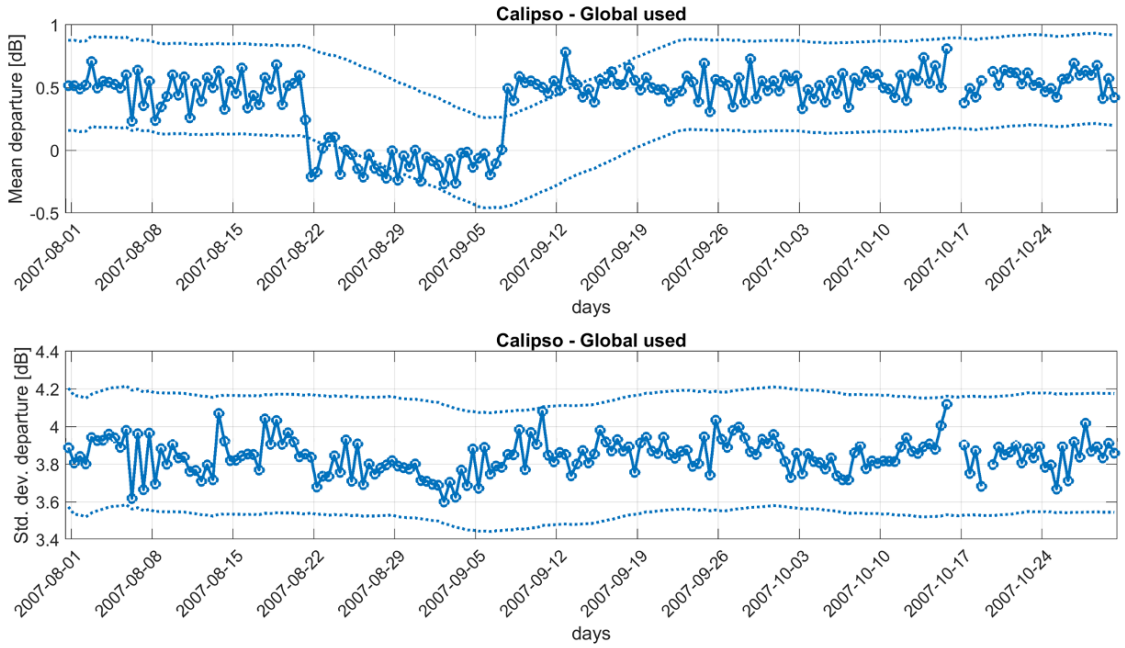

Figure 8.4. *Same as Fig. 8.3., but for CALIPSO lidar backscatter.*

8.4.2. Detection of instrument issues for Aeolus

Many systematic errors in the Earth Explorer mission Aeolus' wind data were first detected or confirmed via ECMWF's HLOS wind O-B departure monitoring. The ECMWF model was found to be trustworthy as a reference when considering statistics over large area/time averages, because the short-range forecast is relatively unbiased compared to "conventional" well-calibrated wind observations i.e. radiosondes, aircraft, radar wind profilers.

Monitoring of Aeolus winds O-B departures against the ECMWF model helped divulge many wind biases in the measurements of the Atmospheric Laser Doppler Instrument (ALADIN) including Elevated dark current rates, likely induced by cosmic rays striking the ALADIN Charge-Coupled Device (ACCD) and hot-pixel related wind biases affecting specific lidar range-bins. Additionally, moon-blinding effects on the star tracker result in pointing (attitude knowledge) wind biases, while calibration-related biases are associated with disparities between star trackers A and B. During the commissioning phase, a discrepancy of 250 meters

in the altitude of range-bins was identified, particularly linked to the star tracker. Furthermore, the varying wind bias along the orbit was attributed to temperature fluctuations across the primary mirror.

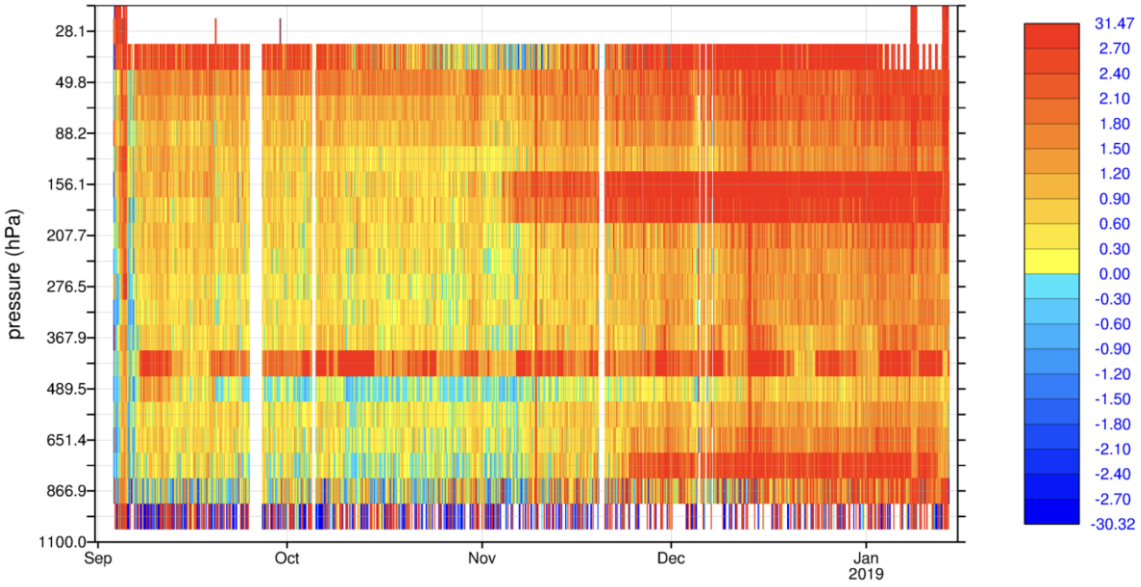

Figure 8.5. *Global mean(O-B) as a function of time (every 3 hours) and pressure (a selection of pressure ranges from surface to near 24 km altitude) for Aeolus L2B Rayleigh-clear HLOS winds. The color-scale has units of m/s.*

ECMWF monitoring helped to highlight several other contributors to wind biases, including imperfect corrections for satellite-induced Line-of-Sight (LOS) velocity, biases related to the Rayleigh-Brillouin look-up table, and imperfections in Mie calibration. Differences in biases observed during October/March ascending/descending orbits were noted, as are biases associated with imperfect Level 2B (L2B) processor quality control (QC) or algorithm settings. Long-term drifts in wind random errors were monitored, influenced by changes in laser emit energy and emit path efficiency for the FM-B laser. Additionally, monitoring helped provide feedback to the European Space Agency (ESA) and industry based on instrumental tests aimed at improving radiometric performance, encompassing efforts to enhance the alignment and divergence of the laser and maintain primary mirror temperature stability.

The automated correction that was developed by the Aeolus DISC of primary-mirror-temperature related HLOS wind biases (reaching ~8 m/s) via O-B statistics has been critical for the success of the mission (e.g., Fig 8.5). The dependence of Rayleigh response (and to a lesser extent Mie response) on the main telescope temperature (gradients) was effectively calibrated against ECMWF O-B statistics of the past. This correction also dealt with the longer time drifts in the global offset wind bias, most strongly seen with the FM-B laser.

8.4.3. Monitoring precipitation radar

At Météo-France, it is planned to use spaceborne radar observations to perform systematic comparisons between NWP models and observations. This monitoring is a powerful tool to

diagnose the weaknesses of the physical parameterizations used in the models. An example of off-line monitoring (performed over a 2-month period) using the reflectivities observed by the Ku-band precipitation radar of GPM, is given here.

The radar simulator available in version 13 of the radiative transfer model RTTOV-SCATT (Geer et al., 2021) is applied to the Météo-France global NWP model ARPEGE (Bouyssel et al., 2022) to simulate DPR reflectivities. The use of RTTOV-SCATT offers a good opportunity to simulate passive and active microwave observations using the same microphysical assumptions. The default configuration of RTTOV-SCATT is employed to simulate reflectivity observations. The ARTS database (Eriksson et al., 2018) is used for frozen hydrometeors, and Mie theory for drops. Frozen hydrometeors characteristics (shapes and PSDs) were inferred with parameter estimation by Geer et al. (2021) using passive microwave observations. Cloud fraction is diagnosed from the cloud cover for large-scale snow and rain. In order to stay consistent with the parameters used operationally at Météo-France and at ECMWF to simulate passive microwave simulations, it is set to 5% over the full column for convective rain and convective snow (i.e. graupel). The bright-band is simulated using a revisited version of the Bauer et al. (2002) parametrization.

Contoured Frequency by Altitude Diagram (CFAD) of the first-guess departures (observations - simulations, in dB) are shown in Figure 8.6 for the Northern hemisphere (left), the tropics (middle panel) and the southern hemisphere (right panel). The total number of samples per altitude level is indicated by the numbers on the right-hand side y-axis. The mean of the first guess departures is indicated by the dashed black line. There is a positive bias of about 3 to 5 dB in the three different hemispheres above the freezing level (above an altitude of approximately 4 km). Conversely, in the tropics, ARPEGE simulations tend to overestimate reflectivity in the rainy levels by an order of approximately 10 dB. This overestimation in the tropics could be related to an imperfect representation of convective hydrometeors in the global NWP model ARPEGE. Indeed, compared to large-scale hydrometeors, convective hydrometeors predominate in the tropics and, thus, have a much larger contribution to the simulated reflectivities. Unlike the prognostic hydrometeors from large-scale processes, the information on convective hydrometeors is diagnosed from the Tiedke/Bechtold convection parameterization. The comparison against DPR observations seems to indicate that this convective scheme tends to overestimate convective hydrometeors contents. On the other hand, this overestimation could also be explained by an imperfect representation of the effect of convective hydrometeors onto simulated reflectivities within the forward operator. This representation has several sources of uncertainties which could be at play for explaining part of the bias: single scattering properties specifications, particle size distribution specifications, sub-grid scale cloud fraction representation, conversions performed to estimate contents from precipitation fluxes. Various sensitivity analysis is currently ongoing at Météo-France in order to disentangle NWP model uncertainties from uncertainties in the forward operator.

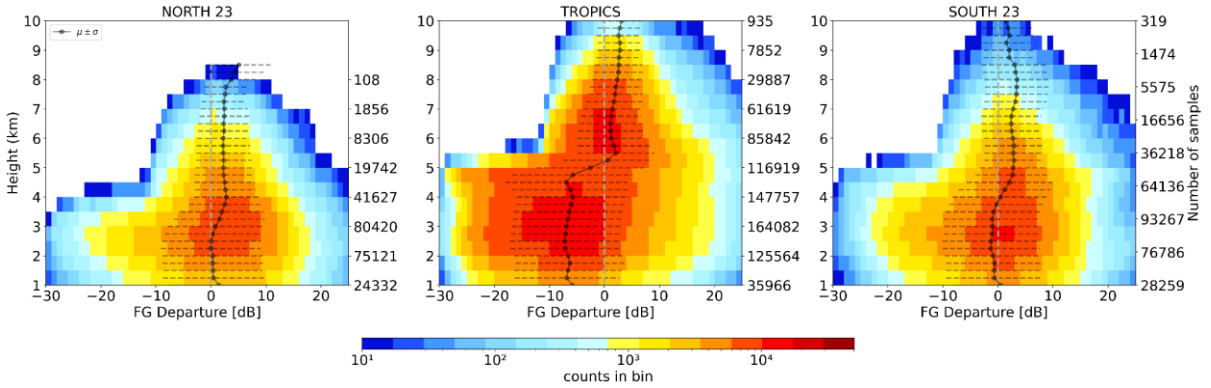

Figure 8.6. Contourned Frequency Diagram (CFAD) of the first-guess departures for the northern hemisphere (left), the tropics (middle) and the southern hemisphere (right panel) for a 2-month period (Jan-Feb 2021). The black solid line represents the mean of the first-guess departures.

8.5. Demonstration of product-level data quality monitoring using data assimilation

Besides raw lidar observations, atmospheric parameters derived from lidar observations can also be evaluated and cross-compared with numerical model simulations that assimilate passive-based retrievals. This is because some parameters included in the product-level lidar data can also be obtained from passive-based retrievals. While a direct comparison of passive-based and active-based retrievals is feasible for those atmospheric parameters, passive-based retrievals are often limited by observing conditions (e.g. cloud free, day time). In comparison, modeled data through assimilation of passive-based observations have much improved data quality with reduced uncertainties and thus can be used for evaluating and inter-comparing with level-2/level-3 lidar products over regions and times that lack passive-based observations/retrievals (e.g. nighttime).

8.5.1. Example of monitoring CALIOP AOD retrievals

An example of such a parameter is aerosol optical depth (AOD). Using the US Navy Aerosol Analysis and Prediction System (NAAPS) AOD data, Campbell et al. (2010) evaluated one year of CALIOP AOD retrievals on both regional and global scales at both daytime and nighttime. NAAPS AOD analyses included assimilation of over-land and over-ocean passive-based AOD retrievals from Moderate Resolution Imaging Spectroradiometer (MODIS) and Multi-angle Imaging Spectroradiometer (MISR). It is concluded from the study that CALIOP AOD data have similar performance at daytime and nighttime, despite the fact that daytime CALIOP observations are much noisier due to solar contamination. It is worth mentioning that AOD analyses from International Cooperative for Aerosol Prediction (ICAP) multi-model ensemble (MME) are currently available with evaluations showing that the MME mean is consistently a top performer relative to the individual contributing models for AOD analyses and forecasts (Sessions et al., 2015; Xian et al., 2019). ICAP-MME is an ensemble of 9 operational aerosol models (CAMS, GEOS-5, MOCAGE, SILAM, NAAPS, MASINGAR, NGAC, BSC MONARCH, and UKMO Unified Model), with each model supporting some form of assimilation (e.g. 2-D, 3-D, 4-D Var or ensemble Kalman filter) of passive-based aerosol

retrievals from Geostationary Equatorial Orbit (GEO) and/or low earth orbit (LEO) sensors. AOD mean analyses from ICAP-MME can and should be used for cross-evaluation of aerosol retrievals from space-borne lidars, especially during nighttime as operational passive-based aerosol retrievals from space-borne sensors are currently not available (e.g. Zhang et al., 2023). It should also be noted that the ICAP-MME has the advantage of providing a measure of uncertainty in the AOD analyses through the ensemble spread, which should be taken into consideration when comparing space-borne lidars with model fields. The multi-model ensemble is powerful in this regard as it accounts for uncertainty in emissions, meteorology, physics, and forward modeling of optical properties as well as different data assimilation methodologies that are not accounted for in single-model ensembles.

A second view on cross-validation can be done by comparing analyses of the same data assimilation system that assimilates different types of observations. If the assimilated observations are linked to the same observable variable, the key similarities and differences between these analyses can be attributed to differences in the information carried by the input observations, as for example in the vertical resolution of the observations, their spatial or temporal sampling, or their prescription of uncertainties in the data assimilation system. Following this approach, Escribano et al. (2022) (ACP) show that the assimilation of the LIVAS mineral dust extinction coefficient (computed from CALIOP profiles) was highly beneficial for the representation of the vertical structure of the mineral dust plumes, as compared with ground-based lidar retrievals; while the impact of mineral dust AOD provide improvements in the larger horizontal structures, as expected. Although this application was not NRT-oriented, positive feedback was established between the assimilation and data providers (for example in filtering criteria or in the definition of uncertainties).

8.5.2. Example of monitoring Aeolus aerosol information

Lidar measurements of particle backscatter as a function of altitude can help to constrain the vertical structure of aerosol fields. Using this information in atmospheric composition forecasting can result in an improved understanding of the evolution of aerosols in time and space. The Aeolus mission was launched in August 2018, carrying onboard the Atmospheric Laser Doppler Instrument (ALADIN), the first ever Doppler wind lidar in space. The mission's aim was to provide profiles of the wind component along the satellite's horizontal line-of-sight (HLOS) direction, from the surface up to the lower stratosphere (~30 km, ~10 hPa), on a global scale (Rennie et al., 2021). In addition to the wind product, advanced retrieval algorithms applied to the satellite data yielded particle spin-off products of the atmospheric constituents sensed by the lidar. One of these products, the L2A particle backscatter mid-bin product calculated by the Standard Correct Algorithm (Flament et al., 2021), was monitored at ECMWF beginning in January 2022, as part of the wider Aeolus Data, Innovation, and Science Cluster (DISC) activities.

Monitoring of this product was carried out using ECMWF's Integrated Forecasting System in atmospheric composition mode (IFS-COMPO). The version of the CAMS IFS-COMPO setup used to monitor the Aeolus L2A particle backscatter assimilated the MODIS Terra and Aqua AOD, alongside the PMAp AOD product from the MetOp B and C satellites. The monitoring was carried out in order to compare the new observations and their model equivalent. The model was calculated using an observation operator, which outputted the particle backscatter

coefficient corresponding to the time and location of the Aeolus observation. In order to monitor any signal from aerosols, the larger backscatter signal from clouds had to first be screened out. A cloud screening was developed where the model trajectory data were used to screen the L2A backscatter values for cloud signals. Data were also filtered by altitude, to reduce the impact of signals from ground contamination and from optically thin cirrus clouds.

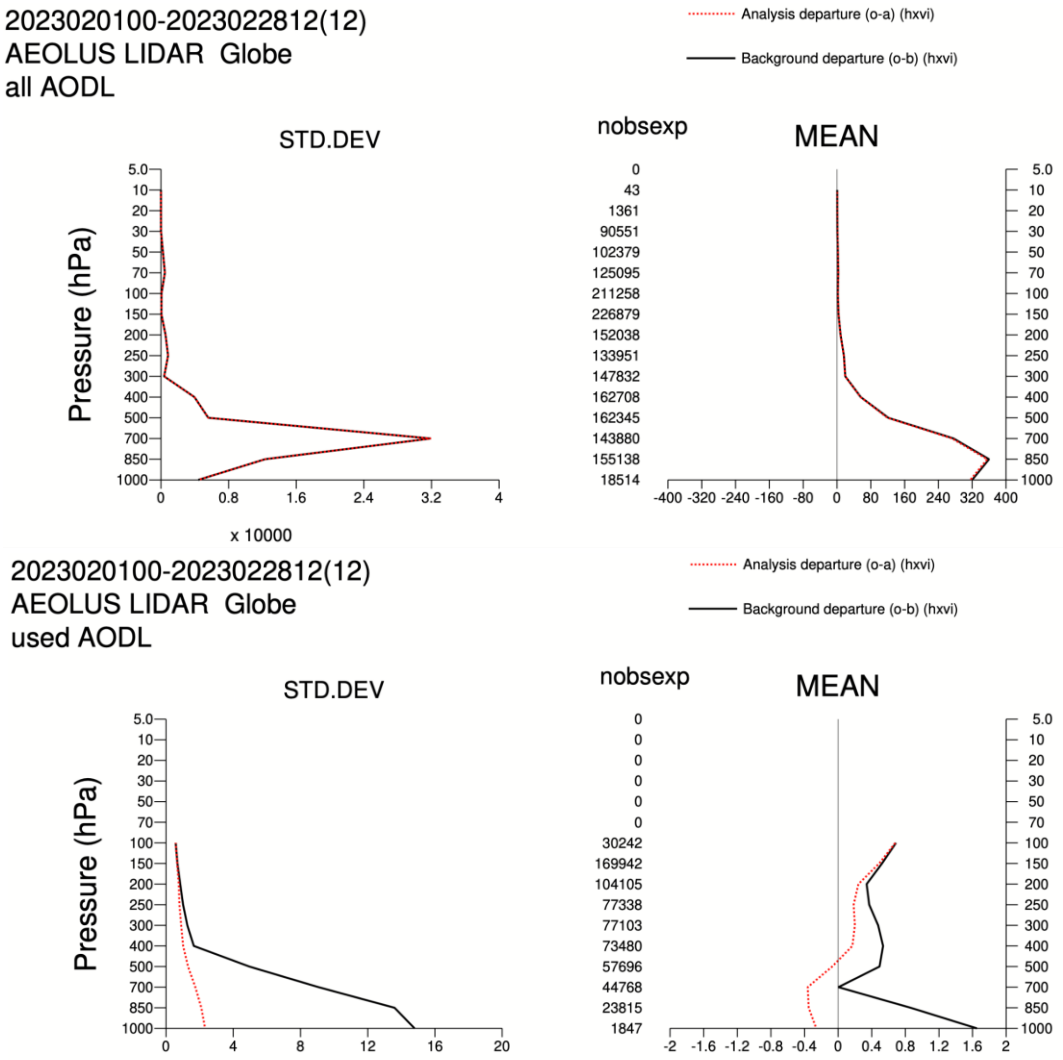

Figure 8.7. *First guess departures (black) and analysis departures (red) of backscatter profiles for February 2023, as a function of atmospheric pressure. Data are averaged over the globe, with the two top plots showing results for all data, and the two bottom plots showing results for data passing the cloud screening. Standard deviation is shown in the left-hand plot of each set, and the mean departures shown on the right-hand plot.*

All data

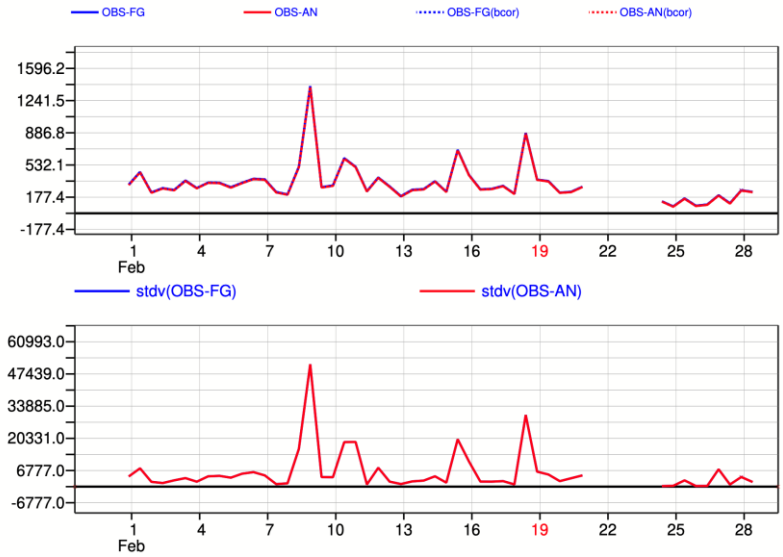

Data passing the cloud screening

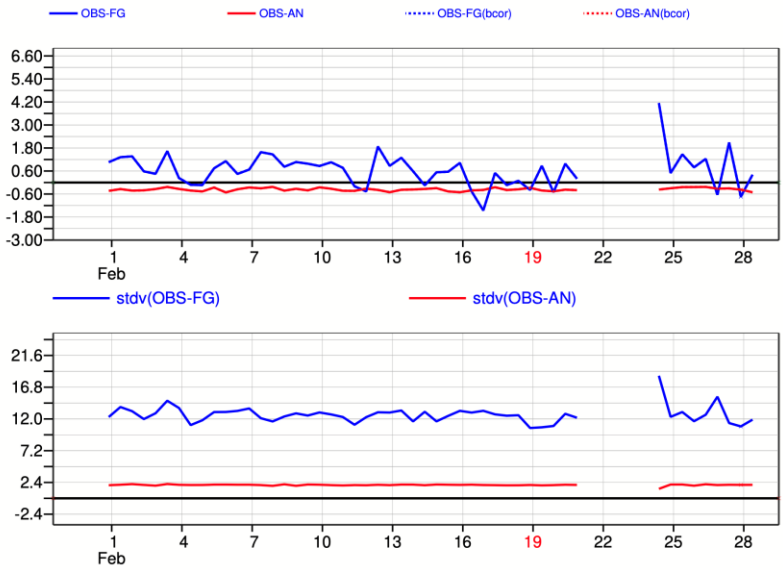

Figure 8.8. *Plots show the time series of the first-guess (blue) and analysis (red) departures for February 2023, and the associated standard deviation for each. Two top plots give statistics for all data, and two bottom plots for data passing the cloud screening.*

Statistics for monitoring and assimilating the L2A particle backscatter product are shown in Figures 8.7 and 8.8. Moreover, the bias and the standard deviation of the first-guess and analysis departures, as a function of the atmospheric pressure are shown in Fig. 8.7. The number of data points used at each altitude is given by the middle number; this is the value passing the criteria for cloud and altitude screening. Statistics are shown for all data in the left two plots, with the right two plots showing the statistics only for data passing the cloud screening.

All units are in 10^{-7}/ (m sr). The solid black lines represent the first guess departures, i.e. the difference between the observation and the model first guess. The red dashed line gives the difference between the measurement and the analysis, where the analysis is the model with the Aeolus backscatter coefficient included in the data assimilation. The assimilation here uses a small, constant value for the observation error, which in turn assigns a relatively large weight to these data in the assimilation. The need for cloud screening is illustrated, with the reduction in bias shown in the right-hand plots, particularly at the 850 hPa level, decreasing from around 360×10^{-7}/ (m sr) to 1×10^{-7}/ (m sr), resulting in a corresponding significant decrease in the standard deviation.

Figure 8.7 shows plots of the backscatter as a function of time, again for the month of February 2023. The left-hand plots show the statistics for all data, and the right for data passing the cloud screening. The top plots show the first-guess departures in blue, and the analysis departures in red, with the standard deviation of the departures shown in the middle plots. As for Figure 8.7, the need for cloud screening is clear, with large variations in the departures and their standard deviations shown on the left. Monitoring statistics as a function of time is crucial to assess any changes in the instrument data quality; here is shown a gap in the data following the satellite going into standby mode for several days, from February 21-24.

8.6. Demonstration of monitoring benefits in regional/local area models

Because of the current limited revisit time of spaceborne radar observations, these data are foreseen to provide less impact on forecast skills than other observations (e.g. ground-based radars, geostationary observations, etc.) to initialize km-scale NWP models. However, their fine vertical resolution and their high sensitivity to hydrometeor characteristics, makes them particularly appealing to monitor km-scale NWP models on high-impact events, especially over oceanic regions over which the coverage of other observations is limited. Météo-France runs a kilometer-scale NWP model over different regions of the globe called AROME (one centered over France in Europe (Brousseau et al., 2016), 5 overseas (Faure et al., 2020)). These models are run at a high horizontal resolution of 1.3 km. Deep convection is explicitly resolved and hydrometeors characteristics are governed by the ICE3 one-moment bulk microphysical scheme.

RTTOV-SCATT v13 is used to simulate DPR reflectivities using AROME 1-h forecasts. The same default configuration, described in sec 6.2.3, is used. Unlike for the ARPEGE global model, hydrometeors usually cover the entire 1.3 km*1.3 km horizontal grid of AROME. Therefore, their associated precipitation fraction is either 100%, or 0%, which removes the uncertainty on this free parameter within the forward operator. Figure 8.9 represents Ku-band non-attenuated reflectivities (top panels) and their associated AROME simulations (bottom panels) at different altitude levels (from left to right) for a heavy precipitation event which hitted Corsica on 17 August 2022. These profiles were observed at the genesis of the event at 02:00 UTC, right before it hitted Corsica at 06:00 UTC. The comparisons between observations and simulations indicate that there is a good agreement between observations and simulations, especially in terms of localization. Besides, as shown in Figure 6.9, fine-scale structures are very well captured by the Ku-band precipitation radar which makes these data an undeniable asset for validating models for which convection is explicitly resolved.

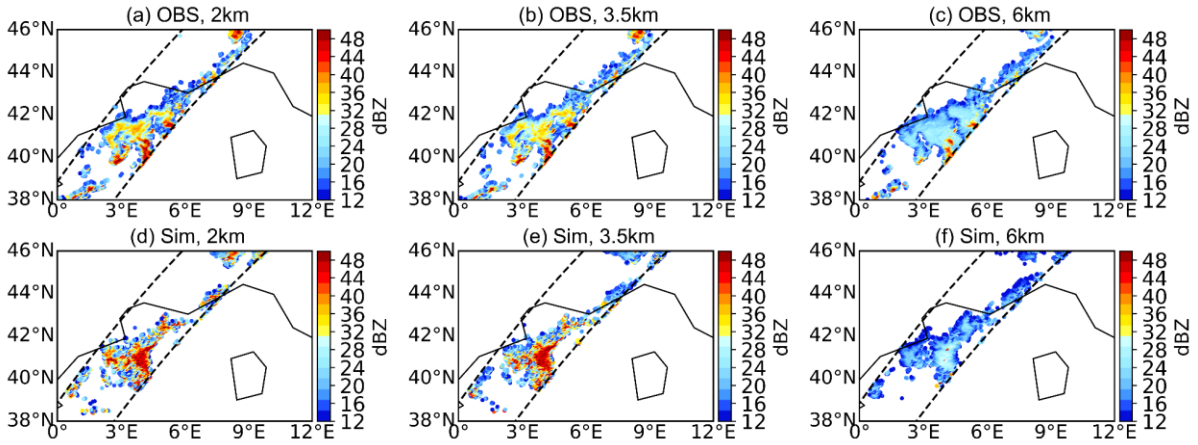

Figure 8.9. *Observed (top panels) and Simulated (bottom panels) Ku-band reflectivities at (from left to right) an altitude of 2 km, 3.5 km and 6 km for a heavy precipitation event over the Mediterranean area on 17 October 2022.*

Radar reflectivities from the DPR/GPM and the CPR/CloudSat instruments have also been simulated at Météo-France with RTTOV-SCATT for the oversea AROME NWP model located over the Caribbean (Duruisseau et al., 2018). Results showed a quite good agreement with the observations but several discrepancies remained in the rainy levels. A lack of precipitating clouds was revealed in the AROME model in the Tropics, which was consistent with other studies conducted on accumulated precipitation forecasts.

Japan Meteorological Agency (JMA) assimilates the GPM satellite observations for making the initial condition of the meso-scale model (MSM) which is the regional forecast model and routinely monitors it. Their monitoring results were also used to validate the cloud microphysics scheme. Ikuta et al. (2021) simulated GPM/GMI and GPM/DPR from the MSM and compared them with observations. As a result, they identified issues with the cloud microphysics scheme and improved the scheme. Figure 8.10 shows the CFADs for the DPR observation and the simulation before and after the improvement. The improved model was closer to observations around the altitude of 3 km and above the altitude of ~6 km, and had improved accuracy in predicting temperature profiles. Based on this previous study, JMA is currently comparing the satellite observation simulations with the observations to evaluate the accuracy of cloud precipitation forecasts in the development of the regional NWP model. These satellite observation simulations are performed using RTTOV-SCATT v13. This model validation is not performed in real-time monitoring, but retroactively over a specific experimental period.

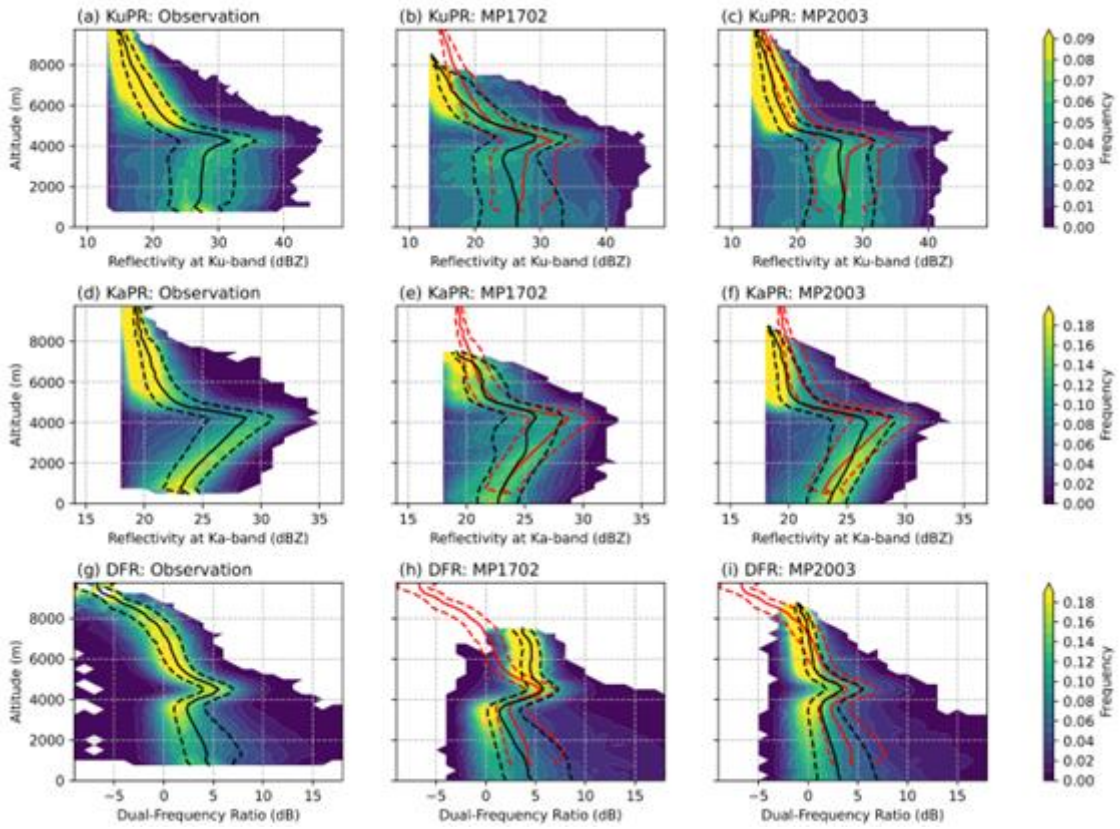

Figure 8.10. *CFADs of (top) Ku-band reflectivity, (middle) Ka-band reflectivity, and (bottom) measured dual-frequency rate. (a), (d), (g) Observation; (b), (e), (h) simulation using the old scheme; and (c), (f), (i) simulation using the current scheme. The solid line shows the median and the dashed lines show the 25th and 75th percentiles. The red lines show the percentiles of observation corresponding to the element. From Ikuta et al. (2021). Use permit not yet obtained.*

8.7. Summary and discussion

In this chapter we have demonstrated the concept and benefit of monitoring cloud, aerosol and precipitation profiles against numerical weather prediction model output within data assimilation systems. Data assimilation combines millions of observations with a physical model to generate a 'best estimate' of the current state of the atmosphere, known as an 'analysis'. New observations can therefore be validated against simulated observations made from analyses, effectively providing correlative measurements from the millions of observations that entered the assimilation system. The effectiveness of the approach relies not only on the quality of the analyses, but the forward models used to simulate observations. For example, we have shown that current NWP systems have sufficient skill to simulate radar reflectivity and lidar backscatter to detect instrument issues much faster than monitoring observations alone. Other techniques available for data assimilation can be leveraged in a monitoring system to improve the validation, such as the incorporation of observation errors, use of bias correction schemes and screening simulated profiles that are known to contain large systematic biases. These techniques help to focus the validation to regions where the model simulations best represent reality.

The capability to use a data assimilation system as a validation tool for cloud and precipitation observations has been made possible by recent advances in both the physical processes represented within NWP and atmospheric composition models and the capability to assimilate observations related to clouds and aerosols. Developments to forward models to simulate complex remote sensing measurements such as radar reflectivity or lidar backscatter have also been crucial to reduce systematic biases and errors when comparing observations with models. Validation is also possible with local area models, which do not necessarily have the full data assimilation capability of global forecast models. Instead monitoring can be performed 'off-line', and concentrated on case studies rather than near-real time monitoring.

In addition to the validation benefits of monitoring, such as improving the quality control of measurements and detecting drifts in calibration, monitoring observations facilitates model evaluation by providing a platform for comparison and the use of profiling observations to improve models. Profiling observations contain huge amounts of information on the structure and microphysical properties of clouds and aerosols, yet paradoxically can be more challenging to interpret. Comparing observations directly with simulated observations allows assumptions to be made in the forward models that are consistent with the assumptions in the model physical parameterizations. Monitoring is also a first-step before assimilation of new observational datasets. By including new observations into the data assimilation system, a positive feedback is introduced: more high-quality observations improves the model analysis, which improves the quality of validation, which in turn improves the quality of the observations.

9. Chapter 9: Gaps and Challenges

Plain language summary

This chapter aims to provide an overview of currently existing challenges and gaps concerning the validation of aerosol and cloud profilers from space identified in the chapters above or during prior activities. These challenges can be manifold, either addressing general knowledge gaps, data coverage gaps, missing reference instruments, validation approaches, etc.

An overview of the currently identified challenges is shown in Table 9.1. It is yet sorted by general, aerosol, and cloud/precipitation related gaps. A more thorough description follows afterwards in this section.

Overview Table

Table 9.1. *Overview of gaps/challenges identified within the activity for a best practice document for validation of aerosol, cloud, and precipitation profiles and proposed recommendations to tackle the challenges.*

Gap/challenge	Recommendations	Section
General		9.1
Geographic gaps	none yet.	9.1.1a
Measurement Gaps	none yet.	9.1.1b
Spatiotemporal representativeness	Use of scanning capabilities. Perform representativeness analysis.	9.1.2
Harmonization of different data sets	Standard QA/QC procedures and measurement setups.	9.1.3
Validation of Level 1 data with ground-based systems	Apply tools developed in CARDINAL to perform level 1 validation.	9.1.4
Private satellite sector	none yet.	9.1.5
Aerosol profiling		9.2
Wavelength dependence of aerosol mixtures	Identify frequent aerosol mixtures and calculate optical properties based on mixing rules and mixing state out of optical properties from pure types.	9.2.1
European background/pollution aerosol	Use of historic data sets to determine characteristic optical properties.	9.2.2

Smoke identification and/or separation	Analysis of existing datasets to propose new sub-categories of smoke.	9.2.3
Impact of dried marine aerosol	Review existing observations. Perform radiative transfer calculations to estimate the impact of even thin layers of dry marine aerosol.	9.2.4
Brown Carbon	Account for brown carbon in additional typing subcategories.	9.2.5
355 + 1064 nm depolarization observations	Analyse JATAC-CPEX datasets to identify the reasons for discrepancies in particle depolarization calculation (e.g. depolarization calibration techniques).	9.2.6
Cloud and precipitation profiling		9.3
Ice cloud retrievals in rain cases	Use data collected at several ACTRIS cloud profiling stations to develop and test radome, rain, and melting layer attenuation correction algorithms.	9.3.1
Validation of CPR Doppler velocity and fall velocity products	Use dual-polarization weather radar observations to estimate reflectivity-weighted mean Doppler CPR velocity. Use Radar Doppler measurements to estimate horizontal wind divergence on large domains. Perform statistical comparisons of ground-based radar observation. Use airborne Doppler measurements.	9.3.2
Ice microphysics	Utilize observations from measurement campaigns that combine remote sensing and aircraft observations and in-situ precipitation observations of snowfall. Implement dual-wavelength approaches to retrieve ice and snow microphysics in networks (e.g. ACTRIS)	9.3.3
Validation of snowfall product	Use weather radar observations in combination with ground-based observations for the validation of rainfall and snowfall products.	9.3.4
Attenuation in embedded supercooled liquid layers	Apply novel machine learning based methods and use multi-frequency cloud radar Doppler spectral observations.	9.3.5
Doppler velocity measurements in convection	Deploy agile adaptive radar strategies along with profiling radar systems.	9.3.6
Accounting for not detected clouds	Use ground-based cloud profiling stations to assess the impact of not resolved liquid-clouds.	9.3.7
Assimilation of cloud products	More efforts in direct assimilation of cloud products in NWP	9.3.8

9.1. General Gaps and challenges

9.1.1. The geographical and measurement gaps

No matter what efforts will be done in future, there will always be a heterogeneous distribution of high quality suborbital reference measurements. However, pointing to the current map for the validation of EarthCARE, it becomes clear that certain regions are significantly undersampled:

Figure 9.1. *Continuously updating map with respect to EarthCARE validation stations on ground. Blue: High power lidar stations, Orange: Cloud radar stations, Green: Synergistic lidar+radar stations. Purple: Other validation measurements. Map shown at: https://www.google.com/maps/d/viewer?mid=1u1BfCIB7Sh4g5HkHqhlMO18LcDJp1MrY&usp=sharing*

a) **Continental Africa**: There is almost no supersite on continental Africa. Here, efforts for **establishing high-quality long-term observations** or even campaigns deployments would be highly desirable.
b) **The Oceans:** There are not many ground observations over the Oceans. However, there is a significant amount of **research vessels** having onboard instruments for high quality atmospheric observations as listed in *Chapter 3* (section 3.2.1.2). Other sea-

borne platforms like commercial vessels and buoys might become more important in future as well. It would be beneficial to **link those activities** also to the validation efforts of spaceborne profilers (**networking, community awareness**) and make the data available.

c) **Oceania**: Currently, Oceania is significantly undersampled. Also here, the establishment of high quality long-term observations shall be envisaged and existing observatories be motivated to join validation efforts and share data.

d) **Northern Asia**: Considering the current map, there are almost no observations for validation in the Asian midlatitudes. Thus, the availability of suited suborbital instrumentation shall be checked and, if applicable, existing observatories and institutions invited to join the global validation effort.

e) **Polar and high latitude regions.** The Arctic and Antarctic are recognized as data sparse regions with only a limited number of observatories. In particular, there is a lack of observations over northern and eastern Greenland, and east of Svalbard. Furthermore, there are almost no lidar observations at 355 nm in the Arctic and Antarctica. It is very expensive and demanding to maintain polar stations, leading to sustainability gaps. The sustainability problem has recently been surveyed and documented by the Copernicus In Situ Coordination Component (Buch et al., 2019).

Measurement gaps

There are certainly also gaps with respect to measurement methodologies. To name a few:

- Humidity measurements (e.g. G-band DAR option).
- Surface-based facilities that can observe, both, clouds and precipitation conditions. For example, the ACTRIS stations are optimized for cloud profiling in non-raining conditions.
- Generally, more measurements for radiation are desired.

9.1.2. Spatio-temporal representativeness

How representative a single station is with respect to the surroundings is important to know for judging the validation results. This challenge is specifically tackled in *Chapter 3* (section 3.4 and recommendations to determine criteria for validation exercises) and strategies/guidance might be very **different depending on the validation target**. On this aspect, the following still remaining challenge is concluded:

Common assessment practices typically use a surface-based reference and bulk comparison metrics (e.g. correlation, bias) to assess performances over a given spatial and temporal domain. Metrics such as correlation, bias, and contingency statistics should be applied to check their relevance. For example, the definition of bias may be ambiguous as it can be defined as an additive satellite QPE-to-reference difference or a multiplicative difference (ratio), sometimes based on conditional (positive) values. The linear correlation is generally insufficient to describe the non-linear and heteroscedastic dependence structure between the satellite estimates and a reference. In addition, the satellite estimates are often assumed to be consistent and display homogeneous performances over their spatial and temporal domain

of comparison. Bulk metrics (correlation, bias, contingency, etc.) are computed over samples actually gathering a variety of scene characteristics (e.g., for precipitation: intermittency, typology, rates) for which the satellite retrieval algorithm is likely to behave differently. More generally the comparison is always performed with estimates ambiguously derived from the satellite sensor observations through the retrieval algorithm and associated assumptions. Individual retrievals are underconstrained by nature and sensitive to unobserved atmospheric parameters (e.g. Stephens & Kummerow, 2007 for precipitation). Combined retrievals inherit the varying sensors' performances and create additional uncertainties with temporal/spatial resampling. Hence bulk error metrics depict averaged space/time properties while the errors tend to be non-stationary and sensitive to parameters not accounted for in the assessment formulation. As a result, the representativeness of any overall satellite assessment or error model is confined to the time and space domain over which it is performed. It tends to be specific to the satellite instrument (e.g. resolution), the retrieval algorithm (and associated version), the space-time-scale and the accuracy of the reference, with limited applicability for other atmospheric regimes, regions, products, etc. Integrated assessment is necessary to track the origin of uncertainties and their propagation through various satellite retrieval algorithms. More informative assessment and information to algorithm improvement can be gained by stratifying (conditioning) the assessment according to relevant factors driving the state of the satellite estimation error. Hence targeting the most significant factors is essential to characterize uncertainties in satellite estimates and lead to a generalization of their assessment.

Nevertheless, currently a study is initiated by ESA investigating this effect with respect to aerosol profiling validation based on long-term reference measurements at a single location in Cabo Verde and CALIPSO/LIVAS data around the site. The outcome of this study might be reported here after finalization of the study.

Furthermore, use of the scanning capabilities of cloud radars to overcome the spatial distance between the two profilers is currently investigated as there is a growing number of scanning cloud radars that can be used for Cal/Val purposes. Already now, scans can be used to retrieve wind profiles within fog, clouds and precipitation. It is currently being investigated in the frame of FRM4radar if cloud radar scans can be used to mimic CPR underflights. This might only be doable for some sites and stations due to specific scanner hardware and meteorological conditions (attenuation of Ka- and especially W-band in rain). Scanning has also the advantage to make use of polarimetric variables and explore their usages for microphysical process understanding and classification of hydrometeors (see gap 9.3.3). Furthermore, developing a method to estimate the spatial distribution of clouds within the scanned area could be envisaged. This could help to develop criteria for statistical comparisons of cloud profiles with the satellite passing close to the site.

As mentioned in Chapter 1 .2, airborne lidar underflights were the most impactful means of validation for the CALIPSO algorithm assessment, therefore there is a clear need for the for airborne validation campaigns (satellite track underpasses), more mobile ground stations (e.g.ship-borne) as well as more light-weight platforms like e.g. balloons and UAVs to collect high quality validation data. Additionally dense ground-based networks for statistical approaches are of high interest.

9.1.3. Harmonization of different data sets

Harmonization of different data sets is tackled in *Chapter 3* and *Chapter 4*, nevertheless, this task is never completed. Next to different instrument specifics (e.g. wavelength, frequency, representativeness) also harmonization among global reference observations is an ongoing effort. First attempts were successfully made, e.g., in the framework of the ATMO-ACCESS pilot, FRM4Radar, and GALION (https://galion.world/) in close collaboration with the ESA Atmospheric Validation Centre (EVDC), and will continue to be made through other programs such as the upcoming EU Horizon project CARGO-ACT (in the EU call for Strengthening the international dimension of ESFRI and/or ERIC research infrastructures). However, **a complete comparability of all data sets is not yet achieved**. This counts for validation purposes as well as for climatological studies.

For example, standardization of in-situ measurements for estimating the particle size distribution properties at the surface in rain/snow conditions is still needed.

The full overview of the current status of the harmonization, links to data formatting templates etc. is listed in Table 4.1. of *Chapter 4*.

As an example for a one specific profiling instrument, ESAs FRM4Radar radar network as a testbed for a path towards Cloud Radar Fiducial reference measurements (FRM) is mentioned in the following. Some QC methods were tested but still following challenges and gaps are identified within the project:

- More hands-on training needed,
- Defining common measurement setups and strategies.
- Common data processing following the same QA/QC routines.

By this, measurement gaps and wrong data acquisition can be minimized.

The FRM4Radar project shows that a homogenization of cloud radar data is possible, but coordinated effort and work is needed which also counts for other instruments and respective networks.

9.1.4. Validation of Level 1 data with ground-based systems

Guidance for validation of L1 data has been tackled in Chapter *5* for aerosol products and *Chapter 6* for cloud and precipitation products.

For the evaluation of the Level 1 products, specific assumptions that introduce additional uncertainties in the validation exercise have to be considered, in terms of the differences that may exist between the satellite profiles and the reference instrument in the operation principle (e.g. HSRL, Elastic, Raman for lidar), the viewing angle and field-of-view, the sampling resolution, and the signal-to-noise ratio. An approach to account for these assumptions is the **development of simulator tools** which use the data from the reference instrument to simulate the L1 products that would be obtained from the satellite based on its design. In the course of the writing, several tools have been developed to simplify validation approaches.

Specifically, simulators to mimic space-born profiles of EarthCARE based on sophisticated ground-based observations have been developed and are currently under testing.

Nevertheless, even though these tools are very helpful, they cannot account for all instances, like, e.g., exact multiple scattering calculation in case of lidar. Furthermore, the tools need to be **instrument-specific adapted for each new spaceborne profiler**. Thus, an open gap/challenge for the future but also historic satellite missions is the development of such tools to facilitate the comparisons between the satellite and the reference instrument for the L1 validation.

9.1.5. Private satellite sector

A general aspect that is considered to be a challenge is the guidance on quality control for the private satellite sector, e.g., by using ACTRIS/ARM data for validation. This is currently not the case, as no private sector aerosol or cloud profiles are in space, but may become an issue soon.

9.2. Aerosol profiling-related gaps and challenges

9.2.1. Wavelength dependence of aerosol mixtures

A good data set of optical properties at different wavelengths for specific, mostly pure, aerosol types is available (e.g. DeLiAn, Floutsi, et al., 2023). Currently, such information is not fully available for aerosol mixtures, which are frequently observed in nature. Furthermore, the optical properties depend on the mixing state, which is usually not fully known. One approach for future studies could be to **calculate optical properties for specific aerosol mixtures** based on mixing rules and mixing state out of optical properties from pure types and then compare these values to existing high-quality observations at multiple wavelengths, e.g. ACTRIS, LALINET, or AD-NET. If satisfying results are achieved, a data homogenization could be envisaged for aerosol mixtures which will help validation approaches but also climatological studies.

9.2.2. Optical properties of European background / pollution aerosol

So far, a full set of optical properties of European background conditions or moderate pollution is rare. The reason is that the aerosol amount is low and mostly confined to the first kilometers for which many ground-based lidars have overlap problems. Nevertheless, spaceborne profiles do more frequently sense in remote areas and are able to take profiles close to the ground. Therefore, studies using historic and novel data sets covering the first kilometers of the atmosphere with backscatter, extinction (Raman or HSRL), and depolarization measurements to **derive background properties** (e.g. ACTRIS dataset) should be envisaged.

9.2.3. Smoke identification and/or separation

Biomass-burning smoke is difficult to characterize and to classify because of changing properties depending on origin, processing during transport, location in the atmosphere (troposphere vs stratosphere). Furthermore, measured optical properties are difficult to differentiate from the optical properties of pollution aerosol. Thus, efforts shall be done to find

suitable measures to differentiate smoke from pollution aerosol. This could lead to proposals for **new sub-categories of smoke**.

9.2.4. Impact of dried marine aerosol

The presence of cubic-like marine aerosol particles under dry conditions was shown, e.g., by Haarig et al. (2017). However, the frequency of occurrence, the vertical distribution (thin layers only or entire marine PBL), and the related radiative impact of dry marine aerosol is unknown. Therefore, it is hard to estimate the effect of misclassification as a dusty-marine mixture. One possible way of addressing this issue, would be to **use several coastal sites** with continuous ground-based lidar observations to estimate the frequency of occurrence (per year) or to investigate lidar observation on **research vessels** (e.g. Bohlmann et al., 2018). However, space-borne observations may lack the required vertical resolution and thus might be simply "biased", although they can be used on statistical basis in regions with only marine aerosol like in the Southern Ocean (Thomas et al., 2022). Studies shall be performed by using radiative transfer calculations to estimate the impact of even thin layers of dry marine aerosol.

9.2.5. Brown Carbon

"Brown carbon" (light-absorbing organic carbon) has attracted interest as a possible cause of climate change. This class of organic carbon, known for its light brownish color, **absorbs strongly in the ultraviolet wavelength range** and less significantly in the visible. But so far it is unclear if it is possible to measure and separate brown carbon from black carbon. BrC is emitted by primary combustion processes of fossil fuels and mostly biomass/biofuel burning but can also be formed as a secondary organic aerosol (SOA) by-product, through a series of photochemical reactions. Global modeling studies have unveiled that BrC-related light absorption and radiative forcing may range from 27% to 70% of that attributed to BC, as documented in the literature. Nevertheless, ongoing scientific debates persist regarding BrC characteristics due to limited BrC-related measurements, coupled with its highly variable chemical composition and optical properties, resulting in significant uncertainties in assessing radiative forcing.

Hence, elucidating the optical properties and sources of carbonaceous aerosols, particularly those of BrC, holds paramount importance. The EC mission can be used, in principle, to retrieve the vertical distribution of aerosol/cloud optical properties to be considered as important sources of uncertainties in estimation of aerosol radiative effect on climate.

In-situ observations of aerosol vertical distribution using aircraft or UAV are tedious and expensive methods, the use of active remote sensing techniques. Lidar techniques complemented with satellite and ground-based passive remote sensors are widely used to characterize the 3-D structures of atmospheric brown clouds (ABCs) over many regions of the world, with particular interest in regions close to areas where biomass burning activities are intense, such as the Amazon Basin and neighboring areas where agricultural development are occurring and in expansion.

The word "ABCs" is used to define the regional scale pollution plumes mainly containing the different types of aerosols from both anthropogenic and natural origins such as mineral dust,

smoke, and urban-industrial pollution plumes in the atmosphere. A bird-eye-view of the earth can identify various ABCs' hotspots over the globe.

EC will provide a set of optical data which may be able to **sub-categorize Carbon based aerosol** and thus enabling to reduce uncertainties with respect to validation but finally also to radiative effect estimations of such aerosols. It should be considered to merge this issue to topic 9.2.3 in the next release of this document.

9.2.6. 355 nm + 1064 nm depolarization observations

Even though related to general aspects of data set harmonization (see 9.1.3), especially the data set of depolarization ratio at 1064 nm is rare and discrepancies have been identified for collocated measurements. Thus, specific efforts shall be envisaged to clarify this issue with **historic data sets** (e.g., JATAC) but also to improve calibration for future measurements. A **dedicated comparison** would also be well received.
Similar accounts for depolarization at 355 nm, even though the data set is much richer and efforts to upgrade lidars for EarthCARE validation have been done recently. Nevertheless, the majority of global lidar observations with depolarization capabilities is still performed at 532 nm only.

9.3. Cloud and precipitation profiling related gaps and challenges

9.3.1. Ice cloud retrievals in rain cases

Currently, quantitative ground-based remote sensing observations of ice clouds are limited to non-rain cases. In the current ACTRIS cloudnet processing, cases of presence of ice above rain and melting-layer are identified and flagged. For such cases, no ice microphysical retrievals are performed, thus limiting ground-based ice cloud observations and Cal/Val capabilities to non-rain cases. A way forward would be to use data collected at several ACTRIS cloud profiling stations to **develop and test radome, rain and melting layer attenuation correction algorithms**.

For example:

- to use cloud radar observations in combination with disdrometers to estimate rain and radome attenuation,
- to use multi-frequency radar observations (Li & Moisseev, 2020) to improve parametrization of melting layer attenuation,
- to use direct overpasses of CPR or coordinated aircraft observations to evaluate the attenuation of ground-based radar systems under different meteorological/precipitation conditions. Differences between ground-based and CPR (or aircraft-borne radar) reflectivities at cloud top are thus caused due to attenuation of the ground-based radar signals. Given appropriate meteorological conditions, this approach can potentially be extended toward the derivation of profiles of the signal extinction.

9.3.2. Validation of CPR Doppler velocity and fall velocity products

Since EarthCARE is the first Doppler radar in space, there are **no methods previously developed for the validation** of spaceborne Doppler radar observations. Additionally, the air

motion contribution to the observed Doppler velocity must be accounted for when employing microphysical retrievals with a terminal fall speed term (Radenz et al., 2018). Furthermore, EarthCARE CPR pulse repetition frequency depends on latitude. Since the pulse repetition frequency affects Doppler velocity observations, validation of Doppler observations should be performed at different latitudes.

Suggested approach are:

- to develop a method to derive terminal fall velocities of raindrops from dual-polarization weather radar observations,
- to apply the extended velocity–azimuth display method to radar Doppler measurements to estimate horizontal wind divergence on large domains from which the air velocity profile can be estimated by solving the continuity equation,
- to derive a method for a statistical comparison of CPR and ground-based observations of cloud velocities, i.e. by using reflectivity-velocity relations, tuned to specific cloud types and geographical locations,
- to additionally use airborne Doppler measurements (e.g. on airborne platforms).

9.3.3. Ice microphysics

There is still lacking knowledge on ice microphysics (number-size distribution, shape distribution, orientation), and their connection to scattering properties of the ice particles, which constitute one of the bigger uncertainties in cloud microphysical retrievals. Thus, it is proposed to utilize observations from measurement campaigns that combine remote sensing and aircraft observations, or coordinated ground-based remote sensing and in situ precipitation observations of snowfall in geographical regions where it occurs to reduce uncertainties in the retrieval algorithms. More and more cloud radar sites perform measurements with more than one wavelength. Developing or implementing a **dual-wavelength retrieval** for ice and snow microphysics in some networks such as ACTRIS might be possible. The implementation has to include common QA/QC standard and data processing routines for the sensors.

9.3.4. Validation of snowfall product

Quantitative estimation of snowfall intensity from radar observations is still rather uncertain (von Lerber et al., 2017). The uncertainty of the estimate appears to be a function of radar wavelength (Schoger et al., 2021). Because of this, there is a need for datasets that can be used for validation of the snowfall product, which minimizes uncertainties and takes into account wavelength dependence. E.g., use **weather radar observations** in combination with ground-based observations for validation of rainfall and snowfall products (i.e. von Lerber et al., 2018).

9.3.5. Attenuation in embedded supercooled liquid layers

Supercooled liquid cloud layers can cause significant radar signal attenuation at mm-wavelengths. The difference in observation geometries between satellite and ground-based remote sensors results in different attenuation profiles. Identification of supercooled liquid layers embedded in ice clouds, which can be identified by a collocated lidar, are limited to the

first layer encountered in the particular viewing geometry. Therefore, **new approaches like machine learning based methods** for identification of embedded supercooled liquid cloud layers (Schimmel et al., 2022) shall be used for validation.
As a first step, the methodology should be applied, trained, tested and validated at several cloud profiling stations. At the same stations, the use of multi-frequency cloud radar Doppler spectral observations to estimate the attenuation caused by the embedded supercooled liquid cloud layers should be applied.

9.3.6. Strategies for evaluating Doppler velocity measurements in convection

The coming decade will feature several new space-borne missions including the ESA-JAXA Earth Cloud Aerosol and Radiation Explorer (EarthCARE), the NASA-Investigation of Convective Updrafts (INCUS) and the NASA-Atmosphere Observing System (AOS) that specifically focuses on improving our understanding of convective processes, evolution, and outcomes (Dolan et al., 2023; Illingworth et al., 2015; Kollias et al., 2022). Despite being deployed hundreds of kilometers above the Earth's surface, these planned missions are expected to offer unprecedented measurement capabilities that in many ways will be superior to those available today from suborbital (airborne and surface-based) platforms.

The systematic collection of observations of convective motion from the ground remains challenging. The most direct way for measuring convective vertical air motions is aircraft in-situ sampling. However, practical hazards and operational costs have resulted in a valuable, but limited, dataset (e.g. LeMone & Zipser, 1980). The use of airborne Doppler radar systems that fly over the top of the convective clouds has eliminated some of the hazards (Heymsfield et al., 2010) but there are only a few aircraft with high altitude capabilities.

Profiling Doppler radar systems (Kumar et al., 2015; Wang et al., 2020) have been also useful in collecting observations of convective vertical air motions. The profiling radars provide a high degree of detail of convective clouds in time and height, and can sample even the most intense convective cores. However, profiling radars potentially have a limited role for direct (rather than statistical) cloud model constraint due to their narrow view of these large, three-dimensional systems. The use of Doppler radar networks and multi-Doppler radar techniques (North et al., 2017; Potvin et al., 2012) can provide a large sampling area, however, recent studies have highlighted a number of uncertainties and shortcomings of traditional multi-Doppler radar retrievals of convective vertical air motion (Oue et al., 2019).

As a result, and despite their importance, there are considerable measurement gaps in convective updrafts. These gaps limit our ability to constrain these important aspects of model parameterization and verification. Observations of the number and magnitude of updrafts contributing to vertical transport in deep convection are not available over the tropical oceans and are rarely available over land. These gaps will not only hinder our efforts to understand convective storms but will also challenge our ability to validate the upcoming, planned spaceborne missions (EarthCARE, INCUS and AOS). In a recent study, Dolan et al. (2023) demonstrated the ability to use agile adaptive radar observations to track convective cores and estimate the convective vertical air motion (Lamer et al., 2023). In the future, surface observatories should deploy **agile adaptive radar strategies** along with profiling radar

systems to provide adequate samples of convective motions to evaluate satellite mission and numerical models.

9.3.7. Accounting for radiatively-important liquid clouds not detected by spaceborne lidars

This section will be completed in the next issue of this document. The main topics are clouds not detected by spaceborne lidar, e.g.:

- Deep ice clouds: embedded mixed-phase layers
- Layered cloud scenes
- Warm liquid clouds within cold rain

Thus, one needs to discuss how observations from cloud profiling remote stations located in various climatological regions can be used to assess the impact of not resolved liquid clouds.

9.3.8. Assimilation of cloud products

An example of the impact of assimilating precipitation products in a regional NWP model is shown in Chapter 8. However, direct assimilation of other cloud products is not yet mentioned because direct assimilation of cloud products is difficult and limited to a few parameters such as IWP (Ice Water Path) and LWP (Liquid Water Path), although they have shown that it might improve forecasts in particular situations (e.g. [RD-3], [RD-4]). More efforts in this direction are desired, especially in the context of the rising interest in data-driven forecast models.

Acknowledgments

Part of the work has been supported by the ESA ACPV (Best practice protocol for validation of Aerosol, Cloud, and Precipitation Profiles) project (Contract no. 4000140645/23/I-NS), and the PANGEA4CalVal project (Grant Agreement no. 101079201) funded by the European Union  . Moreover, part of the work has been possible thanks to the knowhow available on EARLINET, the activities and resources provided by the Research Infrastructure ACTRIS, and the support by the European Commission under the Horizon 2020 – Research and Innovation Framework Programme (H2020-INFRAIA-2020-1) ATMO-ACCESS (Grant Agreement no. 101008004). Part of the work done from NOA team was supported by the CERTAINTY (Cloud-aERosol inTeractions & their impActs IN The earth sYstem) project (Grant Agreement No. 101137680) funded from the Horizon Europe programm, the ESA AIRSENSE (Aerosol and aerosol cloud Interaction from Remote SENSing Enhancement) project (Contract No. 4000142902/23/I-NS), the Hellenic Foundation for Research and Innovation (H.F.R.I.) under the “2nd Call for H.F.R.I. Research Projects to support Post-Doctoral Researchers” (Project Acronym: REVEAL, Project Number: 07222), the ESA L2A+ (Enhanced Aeolus L2A for depolarizing targets and impact on aerosol research and NWP) project (Contract no. 4000139424/22/I-NS), and the ESA ECAMS (EarthCARE ATLID and MSI instruments Synergy for advanced retrieval of aerosol vertical profiles) project (Contract No. 4000146378/24/I-DT-bgh). Work done by Kamil Mroz was performed under a contract with the National Centre for Earth Observation. Isaac Moradi was supported by NASA grant 80NSSC21K1361 and NOAA grant NA24NESX432C0001 (Cooperative Institute for Satellite Earth System Studies - CISESS) at the University of Maryland/ESSIC. David B. Wolff was funded under NASA's Precipitation Measuring Mission (program manager Dr. Will McCarty) Global Precipitation Measurement Ground Validation program (WBS 378289.04.05.02). Pierre Kirstetter was funded by the NASA Global Precipitation Measurement Ground Validation program under Grant 80NSSC21K2045 and the Precipitation Measurement Missions program under Grant 80NSSC19K0681. James Mather was supported by the Atmospheric Radiation Measurement (ARM) User Facility, a U.S. Department of Energy (DOE) Office of Science User Facility managed by the Biological and Environmental Research program. Derek Posselt’s contribution was supported by the Jet Propulsion Laboratory, California Institute of Technology, under a contract with the National Aeronautics and Space Administration (NASA, 80NM0018D0004). Hajime Okamoto was supported by the Japan Aerospace Exploration Agency (EORA3) for the EarthCARE mission; JSPS (KAKENHI grant JP24H00275); Collaborative Research Program of the Research Institute for Applied Mechanics, Kyushu University (Fukuoka Japan). Kaori Sato was supported by the Japan Aerospace Exploration Agency (EORA3) for the EarthCARE mission; JSPS (KAKENHI grants JP22K03721, JP24H00275); Shiseido Female Researcher Science Grant; Collaborative Research Program of the Research Institute for Applied Mechanics, Kyushu University (Fukuoka Japan). Nikos Siomos was supported by the European Union’s Horizon 2020 research and innovation programme under grant agreements No 871115 and by ACTRIS-D, funded by the German Federal Ministry for Education and Research (BMBF) under grant agreements 01LK2001A-K & 01LK2002A-G.

List of acronyms

ACTRIS	Aerosol Cloud and Trace Gasses Research Infrastructure
ALADIN	Atmospheric Laser Doppler Instrument
AOD	Aerosol Optical Depth
API	Application Programming Interface
AROME	Applications of Research to Operations at MEsoscale
ARPEGE	Action de Recherche Petite Echelle Grande Echelle
ASCII	American Standard Code for Information Interchange
AVDC	Aura Validation Data Centre
CALIOP	Cloud-Aerosol Lidar with Orthogonal Polarisation
CALIPSO	Cloud-Aerosol Lidar and Infrared Pathfinder Satellite Observation
CAMS	Copernicus Atmosphere Monitoring Service
CF convention	Climate and Forecast metadata convention
CFAD	Contour Frequency by Altitude Diagram
CloudSat	NASA’s cloud radar mission
CPR	Cloud Profiling Radar
CRTM	Community Radiative Transfer Model
CSV	Comma-separated value
DISC	Data Innovation Science Cluster
DOI	Digital Object Identifier
DPR	Dual-frequency Precipitation Radar
EARLINET	European Aerosol Lidar Network
EarthCARE	Earth, Clouds, Aerosols and Radiation Explorer
EVDC	ESA Validation Data Center
FAIR	Findability, Accessibility, Interoperability, and Reusability
FG	First Guess
GEOMS	Generic Earth Observation Metadata Standard
GMI	GPM Microwave Imager
GPM	Global Precipitation Measurement mission
HDF	Hierarchical Data Format
HLOS	Horizontal Line-Of-Sight
IFS	Integrated Forecasting System of ECMWF
JMA	Japan Meteorological Agency
MODIS	MODerate resolution Imaging Spectroradiometer
NDACC	Network for Detection of Atmospheric Composition Change
netCDF	Network Common Data Form
NWP	Numerical Weather Prediction
PID	Persistent Identifier
RTTOV	Radiative Transfer for TOVS
RTTOV-SCATT	RTTOV multi-scattering scattering package
TIROS	Television InfraRed Observation Satellite
TOVS	TIROS Operational Vertical Sounder
URL	Uniform Resource Locator
UTC	Universal Time Coordinated
XML	Extensible Markup Language

References

Abel, S. J., Boutle, I. A., Waite, K., Fox, S., Brown, P. R. A., Cotton, R., Lloyd, G., Choularton, T. W., & Bower, K. N. (2017). The Role of Precipitation in Controlling the Transition from Stratocumulus to Cumulus Clouds in a Northern Hemisphere Cold-Air Outbreak. *Journal of the Atmospheric Sciences*, *74*(7), 2293–2314. https://doi.org/10.1175/JAS-D-16-0362.1

Abel, S. J., Cotton, R. J., Barrett, P. A., & Vance, A. K. (2014). A comparison of ice water content measurement techniques on the FAAM BAe-146 aircraft. *Atmospheric Measurement Techniques*, *7*(9), 3007–3022. https://doi.org/10.5194/amt-7-3007-2014

Abril-Gago, J., Guerrero-Rascado, J. L., Costa, M. J., Bravo-Aranda, J. A., Sicard, M., Bermejo-Pantaleón, D., Bortoli, D., Granados-Muñoz, M. J., Rodríguez-Gómez, A., Muñoz-Porcar, C., Comerón, A., Ortiz-Amezcua, P., Salgueiro, V., Jiménez-Martín, M. M., & Alados-Arboledas, L. (2022). Statistical validation of Aeolus L2A particle backscatter coefficient retrievals over ACTRIS/EARLINET stations on the Iberian Peninsula. *Atmospheric Chemistry and Physics*, *22*(2), 1425–1451. https://doi.org/10.5194/acp-22-1425-2022

Acquistapace, C., Löhnert, U., Maahn, M., & Kollias, P. (2019). A New Criterion to Improve Operational Drizzle Detection with Ground-Based Remote Sensing. *Journal of Atmospheric and Oceanic Technology*, *36*(5), 781–801. https://doi.org/10.1175/JTECH-D-18-0158.1

Adirosi, E., Montopoli, M., Bracci, A., Porcù, F., Capozzi, V., Annella, C., Budillon, G., Bucchignani, E., Zollo, A. L., Cazzuli, O., Camisani, G., Bechini, R., Cremonini, R., Antonini, A., Ortolani, A., & Baldini, L. (2021). Validation of GPM Rainfall and Drop Size Distribution Products through Disdrometers in Italy. *Remote Sensing*, *13*(11), 2081. https://doi.org/10.3390/rs13112081

Amiridis, V., Balis, D. S., Kazadzis, S., Bais, A., Giannakaki, E., Papayannis, A., & Zerefos, C. (2005). Four-year aerosol observations with a Raman lidar at Thessaloniki, Greece, in the framework of European Aerosol Research Lidar Network (EARLINET). *Journal of Geophysical Research: Atmospheres*, *110*(D21). https://doi.org/10.1029/2005JD006190

Amiridis, V., Wandinger, U., Marinou, E., Giannakaki, E., Tsekeri, A., Basart, S., Kazadzis, S., Gkikas, A., Taylor, M., Baldasano, J., & Ansmann, A. (2013). Optimizing CALIPSO Saharan dust retrievals. *Atmospheric Chemistry and Physics*, *13*(23), 12089–12106. https://doi.org/10.5194/acp-13-12089-2013

Anagnostou, E. N., Morales, C. A., & Dinku, T. (2001). The Use of TRMM Precipitation Radar Observations in Determining Ground Radar Calibration Biases. *Journal of Atmospheric and Oceanic Technology*, *18*(4), 616–628. https://doi.org/10.1175/1520-0426(2001)018<0616:TUOTPR>2.0.CO;2

Anderson, T. L., Charlson, R. J., Winker, D. M., Ogren, J. A., & Holmén, K. (2003). Mesoscale Variations of Tropospheric Aerosols*. *Journal of the Atmospheric Sciences*, *60*(1), 119–136. https://doi.org/10.1175/1520-0469(2003)060<0119:MVOTA>2.0.CO;2

Anderson, T. L., & Ogren, J. A. (1998). Determining Aerosol Radiative Properties Using the TSI 3563 Integrating Nephelometer. *Aerosol Science and Technology*, *29*(1), 57–69. https://doi.org/10.1080/02786829808965551

Ansmann, A., Ohneiser, K., Chudnovsky, A., Baars, H., & Engelmann, R. (2021). CALIPSO Aerosol-Typing Scheme Misclassified Stratospheric Fire Smoke: Case Study From the 2019 Siberian Wildfire Season. *Frontiers in Environmental Science*, *9*. https://doi.org/10.3389/fenvs.2021.769852

Ansmann, A., Wandinger, U., Le Rille, O., Lajas, D., Straume, A. G., Rille, O. Le, Lajas, D., & Straume, A. G. (2007). Particle backscatter and extinction profiling with the spaceborne high-spectral-resolution Doppler lidar ALADIN: methodology and simulations. *Applied Optics*, *46*(26), 6606. https://doi.org/10.1364/AO.46.006606

Ansmann, A., Wandinger, U., Riebesell, M., Weitkamp, C., & Michaelis, W. (1992). Independent measurement of extinction and backscatter profiles in cirrus clouds by using a combined Raman elastic-backscatter lidar. *Appl. Opt.*, *31*(33), 7113–7131. https://doi.org/10.1364/AO.31.007113

Arshinov, Y., Bobrovnikov, S., Serikov, I., Ansmann, A., Wandinger, U., Althausen, D., Mattis, I., & Müller, D. (2005). Daytime operation of a pure rotational Raman lidar by use of a Fabry–Perot interferometer. *Applied Optics*, *44*(17), 3593. https://doi.org/10.1364/AO.44.003593

Aubry, C., Delanoë, J., Gross, S., Ewald, F., Tridon, F., Jourdan, O., & Mioche, G. (2024). Lidar–radar synergistic method to retrieve ice, supercooled water and mixed-phase cloud properties. *Atmospheric Measurement Techniques*, *17*(12), 3863–3881. https://doi.org/10.5194/amt-17-3863-2024

Austin, R. T., Heymsfield, A. J., & Stephens, G. L. (2009). Retrieval of ice cloud microphysical parameters using the CloudSat millimeter-wave radar and temperature. *Journal of Geophysical Research: Atmospheres*, *114*(D8). https://doi.org/10.1029/2008JD010049

Austin, R. T., & Stephens, G. L. (2001). Retrieval of stratus cloud microphysical parameters using millimeter-wave radar and visible optical depth in preparation for CloudSat: 1. Algorithm formulation. *Journal of Geophysical Research: Atmospheres*, *106*(D22), 28233–28242. https://doi.org/10.1029/2000JD000293

Avery, M. A., Ryan, R. A., Getzewich, B. J., Vaughan, M. A., Winker, D. M., Hu, Y., Garnier, A., Pelon, J., & Verhappen, C. A. (2020). CALIOP V4 cloud thermodynamic phase assignment and the impact of near-nadir viewing angles. *Atmospheric Measurement Techniques*, *13*(8), 4539–4563. https://doi.org/10.5194/amt-13-4539-2020

Awaka, J., & Brodzik, S. (2019). Improvements of GPM DPR Rain type Classification Algorithm. *IGARSS 2019 - 2019 IEEE International Geoscience and Remote Sensing Symposium*, 4470–4472. https://doi.org/10.1109/IGARSS.2019.8898365

Awaka, J., Le, M., Brodzik, S., Kubota, T., Masaki, T., Chandrasekar, V., & Iguchi, T. (2021). Development of Precipitation Type Classification Algorithms for a Full Scan Mode of GPM Dual-frequency Precipitation Radar. *Journal of the Meteorological Society of Japan. Ser. II*, *99*(5). https://doi.org/10.2151/jmsj.2021-061

Awaka, J., Le, M., Chandrasekar, V., Yoshida, N., Higashiuwatoko, T., Kubota, T., & Iguchi, T. (2016). Rain Type Classification Algorithm Module for GPM Dual-Frequency Precipitation Radar. *Journal of Atmospheric and Oceanic Technology*, *33*(9), 1887–1898. https://doi.org/10.1175/JTECH-D-16-0016.1

Baars, H., Ansmann, A., Engelmann, R., & Althausen, D. (2008). Continuous monitoring of the boundary-layer top with lidar. *Atmospheric Chemistry and Physics*, *8*(23), 7281–7296. https://doi.org/10.5194/acp-8-7281-2008

Baars, H., Kanitz, T., Engelmann, R., Althausen, D., Heese, B., Komppula, M., Preißler, J., Tesche, M., Ansmann, A., Wandinger, U., Lim, J.-H., Ahn, J. Y., Stachlewska, I. S., Amiridis, V., Marinou, E., Seifert, P., Hofer, J., Skupin, A., Schneider, F., … Zamorano, F. (2016). An overview of the first decade of PollyNET: an emerging network of automated Raman-polarization lidars for continuous aerosol profiling. *Atmospheric Chemistry and Physics*, *16*(8), 5111–5137. https://doi.org/10.5194/acp-16-5111-2016

Baars, H., Radenz, M., Floutsi, A. A., Engelmann, R., Althausen, D., Heese, B., Ansmann, A., Flament, T., Dabas, A., Trapon, D., Reitebuch, O., Bley, S., & Wandinger, U. (2021). Californian Wildfire Smoke Over Europe: A First Example of the Aerosol Observing Capabilities of Aeolus Compared to Ground-Based Lidar. *Geophysical Research Letters*, *48*(8). https://doi.org/10.1029/2020GL092194

Baedi, R. J. . J. P., de Wit, J. J. . J. M., Russchenberg, H. W. . W. J., Erkelens, J. . S., Baptista, J. P. V. P., & Poiares Baptista, J. P. . (2000). Estimating effective radius and liquid water content from

radar and lidar based on the CLARE98 data-set. *Physics and Chemistry of the Earth, Part B: Hydrology, Oceans and Atmosphere*, *25*(10–12), 1057–1062. https://doi.org/10.1016/S1464-1909(00)00152-0

Barker, H. W., Gabriel, P. M., Qu, Z., & Kato, S. (2021). Representativity of cloud-profiling radar observations for data assimilation in numerical weather prediction. *Quarterly Journal of the Royal Meteorological Society*, *147*(736), 1801–1822. https://doi.org/10.1002/qj.3996

Barker, H. W., Jerg, M. P., Wehr, T., Kato, S., Donovan, D. P., & Hogan, R. J. (2011). A 3D cloud-construction algorithm for the EarthCARE satellite mission. *Quarterly Journal of the Royal Meteorological Society*, *137*(657), 1042–1058. https://doi.org/10.1002/qj.824

Barker, H. W., Korolev, A. V., Hudak, D. R., Strapp, J. W., Strawbridge, K. B., & Wolde, M. (2008). A comparison between CloudSat and aircraft data for a multilayer, mixed phase cloud system during the Canadian CloudSat-CALIPSO Validation Project. *Journal of Geophysical Research: Atmospheres*, *113*(D8). https://doi.org/10.1029/2008JD009971

Barker, H. W., & Li, Z. (1997). Interpreting shortwave albedo-transmittance plots: True or apparent anomalous absorption? *Geophysical Research Letters*, *24*(16), 2023–2026. https://doi.org/10.1029/97GL02019

Barros, A., Petersen, W., Schwaller, M., Cifelli, R., Mahoney, K., Peters-Liddard, C., Shepherd, M., Nesbitt, S., Wolff, D., Heymsfield, G., & others. (2014). *NASA GPM-Ground Validation: Integrated Precipitation and Hydrology Experiment 2014 Science Plan.*

Battaglia, A., Haynes, J. M., L'Ecuyer, T., & Simmer, C. (2008). Identifying multiple-scattering-affected profiles in CloudSat observations over the oceans. *Journal of Geophysical Research: Atmospheres*, *113*(D8). https://doi.org/10.1029/2008JD009960

Battaglia, A., & Kollias, P. (2015). Using Ice Clouds for Mitigating the EarthCARE Doppler Radar Mispointing. *IEEE Transactions on Geoscience and Remote Sensing*, *53*(4), 2079–2085. https://doi.org/10.1109/TGRS.2014.2353219

Battaglia, A., & Panegrossi, G. (2020). What Can We Learn from the CloudSat Radiometric Mode Observations of Snowfall over the Ice-Free Ocean? *Remote Sensing*, *12*(20), 3285. https://doi.org/10.3390/rs12203285

Battaglia, A., Tanelli, S., Heymsfield, G. M., & Tian, L. (2014a). The Dual Wavelength Ratio Knee: A Signature of Multiple Scattering in Airborne Ku–Ka Observations. *Journal of Applied Meteorology and Climatology*, *53*(7), 1790–1808. https://doi.org/10.1175/JAMC-D-13-0341.1

Battaglia, A., Tanelli, S., Kobayashi, S., Zrnic, D., Hogan, R. J., & Simmer, C. (2010). Multiple-scattering in radar systems: A review. *Journal of Quantitative Spectroscopy and Radiative Transfer*, *111*(6), 917–947. https://doi.org/10.1016/j.jqsrt.2009.11.024

Battaglia, A., Tanelli, S., Mroz, K., & Tridon, F. (2015). Multiple scattering in observations of the GPM dual-frequency precipitation radar: Evidence and impact on retrievals. *Journal of Geophysical Research: Atmospheres*, *120*(9), 4090–4101. https://doi.org/10.1002/2014JD022866

Battaglia, A., Westbrook, C. D., Kneifel, S., Kollias, P., Humpage, N., Löhnert, U., Tyynelä, J., & Petty, G. W. (2014b). G band atmospheric radars: new frontiers in cloud physics. *Atmospheric Measurement Techniques*, *7*(6), 1527–1546. https://doi.org/10.5194/amt-7-1527-2014

Bauer, M., Genio, A. D. Del, & Lanzante, J. R. (2002). Observed and Simulated Temperature–Humidity Relationships: Sensitivity to Sampling and Analysis. *Journal of Climate*, *15*(2), 203–215. https://doi.org/https://doi.org/10.1175/1520-0442(2002)015<0203:OASTHR>2.0.CO;2

Baumgardner, D., Abel, S. J., Axisa, D., Cotton, R., Crosier, J., Field, P., Gurganus, C., Heymsfield, A., Korolev, A., Krämer, M., Lawson, P., McFarquhar, G., Ulanowski, Z., & Um, J. (2017). Cloud Ice Properties: In Situ Measurement Challenges. *Meteorological Monographs*, *58*, 9.1-9.23.

https://doi.org/10.1175/AMSMONOGRAPHS-D-16-0011.1

Baumgardner, D., Dye, J. E., Gandrud, B. W., & Knollenberg, R. G. (1992). Interpretation of measurements made by the forward scattering spectrometer probe (FSSP-300) during the Airborne Arctic Stratospheric Expedition. *Journal of Geophysical Research: Atmospheres*, *97*(D8), 8035–8046. https://doi.org/10.1029/91JD02728

Bedka, K. M., Nehrir, A. R., Kavaya, M., Barton-Grimley, R., Beaubien, M., Carroll, B., Collins, J., Cooney, J., Emmitt, G. D., Greco, S., Kooi, S., Lee, T., Liu, Z., Rodier, S., & Skofronick-Jackson, G. (2021). Airborne lidar observations of wind, water vapor, and aerosol profiles during the NASA Aeolus calibration and validation (Cal/Val) test flight campaign. *Atmospheric Measurement Techniques*, *14*(6), 4305–4334. https://doi.org/10.5194/amt-14-4305-2021

Belegante, L., Bravo-Aranda, J. A., Freudenthaler, V., Nicolae, D., Nemuc, A., Ene, D., Alados-Arboledas, L., Amodeo, A., Pappalardo, G., D'Amico, G., Amato, F., Engelmann, R., Baars, H., Wandinger, U., Papayannis, A., Kokkalis, P., & Pereira, S. N. (2018). Experimental techniques for the calibration of lidar depolarization channels in EARLINET. *Atmospheric Measurement Techniques*, *11*(2), 1119–1141. https://doi.org/10.5194/amt-11-1119-2018

Benjamin, S. G., Dévényi, D., Weygandt, S. S., Brundage, K. J., Brown, J. M., Grell, G. A., Kim, D., Schwartz, B. E., Smirnova, T. G., Smith, T. L., & Manikin, G. S. (2004). An Hourly Assimilation–Forecast Cycle: The RUC. *Monthly Weather Review*, *132*(2), 495–518. https://doi.org/10.1175/1520-0493(2004)132<0495:AHACTR>2.0.CO;2

Behrangi, A., Lebsock, M., Wong, S., & Lambrigtsen, B. (2012). On the quantification of oceanic rainfall using spaceborne sensors. Journal of Geophysical Research: Atmospheres, 117(D20). https://doi.org/10.1029/2012JD017979

Berg, W., L'Ecuyer, T., & Haynes, J. M. (2010). The distribution of rainfall over oceans from spaceborne radars. Journal of Applied Meteorology and Climatology, 49(3), 535-543. https://doi.org/10.1175/2009JAMC2330.1

Berne, A., & Krajewski, W. F. (2013). Radar for hydrology: Unfulfilled promise or unrecognized potential? *Advances in Water Resources*, *51*, 357–366. https://doi.org/10.1016/j.advwatres.2012.05.005

Beyerle, G. (1994). Untersuchungen stratosphärischer Aerosole vulkanischen Ursprungs und polarer stratosphärischer Wolken mit einem Mehrwellen-Lidar auf Spitzbergen (79°N, 12°E) = Multiwavelength lidar measurements of stratospheric volcanic aerosols and polar stratospheric c. In *Berichte zur Polarforschung (Reports on Polar Research)* (Vol. 138). Alfred Wegener Institute for Polar and Marine Research. https://doi.org/10.2312/BzP_0138_1994

Biele, J., Beyerle, G., & Baumgarten, G. (2000). Polarization Lidar: Correction of instrumental effects. *Optics Express*, *7*(12), 427. https://doi.org/10.1364/OE.7.000427

Biswas, S. K., & Chandrasekar, V. (2018). Cross-Validation of Observations between the GPM Dual-Frequency Precipitation Radar and Ground Based Dual-Polarization Radars. *Remote Sensing*, *10*(11), 1773. https://doi.org/10.3390/rs10111773

Bley, S., Rennie, M., Žagar, N., Sole, M. P., Straume, A. G., Antifaev, J., Candido, S., Carver, R., Fehr, T., von Bismarck, J., Hünerbein, A., Deneke, H., Pinol Sole, M., Straume, A. G., Antifaev, J., Candido, S., Carver, R., Fehr, T., von Bismarck, J., … Deneke, H. (2022). Validation of the Aeolus L2B Rayleigh winds and ECMWF short-range forecasts in the upper troposphere and lower stratosphere using Loon super pressure balloon observations. *Quarterly Journal of the Royal Meteorological Society*, *148*(749), 3852–3868. https://doi.org/10.1002/qj.4391

Bohlmann, S., Baars, H., Radenz, M., Engelmann, R., & Macke, A. (2018). Ship-borne aerosol profiling with lidar over the Atlantic Ocean: from pure marine conditions to complex dust–smoke mixtures. *Atmospheric Chemistry and Physics*, *18*(13), 9661–9679. https://doi.org/10.5194/acp-18-9661-2018

Böhm, J. P. (1992). A general hydrodynamic theory for mixed-phase microphysics. Part III: Riming and aggregation. *Atmospheric Research*, *28*(2), 103–123. https://doi.org/10.1016/0169-8095(92)90023-4

Borne, M., Knippertz, P., Weissmann, M., Witschas, B., Flamant, C., Rios-Berrios, R., & Veals, P. (2024). Validation of Aeolus L2B products over the tropical Atlantic using radiosondes. *Atmospheric Measurement Techniques*, *17*(2), 561–581. https://doi.org/10.5194/amt-17-561-2024

Borovoi, A., Konoshonkin, A., Kustova, N., & Okamoto, H. (2012). Backscattering Mueller matrix for quasi-horizontally oriented ice plates of cirrus clouds: application to CALIPSO signals. *Optics Express*, *20*(27), 28222. https://doi.org/10.1364/OE.20.028222

Botta, G., Aydin, K., & Verlinde, J. (2010). Modeling of Microwave Scattering From Cloud Ice Crystal Aggregates and Melting Aggregates: A New Approach. *IEEE Geoscience and Remote Sensing Letters*, *7*(3), 572–576. https://doi.org/10.1109/LGRS.2010.2041633

Bouyssel, F., Berre, L., Bénichou, H., Chambon, P., Girardot, N., Guidard, V., Loo, C., Mahfouf, J.-F., Moll, P., Payan, C., & Raspaud, D. (2022). The 2020 Global Operational NWP Data Assimilation System at Météo-France. In S. K. Park & L. Xu (Eds.), *Data Assimilation for Atmospheric, Oceanic and Hydrologic Applications (Vol. IV)* (pp. 645–664). Springer International Publishing. https://doi.org/10.1007/978-3-030-77722-7_25

Bracci, A., Baldini, L., Roberto, N., Adirosi, E., Montopoli, M., Scarchilli, C., Grigioni, P., Ciardini, V., Levizzani, V., & Porcù, F. (2021). Quantitative Precipitation Estimation over Antarctica Using Different Ze-SR Relationships Based on Snowfall Classification Combining Ground Observations. *Remote Sensing*, *14*(1), 82. https://doi.org/10.3390/rs14010082

Bracci, A., Sato, K., Baldini, L., Porcù, F., & Okamoto, H. (2023). Development of a methodology for evaluating spaceborne W-band Doppler radar by combined use of Micro Rain Radar and a disdrometer in Antarctica. *Remote Sensing of Environment*, *294*, 113630. https://doi.org/10.1016/j.rse.2023.113630

Brandes, E. A., Zhang, G., & Vivekanandan, J. (2005). Corrigendum. *Journal of Applied Meteorology*, *44*(1). https://doi.org/10.1175/1520-0450(2005)44<186:C>2.0.CO;2

Bravo-Aranda, J. A., De-Arruda-Moreira, G., Navas-Guzmán, F., Granados-Muñoz, M. J., Guerrero-Rascado, J. L., Pozo-Vázquez, D., Arbizu-Barrena, C., Olmo, F. J., Mallet, M., & Alados-Arboledas, L. (2016). PBL height estimation based on lidar depolarisation measurements (POLARIS). *Atmospheric Chemistry and Physics Discussions*, *2016*, 1–24. https://doi.org/10.5194/acp-2016-718

Bringi, V., Mishra, K. V., Thurai, M., Kennedy, P. C., & Raupach, T. H. (2020). Retrieval of lower-order moments of the drop size distribution using CSU-CHILL X-band polarimetric radar: a case study. *Atmospheric Measurement Techniques*, *13*(9), 4727–4750. https://doi.org/10.5194/amt-13-4727-2020

Bringi, V. N., & Chandrasekar, V. (2001). *Polarimetric Doppler Weather Radar*. Cambridge University Press. https://doi.org/10.1017/CBO9780511541094

Brousseau, P., Seity, Y., Ricard, D., & Léger, J. (2016). Improvement of the forecast of convective activity from the AROME-France system. *Quarterly Journal of the Royal Meteorological Society*, *142*(699), 2231–2243. https://doi.org/https://doi.org/10.1002/qj.2822

Bruneau, D., Pelon, J., Blouzon, F., Spatazza, J., Genau, P., Buchholtz, G., Amarouche, N., Abchiche, A., & Aouji, O. (2015). 355-nm high spectral resolution airborne lidar LNG: system description and first results. *Applied Optics*, *54*(29), 8776. https://doi.org/10.1364/AO.54.008776

Buch, E., Madsen, M. S., She, J., Stendel, M., Leth, O. K., Fjæraa, A. M., & Rattenborg, M. (2019). *ARCTIC IN SITU DATA AVAILABILITY*.

https://insitu.copernicus.eu/library/reports/CopernicusArcticDataReportFinalVersion2.1.pdf

Bukovčić, P., Ryzhkov, A., & Zrnić, D. (2020). Polarimetric Relations for Snow Estimation—Radar Verification. *Journal of Applied Meteorology and Climatology*, *59*(5), 991–1009. https://doi.org/10.1175/JAMC-D-19-0140.1

Burton, S. P., Ferrare, R. A., Hostetler, C. A., Hair, J. W., Kittaka, C., Vaughan, M. A., Obland, M. D., Rogers, R. R., Cook, A. L., Harper, D. B., & Remer, L. A. (2010). Using airborne high spectral resolution lidar data to evaluate combined active plus passive retrievals of aerosol extinction profiles. *Journal of Geophysical Research: Atmospheres*, *115*(D4). https://doi.org/10.1029/2009JD012130

Burton, S. P., Ferrare, R. A., Hostetler, C. A., Hair, J. W., Rogers, R. R., Obland, M. D., Butler, C. F., Cook, A. L., Harper, D. B., & Froyd, K. D. (2012). Aerosol classification using airborne High Spectral Resolution Lidar measurements – methodology and examples. *Atmospheric Measurement Techniques*, *5*(1), 73–98. https://doi.org/10.5194/amt-5-73-2012

Burton, S. P., Ferrare, R. A., Vaughan, M. A., Omar, A. H., Rogers, R. R., Hostetler, C. A., & Hair, J. W. (2013). Aerosol classification from airborne HSRL and comparisons with the CALIPSO vertical feature mask. *Atmospheric Measurement Techniques*, *6*(5), 1397–1412. https://doi.org/10.5194/amt-6-1397-2013

Burton, S. P., Hair, J. W., Kahnert, M., Ferrare, R. A., Hostetler, C. A., Cook, A. L., Harper, D. B., Berkoff, T. A., Seaman, S. T., Collins, J. E., Fenn, M. A., & Rogers, R. R. (2015). Observations of the spectral dependence of linear particle depolarization ratio of aerosols using NASA Langley airborne High Spectral Resolution Lidar. *Atmospheric Chemistry and Physics*, *15*(23), 13453–13473. https://doi.org/10.5194/acp-15-13453-2015

Burton, S. P., Hostetler, C. A., Cook, A. L., Hair, J. W., Seaman, S. T., Scola, S., Harper, D. B., Smith, J. A., Fenn, M. A., Ferrare, R. A., Saide, P. E., Chemyakin, E. V., & Müller, D. (2018). Calibration of a high spectral resolution lidar using a Michelson interferometer, with data examples from ORACLES. *Applied Optics*, *57*(21), 6061. https://doi.org/10.1364/AO.57.006061

Campanelli, M., Estellés, V., Tomasi, C., Nakajima, T., Malvestuto, V., & Martínez-Lozano, J. A. (2007). Application of the SKYRAD Improved Langley plot method for the in situ calibration of CIMEL Sun-sky photometers. *Applied Optics*, *46*(14), 2688. https://doi.org/10.1364/AO.46.002688

Campanelli, M., Nakajima, T., & Olivieri, B. (2004). Determination of the solar calibration constant for a sun-sky radiometer: proposal of an in-situ procedure. *Applied Optics*, *43*(3), 651. https://doi.org/10.1364/AO.43.000651

Campbell, J. R., Hlavka, D. L., Welton, E. J., Flynn, C. J., Turner, D. D., Spinhirne, J. D., Scott, V. S., & Hwang, I. H. (2002). Full-Time, Eye-Safe Cloud and Aerosol Lidar Observation at Atmospheric Radiation Measurement Program Sites: Instruments and Data Processing. *Journal of Atmospheric and Oceanic Technology*, *19*(4), 431–442. https://doi.org/10.1175/1520-0426(2002)019<0431:FTESCA>2.0.CO;2

Campbell, J. R., Reid, J. S., Westphal, D. L., Zhang, J., Hyer, E. J., & Welton, E. J. (2010). CALIOP Aerosol Subset Processing for Global Aerosol Transport Model Data Assimilation. *IEEE Journal of Selected Topics in Applied Earth Observations and Remote Sensing*, *3*(2), 203–214. https://doi.org/10.1109/JSTARS.2010.2044868

Campbell, J. R., Sassen, K., & Welton, E. J. (2008). Elevated Cloud and Aerosol Layer Retrievals from Micropulse Lidar Signal Profiles. *Journal of Atmospheric and Oceanic Technology*, *25*(5), 685–700. https://doi.org/10.1175/2007JTECHA1034.1

Camplani A, Sanò P, Casella D, Panegrossi G, Battaglia A. Arctic Weather Satellite Sensitivity to Supercooled Liquid Water in Snowfall Conditions. Remote Sensing. 2024; 16(22):4164. https://doi.org/10.3390/rs16224164

Carroll, B. J., Nehrir, A. R., Kooi, S. A., Collins, J. E., Barton-Grimley, R. A., Notari, A., Harper, D. B., & Lee, J. (2022). Differential absorption lidar measurements of water vapor by the High Altitude Lidar Observatory (HALO): retrieval framework and first results. *Atmospheric Measurement Techniques*, *15*(3), 605–626. https://doi.org/10.5194/amt-15-605-2022

Casella, D., Panegrossi, G., Sanò, P., Marra, A. C., Dietrich, S., Johnson, B. T., & Kulie, M. S. (2017). Evaluation of the GPM-DPR snowfall detection capability: Comparison with CloudSat-CPR. *Atmospheric Research*, *197*, 64–75. https://doi.org/10.1016/j.atmosres.2017.06.018

Casella, G., & Berger, R. L. (1990). Statistical Inference. *Duxbury Press*.

Cazenave, Q., Ceccaldi, M., Delanoë, J., Pelon, J., Gross, S., & Heymsfield, A. (2019). Evolution of DARDAR-CLOUD ice cloud retrievals: new parameters and impacts on the retrieved microphysical properties. *Atmospheric Measurement Techniques*, *12*(5), 2819–2835. https://doi.org/10.5194/amt-12-2819-2019

Ceccaldi, M., Delanoë, J., Hogan, R. J., Pounder, N. L., Protat, A., & Pelon, J. (2013). From CloudSat-CALIPSO to EarthCare: Evolution of the DARDAR cloud classification and its comparison to airborne radar-lidar observations. *Journal of Geophysical Research: Atmospheres*, *118*(14), 7962–7981. https://doi.org/10.1002/jgrd.50579

Chan, M. A., & Comiso, J. C. (2011). Cloud features detected by MODIS but not by CloudSat and CALIOP. *Geophysical Research Letters*, *38*(24). https://doi.org/10.1029/2011GL050063

Chandrasekar, V., Baldini, L., Bharadwaj, N., & Smith, P. L. (2015). *Calibration Procedures for Global Precipitation-Measurement Ground-Validation Radars*.

Chandrasekar, V., Hou, A., Smith, E., Bringi, V. N., Rutledge, S. A., Gorgucci, E., Petersen, W. A., & Jackson, G. S. (2008). POTENTIAL ROLE OF DUAL-POLARIZATION RADAR IN THE VALIDATION OF SATELLITE PRECIPITATION MEASUREMENTS. *Bulletin of the American Meteorological Society*, *89*(8), 1127–1146. https://doi.org/10.1175/2008BAMS2177.1

Chandrasekar, V., Keränen, R., Lim, S., & Moisseev, D. (2013). Recent advances in classification of observations from dual polarization weather radars. *Atmospheric Research*, *119*, 97–111. https://doi.org/10.1016/j.atmosres.2011.08.014

Chang, I., Gao, L., Burton, S. P., Chen, H., Diamond, M. S., Ferrare, R. A., Flynn, C. J., Kacenelenbogen, M., LeBlanc, S. E., Meyer, K. G., Pistone, K., Schmidt, S., Segal-Rozenhaimer, M., Shinozuka, Y., Wood, R., Zuidema, P., Redemann, J., & Christopher, S. A. (2021). Spatiotemporal Heterogeneity of Aerosol and Cloud Properties Over the Southeast Atlantic: An Observational Analysis. *Geophysical Research Letters*, *48*(7). https://doi.org/10.1029/2020GL091469

Chase, R. J., Nesbitt, S. W., McFarquhar, G. M., Wood, N. B., & Heymsfield, G. M. (2022). Direct comparisons between GPM-DPR and CloudSat snowfall retrievals. Journal of Applied Meteorology and Climatology, 61(9), 1257-1271 . https://doi.org/10.1 175/JAMC-D-21-0081 .1

Chazette, P., Marnas, F., & Totems, J. (2014). The mobile Water vapor Aerosol Raman LIdar and its implication in the framework of the HyMeX and ChArMEx programs: application to a dust transport process. *Atmospheric Measurement Techniques*, *7*(6), 1629–1647. https://doi.org/10.5194/amt-7-1629-2014

Chazette, P., Totems, J., Baron, A., Flamant, C., & Bony, S. (2020). Trade-wind clouds and aerosols characterized by airborne horizontal lidar measurements during the EUREC⁴A field campaign. *Earth System Science Data*, *12*(4), 2919–2936. https://doi.org/10.5194/essd-12-2919-2020

Chen, H., Chandrasekar, V., & Bechini, R. (2017). An Improved Dual-Polarization Radar Rainfall Algorithm (DROPS2.0): Application in NASA IFloodS Field Campaign. *Journal of Hydrometeorology*, *18*(4), 917–937. https://doi.org/10.1175/JHM-D-16-0124.1

Chimot, J., Veefkind, J. P., Vlemmix, T., and Levelt, P. F.: Spatial distribution analysis of the OMI aerosol layer height: a pixel-by-pixel comparison to CALIOP observations, Atmos. Meas. Tech., 11, 2257–2277, https://doi.org/10.5194/amt-11-2257-2018, 2018.

Chiu, J. C., Huang, C., Marshak, A., Slutsker, I., Giles, D. M., Holben, B. N., Knyazikhin, Y., & Wiscombe, W. J. (2010). Cloud optical depth retrievals from the Aerosol Robotic Network (AERONET) cloud mode observations. *Journal of Geophysical Research: Atmospheres*, *115*(D14). https://doi.org/10.1029/2009JD013121

Christensen, M. W., Stephens, G. L., & Lebsock, M. D. (2013). Exposing biases in retrieved low cloud properties from CloudSat: A guide for evaluating observations and climate data. *Journal of Geophysical Research: Atmospheres*, *118*(21). https://doi.org/10.1002/2013JD020224

Ciach, G. J., & Krajewski, W. F. (1999). Radar–Rain Gauge Comparisons under Observational Uncertainties. *Journal of Applied Meteorology*, *38*(10), 1519–1525. https://doi.org/10.1175/1520-0450(1999)038<1519:RRGCUO>2.0.CO;2

Clothiaux, E. E., Ackerman, T. P., Mace, G. G., Moran, K. P., Marchand, R. T., Miller, M. A., & Martner, B. E. (2000). Objective Determination of Cloud Heights and Radar Reflectivities Using a Combination of Active Remote Sensors at the ARM CART Sites. *Journal of Applied Meteorology*, *39*(5), 645–665. https://doi.org/10.1175/1520-0450(2000)039<0645:ODOCHA>2.0.CO;2

Cole, J. N. S., Barker, H. W., Qu, Z., Villefranque, N., & Shephard, M. W. (2023). Broadband radiative quantities for the EarthCARE mission: the ACM-COM and ACM-RT products. *Atmospheric Measurement Techniques*, *16*(18), 4271–4288. https://doi.org/10.5194/amt-16-4271-2023

Comerón, A., Muñoz-Porcar, C., Rodríguez-Gómez, A., Sicard, M., Dios, F., Gil-Díaz, C., dos Santos Oliveira, D. C. F., & Rocadenbosch, F. (2023). An explicit formulation for the retrieval of the overlap function in an elastic and Raman aerosol lidar. *Atmospheric Measurement Techniques*, *16*(11), 3015–3025. https://doi.org/10.5194/amt-16-3015-2023

Comerón, A., Sicard, M., & Rocadenbosch, F. (2013). Wavelet Correlation Transform Method and Gradient Method to Determine Aerosol Layering from Lidar Returns: Some Comments. *Journal of Atmospheric and Oceanic Technology*, *30*(6), 1189–1193. https://doi.org/10.1175/JTECH-D-12-00233.1

Cooper, K. B., Roy, R. J., Dengler, R., Monje, R. R., Alonso-Delpino, M., Siles, J. V., Yurduseven, O., Parashare, C., Millan, L., & Lebsock, M. (2021). G-Band Radar for Humidity and Cloud Remote Sensing. *IEEE Transactions on Geoscience and Remote Sensing*, *59*(2), 1106–1117. https://doi.org/10.1109/TGRS.2020.2995325

Cox, C., & Munk, W. (1956). Slopes of the sea surface deduced from photographs of sun glitter. *Bulletin of the Scripps Institution of Oceanography*, *6*(9), 401–488.

D'Adderio, L. P., Porcu, F., Panegrossi, G., Marra, A. C., Sano, P., & Dietrich, S. (2019). Comparison of the GPM DPR Single- and Double-Frequency Products Over the Mediterranean Area. *IEEE Transactions on Geoscience and Remote Sensing*, *57*(12), 9724–9739. https://doi.org/10.1109/TGRS.2019.2928871

D'Almeida, G. A., Koepke, P., & Shettle, E. P. (1991). Atmospheric Aerosols: Global Climatology and Radiative Characteristics. *A. Deepak*, 561.

D'Amico, M. M. G., Holt, A. R., & Capsoni, C. (1998). An anisotropic model of the melting layer. *Radio Science*, *33*(3), 535–552. https://doi.org/10.1029/97RS03049

Darbyshire, E., Morgan, W. T., Allan, J. D., Liu, D., Flynn, M. J., Dorsey, J. R., O'Shea, S. J., Lowe, D., Szpek, K., Marenco, F., Johnson, B. T., Bauguitte, S., Haywood, J. M., Brito, J. F., Artaxo, P., Longo, K. M., & Coe, H. (2019). The vertical distribution of biomass burning pollution over tropical South America from aircraft in situ measurements during SAMBBA. *Atmospheric Chemistry and Physics*, *19*(9), 5771–5790. https://doi.org/10.5194/acp-19-5771-2019

Daskalopoulou, V., Raptis, P. I., Tsekeri, A., Amiridis, V., Kazadzis, S., Ulanowski, Z., Charmandaris, V., Tassis, K., & Martin, W. (2023). Linear polarization signatures of atmospheric dust with the SolPol direct-sun polarimeter. *Atmospheric Measurement Techniques*, *16*(19), 4529–4550. https://doi.org/10.5194/amt-16-4529-2023

Deaconu, L. T., Waquet, F., Josset, D., Ferlay, N., Peers, F., Thieuleux, F., Ducos, F., Pascal, N., Tanré, D., Pelon, J., & Goloub, P. (2017). Consistency of aerosols above clouds characterization from A-Train active and passive measurements. *Atmospheric Measurement Techniques*, *10*(9), 3499–3523. https://doi.org/10.5194/amt-10-3499-2017

Deepak, A., & Gerber, H. E. (1983). Report of the Experts Meeting on Aerosols and their Climatic Effects. *World Climate Program Series*, *55*, 107.

Delahaye, F., Kirstetter, P.-E., Dubreuil, V., Machado, L. A. T., Vila, D. A., & Clark, R. (2015). A consistent gauge database for daily rainfall analysis over the Legal Brazilian Amazon. *Journal of Hydrology*, *527*, 292–304. https://doi.org/10.1016/j.jhydrol.2015.04.012

Delanoë, J., & Hogan, R. J. (2008). A variational scheme for retrieving ice cloud properties from combined radar, lidar, and infrared radiometer. *Journal of Geophysical Research: Atmospheres*, *113*(D7). https://doi.org/10.1029/2007JD009000

Delanoë, J., & Hogan, R. J. (2010). Combined CloudSat-CALIPSO-MODIS retrievals of the properties of ice clouds. *Journal of Geophysical Research: Atmospheres*, *115*(D4). https://doi.org/10.1029/2009JD012346

Delanoë, J. M. E., Heymsfield, A. J., Protat, A., Bansemer, A., & Hogan, R. J. (2014). Normalized particle size distribution for remote sensing application. *Journal of Geophysical Research: Atmospheres*, *119*(7), 4204–4227. https://doi.org/10.1002/2013JD020700

Delanoë, J., Protat, A., Vinson, J.-P., Brett, W., Caudoux, C., Bertrand, F., du Chatelet, J. P., Hallali, R., Barthes, L., Haeffelin, M., Dupont, J.-C., Parent du Chatelet, J., Hallali, R., Barthes, L., Haeffelin, M., & Dupont, J.-C. (2016). BASTA: A 95-GHz FMCW Doppler Radar for Cloud and Fog Studies. *Journal of Atmospheric and Oceanic Technology*, *33*(5), 1023–1038. https://doi.org/10.1175/JTECH-D-15-0104.1

Delrieu, G., Braud, I., Berne, A., Borga, M., Boudevillain, B., Fabry, F., Freer, J., Gaume, E., Nakakita, E., Seed, A., Tabary, P., & Uijlenhoet, R. (2009). Weather radar and hydrology. *Advances in Water Resources*, *32*(7), 969–974. https://doi.org/10.1016/j.advwatres.2009.03.006

Delrieu, G., Wijbrans, A., Boudevillain, B., Faure, D., Bonnifait, L., & Kirstetter, P.-E. (2014). Geostatistical radar–raingauge merging: A novel method for the quantification of rain estimation accuracy. *Advances in Water Resources*, *71*, 110–124. https://doi.org/10.1016/j.advwatres.2014.06.005

Deng, M., Mace, G. G., Wang, Z., & Berry, E. (2015). CloudSat 2C-ICE product update with a new Z e parameterization in lidar-only region. *Journal of Geophysical Research: Atmospheres*, *120*(23). https://doi.org/10.1002/2015JD023600

Deng, M., Mace, G. G., Wang, Z., & Lawson, R. P. (2013). Evaluation of Several A-Train Ice Cloud Retrieval Products with In Situ Measurements Collected during the SPARTICUS Campaign. *Journal of Applied Meteorology and Climatology*, *52*(4), 1014–1030. https://doi.org/10.1175/JAMC-D-12-054.1

Deng, M., Mace, G. G., Wang, Z., & Okamoto, H. (2010). Tropical Composition, Cloud and Climate Coupling Experiment validation for cirrus cloud profiling retrieval using CloudSat radar and CALIPSO lidar. *Journal of Geophysical Research: Atmospheres*, *115*(D10). https://doi.org/10.1029/2009JD013104

Desroziers, G., Berre, L., Chapnik, B., & Poli, P. (2005). Diagnosis of observation, background and analysis-error statistics in observation space. *Quarterly Journal of the Royal Meteorological*

Society, *131*(613), 3385–3396. https://doi.org/10.1256/qj.05.108

Di Girolamo, P., Cacciani, M., di Sarra, A., Fiocco, G., & Fuà, D. (1994). Lidar observations of the Pinatubo aerosol layer at Thule, Greenland. *Geophysical Research Letters*, *21*(13), 1295–1298. https://doi.org/10.1029/93GL02892

Di Girolamo, P., Cosentino, A., Longo, F., Franco, N., Dionisi, D., Summa, D., Lolli, S., Suetta, E., Perna, A., & Zoffoli, S. (2023). *Introducing the Cloud Aerosol Lidar for Global Scale Observations of the Ocean-Land-Atmosphere System: CALIGOLA* (pp. 625–630). https://doi.org/10.1007/978-3-031-37818-8_80

do Carmo, J. P., de Villele, G., Wallace, K., Lefebvre, A., Ghose, K., Kanitz, T., Chassat, F., Corselle, B., Belhadj, T., & Bravetti, P. (2021). ATmospheric LIDar (ATLID): Pre-Launch Testing and Calibration of the European Space Agency Instrument That Will Measure Aerosols and Thin Clouds in the Atmosphere. *Atmosphere*, *12*(1), 76. https://doi.org/10.3390/atmos12010076

Dolan, B., Fuchs, B., Rutledge, S. A., Barnes, E. A., & Thompson, E. J. (2018). Primary Modes of Global Drop Size Distributions. *Journal of the Atmospheric Sciences*, *75*(5), 1453–1476. https://doi.org/10.1175/JAS-D-17-0242.1

Dolan, B., Kollias, P., van den Heever, S. C., Rasmussen, K. L., Oue, M., Luke, E., Lamer, K., Treserras, B. P., Haddad, Z., Stephens, G., & Chandrasekar, V. (2023). Time Resolved Reflectivity Measurements of Convective Clouds. *Geophysical Research Letters*, *50*(22). https://doi.org/10.1029/2023GL105723

Donlon, C. J., Minnett, P. J., Fox, N., & Wimmer, W. (2014). *Strategies for the Laboratory and Field Deployment of Ship-Borne Fiducial Reference Thermal Infrared Radiometers in Support of Satellite-Derived Sea Surface Temperature Climate Data Records* (pp. 557–603). https://doi.org/10.1016/B978-0-12-417011-7.00018-0

Donovan, D. P. (2003). Ice-cloud effective particle size parameterization based on combined lidar, radar reflectivity, and mean Doppler velocity measurements. *Journal of Geophysical Research: Atmospheres*, *108*(D18). https://doi.org/10.1029/2003JD003469

Donovan, D. P. (2016). The Expected Impact of Multiple Scattering on ATLID Signals. *EPJ Web of Conferences*, *119*, 1006. https://doi.org/10.1051/EPJCONF/201611901006

Donovan, D. P., Klein Baltink, H., Henzing, J. S., de Roode, S. R., & Siebesma, A. P. (2015). A depolarisation lidar-based method for the determination of liquid-cloud microphysical properties. *Atmospheric Measurement Techniques*, *8*(1), 237–266. https://doi.org/10.5194/amt-8-237-2015

Donovan, D. P., Kollias, P., Blázquez, A. V., van Zadelhoff, G.-J., Velázquez Blázquez, A., & van Zadelhoff, G.-J. (2023). The generation of EarthCARE L1 test data sets using atmospheric model data sets. *Atmospheric Measurement Techniques*, *16*(21), 5327–5356. https://doi.org/10.5194/amt-16-5327-2023

Donovan, D. P., & van Lammeren, A. C. A. P. (2001). Cloud effective particle size and water content profile retrievals using combined lidar and radar observations: 1. Theory and examples. *Journal of Geophysical Research: Atmospheres*, *106*(D21), 27425–27448. https://doi.org/10.1029/2001JD900243

Donovan, D. P., van Zadelhoff, G.-J., & Wang, P. (2024). The EarthCARE lidar cloud and aerosol profile processor (A-PRO): the A-AER, A-EBD, A-TC and A-ICE products. *EGUsphere*, *2024*, 1–57. https://doi.org/10.5194/egusphere-2024-218

Dubovik, O., Holben, B. N., Lapyonok, T., Sinyuk, A., Mishchenko, M. I., Yang, P., & Slutsker, I. (2002). Non-spherical aerosol retrieval method employing light scattering by spheroids. *Geophysical Research Letters*, *29*(10). https://doi.org/10.1029/2001GL014506

Dubovik, O., Sinyuk, A., Lapyonok, T., Holben, B. N., Mishchenko, M., Yang, P., Eck, T. F., Volten, H.,

Muñoz, O., Veihelmann, B., van der Zande, W. J., Leon, J.-F., Sorokin, M., & Slutsker, I. (2006). Application of spheroid models to account for aerosol particle nonsphericity in remote sensing of desert dust. *Journal of Geophysical Research: Atmospheres*, *111*(D11). https://doi.org/10.1029/2005JD006619

Dubovik O., Li Z., Mishchenko M.I., Tanré D., Karol Y., Bojkov B., Cairns B., Diner D.J., Espinosa W.R., Goloub P., Gu X., Hasekamp O., Hong J., Hou W., Knobelspiesse K.D., Landgraf J., Li L., Litvinov P., Liu Y., Lopatin A., Marbach T., Maring H., Martins V., Meijer Y., Milinevsky G., Mukai S., Parol F., Qiao Y., Remer L., Rietjens J., Sano I., Stammes P., Stamnes S., Sun X., Tabary P., Travis L.D., Waquet F., Xu F., Yan C., & Yin D (2019). Polarimetric remote sensing of atmospheric aerosols: Instruments, methodologies, results, and perspectives, Journal of Quantitative Spectroscopy and Radiative Transfer, 224, pp. 474 - 511, DOI: 10.1016/j.jqsrt.2018.11.024

Durden, S. L., Beauchamp, R. M., Graniello, S., Venkatesh, V., & Tanelli, S. (2023). DPCA-Based Doppler Radar Measurements from Space: Effect of System Errors on Velocity Estimation Performance. *Journal of Atmospheric and Oceanic Technology*, *40*(7), 855–864. https://doi.org/10.1175/JTECH-D-22-0048.1

Durden, S. L., Siqueira, P. R., & Tanelli, S. (2007). On the Use of Multiantenna Radars for Spaceborne Doppler Precipitation Measurements. *IEEE Geoscience and Remote Sensing Letters*, *4*(1), 181–183. https://doi.org/10.1109/LGRS.2006.887136

Duruisseau, F., Chambon, P., Faure, G., & Geer, A. (2018). Development of an active sensor module for the RTTOV-SCATT radiative transfer simulator. *International Precipitation Workshop (IPWG)*.

Eck, T. F., Holben, B. N., Reid, J. S., Arola, A., Ferrare, R. A., Hostetler, C. A., Crumeyrolle, S. N., Berkoff, T. A., Welton, E. J., Lolli, S., Lyapustin, A., Wang, Y., Schafer, J. S., Giles, D. M., Anderson, B. E., Thornhill, K. L., Minnis, P., Pickering, K. E., Loughner, C. P., … Sinyuk, A. (2014). Observations of rapid aerosol optical depth enhancements in the vicinity of polluted cumulus clouds. *Atmospheric Chemistry and Physics*, *14*(21), 11633–11656. https://doi.org/10.5194/acp-14-11633-2014

Eck, T. F., Holben, B. N., Reid, J. S., Dubovik, O., Smirnov, A., O'Neill, N. T., Slutsker, I., & Kinne, S. (1999). Wavelength dependence of the optical depth of biomass burning, urban, and desert dust aerosols. *Journal of Geophysical Research: Atmospheres*, *104*(D24), 31333–31349. https://doi.org/10.1029/1999JD900923

Ehlers, F., Flament, T., Dabas, A., Trapon, D., Lacour, A., Baars, H., & Straume-Lindner, A. G. (2022). Optimization of Aeolus' aerosol optical properties by maximum-likelihood estimation. *Atmospheric Measurement Techniques*, *15*(1), 185–203. https://doi.org/10.5194/amt-15-185-2022

Ehrlich, A., Bierwirth, E., Wendisch, M., Herber, A., & Gayet, J.-F. (2012). Airborne hyperspectral observations of surface and cloud directional reflectivity using a commercial digital camera. *Atmospheric Chemistry and Physics*, *12*(7), 3493–3510. https://doi.org/10.5194/acp-12-3493-2012

Eisinger, M., Marnas, F., Wallace, K., Kubota, T., Tomiyama, N., Ohno, Y., Tanaka, T., Tomita, E., Wehr, T., & Bernaerts, D. (2024). The EarthCARE mission: science data processing chain overview. *Atmospheric Measurement Techniques*, *17*(2), 839–862. https://doi.org/10.5194/amt-17-839-2024

Engelmann, R., Kanitz, T., Baars, H., Heese, B., Althausen, D., Skupin, A., Wandinger, U., Komppula, M., Stachlewska, I. S., Amiridis, V., Marinou, E., Mattis, I., Linné, H., & Ansmann, A. (2016). The automated multiwavelength Raman polarization and water-vapor lidar Polly^{XT}: the neXT generation. *Atmospheric Measurement Techniques*, *9*(4), 1767–1784. https://doi.org/10.5194/amt-9-1767-2016

Eriksson, P., Ekelund, R., Mendrok, J., Brath, M., Lemke, O., & Buehler, S. A. (2018). A general database of hydrometeor single scattering properties atmicrowave and sub-millimetre wavelengths. *Earth System Science Data*, *10*(3), 1301–1326. https://doi.org/10.5194/essd-10-

1301-2018

Eriksson, P., Rydberg, B., Mattioli, V., Thoss, A., Accadia, C., Klein, U., and Buehler, S. A. (2020): Towards an operational Ice Cloud Imager (ICI) retrieval product, Atmos. Meas. Tech., 13, 53–71 , https://doi.org/10.5194/amt-13-53-2020.

Eriksson, P., Ekelund, R., Mendrok, J., Brath, M., Lemke, O., and Buehler, S. A. (2018): A general database of hydrometeor single scattering properties at microwave and sub-millimetre wavelengths, Earth Syst. Sci. Data, 10, 1301–1326, https://doi.org/10.5194/essd-10-1301-2018

ESA. (2019a). *Aeolus Scientific Calibration and Validation Implementation Plan*.

ESA. (2019b). *Aeolus Scientific Calibration and Validation Requirements*.

ESA. (2020). *ESA Cloud_cci Product Validation and Intercomparison Report (PVIR)*. https://climate.esa.int/media/documents/Cloud_Product-Validation-and-Intercomparison-Report-PVIR_v6.0.pdf

Escribano, J., Di Tomaso, E., Jorba, O., Klose, M., Gonçalves Ageitos, M., Macchia, F., Amiridis, V., Baars, H., Marinou, E., Proestakis, E., Urbanneck, C., Althausen, D., Bühl, J., Mamouri, R.-E., & Pérez García-Pando, C. (2022). Assimilating spaceborne lidar dust extinction can improve dust forecasts. *Atmospheric Chemistry and Physics*, *22*(1), 535–560. https://doi.org/10.5194/acp-22-535-2022

Esselborn, M., Wirth, M., Fix, A., Tesche, M., & Ehret, G. (2008). Airborne high spectral resolution lidar for measuring aerosol extinction and backscatter coefficients. *Applied Optics*, *47*(3), 346. https://doi.org/10.1364/AO.47.000346

Estellés, V., Campanelli, M., Smyth, T. J., Utrillas, M. P., & Martínez-Lozano, J. A. (2012). Evaluation of the new ESR network software for the retrieval of direct sun products from CIMEL CE318 and PREDE POM01 sun-sky radiometers. *Atmospheric Chemistry and Physics*, *12*(23), 11619–11630. https://doi.org/10.5194/acp-12-11619-2012

Ewald, F., Gross, S., Hagen, M., Hirsch, L., Delanoë, J., & Bauer-Pfundstein, M. (2019). Calibration of a 35 GHz airborne cloud radar: lessons learned and intercomparisons with 94 GHz cloud radars. *Atmospheric Measurement Techniques*, *12*(3), 1815–1839. https://doi.org/10.5194/amt-12-1815-2019

Ewald, F., Groß, S., Wirth, M., Delanoë, J., Fox, S., & Mayer, B. (2021). Why we need radar, lidar, and solar radiance observations to constrain ice cloud microphysics. *Atmospheric Measurement Techniques*, *14*(7), 5029–5047. https://doi.org/10.5194/amt-14-5029-2021

Ewald, F., Kölling, T., Baumgartner, A., Zinner, T., & Mayer, B. (2016). Design and characterization of specMACS, a multipurpose hyperspectral cloud and sky imager. *Atmospheric Measurement Techniques*, *9*(5), 2015–2042. https://doi.org/10.5194/amt-9-2015-2016

Fabry, F., & Szyrmer, W. (1999). Modeling of the Melting Layer. Part II: Electromagnetic. *Journal of the Atmospheric Sciences*, *56*(20), 3593–3600. https://doi.org/10.1175/1520-0469(1999)056<3593:MOTMLP>2.0.CO;2

Falconi, M. T., von Lerber, A., Ori, D., Marzano, F. S., & Moisseev, D. (2018). Snowfall retrieval at X, Ka and W bands: consistency of backscattering and microphysical properties using BAECC ground-based measurements. *Atmospheric Measurement Techniques*, *11*(5), 3059–3079. https://doi.org/10.5194/amt-11-3059-2018

Faure, G., Chambon, P., & Brousseau, P. (2020). Operational Implementation of the AROME Model in the Tropics: Multiscale Validation of Rainfall Forecasts. *Weather and Forecasting*, *35*(2), 691–710. https://doi.org/https://doi.org/10.1175/WAF-D-19-0204.1

Fernald, F. G. (1984). Analysis of atmospheric lidar observations: some comments. *Appl. Opt.*, *23*(5),

652–653. https://doi.org/10.1364/AO.23.000652

Ferrare, R., Hair, J., Hostetler, C., Shingler, T., Burton, S. P., Fenn, M., Clayton, M., Scarino, A. J., Harper, D., Seaman, S., Cook, A., Crosbie, E., Winstead, E., Ziemba, L., Thornhill, L., Robinson, C., Moore, R., Vaughan, M., Sorooshian, A., … Chellappan, S. (2023). Airborne HSRL-2 measurements of elevated aerosol depolarization associated with non-spherical sea salt. *Frontiers in Remote Sensing*, *4*. https://doi.org/10.3389/frsen.2023.1143944

Fiebig, M., Petzold, A., Wandinger, U., Wendisch, M., Kiemle, C., Stifter, A., Ebert, M., Rother, T., & Leiterer, U. (2002). Optical closure for an aerosol column: Method, accuracy, and inferable properties applied to a biomass-burning aerosol and its radiative forcing. *Journal of Geophysical Research: Atmospheres*, *107*(D21). https://doi.org/10.1029/2000JD000192

Field, P. R., Hogan, R. J., Brown, P. R. A., Illingworth, A. J., Choularton, T. W., & Cotton, R. J. (2005). Parametrization of ice-particle size distributions for mid-latitude stratiform cloud. *Quarterly Journal of the Royal Meteorological Society*, *131*(609), 1997–2017. https://doi.org/10.1256/qj.04.134

Fielding, M. D., Chiu, J. C., Hogan, R. J., & Feingold, G. (2013). 3D cloud reconstructions: Evaluation of scanning radar scan strategy with a view to surface shortwave radiation closure. *Journal of Geophysical Research: Atmospheres*, *118*(16), 9153–9167. https://doi.org/10.1002/jgrd.50614

Fielding, M. D., & Janisková, M. (2020). Direct 4D-Var assimilation of space-borne cloud radar reflectivity and lidar backscatter. Part I: Observation operator and implementation. *Quarterly Journal of the Royal Meteorological Society*, *146*(733), 3877–3899. https://doi.org/10.1002/qj.3878

Fielding, M. D., & Stiller, O. (2019). Characterizing the Representativity Error of Cloud Profiling Observations for Data Assimilation. *Journal of Geophysical Research: Atmospheres*, *124*(7), 4086–4103. https://doi.org/https://doi.org/10.1029/2018JD029949

Fielding, M., & Janisková, M. (2022). Improving NWP forecasts through the direct 4D-Var assimilation of space-borne cloud radar and lidar observations. *EGU General Assembly Conference Abstracts*, EGU22-7441. https://doi.org/10.5194/egusphere-egu22-7441

Flamant, C., Pelon, J., Flamant, P. H., & Durand, P. (1997). Lidar determination of the entrainment zone thickness at the top of the unstable marine atmospheric boundary layer. *Boundary-Layer Meteorology*, *83*(2), 247–284. https://doi.org/10.1023/A:1000258318944

Flamant, P., Cuesta, J., Denneulin, M.-L., Dabas, A., & Huber, D. (2008). ADM-Aeolus retrieval algorithms for aerosol and cloud products. *Tellus A*, *60*(2), 273–288. https://doi.org/10.1111/j.1600-0870.2007.00287.x

Flamant, P., Dabas, A., Martinet, P., Lever, V., Flament, T., Trapon, D., Olivier, M., Cuesta, J., Huber, D., & Lacour, A. (2022). *Aeolus L2A Algorithm Theoretical Baseline Document – Particle spin-off products*.

Flament, T., Trapon, D., Lacour, A., Dabas, A., Ehlers, F., & Huber, D. (2021). Aeolus L2A Aerosol Optical Properties Product: Standard Correct Algorithm and Mie Correct Algorithm. *Atmos. Meas. Tech.*, *14*, 7851–7871.

Floutsi, A. A., Baars, H., Engelmann, R., Althausen, D., Ansmann, A., Bohlmann, S., Heese, B., Hofer, J., Kanitz, T., Haarig, M., Ohneiser, K., Radenz, M., Seifert, P., Skupin, A., Yin, Z., Abdullaev, S. F., Komppula, M., Filioglou, M., Giannakaki, E., … Wandinger, U. (2023). DeLiAn – a growing collection of depolarization ratio, lidar ratio and Ångström exponent for different aerosol types and mixtures from ground-based lidar observations. *Atmospheric Measurement Techniques*, *16*(9), 2353–2379. https://doi.org/10.5194/amt-16-2353-2023

Floutsi, A. A., Baars, H., & Wandinger, U. (2024). HETEAC-Flex: an optimal estimation method for aerosol typing based on lidar-derived intensive optical properties. *Atmospheric Measurement Techniques*, *17*(2), 693–714. https://doi.org/10.5194/amt-17-693-2024

Flynn, C. J., Mendoza, A., Zheng, Y., & Mathur, S. (2007). Novel polarization-sensitive micropulse lidar measurement technique. *Optics Express*, *15*(6), 2785. https://doi.org/10.1364/OE.15.002785

Formenti, P., Elbert, W., Maenhaut, W., Haywood, J., Osborne, S., & Andreae, M. O. (2003). Inorganic and carbonaceous aerosols during the Southern African Regional Science Initiative (SAFARI 2000) experiment: Chemical characteristics, physical properties, and emission data for smoke from African biomass burning. *Journal of Geophysical Research: Atmospheres*, *108*(D13). https://doi.org/10.1029/2002JD002408

Freudenthaler, V. (2016). About the effects of polarising optics on lidar signals and the Δ90 calibration. *Atmospheric Measurement Techniques*, *9*(9), 4181–4255. https://doi.org/10.5194/amt-9-4181-2016

Freudenthaler, V., Esselborn, M., Wiegner, M., Heese, B., Tesche, M., Ansmann, A., Müller, D., Althausen, D., Wirth, M., Fix, A., Ehret, G., Knippertz, P., Toledano, C., Gasteiger, J., Garhammer, M., & Seefeldner, M. (2009). *Depolarization ratio profiling at several wavelengths in pure Saharan dust during SAMUM 2006*. *61*(1). https://doi.org/10.1111/j.1600-0889.2008.00396.x

Freudenthaler, V., Linné, H., Chaikovski, A., Rabus, D., & Gross, S. (2018). EARLINET lidar quality assurance tools. *Atmos. Meas. Tech. Discuss.*

Frey, R. A., Ackerman, S. A., Liu, Y., Strabala, K. I., Zhang, H., Key, J. R., & Wang, X. (2008). Cloud Detection with MODIS. Part I: Improvements in the MODIS Cloud Mask for Collection 5. *Journal of Atmospheric and Oceanic Technology*, *25*(7), 1057–1072. https://doi.org/10.1175/2008JTECHA1052.1

Frisch, S., Shupe, M., Djalalova, I., Feingold, G., & Poellot, M. (2002). The Retrieval of Stratus Cloud Droplet Effective Radius with Cloud Radars. *Journal of Atmospheric and Oceanic Technology*, *19*(6), 835–842. https://doi.org/10.1175/1520-0426(2002)019<0835:TROSCD>2.0.CO;2

Fugal, J. P., & Shaw, R. A. (2009). Cloud particle size distributions measured with an airborne digital in-line holographic instrument. *Atmospheric Measurement Techniques*, *2*(1), 259–271. https://doi.org/10.5194/amt-2-259-2009

G. Feofilov, A., Chepfer, H., Noël, V., Guzman, R., Gindre, C., Ma, P.-L., & Chiriaco, M. (2022). Comparison of scattering ratio profiles retrieved from ALADIN/Aeolus and CALIOP/CALIPSO observations and preliminary estimates of cloud fraction profiles. *Atmospheric Measurement Techniques*.

Ganguly, D., Ginoux, P., Ramaswamy, V., Dubovik, O., Welton, J., Reid, E. A., & Holben, B. N. (2009). Inferring the composition and concentration of aerosols by combining AERONET and MPLNET data: Comparison with other measurements and utilization to evaluate GCM output. *Journal of Geophysical Research: Atmospheres*, *114*(D16). https://doi.org/10.1029/2009JD011895

Garnier, A., Pelon, J., Vaughan, M. A., Winker, D. M., Trepte, C. R., & Dubuisson, P. (2015). Lidar multiple scattering factors inferred from CALIPSO lidar and IIR retrievals of semi-transparent cirrus cloud optical depths over oceans. *Atmospheric Measurement Techniques*, *8*(7), 2759–2774. https://doi.org/10.5194/amt-8-2759-2015

Garnier, A., Pelon, J., Winker, D., Avery, M., Vaughan, M., & Hu, Y. (2023). *Identification of Mixed-Phase Clouds Using Combined CALIPSO Lidar and Imaging Infrared Radiometer Observations* (pp. 817–823). https://doi.org/10.1007/978-3-031-37818-8_105

Garrett, T. J., Fallgatter, C., Shkurko, K., & Howlett, D. (2012). Fall speed measurement and high-resolution multi-angle photography of hydrometeors in free fall. *Atmospheric Measurement Techniques*, *5*(11), 2625–2633. https://doi.org/10.5194/amt-5-2625-2012

Gasteiger, J., Gross, S., Freudenthaler, V., & Wiegner, M. (2011a). Volcanic ash from Iceland over Munich: mass concentration retrieved from ground-based remote sensing measurements. *Atmospheric Chemistry and Physics*, *11*(5), 2209–2223. https://doi.org/10.5194/acp-11-2209-

2011

Gasteiger, J., Wiegner, M., Gross, S., Freudenthaler, V., Toledano, C., Tesche, M., & Kandler, K. (2011b). Modelling lidar-relevant optical properties of complex mineral dust aerosols. *Tellus B: Chemical and Physical Meteorology*, *63*(4), 725. https://doi.org/10.1111/j.1600-0889.2011.00559.x

Gatlin, P. N., Petersen, W. A., Pippitt, J. L., Berendes, T. A., Wolff, D. B., & Tokay, A. (2020). The GPM Validation Network and Evaluation of Satellite-Based Retrievals of the Rain Drop Size Distribution. *Atmosphere*, *11*(9), 1010. https://doi.org/10.3390/atmos11091010

Geer, A. J., Baordo, F., Bormann, N., Chambon, P., English, S. J., Kazumori, M., Lawrence, H., Lean, P., Lonitz, K., & Lupu, C. (2017). The growing impact of satellite observations sensitive to humidity, cloud and precipitation. *Quarterly Journal of the Royal Meteorological Society*, *143*(709), 3189–3206. https://doi.org/10.1002/qj.3172

Geer, A. J., Bauer, P., Lonitz, K., Barlakas, V., Eriksson, P., Mendrok, J., Doherty, A., Hocking, J., & Chambon, P. (2021). Bulk hydrometeor optical properties for microwave and sub-millimetre radiative transfer in RTTOV-SCATT v13.0. *Geoscientific Model Development*, *14*(12), 7497–7526. https://doi.org/10.5194/gmd-14-7497-2021

Gelaro, R., McCarty, W., Suárez, M. J., Todling, R., Molod, A., Takacs, L., Randles, C. A., Darmenov, A., Bosilovich, M. G., Reichle, R., Wargan, K., Coy, L., Cullather, R., Draper, C., Akella, S., Buchard, V., Conaty, A., da Silva, A. M., Gu, W., … Zhao, B. (2017). The Modern-Era Retrospective Analysis for Research and Applications, Version 2 (MERRA-2). *Journal of Climate*, *30*(14), 5419–5454. https://doi.org/10.1175/JCLI-D-16-0758.1

GEOSS. (2005). *The Global Earth Observation System of Systems*.

Getzewich, B. J., Tackett, J. L., Ryan, R. A., Vaughan, M. A., Lee, K. P., Garnier, A. E., Rodier, S. D., Murray, T. D., & Beaumont, K. I. (2024). Summary of the CALIPSO V4.51 Lidar Level 1 and Level 2 Datasets. *In Preparation*.

Getzewich, B. J., Vaughan, M. A., Hunt, W. H., Avery, M. A., Powell, K. A., Tackett, J. L., Winker, D. M., Kar, J., Lee, K.-P., & Toth, T. D. (2018). CALIPSO lidar calibration at 532 nm: version 4 daytime algorithm. *Atmospheric Measurement Techniques*, *11*(11), 6309–6326. https://doi.org/10.5194/amt-11-6309-2018

Giles, D. M., Sinyuk, A., Sorokin, M. G., Schafer, J. S., Smirnov, A., Slutsker, I., Eck, T. F., Holben, B. N., Lewis, J. R., Campbell, J. R., Welton, E. J., Korkin, S. V., & Lyapustin, A. I. (2019). Advancements in the Aerosol Robotic Network (AERONET) Version 3 database – automated near-real-time quality control algorithm with improved cloud screening for Sun photometer aerosol optical depth (AOD) measurements. *Atmospheric Measurement Techniques*, *12*(1), 169–209. https://doi.org/10.5194/amt-12-169-2019

Gimmestad, G., Forrister, H., Grigas, T., O'Dowd, C., & O'Dowd, C. (2017). Comparisons of aerosol backscatter using satellite and ground lidars: implications for calibrating and validating spaceborne lidar. *Scientific Reports*, *7*(1), 42337. https://doi.org/10.1038/srep42337

Gkikas, A., Gialitaki, A., Binietoglou, I., Marinou, E., Tsichla, M., Siomos, N., Paschou, P., Kampouri, A., Voudouri, K. A., Proestakis, E., Mylonaki, M., Papanikolaou, C.-A., Michailidis, K., Baars, H., Straume, A. G., Balis, D., Papayannis, A., Parrinello, T., & Amiridis, V. (2023). First assessment of Aeolus Standard Correct Algorithm particle backscatter coefficient retrievals in the eastern Mediterranean. *Atmospheric Measurement Techniques*, *16*(4), 1017–1042. https://doi.org/10.5194/amt-16-1017-2023

Gorgucci, E., Scarchilli, G., & Chandrasekar, V. (1992). Calibration of radars using polarimetric techniques. *IEEE Transactions on Geoscience and Remote Sensing*, *30*(5), 853–858. https://doi.org/10.1109/36.175319

Gorgucci, E., Scarchilli, G., & Chandrasekar, V. (1999). A procedure to calibrate multiparameter weather radar using properties of the rain medium. *IEEE Transactions on Geoscience and Remote Sensing*, *37*(1), 269–276. https://doi.org/10.1109/36.739161

Gross, S., Esselborn, M., Weinzierl, B., Wirth, M., Fix, A., & Petzold, A. (2013). Aerosol classification by airborne high spectral resolution lidar observations. *Atmospheric Chemistry and Physics*, *13*(5), 2487–2505. https://doi.org/10.5194/acp-13-2487-2013

Gross, S., Freudenthaler, V., Schepanski, K., Toledano, C., Schäfler, A., Ansmann, A., & Weinzierl, B. (2015). Optical properties of long-range transported Saharan dust over Barbados as measured by dual-wavelength depolarization Raman lidar measurements. *Atmospheric Chemistry and Physics*, *15*, 11067–11080.

Gross, S., Freudenthaler, V., Wirth, M., & Weinzierl, B. (2015). Towards an aerosol classification scheme for future EarthCARE lidar observations and implications for research needs. *Atmospheric Science Letters*, *16*(1), 77–82. https://doi.org/10.1002/asl2.524

Gross, S., Gasteiger, J., Freudenthaler, V., Müller, T., Sauer, D., Toledano, C., & Ansmann, A. (2016). Saharan dust contribution to the Caribbean summertime boundary layer – a lidar study during SALTRACE. *Atmospheric Chemistry and Physics*, *16*(18), 11535–11546. https://doi.org/10.5194/acp-16-11535-2016

Gross, S., Tesche, M., Freudenthaler, V., Toledano, C., Wiegner, M., Ansmann, A., Althausen, D., & Seefeldner, M. (2011). Characterization of Saharan dust, marine aerosols and mixtures of biomass-burning aerosols and dust by means of multi-wavelength depolarization and Raman lidar measurements during SAMUM 2. *Tellus B*, *63*(4), 706–724. https://doi.org/10.1111/j.1600-0889.2011.00556.x

Gross, S., Wiegner, M., Freudenthaler, V., & Toledano, C. (2011). Lidar ratio of Saharan dust over Cape Verde Islands: Assessment and error calculation. *Journal of Geophysical Research*, *116*(D15). https://doi.org/10.1029/2010JD015435

Gunn, R., & Kinzer, G. D. (1949). THE TERMINAL VELOCITY OF FALL FOR WATER DROPLETS IN STAGNANT AIR. *Journal of Meteorology*, *6*(4), 243–248. https://doi.org/10.1175/1520-0469(1949)006<0243:TTVOFF>2.0.CO;2

Haarig, M., Ansmann, A., Althausen, D., Klepel, A., Gross, S., Freudenthaler, V., Toledano, C., Mamouri, R.-E., Farrell, D. A., Prescod, D. A., Marinou, E., Burton, S. P., Gasteiger, J., Engelmann, R., & Baars, H. (2017). Triple-wavelength depolarization-ratio profiling of Saharan dust over Barbados during SALTRACE in 2013 and 2014. *Atmospheric Chemistry and Physics*, *17*(17), 10767–10794. https://doi.org/10.5194/acp-17-10767-2017

Haarig, M., Ansmann, A., Baars, H., Jimenez, C., Veselovskii, I., Engelmann, R., & Althausen, D. (2018). Depolarization and lidar ratios at 355, 532, and 1064 nm and microphysical properties of aged tropospheric and stratospheric Canadian wildfire smoke. *Atmospheric Chemistry and Physics*, *18*(16), 11847–11861. https://doi.org/10.5194/acp-18-11847-2018

Haarig, M., Ansmann, A., Engelmann, R., Baars, H., Toledano, C., Torres, B., Althausen, D., Radenz, M., & Wandinger, U. (2022). First triple-wavelength lidar observations of depolarization and extinction-to-backscatter ratios of Saharan dust. *Atmospheric Chemistry and Physics*, *22*(1), 355–369. https://doi.org/10.5194/acp-22-355-2022

Haarig, M., Engelmann, R., Ansmann, A., Veselovskii, I., Whiteman, D. N., & Althausen, D. (2016). 1064 nm rotational Raman lidar for particle extinction and lidar-ratio profiling: cirrus case study. *Atmospheric Measurement Techniques*, *9*(9), 4269–4278. https://doi.org/10.5194/amt-9-4269-2016

Haarig, M., Hünerbein, A., Wandinger, U., Docter, N., Bley, S., Donovan, D., & van Zadelhoff, G.-J. (2023). Cloud top heights and aerosol columnar properties from combined EarthCARE lidar and imager observations: the AM-CTH and AM-ACD products. *Atmospheric Measurement*

Techniques, *16*(23), 5953–5975. https://doi.org/10.5194/amt-16-5953-2023

Habib, E., Ciach, G. J., & Krajewski, W. F. (2004). A method for filtering out raingauge representativeness errors from the verification distributions of radar and raingauge rainfall. *Advances in Water Resources*, *27*(10), 967–980. https://doi.org/10.1016/j.advwatres.2004.08.003

Hagen, M., Ewald, F., Gross, S., Oswald, L., Farrell, D. A., Forde, M., Gutleben, M., Heumos, J., Reimann, J., Tetoni, E., Köcher, G., Marinou, E., Kiemle, C., Li, Q., Chewitt-Lucas, R., Daley, A., Grant, D., & Hall, K. (2021). Deployment of the C-band radar Poldirad on Barbados during EUREC⁴A. *Earth System Science Data*, *13*(12), 5899–5914. https://doi.org/10.5194/essd-13-5899-2021

Hagihara, Y., Ohno, Y., Horie, H., Roh, W., Satoh, M., & Kubota, T. (2023). Global evaluation of Doppler velocity errors of EarthCARE cloud-profiling radar using a global storm-resolving simulation. *Atmospheric Measurement Techniques*, *16*(12), 3211–3219. https://doi.org/10.5194/amt-16-3211-2023

Hagihara, Y., Ohno, Y., Horie, H., Roh, W., Satoh, M., Kubota, T., & Oki, R. (2021). Assessments of Doppler Velocity Errors of EarthCARE Cloud Profiling Radar Using Global Cloud System Resolving Simulations: Effects of Doppler Broadening and Folding. *IEEE Transactions on Geoscience and Remote Sensing*, *60*, 1–9. https://doi.org/10.1109/TGRS.2021.3060828

Hagihara, Y., Okamoto, H., & Luo, Z. J. (2014). Joint analysis of cloud top heights from CloudSat and CALIPSO: New insights into cloud top microphysics. *Journal of Geophysical Research: Atmospheres*, *119*(7), 4087–4106. https://doi.org/10.1002/2013JD020919

Hagihara, Y., Okamoto, H., & Yoshida, R. (2010). Development of a combined CloudSat-CALIPSO cloud mask to show global cloud distribution. *Journal of Geophysical Research: Atmospheres*, *115*(D4). https://doi.org/10.1029/2009JD012344

Hair, J. W., Hostetler, C. A., Cook, A. L., Harper, D. B., Ferrare, R. A., Mack, T. L., Welch, W., Izquierdo, L. R., & Hovis, F. E. (2008). Airborne High Spectral Resolution Lidar for profiling aerosol optical properties. *Applied Optics*, *47*(36), 6734. https://doi.org/10.1364/AO.47.006734

Ham, S.-H., Kato, S., Rose, F. G., Sun-Mack, S., Chen, Y., Miller, W. F., & Scott, R. C. (2022). Combining Cloud Properties from CALIPSO, CloudSat, and MODIS for Top-of-Atmosphere (TOA) Shortwave Broadband Irradiance Computations: Impact of Cloud Vertical Profiles. *Journal of Applied Meteorology and Climatology*, *61*(10), 1449–1471. https://doi.org/10.1175/JAMC-D-21-0260.1

Ham, S., Kato, S., Barker, H. W., Rose, F. G., & Sun-Mack, S. (2015). Improving the modelling of short-wave radiation through the use of a 3D scene construction algorithm. *Quarterly Journal of the Royal Meteorological Society*, *141*(690), 1870–1883. https://doi.org/10.1002/qj.2491

Ham, S., Kato, S., Rose, F. G., Winker, D., L'Ecuyer, T., Mace, G. G., Painemal, D., Sun-Mack, S., Chen, Y., & Miller, W. F. (2017). Cloud occurrences and cloud radiative effects (CREs) from CERES-CALIPSO-CloudSat-MODIS (CCCM) and CloudSat radar-lidar (RL) products. *Journal of Geophysical Research: Atmospheres*, *122*(16), 8852–8884. https://doi.org/10.1002/2017JD026725

Hang, Y., L'Ecuyer, T. S., Henderson, D. S., Matus, A. V., & Wang, Z. (2019). Reassessing the Effect of Cloud Type on Earth's Energy Balance in the Age of Active Spaceborne Observations. Part II: Atmospheric Heating. *Journal of Climate*, *32*(19), 6219–6236. https://doi.org/10.1175/JCLI-D-18-0754.1

Hansen, J., Russell, G., Rind, D., Stone, P., Lacis, A., Lebedeff, S., Ruedy, R., & Travis, L. (1983). Efficient Three-Dimensional Global Models for Climate Studies: Models I and II. *Monthly Weather Review*, *111*(4), 609–662. https://doi.org/10.1175/1520-0493(1983)111<0609:ETDGMF>2.0.CO;2

Hashino, T., Satoh, M., Hagihara, Y., Kato, S., Kubota, T., Matsui, T., Nasuno, T., Okamoto, H., & Sekiguchi, M. (2016). *Evaluating Arctic cloud radiative effects simulated by NICAM with A-train*. *121*(12), 7041–7063.

Hashino, T., Satoh, M., Hagihara, Y., Kubota, T., Matsui, T., Nasuno, T., & Okamoto, H. (2013). Evaluating cloud microphysics from NICAM against CloudSat and CALIPSO. *Journal of Geophysical Research: Atmospheres*, *118*(13), 7273–7292. https://doi.org/10.1002/jgrd.50564

Hassell, D., Gregory, J., Blower, J., Lawrence, B. N., & Taylor, K. E. (2017). A data model of the Climate and Forecast metadata conventions (CF-1.6) with a software implementation (cf-python v2.1). *Geoscientific Model Development*, *10*(12), 4619–4646. https://doi.org/10.5194/gmd-10-4619-2017

Haynes, J. M., L'Ecuyer, T. S., Stephens, G. L., Miller, S. D., Mitrescu, C., Wood, N. B., & Tanelli, S. (2009). Rainfall retrieval over the ocean with spaceborne W-band radar. *Journal of Geophysical Research: Atmospheres*, *114*(D8). https://doi.org/10.1029/2008JD009973

Hegglin, M. I., Tegtmeier, S., Anderson, J., Bourassa, A. E., Brohede, S., Degenstein, D., Froidevaux, L., Funke, B., Gille, J., Kasai, Y., Kyrölä, E. T., Lumpe, J., Murtagh, D., Neu, J. L., Pérot, K., Remsberg, E. E., Rozanov, A., Toohey, M., Urban, J., … Weigel, K. (2021). Overview and update of the SPARC Data Initiative: comparison of stratospheric composition measurements from satellite limb sounders. *Earth System Science Data*, *13*(5), 1855–1903. https://doi.org/10.5194/essd-13-1855-2021

Heistermann, M., Collis, S., Dixon, M. J., Giangrande, S., Helmus, J. J., Kelley, B., Koistinen, J., Michelson, D. B., Peura, M., Pfaff, T., & Wolff, D. B. (2015). The Emergence of Open-Source Software for the Weather Radar Community. *Bulletin of the American Meteorological Society*, *96*(1), 117–128. https://doi.org/10.1175/BAMS-D-13-00240.1

Heistermann, M., Jacobi, S., & Pfaff, T. (2013). Technical Note: An open source library for processing weather radar data (<i>wradlib</i>). *Hydrology and Earth System Sciences*, *17*(2), 863–871. https://doi.org/10.5194/hess-17-863-2013

Helmus, J. J., & Collis, S. M. (2016). The Python ARM Radar Toolkit (Py-ART), a Library for Working with Weather Radar Data in the Python Programming Language. *Journal of Open Research Software*, *4*(1), 25. https://doi.org/10.5334/jors.119

Henderson, D. S., L'Ecuyer, T., Stephens, G., Partain, P., & Sekiguchi, M. (2013). A Multisensor Perspective on the Radiative Impacts of Clouds and Aerosols. *Journal of Applied Meteorology and Climatology*, *52*(4), 853–871. https://doi.org/10.1175/JAMC-D-12-025.1

Henja, A., & Michelson, D. (2012). Improving the quality of European weather radar composites with the BALTRAD toolbox. *Proceedings of the Seventh European Conference on Radar in Meteorology and Hydrology*.

Hersbach, H., Bell, B., Berrisford, P., Hirahara, S., Horányi, A., Muñoz-Sabater, J., Nicolas, J., Peubey, C., Radu, R., Schepers, D., Simmons, A., Soci, C., Abdalla, S., Abellan, X., Balsamo, G., Bechtold, P., Biavati, G., Bidlot, J., Bonavita, M., … Thépaut, J.-N. (2020). The ERA5 global reanalysis. *Quarterly Journal of the Royal Meteorological Society*, *146*(730), 1999–2049. https://doi.org/https://doi.org/10.1002/qj.3803

Herzfeld, U., Hayes, A., Palm, S., Hancock, D., Vaughan, M., & Barbieri, K. (2021). Detection and Height Measurement of Tenuous Clouds and Blowing Snow in ICESat-2 ATLAS Data. *Geophysical Research Letters*, *48*(17). https://doi.org/10.1029/2021GL093473

Heymsfield, A. J., Bansemer, A., Poellot, M. R., & Wood, N. (2015). Observations of Ice Microphysics through the Melting Layer. *Journal of the Atmospheric Sciences*, *72*(8), 2902–2928. https://doi.org/10.1175/JAS-D-14-0363.1

Heymsfield, G. M., Tian, L., Heymsfield, A. J., Li, L., & Guimond, S. (2010). Characteristics of Deep

Tropical and Subtropical Convection from Nadir-Viewing High-Altitude Airborne Doppler Radar. *Journal of the Atmospheric Sciences*, *67*(2), 285–308. https://doi.org/10.1175/2009JAS3132.1

Heymsfield, G. M., Walker McLinden, M. L., Liao, L., Helms, C. N., & Guimond, S. (2023). NASA high altitude airborne weather radars. In *Advances in Weather Radar. Volume 1: Precipitation sensing platforms* (pp. 231–282). Institution of Engineering and Technology. https://doi.org/10.1049/SBRA557F_ch7

Hitschfeld, W., & Bordan, J. (1954). ERRORS INHERENT IN THE RADAR MEASUREMENT OF RAINFALL AT ATTENUATING WAVELENGTHS. *Journal of Meteorology*, *11*(1), 58–67. https://doi.org/10.1175/1520-0469(1954)011<0058:EIITRM>2.0.CO;2

Hlavka, D. L., Palm, S. P., Hart, W. D., Spinhirne, J. D., McGill, M. J., & Welton, E. J. (2005). Aerosol and cloud optical depth from GLAS: Results and verification for an October 2003 California fire smoke case. *Geophysical Research Letters*, *32*(22). https://doi.org/10.1029/2005GL023413

Hlavka, D. L., Yorks, J. E., Young, S. A., Vaughan, M. A., Kuehn, R. E., McGill, M. J., & Rodier, S. D. (2012). Airborne validation of cirrus cloud properties derived from CALIPSO lidar measurements: Optical properties. *Journal of Geophysical Research: Atmospheres*, *117*(D9). https://doi.org/10.1029/2011JD017053

Hofer, J., Ansmann, A., Althausen, D., Engelmann, R., Baars, H., Fomba, K. W., Wandinger, U., Abdullaev, S. F., & Makhmudov, A. N. (2020). Optical properties of Central Asian aerosol relevant for spaceborne lidar applications and aerosol typing at 355 and 532 nm. *Atmospheric Chemistry and Physics*, *20*(15), 9265–9280. https://doi.org/10.5194/acp-20-9265-2020

Hogan, R., & Connor, E. (2004). *Facilitating cloud radar and lidar algorithms: the Cloudnet Instrument Synergy/Target Categorization product*.

Hogan, R. J. (1998). Dual-wavelength radar studies of clouds. *Diss. University of Reading*.

Hogan, R. J., Bouniol, D., Ladd, D. N., O'Connor, E. J., & Illingworth, A. J. (2003). Absolute Calibration of 94/95-GHz Radars Using Rain. *Journal of Atmospheric and Oceanic Technology*, *20*(4), 572–580. https://doi.org/10.1175/1520-0426(2003)20<572:ACOGRU>2.0.CO;2

Hogan, R. J., Gaussiat, N., & Illingworth, A. J. (2005). Stratocumulus Liquid Water Content from Dual-Wavelength Radar. *Journal of Atmospheric and Oceanic Technology*, *22*(8), 1207–1218. https://doi.org/10.1175/JTECH1768.1

Hogan, R. J., Honeyager, R., Tyynelä, J., & Kneifel, S. (2017). Calculating the millimetre-wave scattering phase function of snowflakes using the self-similar Rayleigh–Gans Approximation. *Quarterly Journal of the Royal Meteorological Society*, *143*(703), 834–844. https://doi.org/10.1002/qj.2968

Holben, B. N., Eck, T. F., Slutsker, I., Tanré, D., Buis, J. P., Setzer, A., Vermote, E., Reagan, J. A., Kaufman, Y. J., Nakajima, T., Lavenu, F., Jankowiak, I., & Smirnov, A. (1998). AERONET - A federated instrument network and data archive for aerosol characterization. *Remote Sensing of Environment*, *66*(1), 1–16. https://doi.org/10.1016/S0034-4257(98)00031-5

Holzer-Popp, T., de Leeuw, G., Griesfeller, J., Martynenko, D., Klüser, L., Bevan, S., Davies, W., Ducos, F., Deuzé, J. L., Graigner, R. G., Heckel, A., von Hoyningen-Hüne, W., Kolmonen, P., Litvinov, P., North, P., Poulsen, C. A., Ramon, D., Siddans, R., Sogacheva, L., … Pinnock, S. (2013). Aerosol retrieval experiments in the ESA Aerosol_cci project. *Atmospheric Measurement Techniques*, *6*(8), 1919–1957. https://doi.org/10.5194/amt-6-1919-2013

Horie, H., Iguchi, T., Hanado, H., Kuroiwa, H., Okamoto, H., & Kumagai, H. (2000). Development of a 95-GHz airborne cloud profiling radar (SPIDER) - Technical aspects. *IEICE Transactions on Communications*, *E83B*, 2010–2020.

Hou, A. Y., Kakar, R. K., Neeck, S., Azarbarzin, A. A., Kummerow, C. D., Kojima, M., Oki, R., Nakamura,

K., & Iguchi, T. (2014). The Global Precipitation Measurement Mission. *Bulletin of the American Meteorological Society*, *95*(5), 701–722. https://doi.org/10.1175/BAMS-D-13-00164.1

Houze, R. A., McMurdie, L. A., Petersen, W. A., Schwaller, M. R., Baccus, W., Lundquist, J. D., Mass, C. F., Nijssen, B., Rutledge, S. A., Hudak, D. R., Tanelli, S., Mace, G. G., Poellot, M. R., Lettenmaier, D. P., Zagrodnik, J. P., Rowe, A. K., DeHart, J. C., Madaus, L. E., Barnes, H. C., & Chandrasekar, V. (2017). The Olympic Mountains Experiment (OLYMPEX). *Bulletin of the American Meteorological Society*, *98*(10), 2167–2188. https://doi.org/10.1175/BAMS-D-16-0182.1

Hu, Q., Goloub, P., Veselovskii, I., Bravo-Aranda, J.-A., Popovici, I. E., Podvin, T., Haeffelin, M., Lopatin, A., Dubovik, O., Pietras, C., Huang, X., Torres, B., & Chen, C. (2019). Long-range-transported Canadian smoke plumes in the lower stratosphere over northern France. *Atmospheric Chemistry and Physics*, *19*(2), 1173–1193. https://doi.org/10.5194/acp-19-1173-2019

Hu, Q., Wang, H., Goloub, P., Li, Z., Veselovskii, I., Podvin, T., Li, K., & Korenskiy, M. (2020). The characterization of Taklamakan dust properties using a multiwavelength Raman polarization lidar in Kashi, China. *Atmospheric Chemistry and Physics*, *20*(22), 13817–13834. https://doi.org/10.5194/acp-20-13817-2020

Hu, Y., Vaughan, M., Liu, Z., Powell, K., & Rodier, S. (2007). Retrieving Optical Depths and Lidar Ratios for Transparent Layers Above Opaque Water Clouds From CALIPSO Lidar Measurements. *IEEE Geoscience and Remote Sensing Letters*, *4*(4), 523–526. https://doi.org/10.1109/LGRS.2007.901085

Huang, X., Chen, X., Zhou, D. K., & Liu, X. (2016). An Observationally Based Global Band-by-Band Surface Emissivity Dataset for Climate and Weather Simulations. *Journal of the Atmospheric Sciences*, *73*(9), 3541–3555. https://doi.org/10.1175/JAS-D-15-0355.1

Huang, Y., Kok, J. F., Saito, M., & Muñoz, O. (2023). Single-scattering properties of ellipsoidal dust aerosols constrained by measured dust shape distributions. *Atmospheric Chemistry and Physics*, *23*(4), 2557–2577. https://doi.org/10.5194/acp-23-2557-2023

Hudak, D., Rodriguez, P., & Donaldson, N. (2008). Validation of the CloudSat precipitation occurrence algorithm using the Canadian C band radar network. *Journal of Geophysical Research: Atmospheres*, *113*(D8). https://doi.org/10.1029/2008JD009992

Hunt, W. H., Winker, D. M., Vaughan, M. A., Powell, K. A., Lucker, P. L., & Weimer, C. (2009). CALIPSO Lidar Description and Performance Assessment. *Journal of Atmospheric and Oceanic Technology*, *26*(7), 1214–1228. https://doi.org/10.1175/2009JTECHA1223.1

Huuskonen, A., Saltikoff, E., & Holleman, I. (2014). The Operational Weather Radar Network in Europe. *Bulletin of the American Meteorological Society*, *95*(6), 897–907. https://doi.org/10.1175/BAMS-D-12-00216.1

Iacono, M. J., Delamere, J. S., Mlawer, E. J., Shephard, M. W., Clough, S. A., & Collins, W. D. (2008). Radiative forcing by long-lived greenhouse gases: Calculations with the AER radiative transfer models. *Journal of Geophysical Research: Atmospheres*, *113*(D13). https://doi.org/10.1029/2008JD009944

Iarlori, M., Madonna, F., Rizi, V., Trickl, T., & Amodeo, A. (2015). Effective resolution concepts for lidar observations. *Atmospheric Measurement Techniques*, *8*(12), 5157–5176. https://doi.org/10.5194/amt-8-5157-2015

Iguchi, T. (2020). Dual-Frequency Precipitation Radar (DPR) on the Global Precipitation Measurement (GPM) Mission's Core Observatory. In *Advances in Global Change Research* (pp. 183–192). Springer International Publishing. https://doi.org/10.1007/978-3-030-24568-9_11

Iguchi, T., Kozu, T., Meneghini, R., Awaka, J., & Okamoto, K. K. (2000). Rain-Profiling Algorithm for the TRMM Precipitation Radar. *Journal of Applied Meteorology*, *39*(12), 2038–2052. https://doi.org/10.1175/1520-0450(2001)040<2038:RPAFTT>2.0.CO;2

Iguchi, T., Seto, S., Meneghini, R., Yoshida, N., Awaka, J., Le, M., Chandrasekar, V., Brodzik, S., Tanelli, S., Kanemaru, K., Masaki, T., Kubota, T., & Nobuhiro, T. (2023). *GPM/DPR Level-2, Algorithm Theoretical Basis Document*.

Ikuta, Y., Satoh, M., Sawada, M., Kusabiraki, H., & Kubota, T. (2021). Improvement of the Cloud Microphysics Scheme of the Mesoscale Model at the Japan Meteorological Agency Using Spaceborne Radar and Microwave Imager of the Global Precipitation Measurement as Reference. *Monthly Weather Review*, *149*(11), 3803–3819. https://doi.org/https://doi.org/10.1175/MWR-D-21-0066.1

Illingworth, A. J., Barker, H. W., Beljaars, A., Ceccaldi, M., Chepfer, H., Clerbaux, N., Cole, J., Delanoë, J., Domenech, C., Donovan, D. P., Fukuda, S., Hirakata, M., Hogan, R. J., Huenerbein, A., Kollias, P., Kubota, T., Nakajima, T. Y., Nakajima, T. Y., Nishizawa, T., … van Zadelhoff, G.-J. (2015). The EarthCARE Satellite: The Next Step Forward in Global Measurements of Clouds, Aerosols, Precipitation, and Radiation. *Bulletin of the American Meteorological Society*, *96*(8), 1311–1332. https://doi.org/10.1175/BAMS-D-12-00227.1

Illingworth, A. J., Hogan, R. J., O'Connor, E. J., Bouniol, D., Brooks, M. E., Delanoë, J., Donovan, D. P., Eastment, J. D., Gaussiat, N., Goddard, J. W. F., Haeffelin, M., Klein Baltinik, H., Krasnov, O. A., Pelon, J., Piriou, J. M., Protat, A., Russchenberg, H. W. J., Seifert, A., Tompkins, A. M., … Wrench, C. L. (2007). Cloudnet: Continuous Evaluation of Cloud Profiles in Seven Operational Models Using Ground-Based Observations. *Bulletin of the American Meteorological Society*, *88*(6), 883–898. https://doi.org/10.1175/BAMS-88-6-883

Intrieri, J. M., Stephens, G. L., Eberhard, W. L., & Uttal, T. (1993). A Method for Determining Cirrus Cloud Particle Sizes Using Lidar and Radar Backscatter Technique. *Journal of Applied Meteorology*, *32*(6), 1074–1082. https://doi.org/10.1175/1520-0450(1993)032<1074:AMFDCC>2.0.CO;2

Irbah, A., Delanoë, J., van Zadelhoff, G.-J., Donovan, D. P., Kollias, P., Treserras, B. P., Mason, S., Hogan, R. J., Tatarevic, A., Puigdomènech Treserras, B., Mason, S., Hogan, R. J., & Tatarevic, A. (2023). The classification of atmospheric hydrometeors and aerosols from the EarthCARE radar and lidar: the A-TC, C-TC and AC-TC products. *Atmospheric Measurement Techniques*, *16*(11), 2795–2820. https://doi.org/10.5194/amt-16-2795-2023

Ishida, H., & Nakajima, T. Y. (2009). Development of an unbiased cloud detection algorithm for a spaceborne multispectral imager. *Journal of Geophysical Research: Atmospheres*, *114*(D7). https://doi.org/10.1029/2008JD010710

Ishii, S., Kishibuchi, K., Takenaka, H., Jin, Y., Nishizawa, T., Sugimoto, N., Iwai, H., Aoki, M., Kawamura, S., & Okamoto, H. (2022). 355-nm direct-detection Doppler wind lidar for vertical atmospheric motion measurement. *Applied Optics*, *61*(27), 7925. https://doi.org/10.1364/AO.460219

Iwai, H., Ishii, S., Oda, R., Mizutani, K., Sekizawa, S., & Murayama, Y. (2013). Performance and Technique of Coherent 2-μm Differential Absorption and Wind Lidar for Wind Measurement. *Journal of Atmospheric and Oceanic Technology*, *30*(3), 429–449. https://doi.org/10.1175/JTECH-D-12-00111.1

Iwasaki, S., & Okamoto, H. (2001). Analysis of the enhancement of backscattering by nonspherical particles with flat surfaces. *Applied Optics*, *40*(33), 6121. https://doi.org/10.1364/AO.40.006121

Jager, H., & Hofmann, D. (1991). Midlatitude lidar backscatter to mass, area, and extinction conversion model based on in situ aerosol measurements from 1980 to 1987. *Applied Optics* , *30*, 127–138.

Janisková, M., & Fielding, M. D. (2020). Direct 4D-Var assimilation of space-borne cloud radar and lidar observations. Part II: Impact on analysis and subsequent forecast. *Quarterly Journal of the Royal Meteorological Society*, *146*(733), 3900–3916. https://doi.org/10.1002/qj.3879

Janjić, T., Bormann, N., Bocquet, M., Carton, J. A., Cohn, S. E., Dance, S. L., Losa, S. N., Nichols, N.

K., Potthast, R., Waller, J. A., & Weston, P. (2018). On the representation error in data assimilation. *Quarterly Journal of the Royal Meteorological Society*, *144*(713), 1257–1278. https://doi.org/10.1002/qj.3130

JAXA. (2024). *EarthCARE JAXA Level 2 Algorithm Theoretical Basis Document (L2 ATBD)*.

Jensen, M. P., Petersen, W. A., Bansemer, A., Bharadwaj, N., Carey, L. D., Cecil, D. J., Collis, S. M., Genio, A. D. Del, Dolan, B., Gerlach, J., Giangrande, S. E., Heymsfield, A., Heymsfield, G., Kollias, P., Lang, T. J., Nesbitt, S. W., Neumann, A., Poellot, M., Rutledge, S. A., … Zipser, E. J. (2016). The Midlatitude Continental Convective Clouds Experiment (MC3E). *Bulletin of the American Meteorological Society*, *97*(9), 1667–1686. https://doi.org/10.1175/BAMS-D-14-00228.1

Jimenez, C., Ansmann, A., Engelmann, R., Donovan, D., Malinka, A., Seifert, P., Wiesen, R., Radenz, M., Yin, Z., Bühl, J., Schmidt, J., Barja, B., Wandinger, U., Seifert, P., Wandinger, U., Wiesen, R., Radenz, M., Yin, Z., Bühl, J., … Wandinger, U. (2020). The dual-field-of-view polarization lidar technique: a new concept in monitoring aerosol effects in liquid-water clouds – case studies. *Atmospheric Chemistry and Physics*, *20*(23).

Jin, Y., Nishizawa, T., Sugimoto, N., Ishii, S., Aoki, M., Sato, K., & Okamoto, H. (2020). Development of a 355-nm high-spectral-resolution lidar using a scanning Michelson interferometer for aerosol profile measurement. *Optics Express*, *28*(16), 23209. https://doi.org/10.1364/OE.390987

Jin, Y., Nishizawa, T., Sugimoto, N., Takakura, S., Aoki, M., Ishii, S., Yamazaki, A., Kudo, R., Yumimoto, K., Sato, K., & Okamoto, H. (2022). Demonstration of aerosol profile measurement with a dual-wavelength high-spectral-resolution lidar using a scanning interferometer. *Applied Optics*, *61*(13), 3523. https://doi.org/10.1364/AO.451707

Josset, D., Pelon, J., Garnier, A., Hu, Y., Vaughan, M., Zhai, P., Kuehn, R., & Lucker, P. (2012). Cirrus optical depth and lidar ratio retrieval from combined CALIPSO-CloudSat observations using ocean surface echo. *Journal of Geophysical Research: Atmospheres*, *117*(D5). https://doi.org/10.1029/2011JD016959

Josset, D., Rogers, R., Pelon, J., Hu, Y., Liu, Z., Omar, A., & Zhai, P.-W. (2011). CALIPSO lidar ratio retrieval over the ocean. *Opt. Express*, *19*(19), 18696–18706. https://doi.org/10.1364/OE.19.018696

Kacenelenbogen, M., Redemann, J., Vaughan, M. A., Omar, A. H., Russell, P. B., Burton, S., Rogers, R. R., Ferrare, R. A., & Hostetler, C. A. (2014). An evaluation of CALIOP/CALIPSO's aerosol-above-cloud detection and retrieval capability over North America. *Journal of Geophysical Research: Atmospheres*, *119*(1), 230–244. https://doi.org/10.1002/2013JD020178

Kacenelenbogen, M., Vaughan, M. A., Redemann, J., Hoff, R. M., Rogers, R. R., Ferrare, R. A., Russell, P. B., Hostetler, C. A., Hair, J. W., & Holben, B. N. (2011). An accuracy assessment of the CALIOP/CALIPSO version 2/version 3 daytime aerosol extinction product based on a detailed multi-sensor, multi-platform case study. *Atmospheric Chemistry and Physics*, *11*(8), 3981–4000. https://doi.org/10.5194/acp-11-3981-2011

Kahn, R. A., Gaitley, B. J., Garay, M. J., Diner, D. J., Eck, T. F., Smirnov, A., & Holben, B. N. (2010). Multiangle Imaging SpectroRadiometer global aerosol product assessment by comparison with the Aerosol Robotic Network. *Journal of Geophysical Research: Atmospheres*, *115*(D23). https://doi.org/10.1029/2010JD014601

Kahn, R. A., Garay, M. J., Nelson, D. L., Levy, R. C., Bull, M. A., Diner, D. J., Martonchik, J. V., Hansen, E. G., Remer, L. A., & Tanré, D. (2011). Response to "Toward unified satellite climatology of aerosol properties. 3. MODIS versus MISR versus AERONET." *Journal of Quantitative Spectroscopy and Radiative Transfer*, *112*(5), 901–909. https://doi.org/10.1016/j.jqsrt.2010.11.001

Kalesse, H., & Kollias, P. (2013). Climatology of High Cloud Dynamics Using Profiling ARM Doppler Radar Observations. *Journal of Climate*, *26*(17), 6340–6359. https://doi.org/10.1175/JCLI-D-12-

00695.1

Kanemaru, K., & Hanado, H. (2023). Precipitation Judgement of The Dual-Frequency Precipitation Radar in Gpm Version 7. *IGARSS 2023 - 2023 IEEE International Geoscience and Remote Sensing Symposium*, 3796–3798. https://doi.org/10.1109/IGARSS52108.2023.10282964

Kanemaru, K., Hanado, H., & Nakagawa, K. (2021). Improvement of the Clutter Removal Method for the Spaceborne Precipitation Radars. *2021 IEEE International Geoscience and Remote Sensing Symposium IGARSS*, 840–843. https://doi.org/10.1109/IGARSS47720.2021.9554974

Kanemaru, K., Iguchi, T., Masaki, T., & Kubota, T. (2020). Estimates of Spaceborne Precipitation Radar Pulsewidth and Beamwidth Using Sea Surface Echo Data. *IEEE Transactions on Geoscience and Remote Sensing*, *58*(8), 5291–5303. https://doi.org/10.1109/TGRS.2019.2963090

Kanitz, T., Ansmann, A., Foth, A., Seifert, P., Wandinger, U., Engelmann, R., Baars, H., Althausen, D., Casiccia, C., & Zamorano, F. (2014). Surface matters: limitations of CALIPSO V3 aerosol typing in coastal regions. *Atmospheric Measurement Techniques*, *7*(7), 2061–2072. https://doi.org/10.5194/amt-7-2061-2014

Kar, J., Lee, K.-P., Vaughan, M. A., Tackett, J. L., Trepte, C. R., Winker, D. M., Lucker, P. L., & Getzewich, B. J. (2019). CALIPSO level 3 stratospheric aerosol profile product: version 1.00algorithm description and initial assessment. *Atmospheric Measurement Techniques*, *12*(11), 6173–6191. https://doi.org/10.5194/amt-12-6173-2019

Kar, J., Vaughan, M. A., Lee, K.-P., Tackett, J. L., Avery, M. A., Garnier, A., Getzewich, B. J., Hunt, W. H., Josset, D., Liu, Z., Lucker, P. L., Magill, B., Omar, A. H., Pelon, J., Rogers, R. R., Toth, T. D., Trepte, C. R., Vernier, J.-P., Winker, D. M., & Young, S. A. (2018). CALIPSO lidar calibration at 532 nm: version 4 nighttime algorithm. *Atmospheric Measurement Techniques*, *11*(3), 1459–1479. https://doi.org/10.5194/amt-11-1459-2018

Karlsson, K.-G., & Devasthale, A. (2018). Inter-Comparison and Evaluation of the Four Longest Satellite-Derived Cloud Climate Data Records: CLARA-A2, ESA Cloud CCI V3, ISCCP-HGM, and PATMOS-x. *Remote Sensing*, *10*(10), 1567. https://doi.org/10.3390/rs10101567

Kato, S., Loeb, N. G., Rose, F. G., Doelling, D. R., Rutan, D. A., Caldwell, T. E., Yu, L., & Weller, R. A. (2013). Surface Irradiances Consistent with CERES-Derived Top-of-Atmosphere Shortwave and Longwave Irradiances. *Journal of Climate*, *26*(9), 2719–2740. https://doi.org/10.1175/JCLI-D-12-00436.1

Kato, S., Rose, F. G., Sun-Mack, S., Miller, W. F., Chen, Y., Rutan, D. A., Stephens, G. L., Loeb, N. G., Minnis, P., Wielicki, B. A., Winker, D. M., Charlock, T. P., Stackhouse, P. W., Xu, K.-M., & Collins, W. D. (2011). Improvements of top-of-atmosphere and surface irradiance computations with CALIPSO-, CloudSat-, and MODIS-derived cloud and aerosol properties. *Journal of Geophysical Research*, *116*(D19), D19209. https://doi.org/10.1029/2011JD016050

Katsumata, M., Taniguchi, K., & Nishizawa, T. (2020). An Attempt to Retrieve Continuous Water Vapor Profiles in Marine Lower Troposphere Using Shipboard Raman/Mie Lidar System. *SOLA*, *16A*(Special_Edition), 6–11. https://doi.org/10.2151/sola.16A-002

Ke, J., Sun, Y., Dong, C., Zhang, X., Wang, Z., Lyu, L., Zhu, W., Ansmann, A., Su, L., Bu, L., Xiao, D., Wang, S., Chen, S., Liu, J., Chen, W., & Liu, D. (2022). Development of China's first space-borne aerosol-cloud high-spectral-resolution lidar: retrieval algorithm and airborne demonstration. *PhotoniX*, *3*(1), 17. https://doi.org/10.1186/s43074-022-00063-3

Kealy, J. C., Marenco, F., Marsham, J. H., Garcia-Carreras, L., Francis, P. N., Cooke, M. C., & Hocking, J. (2017). Clouds over the summertime Sahara: an evaluation of Met Office retrievals from Meteosat Second Generation using airborne remote sensing. *Atmospheric Chemistry and Physics*, *17*(9), 5789–5807. https://doi.org/10.5194/acp-17-5789-2017

Kennedy, A., Scott, A., Loeb, N., Sczepanski, A., Lucke, K., Marquis, J., & Waugh, S. (2022). Bringing

Microphysics to the Masses: The Blowing Snow Observations at the University of North Dakota: Education through Research (BLOWN-UNDER) Campaign. *Bulletin of the American Meteorological Society*, *103*(1). https://doi.org/10.1175/BAMS-D-20-0199.1

Kezoudi, M., Keleshis, C., Antoniou, P., Biskos, G., Bronz, M., Constantinides, C., Desservettaz, M., Gao, R.-S., Girdwood, J., Harnetiaux, J., Kandler, K., Leonidou, A., Liu, Y., Lelieveld, J., Marenco, F., Mihalopoulos, N., Močnik, G., Neitola, K., Paris, J.-D., … Sciare, J. (2021). The Unmanned Systems Research Laboratory (USRL): A New Facility for UAV-Based Atmospheric Observations. *Atmosphere*, *12*(8), 1042. https://doi.org/10.3390/atmos12081042

Khaykin, S., Legras, B., Bucci, S., Sellitto, P., Isaksen, L., Tencé, F., Bekki, S., Bourassa, A., Rieger, L., Zawada, D., Jumelet, J., & Godin-Beekmann, S. (2020). The 2019/20 Australian wildfires generated a persistent smoke-charged vortex rising up to 35 km altitude. *Communications Earth & Environment*, *1*(1). https://doi.org/10.1038/s43247-020-00022-5

Kikuchi, M., Okamoto, H., Sato, K., Suzuki, K., Cesana, G., Hagihara, Y., Takahashi, N., Hayasaka, T., & Oki, R. (2017). Development of Algorithm for Discriminating Hydrometeor Particle Types With a Synergistic Use of CloudSat and CALIPSO. *Journal of Geophysical Research: Atmospheres*, *122*(20). https://doi.org/10.1002/2017JD027113

Kim, H.-S., Chung, Y.-S., & Kim, J.-T. (2014). Spatio-temporal variations of optical properties of aerosols in East Asia measured by MODIS and relation to the ground-based mass concentrations observed in central Korea during 2001~2010. *Asia-Pacific Journal of Atmospheric Sciences*, *50*(2), 191–200. https://doi.org/10.1007/s13143-014-0007-8

Kim, M.-H., Omar, A. H., Tackett, J. L., Vaughan, M. A., Winker, D. M., Trepte, C. R., Hu, Y., Liu, Z., Poole, L. R., Pitts, M. C., Kar, J., & Magill, B. E. (2018). The CALIPSO version 4 automated aerosol classification and lidar ratio selection algorithm. *Atmospheric Measurement Techniques*, *11*(11), 6107–6135. https://doi.org/10.5194/amt-11-6107-2018

Kim, M.-H., Yeo, H., Park, S., Park, D.-H., Omar, A., Nishizawa, T., Shimizu, A., & Kim, S.-W. (2021). Assessing CALIOP-Derived Planetary Boundary Layer Height Using Ground-Based Lidar. Remote Sensing, 13(8), 1496. https://doi.org/10.3390/rs13081496

Kim, M., Kim, S., Yoon, S., & Omar, A. H. (2013). Comparison of aerosol optical depth between CALIOP and MODIS-Aqua for CALIOP aerosol subtypes over the ocean. Journal of Geophysical Research: Atmospheres, 118(23). https://doi.org/10.1002/2013JD019527

Kim, M., Omar, A. H., Vaughan, M. A., Winker, D. M., Trepte, C. R., Hu, Y., Liu, Z., & Kim, S. (2017). Quantifying the low bias of CALIPSO's column aerosol optical depth due to undetected aerosol layers. Journal of Geophysical Research: Atmospheres, 122(2), 1098–1113. https://doi.org/10.1002/2016JD025797

Kim, S.-W., Chung, E.-S., Yoon, S.-C., Sohn, B.-J., & Sugimoto, N. (2011). Intercomparisons of cloud-top and cloud-base heights from ground-based Lidar, CloudSat and CALIPSO measurements. International Journal of Remote Sensing, 32(4), 1179–1197. https://doi.org/10.1080/01431160903527439

Kinne, S., Lohmann, U., Feichter, J., Schulz, M., Timmreck, C., Ghan, S., Easter, R., Chin, M., Ginoux, P., Takemura, T., Tegen, I., Koch, D., Herzog, M., Penner, J., Pitari, G., Holben, B., Eck, T., Smirnov, A., Dubovik, O., … Kaufman, Y. (2003). Monthly averages of aerosol properties: A global comparison among models, satellite data, and AERONET ground data. Journal of Geophysical Research: Atmospheres, 108(D20). https://doi.org/10.1029/2001JD001253

Kirstetter, P.-E., Hong, Y., Gourley, J. J., Chen, S., Flamig, Z., Zhang, J., Schwaller, M., Petersen, W., & Amitai, E. (2012). Toward a Framework for Systematic Error Modeling of Spaceborne Precipitation Radar with NOAA/NSSL Ground Radar–Based National Mosaic QPE. Journal of Hydrometeorology, 13(4), 1285–1300. https://doi.org/10.1175/JHM-D-11-0139.1

Kirstetter, P., Gourley, J. J., Hong, Y., Zhang, J., Moazamigoodarzi, S., Langston, C., & Arthur, A.

(2015). Probabilistic precipitation rate estimates with ground-based radar networks. Water Resources Research, 51(3), 1422–1442. https://doi.org/10.1002/2014WR015672

Kittaka, C., Winker, D. M., Vaughan, M. A., Omar, A., & Remer, L. A. (2011). Intercomparison of column aerosol optical depths from CALIPSO and MODIS-Aqua. Atmospheric Measurement Techniques, 4(2), 131–141. https://doi.org/10.5194/amt-4-131-2011

Klett, J. D. (1985). Lidar inversion with variable backscatter/extinction ratios. Applied Optics, 24(11), 1638. https://doi.org/10.1364/AO.24.001638

Kneifel, S., Kollias, P., Battaglia, A., Leinonen, J., Maahn, M., Kalesse, H., & Tridon, F. (2016). First observations of triple-frequency radar Doppler spectra in snowfall: Interpretation and applications. *Geophysical Research Letters*, *43*(5), 2225–2233. https://doi.org/10.1002/2015GL067618

Kneifel, S., & Moisseev, D. (2020). Long-Term Statistics of Riming in Nonconvective Clouds Derived from Ground-Based Doppler Cloud Radar Observations. *Journal of the Atmospheric Sciences*, *77*(10), 3495–3508. https://doi.org/10.1175/JAS-D-20-0007.1

Kneifel, S., von Lerber, A., Tiira, J., Moisseev, D., Kollias, P., & Leinonen, J. (2015). Observed relations between snowfall microphysics and triple-frequency radar measurements. *Journal of Geophysical Research: Atmospheres*, *120*(12), 6034–6055. https://doi.org/10.1002/2015JD023156

Kneifel, S., and Coauthors, (2018): Summer Snowfall Workshop: Scattering Properties of Realistic Frozen Hydrometeors from Simulations and Observations, as well as Defining a New Standard for Scattering Databases. Bull. Amer. Meteor. Soc., 99, ES55–ES58, https://doi.org/10.1175/BAMS-D-17-0208.1.

Knight, C. A., & Miller, L. J. (1993). First Radar Echoes from Cumulus Clouds. *Bulletin of the American Meteorological Society*, *74*(2), 179–188. https://doi.org/10.1175/1520-0477(1993)074<0179:FREFCC>2.0.CO;2

Knobelspiesse, K., Cairns, B., Redemann, J., Bergstrom, R. W., & Stohl, A. (2011): Simultaneous retrieval of aerosol and cloud properties during the MILAGRO field campaign, Atmos. Chem. Phys., 11, 6245–6263, https://doi.org/10.5194/acp-11-6245-2011

Knollenberg, R. G. (1970). The Optical Array: An Alternative to Scattering or Extinction for Airborne Particle Size Determination. *Journal of Applied Meteorology*, *9*(1), 86–103. https://doi.org/10.1175/1520-0450(1970)009<0086:TOAAAT>2.0.CO;2

Kobayashi, S., Kumagai, H., & Iguchi, T. (2003). Accuracy Evaluation of Doppler Velocity on a Spaceborne Weather Radar through a Random Signal Simulation. *Journal of Atmospheric and Oceanic Technology*, *20*(6), 944–949. https://doi.org/10.1175/1520-0426(2003)020<0944:AEODVO>2.0.CO;2

Kojima, M., Miura, T., Furukawa, K., Hyakusoku, Y., Ishikiri, T., Kai, H., Iguchi, T., Hanado, H., & Nakagawa, K. (2012). Dual-frequency precipitation radar (DPR) development on the global precipitation measurement (GPM) core observatory. In *SPIE Proceedings*. SPIE. https://doi.org/10.1117/12.976823

Kollias, P., Battaglia, A., Lamer, K., Treserras, B. P., & Braun, S. A. (2022). Mind the Gap - Part 3: Doppler Velocity Measurements From Space. *Frontiers in Remote Sensing*, *3*. https://doi.org/10.3389/frsen.2022.860284

Kollias, P., Bharadwaj, N., Widener, K., Jo, I., & Johnson, K. (2014). Scanning ARM Cloud Radars. Part I: Operational Sampling Strategies. *Journal of Atmospheric and Oceanic Technology*, *31*(3), 569–582. https://doi.org/10.1175/JTECH-D-13-00044.1

Kollias, P., Clothiaux, E. E., Miller, M. A., Albrecht, B. A., Stephens, G. L., & Ackerman, T. P. (2007). Millimeter-Wavelength Radars: New Frontier in Atmospheric Cloud and Precipitation Research. *Bulletin of the American Meteorological Society*, *88*(10), 1608–1624.

https://doi.org/10.1175/BAMS-88-10-1608

Kollias, P., Puidgomènech Treserras, B., Battaglia, A., Borque, P. C., & Tatarevic, A. (2023). Processing reflectivity and Doppler velocity from EarthCARE's cloud-profiling radar: the C-FMR, C-CD and C-APC products. *Atmospheric Measurement Techniques*, *16*(7), 1901–1914. https://doi.org/10.5194/amt-16-1901-2023

Kollias, P., Puigdomènech Treserras, B., & Protat, A. (2019). Calibration of the 2007–2017 record of Atmospheric Radiation Measurements cloud radar observations using CloudSat. *Atmospheric Measurement Techniques*, *12*(9), 4949–4964. https://doi.org/10.5194/amt-12-4949-2019

Kong, S., Sato, K., & Bi, L. (2022). Lidar Ratio–Depolarization Ratio Relations of Atmospheric Dust Aerosols: The Super-Spheroid Model and High Spectral Resolution Lidar Observations. *Journal of Geophysical Research: Atmospheres*, *127*(4). https://doi.org/10.1029/2021JD035629

Koopman R. (2021). *EarthCARE Scientific Validation Implementation Plan (VIP)*. https://www.eorc.jaxa.jp/EARTHCARE/document/EC-PL-ESA-SYS-1049 EC Validation Plan__1.2__2021-02-26.pdf

Kotarba, A. Z. (2020). Calibration of global MODIS cloud amount using CALIOP cloud profiles. *Atmospheric Measurement Techniques*, *13*(9), 4995–5012. https://doi.org/10.5194/amt-13-4995-2020

Kotarba, A. Z. (2022a). Errors in global cloud climatology due to transect sampling with the CALIPSO satellite lidar mission. *Atmospheric Research*, *279*, 106379. https://doi.org/10.1016/j.atmosres.2022.106379

Kotarba, A. Z. (2022b). Impact of the revisit frequency on cloud climatology for CALIPSO, EarthCARE, Aeolus, and ICESat-2 satellite lidar missions. *Atmospheric Measurement Techniques*, *15*(14), 4307–4322. https://doi.org/10.5194/amt-15-4307-2022

Kotarba, A. Z., & Solecki, M. (2021). Uncertainty Assessment of the Vertically-Resolved Cloud Amount for Joint CloudSat–CALIPSO Radar–Lidar Observations. *Remote Sensing*, *13*(4), 807. https://doi.org/10.3390/rs13040807

Kotthaus, S., Bravo-Aranda, J. A., Collaud Coen, M., Guerrero-Rascado, J. L., Costa, M. J., Cimini, D., O'Connor, E. J., Hervo, M., Alados-Arboledas, L., Jiménez-Portaz, M., Mona, L., Ruffieux, D., Illingworth, A., & Haeffelin, M. (2023). Atmospheric boundary layer height from ground-based remote sensing: a review of capabilities and limitations. *Atmospheric Measurement Techniques*, *16*(2), 433–479. https://doi.org/10.5194/amt-16-433-2023

Kotz, S., Johnson, N. L., & Read, C. B. (1988). Encyclopedia of statistical sciences. *Wiley, New York, 1982-1988*.

Kovilakam, M., Thomason, L., & Knepp, T. (2023). SAGE III/ISS aerosol/cloud categorization and its impact on GloSSAC. *Atmospheric Measurement Techniques*, *16*(10), 2709–2731. https://doi.org/10.5194/amt-16-2709-2023

Kozu, T., Kawanishi, T., Kuroiwa, H., Kojima, M., Oikawa, K., Kumagai, H., Okamoto, K., Okumura, M., Nakatsuka, H., & Nishikawa, K. (2001). Development of precipitation radar onboard the Tropical Rainfall Measuring Mission (TRMM) satellite. *IEEE Transactions on Geoscience and Remote Sensing*, *39*(1), 102–116. https://doi.org/10.1109/36.898669

Krämer, M., Rolf, C., Spelten, N., Afchine, A., Fahey, D., Jensen, E., Khaykin, S., Kuhn, T., Lawson, P., Lykov, A., Pan, L. L. L., Riese, M., Rollins, A., Stroh, F., Thornberry, T., Wolf, V., Woods, S., Spichtinger, P., Quaas, J., & Sourdeval, O. (2020). A microphysics guide to cirrus – Part 2: Climatologies of clouds and humidity from observations. *Atmospheric Chemistry and Physics*, *20*(21), 12569–12608. https://doi.org/10.5194/acp-20-12569-2020

Kubota, T., Iguchi, T., Kojima, M., Liao, L., Masaki, T., Hanado, H., Meneghini, R., & Oki, R. (2016). A

Statistical Method for Reducing Sidelobe Clutter for the Ku-Band Precipitation Radar on board the GPM Core Observatory. *Journal of Atmospheric and Oceanic Technology*, *33*(7), 1413–1428. https://doi.org/10.1175/JTECH-D-15-0202.1

Kubota, T., Iguchi, T., Masaki, T., Yoshida, N., & Oki, R. (2018). Development of A Statistical Method for Reducing Sidelobe Clutter in High Sensitivity Mode of GPM/Kapr. *IGARSS 2018 - 2018 IEEE International Geoscience and Remote Sensing Symposium*, 8347–8348. https://doi.org/10.1109/IGARSS.2018.8519100

Kubota, T., Seto, S., Satoh, M., Nasuno, T., Iguchi, T., Masaki, T., Kwiatkowski, J. M., & Oki, R. (2020). Cloud Assumption of Precipitation Retrieval Algorithms for the Dual-Frequency Precipitation Radar. *Journal of Atmospheric and Oceanic Technology*, *37*(11), 2015–2031. https://doi.org/10.1175/JTECH-D-20-0041.1

Kudo, R., Diémoz, H., Estellés, V., Campanelli, M., Momoi, M., Marenco, F., Ryder, C. L., Ijima, O., Uchiyama, A., Nakashima, K., Yamazaki, A., Nagasawa, R., Ohkawara, N., & Ishida, H. (2021). Optimal use of the Prede POM sky radiometer for aerosol, water vapor, and ozone retrievals. *Atmospheric Measurement Techniques*, *14*(5), 3395–3426. https://doi.org/10.5194/amt-14-3395-2021

Kudo, R., Higurashi, A., Oikawa, E., Fujikawa, M., Ishimoto, H., & Nishizawa, T. (2023). Global 3-D distribution of aerosol composition by synergistic use of CALIOP and MODIS observations. *Atmospheric Measurement Techniques*, *16*(16), 3835–3863. https://doi.org/10.5194/amt-16-3835-2023

Kudo, R., Nishizawa, T., & Aoyagi, T. (2016). Vertical profiles of aerosol optical properties and the solar heating rate estimated by combining sky radiometer and lidar measurements. *Atmospheric Measurement Techniques*, *9*(7), 3223–3243. https://doi.org/10.5194/amt-9-3223-2016

Kumar, V. V, Jakob, C., Protat, A., Williams, C. R., & May, P. T. (2015). Mass-Flux Characteristics of Tropical Cumulus Clouds from Wind Profiler Observations at Darwin, Australia. *Journal of the Atmospheric Sciences*, *72*(5), 1837–1855. https://doi.org/10.1175/JAS-D-14-0259.1

Kummerow, C., Barnes, W., Kozu, T., Shiue, J., & Simpson, J. (1998). The Tropical Rainfall Measuring Mission (TRMM) Sensor Package. *Journal of Atmospheric and Oceanic Technology*, *15*(3), 809–817. https://doi.org/10.1175/1520-0426(1998)015<0809:TTRMMT>2.0.CO;2

Kummerow, C., Simpson, J., Thiele, O., Barnes, W., Chang, A. T. C., Stocker, E., Adler, R. F., Hou, A., Kakar, R., Wentz, F., Ashcroft, P., Kozu, T., Hong, Y., Okamoto, K., Iguchi, T., Kuroiwa, H., Im, E., Haddad, Z., Huffman, G., … Nakamura, K. (2000). The Status of the Tropical Rainfall Measuring Mission (TRMM) after Two Years in Orbit. *Journal of Applied Meteorology*, *39*(12), 1965–1982. https://doi.org/10.1175/1520-0450(2001)040<1965:TSOTTR>2.0.CO;2

Kuo, K.-S., Olson, W. S., Johnson, B. T., Grecu, M., Tian, L., Clune, T. L., van Aartsen, B. H., Heymsfield, A. J., Liao, L., & Meneghini, R. (2016). The Microwave Radiative Properties of Falling Snow Derived from Nonspherical Ice Particle Models. Part I: An Extensive Database of Simulated Pristine Crystals and Aggregate Particles, and Their Scattering Properties. *Journal of Applied Meteorology and Climatology*, *55*(3), 691–708. https://doi.org/10.1175/JAMC-D-15-0130.1

L'Ecuyer, T. S., Hang, Y., Matus, A. V., & Wang, Z. (2019). Reassessing the Effect of Cloud Type on Earth's Energy Balance in the Age of Active Spaceborne Observations. Part I: Top of Atmosphere and Surface. *Journal of Climate*, *32*(19).

L'Ecuyer, T. S., & Jiang, J. H. (2010). Touring the atmosphere aboard the A-Train. *Physics Today*, *63*(7), 36–41. https://doi.org/10.1063/1.3463626

L'Ecuyer, T. S., Mateling, M., Shannon, K., Chepfer, H., Feofilov, A., Wood, N., & Shupe, M. (2024). Polar snowfall observations from CloudSat and CALIPSO. *In Preparation*.

L'Ecuyer, T. S., & Stephens, G. L. (2002). An Estimation-Based Precipitation Retrieval Algorithm for

Attenuating Radars. *Journal of Applied Meteorology*, *41*(3), 272–285. https://doi.org/10.1175/1520-0450(2002)041<0272:AEBPRA>2.0.CO;2

L'Ecuyer, T. S., Wood, N. B., Haladay, T., Stephens, G. L., & Stackhouse, P. W. (2008). Impact of clouds on atmospheric heating based on the R04 CloudSat fluxes and heating rates data set. *Journal of Geophysical Research: Atmospheres*, *113*(D8). https://doi.org/10.1029/2008JD009951

Laj, P., Myhre, C. L., Riffault, V., Amiridis, V., Fuchs, H., Eleftheriadis, K., Petäjä, T., Salameh, T., Kivekäs, N., Juurola, E., Saponaro, G., Philippin, S., Cornacchia, C., Arboledas, L. A., Baars, H., Claude, A., Mazière, M. De, Dils, B., Dufresne, M., … Vana, M. (2024). Aerosol, Clouds and Trace Gases Research Infrastructure (ACTRIS): The European Research Infrastructure Supporting Atmospheric Science. *Bulletin of the American Meteorological Society*, *105*(7), E1098–E1136. https://doi.org/10.1175/BAMS-D-23-0064.1

Lakshmanan, V. (2007). *Overview of radar data compression* (R. W. Heymann, B. Huang, & I. Gladkova (eds.); p. 668308). https://doi.org/10.1117/12.740171

Lamer, K., Kollias, P., Battaglia, A., & Preval, S. (2020). Mind the gap – Part 1: Accurately locating warm marine boundary layer clouds and precipitation using spaceborne radars. *Atmospheric Measurement Techniques*, *13*(5), 2363–2379. https://doi.org/10.5194/amt-13-2363-2020

Lamer, K., Kollias, P., Luke, E. P., Treserras, B. P., Oue, M., & Dolan, B. (2023). Multisensor Agile Adaptive Sampling (MAAS): A Methodology to Collect Radar Observations of Convective Cell Life Cycle. *Journal of Atmospheric and Oceanic Technology*, *40*(11), 1509–1522. https://doi.org/https://doi.org/10.1175/JTECH-D-23-0043.1

Lasser, M., O, S., & Foelsche, U. (2019). Evaluation of GPM-DPR precipitation estimates with WegenerNet gauge data. *Atmospheric Measurement Techniques*, *12*(9), 5055–5070. https://doi.org/10.5194/amt-12-5055-2019

Le, M., & Chandrasekar, V. (2019). Ground Validation of Surface Snowfall Algorithm in GPM Dual-Frequency Precipitation Radar. *Journal of Atmospheric and Oceanic Technology*, *36*(4), 607–619. https://doi.org/10.1175/JTECH-D-18-0098.1

Le, M., Chandrasekar, V., & Biswas, S. (2016). Evaluation and Validation of GPM Dual-Frequency Classification Module after Launch. *Journal of Atmospheric and Oceanic Technology*, *33*(12), 2699–2716. https://doi.org/10.1175/JTECH-D-15-0253.1

Lebel, T., Bastin, G., Obled, C., & Creutin, J. D. (1987). On the accuracy of areal rainfall estimation: A case study. *Water Resources Research*, *23*(11), 2123–2134. https://doi.org/10.1029/WR023i011p02123

LeBlanc, S. E., Segal-Rozenhaimer, M., Redemann, J., Flynn, C., Johnson, R. R., Dunagan, S. E., Dahlgren, R., Kim, J., Choi, M., da Silva, A., Castellanos, P., Tan, Q., Ziemba, L., Lee Thornhill, K., & Kacenelenbogen, M. (2022). Airborne observations during KORUS-AQ show that aerosol optical depths are more spatially self-consistent than aerosol intensive properties. *Atmospheric Chemistry and Physics*, *22*(17), 11275–11304. https://doi.org/10.5194/acp-22-11275-2022

Lebsock, M. D., & L'Ecuyer, T. S. (2011). The retrieval of warm rain from CloudSat. *Journal of Geophysical Research*, *116*(D20), D20209. https://doi.org/10.1029/2011JD016076

Lebsock, M. D., L'Ecuyer, T. S., & Stephens, G. L. (2011). Detecting the Ratio of Rain and Cloud Water in Low-Latitude Shallow Marine Clouds. *Journal of Applied Meteorology and Climatology*, *50*(2), 419–432. https://doi.org/10.1175/2010JAMC2494.1

Lebsock, M. D., & Suzuki, K. (2016). Uncertainty Characteristics of Total Water Path Retrievals in Shallow Cumulus Derived from Spaceborne Radar/Radiometer Integral Constraints. *Journal of Atmospheric and Oceanic Technology*, *33*(8), 1597–1609. https://doi.org/10.1175/JTECH-D-16-0023.1

Lee, L., Zhang, J., Reid, J. S., & Yorks, J. E. (2019). Investigation of CATS aerosol products and application toward global diurnal variation of aerosols. *Atmospheric Chemistry and Physics*, *19*(19), 12687–12707. https://doi.org/10.5194/acp-19-12687-2019

Leinonen, J. (2014). High-level interface to T-matrix scattering calculations: architecture, capabilities and limitations. *Optics Express*, *22*(2), 1655. https://doi.org/10.1364/OE.22.001655

Leinonen, J., Kneifel, S., Moisseev, D., Tyynelä, J., Tanelli, S., & Nousiainen, T. (2012). Evidence of nonspheroidal behavior in millimeter-wavelength radar observations of snowfall. *Journal of Geophysical Research: Atmospheres*, *117*(D18). https://doi.org/10.1029/2012JD017680

Leinonen, J., Lebsock, M. D., Stephens, G. L., & Suzuki, K. (2016). Improved Retrieval of Cloud Liquid Water from CloudSat and MODIS. *Journal of Applied Meteorology and Climatology*, *55*(8), 1831–1844. https://doi.org/10.1175/JAMC-D-16-0077.1

Leinonen, J., & Moisseev, D. (2015). What do triple-frequency radar signatures reveal about aggregate snowflakes? *Journal of Geophysical Research: Atmospheres*, *120*(1), 229–239. https://doi.org/10.1002/2014JD022072

Leinonen, J., & Szyrmer, W. (2015). Radar signatures of snowflake riming: A modeling study. *Earth and Space Science*, *2*(8), 346–358. https://doi.org/10.1002/2015EA000102

LeMone, M. A., & Zipser, E. J. (1980). Cumulonimbus Vertical Velocity Events in GATE. Part I: Diameter, Intensity and Mass Flux. *Journal of Atmospheric Sciences*, *37*(11), 2444–2457. https://doi.org/https://doi.org/10.1175/1520-0469(1980)037<2444:CVVEIG>2.0.CO;2

Levy, R. C., Leptoukh, G. G., Kahn, R., Zubko, V., Gopalan, A., & Remer, L. A. (2009). A Critical Look at Deriving Monthly Aerosol Optical Depth From Satellite Data. *IEEE Transactions on Geoscience and Remote Sensing*, *47*(8), 2942–2956. https://doi.org/10.1109/TGRS.2009.2013842

Levy, R. C., Mattoo, S., Munchak, L. A., Remer, L. A., Sayer, A. M., Patadia, F., & Hsu, N. C. (2013). The Collection 6 MODIS aerosol products over land and ocean. *Atmospheric Measurement Techniques*, *6*(11), 2989–3034. https://doi.org/10.5194/amt-6-2989-2013

Lewis, J. R., Welton, E. J., Molod, A. M., & Joseph, E. (2013). Improved boundary layer depth retrievals from MPLNET. *Journal of Geophysical Research: Atmospheres*, *118*(17), 9870–9879. https://doi.org/10.1002/jgrd.50570

Li, H., & Moisseev, D. (2019). Melting Layer Attenuation at Ka- and W-Bands as Derived From Multifrequency Radar Doppler Spectra Observations. *Journal of Geophysical Research: Atmospheres*, *124*(16), 9520–9533. https://doi.org/10.1029/2019JD030316

Li, H., & Moisseev, D. (2020). Two Layers of Melting Ice Particles Within a Single Radar Bright Band: Interpretation and Implications. *Geophysical Research Letters*, *47*(13), e2020GL087499.

Li, H., Tiira, J., von Lerber, A., & Moisseev, D. (2020). Towards the connection between snow microphysics and melting layer: insights from multifrequency and dual-polarization radar observations during BAECC. *Atmospheric Chemistry and Physics*, *20*(15), 9547–9562. https://doi.org/10.5194/acp-20-9547-2020

Li, L., Heymsfield, G. M., Tian, L., & Racette, P. E. (2005). Measurements of Ocean Surface Backscattering Using an Airborne 94-GHz Cloud Radar—Implication for Calibration of Airborne and Spaceborne W-Band Radars. *Journal of Atmospheric and Oceanic Technology*, *22*(7), 1033–1045. https://doi.org/10.1175/JTECH1722.1

Liao, L., & Meneghini, R. (2019). Physical Evaluation of GPM DPR Single- and Dual-Wavelength Algorithms. *Journal of Atmospheric and Oceanic Technology*, *36*(5), 883–902. https://doi.org/10.1175/JTECH-D-18-0210.1

Liao, L., & Meneghini, R. (2022). GPM DPR Retrievals: Algorithm, Evaluation, and Validation. *Remote*

Sensing, *14*(4), 843. https://doi.org/10.3390/rs14040843

Liao, L., Meneghini, R., Tian, L., & Heymsfield, G. M. (2009). Measurements and Simulations of Nadir-Viewing Radar Returns from the Melting Layer at X and W Bands. *Journal of Applied Meteorology and Climatology*, *48*(11), 2215–2226. https://doi.org/10.1175/2009JAMC2033.1

Lieke, K., Kandler, K., Scheuvens, D., Emmel, C., Von Glahn, C., Petzold, A., Weinzierl, B., Veira, A., Ebert, M., Weinbruch, S., Schütz, L., Glahn, C. Von, Petzold, A., Weinzierl, B., Veira, A., Ebert, M., Weinbruch, S., & Schütz, L. (2011). Particle chemical properties in the vertical column based on aircraft observations in the vicinity of Cape Verde Islands. *Tellus B: Chemical and Physical Meteorology*, *63*(4), 497. https://doi.org/10.1111/j.1600-0889.2011.00553.x

Liu, B., Ma, Y., Gong, W. et al. Comparison of AOD from CALIPSO, MODIS, and Sun Photometer under Different Conditions over Central China. Sci Rep 8, 10066 (2018). https://doi.org/10.1038/s41598-018-28417-7

Liu, C., Shen, X., & Gao, W. (2018). Intercomparison of CALIOP, MODIS, and AERONET aerosol optical depth over China during the past decade. *International Journal of Remote Sensing*, *39*(21), 7251–7275. https://doi.org/10.1080/01431161.2018.1466070

Liu, G. (2008). Deriving snow cloud characteristics from CloudSat observations. *Journal of Geophysical Research: Atmospheres*, *113*(D8). https://doi.org/https://doi.org/10.1029/2007JD009766

Liu, Q., Huang, Z., Liu, J., Chen, W., Dong, Q., Wu, S., Dai, G., Li, M., Li, W., Li, Z., Song, X., & Xie, Y. (2024). Validation of initial observation from the first spaceborne high-spectral-resolution lidar with a ground-based lidar network. *Atmospheric Measurement Techniques*, *17*(5), 1403–1417. https://doi.org/10.5194/amt-17-1403-2024

Liu, Z., Kar, J., Zeng, S., Tackett, J., Vaughan, M., Avery, M., Pelon, J., Getzewich, B., Lee, K.-P., Magill, B., Omar, A., Lucker, P., Trepte, C., & Winker, D. (2019). Discriminating between clouds and aerosols in the CALIOP version 4.1 data products. *Atmospheric Measurement Techniques*, *12*(1), 703–734. https://doi.org/10.5194/amt-12-703-2019

Liu, Z., Marchand, R., & Ackerman, T. (2010). A comparison of observations in the tropical western Pacific from ground-based and satellite millimeter-wavelength cloud radars. *Journal of Geophysical Research: Atmospheres*, *115*(D24). https://doi.org/10.1029/2009JD013575

Liu, Z., Winker, D., Omar, A., Vaughan, M., Kar, J., Trepte, C., Hu, Y., & Schuster, G. (2015). Evaluation of CALIOP 532 nm aerosol optical depth over opaque water clouds. *Atmospheric Chemistry and Physics*, *15*(3), 1265–1288. https://doi.org/10.5194/acp-15-1265-2015

Loew, A., Bell, W., Brocca, L., Bulgin, C. E., Burdanowitz, J., Calbet, X., Donner, R. V., Ghent, D., Gruber, A., Kaminski, T., Kinzel, J., Klepp, C., Lambert, J., Schaepman-Strub, G., Schröder, M., & Verhoelst, T. (2017). Validation practices for satellite-based Earth observation data across communities. *Reviews of Geophysics*, *55*(3), 779–817. https://doi.org/10.1002/2017RG000562

Löffler-Mang, M., & Joss, J. (2000). An Optical Disdrometer for Measuring Size and Velocity of Hydrometeors. *Journal of Atmospheric and Oceanic Technology*, *17*(2), 130–139. https://doi.org/10.1175/1520-0426(2000)017<0130:AODFMS>2.0.CO;2

Lopatin, A., Dubovik, O., Chaikovsky, A., Goloub, P., Lapyonok, T., Tanré, D., & Litvinov, P. (2013). Enhancement of aerosol characterization using synergy of lidar and sun-photometer coincident observations: the GARRLiC algorithm. *Atmospheric Measurement Techniques*, *6*(8), 2065–2088. https://doi.org/10.5194/amt-6-2065-2013

Lopatin, A., Dubovik, O., Fuertes, D., Stenchikov, G., Lapyonok, T., Veselovskii, I., Wienhold, F. G., Shevchenko, I., Hu, Q., & Parajuli, S. (2021). Synergy processing of diverse ground-based remote sensing and in situ data using the GRASP algorithm: applications to radiometer, lidar and radiosonde observations. *Atmospheric Measurement Techniques*, *14*(3), 2575–2614. https://doi.org/10.5194/amt-14-2575-2021

Louf, V., Protat, A., Warren, R. A., Collis, S. M., Wolff, D. B., Raunyiar, S., Jakob, C., & Petersen, W. A. (2019). An Integrated Approach to Weather Radar Calibration and Monitoring Using Ground Clutter and Satellite Comparisons. *Journal of Atmospheric and Oceanic Technology*, *36*(1), 17–39. https://doi.org/10.1175/JTECH-D-18-0007.1

Lux, O., Lemmerz, C., Weiler, F., Marksteiner, U., Witschas, B., Rahm, S., Geiß, A., & Reitebuch, O. (2020). Intercomparison of wind observations from the European Space Agency's Aeolus satellite mission and the ALADIN Airborne Demonstrator. *Atmospheric Measurement Techniques*, *13*(4), 2075–2097. https://doi.org/10.5194/amt-13-2075-2020

Lux, O., Lemmerz, C., Weiler, F., Marksteiner, U., Witschas, B., Rahm, S., Schäfler, A., & Reitebuch, O. (2018). Airborne wind lidar observations over the North Atlantic in 2016 for the pre-launch validation of the satellite mission Aeolus. *Atmospheric Measurement Techniques*, *11*(6), 3297–3322. https://doi.org/10.5194/amt-11-3297-2018

Ma, X., Bartlett, K., Harmon, K., & Yu, F. (2013). Comparison of AOD between CALIPSO and MODIS: significant differences over major dust and biomass burning regions. *Atmospheric Measurement Techniques*, *6*(9), 2391–2401. https://doi.org/10.5194/amt-6-2391-2013

Maahn, M., Burgard, C., Crewell, S., Gorodetskaya, I. V., Kneifel, S., Lhermitte, S., Van Tricht, K., van Lipzig, N. P. M., Tricht, K. Van, & van Lipzig, N. P. M. (2014). How does the spaceborne radar blind zone affect derived surface snowfall statistics in polar regions? *Journal of Geophysical Research: Atmospheres*, *119*(24). https://doi.org/10.1002/2014JD022079

Maahn, M., Moisseev, D., Steinke, I., Maherndl, N., & Shupe, M. D. (2024). Introducing the Video In Situ Snowfall Sensor (VISSS). *Atmospheric Measurement Techniques*, *17*(2), 899–919. https://doi.org/10.5194/amt-17-899-2024

Mace, G. G., & Zhang, Q. (2014). The CloudSat radar-lidar geometrical profile product (RL-GeoProf): Updates, improvements, and selected results. *Journal of Geophysical Research: Atmospheres*, *119*(15), 9441–9462. https://doi.org/10.1002/2013JD021374

Maesaka, T. (2018). Cloud radars. Remote Sensing of Clouds and Precipitation. *Andronache, C. (Ed.), Springer Remote Sensing/Photogrammetry, Springer International Publishing*, 137–152.

Mamouri, R. E., Amiridis, V., Papayannis, A., Giannakaki, E., Tsaknakis, G., & Balis, D. S. (2009). Validation of CALIPSO space-borne-derived attenuated backscatter coefficient profiles using a ground-based lidar in Athens, Greece. *Atmospheric Measurement Techniques*, *2*(2), 513–522. https://doi.org/10.5194/amt-2-513-2009

Marchand, R., Ackerman, T., Smyth, M., & Rossow, W. B. (2010). A review of cloud top height and optical depth histograms from MISR, ISCCP, and MODIS. *Journal of Geophysical Research: Atmospheres*, *115*(D16). https://doi.org/10.1029/2009JD013422

Marchand, R., Mace, G. G., Ackerman, T., & Stephens, G. (2008). Hydrometeor Detection Using Cloudsat—An Earth-Orbiting 94-GHz Cloud Radar. *Journal of Atmospheric and Oceanic Technology*, *25*(4), 519–533. https://doi.org/10.1175/2007JTECHA1006.1

Marcos, C., & Rodríguez, A. (2019). Algorithm Theoretical Basis Document for the Precipitation Product Processors of the NWC/GEO. *EUMETSAT NWC SAF*.

Mardiana, R., Iguchi, T., & Takahashi, N. (2004). A dual-frequency rain profiling method without the use of a surface reference technique. *IEEE Transactions on Geoscience and Remote Sensing*, *42*(10), 2214–2225. https://doi.org/10.1109/TGRS.2004.834647

Marenco, F., Amiridis, V., Marinou, E., Tsekeri, A., & Pelon, J. (2014). Airborne verification of CALIPSO products over the Amazon: a case study of daytime observations in a complex atmospheric scene. *Atmospheric Chemistry and Physics*, *14*(21), 11871–11881. https://doi.org/10.5194/acp-14-11871-2014

Marenco, F., Johnson, B., Langridge, J. M., Mulcahy, J., Benedetti, A., Remy, S., Jones, L., Szpek, K., Haywood, J., Longo, K., & Artaxo, P. (2016). On the vertical distribution of smoke in the Amazonian atmosphere during the dry season. *Atmospheric Chemistry and Physics*, *16*(4), 2155–2174. https://doi.org/10.5194/acp-16-2155-2016

Marenco, F., Johnson, B., Turnbull, K., Newman, S., Haywood, J., Webster, H., & Ricketts, H. (2011). Airborne lidar observations of the 2010 Eyjafjallajökull volcanic ash plume. *Journal of Geophysical Research*, *116*. https://doi.org/10.1029/2011JD016396

Marenco, F., Santacesaria, V., Bais, A. F., Balis, D., di Sarra, A., Papayannis, A., & Zerefos, C. (1997). Optical properties of tropospheric aerosols determined by lidar and spectrophotometric measurements (Photochemical Activity and Solar Ultraviolet Radiation campaign). *Applied Optics*, *36*(27), 6875. https://doi.org/10.1364/AO.36.006875

Marks, D. A., Wolff, D. B., Carey, L. D., & Tokay, A. (2011). Quality Control and Calibration of the Dual-Polarization Radar at Kwajalein, RMI. *Journal of Atmospheric and Oceanic Technology*, *28*(2), 181–196. https://doi.org/10.1175/2010JTECHA1462.1

Marseille, G., de Kloe, J., Marksteiner, U., Reitebuch, O., Rennie, M., & de Haan, S. (2022). NWP calibration applied to Aeolus Mie channel winds. *Quarterly Journal of the Royal Meteorological Society*, *148*(743), 1020–1034. https://doi.org/10.1002/qj.4244

Marshak, A., Davis, A., Wiscombe, W., Ridgway, W., & Cahalan, R. (1998). Biases in Shortwave Column Absorption in the Presence of Fractal Clouds. *Journal of Climate*, *11*(3), 431–446. https://doi.org/10.1175/1520-0442(1998)011<0431:BISCAI>2.0.CO;2

Masaki, T., Iguchi, T., Kanemaru, K., Furukawa, K., Yoshida, N., Kubota, T., & Oki, R. (2020). Calibration of the Dual-Frequency Precipitation Radar Onboard the Global Precipitation Measurement Core Observatory. *IEEE Transactions on Geoscience and Remote Sensing*, *60*, 1–16. https://doi.org/10.1109/TGRS.2020.3039978

Mason, S. L., Chiu, C. J., Hogan, R. J., Moisseev, D., & Kneifel, S. (2018). Retrievals of Riming and Snow Density From Vertically Pointing Doppler Radars. *Journal of Geophysical Research: Atmospheres*, *123*(24). https://doi.org/10.1029/2018JD028603

Mason, S. L., Chiu, J. C., Hogan, R. J., & Tian, L. (2017). Improved rain rate and drop size retrievals from airborne Doppler radar. *Atmospheric Chemistry and Physics*, *17*(18), 11567–11589. https://doi.org/10.5194/acp-17-11567-2017

Mason, S. L., Hogan, R. J., Bozzo, A., & Pounder, N. L. (2023). A unified synergistic retrieval of clouds, aerosols, and precipitation from EarthCARE: the ACM-CAP product. *Atmospheric Measurement Techniques*, *16*(13), 3459–3486. https://doi.org/10.5194/amt-16-3459-2023

Mason, S. L., Hogan, R. J., Westbrook, C. D., Kneifel, S., Moisseev, D., & von Terzi, L. (2019). The importance of particle size distribution and internal structure for triple-frequency radar retrievals of the morphology of snow. *Atmospheric Measurement Techniques*, *12*(9), 4993–5018. https://doi.org/10.5194/amt-12-4993-2019

Masuda, K., Ishimoto, H., & Mano, Y. (2012). Efficient method of computing a geometric optics integral for light scattering by nonspherical particles. *Papers in Meteorology and Geophysics*, *63*, 15–19. https://doi.org/10.2467/mripapers.63.15

Matrosov, S. Y. (2011). Feasibility of using radar differential Doppler velocity and dual-frequency ratio for sizing particles in thick ice clouds. *Journal of Geophysical Research*, *116*(D17), D17202. https://doi.org/10.1029/2011JD015857

Matrosov, S. Y. Y. (2008). Assessment of Radar Signal Attenuation Caused by the Melting Hydrometeor Layer. *IEEE Transactions on Geoscience and Remote Sensing*, *46*(4), 1039–1047. https://doi.org/10.1109/TGRS.2008.915757

Mattis, I., D'Amico, G., Baars, H., Amodeo, A., Madonna, F., & Iarlori, M. (2016). EARLINET Single Calculus Chain – technical – Part 2: Calculation of optical products. *Atmospheric Measurement Techniques*, *9*(7), 3009–3029. https://doi.org/10.5194/amt-9-3009-2016

May, R. M., Goebbert, K. H., Thielen, J. E., Leeman, J. R., Camron, M. D., Bruick, Z., Bruning, E. C., Manser, R. P., Arms, S. C., & Marsh, P. T. (2022). MetPy: A Meteorological Python Library for Data Analysis and Visualization. *Bulletin of the American Meteorological Society*, *103*(10). https://doi.org/10.1175/BAMS-D-21-0125.1

May, E., Rydberg, B., Kaur, I., Mattioli, V., Hallborn, H., and Eriksson, P. (2024): The Ice Cloud Imager: retrieval of frozen water column properties, Atmos. Meas. Tech., 17, 5957–5987, https://doi.org/10.5194/amt-17-5957-2024

McComiskey, A., & Feingold, G. (2012). The scale problem in quantifying aerosol indirect effects. *Atmospheric Chemistry and Physics*, *12*(2), 1031–1049. https://doi.org/10.5194/acp-12-1031-2012

McCusker, K., Baran, A. J., Westbrook, C., Fox, S., Eriksson, P., Cotton, R., Delanoë, J., and Ewald, F. (2024): The first microwave and submillimetre closure study using particle models of oriented ice hydrometeors to simulate polarimetric measurements of ice clouds, Atmos. Meas. Tech., 17, 3533–3552, https://doi.org/10.5194/amt-17-3533-2024.

McFarquhar, G. M., Baumgardner, D., Bansemer, A., Abel, S. J., Crosier, J., French, J., Rosenberg, P., Korolev, A., Schwarzoenboeck, A., Leroy, D., Um, J., Wu, W., Heymsfield, A. J., Twohy, C., Detwiler, A., Field, P., Neumann, A., Cotton, R., Axisa, D., & Dong, J. (2017). Processing of Ice Cloud In Situ Data Collected by Bulk Water, Scattering, and Imaging Probes: Fundamentals, Uncertainties, and Efforts toward Consistency. *Meteorological Monographs*, *58*, 11.1-11.33. https://doi.org/10.1175/AMSMONOGRAPHS-D-16-0007.1

McFarquhar, G. M., & Black, R. A. (2004). Observations of Particle Size and Phase in Tropical Cyclones: Implications for Mesoscale Modeling of Microphysical Processes. *Journal of the Atmospheric Sciences*, *61*(4), 422–439. https://doi.org/10.1175/1520-0469(2004)061%3C0422:OOPSAP%3E2.0.CO;2

McFarquhar, G. M., & Heymsfield, A. J. (1998). The Definition and Significance of an Effective Radius for Ice Clouds. *Journal of the Atmospheric Sciences*, *55*(11), 2039–2052. https://doi.org/10.1175/1520-0469(1998)055%3C2039:TDASOA%3E2.0.CO;2

McFarquhar, G. M., Zhang, G., Poellot, M. R., Kok, G. L., McCoy, R., Tooman, T., Fridlind, A., & Heymsfield, A. J. (2007). Ice properties of single-layer stratocumulus during the Mixed-Phase Arctic Cloud Experiment: 1. Observations. *Journal of Geophysical Research: Atmospheres*, *112*(D24). https://doi.org/10.1029/2007JD008633

McGill, M., Hlavka, D., Hart, W., Scott, V. S., Spinhirne, J., & Schmid, B. (2002). Cloud Physics Lidar: instrument description and initial measurement results. *Applied Optics*, *41*(18), 3725. https://doi.org/10.1364/AO.41.003725

McGill, M. J., Vaughan, M. A., Trepte, C. R., Hart, W. D., Hlavka, D. L., Winker, D. M., & Kuehn, R. (2007). Airborne validation of spatial properties measured by the CALIPSO lidar. *Journal of Geophysical Research: Atmospheres*, *112*(D20). https://doi.org/10.1029/2007JD008768

McIlhattan, E. A., L'Ecuyer, T. S., Miller, N. B., L'Ecuyer, T. S., & Miller, N. B. (2017). Observational Evidence Linking Arctic Supercooled Liquid Cloud Biases in CESM to Snowfall Processes. *Journal of Climate*, *30*(12), 4477–4495. https://doi.org/10.1175/JCLI-D-16-0666.1

McPherson, C. J., Reagan, J. A., Schafer, J., Giles, D., Ferrare, R., Hair, J., & Hostetler, C. (2010). AERONET, airborne HSRL, and CALIPSO aerosol retrievals compared and combined: A case study. *Journal of Geophysical Research: Atmospheres*, *115*(D4). https://doi.org/10.1029/2009JD012389

Mech, M., Kliesch, L.-L., Anhäuser, A., Rose, T., Kollias, P., & Crewell, S. (2019). Microwave Radar/radiometer for Arctic Clouds (MiRAC): first insights from the ACLOUD campaign. *Atmospheric Measurement Techniques*, *12*(9), 5019–5037. https://doi.org/10.5194/amt-12-5019-2019

Mech, M., Maahn, M., Kneifel, S., Ori, D., Orlandi, E., Kollias, P., Schemann, V., & Crewell, S. (2020). PAMTRA 1.0: the Passive and Active Microwave radiative TRAnsfer tool for simulating radiometer and radar measurements of the cloudy atmosphere. *Geoscientific Model Development*, *13*(9), 4229–4251. https://doi.org/10.5194/gmd-13-4229-2020

Mech, M., Orlandi, E., Crewell, S., Ament, F., Hirsch, L., Hagen, M., Peters, G., & Stevens, B. (2014). HAMP – the microwave package on the High Altitude and LOng range research aircraft (HALO). *Atmospheric Measurement Techniques*, *7*(12), 4539–4553. https://doi.org/10.5194/amt-7-4539-2014

Meneghini, R., Eckerman, J., & Atlas, D. (1983). Determination of Rain Rate from a Spaceborne Radar Using Measurements of Total Attenuation. *IEEE Transactions on Geoscience and Remote Sensing*, *GE-21*(1), 34–43. https://doi.org/10.1109/TGRS.1983.350528

Meneghini, R., Kim, H., Liao, L., Kwiatkowski, J., & Iguchi, T. (2021). Path Attenuation Estimates for the GPM Dual-frequency Precipitation Radar (DPR). *Journal of the Meteorological Society of Japan. Ser. II*, *99*(1), 181–200. https://doi.org/10.2151/jmsj.2021-010

Menzel, W. P., Frey, R. A., Zhang, H., Wylie, D. P., Moeller, C. C., Holz, R. E., Maddux, B., Baum, B. A., Strabala, K. I., & Gumley, L. E. (2008). MODIS Global Cloud-Top Pressure and Amount Estimation: Algorithm Description and Results. *Journal of Applied Meteorology and Climatology*, *47*(4), 1175–1198. https://doi.org/10.1175/2007JAMC1705.1

Michailidis, K., Koukouli, M.-E., Balis, D., Veefkind, J. P., de Graaf, M., Mona, L., Papagianopoulos, N., Pappalardo, G., Tsikoudi, I., Amiridis, V., Marinou, E., Gialitaki, A., Mamouri, R.-E., Nisantzi, A., Bortoli, D., Costa, M. J., Salgueiro, V., Papayannis, A., Mylonaki, M., … Baars, H. (2023). Validation of the TROPOMI/S5P aerosol layer height using EARLINET lidars. *Atmospheric Chemistry and Physics*, *23*(3), 1919–1940. https://doi.org/10.5194/acp-23-1919-2023

Mielonen, T., Arola, A., Komppula, M., Kukkonen, J., Koskinen, J., de Leeuw, G., & Lehtinen, K. E. J. (2009). Comparison of CALIOP level 2 aerosol subtypes to aerosol types derived from AERONET inversion data. *Geophysical Research Letters*, *36*(18). https://doi.org/10.1029/2009GL039609

Mishchenko, M. I., and L. D. Travis (1997), Satellite retrieval of aerosol properties over the ocean using measurements of reflected sunlight: Effect of instrumental errors and aerosol absorption, J. Geophys. Res., 102(D12), 13543–13553, doi:10.1029/97JD01124

Mona, L., Amodeo, A., Pandolfi, M., & Pappalardo, G. (2006). Saharan dust intrusions in the Mediterranean area: Three years of Raman lidar measurements. *Journal of Geophysical Research: Atmospheres*, *111*(D16), n/a—-n/a. https://doi.org/10.1029/2005JD006569

Mona, L., Pappalardo, G., Amodeo, A., D'Amico, G., Madonna, F., Boselli, A., Giunta, A., Russo, F., & Cuomo, V. (2009). One year of CNR-IMAA multi-wavelength Raman lidar measurements in coincidence with CALIPSO overpasses: Level 1 products comparison. *Atmospheric Chemistry and Physics*. https://doi.org/10.5194/acp-9-7213-2009

Moody, E. G., King, M. D., Schaaf, C. B., Hall, D. K., & Platnick, S. (2007). Northern Hemisphere five-year average (2000–2004) spectral albedos of surfaces in the presence of snow: Statistics computed from Terra MODIS land products. *Remote Sensing of Environment*, *111*(2–3), 337–345. https://doi.org/10.1016/j.rse.2007.03.026

Moradi, I., Johnson, B., Stegmann, P., Holdaway, D., Heymsfield, G., Gelaro, R., & McCarty, W. (2023). Developing a Radar Signal Simulator for the Community Radiative Transfer Model. *IEEE Transactions on Geoscience and Remote Sensing*, *61*, 1–13. https://doi.org/10.1109/TGRS.2023.3330067

Moradi, I., Stegmann, P., Johnson, B., Barlakas, V., Eriksson, P., Geer, A., Gelaro, R., Kalluri, S., Kleist, D., Liu, Q., & Mccarty, W. (2022). Implementation of a Discrete Dipole Approximation Scattering Database Into Community Radiative Transfer Model. *Journal of Geophysical Research: Atmospheres*, *127*(24). https://doi.org/10.1029/2022JD036957

Morcrette, J.-J., Barker, H. W., Cole, J. N. S., Iacono, M. J., & Pincus, R. (2008). Impact of a New Radiation Package, McRad, in the ECMWF Integrated Forecasting System. *Monthly Weather Review*, *136*(12), 4773–4798. https://doi.org/10.1175/2008MWR2363.1

Moroney, C., Davies, R., & Muller, J.-P. (2002). Operational retrieval of cloud-top heights using MISR data. *IEEE Transactions on Geoscience and Remote Sensing*, *40*(7), 1532–1540. https://doi.org/10.1109/TGRS.2002.801150

Morys, M., Mims, F. M., Hagerup, S., Anderson, S. E., Baker, A., Kia, J., & Walkup, T. (2001). Design, calibration, and performance of MICROTOPS II handheld ozone monitor and Sun photometer. *Journal of Geophysical Research: Atmospheres*, *106*(D13), 14573–14582. https://doi.org/10.1029/2001JD900103

Mróz, K., Battaglia, A., Kneifel, S., D'Adderio, L. P., & Dias Neto, J. (2020). Triple-Frequency Doppler Retrieval of Characteristic Raindrop Size. *Earth and Space Science*, *7*(3). https://doi.org/10.1029/2019EA000789

Mróz, K., Battaglia, A., Kneifel, S., von Terzi, L., Karrer, M., & Ori, D. (2021). Linking rain into ice microphysics across the melting layer in stratiform rain: a closure study. *Atmospheric Measurement Techniques*, *14*(1), 511–529. https://doi.org/10.5194/amt-14-511-2021

Mroz, K., Montopoli, M., Battaglia, A., Panegrossi, G., Kirstetter, P., & Baldini, L. (2021). Cross-validation of active and passive microwave snowfall products over the continental United States. *Journal of Hydrometeorology*. https://doi.org/10.1175/JHM-D-20-0222.1

Mroz, K., Treserras, B. P., Battaglia, A., Kollias, P., Tatarevic, A., & Tridon, F. (2023). Cloud and precipitation microphysical retrievals from the EarthCARE Cloud Profiling Radar: the C-CLD product. *Atmospheric Measurement Techniques*, *16*(11), 2865–2888. https://doi.org/10.5194/amt-16-2865-2023

Müller, D., Hostetler, C. A., Ferrare, R. A., Burton, S. P., Chemyakin, E., Kolgotin, A., Hair, J. W., Cook, A. L., Harper, D. B., Rogers, R. R., Hare, R. W., Cleckner, C. S., Obland, M. D., Tomlinson, J., Berg, L. K., & Schmid, B. (2014). Airborne Multiwavelength High Spectral Resolution Lidar (HSRL-2) observations during TCAP 2012: vertical profiles of optical and microphysical properties of a smoke/urban haze plume over the northeastern coast of the US. *Atmospheric Measurement Techniques*, *7*(10), 3487–3496. https://doi.org/10.5194/amt-7-3487-2014

Müller, D., Wandinger, U., & Ansmann, A. (1999). Microphysical particle parameters from extinction and backscatter lidar data by inversion with regularization: theory. *Applied Optics*, *38*(12), 2346. https://doi.org/10.1364/AO.38.002346

Myagkov, A., Kneifel, S., & Rose, T. (2020). Evaluation of the reflectivity calibration of W-band radars based on observations in rain. *Atmospheric Measurement Techniques*, *13*(11), 5799–5825. https://doi.org/10.5194/amt-13-5799-2020

Myagkov, A., Seifert, P., Wandinger, U., Bühl, J., & Engelmann, R. (2016). Relationship between temperature and apparent shape of pristine ice crystals derived from polarimetric cloud radar observations during the ACCEPT campaign. *Atmospheric Measurement Techniques*, *9*(8), 3739–3754. https://doi.org/10.5194/amt-9-3739-2016

Nakajima, T., Campanelli, M., Che, H., Estellés, V., Irie, H., Kim, S.-W., Kim, J., Liu, D., Nishizawa, T., Pandithurai, G., Soni, V. K., Thana, B., Tugjsurn, N.-U., Aoki, K., Go, S., Hashimoto, M., Higurashi, A., Kazadzis, S., Khatri, P., … Yamazaki, A. (2020). An overview of and issues with sky radiometer technology and SKYNET. *Atmospheric Measurement Techniques*, *13*(8), 4195–4218. https://doi.org/10.5194/amt-13-4195-2020

Nakajima, T., & Tanaka, M. (1986). Matrix formulations for the transfer of solar radiation in a plane-parallel scattering atmosphere. *Journal of Quantitative Spectroscopy and Radiative Transfer*, *35*(1), 13–21. https://doi.org/10.1016/0022-4073(86)90088-9

Nakajima, T., & Tanaka, M. (1988). Algorithms for radiative intensity calculations in moderately thick atmospheres using a truncation approximation. *Journal of Quantitative Spectroscopy and Radiative Transfer*, *40*(1), 51–69. https://doi.org/10.1016/0022-4073(88)90031-3

Nakajima, T., Tonna, G., Rao, R., Boi, P., Kaufman, Y., & Holben, B. (1996). Use of sky brightness measurements from ground for remote sensing of particulate polydispersions. *Applied Optics*, *35*(15), 2672. https://doi.org/10.1364/AO.35.002672

Nakajima, T., Tsukamoto, M., Tsushima, Y., Numaguti, A., & Kimura, T. (2000). Modeling of the radiative process in an atmospheric general circulation model. *Applied Optics*, *39*(27), 4869. https://doi.org/10.1364/AO.39.004869

Nakajima, T. Y., Ishida, H., Nagao, T. M., Hori, M., Letu, H., Higuchi, R., Tamaru, N., Imoto, N., & Yamazaki, A. (2019). Theoretical basis of the algorithms and early phase results of the GCOM-C (Shikisai) SGLI cloud products. *Progress in Earth and Planetary Science*, *6*(1), 52. https://doi.org/10.1186/s40645-019-0295-9

Nakajima, T., Yoon, S., Ramanathan, V., Shi, G., Takemura, T., Higurashi, A., Takamura, T., Aoki, K., Sohn, B., Kim, S., Tsuruta, H., Sugimoto, N., Shimizu, A., Tanimoto, H., Sawa, Y., Lin, N., Lee, C., Goto, D., & Schutgens, N. (2007). Overview of the Atmospheric Brown Cloud East Asian Regional Experiment 2005 and a study of the aerosol direct radiative forcing in east Asia. *Journal of Geophysical Research: Atmospheres*, *112*(D24). https://doi.org/10.1029/2007JD009009

Nakamura, K., & Furukawa, K. (2023). Estimation of Doppler Velocity Degradation Due to Difference in Beam-Pointing Directions. *IEEE Geoscience and Remote Sensing Letters*, *20*, 1–5. https://doi.org/10.1109/LGRS.2023.3250387

Nappo, C. J., Caneill, J. Y., Furman, R. W., Gifford, F. A., Kaimal, J. C., Kramer, M. L., Lockhart, T. J., Pendergast, M. M., Pielke, R. A., Randerson, D., Shreffler, J. H., & Wyngaard, J. C. (1982). The Workshop on the Representativeness of Meteorological Observations, June 1981, Boulder, Colo. *Bulletin of the American Meteorological Society*, *63*(7), 761–764. http://www.jstor.org/stable/26222836

Nesbitt, S. W., Zipser, E. J., & Cecil, D. J. (2000). A Census of Precipitation Features in the Tropics Using TRMM: Radar, Ice Scattering, and Lightning Observations. *Journal of Climate*, *13*(23), 4087–4106. https://doi.org/10.1175/1520-0442(2000)013<4087:ACOPFI>2.0.CO;2

Neuper, M., & Ehret, U. (2019). Quantitative precipitation estimation with weather radar using a data- and information-based approach. *Hydrology and Earth System Sciences*, *23*(9), 3711–3733. https://doi.org/10.5194/hess-23-3711-2019

Nicolae, D., Vasilescu, J., Talianu, C., Binietoglou, I., Nicolae, V., Andrei, S., & Antonescu, B. (2018). A neural network aerosol-typing algorithm based on lidar data. *Atmospheric Chemistry and Physics*, *18*(19), 14511–14537. https://doi.org/10.5194/acp-18-14511-2018

Nishizawa, T., Jin, Y., Sugimoto, N., Sato, K., Fujikawa, M., Ishii, S., Aoki, M., Nakagawa, K., & Okamoto, H. (2021). Observation of clouds, aerosols, and precipitation by multiple-field-of-view multiple-scattering polarization lidar at 355 nm. *Journal of Quantitative Spectroscopy and Radiative Transfer*, *271*, 107710. https://doi.org/10.1016/j.jqsrt.2021.107710

Nishizawa, T., Kudo, R., Oikawa, E., Higurashi, A., Jin, Y., Sugimoto, N., Sato, K., & Okamoto, H. (2024). Algorithm to retrieve aerosol optical properties using lidar measurements on board the EarthCARE satellite. *Atmospheric Measurement Techniques Discussions*, *2024*, 1–24. https://doi.org/10.5194/amt-2024-100

Nishizawa, T., Okamoto, H., Sugimoto, N., Matsui, I., Shimizu, A., & Aoki, K. (2007). An algorithm that

retrieves aerosol properties from dual-wavelength polarized lidar measurements. *Journal of Geophysical Research: Atmospheres*, *112*(D6). https://doi.org/10.1029/2006JD007435

Nishizawa, T., Okamoto, H., Takemura, T., Sugimoto, N., Matsui, I., & Shimizu, A. (2008). Aerosol retrieval from two-wavelength backscatter and one-wavelength polarization lidar measurement taken during the MR01K02 cruise of the R/V Mirai and evaluation of a global aerosol transport model. *Journal of Geophysical Research: Atmospheres*, *113*(D21). https://doi.org/10.1029/2007JD009640

Nishizawa, T., Sugimoto, N., Matsui, I., Shimizu, A., Hara, Y., Itsushi, U., Yasunaga, K., Kudo, R., & Kim, S.-W. (2017). Ground-based network observation using Mie–Raman lidars and multi-wavelength Raman lidars and algorithm to retrieve distributions of aerosol components. *Journal of Quantitative Spectroscopy and Radiative Transfer*, *188*, 79–93. https://doi.org/10.1016/j.jqsrt.2016.06.031

Nishizawa, T., Sugimoto, N., Matsui, I., Shimizu, A., & Okamoto, H. (2011). Algorithms to retrieve optical properties of three component aerosols from two-wavelength backscatter and one-wavelength polarization lidar measurements considering nonsphericity of dust. *Journal of Quantitative Spectroscopy and Radiative Transfer*, *112*(2), 254–267. https://doi.org/10.1016/j.jqsrt.2010.06.002

Noël, B., van de Berg, W. J., van Wessem, J. M., van Meijgaard, E., van As, D., Lenaerts, J. T. M., Lhermitte, S., Munneke, P. K., Smeets, C. J. P. P., van Ulft, L. H., van de Wal, R. S. W., & van den Broeke, M. R. (2018). Modelling the climate and surface mass balance of polar ice sheets using RACMO2 – Part~1: Greenland (1958–2016). *The Cryosphere*, *12*(3), 811–831. https://doi.org/10.5194/tc-12-811-2018

Noel, V., & Sassen, K. (2005). Study of planar ice crystal orientations in ice clouds from scanning polarization lidar observations. *Journal of Applied Meteorology*, *44*(5), 653–664. https://doi.org/10.1175/JAM2223.1

North, K. W., Oue, M., Kollias, P., Giangrande, S. E., Collis, S. M., & Potvin, C. K. (2017). Vertical air motion retrievals in deep convective clouds using the ARM scanning radar network in Oklahoma during MC3E. *Atmospheric Measurement Techniques*, *10*(8), 2785–2806. https://doi.org/10.5194/amt-10-2785-2017

Nowottnick, E. P., Christian, K. E., Yorks, J. E., McGill, M. J., Midzak, N., Selmer, P. A., Lu, Z., Wang, J., & Salinas, S. V. (2022). Aerosol Detection from the Cloud–Aerosol Transport System on the International Space Station: Algorithm Overview and Implications for Diurnal Sampling. *Atmosphere*, *13*(9), 1439. https://doi.org/10.3390/atmos13091439

O'Connor, E. J., Illingworth, A. J., & Hogan, R. J. (2004). A Technique for Autocalibration of Cloud Lidar. *Journal of Atmospheric and Oceanic Technology*, *21*(5), 777–786. https://doi.org/10.1175/1520-0426(2004)021<0777:ATFAOC>2.0.CO;2

O'Sullivan, D., Marenco, F., Ryder, C. L., Pradhan, Y., Kipling, Z., Johnson, B., Benedetti, A., Brooks, M., McGill, M., Yorks, J., & Selmer, P. (2020). Models transport Saharan dust too low in the atmosphere: a comparison of the MetUM and CAMS forecasts with observations. *Atmospheric Chemistry and Physics*, *20*(21), 12955–12982. https://doi.org/10.5194/acp-20-12955-2020

Okamoto, H. (2002). Information content of the 95-GHz cloud radar signals: Theoretical assessment of effects of nonsphericity and error evaluation of the discrete dipole approximation. *Journal of Geophysical Research: Atmospheres*, *107*(D22). https://doi.org/10.1029/2001JD001386

Okamoto, H., Nishizawa, T., Takemura, T., Kumagai, H., Kuroiwa, H., Sugimoto, N., Matsui, I., Shimizu, A., Emori, S., Kamei, A., & Nakajima, T. (2007). Vertical cloud structure observed from shipborne radar and lidar: Midlatitude case study during the MR01/K02 cruise of the research vessel Mirai. *Journal of Geophysical Research: Atmospheres*, *112*(D8). https://doi.org/10.1029/2006JD007628

Okamoto, H., Nishizawa, T., Takemura, T., Sato, K., Kumagai, H., Ohno, Y., Sugimoto, N., Shimizu, A.,

Matsui, I., & Nakajima, T. (2008). Vertical cloud properties in the tropical western Pacific Ocean: Validation of the CCSR/NIES/FRCGC GCM by shipborne radar and lidar. *Journal of Geophysical Research: Atmospheres*, *113*(D24). https://doi.org/10.1029/2008JD009812

Okamoto, H., Sato, K., Borovoi, A., Ishimoto, H., Masuda, K., Konoshonkin, A., & Kustova, N. (2019). Interpretation of lidar ratio and depolarization ratio of ice clouds using spaceborne high-spectral-resolution polarization lidar. *Optics Express*, *27*(25), 36587. https://doi.org/10.1364/OE.27.036587

Okamoto, H., Sato, K., Borovoi, A., Ishimoto, H., Masuda, K., Konoshonkin, A., & Kustova, N. (2020). Wavelength dependence of ice cloud backscatter properties for space-borne polarization lidar applications. *Optics Express*, *28*(20), 29178. https://doi.org/10.1364/OE.400510

Okamoto, H., Sato, K., & Hagihara, Y. (2010). Global analysis of ice microphysics from CloudSat and CALIPSO: Incorporation of specular reflection in lidar signals. *Journal of Geophysical Research: Atmospheres*, *115*(D22). https://doi.org/10.1029/2009JD013383

Okamoto, H., Sato, K., Nishizawa, T., Jin, Y., Nakajima, T. Y., Wang, M., Satoh, M., Suzuki, K., Roh, W., Yamauchi, A., Horie, H., Ohno, Y., Hagihara, Y., Ishimoto, H., Kudo, R., Kubota, T., & Tanaka, T. (2024). JAXA Level2 algorithms for EarthCARE mission from single to four sensors: new perspective of cloud, aerosol, radiation and dynamics. *Atmos. Meas. Tech.*

Okamoto, H., Sato, K., Nishizawa, T., Jin, Y., Ogawa, S., Ishimoto, H., Hagihara, Y., Oikawa, E., & Kikuchi, M. (2024). Cloud mask and cloud type classification using EarthCARE CPR and ATLID. *Atmos. Meas. Tech.*

Okamoto, H., Sato, K., Nishizawa, T., Sugimoto, N., Makino, T., Jin, Y., Shimizu, A., Takano, T., & Fujikawa, M. (2016). Development of a multiple-field-of-view multiple-scattering polarization lidar: comparison with cloud radar. *Optics Express*, *24*(26), 30053. https://doi.org/10.1364/OE.24.030053

Okamoto, K. K. (2003). A Short History of the TRMM Precipitation Radar. In *Cloud Systems, Hurricanes, and the Tropical Rainfall Measuring Mission (TRMM)* (pp. 187–195). American Meteorological Society. https://doi.org/10.1007/978-1-878220-63-9_16

Okata, M., Nakajima, T. Y., Suzuki, K., Inoue, T., Nakajima, T. Y., & Okamoto, H. (2017). A study on radiative transfer effects in 3-D cloudy atmosphere using satellite data. *Journal of Geophysical Research: Atmospheres*, *122*(1), 443–468. https://doi.org/10.1002/2016JD025441

Olson, W. S., Bauer, P., Viltard, N. F., Johnson, D. E., Tao, W.-K., Meneghini, R., & Liao, L. (2001). A Melting-Layer Model for Passive/Active Microwave Remote Sensing Applications. Part I: Model Formulation and Comparison with Observations. *Journal of Applied Meteorology*, *40*(7), 1145–1163. https://doi.org/10.1175/1520-0450(2001)040<1145:AMLMFP>2.0.CO;2

Omar, A. H., Winker, D. M., Tackett, J. L., Giles, D. M., Kar, J., Liu, Z., Vaughan, M. A., Powell, K. A., & Trepte, C. R. (2013). CALIOP and AERONET aerosol optical depth comparisons: One size fits none. *Journal of Geophysical Research: Atmospheres*, *118*(10), 4748–4766. https://doi.org/10.1002/jgrd.50330

Omar, A. H., Winker, D. M., Vaughan, M. A., Hu, Y., Trepte, C. R., Ferrare, R. A., Lee, K.-P., Hostetler, C. A., Kittaka, C., Rogers, R. R., Kuehn, R. E., & Liu, Z. (2009). The CALIPSO Automated Aerosol Classification and Lidar Ratio Selection Algorithm. *Journal of Atmospheric and Oceanic Technology*, *26*(10), 1994–2014. https://doi.org/10.1175/2009JTECHA1231.1

Oo, M. and Holz, R. (2011). Improving the CALIOP aerosol optical depth using combined MODIS-CALIOP observations and CALIOP integrated attenuated total color ratio, J. Geophys. Res., 116,D14201, 15 pp., doi:10.1029/2010JD014894.

Ori, D., Maestri, T., Rizzi, R., Cimini, D., Montopoli, M., & Marzano, F. S. (2014). Scattering properties of modeled complex snowflakes and mixed-phase particles at microwave and millimeter frequencies. *Journal of Geophysical Research: Atmospheres*, *119*(16), 9931–9947.

https://doi.org/10.1002/2014JD021616

Osborne, S. R., & Haywood, J. M. (2005). Aircraft observations of the microphysical and optical properties of major aerosol species. *Atmospheric Research*, *73*(3–4), 173–201. https://doi.org/10.1016/j.atmosres.2004.09.002

Oue, M., Kollias, P., Shapiro, A., Tatarevic, A., & Matsui, T. (2019). Investigation of observational error sources in multi-Doppler-radar three-dimensional variational vertical air motion retrievals. *Atmospheric Measurement Techniques*, *12*(3), 1999–2018. https://doi.org/10.5194/amt-12-1999-2019

Overeem, A., van den Besselaar, E., van der Schrier, G., Meirink, J. F., van der Plas, E., & Leijnse, H. (2023). EURADCLIM: the European climatological high-resolution gauge-adjusted radar precipitation dataset. *Earth System Science Data*, *15*(3), 1441–1464. https://doi.org/10.5194/essd-15-1441-2023

Painemal, D., Clayton, M., Ferrare, R., Burton, S., Josset, D., & Vaughan, M. (2019). Novel aerosol extinction coefficients and lidar ratios over the ocean from CALIPSO–CloudSat: evaluation and global statistics. *Atmospheric Measurement Techniques*, *12*(4), 2201–2217. https://doi.org/10.5194/amt-12-2201-2019

Palm, S. P., Yang, Y., Herzfeld, U., Hancock, D., Hayes, A., Selmer, P., Hart, W., & Hlavka, D. (2021). ICESat-2 Atmospheric Channel Description, Data Processing and First Results. *Earth and Space Science*, *8*(8). https://doi.org/10.1029/2020EA001470

Papagiannopoulos, N., Mona, L., Alados-Arboledas, L., Amiridis, V., Baars, H., Binietoglou, I., Bortoli, D., D'Amico, G., Giunta, A., Guerrero-Rascado, J. L., Schwarz, A., Pereira, S., Spinelli, N., Wandinger, U., Wang, X., & Pappalardo, G. (2016). CALIPSO climatological products: evaluation and suggestions from EARLINET. *Atmospheric Chemistry and Physics*, *16*(4), 2341–2357. https://doi.org/10.5194/acp-16-2341-2016

Papagiannopoulos Nikolaos, Mona Lucia, Amiridis Vassilis, Binietoglou Ioannis, DÁmico Giuseppe, Guma-Claramunt P., Schwarz Anja, Alados-Arboledas Lucas, Amodeo Aldo, Apituley Arnoud, Baars Holger, Bortoli Daniele, Comeron Adolfo, Guerrero-Rascado Juan Luis, Kokkalis Panos, Nicolae Doina, Papayannis Alex, Pappalardo Gelsomina, Wandinger Ulla, & Wiegner Matthias. (2018). An automatic aerosol classification for earlinet: application and results. *EPJ Web Conf.*, *176*, 9012. https://doi.org/10.1051/epjconf/201817609012

Pappalardo, G., Amodeo, A., Apituley, A., Comeron, A., Freudenthaler, V., Linné, H., Ansmann, A., Bösenberg, J., D'Amico, G., Mattis, I., Mona, L., Wandinger, U., Amiridis, V., Alados-Arboledas, L., Nicolae, D., & Wiegner, M. (2014). EARLINET: towards an advanced sustainable European aerosol lidar network. *Atmospheric Measurement Techniques*, *7*(8), 2389–2409. https://doi.org/10.5194/amt-7-2389-2014

Pappalardo, G., Wandinger, U., Mona, L., Hiebsch, A., Mattis, I., Amodeo, A., Ansmann, A., Seifert, P., Linné, H., Apituley, A., Arboledas, L. A., Balis, D., Chaikovsky, A., D'Amico, G., Tomasi, F. De, Freudenthaler, V., Giannakaki, E., Giunta, A., Grigorov, I., … Wiegner, M. (2010). EARLINET correlative measurements for CALIPSO: First intercomparison results. *Journal of Geophysical Research: Atmospheres*, *115*(D4). https://doi.org/10.1029/2009JD012147

Park, H. S., Ryzhkov, A. V., Zrnić, D. S., & Kim, K.-E. (2009). The Hydrometeor Classification Algorithm for the Polarimetric WSR-88D: Description and Application to an MCS. *Weather and Forecasting*, *24*(3), 730–748. https://doi.org/10.1175/2008WAF2222205.1

Park, S. S., Kim, S.-W., Song, C.-K., Park, J.-U., & Bae, K.-H. (2020). Spatio-Temporal Variability of Aerosol Optical Depth, Total Ozone and NO2 Over East Asia: Strategy for the Validation to the GEMS Scientific Products. *Remote Sensing*, *12*(14), 2256. https://doi.org/10.3390/rs12142256

Paschou, P., Siomos, N., Marinou, E., Baars, H., Gkikas, A., Georgoussis, G., Althausen, D., Engelmann, R., von Bismarck, J., Fehr, T., & Amiridis, V. (2023). *First Results from the Aeolus*

Reference Lidar eVe During the Tropical Campaign JATAC at Cabo Verde (pp. 795–801). https://doi.org/10.1007/978-3-031-37818-8_102

Paschou, P., Siomos, N., Tsekeri, A., Louridas, A., Georgoussis, G., Freudenthaler, V., Binietoglou, I., Tsaknakis, G., Tavernarakis, A., Evangelatos, C., von Bismarck, J., Kanitz, T., Meleti, C., Marinou, E., & Amiridis, V. (2022). The eVe reference polarisation lidar system for the calibration and validation of the Aeolus L2A product. *Atmospheric Measurement Techniques*, *15*(7), 2299–2323. https://doi.org/10.5194/amt-15-2299-2022

Pauly, R. M., Yorks, J. E., Hlavka, D. L., McGill, M. J., Amiridis, V., Palm, S. P., Rodier, S. D., Vaughan, M. A., Selmer, P. A., Kupchock, A. W., Baars, H., & Gialitaki, A. (2019). Cloud-Aerosol Transport System (CATS) 1064 nm calibration and validation. *Atmospheric Measurement Techniques*, *12*(11), 6241–6258. https://doi.org/10.5194/amt-12-6241-2019

Peral, E., Tanelli, S., Statham, S., Joshi, S., Imken, T., Price, D., Sauder, J., Chahat, N., & Williams, A. (2019). RainCube: the first ever radar measurements from a CubeSat in space. *Journal of Applied Remote Sensing*, *13*(03), 1. https://doi.org/10.1117/1.JRS.13.032504

Petersen, W. A., Kirstetter, P.-E., Wang, J., Wolff, D. B., & Tokay, A. (2020). *The GPM Ground Validation Program* (pp. 471–502). https://doi.org/10.1007/978-3-030-35798-6_2

Petersen, W. A., L'Ecuyer, T., & Moisseev, D. (2011). The NASA CloudSat/GPM Light Precipitation Validation Experiment (LPVEx). *The Earth Observer*, *23*(4), 4–8.

Petersen, W., Kirstetter, P., Wolff, D., Kidd, C., Tokay, A., Chandrasekar, V., Grecu, M., Huffman, G., & Jackson, G. S. (2016). Gpm Level 1 Science Requirements: Science and Performance Viewed from the Ground. *NASA Technical Report*.

Petersen, W., & Krajewski, W. (2013). *Status Update on the GPM Ground Validation Iowa Flood Studies (IFloodS) Field Experiment*. 13345.

Petracca, M., D'Adderio, L. P., Porcù, F., Vulpiani, G., Sebastianelli, S., & Puca, S. (2018). Validation of GPM Dual-Frequency Precipitation Radar (DPR) Rainfall Products over Italy. *Journal of Hydrometeorology*, *19*(5), 907–925. https://doi.org/10.1175/JHM-D-17-0144.1

Pettersen, C., Bliven, L. F., von Lerber, A., Wood, N. B., Kulie, M. S., Mateling, M. E., Moisseev, D. N., Munchak, S. J., Petersen, W. A., & Wolff, D. B. (2020). The Precipitation Imaging Package: Assessment of Microphysical and Bulk Characteristics of Snow. *Atmosphere*, *11*(8), 785. https://doi.org/10.3390/atmos11080785

Petty, G. W., & Huang, W. (2010). Microwave Backscatter and Extinction by Soft Ice Spheres and Complex Snow Aggregates. *Journal of the Atmospheric Sciences*, *67*(3), 769–787. https://doi.org/10.1175/2009JAS3146.1

Petzold, A., Veira, A., Mund, S., Esselborn, M., Kiemle, C., Weinzierl, B., Hamburger, T., Ehret, G., Lieke, K., & Kandler, K. (2011). Mixing of mineral dust with urban pollution aerosol over Dakar (Senegal): impact on dust physico-chemical and radiative properties. *Tellus B: Chemical and Physical Meteorology*, *63*(4), 619. https://doi.org/10.1111/j.1600-0889.2011.00547.x

Peura, M. (2002). *Computer vision methods for anomaly removal*. 312–317.

Pfreundschuh, S., Eriksson, P., Buehler, S. A., Brath, M., Duncan, D., Larsson, R., and Ekelund, R. (2020): Synergistic radar and radiometer retrievals of ice hydrometeors, Atmos. Meas. Tech., 13, 4219–4245, https://doi.org/10.5194/amt-13-4219-2020.

Planche, C., Wobrock, W., & Flossmann, A. I. (2014). The continuous melting process in a cloud-scale model using a bin microphysics scheme. *Quarterly Journal of the Royal Meteorological Society*, *140*(683), 1986–1996. https://doi.org/10.1002/qj.2265

Platnick, S., King, M. D. D., Ackerman, S. A. A., Menzel, W. P. P., Baum, B. A. A., Riedi, J. C. C., &

Frey, R. A. A. (2003). The MODIS cloud products: algorithms and examples from terra. *IEEE Transactions on Geoscience and Remote Sensing*, *41*(2), 459–473. https://doi.org/10.1109/TGRS.2002.808301

Potvin, C. K., Shapiro, A., & Xue, M. (2012). Impact of a Vertical Vorticity Constraint in Variational Dual-Doppler Wind Analysis: Tests with Real and Simulated Supercell Data. *Journal of Atmospheric and Oceanic Technology*, *29*(1), 32–49. https://doi.org/https://doi.org/10.1175/JTECH-D-11-00019.1

Powell, K. A., Hostetler, C. A., Vaughan, M. A., Lee, K.-P., Trepte, C. R., Rogers, R. R., Winker, D. M., Liu, Z., Kuehn, R. E., Hunt, W. H., & Young, S. A. (2009). CALIPSO Lidar Calibration Algorithms. Part I: Nighttime 532-nm Parallel Channel and 532-nm Perpendicular Channel. *Journal of Atmospheric and Oceanic Technology*, *26*(10), 2015–2033. https://doi.org/10.1175/2009JTECHA1242.1

Proestakis, E., Amiridis, V., Marinou, E., Binietoglou, I., Ansmann, A., Wandinger, U., Hofer, J., Yorks, J., Nowottnick, E., Makhmudov, A., Papayannis, A., Pietruczuk, A., Gialitaki, A., Apituley, A., Szkop, A., Porcar, C. M., Bortoli, D., Dionisi, D., Althausen, D., … Pappalardo, G. (2019). EARLINET evaluation of the CATS Level 2 aerosol backscatter coefficient product. *Atmospheric Chemistry and Physics*, *19*(18), 11743–11764. https://doi.org/10.5194/acp-19-11743-2019

Protat, A., Bouniol, D., Delanoë, J., O'Connor, E., May, P. T., Plana-Fattori, A., Hasson, A., Görsdorf, U., & Heymsfield, A. J. (2009). Assessment of Cloudsat Reflectivity Measurements and Ice Cloud Properties Using Ground-Based and Airborne Cloud Radar Observations. *Journal of Atmospheric and Oceanic Technology*, *26*(9), 1717–1741. https://doi.org/10.1175/2009JTECHA1246.1

Protat, A., Bouniol, D., O'Connor, E. J., Klein Baltink, H., Verlinde, J., & Widener, K. (2011). CloudSat as a Global Radar Calibrator. *Journal of Atmospheric and Oceanic Technology*, *28*(3), 445–452. https://doi.org/10.1175/2010JTECHA1443.1

Protat, A., Pelon, J., Grand, N., Delville, P., Laborie, P., Vinson, J.-P., Bouniol, D., Bruneau, D., Chepfer, H., Delanoe, J., Haeffelin, M., Noel, V., & Tinel, C. (2004). Le projet Rali : combinaison d'un radar et d'un lidar pour l'étude des nuages faiblement précipitants. *La Météorologie*, *8*(47), 23. https://doi.org/10.4267/2042/36076

Qu, Z., Barker, H. W., Cole, J. N. S., & Shephard, M. W. (2023). Across-track extension of retrieved cloud and aerosol properties for the EarthCARE mission: the ACMB-3D product. *Atmospheric Measurement Techniques*, *16*(9), 2319–2331. https://doi.org/10.5194/amt-16-2319-2023

Qu, Z., Donovan, D. P., Barker, H. W., Cole, J. N. S., Shephard, M. W., & Huijnen, V. (2023). Numerical model generation of test frames for pre-launch studies of EarthCARE's retrieval algorithms and data management system. *Atmospheric Measurement Techniques*, *16*(20), 4927–4946. https://doi.org/10.5194/amt-16-4927-2023

Radenz, M., Bühl, J., Lehmann, V., Görsdorf, U., & Leinweber, R. (2018). Combining cloud radar and radar wind profiler for a value added estimate of vertical air motion and particle terminal velocity within clouds. *Atmospheric Measurement Techniques*, *11*(10), 5925–5940. https://doi.org/10.5194/amt-11-5925-2018

Radenz, M., Bühl, J., Seifert, P., Baars, H., Engelmann, R., Barja González, B., Mamouri, R.-E., Zamorano, F., Ansmann, A., González, B. B., Mamouri, R.-E., Zamorano, F., & Ansmann, A. (2021). Hemispheric contrasts in ice formation in stratiform mixed-phase clouds: disentangling the role of aerosol and dynamics with ground-based remote sensing. *Atmospheric Chemistry and Physics*, *21*(23), 17969–17994. https://doi.org/10.5194/acp-21-17969-2021

Rahman, H., Pinty, B., & Verstraete, M. M. (1993). Coupled surface-atmosphere reflectance (CSAR) model: 2. Semiempirical surface model usable with NOAA advanced very high resolution radiometer data. *Journal of Geophysical Research: Atmospheres*, *98*(D11), 20791–20801. https://doi.org/10.1029/93JD02072

Rasmussen, R., Dixon, M., Vasiloff, S., Hage, F., Knight, S., Vivekanandan, J., & Xu, M. (2003). Snow Nowcasting Using a Real-Time Correlation of Radar Reflectivity with Snow Gauge Accumulation. *Journal of Applied Meteorology*, *42*(1), 20–36. https://doi.org/10.1175/1520-0450(2003)042<0020:SNUART>2.0.CO;2

Ravetta, F., Mariage, V., Brousse, E., d'Almeida, E., Ferreira, F., Pelon, J., & Victori, S. (2020). BeCOOL: A Balloon-Borne Microlidar System Designed for Cirrus and Convective Overshoot Monitoring. *EPJ Web of Conferences*, *237*, 07003. https://doi.org/10.1051/epjconf/202023707003

Redemann, J., Schmid, B., Eilers, J. A., Kahn, R., Levy, R. C., Russell, P. B., Livingston, J. M., Hobbs, P. V., Smith, W. L., & Holben, B. N. (2005). Suborbital Measurements of Spectral Aerosol Optical Depth and Its Variability at Subsatellite Grid Scales in Support of CLAMS 2001. *Journal of the Atmospheric Sciences*, *62*(4), 993–1007. https://doi.org/10.1175/JAS3387.1

Redemann, J., Turco, R. P., Liou, K. N., Hobbs, P. V., Hartley, W. S., Bergstrom, R. W., Browell, E. V., & Russell, P. B. (2000). Case studies of the vertical structure of the direct shortwave aerosol radiative forcing during TARFOX. *Journal of Geophysical Research: Atmospheres*, *105*(D8), 9971–9979. https://doi.org/10.1029/1999JD901042

Redemann, J., Vaughan, M. A., Zhang, Q., Shinozuka, Y., Russell, P. B., Livingston, J. M., Kacenelenbogen, M., & Remer, L. A. (2012). The comparison of MODIS-Aqua (C5) and CALIOP (V2 & V3) aerosol optical depth. *Atmospheric Chemistry and Physics*, *12*(6), 3025–3043. https://doi.org/10.5194/acp-12-3025-2012

Redemann, J., Wood, R., Zuidema, P., Doherty, S. J., Luna, B., LeBlanc, S. E., Diamond, M. S., Shinozuka, Y., Chang, I. Y., Ueyama, R., Pfister, L., Ryoo, J.-M., Dobracki, A. N., da Silva, A. M., Longo, K. M., Kacenelenbogen, M. S., Flynn, C. J., Pistone, K., Knox, N. M., … Gao, L. (2021). An overview of the ORACLES (ObseRvations of Aerosols above CLouds and their intEractionS) project: aerosol–cloud–radiation interactions in the southeast Atlantic basin. *Atmospheric Chemistry and Physics*, *21*(3), 1507–1563. https://doi.org/10.5194/acp-21-1507-2021

Reichardt, J., & Reichardt, S. (2003). Effect of multiple scattering on depolarization measurements with spaceborne lidars. *Applied Optics, Vol. 42, Issue 18, Pp. 3620-3633*, *42*(18), 3620–3633. https://doi.org/10.1364/AO.42.003620

Reitebuch, O., Lemmerz, C., Nagel, E., Paffrath, U., Durand, Y., Endemann, M., Fabre, F., & Chaloupy, M. (2009). The Airborne Demonstrator for the Direct-Detection Doppler Wind Lidar ALADIN on ADM-Aeolus. Part I: Instrument Design and Comparison to Satellite Instrument. *Journal of Atmospheric and Oceanic Technology*, *26*(12), 2501–2515. https://doi.org/10.1175/2009JTECHA1309.1

Remer, L. A., Tanré, D., Kaufman, Y. J., Ichoku, C., Mattoo, S., Levy, R., Chu, D. A., Holben, B., Dubovik, O., Smirnov, A., Martins, J. V., Li, R. -R., & Ahmad, Z. (2002). Validation of MODIS aerosol retrieval over ocean. *Geophysical Research Letters*, *29*(12). https://doi.org/10.1029/2001GL013204

Ren, G., Pan, B., Wang, J., An, D., Yang, M., & Liu, H. (2023). Spatiotemporal distribution of dust aerosol optical properties from CALIPSO and CATS observations in Xinjiang, China. *Journal of Atmospheric and Solar-Terrestrial Physics*, *243*, 106006. https://doi.org/https://doi.org/10.1016/j.jastp.2023.106006

Renard, J.-B., Dulac, F., Berthet, G., Lurton, T., Vignelles, D., Jégou, F., Tonnelier, T., Jeannot, M., Couté, B., Akiki, R., Verdier, N., Mallet, M., Gensdarmes, F., Charpentier, P., Mesmin, S., Duverger, V., Dupont, J.-C., Elias, T., Crenn, V., … Daugeron, D. (2016). LOAC: a small aerosol optical counter/sizer for ground-based and balloon measurements of the size distribution and nature of atmospheric particles – Part 1: Principle of measurements and instrument evaluation. Atmospheric Measurement Techniques, 9(4), 1721–1742. https://doi.org/10.5194/amt-9-1721-2016

Rennie, M., & Isaksen, L. (2020). The NWP impact of Aeolus Level-2B Winds at ECMWF.

Rennie, M. P., Isaksen, L., Weiler, F., de Kloe, J., Kanitz, T., & Reitebuch, O. (2021). The impact of <scp>Aeolus</scp> wind retrievals on <scp>ECMWF</scp> global weather forecasts. Quarterly Journal of the Royal Meteorological Society, 147(740), 3555–3586. https://doi.org/10.1002/qj.4142

Rennie, M., Tan, D., Andersson, E., Poli, P., Dabas, A., De Kloe, J., Marseille, G.-J., & Stoffelen, A. (2020). Aeolus Level-2B algorithm theoretical basis document (mathematical description of the Aeolus Level-2B processor).

Rieger, L. A., Zawada, D. J., Bourassa, A. E., & Degenstein, D. A. (2019). A Multiwavelength Retrieval Approach for Improved OSIRIS Aerosol Extinction Retrievals. Journal of Geophysical Research: Atmospheres, 124(13), 7286–7307. https://doi.org/10.1029/2018JD029897

Rogers, R. R., Hair, J. W., Hostetler, C. A., Ferrare, R. A., Obland, M. D., Cook, A. L., Harper, D. B., Burton, S. P., Shinozuka, Y., McNaughton, C. S., Clarke, A. D., Redemann, J., Russell, P. B., Livingston, J. M., & Kleinman, L. I. (2009). NASA LaRC airborne high spectral resolution lidar aerosol measurements during MILAGRO: observations and validation. *Atmospheric Chemistry and Physics*, *9*(14), 4811–4826. https://doi.org/10.5194/acp-9-4811-2009

Rogers, R. R., Hostetler, C. A., Hair, J. W., Ferrare, R. A., Liu, Z., Obland, M. D., Harper, D. B., Cook, A. L., Powell, K. A., Vaughan, M. A., & Winker, D. M. (2011). Assessment of the CALIPSO Lidar 532 nm attenuated backscatter calibration using the NASA LaRC airborne High Spectral Resolution Lidar. *Atmospheric Chemistry and Physics*, *11*(3), 1295–1311. https://doi.org/10.5194/acp-11-1295-2011

Rogers, R. R., Vaughan, M. A., Hostetler, C. A., Burton, S. P., Ferrare, R. A., Young, S. A., Hair, J. W., Obland, M. D., Harper, D. B., Cook, A. L., & Winker, D. M. (2014). Looking through the haze: evaluating the CALIPSO level 2 aerosol optical depth using airborne high spectral resolution lidar data. *Atmospheric Measurement Techniques*, *7*(12), 4317–4340. https://doi.org/10.5194/amt-7-4317-2014

Roh, W., Satoh, M., Hashino, T., Matsugishi, S., Nasuno, T., & Kubota, T. (2023). Introduction to EarthCARE synthetic data using a global storm-resolving simulation. *Atmospheric Measurement Techniques*, *16*(12), 3331–3344. https://doi.org/10.5194/amt-16-3331-2023

Rosenberg, P. D., Dean, A. R., Williams, P. I., Dorsey, J. R., Minikin, A., Pickering, M. A., & Petzold, A. (2012). Particle sizing calibration with refractive index correction for light scattering optical particle counters and impacts upon PCASP and CDP data collected during the Fennec campaign. *Atmospheric Measurement Techniques*, *5*(5), 1147–1163. https://doi.org/10.5194/amt-5-1147-2012

Rossow, W. B., & Schiffer, R. A. (1999). Advances in Understanding Clouds from ISCCP. *Bulletin of the American Meteorological Society*, *80*(11), 2261–2288. https://doi.org/10.1175/1520-0477(1999)080<2261:AIUCFI>2.0.CO;2

Roy, R. J., Carswell, J., Sanchez-Barbetty, M., Maese, T., & Springmann, J. (2023). The Tomorrow.io Pathfinder Mission: Software-Defined Ka-band Precipitation Radar in Space. *2023 IEEE Radar Conference (RadarConf23)*, 1–6. https://doi.org/10.1109/RadarConf2351548.2023.10149672

Roy, R. J., M. Lebsock, L. Millán and K. B. Cooper, (2020). Validation of a G-band differential absorption cloud radar for humidity remote sensing, J. Atmos. Ocean. Technol., vol. 37, no. 6, pp. 1085-1 102

Rubin, J. I., Reid, J. S., Hansen, J. A., Anderson, J. L., Holben, B. N., Xian, P., Westphal, D. L., & Zhang, J. (2017). Assimilation of AERONET and MODIS AOT observations using variational and ensemble data assimilation methods and its impact on aerosol forecasting skill. *Journal of Geophysical Research: Atmospheres*, *122*(9), 4967–4992. https://doi.org/10.1002/2016JD026067

Russchenberg, H. W. J., & Ligthart, L. P. (1996). Backscattering by and propagation through the melting layer of precipitation: a new polarimetric model. *IEEE Transactions on Geoscience and Remote*

Sensing, *34*(1), 3–14. https://doi.org/10.1109/36.481885

Russell, P. B., Kinne, S. A., & Bergstrom, R. W. (1997). Aerosol climate effects: Local radiative forcing and column closure experiments. *Journal of Geophysical Research: Atmospheres*, *102*(D8), 9397–9407. https://doi.org/10.1029/97JD00112

Ryan, R. A., Vaughan, M. A., Rodier, S. D., Tackett, J. L., Reagan, J. A., Ferrare, R. A., Hair, J. W., & Getzewich, B. J. (2024). Total column optical depths retrieved from CALIPSO lidar ocean surface backscatter. *Atmospheric Measurement Techniques, 17(22), 6517-6545. https://doi.org/10.5194/amt-17-6517-2024*

Ryder, C. L., Marenco, F., Brooke, J. K., Estelles, V., Cotton, R., Formenti, P., McQuaid, J. B., Price, H. C., Liu, D., Ausset, P., Rosenberg, P. D., Taylor, J. W., Choularton, T., Bower, K., Coe, H., Gallagher, M., Crosier, J., Lloyd, G., Highwood, E. J., & Murray, B. J. (2018). Coarse-mode mineral dust size distributions, composition and optical properties from AER-D aircraft measurements over the tropical eastern Atlantic. *Atmospheric Chemistry and Physics*, *18*(23), 17225–17257. https://doi.org/10.5194/acp-18-17225-2018

Ryder, C. L., McQuaid, J. B., Flamant, C., Rosenberg, P. D., Washington, R., Brindley, H. E., Highwood, E. J., Marsham, J. H., Parker, D. J., Todd, M. C., Banks, J. R., Brooke, J. K., Engelstaedter, S., Estelles, V., Formenti, P., Garcia-Carreras, L., Kocha, C., Marenco, F., Sodemann, H., … Woolley, A. (2015). Advances in understanding mineral dust and boundary layer processes over the Sahara from Fennec aircraft observations. *Atmospheric Chemistry and Physics*, *15*(14), 8479–8520. https://doi.org/10.5194/acp-15-8479-2015

Ryzhkov, A., Zhang, P., Bukovčić, P., Zhang, J., & Cocks, S. (2022). Polarimetric Radar Quantitative Precipitation Estimation. *Remote Sensing*, *14*(7), 1695. https://doi.org/10.3390/rs14071695

Ryzhkov, A. V., Giangrande, S. E., Melnikov, V. M., & Schuur, T. J. (2005). Calibration Issues of Dual-Polarization Radar Measurements. *Journal of Atmospheric and Oceanic Technology*, *22*(8), 1138–1155. https://doi.org/10.1175/JTECH1772.1

Ryzhkov, A. V., Schuur, T. J., Burgess, D. W., Heinselman, P. L., Giangrande, S. E., & Zrnic, D. S. (2005). The Joint Polarization Experiment: Polarimetric Rainfall Measurements and Hydrometeor Classification. *Bulletin of the American Meteorological Society*, *86*(6), 809–824. https://doi.org/10.1175/BAMS-86-6-809

Saito, M., Yang, P., Ding, J., & Liu, X. (2021). A comprehensive database of the optical properties of irregular aerosol particles for radiative transfer simulations. *Journal of the Atmospheric Sciences*. https://doi.org/10.1175/JAS-D-20-0338.1

Saltikoff, E., Haase, G., Delobbe, L., Gaussiat, N., Martet, M., Idziorek, D., Leijnse, H., Novák, P., Lukach, M., & Stephan, K. (2019). OPERA the Radar Project. *Atmosphere*, *10*(6), 320. https://doi.org/10.3390/atmos10060320

Sassen, K. (2003). *Polarization in lidar: a review* (J. A. Shaw & J. S. Tyo (eds.); p. 151). https://doi.org/10.1117/12.507006

Sassen, K., Kayetha, V. K., & Zhu, J. (2012). Ice cloud depolarization for nadir and off-nadir CALIPSO measurements. *Geophysical Research Letters*, *39*(20). https://doi.org/10.1029/2012GL053116

Sassen, K., & Wang, Z. (2008). Classifying clouds around the globe with the CloudSat radar: 1-year of results. *Geophysical Research Letters*, *35*(4). https://doi.org/10.1029/2007GL032591

Sassen, K., Wang, Z., & Liu, D. (2008). Global distribution of cirrus clouds from CloudSat/Cloud-Aerosol Lidar and Infrared Pathfinder Satellite Observations (CALIPSO) measurements. *Journal of Geophysical Research: Atmospheres*, *113*(D8). https://doi.org/10.1029/2008JD009972

Sato, K., & Okamoto, H. (2006). Characterization of Ze and LDR of nonspherical and inhomogeneous ice particles for 95-GHz cloud radar: Its implication to microphysical retrievals. *Journal of*

Geophysical Research: Atmospheres, *111*(D22). https://doi.org/10.1029/2005JD006959

Sato, K., & Okamoto, H. (2011). Refinement of global ice microphysics using spaceborne active sensors. *Journal of Geophysical Research*, *116*(D20), D20202. https://doi.org/10.1029/2011JD015885

Sato, K., & Okamoto, H. (2020). *Application of Single and Multiple-Scattering Theories to Analyses of Space-Borne Cloud Radar and Lidar Data* (pp. 1–37). https://doi.org/10.1007/978-3-030-38696-2_1

Sato, K., & Okamoto, H. (2023). Global Analysis of Height-Resolved Ice Particle Categories From Spaceborne Lidar. *Geophysical Research Letters*, *50*(17). https://doi.org/10.1029/2023GL105522

Sato, K., Okamoto, H., & Ishimoto, H. (2018). Physical model for multiple scattered space-borne lidar returns from clouds. *Opt. Express*, *26*(6), A301–A319. https://doi.org/10.1364/OE.26.00A301

Sato, K., Okamoto, H., & Ishimoto, H. (2019). Modeling the depolarization of space-borne lidar signals. *Optics Express*, *27*(4), A117. https://doi.org/10.1364/OE.27.00A117

Sato, K., Okamoto, H., Nishizawa, T., Jin, Y., Nakajima, T., Wang, M., Satoh, M., Roh, W., Ishimoto, H., & Kudo, R. (2024). JAXA Level 2 cloud and precipitation microphysics retrievals based on EarthCARE CPR, ATLID and MSI. *Atmospheric Measurement Techniques Discussions*, *2024*, 1–15. https://doi.org/10.5194/amt-2024-99

Sato, K., Okamoto, H., Yamamoto, M. K., Fukao, S., Kumagai, H., Ohno, Y., Horie, H., & Abo, M. (2009). 95-GHz Doppler radar and lidar synergy for simultaneous ice microphysics and in-cloud vertical air motion retrieval. *Journal of Geophysical Research: Atmospheres*, *114*(D3). https://doi.org/10.1029/2008JD010222

Satoh, M., Matsuno, T., Tomita, H., Miura, H., Nasuno, T., & Iga, S. (2008). Nonhydrostatic icosahedral atmospheric model (NICAM) for global cloud resolving simulations. *Journal of Computational Physics*, *227*(7), 3486–3514. https://doi.org/10.1016/j.jcp.2007.02.006

Satoh, M., Tomita, H., Yashiro, H., Miura, H., Kodama, C., Seiki, T., Noda, A. T., Yamada, Y., Goto, D., Sawada, M., Miyoshi, T., Niwa, Y., Hara, M., Ohno, T., Iga, S., Arakawa, T., Inoue, T., & Kubokawa, H. (2014). The Non-hydrostatic Icosahedral Atmospheric Model: description and development. *Progress in Earth and Planetary Science*, *1*(1), 18. https://doi.org/10.1186/s40645-014-0018-1

Sauvageot, H., & Omar, J. (1987). Radar Reflectivity of Cumulus Clouds. *Journal of Atmospheric and Oceanic Technology*, *4*(2), 264–272. https://doi.org/10.1175/1520-0426(1987)004<0264:RROCC>2.0.CO;2

Sayer, A. M. (2020). How Long Is Too Long? Variogram Analysis of AERONET Data to Aid Aerosol Validation and Intercomparison Studies. *Earth and Space Science*, *7*(9). https://doi.org/10.1029/2020EA001290

Sayer, A. M., Govaerts, Y., Kolmonen, P., Lipponen, A., Luffarelli, M., Mielonen, T., Patadia, F., Popp, T., Povey, A. C., Stebel, K., & Witek, M. L. (2020). A review and framework for the evaluation of pixel-level uncertainty estimates in satellite aerosol remote sensing. *Atmospheric Measurement Techniques*, *13*(2), 373–404. https://doi.org/10.5194/amt-13-373-2020

Sayer, A. M., Smirnov, A., Hsu, N. C., & Holben, B. N. (2012). A pure marine aerosol model, for use in remote sensing applications. *Journal of Geophysical Research: Atmospheres*, *117*(D5). https://doi.org/10.1029/2011JD016689

Sayer, A. M., Thomas, G. E., Palmer, P. I., & Grainger, R. G. (2010). Some implications of sampling choices on comparisons between satellite and model aerosol optical depth fields. *Atmospheric Chemistry and Physics*, *10*(22), 10705–10716. https://doi.org/10.5194/acp-10-10705-2010

Scarchilli, G., Gorgucci, V., Chandrasekar, V., & Dobaie, A. (1996). Self-consistency of polarization diversity measurement of rainfall. *IEEE Transactions on Geoscience and Remote Sensing*, *34*(1), 22–26. https://doi.org/10.1109/36.481887

Schaaf, C. B., Gao, F., Strahler, A. H., Lucht, W., Li, X., Tsang, T., Strugnell, N. C., Zhang, X., Jin, Y., Muller, J.-P., Lewis, P., Barnsley, M., Hobson, P., Disney, M., Roberts, G., Dunderdale, M., Doll, C., d'Entremont, R. P., Hu, B., … Roy, D. (2002). First operational BRDF, albedo nadir reflectance products from MODIS. *Remote Sensing of Environment*, *83*(1–2), 135–148. https://doi.org/10.1016/S0034-4257(02)00091-3

Schillinger, M., Morancais, D., Fabre, F., & Culoma, A. J. (2003). ALADIN: the lidar instrument for the AEOLUS mission. In *SPIE Proceedings*. SPIE. https://doi.org/10.1117/12.463024

Schimmel, W., Kalesse-Los, H., Maahn, M., Vogl, T., Foth, A., Garfias, P. S., & Seifert, P. (2022). Identifying cloud droplets beyond lidar attenuation from vertically pointing cloud radar observations using artificial neural networks. *Atmospheric Measurement Techniques*, *15*(18), 5343–5366. https://doi.org/10.5194/amt-15-5343-2022

Schmidt, J., Wandinger, U., & Malinka, A. (2013). Dual-field-of-view Raman lidar measurements for the retrieval of cloud microphysical properties. *Applied Optics*, *52*(11), 2235. https://doi.org/10.1364/AO.52.002235

Schoeberl, M., Jensen, E., Wang, T., Taha, G., Ueyama, R., Wang, Y., DeLand, M., & Dessler, A. (2021). Cloud and Aerosol Distributions From SAGE III/ISS Observations. *Journal of Geophysical Research: Atmospheres*, *126*(23). https://doi.org/10.1029/2021JD035550

Schoger, S. Y., Moisseev, D., von Lerber, A., Crewell, S., & Ebell, K. (2021). Snowfall-Rate Retrieval for K- and W-Band Radar Measurements Designed in Hyytiälä, Finland, and Tested at Ny-Ålesund, Svalbard, Norway. *Journal of Applied Meteorology and Climatology*, *60*(3), 273–289. https://doi.org/10.1175/JAMC-D-20-0095.1

Schönhuber, M., Lammer, G., & Randeu, W. L. (2007). One decade of imaging precipitation measurement by 2D-video-distrometer. *Advances in Geosciences*, *10*, 85–90. https://doi.org/10.5194/adgeo-10-85-2007

Schulte, R. M., Lebsock, M. D., & Haynes, J. M. (2023). What CloudSat cannot see: liquid water content profiles inferred from MODIS and CALIOP observations. *Atmospheric Measurement Techniques*, *16*(14), 3531–3546. https://doi.org/10.5194/amt-16-3531-2023

Schuster, G. L., Dubovik, O., & Holben, B. N. (2006). Angstrom exponent and bimodal aerosol size distributions. *Journal of Geophysical Research: Atmospheres*, *111*(D7). https://doi.org/10.1029/2005JD006328

Schuster, G. L., Vaughan, M., MacDonnell, D., Su, W., Winker, D., Dubovik, O., Lapyonok, T., & Trepte, C. (2012). Comparison of CALIPSO aerosol optical depth retrievals to AERONET measurements, and a climatology for the lidar ratio of dust. *Atmospheric Chemistry and Physics*, *12*(16), 7431–7452. https://doi.org/10.5194/acp-12-7431-2012

Schwaller, M. R., & Morris, K. R. (2011). A Ground Validation Network for the Global Precipitation Measurement Mission. *Journal of Atmospheric and Oceanic Technology*, *28*(3), 301–319. https://doi.org/10.1175/2010JTECHA1403.1

Scott, R. C., Rose, F. G., Stackhouse, P. W., Loeb, N. G., Kato, S., Doelling, D. R., Rutan, D. A., Taylor, P. C., & Smith, W. L. (2022). Clouds and the Earth's Radiant Energy System (CERES) Cloud Radiative Swath (CRS) Edition 4 Data Product. *Journal of Atmospheric and Oceanic Technology*, *39*(11), 1781–1797. https://doi.org/10.1175/JTECH-D-22-0021.1

Scovell, R., Gaussiat, N., & Mittermaier, M. (2013, August). *RECENT IMPROVEMENTS TO THE QUALITY CONTROL OF RADAR DATA FOR THE OPERA DATA CENTRE*.

Seela, B. K., Janapati, J., Lin, P.-L., Lan, C.-H., & Huang, M.-Q. (2024). Evaluation of GPM DPR Rain Parameters with North Taiwan Disdrometers. *Journal of Hydrometeorology*, *25*(1), 47–64. https://doi.org/10.1175/JHM-D-23-0027.1

Sekiguchi, M., & Nakajima, T. (2008). A k-distribution-based radiation code and its computational optimization for an atmospheric general circulation model. *Journal of Quantitative Spectroscopy and Radiative Transfer*, *109*(17–18), 2779–2793. https://doi.org/10.1016/j.jqsrt.2008.07.013

Sellitto, P., Bucci, S., & Legras, B. (2020). Comparison of ISS–CATS and CALIPSO–CALIOP Characterization of High Clouds in the Tropics. *Remote Sensing*, *12*(23), 3946. https://doi.org/10.3390/rs12233946

Sessions, W. R., Reid, J. S., Benedetti, A., Colarco, P. R., da Silva, A., Lu, S., Sekiyama, T., Tanaka, T. Y., Baldasano, J. M., Basart, S., Brooks, M. E., Eck, T. F., Iredell, M., Hansen, J. A., Jorba, O. C., Juang, H.-M. H., Lynch, P., Morcrette, J.-J., Moorthi, S., … Westphal, D. L. (2015). Development towards a global operational aerosol consensus: basic climatological characteristics of the International Cooperative for Aerosol Prediction Multi-Model Ensemble (ICAP-MME). *Atmospheric Chemistry and Physics*, *15*(1), 335–362. https://doi.org/10.5194/acp-15-335-2015

Seto, S., Iguchi, T., Meneghini, R., Awaka, J., Kubota, T., Masaki, T., & Takahashi, N. (2021). The Precipitation Rate Retrieval Algorithms for the GPM Dual-frequency Precipitation Radar. *Journal of the Meteorological Society of Japan. Ser. II*, *99*(2). https://doi.org/10.2151/jmsj.2021-011

Seto, S., Kubota, T., Masaki, T., Takahashi, N., & Iguchi, T. (2020). Preliminary Analysis of Experimental Product for the New Scan Pattern of GPM/DPR. *IGARSS 2020 - 2020 IEEE International Geoscience and Remote Sensing Symposium*, 3593–3596. https://doi.org/10.1109/IGARSS39084.2020.9323276

Sheridan, P. J., Andrews, E., Ogren, J. A., Tackett, J. L., & Winker, D. M. (2012). Vertical profiles of aerosol optical properties over central Illinois and comparison with surface and satellite measurements. *Atmospheric Chemistry and Physics*, *12*(23), 11695–11721. https://doi.org/10.5194/acp-12-11695-2012

Shimizu, A., Sugimoto, N., Matsui, I., Arao, K., Uno, I., Murayama, T., Kagawa, N., Aoki, K., Uchiyama, A., & Yamazaki, A. (2004). Continuous observations of Asian dust and other aerosols by polarization lidars in China and Japan during ACE-Asia. *Journal of Geophysical Research: Atmospheres*, *109*(D19). https://doi.org/10.1029/2002JD003253

Shinozuka, Y., Kacenelenbogen, M. S., Burton, S. P., Howell, S. G., Zuidema, P., Ferrare, R. A., LeBlanc, S. E., Pistone, K., Broccardo, S., Redemann, J., Schmidt, K. S., Cochrane, S. P., Fenn, M., Freitag, S., Dobracki, A., Segal-Rosenheimer, M., & Flynn, C. J. (2020). Daytime aerosol optical depth above low-level clouds is similar to that in adjacent clear skies at the same heights: airborne observation above the southeast Atlantic. *Atmospheric Chemistry and Physics*, *20*(19), 11275–11285. https://doi.org/10.5194/acp-20-11275-2020

Shinozuka, Y., & Redemann, J. (2011). Horizontal variability of aerosol optical depth observed during the ARCTAS airborne experiment. *Atmospheric Chemistry and Physics*, *11*(16), 8489–8495. https://doi.org/10.5194/acp-11-8489-2011

Shipley, S. T., Tracy, D. H., Eloranta, E. W., Trauger, J. T., Sroga, J. T., Roesler, F. L., & Weinman, J. A. (1983). High spectral resolution lidar to measure optical scattering properties of atmospheric aerosols 1: Theory and instrumentation. *Applied Optics*, *22*(23), 3716. https://doi.org/10.1364/AO.22.003716

Shupe, M. D., Daniel, J. S., de Boer, G., Eloranta, E. W., Kollias, P., Long, C. N., Luke, E. P., Turner, D. D., & Verlinde, J. (2008). A Focus On Mixed-Phase Clouds. *Bulletin of the American Meteorological Society*, *89*(10), 1549–1562. https://doi.org/10.1175/2008BAMS2378.1

Shupe, M. D., Kollias, P., Matrosov, S. Y., & Schneider, T. L. (2004). Deriving Mixed-Phase Cloud Properties from Doppler Radar Spectra. *Journal of Atmospheric and Oceanic Technology*, *21*(4),

660–670. https://doi.org/10.1175/1520-0426(2004)021<0660:DMCPFD>2.0.CO;2

Silberstein, D. S., Wolff, D. B., Marks, D. A., Atlas, D., & Pippitt, J. L. (2008). Ground Clutter as a Monitor of Radar Stability at Kwajalein, RMI. *Journal of Atmospheric and Oceanic Technology*, *25*(11), 2037–2045. https://doi.org/10.1175/2008JTECHA1063.1

Silva Dias, M. A. F., Rutledge, S., Kabat, P., Silva Dias, P. L., Nobre, C., Fisch, G., Dolman, A. J., Zipser, E., Garstang, M., Manzi, A. O., Fuentes, J. D., Rocha, H. R., Marengo, J., Plana-Fattori, A., Sá, L. D. A., Alvalá, R. . C. S., Andreae, M. O., Artaxo, P., Gielow, R., & Gatti, L. (2002). Cloud and rain processes in a biosphere-atmosphere interaction context in the Amazon Region. *Journal of Geophysical Research: Atmospheres*, *107*(D20). https://doi.org/10.1029/2001JD000335

Sinyuk, A., Holben, B. N., Eck, T. F., Giles, D. M., Slutsker, I., Korkin, S., Schafer, J. S., Smirnov, A., Sorokin, M., & Lyapustin, A. (2020). The AERONET Version 3 aerosol retrieval algorithm, associated uncertainties and comparisons to Version 2. *Atmospheric Measurement Techniques*, *13*(6), 3375–3411. https://doi.org/10.5194/amt-13-3375-2020

Siomos, N., Balis, D. S., Voudouri, K. A., Giannakaki, E., Filioglou, M., Amiridis, V., Papayannis, A., & Fragkos, K. (2018). Are EARLINET and AERONET climatologies consistent? The case of Thessaloniki, Greece. *Atmospheric Chemistry and Physics*, *18*(16), 11885–11903. https://doi.org/10.5194/acp-18-11885-2018

Siomos, N., Binietoglou, I., Paschou, P., Adam, M., D'Amico, G., Gast, B., Haarig, M., & Freudenthaler, V. (2023). ARC and ATLAS: CARS software tools for the data analysis and quality assurance of lidar measurements performed within ACTRIS. *EGU General Assembly Conference Abstracts*. https://doi.org/10.5194/egusphere-egu23-13218

Skaropoulos, N. C., & Russchenberg, H. W. J. (2003). Simulations of Doppler spectra in the melting layer of precipitation. *Geophysical Research Letters*, *30*(12). https://doi.org/10.1029/2003GL016959

Skofronick-Jackson, G., Hudak, D., Petersen, W., Nesbitt, S. W., Chandrasekar, V., Durden, S., Gleicher, K. J., Huang, G.-J., Joe, P., Kollias, P., Reed, K. A., Schwaller, M. R., Stewart, R., Tanelli, S., Tokay, A., Wang, J. R., & Wolde, M. (2015). Global Precipitation Measurement Cold Season Precipitation Experiment (GCPEx): For Measurement Sake Let it Snow. *Bulletin of the American Meteorological Society*, *96*(10), 1719–1741. https://doi.org/10.1175/BAMS-D-13-00262.1

Skofronick-Jackson, G., Petersen, W. A., Berg, W., Kidd, C., Stocker, E. F., Kirschbaum, D. B., Kakar, R., Braun, S. A., Huffman, G. J., Iguchi, T., Kirstetter, P. E., Kummerow, C., Meneghini, R., Oki, R., Olson, W. S., Takayabu, Y. N., Furukawa, K., & Wilheit, T. (2017). The Global Precipitation Measurement (GPM) Mission for Science and Society. *Bulletin of the American Meteorological Society*, *98*(8), 1679–1695. https://doi.org/10.1175/BAMS-D-15-00306.1

Skofronick-Jackson, G., Kirschbaum, D., Petersen, W., Huffman, G., Kidd, C., Stocker, E., & Kakar, R. (2018). The Global Precipitation Measurement (GPM) mission's scientific achievements and societal contributions: reviewing four years of advanced rain and snow observations. *Quarterly Journal of the Royal Meteorological Society*, *144*(S1), 27–48. https://doi.org/10.1002/qj.3313

Smirnov, A., Holben, B. N., Sakerin, S. M., Kabanov, D. M., Slutsker, I., Chin, M., Diehl, T. L., Remer, L. A., Kahn, R., Ignatov, A., Liu, L., Mishchenko, M., Eck, T. F., Kucsera, T. L., Giles, D., & Kopelevich, O. V. (2006). Ship-based aerosol optical depth measurements in the Atlantic Ocean: Comparison with satellite retrievals and GOCART model. *Geophysical Research Letters*, *33*(14). https://doi.org/10.1029/2006GL026051

Smirnov, A., Holben, B. N., Slutsker, I., Giles, D. M., McClain, C. R., Eck, T. F., Sakerin, S. M., Macke, A., Croot, P., Zibordi, G., Quinn, P. K., Sciare, J., Kinne, S., Harvey, M., Smyth, T. J., Piketh, S., Zielinski, T., Proshutinsky, A., Goes, J. I., … Jourdin, F. (2009). Maritime Aerosol Network as a component of Aerosol Robotic Network. *Journal of Geophysical Research: Atmospheres*, *114*(D6). https://doi.org/10.1029/2008JD011257

Smith, H. R., Ulanowski, Z., Kaye, P. H., Hirst, E., Stanley, W., Kaye, R., Wieser, A., Stopford, C., Kezoudi, M., Girdwood, J., Greenaway, R., & Mackenzie, R. (2019). The Universal Cloud and Aerosol Sounding System (UCASS): a low-cost miniature optical particle counter for use in dropsonde or balloon-borne sounding systems. *Atmospheric Measurement Techniques*, *12*(12), 6579–6599. https://doi.org/10.5194/amt-12-6579-2019

Smith, W. L., Hansen, C., Bucholtz, A., Anderson, B. E., Beckley, M., Corbett, J. G., Cullather, R. I., Hines, K. M., Hofton, M., Kato, S., Lubin, D., Moore, R. H., Rosenhaimer, M. S., Redemann, J., Schmidt, S., Scott, R., Song, S., Barrick, J. D., Blair, J. B., … Winstead, E. (2017). Arctic Radiation-IceBridge Sea and Ice Experiment: The Arctic Radiant Energy System during the Critical Seasonal Ice Transition. *Bulletin of the American Meteorological Society*, *98*(7), 1399–1426. https://doi.org/10.1175/BAMS-D-14-00277.1

Sogacheva, L., Denisselle, M., Kolmonen, P., Virtanen, T. H., North, P., Henocq, C., Scifoni, S., & Dransfeld, S. (2022). Extended validation and evaluation of the OLCI–SLSTR SYNERGY aerosol product (SY_2_AOD) on Sentinel-3. *Atmospheric Measurement Techniques*, *15*(18), 5289–5322. https://doi.org/10.5194/amt-15-5289-2022

Sokol, A. B., & Storelvmo, T. (2024). The Spatial Heterogeneity of Cloud Phase Observed by Satellite. *Journal of Geophysical Research: Atmospheres*, *129*(3). https://doi.org/10.1029/2023JD039751

Speirs, P., Gabella, M., & Berne, A. (2017). A Comparison between the GPM Dual-Frequency Precipitation Radar and Ground-Based Radar Precipitation Rate Estimates in the Swiss Alps and Plateau. *Journal of Hydrometeorology*, *18*(5), 1247–1269. https://doi.org/10.1175/JHM-D-16-0085.1

Spinhirne, J. D., Rall, J. A. R., & Scott, V. S. (1995). Compact Eye Safe Lidar Systems. *The Review of Laser Engineering*, *23*(2), 112–118. https://doi.org/10.2184/lsj.23.112

Stachlewska, I. S., Neuber, R., Lampert, A., Ritter, C., & Wehrle, G. (2010). AMALi – the Airborne Mobile Aerosol Lidar for Arctic research. *Atmospheric Chemistry and Physics*, *10*(6), 2947–2963. https://doi.org/10.5194/acp-10-2947-2010

Stephens, G. L., & Kummerow, C. D. (2007). The Remote Sensing of Clouds and Precipitation from Space: A Review. *Journal of the Atmospheric Sciences*, *64*(11), 3742–3765. https://doi.org/10.1175/2006JAS2375.1

Stephens, G. L., Vane, D. G., Boain, R. J., Mace, G. G., Sassen, K., Wang, Z., Illingworth, A. J., O'connor, E. J., Rossow, W. B., Durden, S. L., Miller, S. D., Austin, R. T., Benedetti, A., & Mitrescu, C. (2002). THE CLOUDSAT MISSION AND THE A-TRAIN. *Bulletin of the American Meteorological Society*, *83*(12), 1771–1790. https://doi.org/10.1175/BAMS-83-12-1771

Stephens, G. L., Vane, D. G., Tanelli, S., Im, E., Durden, S., Rokey, M., Reinke, D., Partain, P., Mace, G. G., Austin, R., L'Ecuyer, T., Haynes, J., Lebsock, M., Suzuki, K., Waliser, D., Wu, D., Kay, J., Gettelman, A., Wang, Z., & Marchand, R. (2008). CloudSat mission: Performance and early science after the first year of operation. *Journal of Geophysical Research: Atmospheres*, *113*(D8). https://doi.org/10.1029/2008JD009982

Stephens, G., Winker, D., Pelon, J., Trepte, C., Vane, D., Yuhas, C., L'Ecuyer, T., Lebsock, M., L'Ecuyer, T., & Lebsock, M. (2018). CloudSat and CALIPSO within the A-Train: Ten Years of Actively Observing the Earth System. *Bulletin of the American Meteorological Society*, *99*(3), 569–581. https://doi.org/10.1175/BAMS-D-16-0324.1

Stocker, E. F., Alquaied, F., Bilanow, S., Ji, Y., & Jones, L. (2018). TRMM Version 8 Reprocessing Improvements and Incorporation into the GPM Data Suite. *Journal of Atmospheric and Oceanic Technology*, *35*(6), 1181–1199. https://doi.org/10.1175/JTECH-D-17-0166.1

Stoffelen, A., Pailleux, J., Källén, E., Vaughan, J. M., Isaksen, L., Flamant, P., Wergen, W., Andersson, E., Schyberg, H., Culoma, A., Meynart, R., Endemann, M., & Ingmann, P. (2005). THE ATMOSPHERIC DYNAMICS MISSION FOR GLOBAL WIND FIELD MEASUREMENT. *Bulletin of*

the American Meteorological Society, *86*(1), 73–88. https://doi.org/10.1175/BAMS-86-1-73

Straka, J. M., Zrnić, D. S., & Ryzhkov, A. V. (2000). Bulk Hydrometeor Classification and Quantification Using Polarimetric Radar Data: Synthesis of Relations. *Journal of Applied Meteorology*, *39*(8), 1341–1372. https://doi.org/10.1175/1520-0450(2000)039<1341:BHCAQU>2.0.CO;2

Straume, A. G., Rennie, M., Isaksen, L., de Kloe, J., Marseille, G. J., Stoffelen, A., Flament, T., Stieglitz, H., Dabas, A., Huber, D., & Reitebuch, O. (2020). ESA's space-based Doppler wind lidar mission Aeolus–First wind and aerosol product assessment results. *EPJ Web of Conferences*.

Straume, A. G., Schuettemeyer, D., Von Bismarck, J., Kanitz, T., & Fehr, T. (2019). *Aeolus Scientific Calibration and Validation Implementation Plan*.

Stubenrauch, C. J., Kinne, S., Mandorli, G., Rossow, W. B., Winker, D. M., Ackerman, S. A., Chepfer, H., Girolamo, L. Di, Garnier, A., Heidinger, A., Karlsson, K.-G., Meyer, K., Minnis, P., Platnick, S., Stengel, M., Sun-Mack, S., Veglio, P., Walther, A., Cai, X., … Zhao, G. (2024). Lessons Learned from the Updated GEWEX Cloud Assessment Database. *Surveys in Geophysics*. https://doi.org/10.1007/s10712-024-09824-0

Sugimoto, N., Matsui, I., Shimizu, A., Nishizawa, T., Hara, Y., Xie, C., Uno, I., Yumimoto, K., Wang, Z., & Yoon, S.-C. (2008). Lidar network observations of tropospheric aerosols. In *SPIE Proceedings*. SPIE. https://doi.org/10.1117/12.806540

Sugimoto, N., Matsui, I., Shimizu, A., Uno, I., Asai, K., Endoh, T., & Nakajima, T. (2002). Observation of dust and anthropogenic aerosol plumes in the Northwest Pacific with a two-wavelength polarization lidar on board the research vessel Mirai. *Geophysical Research Letters*, *29*(19). https://doi.org/10.1029/2002GL015112

Sugimoto N., Nishizawa T., Liu X., Matsui I., Shimizu A., Zhang Y., Kim Y.J., Li R., & Liu J. (2009): Continuous Observations of Aerosol Profiles with a Two-Wavelength Mie-Scattering Lidar in Guangzhou in PRD2006. J. Appl. Meteor. Climatol., 48, 1822–1830, https://doi.org/10.1175/2009JAMC2089.1

Sugimoto, N., Uno, I., Nishikawa, M., Shimizu, A., Matsui, I., Dong, X., Chen, Y., & Quan, H. (2003). Record heavy Asian dust in Beijing in 2002: Observations and model analysis of recent events. *Geophysical Research Letters*, *30*(12). https://doi.org/10.1029/2002GL016349

Sun, X. J., Li, H. R., Barker, H. W., Zhang, R. W., Zhou, Y. B., & Liu, L. (2015). Satellite-based estimation of cloud-base heights using constrained spectral radiance matching. *Quarterly Journal of the Royal Meteorological Society*, *142*(694), 224–232. https://doi.org/10.1002/qj.2647

Sy, O. O., & Tanelli, S. (2023). Recovering the Elusive Spectral Width From Spaceborne Doppler Profiling Radar Measurements: The "ExpliSyT" Approach. *IEEE Transactions on Geoscience and Remote Sensing*, *61*, 1–23. https://doi.org/10.1109/TGRS.2023.3279767

Sy, O. O., Tanelli, S., Durden, S. L., Peral, E., Sacco, G.-F., Chahat, N. E., Hristova-Veleva, S., Heymsfield, A. J., Bansemer, A., Knosp, B., Dobrowalski, G., Li, P. P., & Vu, Q. (2022). Scientific Products From the First Radar in a CubeSat (RainCube): Deconvolution, Cross-Validation, and Retrievals. *IEEE Transactions on Geoscience and Remote Sensing*, *60*, 1–20. https://doi.org/10.1109/TGRS.2021.3073990

Sy, O. O., Tanelli, S., Kollias, P., & Ohno, Y. (2014). Application of Matched Statistical Filters for EarthCARE Cloud Doppler Products. *IEEE Transactions on Geoscience and Remote Sensing*, *52*(11), 7297–7316. https://doi.org/10.1109/TGRS.2014.2311031

Szyrmer, W., & Zawadzki, I. (2014). Snow Studies. Part III: Theoretical Derivations for the Ensemble Retrieval of Snow Microphysics from Dual-Wavelength Vertically Pointing Radars. *Journal of the Atmospheric Sciences*, *71*(3), 1158–1170. https://doi.org/10.1175/JAS-D-12-0285.1

Tackett, J. L., Kar, J., Vaughan, M. A., Getzewich, B. J., Kim, M.-H., Vernier, J.-P., Omar, A. H., Magill,

B. E., Pitts, M. C., & Winker, D. M. (2023). The CALIPSO version 4.5 stratospheric aerosol subtyping algorithm. *Atmospheric Measurement Techniques*, *16*(3), 745–768. https://doi.org/10.5194/amt-16-745-2023

Tackett, J. L., Winker, D. M., Getzewich, B. J., Vaughan, M. A., Young, S. A., & Kar, J. (2018). CALIPSO lidar level 3 aerosol profile product: version 3 algorithm design. *Atmospheric Measurement Techniques*, *11*(7), 4129–4152. https://doi.org/10.5194/amt-11-4129-2018

Taha, G., Loughman, R., Zhu, T., Thomason, L., Kar, J., Rieger, L., & Bourassa, A. (2021). OMPS LP Version 2.0 multi-wavelength aerosol extinction coefficient retrieval algorithm. *Atmospheric Measurement Techniques*, *14*(2), 1015–1036. https://doi.org/10.5194/amt-14-1015-2021

Takahashi, N., Hanado, H., Nakamura, K., Kanemaru, K., Nakagawa, K., Iguchi, T., Nio, T., Kubota, T., Oki, R., & Yoshida, N. (2016). Overview of the End-of-Mission Observation Experiments of Precipitation Radar Onboard the Tropical Rainfall Measuring Mission Satellite. *IEEE Transactions on Geoscience and Remote Sensing*, *54*(6), 3450–3459. https://doi.org/10.1109/TGRS.2016.2518221

Takamura, T., & Nakajima, T. (2004). Overview of SKYNET and its activities. *Opt. Pura Apl*, *37*, 3303–3308.

Takamura, T., Sasano, Y., & Hayasaka, T. (1994). Tropospheric aerosol optical properties derived from lidar, sun photometer, and optical particle counter measurements. *Applied Optics*, *33*(30), 7132. https://doi.org/10.1364/AO.33.007132

Takemura, T., Nakajima, T., Dubovik, O., Holben, B. N., & Kinne, S. (2002). Single-Scattering Albedo and Radiative Forcing of Various Aerosol Species with a Global Three-Dimensional Model. *Journal of Climate*, *15*(4), 333–352. https://doi.org/10.1175/1520-0442(2002)015<0333:SSAARF>2.0.CO;2

Tan, D. G. H., Andersson, E., De Kloe, J., Marseille, G.-J., Stoffelen, A., Poli, P., Denneulin, M.-L., Dabas, A., Huber, D., Reitebuch, O., Flamant, P., Le Rille, O., & Nett, H. (2008). The ADM-Aeolus wind retrieval algorithms. *Tellus A: Dynamic Meteorology and Oceanography*, *60*(2), 191. https://doi.org/10.1111/j.1600-0870.2007.00285.x

Tan, J., Petersen, W. A., Kirchengast, G., Goodrich, D. C., & Wolff, D. B. (2018). Evaluation of Global Precipitation Measurement Rainfall Estimates against Three Dense Gauge Networks. *Journal of Hydrometeorology*, *19*(3), 517–532. https://doi.org/10.1175/JHM-D-17-0174.1

Tanelli, S., Durden, S. L., Im, E., Pak, K. S., Reinke, D. G., Partain, P., Haynes, J. M., & Marchand, R. T. (2008). CloudSat's Cloud Profiling Radar After Two Years in Orbit: Performance, Calibration, and Processing. *IEEE Transactions on Geoscience and Remote Sensing*, *46*(11), 3560–3573. https://doi.org/10.1109/TGRS.2008.2002030

Tanelli, S., Im, E., Durden, S. L., Facheris, L., & Giuli, D. (2002). The Effects of Nonuniform Beam Filling on Vertical Rainfall Velocity Measurements with a Spaceborne Doppler Radar. *Journal of Atmospheric and Oceanic Technology*, *19*(7), 1019–1034. https://doi.org/10.1175/1520-0426(2002)019<1019:TEONBF>2.0.CO;2

Tanelli, S., Im, E., Kobayashi, S., Mascelloni, R., & Facheris, L. (2005). Spaceborne Doppler Radar Measurements of Rainfall: Correction of Errors Induced by Pointing Uncertainties. *Journal of Atmospheric and Oceanic Technology*, *22*(11), 1676–1690. https://doi.org/10.1175/JTECH1797.1

Tanelli, S., Sacco, G. F., Durden, S. L., & Haddad, Z. S. (2012). *Impact of non-uniform beam filling on spaceborne cloud and precipitation radar retrieval algorithms* (T. Hayasaka, K. Nakamura, & E. Im (eds.); p. 852308). https://doi.org/10.1117/12.977375

Tang, G., Wen, Y., Gao, J., Long, D., Ma, Y., Wan, W., & Hong, Y. (2017). Similarities and differencesbetween three coexisting spaceborne radars in global rainfall and snowfall estimation. Water resources research, 53(5), 3835-3853. https://doi.org/10.1002/2016WR019961

Tesche, M., Ansmann, A., Müller, D., Althausen, D., Engelmann, R., Freudenthaler, V., & Gross, S. (2009). Vertically resolved separation of dust and smoke over Cape Verde using multiwavelength Raman and polarization lidars during Saharan Mineral Dust Experiment 2008. *Journal of Geophysical Research: Atmospheres*, *114*(D13). https://doi.org/10.1029/2009JD011862

Tesche, M., Wandinger, U., Ansmann, A., Althausen, D., Müller, D., & Omar, A. H. (2013). Ground-based validation of CALIPSO observations of dust and smoke in the Cape Verde region. *Journal of Geophysical Research: Atmospheres*, *118*(7), 2889–2902. https://doi.org/https://doi.org/10.1002/jgrd.50248

Testud, J., Oury, S., Black, R. A., Amayenc, P., & Dou, X. (2001). The Concept of "Normalized" Distribution to Describe Raindrop Spectra: A Tool for Cloud Physics and Cloud Remote Sensing. *Journal of Applied Meteorology*, *40*(6), 1118–1140. https://doi.org/10.1175/1520-0450(2001)040<1118:TCONDT>2.0.CO;2

Tetoni, E., Ewald, F., Hagen, M., Köcher, G., Zinner, T., & Gross, S. (2021). Retrievals of ice microphysics using dual-wavelength polarimetric radar observations during stratiform precipitation events. *Atmospheric Measurement Techniques Discussions*.

Tetoni, E., Ewald, F., Hagen, M., Köcher, G., Zinner, T., & Groß, S. (2022). Retrievals of ice microphysical properties using dual-wavelength polarimetric radar observations during stratiform precipitation events. *Atmospheric Measurement Techniques*, *15*(13), 3969–3999. https://doi.org/10.5194/amt-15-3969-2022

Thomas, L., Cartwright, J. C., & Wareing, D. P. (1990). Lidar observations of the horizontal orientation of ice crystals in cirrus clouds. *Tellus, Series B*, *42 B*(2). https://doi.org/10.3402/tellusb.v42i2.15206

Thomas, M. A., Devasthale, A., & Kahnert, M. (2022). Marine aerosol properties over the Southern Ocean in relation to the wintertime meteorological conditions. *Atmospheric Chemistry and Physics*, *22*(1), 119–137. https://doi.org/10.5194/acp-22-119-2022

Thomason, L. W., Moore, J. R., Pitts, M. C., Zawodny, J. M., & Chiou, E. W. (2010). An evaluation of the SAGE III version 4 aerosol extinction coefficient and water vapor data products. *Atmospheric Chemistry and Physics*, *10*(5), 2159–2173. https://doi.org/10.5194/acp-10-2159-2010

Thorsen, T. J., Ferrare, R. A., Hostetler, C. A., Vaughan, M. A., & Fu, Q. (2017). The impact of lidar detection sensitivity on assessing aerosol direct radiative effects. *Geophysical Research Letters*, *44*(17), 9059–9067. https://doi.org/10.1002/2017GL074521

Thorsen, T. J., Fu, Q., & Comstock, J. (2011). Comparison of the CALIPSO satellite and ground-based observations of cirrus clouds at the ARM TWP sites. *Journal of Geophysical Research: Atmospheres*, *116*(D21). https://doi.org/10.1029/2011JD015970

Thorsen, T. J., Fu, Q., Newsom, R. K., Turner, D. D., & Comstock, J. M. (2015). Automated Retrieval of Cloud and Aerosol Properties from the ARM Raman Lidar. Part I: Feature Detection. *Journal of Atmospheric and Oceanic Technology*, *32*(11), 1977–1998. https://doi.org/10.1175/JTECH-D-14-00150.1

Tinel, C., Testud, J., Pelon, J., Hogan, R. J., Protat, A., Delanoë, J., & Bouniol, D. (2005). The Retrieval of Ice-Cloud Properties from Cloud Radar and Lidar Synergy. *Journal of Applied Meteorology*, *44*(6), 860–875. https://doi.org/10.1175/JAM2229.1

Toledo, F., Delanoë, J., Haeffelin, M., Dupont, J.-C., Jorquera, S., & Le Gac, C. (2020). Absolute calibration method for frequency-modulated continuous wave (FMCW) cloud radars based on corner reflectors. *Atmospheric Measurement Techniques*, *13*(12), 6853–6875. https://doi.org/10.5194/amt-13-6853-2020

Tomita, H., & Satoh, M. (2004). A new dynamical framework of nonhydrostatic global model using the icosahedral grid. *Fluid Dynamics Research*, *34*(6), 357–400.

https://doi.org/10.1016/j.fluiddyn.2004.03.003

Toohey, M., & von Clarmann, T. (2013). Climatologies from satellite measurements: the impact of orbital sampling on the standard error of the mean. *Atmospheric Measurement Techniques*, *6*(4), 937–948. https://doi.org/10.5194/amt-6-937-2013

Tornow, F., Barker, H. W., & Domenech, C. (2015). On the use of simulated photon paths to co-register top-of-atmosphere radiances in EarthCARE radiative closure experiments. *Quarterly Journal of the Royal Meteorological Society*, *141*(693), 3239–3251. https://doi.org/10.1002/qj.2606

Toth, T. D., Campbell, J. R., Reid, J. S., Tackett, J. L., Vaughan, M. A., Zhang, J., & Marquis, J. W. (2018). Minimum aerosol layer detection sensitivities and their subsequent impacts on aerosol optical thickness retrievals in CALIPSO level 2 data products. *Atmospheric Measurement Techniques*, *11*(1), 499–514. https://doi.org/10.5194/amt-11-499-2018

Trepte, C. . R., Cambaliza, C. M., Dubovik, O., Kim, S. . W., & Schuster, G. . L. (2023). *Models, in Situ, and Remote Sensing of Aerosols (MIRA): Formation of an International Working Group*.

Tricht, K. Van, Lhermitte, S., Lenaerts, J. T. M., Gorodetskaya, I. V, L'Ecuyer, T. S., Noël, B., van den Broeke, M. R., Turner, D. D., & van Lipzig, N. P. M. (2016). Clouds enhance Greenland ice sheet meltwater runoff. *Nature Communications*, *7*(1), 10266. https://doi.org/10.1038/ncomms10266

Tridon, F., Battaglia, A., Chase, R. J., Turk, F. J., Leinonen, J., Kneifel, S., Mroz, K., Finlon, J., Bansemer, A., Tanelli, S., Heymsfield, A. J., & Nesbitt, S. W. (2019). The Microphysics of Stratiform Precipitation During OLYMPEX: Compatibility Between Triple-Frequency Radar and Airborne In Situ Observations. *Journal of Geophysical Research: Atmospheres*, *124*(15), 8764–8792. https://doi.org/10.1029/2018JD029858

Tridon, F., Battaglia, A., & Kneifel, S. (2020). Estimating total attenuation using Rayleigh targets at cloud top: applications in multilayer and mixed-phase clouds observed by ground-based multifrequency radars. *Atmospheric Measurement Techniques*, *13*(9), 5065–5085. https://doi.org/10.5194/amt-13-5065-2020

Tsekeri, A., Amiridis, V., Lopatin, A., Marinou, E., Giannakaki, E., Pikridas, M., Sciare, J., Liakakou, E., Gerasopoulos, E., Duesing, S., Corbin, J. C., Gysel, M., Bukowiecki, N., Baars, H., Engelmann, R., Wehner, B., Kottas, M., Mamali, D., Kokkalis, P., … Goloub, P. (2018). Aerosol absorption profiling from the synergy of lidar and sun-photometry: the ACTRIS-2 campaigns in Germany, Greece and Cyprus. *EPJ Web of Conferences*, *176*, 08005. https://doi.org/10.1051/epjconf/201817608005

Tsekeri, A., Amiridis, V., Marenco, F., Nenes, A., Marinou, E., Solomos, S., Rosenberg, P., Trembath, J., Nott, G. J., Allan, J., Le Breton, M., Bacak, A., Coe, H., Percival, C., & Mihalopoulos, N. (2017). Profiling aerosol optical, microphysical and hygroscopic properties in ambient conditions by combining in situ and remote sensing. *Atmospheric Measurement Techniques*, *10*(1), 83–107. https://doi.org/10.5194/amt-10-83-2017

Tukiainen, S., O'Connor, E., Korpinen, A., O'Connor, E., & Korpinen, A. (2020). CloudnetPy: A Python package for processing cloud remote sensing data. *Journal of Open Source Software*, *5*(53), 2123. https://doi.org/10.21105/joss.02123

Turk, F. J., Ringerud, S. E., Camplani, A., Casella, D., Chase, R. J., Ebtehaj, A., Gong, J., Kulie, M., Liu, G., Milani, L., Panegrossi, G., Padullés, R., Rysman, J.-F., Sanò, P., Vahedizade, S., & Wood, N. B. (2021). Applications of a CloudSat-TRMM and CloudSat-GPM Satellite Coincidence Dataset. *Remote Sensing*, *13*(12), 2264. https://doi.org/10.3390/rs13122264

Turnbull, K., Johnson, B., Marenco, F., Haywood, J., Minikin, A., Weinzierl, B., Schlager, H., Schumann, U., Leadbetter, S., & Woolley, A. (2012). A case study of observations of volcanic ash from the Eyjafjallajökull eruption: 1. In situ airborne observations. *Journal of Geophysical Research: Atmospheres*, *117*(D20). https://doi.org/10.1029/2011JD016688

Turner, D. D., Ferrare, R. A., Brasseur, L. A. H., Feltz, W. F., & Tooman, T. P. (2002). Automated Retrievals of Water Vapor and Aerosol Profiles from an Operational Raman Lidar. *Journal of Atmospheric and Oceanic Technology*, *19*(1), 37–50. https://doi.org/10.1175/1520-0426(2002)019<0037:AROWVA>2.0.CO;2

Tyynelä, J., Leinonen, J., Moisseev, D., & Nousiainen, T. (2011). Radar Backscattering from Snowflakes: Comparison of Fractal, Aggregate, and Soft Spheroid Models. *Journal of Atmospheric and Oceanic Technology*, *28*(11), 1365–1372. https://doi.org/10.1175/JTECH-D-11-00004.1

Ulanowski, Z., Bailey, J., Lucas, P. W., Hough, J. H., & Hirst, E. (2007). Alignment of atmospheric mineral dust due to electric field. *Atmospheric Chemistry and Physics*, *7*(24), 6161–6173. https://doi.org/10.5194/acp-7-6161-2007

Vaillant de Guélis, T., Vaughan, M. A., Winker, D. M., & Liu, Z. (2021). Two-dimensional and multi-channel feature detection algorithm for the CALIPSO lidar measurements. *Atmospheric Measurement Techniques*, *14*(2), 1593–1613. https://doi.org/10.5194/amt-14-1593-2021

van de Poll, H. M., Grubb, H., & Astin, I. (2006). Sampling uncertainty properties of cloud fraction estimates from random transect observations. *Journal of Geophysical Research: Atmospheres*, *111*(D22). https://doi.org/10.1029/2006JD007189

van den Heever, S. C., Haddad, Z., Tanelli, S., Stephens, G., Posselt, D., Kim, Y., Brown, S., Braun, S., Grant, L., Kollias, P., Luo, Z., Mace, G., Marinescu, P., Padmanabhan, S., Partain, P., Petersen, W., Prasanth, S., Rasmussen, K., Reising, S., … INCUS Mission team. (2022). The INCUS Mission. *EGU*.

van Zadelhoff, G.-J., Donovan, D. P., & Wang, P. (2023). Detection of aerosol and cloud features for the EarthCARE atmospheric lidar (ATLID): the ATLID FeatureMask (A-FM) product. *Atmospheric Measurement Techniques*, *16*(15), 3631–3651. https://doi.org/10.5194/amt-16-3631-2023

van Zadelhoff, G. -J., Donovan, D. P., Klein Baltink, H., Boers, R., Baltink, H. K., & Boers, R. (2004). Comparing ice cloud microphysical properties using CloudNET and Atmospheric Radiation Measurement Program data. *Journal of Geophysical Research: Atmospheres*, *109*(D24). https://doi.org/10.1029/2004JD004967

Vaughan, M. A. ., Powell, K. A. ., Winker, D. M. ., Hostetler, C. A. ., Kuehn, R. E. ., Hunt, W. H. ., Getzewich, B. J. ., Young, S. A. ., Liu, Z. ., & McGill, M. J. (2009). Fully Automated Detection of Cloud and Aerosol Layers in the CALIPSO Lidar Measurements. *Journal of Atmospheric and Oceanic Technology*, *26*(10), 2034–2050. https://doi.org/10.1175/2009JTECHA1228.1

Vaughan, M. A., Liu, Z., McGill, M. J., Hu, Y., & Obland, M. D. (2010). On the spectral dependence of backscatter from cirrus clouds: Assessing CALIOP's 1064 nm calibration assumptions using cloud physics lidar measurements. *Journal of Geophysical Research: Atmospheres*, *115*(D14). https://doi.org/10.1029/2009JD013086

Vaughan, M., Garnier, A., Josset, D., Avery, M., Lee, K.-P., Liu, Z., Hunt, W., Pelon, J., Hu, Y., Burton, S., Hair, J., Tackett, J. L., Getzewich, B., Kar, J., & Rodier, S. (2019). CALIPSO lidar calibration at 1064 nm: version 4 algorithm. *Atmospheric Measurement Techniques*, *12*(1), 51–82. https://doi.org/10.5194/amt-12-51-2019

Velázquez-Blázquez, A., Baudrez, E., Clerbaux, N., & Domenech, C. (2024). Unfiltering of the EarthCARE Broadband Radiometer (BBR) observations: the BM-RAD product. *Atmospheric Measurement Techniques*, *17*(14), 4245–4256. https://doi.org/10.5194/amt-17-4245-2024

Velázquez-Blázquez, A., Baudrez, E., Clerbaux, N., Domenech, C., Marañón, R. G., & Madenach, N. (2024). Towards instantaneous top-of-atmosphere fluxes from EarthCARE: The BMA-FLX product. *Atmospheric Measurement Techniques, to Be Submitted*.

Venkata, S. L., & Reagan, J. A. (2016). Aerosol Retrievals from CALIPSO Lidar Ocean Surface Returns.

Remote Sensing, *8*(12). https://doi.org/10.3390/rs8121006

Veselovskii, I., Whiteman, D. N., Korenskiy, M., Suvorina, A., & Pérez-Ramírez, D. (2015). Use of rotational Raman measurements in multiwavelength aerosol lidar for evaluation of particle backscattering and extinction. *Atmospheric Measurement Techniques*, *8*(10), 4111–4122. https://doi.org/10.5194/amt-8-4111-2015

Villarini, G., & Krajewski, W. F. (2010). Review of the Different Sources of Uncertainty in Single Polarization Radar-Based Estimates of Rainfall. *Surveys in Geophysics*, *31*(1), 107–129. https://doi.org/10.1007/s10712-009-9079-x

Vivone, G., D'Amico, G., Summa, D., Lolli, S., Amodeo, A., Bortoli, D., & Pappalardo, G. (2021). Atmospheric boundary layer height estimation from aerosol lidar: a new approach based on morphological image processing techniques. *Atmospheric Chemistry and Physics*, *21*(6), 4249–4265. https://doi.org/10.5194/acp-21-4249-2021

Voigt, C., Schumann, U., Jurkat, T., Schäuble, D., Schlager, H., Petzold, A., Gayet, J.-F., Krämer, M., Schneider, J., Borrmann, S., Schmale, J., Jessberger, P., Hamburger, T., Lichtenstern, M., Scheibe, M., Gourbeyre, C., Meyer, J., Kübbeler, M., Frey, W., … Dörnbrack, A. (2010). In-situ observations of young contrails – overview and selected results from the CONCERT campaign. *Atmospheric Chemistry and Physics*, *10*(18), 9039–9056. https://doi.org/10.5194/acp-10-9039-2010

Voigt, C., Schumann, U., Minikin, A., Abdelmonem, A., Afchine, A., Borrmann, S., Boettcher, M., Buchholz, B., Bugliaro, L., Costa, A., Curtius, J., Dollner, M., Dörnbrack, A., Dreiling, V., Ebert, V., Ehrlich, A., Fix, A., Forster, L., Frank, F., … Zöger, M. (2017). ML-CIRRUS: The Airborne Experiment on Natural Cirrus and Contrail Cirrus with the High-Altitude Long-Range Research Aircraft HALO. *Bulletin of the American Meteorological Society*, *98*(2), 271–288. https://doi.org/10.1175/BAMS-D-15-00213.1

von Clarmann, T. (2006). Validation of remotely sensed profiles of atmospheric state variables: strategies and terminology. *Atmospheric Chemistry and Physics*, *6*(12), 4311–4320. https://doi.org/10.5194/acp-6-4311-2006

von Lerber, A., Moisseev, D., Bliven, L. F., Petersen, W., Harri, A.-M., & Chandrasekar, V. (2017). Microphysical Properties of Snow and Their Link to Ze–S Relations during BAECC 2014. *Journal of Applied Meteorology and Climatology*, *56*(6), 1561–1582. https://journals.ametsoc.org/view/journals/apme/56/6/jamc-d-16-0379.1.xml

von Lerber, A., Moisseev, D., Leinonen, J., Koistinen, J., & Hallikainen, M. T. (2015). Modeling Radar Attenuation by a Low Melting Layer With Optimized Model Parameters at C-Band. *IEEE Transactions on Geoscience and Remote Sensing*, *53*(2), 724–737. https://doi.org/10.1109/TGRS.2014.2327148

von Lerber, A., Moisseev, D., Marks, D. A., Petersen, W., Harri, A.-M., & Chandrasekar, V. (2018). Validation of GMI Snowfall Observations by Using a Combination of Weather Radar and Surface Measurements. *Journal of Applied Meteorology and Climatology*, *57*(4), 797–820. https://journals.ametsoc.org/view/journals/apme/57/4/jamc-d-17-0176.1.xml

Voudouri, K. A., Giannakaki, E., Komppula, M., & Balis, D. (2020). Variability in cirrus cloud properties using a Polly^{XT} Raman lidar over high and tropical latitudes. *Atmospheric Chemistry and Physics*, *20*(7), 4427–4444. https://doi.org/10.5194/acp-20-4427-2020

Voudouri, K. A., Siomos, N., Michailidis, K., Papagiannopoulos, N., Mona, L., Cornacchia, C., Nicolae, D., & Balis, D. (2019). Comparison of two automated aerosol typing methods and their application to an EARLINET station. *Atmospheric Chemistry and Physics*, *19*(16), 10961–10980. https://doi.org/10.5194/acp-19-10961-2019

Voudouri, K., Fountoukidis, P., Siomos, N., Dema, C., Balis, D., & D'Amico, G. (2023). *Sensitivity Study on the Performance of the Single Calculus Chain Aerosol Layering Module* (pp. 19–24).

https://doi.org/10.1007/978-3-031-37818-8_3

Walther, B. A., & Moore, J. L. (2005). The concepts of bias, precision and accuracy, and their use in testing the performance of species richness estimators, with a literature review of estimator performance. *Ecography*, *28*(6), 815–829. https://doi.org/10.1111/j.2005.0906-7590.04112.x

Wandinger, U., & Ansmann, A. (2002). Experimental determination of the lidar overlap profile with Raman lidar. *Appl. Opt.*, *41*(3), 511–514. https://doi.org/10.1364/AO.41.000511

Wandinger, U., Haarig, M., Baars, H., Donovan, D., & van Zadelhoff, G.-J. (2023a). Cloud top heights and aerosol layer properties from EarthCARE lidar observations: the A-CTH and A-ALD products. *Atmospheric Measurement Techniques*, *16*(17), 4031–4052. https://doi.org/10.5194/amt-16-4031-2023

Wandinger, U., Floutsi, A. A., Baars, H., Haarig, M., Ansmann, A., Hünerbein, A., Docter, N., Donovan, D., van Zadelhoff, G.-J., Mason, S., & Cole, J. (2023b). HETEAC – the Hybrid End-To-End Aerosol Classification model for EarthCARE. *Atmospheric Measurement Techniques*, *16*(10), 2485–2510. https://doi.org/10.5194/amt-16-2485-2023

Wandinger, U., Floutsi, A. A., Baars, H., Haarig, M., Ansmann, A., Hünerbein, A., Docter, N., Donovan, D., van Zadelhoff, G.-J., Mason, S., & Cole, J. (2023c). *HETEAC – The Hybrid End-To-End Aerosol Classification model for EarthCARE: Look-Up Table (LUT) for aerosol mixtures*.

Wandinger, U., Tesche, M., Seifert, P., Ansmann, A., Müller, D., & Althausen, D. (2010). Size matters: Influence of multiple scattering on CALIPSO light-extinction profiling in desert dust. *Geophysical Research Letters*, *37*(10).

Wang, D., Giangrande, S. E., Feng, Z., Hardin, J. C., & Prein, A. F. (2020). Updraft and Downdraft Core Size and Intensity as Revealed by Radar Wind Profilers: MCS Observations and Idealized Model Comparisons. *Journal of Geophysical Research: Atmospheres*, *125*(11). https://doi.org/10.1029/2019JD031774

Wang, M., Nakajima, T. Y., Roh, W., Satoh, M., Suzuki, K., Kubota, T., & Yoshida, M. (2023). Evaluation of the spectral misalignment on the Earth Clouds, Aerosols and Radiation Explorer/multi-spectral imager cloud product. *Atmospheric Measurement Techniques*, *16*(2), 603–623. https://doi.org/10.5194/amt-16-603-2023

Warren, R. A., Protat, A., Siems, S. T., Ramsay, H. A., Louf, V., Manton, M. J., & Kane, T. A. (2018). Calibrating Ground-Based Radars against TRMM and GPM. *Journal of Atmospheric and Oceanic Technology*, *35*(2), 323–346. https://doi.org/10.1175/JTECH-D-17-0128.1

Watters, D., Battaglia, A., Mroz, K., & Tridon, F. (2018). Validation of the GPM Version-5 Surface Rainfall Products over Great Britain and Ireland. *Journal of Hydrometeorology*, *19*(10), 1617–1636. https://doi.org/10.1175/JHM-D-18-0051.1

Wehr, T., Kubota, T., Tzeremes, G., Wallace, K., Nakatsuka, H., Ohno, Y., Koopman, R., Rusli, S., Kikuchi, M., Eisinger, M., Tanaka, T., Taga, M., Deghaye, P., Tomita, E., & Bernaerts, D. (2023). The EarthCARE mission – science and system overview. *Atmospheric Measurement Techniques*, *16*(15), 3581–3608. https://doi.org/10.5194/amt-16-3581-2023

Weiler, F., Rennie, M., Kanitz, T., Isaksen, L., Checa, E., de Kloe, J., Okunde, N., & Reitebuch, O. (2021). Correction of wind bias for the lidar on board Aeolus using telescope temperatures. *Atmospheric Measurement Techniques*, *14*(11), 7167–7185. https://doi.org/10.5194/amt-14-7167-2021

Weinzierl, B., Ansmann, A., Prospero, J. M., Althausen, D., Benker, N., Chouza, F., Dollner, M., Farrell, D., Fomba, W. K., Freudenthaler, V., Gasteiger, J., Gross, S., Haarig, M., Heinold, B., Kandler, K., Kristensen, T. B., Mayol-Bracero, O. L., Müller, T., Reitebuch, O., … Walser, A. (2017). The Saharan Aerosol Long-Range Transport and Aerosol–Cloud-Interaction Experiment: Overview and Selected Highlights. *Bulletin of the American Meteorological Society*, *98*(7), 1427–1451.

https://doi.org/10.1175/BAMS-D-15-00142.1

Welton, E. J., & Campbell, J. R. (2002). Micropulse Lidar Signals: Uncertainty Analysis. *Journal of Atmospheric and Oceanic Technology*, *19*(12), 2089–2094. https://doi.org/10.1175/1520-0426(2002)019<2089:MLSUA>2.0.CO;2

Wendisch, M., Müller, D., Schell, D., & Heintzenberg, J. (2001). An Airborne Spectral Albedometer with Active Horizontal Stabilization. *Journal of Atmospheric and Oceanic Technology*, *18*(11), 1856–1866. https://doi.org/10.1175/1520-0426(2001)018<1856:AASAWA>2.0.CO;2

Wilkinson, M. D., Dumontier, M., Aalbersberg, Ij. J., Appleton, G., Axton, M., Baak, A., Blomberg, N., Boiten, J.-W., da Silva Santos, L. B., Bourne, P. E., Bouwman, J., Brookes, A. J., Clark, T., Crosas, M., Dillo, I., Dumon, O., Edmunds, S., Evelo, C. T., Finkers, R., … Mons, B. (2016). The FAIR Guiding Principles for scientific data management and stewardship. *Scientific Data*, *3*(1). https://doi.org/10.1038/sdata.2016.18

Williams, C. R., Ecklund, W. L., & Gage, K. S. (1995). Classification of Precipitating Clouds in the Tropics Using 915-MHz Wind Profilers. *Journal of Atmospheric and Oceanic Technology*, *12*(5), 996–1012. https://doi.org/10.1175/1520-0426(1995)012<0996:COPCIT>2.0.CO;2

Winker, D., Cai, X., Vaughan, M., Garnier, A., Magill, B., Avery, M., & Getzewich, B. (2024). A Level 3 monthly gridded ice cloud dataset derived from 12 years of CALIOP measurements. *Earth System Science Data*, *16*(6), 2831–2855. https://doi.org/10.5194/essd-16-2831-2024

Winker, D. M. M., Couch, R. H. H., & McCormick, M. P. P. (1996). An overview of LITE: NASA's Lidar In-space Technology Experiment. *Proceedings of the IEEE*, *84*(2), 164–180. https://doi.org/10.1109/5.482227

Winker, D. M., Pelon, J., Coakley, J. A., Ackerman, S. A., Charlson, R. J., Colarco, P. R., Flamant, P., Fu, Q., Hoff, R. M., Kittaka, C., Kubar, T. L., Treut, H. Le, McCormick, M. P., Mégie, G., Poole, L., Powell, K., Trepte, K., Vaughan, M. A., Wielicki, B. A., … Wielicki, B. A. (2010). The Calipso Mission: A Global 3D View of Aerosols and Clouds. *Bulletin of the American Meteorological Society*. https://doi.org/10.1175/2010BAMS3009.1

Winker, D. M., Tackett, J. L., Getzewich, B. J., Liu, Z., Vaughan, M. A., & Rogers, R. R. (2013). The global 3-D distribution of tropospheric aerosols as characterized by CALIOP. *Atmospheric Chemistry and Physics*, *13*(6), 3345–3361. https://doi.org/10.5194/acp-13-3345-2013

Wirth, M., Fix, A., Mahnke, P., Schwarzer, H., Schrandt, F., & Ehret, G. (2009). The airborne multi-wavelength water vapor differential absorption lidar WALES: system design and performance. *Applied Physics B*, *96*(1), 201–213. https://doi.org/10.1007/s00340-009-3365-7

Witkowski, M. M., Vane, D., & Livermore, T. (2018). CloudSat - Life in Daylight Only Operations (DO-Op). In *2018 SpaceOps Conference*. American Institute of Aeronautics and Astronautics. https://doi.org/10.2514/6.2018-2562

Witschas, B., Lemmerz, C., Geiß, A., Lux, O., Marksteiner, U., Rahm, S., Reitebuch, O., & Weiler, F. (2020). First validation of Aeolus wind observations by airborne Doppler wind lidar measurements. *Atmospheric Measurement Techniques*, *13*(5), 2381–2396. https://doi.org/10.5194/amt-13-2381-2020

Witschas, B., Rahm, S., Dörnbrack, A., Wagner, J., & Rapp, M. (2017). Airborne Wind Lidar Measurements of Vertical and Horizontal Winds for the Investigation of Orographically Induced Gravity Waves. *Journal of Atmospheric and Oceanic Technology*, *34*(6), 1371–1386. https://doi.org/10.1175/JTECH-D-17-0021.1

Wolff, D. B., Marks, D. A., Amitai, E., Silberstein, D. S., Fisher, B. L., Tokay, A., Wang, J., & Pippitt, J. L. (2005). Ground Validation for the Tropical Rainfall Measuring Mission (TRMM). *Journal of Atmospheric and Oceanic Technology*, *22*(4), 365–380. https://doi.org/10.1175/JTECH1700.1

Wolff, D. B., Marks, D. A., & Petersen, W. A. (2015). General Application of the Relative Calibration Adjustment (RCA) Technique for Monitoring and Correcting Radar Reflectivity Calibration. *Journal of Atmospheric and Oceanic Technology*, *32*(3), 496–506. https://doi.org/10.1175/JTECH-D-13-00185.1

Wood, N. B., & L'Ecuyer, T. S. (2021). What millimeter-wavelength radar reflectivity reveals about snowfall: an information-centric analysis. *Atmospheric Measurement Techniques*, *14*(2), 869–888. https://doi.org/10.5194/amt-14-869-2021

Wood, N. B., L'Ecuyer, T. S., Heymsfield, A. J., & Stephens, G. L. (2015). Microphysical Constraints on Millimeter-Wavelength Scattering Properties of Snow Particles. *Journal of Applied Meteorology and Climatology*, *54*(4), 909–931. https://doi.org/10.1175/JAMC-D-14-0137.1

Wood, R., & Hartmann, D. L. (2006). Spatial Variability of Liquid Water Path in Marine Low Cloud: The Importance of Mesoscale Cellular Convection. *Journal of Climate*, *19*(9), 1748–1764. https://doi.org/10.1175/JCLI3702.1

World Meteorological Organisation. (2015). *Commission for Basic Systems, Open programme area group on integrated observing systems, Inter-programme expert team on satellite utilization and products, SCOPE-Nowcasting Pilot Project 2 : Globally consistent Volcanic Ash Products, Final report: Meeting on the Intercomparison of Satellite-based Volcanic Ash Retrieval Algorithms*.

Wu, D., Wang, Z., Wang, B., Zhou, J., & Wang, Y. (2010). CALIPSO validation using ground-based lidar in Hefei (31.9°N, 117.2°E), China. *Applied Physics* , *102*(1), 185–195. https://doi.org/10.1007/s00340-010-4243-z

Wu, W., & McFarquhar, G. M. (2018). Statistical Theory on the Functional Form of Cloud Particle Size Distributions. *Journal of the Atmospheric Sciences*, *75*(8), 2801–2814. https://doi.org/10.1175/JAS-D-17-0164.1

Wu, Z., Zhang, Y., Zhang, L., Hao, X., Lei, H., & Zheng, H. (2019). Validation of GPM Precipitation Products by Comparison with Ground-Based Parsivel Disdrometers over Jianghuai Region. *Water*, *11*(6), 1260. https://doi.org/10.3390/w11061260

Xian, P., Reid, J. S., Hyer, E. J., Sampson, C. R., Rubin, J. I., Ades, M., Asencio, N., Basart, S., Benedetti, A., Bhattacharjee, P. S., Brooks, M. E., Colarco, P. R., da Silva, A. M., Eck, T. F., Guth, J., Jorba, O., Kouznetsov, R., Kipling, Z., Sofiev, M., … Zhang, J. (2019). Current state of the global operational aerosol multi-model ensemble: An update from the International Cooperative for Aerosol Prediction (ICAP). *Quarterly Journal of the Royal Meteorological Society*, *145*(S1), 176–209. https://doi.org/10.1002/qj.3497

Xu, F., Gao, L., Redemann, J., Flynn, C. J., Espinosa, W. R., da Silva, A. M., Stamnes, S., Burton, S. P., Liu, X., Ferrare, R., Cairns, B., & Dubovik, O. (2021). A Combined Lidar-Polarimeter Inversion Approach for Aerosol Remote Sensing Over Ocean. *Frontiers in Remote Sensing*, *2*. https://doi.org/10.3389/frsen.2021.620871

Yamauchi, A., Suzuki, K., Oikawa, E., Sekiguchi, M., Nagao, T., & Ishida, H. (2024). Description and validation of the Japanese algorithm for radiative flux and heating rate products with all four EarthCARE instruments: Pre-launch test with A-Train. *Atmospheric Measurement Techniques Discussions*, *2024*, 1–24. https://doi.org/10.5194/amt-2024-78

Yang, C. K., Chiu, J. C., Marshak, A., Feingold, G., Várnai, T., Wen, G., Yamaguchi, T., & Jan van Leeuwen, P. (2022). Near-Cloud Aerosol Retrieval Using Machine Learning Techniques, and Implied Direct Radiative Effects. *Geophysical Research Letters*, *49*(20). https://doi.org/10.1029/2022GL098274

Yang, P., Liou, K. N., Wyser, K., & Mitchell, D. (2000). Parameterization of the scattering and absorption properties of individual ice crystals. *Journal of Geophysical Research: Atmospheres*, *105*(D4), 4699–4718. https://doi.org/https://doi.org/10.1029/1999JD900755

Yorks, J. E., Hlavka, D. L., Vaughan, M. A., McGill, M. J., Hart, W. D., Rodier, S., & Kuehn, R. (2011). Airborne validation of cirrus cloud properties derived from CALIPSO lidar measurements: Spatial properties. *Journal of Geophysical Research*, *116*(D19), D19207. https://doi.org/10.1029/2011JD015942

Yorks, J. E., McGill, M. J., Palm, S. P., Hlavka, D. L., Selmer, P. A., Nowottnick, E. P., Vaughan, M. A., Rodier, S. D., & Hart, W. D. (2016). An overview of the CATS level 1 processing algorithms and data products. *Geophysical Research Letters*, *43*(9), 4632–4639. https://doi.org/10.1002/2016GL068006

Yorks, J. E., Palm, S. P., Hlavka, D. L., McGill, M. J., Nowottnick, E., Selmer, P., & Hart, W. D. (2015). *The Cloud-Aerosol Transport System (CATS) algorithm theoretical basis document*.

Yorks, J. E., Selmer, P. A., Kupchock, A., Nowottnick, E. P., Christian, K. E., Rusinek, D., Dacic, N., & McGill, M. J. (2021). Aerosol and Cloud Detection Using Machine Learning Algorithms and Space-Based Lidar Data. *Atmosphere*, *12*(5), 606. https://doi.org/10.3390/atmos12050606

Yoshida, R., Okamoto, H., Hagihara, Y., & Ishimoto, H. (2010). *Global analysis of cloud phase and ice crystal orientation from Cloud-Aerosol Lidar and Infrared Pathfinder Satellite Observation (CALIPSO) data using attenuated backscattering and depolarization ratio*. *115*. https://doi.org/10.1029/2009JD012334

Young, G., Jones, H. M., Choularton, T. W., Crosier, J., Bower, K. N., Gallagher, M. W., Davies, R. S., Renfrew, I. A., Elvidge, A. D., Darbyshire, E., Marenco, F., Brown, P. R. A., Ricketts, H. M. A., Connolly, P. J., Lloyd, G., Williams, P. I., Allan, J. D., Taylor, J. W., Liu, D., & Flynn, M. J. (2016). Observed microphysical changes in Arctic mixed-phase clouds when transitioning from sea ice to open ocean. *Atmospheric Chemistry and Physics*, *16*(21), 13945–13967. https://doi.org/10.5194/acp-16-13945-2016

Young, S. A., & Vaughan, M. A. (2009). The Retrieval of Profiles of Particulate Extinction from Cloud-Aerosol Lidar Infrared Pathfinder Satellite Observations (CALIPSO) Data: Algorithm Description. *Journal of Atmospheric and Oceanic Technology*, *26*(6), 1105–1119. https://doi.org/10.1175/2008JTECHA1221.1

Young, S. A., Vaughan, M. A., Garnier, A., Tackett, J. L., Lambeth, J. D., & Powell, K. A. (2018). Extinction and optical depth retrievals for CALIPSO's Version 4 data release. *Atmospheric Measurement Techniques*, *11*(10), 5701–5727. https://doi.org/10.5194/amt-11-5701-2018

Young, S. A., Vaughan, M. A., Kuehn, R. E., & Winker, D. M. (2013). The Retrieval of Profiles of Particulate Extinction from Cloud–Aerosol Lidar and Infrared Pathfinder Satellite Observations (CALIPSO) Data: Uncertainty and Error Sensitivity Analyses. *Journal of Atmospheric and Oceanic Technology*, *30*(3), 395–428. https://doi.org/10.1175/JTECH-D-12-00046.1

Yu, Y., Kalashnikova, O. V., Garay, M. J., Lee, H., Choi, M., Okin, G. S., Yorks, J. E., Campbell, J. R., & Marquis, J. (2021). A global analysis of diurnal variability in dust and dust mixture using CATS observations. *Atmospheric Chemistry and Physics*, *21*(3), 1427–1447. https://doi.org/10.5194/acp-21-1427-2021

Yuter, S. E., Houze, R. A., Smith, E. A., Wilheit, T. T., & Zipser, E. (2005). Physical Characterization of Tropical Oceanic Convection Observed in KWAJEX. *Journal of Applied Meteorology*, *44*(4), 385–415. https://doi.org/10.1175/JAM2206.1

Zawadzki, I. I. (1975). On Radar-Raingage Comparison. *Journal of Applied Meteorology*, *14*(8), 1430–1436. https://doi.org/10.1175/1520-0450(1975)014<1430:ORRC>2.0.CO;2

Zhang, J., Howard, K., Langston, C., Kaney, B., Qi, Y., Tang, L., Grams, H., Wang, Y., Cocks, S., Martinaitis, S., Arthur, A., Cooper, K., Brogden, J., & Kitzmiller, D. (2016). Multi-Radar Multi-Sensor (MRMS) Quantitative Precipitation Estimation: Initial Operating Capabilities. *Bulletin of the American Meteorological Society*, *97*(4), 621–638. https://doi.org/10.1175/BAMS-D-14-00174.1

Zhang, J., Howard, K., Langston, C., Vasiloff, S., Kaney, B., Arthur, A., Cooten, S. Van, Kelleher, K., Kitzmiller, D., Ding, F., Seo, D.-J., Wells, E., Dempsey, C., Van Cooten, S., Kelleher, K., Kitzmiller, D., Ding, F., Seo, D.-J., Wells, E., & Dempsey, C. (2011). National Mosaic and Multi-Sensor QPE (NMQ) System: Description, Results, and Future Plans. *Bulletin of the American Meteorological Society*, *92*(10), 1321–1338. https://doi.org/10.1175/2011BAMS-D-11-00047.1

Zhang, J., Reid, J. S., Miller, S. D., Román, M., Wang, Z., Spurr, R. J. D., & Jaker, S. (2023). Sensitivity studies of nighttime top-of-atmosphere radiances from artificial light sources using a 3-D radiative transfer model for nighttime aerosol retrievals. *Atmospheric Measurement Techniques*, *16*(10), 2531–2546. https://doi.org/10.5194/amt-16-2531-2023

Zhang, M. H., Hack, J. J., Kiehl, J. T., & Cess, R. D. (1994). Diagnostic study of climate feedback processes in atmospheric general circulation models. *Journal of Geophysical Research: Atmospheres*, *99*(D3), 5525–5537. https://doi.org/10.1029/93JD03523

Zhu, Z., Kollias, P., Luke, E., & Yang, F. (2022). New insights on the prevalence of drizzle in marine stratocumulus clouds based on a machine learning algorithm applied to radar Doppler spectra. *Atmospheric Chemistry and Physics*, *22*(11), 7405–7416. https://doi.org/10.5194/acp-22-7405-2022